

**MOVING FINITE ELEMENT SOLUTION OF
DISCONTINUOUS OPEN CHANNEL FLOW**

by

© SYED M. AFAQ MOIN, B.E., M.S.

A Thesis

Submitted to the School of Graduate Studies

in Partial Fulfilment of the Requirements

for the Degree

Doctor of Philosophy

McMaster University

May 1988

MOVING FINITE ELEMENT SOLUTION OF
DISCONTINUOUS OPEN CHANNEL FLOW

DOCTOR OF PHILOSOPHY
(Civil Engineering)

McMASTER UNIVERSITY
Hamilton, Ontario

TITLE: Moving Finite Element Solution of Discontinuous Open Channel Flow

AUTHOR: Syed M. Afaq Moin, B.E. (Osmania University)
M.S. (University of Nevada)

SUPERVISORS: Professor A.A. Smith
Dr. D.C.L. Lam

NUMBER OF PAGES: xxii, 492

بِسْمِ اللَّهِ الرَّحْمَنِ الرَّحِيمِ

اقْرَأْ بِاسْمِ رَبِّكَ الَّذِي خَلَقَ ۝ خَلَقَ الْإِنْسَانَ مِنْ عَلَقٍ ۝ اقْرَأْ وَرَبُّكَ الْأَكْرَمُ ۝ الَّذِي عَلَّمَ بِالْقَلَمِ ۝ عَلَّمَ الْإِنْسَانَ مَا لَمْ يَعْلَمْ

In the name of God, the Beneficent, the Merciful

Read in the name of your Lord Who creates,
creates man from a clot
Read, for your Lord is most Generous
[it is He] Who teaches by means of the Pen
teaches man what he does not know.

(Surah: The Clot, Verses 1 - 5)

ABSTRACT

Over the years, rapidly varying channel flow and discontinuities in the solution of fluid mechanics problems have provided stimulation and challenge to numerical modelers. Traditional finite difference and finite element methods produce accurate but oscillatory solutions. Attempts to selectively eliminate these parasitic waves have been only partially successful in that the cost of a smoother profile was a lower accuracy solution. It is common to employ either internal and external dissipation parameters or a provision of dispersive interface.

In this thesis, the problem of rapidly varying open channel flow is represented by a pair of nonlinear partial differential equations which are solved by a powerful moving finite element technique. The method developed in this research is based on the linking of a novel Lagrangian mode solution with the convenience of the Eulerian grid at each time step. This second order scheme was employed in solving a variety of devised and reported open channel flow problems with near discontinuities.

Comparisons with solutions obtained using the finite difference and finite element methods with Crank-Nicholson centred weightings demonstrates the quality improvements which have been achieved by this moving element scheme. The basic scheme was further generalized in both spatial and temporal dimensions. Sensitivity analysis of these generalized parameters established the grid size relaxations for a variety of problems. The moving element technique solved near discontinuous and gradually varied flow problems both in supercritical and subcritical regimes.

An alternate form of Petrov-Galerkin weighting function was tested and found to give promising results. Further experimentation and testing are required before implementation.

The robustness of the solution procedure is indicated by the adaptation of the model from the numerical and laboratory experiment stage to field problems. The model was successfully applied to the Teton Dam break flood and flood routing problem in the (Ontario) Grand River basin. Sensitivity analysis with very mild sloped channels with topographical features such as sudden expansions and off-channel storage suggest that the Eulerian-Lagrangian mode algorithm provides the missing link between the fluid mechanics of discontinuities and a practical tool for the modelling of rapidly varying open channel flow.

ACKNOWLEDGEMENTS

I wish to express my sincere gratitude to my supervisors, Dr. A.A. Smith and Dr. D.C.L. Lam, for their invaluable guidance and encouragement during the course of graduate work in general and this research in particular.

I should also like to thank Dr. F. Mirza and Dr. H. Woo for their continuing interest in this work. Special thanks are due to Mr. D.W. Brown, my supervisor at Environment Canada for taking keen interest in this work. I am grateful to my employer, Environment Canada for endorsing my studies and allowing time to write the thesis.

I would like to thank Mrs. L. Minshall of the Grand River Conservation Authority for providing data on the Grand River floods.

Thanks are also due to S. Babij for typing the manuscript and the staff of the Engineering Word Processing Centre for their effort.

Lastly, I would like to show appreciation to my parents, Syed Moinuddin and Sarwar Khatoon, my wife Khalda, and my children Harith, Umamah and Hamzah for their encouragement and perseverance throughout my studies, and to them I dedicate my thesis.

TABLE OF CONTENTS

	Page
Abstract	iii
Acknowledgements	v
List of Figures	xi
List of Tables	xxii
1. Introduction	1
2. Definition of Problem	4
2.1 Oscillation in Convection Dominated Flows	4
2.2 Compromises in Rapidly Varying Open Channel Flows	7
2.3 Open Channel Flow Equations	10
2.3.1 Non-divergent form	14
2.3.2 Characteristic form	14
2.3.3 Conservation or Divergent form	16
2.4 Statement of Objectives	17
3. Literature Review	19
3.1 Introduction	19
3.2 Convection Dominated Flows in Fluid Mechanics	20
3.3 Solution of Open Channel Flow Equations	33
3.3.1 Discontinuous or Rapidly Varied Flow Solution	34
3.3.1.1 Finite Difference Methods	35
3.3.1.2 Finite Element Methods	52
3.3.2 Continuous or Gradually Varied Flow Solution	55
3.3.2.1 Finite Difference Methods	57
3.3.2.2 Finite Element Methods	62
3.4 On Dissipative and Dispersive Interfaces	63
3.4.1 Isolation of Discontinuity	65
3.4.2 Dissipative Interfaces and Inconsistent Equations	67
3.4.3 Numerical Damping Devices	71

TABLE OF CONTENTS (continued)

	Page
3.5 Summary	74
4. Development of Methodology	77
4.1 Introduction	77
4.2 Moving Element Solution of St. Venant Open Channel Flow Equations	78
4.2.1 Governing Equations	82
4.2.2 Basis Functions and Isoparametric Elements	87
4.2.3 Numerical Integration	95
4.2.3.1 Computation of Derivatives	96
4.2.3.2 Computation of Flux Terms	101
4.3 Boundary Elements	103
4.3.1 Upstream Boundary	103
4.3.1.1 Triangular Element	104
4.3.1.2 Trapezoidal Element	111
4.3.2 Downstream Boundary	113
4.4 Discretized Form of Difference Equations	115
4.5 Solution Procedure	123
4.6 Extension to Eulerian - Lagrangian Concept	128
4.6.1 Two-Point Linear Interpolation	128
4.6.2 Three-Point Lagrangian Interpolation	130
4.6.3 Mixed Linear - Lagrangian Interpolation	132
4.6.4 Choice of Eulerian-Lagrangian Scheme Over Lagrangian Scheme	133
4.7 Generalization of the Solution Procedure	135
4.7.1 Temporal Generalization	138
4.7.2 Spatial Generalization	140
4.8 Employment of Petro-Galerkin Basis Function	143
4.9 Extension of Methodology to Nonprismatic Channels	146
4.9.1 Convective Acceleration and Pressure Terms	147
4.9.2 Off-Channel Storage	149
4.10 Summary	152

TABLE OF CONTENTS (continued)

	Page
5. Numerical Experiments	154
5.1 Introduction	154
5.2 Design of Experiments	155
5.2.1 Test A - Supercritical Surge Moving Downstream	156
5.2.2 Test B - Subcritical Surge Moving Downstream	158
5.2.3 Test C - Subcritical Surge Moving Upstream	164
5.2.4 Test D - Continuous Flow Simulation	166
5.2.5 Test E1 - Surge Through Choke-Horizontal Constriction	169
5.2.6 Test E2 - Surge Over Hump-Vertical Constriction	173
5.2.7 Discussion of Results	181
5.2.7.1 Shape of the Front	181
5.2.7.2 Speed of the Wave	182
5.2.7.3 Conservation of Mass	183
5.2.7.4 Steepness of Front	184
5.2.7.5 Handling of Nonprismatic Cross-Sections	185
5.2.7.6 Direction of Front	186
5.3 Sensitivity Analysis	187
5.3.1 Variation of Time-step	189
5.3.2 Variation of Element Size	194
5.3.3 Variation of Temporal Weighting Factor	198
5.3.4 Variation of Spatial Weighting Factor	204
5.3.5 Variation of Channel Roughness	208
5.3.6 Variation of Temporal Acceleration	213
5.3.7 Summary of Sensitivity	215
5.4 Comparison with Other Techniques	219
5.4.1 Selection of Finite Difference and Finite Element Models	219
5.4.2 Finite Difference Method	223
5.4.3 Finite Element Method	226
5.4.4 Petrov-Galerkin Based Method	231
5.4.5 Lagrangian Method	241
5.4.6 Summary of Comparisons	252
5.5 Tests on Nonprismatic Channel	252
5.5.1 Diverging Channel	254
5.5.2 Converging Channel	256
5.6 Miscellaneous Experiments	262
5.6.1 Mass Conservation and Time Step	262
5.6.2 Mass Conservation and Interpolation Scheme	263
5.6.3 Wave Steepening	271
5.6.4 Emulation of Bridges and Reservoirs	271

TABLE OF CONTENTS (continued)

	Page
5.7 Summary	274
6. Description of Computer Program	276
6.1 Introduction	276
6.2 Development on Mainframe Computers	277
6.3 Tests on Personal Computers	286
6.3.1 Hardware/Software Description	287
6.3.2 Comparison of Operating Environments	290
6.3.3 Other Testing on Microcomputers	294
6.3.4 Summary	295
6.4 Input Requirements	295
6.5 Output Description	296
6.6 Summary	298
7. Applications	300
7.1 Introduction	300
7.2 Teton Dam Failure	301
7.2.1 Physical Description	303
7.2.2 Initial and Boundary Conditions	307
7.2.3 Model Set-up	308
7.2.4 Discussion of Results	309
7.3 Teton Dam Failure Flood Simulation with Prismatic Channel	325
7.3.1 Channel Description	325
7.3.2 Initial and Boundary Conditions	328
7.3.3 Model Set-up	328
7.3.4 Discussion of Results	329
7.4 Teton Dam Failure Hydrograph on Mild Sloped Non-Prismatic Channel	333
7.4.1 Channel Description	333
7.4.2 Initial and Boundary Conditions	334
7.4.3 Model Set-up	334
7.4.4 Discussion of Results	335

TABLE OF CONTENTS (continued)

	Page
7.5 Grand River Flood Routing - Continuous Flow Modelling	350
7.5.1 Channel Description	354
7.5.2 Initial and Boundary Conditions	355
7.5.3 Model Set-up	355
7.5.4 Discussion of Results	356
7.5.4.1 Simulation of Stage Hydrograph at York	356
7.5.4.2 Attenuation and Translation of Flood Wave	358
7.5.4.3 Hysteresis or Looping Effect	362
7.5.4.4 Water Surface Profile	366
7.6 Grand River Flood Simulation with Hypothetical Dam-Break Hydrograph	370
7.7 Laboratory Experiment Verifications	373
7.7.1 Egiazarov's Experiment	373
7.7.2 Faure's Experiment	376
7.8 Summary	386
8. Summary, Conclusions and Recommendations	388
8.1 Summary	388
8.2 Conclusions	390
8.3 Recommendations	392
Appendix A Nomenclature and Glossary of Terms	394
Appendix B Nodal Contributions at the Upstream Boundary for Supercritical Flow Conditions	402
Appendix C Nodal Contributions of the Lateral Flow Component in the Momentum Conservation Equation	404
Appendix D Nodal Contributions for the Collapsed Quadilateral Elements	405
Appendix E Coefficients of Bi-Tridiagonal Matrix	407
Appendix F More Numerical Experiments' Graphical Results	409
Appendix G Input File Description	453
Appendix H Output File Echoing Input Data	457
Appendix I Envelopes of Maximum Flows and Highest Elevations with Associated Times	460
Appendix J Channel Cross-Sections for Teton River and Grand River	461
Bibliography	484

LIST OF FIGURES

Figure		Page
3.1(a)	Oscillatory Solution in Fluid Mechanics. Solution of Burger's Equation. After Bonnerot and Jamet (1975)	22
3.1(b)	Oscillatory Solution in Open Channel Hydraulics. Solution of Stationary Hydraulic Jump. After Katopodes (1984)	23
3.2	Clipping, Overshooting, Dispersion and Negative Concentration Errors in Finite Difference and Finite Element Schemes. After Lam (1978)	28
3.3	Finite Elements in Space and Time at a Typical Time Step.	29
3.4	Solution of a Concentration Front Movement by the Space-Time Finite Elements. After Varoglu and Finn (1980)	31
3.5	Vasiliev's Oblique Grid for the Finite Difference Method.	40
3.6	Priessmann's Weighted Four-Point Implicit Scheme.	44
3.7	Leap-Frog Explicit Scheme Employed in USTFLO Program.	49
3.8	Diffusive One and Two-Steps Explicit Schemes employed by Terzedis and Strelkoff (1970).	50
3.9	Weighting Function for the Galerkin Scheme	54
3.10	Weighting Function for the Dissipative Galerkin Method.	54
3.11	Isolation of Discontinuity by the Characteristic Equations.	66
3.12	Improvement in a Discontinuous Front solution with a Dissipative Interface. After Katopodes (1984).	69
4.1	Solution Strip of Space-Time Moving Finite Elements	80
4.2	Eularian Space-Time Grid	81
4.3	Lagrangian Space-Time Grid	83
4.4	Eularian- Lagrangian Space-Time Grid	84
4.5	Solution Domain of Space-Time Finite Elements	89
4.6	Typical Trapezoidal Element	105

LIST OF FIGURES (continued)

Figure		Page
4.7(a)	Varoglu and Finn's Upstream Boundary Triangular Element	106
4.7(b)	Proposed Alternate Form of Upstream Boundary Element	106
4.8	Upstream Boundary Triangular Element	107
4.9	Upstream Boundary Trapezoidal Element	112
4.10	Downstream Boundary Trapezoidal Element	114
4.11	Eularian-Lagrangian Time Step	129
4.12	Two and Three Point Lagrangian Interpolation Scheme	131
4.13	Main Channel and Storage Flow Dynamics	150
4.14	Approximation of Conveyance and Storage Flow Interchange	151
5.1	Water Surface Profiles for Test 'A' - Supercritical Surge in Frictionless Channel.	159
5.2	Water Surface Profiles for Test 'B' - Subcritical Surge in Frictionless Channel.	162
5.3	Flow Hydrograph at Channel Mid-Point for Test 'B'. Subcritical Surge in Frictionless Channel.	163
5.4	Influence of Channel Roughness on Water Surface Profiles for Test 'B'.	165
5.5	Water Surface Profiles for Test 'C' - Subcritical Surge Moving Upstream in Trapezoidal Channel.	167
5.6	Flow Hydrographs at Upstream and Downstream Boundaries and Channel Mid-Point for Test 'D' - Continuous Flow Simulation.	170
5.7	Plan Layout for Test 'E1' - Flow Through a Choke.	171
5.8	Water Surface Profiles for Test 'E1' - Flow Through a Choke.	174
5.9	Water Surface Profiles for Test 'E1' - Flow Through a Choke.	175
5.10	Flow Hydrographs for Flow Through a Choke - Test 'E1'.	176
5.11	Cross-Sectional Profile of an Obstruction (Hump) in a Channel for Test 'E2'.	178

LIST OF FIGURES (continued)

Figure		Page
5.12	Water Surface Profiles for Test 'E2' - Flow over a Hump.	179
5.13	Flow Hydrographs at Hump for Test 'E2'.	180
5.14	Time Step Sensitivity for Test 'B' - Subcritical Surge Moving Downstream.	191
5.15	Time Step Sensitivity for Test 'C' - Subcritical Surge Moving Upstream.	193
5.16	Time Step Sensitivity for Test 'D' - Continuous Flow Simulation.	195.
5.17	Time Step Sensitivity for Test 'D' - Continuous Flow Simulation.	196
5.18	Element Length Sensitivity for Test 'B' - Subcritical Surge Moving Downstream.	199
5.19	Sensitivity of Varying Temporal Weighting Parameter, θ , for Test 'A' - Supercritical Surge in Frictionless Channel.	202
5.20	Sensitivity of Varying Temporal Weighting Parameter, θ , for Test 'C' - Subcritical Surge Moving Upstream.	203
5.21	Sensitivity of Varying Spatial Weighting Parameter, β , for Test 'B' - Subcritical Surge Moving Downstream.	206
5.22	Sensitivity of Varying Spatial Weighting Parameter, β , for Test 'B' - Subcritical Surge Moving Downstream.	207
5.23	Sensitivity of Varying Channel Roughness Coefficient, n , for Test 'B' - Stage Profiles at Time = 120 Sec.	211
5.24	Sensitivity of Varying Channel Roughness Coefficient, n , for Test 'B' - Flow Profiles at Time = 120 Sec.	212
5.25	Sensitivity of Varying Temporal Acceleration at Upstream Boundary for Test 'B'.	216
5.26	Exploded Window with Exaggerated Vertical Scales From 5.25.	217
5.27	Sensitivity of Varying Temporal Acceleration at Downstream Boundary for Test 'C'.	218
5.28	Comparison of Moving Element Method with Finite Difference Method for Test 'A'.	225

LIST OF FIGURES (continued)

Figure		Page
5.29	Comparison of Moving Element Method with Finite Difference Method for Test 'B'.	227
5.30	Comparison of Moving Element Method with Finite Element Method for Test 'A'.	229
5.31	Comparison of Moving Element Method with Finite Element Method for Test 'B'.	230
5.32	Comparison of Basic Moving Element Method with Petrov-Galerkin Based Moving Element for Test 'B' - Dissipation Level, $\epsilon = 0.1$.	233
5.33	Comparison of Basic Moving Element Method with Petrov-Galerkin Based Moving Element for Test 'B' - Dissipation Level, $\epsilon = 0.15$.	234
5.34	Comparison of Basic Moving Element Method with Petrov-Galerkin Based Moving Element for Test 'B' - Dissipation Level, $\epsilon = 0.25$.	235
5.35	Comparison of Basic Moving Element Method with Petrov-Galerkin Based Moving Element for Test 'B' - Dissipation Level, $\epsilon = -0.1$.	236
5.36	Comparison of Basic Moving Element Method with Petrov-Galerkin Based Moving Element for Test 'B' - Flow Profiles for Dissipation Level, $\epsilon = 0.1$.	237
5.37	Comparison of Basic Moving Element Method with Petrov-Galerkin Based Moving Element for Test 'B' - Stage Profiles for Dissipation Level, $\epsilon = 0.1$ and Temporal Acceleration at U/S Boundary of $162.67 \text{ m}^3/\text{s}^2$.	239
5.38	Exploded Window with Exaggerated Vertical Scale for Controlling Spikes in 5.32 to 5.35.	240
5.39	Comparison of Eulerian - Lagrangian Linked Algorithm with Lagrangian Solution for Test 'B' - Temporal Weighting Factor = 0.5.	243
5.40	Influence of Temporal Weighting Parameter on Lagrangian Solution for Test 'B'.	245
5.41	Comparison of Eulerian - Lagrangian Linked Algorithm with Lagrangian Solution for Test 'B' - Temporal Weighting Factor = 0.75.	246
5.42	Lagrangian Mode Solution of Test 'D' - Time Step = 30 Sec.	248

LIST OF FIGURES (continued)

Figure		Page
5.43	Lagrangian Mode Solution of Test 'D' - Time Step = 60 and 600 Sec.	249
5.44	Lagrangian Mode Solution of Test 'D' - Time Step = 120 Sec.	250
5.45	Lagrangian Mode Solution of Test 'D' - Time Step = 300 Sec.	251
5.46	Surge Movement in Non-Prismatic Diverging Channel - Influence of Channel Roughness.	255
5.47	Stage Profile Sensitivity for Degree of Non-Prismatic Channel Form - Diverging Channels.	257
5.48	Flow Profile Sensitivity for Degree of Non-Prismatic Channel Form - Diverging Channels.	258
5.49	Surge Movement in Non-Prismatic Converging Channel - Influence of Channel Roughness.	259
5.50	Stage Profile Sensitivity for Degree of Non-Prismatic Channel Form - Converging Channels.	260
5.51	Flow Profile Sensitivity for Degree of Non-Prismatic Channel Form - Converging Channels.	261
5.52	Comparison of Mass Conservation Characteristics of Eulerian-Lagrangian and Lagrangian Models.	264
5.53	Effect on Mass Conservation with Time Step for Test 'B'.	265
5.54	Comparison of Interpolation Schemes at Eulerian Step for Test 'A'.	267
5.55	Exploded Window Showing Influence of Interpolation Schemes for Test 'A'.	268
5.56	Comparison of Interpolation Schemes at Eulerian Step for Test 'B'.	269
5.57	Introduction of Clipping Errors in Time with Interpolation Schemes.	270
5.58	Dynamic Effects of Wave Steepening, Maturing and Breaking.	272
6.1	Simplified Flow Chart of Moving Element Model.	281
6.2	Channel Cross-section Definition in Moving Element Model.	282
7.1	Location Map of Teton Dam Break Flood Study	302

LIST OF FIGURES (continued)

Figure		Page
7.2	Typical Channel Cross-section with Conveying and Storage Zones Adopted for Moving Element Model	305
7.3	Envelopes of Maximum Flows for Teton Dam Break Flood with Bed Elevations of 4817 and 4837 ft at Mile 16.0	310
7.4	Choking Provided by Steep to Mild Slope Change at Mile 16.0 - Steady State Profile	312
7.5	Envelope of Maximum Elevations for Teton Dam Break Flood with Bed Elevation of 4817 ft at Mile 16.0	315
7.6	Envelope of Maximum Elevations for Teton Dam Break Flood with Bed Elevation of 4837 ft at Mile 16.0	316
7.7	Envelopes of Maximum Flow Depths for Teton Dam Break Flood with Bed Elevations of 4817 and 4837 ft at Mile 16.0	317
7.8	Times of Maximum Elevation for Teton Dam Break Flood with Bed Elevations of 4817 and 4837 ft at Mile 16.0	319
7.9	Times for Maximum Elevation and Discharge for Teton Dam Break Flood	320
7.10	Flow Attenuation and Lag for Teton Dam Break Flood - Mile 0.0 to 20.0	321
7.11	Flow Attenuation and Lag for Teton Dam Break Flood - Mile 20.0 to 59.5	322
7.12	Stage Hydrographs for Teton Dam Break Flood Mile 0.0 to 20.0	323
7.13	Stage Hydrographs for Teton Dam Break Flood Mile 20.0 to 59.5	324
7.14	Prismatic Channel Cross-section with Teton Dam Break Flood - Mile 0.0 to 5.0	326
7.15	Prismatic Channel Cross-section with Teton Dam Break Flood - Mile 10.0 to 50.0	327
7.16	Comparison of Moving Element Models (Divergent and Non-Divergent) with DAMBRK and SMPDBK for Maximum Depths	330
7.17	Comparison of Moving Element Models (Divergent and Non-Divergent) with DAMBRK and SMPDBK for Maximum Discharges	331

LIST OF FIGURES (continued)

Figure		Page
7.18	Comparison of Moving Element Model with DAMBRK and SMPDBK for Times to Maximum Depth	332
7.19	Envelope of Maximum Elevation for Teton River Channel Cross-section and Dam Break Hydrographs on a Mild Sloped Channel	336
7.20	Envelope of Maximum Elevation for Teton River Channel Cross-section and Dam Break Hydrographs on a Mild Sloped Channel	337
7.21	Envelope of Maximum Elevation for Teton River Channel Cross-section and Dam Break Hydrographs on a Mild Sloped Channel	338
7.22	Envelope of Maximum Discharge for Teton River Channel Cross-section and Dam Break Hydrographs on a Mild Sloped Channel	339
7.23	Envelope of Maximum Discharge for Teton River Channel Cross-section and Dam Break Hydrographs on a Mild Sloped Channel	340
7.24	Envelope of Maximum Discharge for Teton River Channel Cross-section and Dam Break Hydrographs on a Mild Sloped Channel	341
7.25	Flow Attenuation and Lag for Teton Dam Break Hydrograph on a Mild Sloped Channel	343
7.26	Stage Hydrographs for Teton Dam Break Flood on a Mild Sloped Channel	344
7.27	Comparison of Steep and Mild River Models for Discharge Hydrographs at Mile 15.0	345
7.28	Comparison of Steep and Mild River Models for Stage Hydrographs at Mile 15.0	347
7.29	Sensitivity of Channel Roughness Change at Mile 0.0 - Maximum Stage Envelopes for Mild Slope Model	348
7.30	Sensitivity of Channel Roughness Change at Mile 0.0 - Maximum Discharge Envelopes for Mild Slope Model	349
7.31	Location Map of Grand River Flood Routing Model Study Brantford to Lake Erie Reach	351
7.32	Comparison of Observed and Computed Stage Hydrographs at York Gauge for Flood of May 1974	357
7.33	Simulated Stage Hydrograph at York Gauge for Flood of April 1975	359

LIST OF FIGURES (continued)

Figure		Page
7.34	Comparison of Observed and Computed Stage Hydrographs at York Gauge for Flood of April 1979	360
7.35	Influence of Lateral Flow on Stage Hydrographs at York Gauge for Flood of May 1974	361
7.36	Flow Attenuation and Lag for Grand River Flood of May 1974 Between Brantford and York Gauge	363
7.37	Flow Attenuation and Lag for Grand River Flood of April 1975 Between Brantford and York Gauge	364
7.38	Flow Attenuation and Lag for Grand River Flood of April 1974 Between Brantford and York Gauge	365
7.39	Hysteresis Effects at Brantford Gauge for the Stage versus Discharge Relationship	367
7.40	Hysteresis Effects at York Gauge for the Stage versus Discharge Relationship	368
7.41	Maximum Stage Envelope for Grand River Flood of May 1974	369
7.42	Flow Attenuation and Lag for Grand River Hypothetical Flood Between Brantford and York Gauge	371
7.43	Maximum Stage Envelope for Grand River Hypothetical Flood	372
7.44	Influence of Higher Flow on Hysteresis Effects at York Gauge for the Stage versus Discharge Relationship	374
7.45	Comparison of Stage Profiles at 5, 15, 30 and 45 Sec. - Egiazarov's Experiment	377
7.46	Advancement of Surge in Time for Depth of Flow - Egiazarov's Experiment	378
7.47	Advancement of Surge in Time for Discharge - Egiazarov's Experiment	379
7.48	Comparison of Stage Profiles at 20 and 40 Sec. for Faure's Experiment	382
7.49	Comparison of Surge Arrival Times Between Observed and Computed Discharge Hydrograph for Faure's Experiment at 31.5 M	383

LIST OF FIGURES (continued)

Figure		Page
7.50	Comparison of Surge Arrival Times Between Observed and Computed Discharge Hydrograph for Favre's Experiment at 43.5 M	384
7.51	Comparison of Surge Arrival Times Between Observed and Computed Discharge Hydrograph for Favre's Experiment at 55.5 M	385
App. F.1.1	Impact of Choke Size - Stagegraphs at U/S Boundary	412
App. F.1.2	Impact of Choke Size - Stagegraphs at Choke Section	413
App. F.1.3	Impact of Choke Size - Hydrographs at Choke Section	414
App. F.1.4	Impact of Choke Size - Hydrographs at D/S Boundary	415
App. F.1.5	Surge Progress Through Choke at Time = 60.0 Seconds	416
App. F.1.6	Surge Progress Through Choke at Time = 120.0 Seconds	417
App. F.1.7	Surge Progress Through Choke at Time = 180.0 Seconds	418
App. F.1.8	Surge Progress Through Choke at Time = 240.0 Seconds	419
App. F.1.9	Surge Progress Through Choke at Time = 300.0 Seconds	420
App. F.1.10	Surge Progress Through Choke - Grid Size Sensitivity	421
App. F.1.11	TWF Sensitivity on Surge Progress - Fine Grid Size	422
App. F.1.12	TWF Sensitivity on Surge Progress - Fine Grid Size	423
App. F.1.13	TWF Sensitivity on Surge Progress - Fine Grid Size	424
App. F.1.14	TWF Sensitivity on Surge Progress - Fine Grid Size	425
App. F.1.15	TWF Sensitivity on Surge Progress - Fine Grid Size	426
App. F.1.16	Time Step Sensitivity on Surge Progression	427
App. F.1.17	TWF Sensitivity on Surge Progression	428
App. F.2.1	Test E2 - Flow Profile Over Hump	429
App. F.2.2	Test E2 - Velocity Profile Over Hump	430
App. F.2.3	Test E2 - Flow Hydrographs Around Hump	431

LIST OF FIGURES (continued)

Figure		Page
App. F.2.4	Constriction with Hump - Stage Profiles	432
App. F.2.5	Constriction with Hump - Velocity Profiles	433
App. F.2.6	Constriction with Hump - Flow Profiles	434
App. F.3.1	Surge Through an Expansion - Stage Profiles at 120 Sec	435
App. F.3.2	Surge Through an Expansion - Flow Profiles at 120 Sec	436
App. F.3.3	Surge Through an Expansion - Fine Grid Size, Stage	437
App. F.3.4	Surge Through an Expansion - Fine-Grid Size, Flow	438
App. F.4.1	Stage Profiles with Time step = 5 Sec	439
App. F.4.2	SWF Sensitivity for Advanced TWF	440
App. F.4.3	SWF Sensitivity for Centered TWF	441
App. F.4.4	SWF Sensitivity for Centered TWF	442
App. F.4.5	Comparison of ME and FD	443
App. F.4.6	Comparison of ME and FD	444
App. F.4.7	Comparison of ME and FD	445
App. F.4.8	Comparison of ME and FE	446
App. F.5.1	Channel Roughness Sensitivity on Surge Location	447
App. F.5.2	Element Size Sensitivity on Front Shape	448
App. F.5.3	TWF Sensitivity on Front Shape	449
App. F.5.4	TWF Sensitivity on Front Shape	450
App. F.5.5	Interpolation Sensitivity at Eulerian Regridding Step	451
App. F.5.6	Wave Steepening and Breaking - Discontinuity in Domain	452
App. J.1.1	Section at Mile 0.0	462
App. J.1.2	Section at Mile 5.0	463
App. J.1.3	Section at Mile 8.5	464

LIST OF FIGURES (continued)

Figure		Page
App. J.1.4	Section at Mile 16.0	465
App. J.1.5	Section at Mile 22.5	466
App. J.1.6	Section at Mile 27.5	467
App. J.1.7	Section at Mile 32.5	468
App. J.1.8	Section at Mile 37.5	469
App. J.1.9	Section at Mile 41.0	470
App. J.1.10	Section at Mile 43.0	471
App. J.1.11	Section at Mile 51.5	472
App. J.1.12	Section at Mile 59.5	473
App. J.2.1	Section at Mile 0.0	474
App. J.2.2	Section at Mile 8.0	475
App. J.2.3	Section at Mile 16.0	476
App. J.2.4	Section at Mile 24.0	477
App. J.2.5	Section at Mile 28.0	478
App. J.2.6	Section at Mile 35.0	479
App. J.2.7	Section at Mile 38.5	480
App. J.2.8	Section at Mile 45.0	481
App. J.2.9	Section at Mile 53.0	482
App. J.2.10	Section at Mile 60.0	483

LIST OF TABLES

Table		Page
3.1	Summary of Reviewed Models and Techniques	74
5.0	Summary of Numerical Experiments	188
5.1	Sensitivity Analysis of Varying Computation Time Step	190
5.2	Sensitivity Analysis of Varying Element Length	197
5.3	Sensitivity Analysis of Varying Temporal Weighting Parameter, θ	201
5.4	Sensitivity Analysis of Varying Spatial Weighting Parameter, β	205
5.5	Sensitivity Analysis of Varying Manning's Roughness Coefficient, n	210
5.6	Sensitivity Analysis of Varying Temporal Acceleration, dQ/dt	214
5.6(a)	Summary of Sensitivity Analysis	220
5.7	Comparison of Moving Element and Finite Difference Methods	224
5.8	Comparison of Moving Element and Finite Element Methods	228
5.9	Comparison of Moving Element and Petrov- Galerkin Based Methods	232
5.10	Comparison of Eulerian-Lagrangian and Lagrangian Methods	242
5.11	Comparison of Moving Element Method with Other Numerical Techniques	253
6.1	Hardware Configurations of Micro-Computers	288
6.2	Comparison of Execution Time for Different PC Configurations relative to CDC Cyber Performance	289
6.3	Relative Execution Time for Test Cases using Different Hardware/Software Configurations	292
7.1	Channel Properties for the Teton Dam Break Flood Model	306
7.2	Two-Dimensional Flow Aspects Following the Teton Dam Break	314
7.3	Channel Properties for the Grand River Flood Routing Model	352
7.4	Simulation Characteristics for Grand River Flood Routing	353

CHAPTER 1

INTRODUCTION

Sudden release of water in a channel following the breach of a dam is considered as a discontinuous flow problem in a limiting sense. Such problems have invited interests from many disciplines. Two related fields are in fluid mechanics and open channel hydraulics. Problems encountered in solving discontinuities in any field are well documented.

While research concentrated in developing new and innovative techniques in fluid mechanics, hydraulic engineers primarily concentrated in devising practical tools to solve the problems. The difficulty in solving rapidly varying flow resides in the oscillatory behaviour of many discretized difference forms of the governing differential equations. The current research was concentrated on an attempt to bridge the two disciplines by doing justice to the mechanics of fluid behaviour, while responding to the practical aspects of unsteady flow modelling.

The unsteady flow hydraulics for near discontinuous or rapidly varying flows is described by the divergent or conservative form of equations due to Barre De St. Venant. The pair of equations account for the conservation of volume and momentum within the solution domain. Mathematically, the two equations are non-linear partial differential equations of hyperbolic type. A complete solution requires specification of initial and boundary conditions. In the form in which these equations are written they cannot be solved analytically. Since the advent of computers, a variety of numerical solutions of the St. Venant equations have been proposed. This

study addresses this aspect of numerical solution by a new Eulerian-Lagrangian based finite element method.

The study was carried out in five stages described in the following chapters. In Chapter 2, the scope of the study is defined, objectives are set and the governing equations along with necessary initial and boundary conditions are established. Chapter 3 documents the literature review carried out in support of the research. The Eulerian-Lagrangian linked algorithm, named the moving element method, is developed in Chapter 4. This chapter also provides details on the generalization from idealized conditions to practical field problems.

Chapter 5 documents the setting up of a number of numerical experiments, model testing and sensitivity studies. Alternative forms of solution in pure Lagrangian mode and Petrov-Galerkin based schemes are also tested. Improvements in results over the finite difference and finite element methods are demonstrated. The computer model developed to carry out the numerical analysis is described in Chapter 6.

Testing on mainframe machines and the successful transfer to a variety of personal computers is documented in this chapter and model input and output are explained.

In Chapter 7, the model application to simulate the Teton Dam break flood and flood routing in the Grand River are described along with some laboratory experiment verification. Chapter 8 provides a summary of the model development, testing and implementation, conclusions are drawn from the study and recommendations for future work are suggested. As a certain amount of the comparisons in Chapter 7 involve the Imperial System of units, these were also employed in this work for the sake of consistency.

All figures and tables appear following their reference. Where appropriate, reference is made to Appendices. The variables used in this work are summarized in Appendix 'A' and defined following their first declaration. The source code for the computer program, an executable module, an example input file and a sample output are provided on a floppy diskette appended to the printed thesis. The list of references provided in this thesis is also enclosed on a diskette as an ASCII file.

CHAPTER 2

DEFINITION OF PROBLEM

To obtain a reasonable solution, the problem has to be posed properly. For the study of open channel flow hydraulics, this requires the specification of the governing equations and the associated initial conditions and boundary conditions. In this chapter, a brief description of problems encountered in solving discontinuous or rapidly varying flow phenomenon is presented. This problem definition is studied separately for the numerical aspects of convection dominated flow equations and application aspects of open channel equations. As a variety of open channel flow equations have been proposed in the past, these are classified according to their use. Lastly, the study objectives are developed for addressing the problem so defined.

2.1 Oscillations in Convection Dominated Flows

Although there are a variety of ways of posing open channel flow equations, all these lead to a pair of non-linear partial differential equations of hyperbolic type. These equations when formulated represent the conservation of mass (strictly speaking volume), and some form of momentum. In a generic form, these equations are written as:

Mass Conservation

$$\frac{\partial}{\partial t} f_1(y) + \frac{\partial}{\partial x} g_1(u) - h_1 = 0 \quad (2.1)$$

Momentum Conservation

$$\frac{\partial}{\partial t} g_1(u) + \frac{\partial}{\partial x} [g_2(u) + f_2(y)] - h_2 = 0 \quad (2.2)$$

where:

Mass Conservation terms:

- (1) The first term of Equation (2.1) describes the rate of rise reflecting changes in the storage due to change of water surface elevation with time.
- (2) The second term accounts for the prism and wedge storage variations in space.
- (3) Lateral inflow and outflow term accounting for the net mass change both spatially and temporally besides the storage terms in (1) and (2).

Momentum Conservation terms:

- (4) The first term of Equation (2.2) provides for the acceleration due to time variation in the flow field.
- (5) The second term of momentum equation explains the convective acceleration due to a spatial gradient of both velocity and depth.
- (6) The third term accounts for the pressure force terms.
- (7) The term h_2 in Equation (2.2) shows a balance of acceleration effects contributions of lateral inflow (zero for outflow), gravity body force provided by a sloping channel bed and corresponding frictional force effects on the wetted surface.

In the above equations $f_1(\)$, $f_2(\)$, $g_1(\)$ and $g_2(\)$ are functions of the dependent variables. Specific forms of these equations are described in later sections.

These equations have no closed form solution, unless they are simplified to an extent that they cease to be of practical interest. The pair of equations further

require initial and boundary conditions when their solution is sought by any of the numerical techniques.

Numerical solutions of any partial equations such as Equations (2.1) and (2.2) require discretization of the continuous terms into finite difference form. Such approximations are achieved by a variety of techniques. Finite difference and finite element methods are two most commonly used.

For problems with gradual variation in both spatial and temporal senses, experience in solving such equations has been a success. When faced with problems involving steep spatial and temporal gradients, historically, all numerical methods have failed to produce satisfactory results. Common problems reported for steep fronted solution include node to node oscillations, clipping and overshooting, negative values of variables, etc.

When the resulting numerical solutions exhibit node to node oscillations, it is commonly referred as a saw-tooth solution or one marred by the presence of parasitic waves. In the literature, these oscillations are commonly called 'wiggles' and this term is used widely here.

Considerable effort has gone into explaining the mechanisms that precipitate the growth of an oscillatory behaviour. The most common approach is the use of Fourier analysis of the linearized governing equations. These Fourier analyses study the properties of waves of different lengths in a discretized domain.

By Fourier analysis of the linearized wave equations, Gray and Lynch (1980) have shown that the $2\Delta x$ waves are not dissipated and that they travel at different speeds when compared with other wave components. These oscillations are common for many of the discretization procedures in finite difference and finite element techniques. From this perspective, the discretization schemes are sometimes

called non-dissipative if the node to node oscillations are preserved in the difference forms.

Many governing equations which explain the physical processes of fluid mechanics are nonlinear. The node to node problems are then further exacerbated from oscillations generated by the nonlinearities. These problems are common even when idealized field conditions are assumed. For example, in solving open channel flow equations, a prismatic channel maybe assumed. Problems in the field setting and their solutions are therefore compounded when the finite difference and finite element discretization is over a nonlinear domain, i.e. one in which the variables violate the holistic assumptions.

The foregoing then leads to the development of the first objective for this research. The objective is to develop alternate techniques for solving a pair of nonlinear partial differential equations of hyperbolic type in the presence of steep spatial and temporal gradients. In this research the pair of equations describe open channel hydraulics. This is further elaborated in the next section.

2.2 Compromises in Rapidly Varying Open Channel Flows

The problems defined in the previous section are also present when solving unsteady flow equations for open channel flows. The physics of open channel flow is explained by a pair of equations accounting for mass or volume continuity and conservation of some form of momentum. The solution further requires initial and boundary conditions. By its nature this system of equations constitutes a problem of nonlinear hyperbolic partial differential equations.

One of the properties of hyperbolic equations is to propagate any discontinuity introduced at its boundary without change. No mechanisms exist to dissipate

or disperse the perturbation, unlike elliptic or parabolic equations for example. Therefore, any oscillatory solution that is developed will propagate without change in its form, if the solution is free from stability, convergency and consistency problems.

As the research is concentrated in the field of open channel hydraulics, the problem is defined in this frame of reference. Before describing the existing solution techniques, it is prudent to define a variety of terms commonly employed throughout this thesis.

Dam-break flood: A hypothetical dam-break flood results from instantaneous removal of a structure holding back initially quiescent water at a finite depth and of infinite capacity to sustain the flow rate for the duration of simulation.

Other terms commonly used in the same context are dam-burst or dam-breach floods. The only scenario where the concept of near instantaneous failure can be realized is for concrete arch dams. The second postulation of infinite capacity of the reservoir is rarely true. Dam-break floods generate two fronts, a strong front advancing down the valley and a weak front receding into the reservoir. The U.S. Army Corps of Engineers, Hydrologic Engineering Center (HEC, 1977) provided information on breach characteristics and different modes of failure depending upon the material of construction.

Rapidly Varying Flow: Near discontinuous flow or rapidly varying flow are synonymous with dam-break flood. In the presence of such flow conditions, the domain experiences large temporal and spatial gradients of velocity, discharge and depth of flow. The flow is marked with discontinuities by the formation of standing and moving hydraulic jumps.

Gradually Varying Flow: In contrast to the rapidly varying flows, gradually varying flow exhibit a continuous surface. The spatial and temporal gradients are very small and at any point the water level and flow change slowly. This is the most common type of unsteady flow in natural channels. This flow type is also referred as continuous flow.

Traditionally, the unsteady flow hydraulic models for studying dam-break floods evolved from their continuous simulation counterparts. Most of the numerical techniques provide adequate solutions for gradually varying flows and by advancing the temporal weighting parameter. These techniques, however, lead to oscillatory waves when the solution is sought at numerically more accurate centered Crank-Nicholson weighting especially for rapidly varied flow.

In order to obtain a smooth solution, i.e. free from parasitic waves three different techniques are commonly employed. These provide a smooth, non-oscillatory albeit dispersive surface. These methods, reviewed in Chapter 3 are:

- external dissipative mechanisms
- internal dissipative parameters
- dissipative interfaces.

The first method requires the addition of external higher order derivatives and a dissipation constant. This is a popular method in many finite element based models. The second technique provides for selective dissipation of the oscillatory waves by advancing the temporal weighting of an otherwise centered Crank-Nicholson scheme. This is the most frequently used method among numerical solutions. Dissipative interfaces are introduced in the solution by replacing those variables at the current time level associated with the time derivatives with a

weighted average. This averaging process, which requires a dissipation parameter, provides an interface.

The foregoing provides the basis for the second requirement of this research. The objective then is to develop an accurate numerical scheme for open channel flow equations capable of handling hydraulic transients preferably without any dissipative aids.

2.3 Open Channel Flow Equations

Saint-Venant (1871) first proposed and developed the basic theory to explain the process of propagation of waves in open channels. The fluid mechanics is explained by a pair of partial differential equations representing the conservation of mass (strictly speaking volume) and momentum of flow in the channel. In the literature these equations are commonly referred to as the St. Venant equations.

There are excellent references where the development of these equations and associated assumptions are expounded. Abbott (1979) provides the theoretical framework, assumptions and common simplifications. Since there are a variety of ways in which the open channel flow can be represented, it is important to provide consistent definitions of all the variables and parameters. The flow equations as employed in this research are:

$$\frac{\partial A}{\partial t} + \frac{\partial Q}{\partial x} - q = 0 \quad (2.1a)$$

$$\frac{\partial Q}{\partial t} + \frac{\partial}{\partial x} (Qu) + g \frac{\partial}{\partial x} (A \bar{y}) - gA(S_0 - S_f) - u_x q = 0 \quad (2.2a)$$

Being stated for the first time, the following definitions are used throughout this thesis:

- t = independent variable, time (basic unit is second, T)
 x = independent variable, distance measured from the upstream boundary; positive in the downstream direction (metre or feet, L)
 $Q(x,t)$ = discharge or flow rate (m^3/s and cfs, L^3T^{-1})
 $y(x,t)$ = depth of flow (metre or feet, L)
 $h(x,t)$ = stage or water surface elevation above an arbitrary datum (metre or feet, L)
 S_o = channel bed slope (dimensionless)
 $S_f(Q,h)$ = frictional slope (dimensionless). It is also a measure of forces exerted on water by the wetted surface
 $b(u, \xi)$ = channel width at depth ' ξ ' and location, x (L)
 $A(b,t)$ = cross-sectional area of the channel (L)
 $V = Q/A$ = velocity averaged over the cross sectional area (LT^{-1})
 q = lateral flow rate per unit length of channel (L^2T^{-1}) positive for inflow and negative for outflow
 u_x = velocity of lateral flow component in positive 'x' direction, contributing to channel momentum, zero for lateral outflow, positive or negative value for lateral inflow
 P/ρ = pressure exerted by the water body

This is also the same as $gA\bar{y}$

where

- \bar{y} = depth of centroid of the cross-section (metre or feet, L)
 z = thalweg or channel bed elevation above an arbitrary datum

The following relationships further define the variables noted above

$$S_f = \frac{Q^2 n^2}{K^2 A^2 R^{4/3}} \quad (2.3)$$

where

n = Manning's roughness coefficient

$R = A/P$ = hydraulic radius (L)

P = wetted perimeter or surface (L)

K^2 = a constant to reflect units used

($K^2 = 1.0$ for metric system and $K^2 = 2.208$ for Imperial units)

$$C^2, c^2 = \frac{gA}{T} = gD \quad (2.4)$$

where

C, c = celerity of wave (LT^{-1})

T = top width of channel at a given flow (L)

D = hydraulic depth (L)

g = acceleration due to gravity (LT^{-2})

$$F_r = \frac{u}{\sqrt{gD}} \quad (2.5)$$

where

F_r = Froude Number, a relative measure of the inertial forces to gravitational forces

$$\frac{y}{y} = \frac{\int_0^y b(x, \vartheta) (h - \vartheta) d\vartheta}{\int_0^y b(x, \vartheta) d\vartheta} = \frac{\int_0^y b(x, \vartheta) (h - \vartheta) d\vartheta}{A} \quad (2.6)$$

where

\bar{y} = depth of centroid below the water surface

Other variables and definitions follow their first occurrence.

The two open channel flow equations attributed to the 1871 paper of de Saint-Venant in their original form are given as follows:

$$\frac{\partial w}{\partial t} + \frac{\partial(wu)}{\partial x} = 0 \quad (2.7)$$

and

$$\frac{\partial \epsilon}{\partial s} + \frac{1}{g} \frac{\partial u}{\partial t} + \frac{u}{g} \frac{\partial u}{\partial s} + \frac{\chi}{w} \frac{F}{\rho g} \quad (2.8)$$

where

w = the cross-sectional area

u = the mean velocity

ϵ = the position of water surface above a reference level

$\chi F/w\rho g$ = the friction slope

ρ = the density of water

g = the specific weight

gF = the boundary friction per unit area

and s = the length along the rectangular prismatic channel

In essence, the above two governing equations have remained unchanged over the last hundred years. A variety of modifications, enhancements, simplifications and alternative form of equations have been developed. Such equations can, however, be shown to reduce or alter to the equations as described by Saint-Venant.

There are three alternate forms from two basic formulations of the unsteady flow equations depending on their emphasis on the momentum conservation principle. These alternate forms also provide physically consistent numerical solutions of the unsteady flow problem under various conditions. these are:

1. Non-Divergent form

2. Characteristic form

3. Conservation or Divergent form

There are again a number of ways in which the dependent variables are defined. For example the flow conditions can be specified as the discharge rate or velocity. Similarly, the depth of flow can be described alternately as the position of the water surface above a reference datum. For the sake of consistency, the dependent variables used in this research consist of discharge and depth of flow.

2.3.1 Non-Divergent Form

This is the most common form of the St. Venant flow equations, and is employed numerical models. As this formulation is rooted in the resolution of an energy balance, the equations are also referred to as the energy based form.

Conservation of Volume

$$T \frac{\partial y}{\partial t} + \frac{\partial Q}{\partial x} = q \quad (2.9)$$

Conservation of Momentum

$$\frac{\partial Q}{\partial t} + \frac{\partial}{\partial x} (Qu) + gA \frac{\partial y}{\partial x} - gA S_o + gA S_f - u_x q = 0 \quad (2.10)$$

Since the Rankine-Hugoniot conditions are not satisfied across a shock or discontinuity, this non-divergent form of the unsteady flow equations should not be used for problems with steep temporal and spatial gradients.

2.3.2 Characteristic Form

By multiplying the terms of the continuity equation (Equation 2.9) by the wave celerity, c , and alternately adding and subtracting the resulting equation to the

momentum conservation equation, the result can be reduced to the characteristic form. These equations are written in terms of the forward and backward characteristics as follows:

Forward Characteristic:

$$\begin{aligned} \frac{\partial Q}{\partial t} + (u+c) \frac{\partial Q}{\partial x} - (u-c) \frac{\partial A}{\partial t} - (u^2 - c^2) \frac{\partial A}{\partial x} \\ - gA S_o + gA S_f + (u_x - c)q = 0 \end{aligned} \quad (2.11)$$

Backward Characteristic:

$$\begin{aligned} \frac{\partial Q}{\partial t} + (u-c) \frac{\partial Q}{\partial x} - (u+c) \frac{\partial A}{\partial t} - (u^2 - c^2) \frac{\partial A}{\partial x} \\ - gA S_o + gA S_f + (u_x + c)q = 0 \end{aligned} \quad (2.12)$$

For two reasons the characteristic form of equations provide more accurate numerical solution. First, by its very nature the solution for hyperbolic equations follow the characteristics and hence this form provides the best vehicle. Secondly, unlike the non-divergent form, the characteristic equations and their difference forms lead to well conditioned matrices. The coefficients of the resulting sets of equations are of the same order of magnitude hence roundoff errors have less impact on the overall solution.

As will be documented in Chapter 3, this form of the equations is not suitable in the presence of shocks (the characteristics will intersect) and for simulating wave movement in natural channels (existence of reflected waves).

2.3.3 Conservation or Divergent Form

It was noted that, the non-divergent form of equations, because of their energy balancing properties, could balance or account for energy loss across a discontinuity while the momentum is violated. This can be rectified by adopting a divergent form of the equations which explicitly balances the momentum.

For the conservation of volume and momentum (and, by extension, energy), the divergent form embodies the Rankine-Hugoniot shock conditions. The unsteady flow equations in this and other forms have been commonly employed in studying near discontinuous flows.

Conservation of Volume

$$\frac{\partial A}{\partial t} + \frac{\partial Q}{\partial x} = q \quad (2.13)$$

Conservation of Momentum

$$\frac{\partial Q}{\partial t} + \frac{\partial}{\partial x} (Qu) + \frac{\partial}{\partial x} \left(\frac{P}{\rho} \right) - gA S_o + gA S_f - u_x q = 0 \quad (2.14)$$

Alternate form of Equation 2.14

$$\frac{\partial Q}{\partial t} + \frac{\partial}{\partial x} (Qu) + g \frac{\partial}{\partial x} (A \bar{y}) - gA S_o + gA S_f - u_x q = 0 \quad (2.15)$$

As the objectives stated before stress the solution of open channel flow equations for rapidly varying flows associated with dam-breach phenomenon or discontinuous flows, the above equations are used. Equations (2.13) and (2.14) and associated boundary and initial conditions define the problem definition.

Initial Conditions

$$Q(x,0) = F_1(x) \quad (2.16)$$

$$y(x,0) = F_2(x) \quad (2.17)$$

Boundary Conditions**Upstream**

$$Q(0,t) = G_1(t) \quad (2.18)$$

or

$$y(0,t) = G_2(t) \quad (2.19)$$

Downstream

$$Q(L,t) = H_1(t) \quad (2.20)$$

or

$$y(L,t) = H_2(t) \quad (2.21)$$

or

$$Q(L,t) = H_3\{y(L,t)\} \quad (2.22)$$

To avoid non-trivial solution, Equations (2.18) and (2.20) should not be specified concurrently. F, G and H are known functions.

2.4 Statement of Objectives

From the definition of problems two major objectives were listed in previous sections. These are restated and other secondary objectives developed. These are stated as follows:

1. The primary objective of this research is to develop, test and implement an improved numerical solution of a pair of nonlinear partial differential equations of hyperbolic type which represent the divergent form of the equations of open channel flow.

2. The numerical solution should be capable of handling discontinuities both internally as initial conditions and externally by introduction at the boundaries. Further, the technique should achieve results without prejudicing the integrity of equations as employed.
3. The proposed methodology would extend existing Lagrangian based solutions of single equation problems in fluid mechanics to open channel flow problems with coupled dependent variables.
4. The technique should be capable of eliminating oscillations commonly found in discontinuous flow solutions without adding internal or external dissipation parameters.
5. The solution procedure would be generalized in both spatial and temporal weighting senses and the impact of such generalization would be studied.
6. Controlled numerical experiments would be devised to evaluate model capabilities and establish limitations.
7. The numerical scheme would be extended from the controlled experiment stage to simulate dam-break floods in natural channels. The governing equations would be improved by adding or altering the appropriate terms.
8. The portability of the computer algorithm would be tested by first downloading the program from the mainframe computers to personal computers and then by adapting to a variety of microcomputers.

CHAPTER 3

LITERATURE REVIEW

3.1 Introduction

The literature is abundant in both theoretical development of procedures for dam-breach/floodwave routing and their practical applications. There are two noteworthy documents which chronicled these developments. Miller and Yevjevich (1975) prepared a bibliography containing 1885 references on unsteady flows in open channels. Wurbs (1985) presented a chronological annotated bibliography of 189 references on dam-breach and associated flood routing phenomenon. Furthermore, a workshop was organized by the United States Water Resources Council, Hydrology Committee in 1977. The proceedings from this workshop on Dam-Break Flood Routing summarizes the experience in practical applications of several models by sixteen agencies.

Instead of reiterating the theoretical developments, modelling and practical experiences, the presentation in this chapter is organized to highlight particular techniques employed classified as follows:

- (i) Dam-break and associated flood routing being a convection dominated flow problem in fluid mechanics, theoretical aspects of these associated fields are discussed;
- (ii) The flood wave generated by dam-breach in a theoretical or limiting sense introduces a discontinuity in the flow domain. The techniques related to handling such discontinuity by the finite difference and finite element methods are addressed;

- (iii) Field problems have to be concerned with smearing and damping of this discontinuity by external variables in the form of bed roughness, eddies, etc. Also, the flood-wave after travelling a certain distance, due to peak flow attenuation adopt a more or less continuous flow profile and flow varies gradually from point to point. Finite difference and finite element techniques employed in solving the continuous flow problem are presented next; and
- (iv) Numerous references are available on problems related to oscillatory solutions in convection dominated fluid flows. In the last section a summary of different damping techniques with reference to open channel flows is discussed.

3.2 Convection Dominated Flows in Fluid Mechanics

Many problems in the field of fluid mechanics are concerned with advection or convection dominated flows. Examples are the Navier-Stokes equations, and diffusion-dispersion equations describing the distribution of momentum, temperature or concentration. Such problems are similar to those handled by the open channel flows equations. It is not, then, uncommon to observe oscillatory solutions or wiggles when studying these problems. As a simple case the equation of advection-dispersion problem is stated as

$$\frac{\partial C}{\partial t} + \frac{\partial C \bar{u}}{\partial x} = K \frac{\partial^2 C}{\partial x^2} \quad (3.1)$$

The second term on the left hand side accounts for the advective transport of a substance, C, in a non-uniform flow or velocity field, u. The term on the right hand side describes the molecular or eddy dispersion at a rate, K. Typically, this

problem is related by the Peclet Number, P_e , defined as

$$P_e = \frac{uL}{K} \quad (3.2)$$

where L is a characteristic length. In a finite difference scheme, the characteristic length is the reach length, or Δx . When P_e is small (< 1), there is enough dispersion or diffusion present that it overcomes the oscillatory solution associated with the advection component. However, problems arise when P_e is large (> 10) when advection dominates. The limiting case is when K is equal to zero and Peclet No. is infinite. This is similar to open channel flow equations in the absence of bed roughness. Writing the conservation of mass and momentum equations

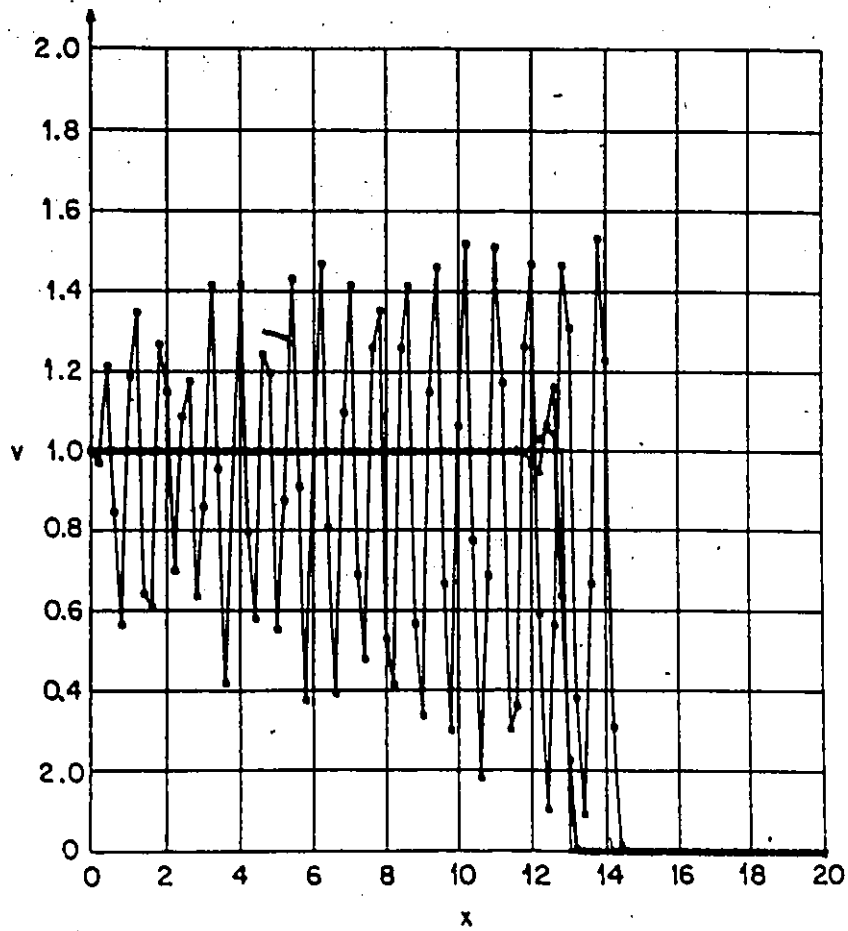
$$\frac{\partial A}{\partial t} + \frac{\partial(Au)}{\partial x} = 0 \quad (3.3)$$

$$\frac{\partial Q}{\partial t} + \frac{\partial(Qu)}{\partial x} = -g \frac{\partial}{\partial x} (A \bar{y}) \quad (3.4)$$

Comparing Equations (3.3) and (3.4) with Equation (3.1) indicate the complexities in solving open channel flow equations. This is imposed by the requirement of simultaneous satisfaction of dependent variables in two equations. Another reason of complexity is due to the coupling of various terms.

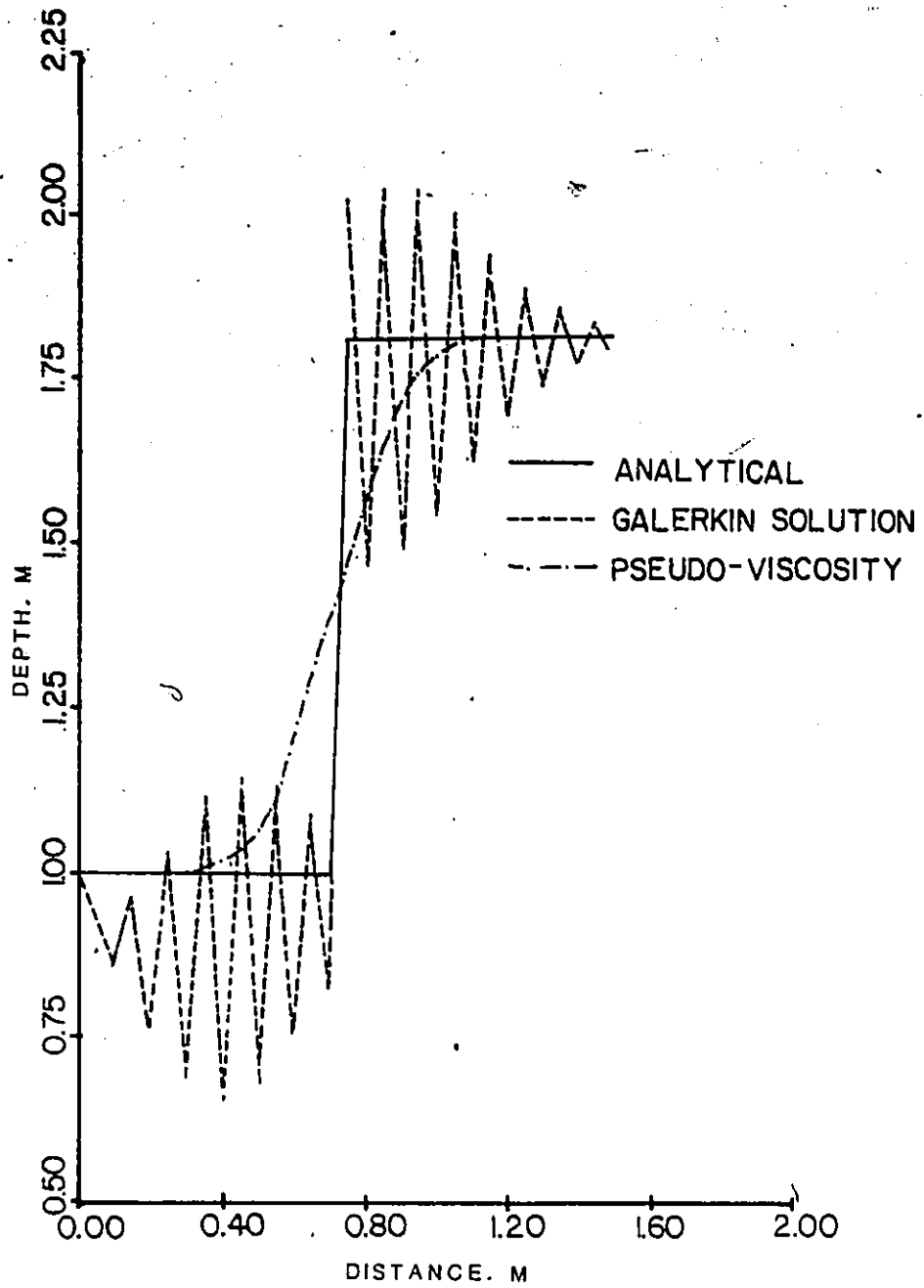
Having established the necessary common features of the open channel flows and convection-dominated transport, attention is now focussed on the treatment of the problems, viz. the presence of oscillations as shown in Figures 3.1(a) and (b).

The advent of the computer has resulted in the employment of various methods for the numerical solution of the partial differential equations for many physical processes. As a variety of techniques emerged for solving convection dominated flows, there appeared a corresponding volume of literature on the oscillatory nature of solutions and techniques to suppress these parasitic oscillations.



Burgers equation: propagation of a discontinuity. * = exact solution; \square = computed solution with no pseudoviscosity; \triangle = computed solution with simple pseudoviscosity
 \circ = computed solution with iterated pseudoviscosity

Fig. 3.1(a) Oscillatory Solution in Fluid Mechanics. Solution of Burger's Equation. After Bonnerot and Jamet (1975)



Galerkin Simulation of Hydraulic Jump

3.1(b) Oscillatory Solution in Open Channel Hydraulics. Solution of Stationary Hydraulic Jump. After Katopodes (1984)

These numerical techniques were further enhanced with the employment of the finite element method and variations there of.

In 1981, the American Society of Mechanical Engineers organized a workshop to specifically address the subject of convection-dominated flows in fluid mechanics. Among a number of papers which described several alternative procedures, there were two excellent papers which summarized the nature of the problem, possible reasons and suggested remedies.

Leonard (1981) provided a brief history of computational fluid dynamics modelling. The paper centred on the appearance of oscillations in the solution and their interpretation and gave a detailed description of problems associated with the discretization of the spatial derivative, ie. the advection term.

Leonard theorized that when the cell Peclet number, described in Equation (3.1), P_c is greater than 2.0, the second-order central difference scheme results in an oscillatory solution where as the first-order upstream differencing scheme becomes artificially diffusive. Leonard proposed two other higher-order schemes which were claimed to be both stable and accurate under high convection conditions. A literature search for this work, however, failed to reveal use or success of similar higher order terms in open channel flows. The use of upwind-weighted differencing in suppressing the oscillations was questioned. Roach (1976) analyzed the same problem with a suggestion that the use of upwind-weighted differencing of the convection terms is actually fictitious in view of the stability being achieved at the expense of false numerical diffusion. This is equivalent to using the central differencing and adding an artificial diffusion term. Roach further suggested possible solutions if the wiggles are a result of the boundary conditions.

A second paper by Gresho and Lee (1981) in the same proceedings provides a summary of different techniques used in suppressing the oscillations. The topics covered for these parasitic oscillation range from the simple heat conduction to the more complicated Navier-Stokes equations. The paper argued very strongly against indiscriminate treatment of the wiggles by means of suppressants such as artificial damping mechanisms. The authors argue in support of refining the grid rather than retaining a coarse mesh and adding external and redundant terms. The reason for the oscillations, it is theorized, is related to the discretization of the solution domain and not necessarily the finite element or finite difference techniques. Further, if the discretization of the partial differential equation is consistent then in the limit of a fine mesh the finite difference solution should approach the analytical solution if one exists.

The paper equates the oscillatory nature of solution to a signal that there are problems either with the discretization scheme, the boundary conditions or parameter selection. The paper concludes that the 'sedatives' introduced by schemes which set out to suppress the oscillations a priori induces a false sense of security that the solution is representative and that moreover such schemes can damp out more than just oscillations and may suppress information.

The paper is strongly critical of any upwind weighting scheme, be it a finite difference or finite element technique. Huyakorn (1977) and Huyakorn and Nilkuha (1979) have reported progress in employing upwind weighting schemes in the finite element discretization for the advective-dispersion problem. Gresho and Lee (1981) have, however, argued against the 'theoretically unsound basis' of the scheme and questioned its ad hoc nature for obtaining an optimum weighting factor. It also

appears that there is no easy way to optimize this factor especially for time-variant problem.

There are certainly other papers which tend to support the arguments put forward by Leonard (1981) and Gresho and Lee (1981). Lee et al (1976) and Gresho and Lee (1978) tested and compared several numerical methods for the convection dominated flows. These papers summarized the following points which are relevant to the dambreak problems.

- a) In the absence of diffusive or dispersive agents or when their influence is insignificant (corresponding to a high cell Peclet Number), conventional finite element methods even with linear elements are more accurate than central finite difference schemes.
- b) The first signs of oscillations are directly linked to the grid coarseness. Other reasons to cause these oscillations are too-steep waveform, too-high cell Peclet number and fixed outflow boundary condition. Oscillations which resulted from grid coarseness or steep-wave form are dispersion wiggles (i.e. shorter wave components advecting at the wrong speed) and can be reduced to an acceptable level by refining the mesh configuration.

On the contrary if the same oscillations are suppressed by employing, for example, the upwind weighting technique, then it no doubts provides a smooth solution. It will also be shown later in this chapter that in many cases such external variables causes the solution to be that of an entirely different problem.

Still within the domain of convection dominated flows, most of the solution procedures have concentrated on finite differences in space and time. Examples can be found in Book et al (1975) and Martin (1975). Others have employed a combination of Galerkin based finite elements in space and finite difference in time. Reference is

made to Adey and Brebbia (1973), Dailey and Harleman (1973), and Smith, et al (1973). Lam (1977), Ehlig (1977), Mercer and Faust (1977) and Smith (1977) compared various finite difference and finite element techniques for selected tests. The results from the review and comparison indicate that when the diffusive terms dominate (associated with low cell Peclet Number) all methods give satisfactory results. When convection terms dominate (i.e. high cell Peclet Number) all techniques exhibited problems like oscillations, overshooting, clipping, numerical diffusion and negative values of dependent variables (concentration cannot be negative).

Figure 3.2, reproduced from Lam (1977), indicates the nature and degree of problems for highly convection dominated flows. In this example, the central differencing scheme and box scheme are oscillatory; upstream weighted differences introduces artificial differencing and when flux correction is employed to suppress the wiggles in upstream weighted schemes results in smearing and clipping errors.

Bonnerot and Jamet (1974, 1977) and Jamet and Bonnerot (1975) presented three papers on the concept of space-time elements for the solution of Stefan Problem. The central theme in these papers revolved around the use of time, an independent variable, similar to the space dimension. The Galerkin method of weighted residuals is then applied with two-dimensional space-time elements for a one-dimensional problem in space and three-dimensional elements for two-dimensional space problems. The solution is obtained for a slice of time step and advanced in a likewise fashion. A typical solution strip is shown in Figure 3.3.

The space-time finite element technique was furthered by Varoglu and Finn (1978, 1980) and Finn and Varoglu (1979). These applications related to advection-diffusion problems in one and two dimensions and the solution of Burger's Equation. The method introduced a combination of linear triangular and four node

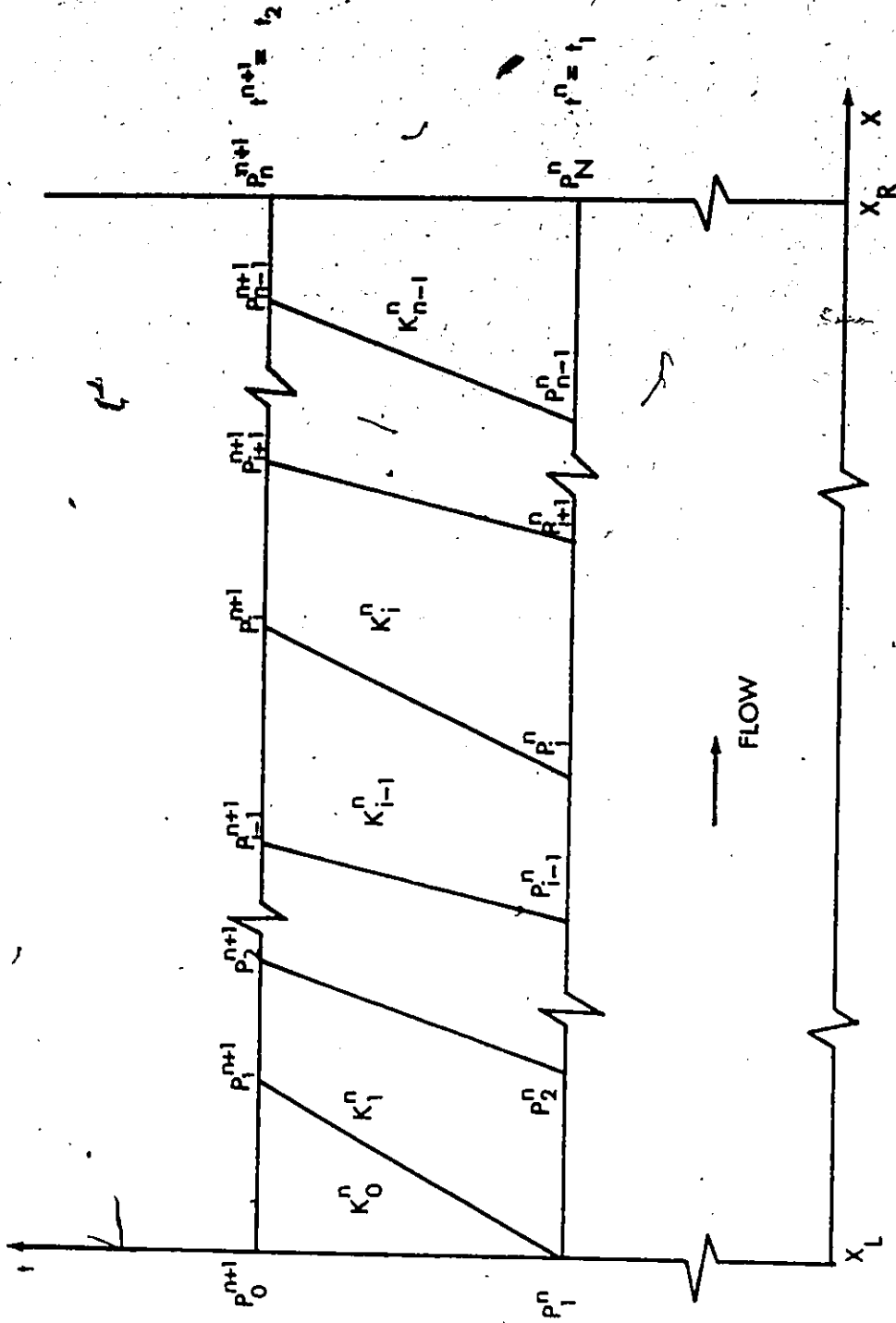
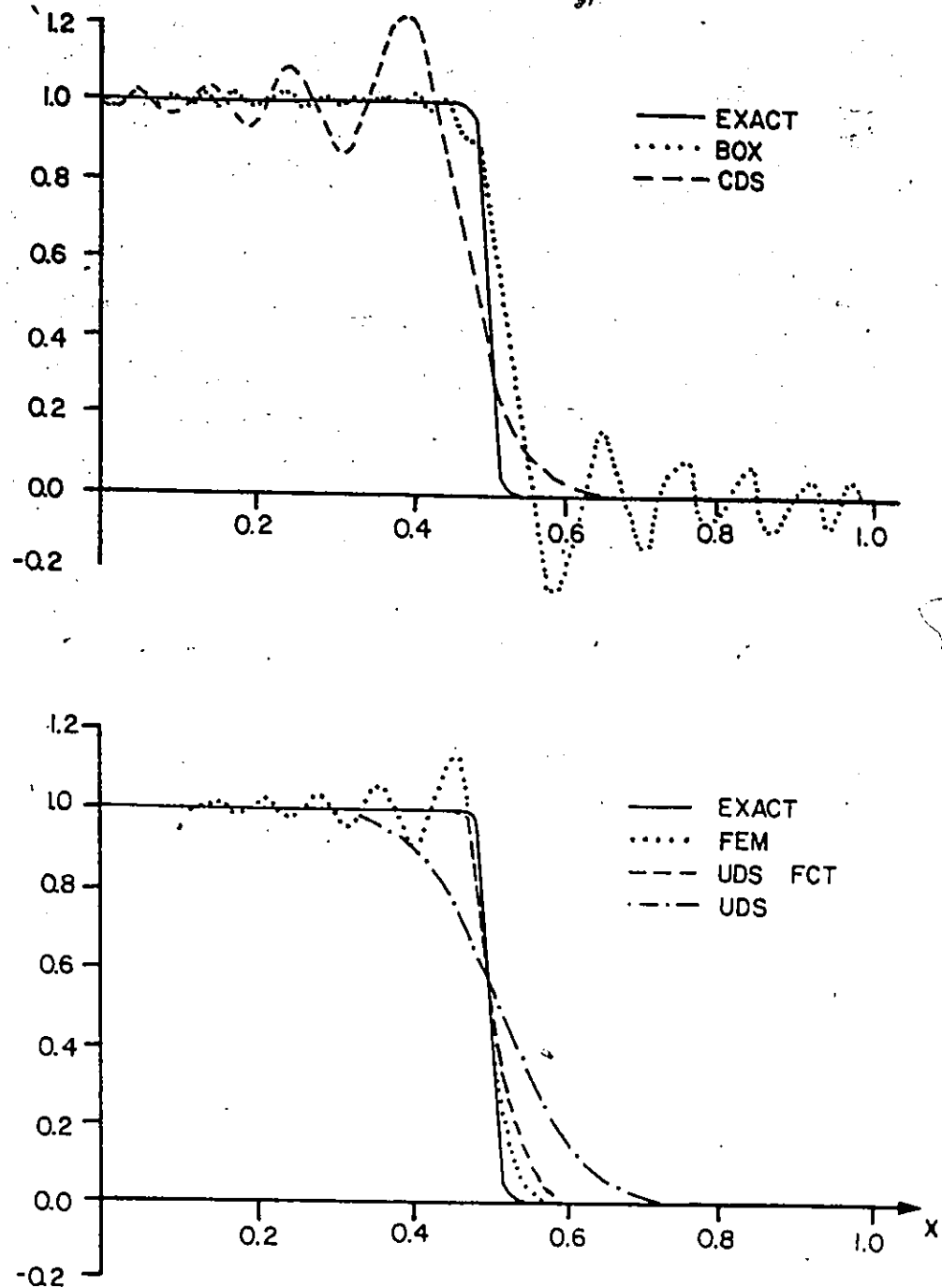


Fig. 3.3 Finite Elements in Space and Time at a Typical Time Step.



BOX = box scheme; CDS = central differencing scheme; FEM = finite element (Galerkin) methods with linear basis function; UDS + FCT = upstream differencing scheme plus flux-corrected transport; UDS = upstream differencing.

Fig. 3.2

Clipping, Overshooting, Dispersion and Negative Concentration Errors in Finite Difference and Finite Element Schemes. After Lam (1978)

isoparametric space-time finite elements. The stability was achieved by incorporating the "method of characteristics" into the finite element method. Varoglu and Finn demonstrated that this technique reduces to the finite element method proposed by Gray and Pinder (1976) for the pure diffusion case. When the diffusion parameter 'K' in equation 3.1 is zero, the problem is that of pure advection and of hyperbolic type. Under these circumstances the technique reverts to the method of characteristics which is superior for hyperbolic equations. A cautionary note that this technique and the method of characteristics as employed in open channel flows have different connotations. Figure 3.4 reproduced from Varoglu and Finn (1978) demonstrates the improvement in the solution for the same problem described in Figure 3.2.

Miller and Miller (1981) and Miller (1981) presented an elegant moving finite element scheme for dealing with problems whose solution develop near-shocks. In this technique the governing equations are transformed to allow displacements of the nodes; the transformed equations are then subject to usual error minimization requirements by a least square method. This step resulted in the normal basis function for the governing equations, while the equation explaining the nodal displacements yields a discontinuous basis function.

This technique was applied by Gelinas et al (1981) to a variety of problems in fluid mechanics. Although the method showed considerable improvements over any existing technique, it introduced four extra parameters with no explanations to relate them to a given problem. Further, all solutions presented were either with a dissipation variable present or the discontinuity already positioned within the domain. No results were shown for a dissipation free problem or where a discontinuity is introduced through the boundaries. Lastly, the technique required very small time

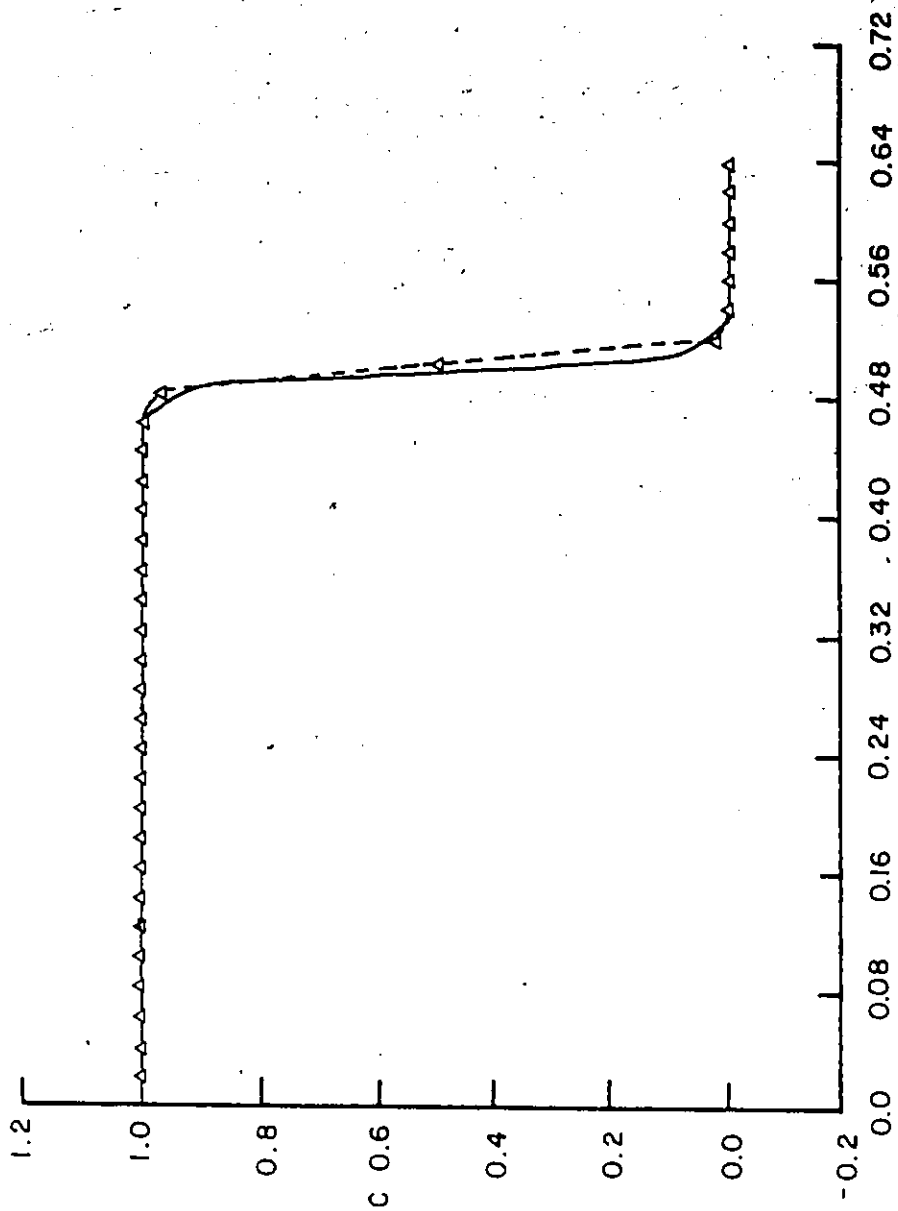


Fig. 3.4 Solution of a Concentration Front Movement by the Space-Time Finite Elements. After Voruglu and Finn (1980)

steps which would have serious implications if the model is adopted for a life-size problem.

Gray (1976) demonstrates that node to node oscillations of length $2 \Delta x$, are common in shallow water equations, and Gray and Lynch (1977) compared the behaviour of a number of time-stepping schemes for simplified tidal equations. In that study, Gray and Lynch used Fourier analysis to examine the fate of $2 \Delta x$ length waves. The analytically obtained modulus and phase of the propagation factor for the following time-stepping methods were compared with the numerically discretized schemes:

- (i) Crank-Nicholson scheme
- (ii) Finite Elements in time
- (iii) Leap Frog scheme
- (iv) Split-Step scheme
- (v) Partially corrected and Second Order Adams-Bashforth scheme
- (vi) Lax Wendroff scheme
- (vii) Two and Three Level Semi-implicit scheme, and
- (viii) Wave equations

Some very interesting and important conclusions were drawn from this work.

Quoting from Gray and Lynch (1977).

"Ten different schemes for marching through time have been analysed. Of these schemes only the Crank-Nicholson, leap frog, split step and wave equations exactly conserve mass and momentum in the absence of friction ... The Lax-Wendroff and finite element in time schemes are both heavily damped. The Lax-Wendroff Scheme does damp the waves length $2 \Delta x$ while the finite element algorithm does not. The wave equation scheme also damps the waves of length $2 \Delta x$ ".

The review further reinforces the dictum that whenever damping is added to a computational procedure, it should be physically realistic and not a convenience to obtain a smooth, though possibly error prone, solution.

3.3 Solution of Open Channel Flow Equations

It is almost universal to employ some form of the St. Venant equations when studying unsteady open channel flow problems. The treatise formulated by Barre De Saint-Venant (1871) also traces to the earlier application of the theory of unsteady flow hydraulics to dam-break problem.

In literature, the St. Venant Equations are found in a variety of equivalent forms. Most of this equivalency is, however, obtained by mere mathematical transformations or by expressing the boundary forces in different forms. Barre De St. Venant (1871) presented the equations as follows

$$\frac{\partial A}{\partial t} + \frac{\partial(AV)}{\partial x} = 0 \quad (3.5)$$

$$\frac{\partial z}{\partial x} = \frac{1}{g} \frac{\partial V}{\partial t} + \frac{V}{g} \frac{\partial V}{\partial x} + S_f \quad (3.6)$$

Subsequently, with discharge being a more easily accessible quantity, the momentum equation has been written in terms of discharge 'Q' instead of velocity 'V' as the dependent variable. Others have also employed a dimensionless form of the equations.

Thus, establishing the common source of the various forms of the governing equation, this literature search is further subdivided into two major categories respecting the nature of the problem. Namely, these are the discontinuous or rapidly varied and continuous or gradually varied flow solutions.

3.3.1 Discontinuous or Rapidly Varied Flow Solution

When compared to other fields in fluid mechanics, the concept of a discontinuity in open channel flows is rare except for the case of a hydraulic jump. Even then, the surface is disturbed to such an extent that the assumption of a truly vertical wall is seldom found. However, it is quite common to refer to flood waves resulting from a dam breach phenomenon or sudden closure of turbine gates (and the subsequent upstream positive wave) as discontinuities.

There are a number of methods available for studying this problem of unsteady, varied flow. These may be broadly divided into (a) hydraulic or dynamic flood-routing method and (b) other simpler flood-routing techniques. The latter group includes purely empirical methods, analogies, hydrologic (or storage) routing, kinematic flood routing and linearization of the St. Venant Equations. It is acknowledged that when steep channel bed slopes are encountered, results from these simpler methods are reasonable. This approach is, however, inadequate for channel of mild slope or when interaction with other land features is significant.

The literature review in this section is limited to dynamic flood routing methods. Reference is made to a number of excellent papers which have provided concise reviews of simpler flood routing techniques. These include Fread (1982), Linsley, Kohler and Paulhus (1982), Miller (1971) and Wurbs (1985). A number of other investigators, Wurbs (1986), Land (1980), Strelkoff et al (1977), to name a few have carried out studies to compare and evaluate various dynamic and simplified routing models.

The solution of dam-break flood routing problems is most commonly achieved using finite-difference methods. With the emergence of the finite element

method as an equivalent and numerically sound alternative, the literature search is next subdivided into finite difference and finite element techniques.

3.3.1.1 Finite Difference Methods

A review of literature has revealed that in most cases the investigators have extended the finite difference techniques used erstwhile in continuous flow situations. Hence, there is little information on thorough numerical treatment for discontinuous flow analysis relying instead on experiences in computational fluid dynamics.

Abbott (1974) provides an excellent dissertation on the numerical techniques for analyzing continuous and discontinuous flows. Abbott raised some fundamental questions about the validity of certain formulations of the energy-momentum equations. The paper resolves this question by resorting to Newton's second law of motion. From this consideration, Abbott maintains that only mass-momentum combination should be used for studying discontinuous flows. This was demonstrated by computing the celerity of the wave and jump conditions for both conservative momentum and energy-based momentum equations. In summary, the following combination of mass-momentum are recommended.

$$\frac{\partial f}{\partial t} + \frac{\partial g(f)}{\partial x} = 0 \quad (3.7)$$

$$f = \begin{bmatrix} h \\ uh \end{bmatrix}, \quad g(f) = \begin{bmatrix} uh \\ u^2h + gh^2/2 \end{bmatrix} \quad (3.8)$$

where the vector 'f' describes "levels" and g(f) represents the corresponding "flux densities". The following combination based on work-energy principle are specifically not recommended

$$f = \begin{bmatrix} h \\ u \end{bmatrix}, g(f) = \begin{bmatrix} uh \\ u^2/2 + gh \end{bmatrix} \quad (3.9)$$

In the foregoing, u is the fluid velocity along x direction, h , the depth of fluid. Equations (3.7) and (3.8) simultaneously satisfy conservation laws for continuous and discontinuous flows and hence are called genuine weak solutions.

Abbott further discusses the non-equivalence of the difference schemes and the differential equations and introduces the ' α -algorithm' for providing a dissipative interface to an otherwise non-dissipative difference equation. Thus

$$f'_i = \alpha f_{i-1} + (1 - 2\alpha) f_i + \alpha f_{i+1} \quad (3.10)$$

$$0 \leq \alpha \leq 0.5.$$

where f'_i is any dependent variable and $0 < \alpha < 0.5$

Abbott concludes with a paradox that the use of a higher Courant number give excellent results which are often marginally better than from a much smaller Courant number. This is argued from the viewpoint that with the higher Courant number information from the boundaries is injected into the interior of the solution domain thus refreshing computation and reducing information loss.

Franz (1977) discusses the problems, pitfalls and partial solutions associated with dam-break flood wave analysis. The paper is divided in two parts; the first part addresses the practical aspects and field problems whereas the other part is devoted to problems related to numerical adequacies and inadequacies. The discussion focusses on variations in the representation of various terms in the shallow water equations. The problems associated with the generalization of techniques developed for prismatic rectangular channels to non-prismatic sections are highlighted and remedies put forward.

Franz acknowledged that for the method of characteristic, conservation errors for discontinuous flows were expected because most techniques are not valid near the discontinuities where characteristics of the same family cross. Such crossing of characteristics indicates the formation of a bore. Terzidis and Strelkoff (1970) also show that errors in conservation result and that the speed of the front of the wave is in error. Franz (1977) traces the problems with conservation in volume to an inconsistency in the approximation of the non-prismatic term.

The paper also explores problems due of nonlinear instabilities associated with nonlinear momentum flux terms together with difference operators which cause the transfer of energy to shorter wave lengths. Such transfer then manifests as oscillations with a wavelength of as $2 \Delta x$. The paper briefly describes the use of the dissipative interface proposed by Abbott, its success for prismatic channels and a general lack of success when applied to non-prismatic channels.

With the foregoing material describing the generalities, attention is now focussed on specific examples in the finite difference methods, their successes or a lack thereof. This discussion addresses the three popular approaches in discretizing the solution domain, i.e. implicit, explicit and characteristic methods.

A. Implicit Method

A number of workers address the problem of near discontinuities as shock waves but most of the experience has been restricted to the fields of hydrodynamics and gas dynamics. Vasiliev et al (1965) address the question of shock wave propagation in the context of open channel flows. Utilizing the work in gas dynamics, the conservation of mass and momentum are derived employing the non-divergent form as a variation of Equations (2.9) and (2.10)

$$\frac{\partial Q}{\partial x} + \frac{\partial A}{\partial t} = 0 \quad (2.9a)$$

$$\frac{\partial Q}{\partial t} + 2v \frac{\partial Q}{\partial x} + (C^2 - v^2) \frac{\partial A}{\partial x} = gA \left[S_o - \frac{\partial h}{\partial x} \Big|_{A=\text{const.}} - \frac{Q|Q|}{K^2} \right] \quad (2.10a)$$

All the variables are as defined in Chapter 2, except for C^2 which is defined in terms of the pressure term (P/ρ) as follows:

$$C^2 = \frac{\partial}{\partial A} \left[\frac{P}{\rho} \right] \quad \text{and} \quad \frac{P}{\rho} = g \int_0^h (h - \xi) b(x, \xi) d\xi \quad (3.11)$$

$b(x, \xi)$ = width at any location x and dependent of its position above the datum

The solution is obtained with a two-stage predictor-corrector scheme employed successfully for solving gas dynamics equation. The time and space derivatives of the first stage at an intermediate time level are given as

$$\frac{\partial f}{\partial t} = \frac{f_i^{k+1/2} - f_i^k}{\Delta t} \quad \text{and} \quad \frac{\partial f}{\partial x} = \frac{f_{i+1}^{k+1/2} - f_{i-1}^{k+1/2}}{x_{i+1}^{k+1/2} - x_{i-1}^{k+1/2}} \quad (3.12)$$

Before the second-level is implemented an averaging operation is performed to reassign the value of the dependent variable, say f , as

$$f_{i+1/2}^{k+1/2} = \frac{3}{8} (f_i^{k+1/2} + f_{i+1}^{k+1/2}) + \frac{1}{8} (f_{i-1}^{k+1/2} + f_{i+1}^{k+1/2}) \quad \text{for } i = 2, \dots, n-2 \quad (3.13)$$

$$f_{i+1/2}^{k+1/2} = \frac{1}{2} (f_i^{k+1/2} + f_{i+1}^{k+1/2}) \quad \text{for } i = 1, n-1$$

At the corrector stage, the equivalent of equation 3-12 was

$$\frac{\partial f}{\partial t} = \frac{f_i^{k+1} - f_i^k}{\Delta t} \quad \text{and} \quad \frac{\partial f}{\partial x} = \frac{f_{i+1/2}^{k+1/2} - f_{i-1/2}^{k+1/2}}{x_{i+1/2}^{k+1/2} - x_{i-1/2}^{k+1/2}} \quad (3.14)$$

Vasiliev et al. provide results from prismatic channel and laboratory experiments.

With the support of a number of agencies, research on dam-break flood modelling was carried out at the University of California at Davis. A total of six models were developed; three of these models were based on the complete St. Venant

Equations while others were simplifications of the same. The findings were presented by Strelkoff et al (1977).

Limiting the discussion to the implicit model, Strelkoff et al. employed a scheme proposed earlier by Vasiliev (1970). This model also used a two-stage predictor-corrector method with one difference. At the predictor step the scheme employs the characteristic form of equations whereas at the corrector stage a momentum-form of the conservation equation is used. The use of the conservation based equation allows the technique to be used in tracking the front. Vasiliev (1970) limits the use to zones above and below the discontinuity while tracing the location and size of the discontinuity by separate equations. The corrector step is executed in an explicit manner, while the predictor step is linearized and fully implicit. The novelty of the Vasiliev scheme is in the discretization of the differential equations using an oblique grid (Figure 3.5) rather than the usual rectangular grid. The derivatives with respect to x and t are then written as:

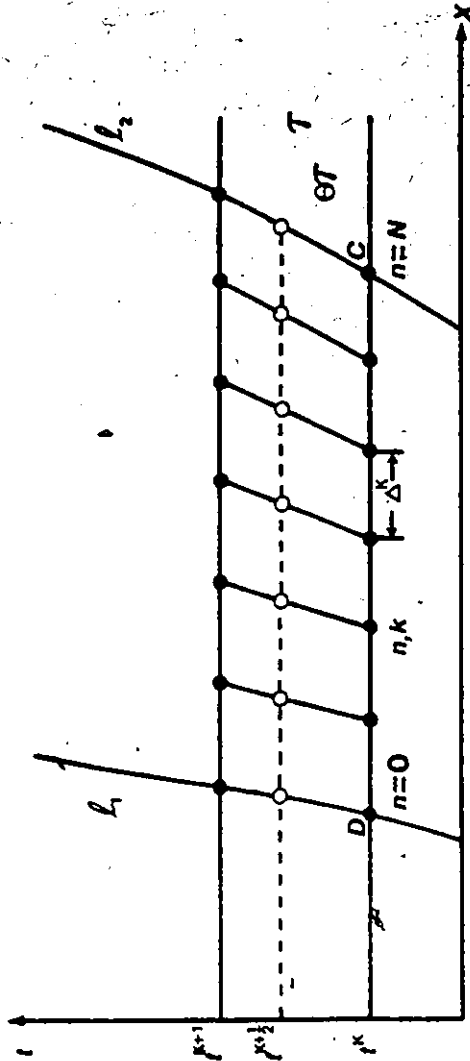
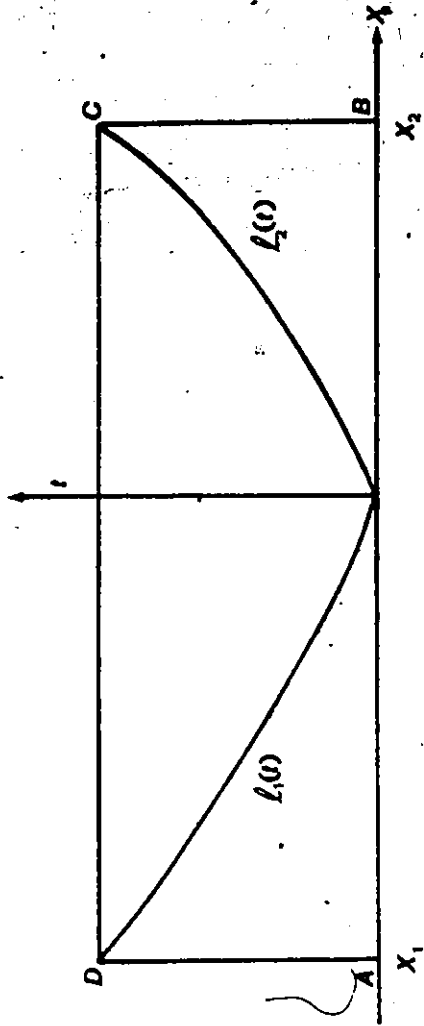
$$\frac{\partial f}{\partial x} = \frac{f_{i+1}^{n+\theta} - f_{i-1}^{n+\theta}}{2\Delta^{n+\theta}} \quad (3.15)$$

$$\frac{\partial f}{\partial t} = \frac{f_i^{n+\theta} - f_i^n}{\theta\Delta t} - \frac{x_i^{n+\theta} - x_i^n}{\theta\Delta t} \cdot \frac{f_{i+1}^{n+\theta} - f_{i-1}^{n+\theta}}{2\Delta^{n+\theta}} \quad (3.16)$$

where 'f' is any dependent variable

At the predictor step the characteristic equations are

$$\begin{aligned} & \left[\frac{\partial Q}{\partial t} + (V \pm C) \frac{\partial Q}{\partial x} \right] + B(-V \pm C) \left[\frac{\partial z}{\partial t} + (V \pm C) \frac{\partial z}{\partial x} \right] \\ & = \left[B S_o + \frac{\partial A}{\partial x} \right]_h V^2 - \frac{gA}{K^2} |Q| Q \end{aligned} \quad (3.17)$$



(a) Domain in which the solution is sought
 (b) The moving grid

Fig. 3.5 Vasiliev's Oblique Grid for the Finite Difference Method.

with all the variables as defined before. The predictor step computes the dependent variables Q and z at an intermediate level, $n + \theta$ with $0 \leq \theta \leq 1$. The equations for the corrector step in explicit mode are written as

$$A_i^{n+1} = \frac{1}{\Delta^{n+1}} \left[\Delta^n A_i^n - \Delta t (Q_{i+1/2}^{n+\theta} - Q_{i-1/2}^{n+\theta}) \right. \\ \left. + A_{i+1/2}^{n+\theta} (x_{i+1/2}^{n+1} - x_{i+1/2}^n) - A_{i-1/2}^{n+\theta} (x_{i-1/2}^{n+1} - x_{i-1/2}^n) \right] \quad (3.18)$$

$$Q_i^{n+1} = \frac{1}{\Delta^{n+1}} \left[\Delta^n Q_i^n - \Delta t \left\{ P_{i+1/2}^{n+\theta} - P_{i-1/2}^{n+\theta} + (QV)_{i+1/2}^{n+\theta} - (QV)_{i-1/2}^{n+\theta} \right\} \right. \\ \left. + Q_{i+1/2}^{n+\theta} (x_{i+1/2}^{n+1} - x_{i+1/2}^n) - Q_{i-1/2}^{n+\theta} (x_{i-1/2}^{n+1} - x_{i-1/2}^n) \right. \\ \left. - Y_i^{n+\theta} \left\{ \frac{z_o(x_{i+1/2}^{n+\theta}) - z_o(x_{i-1/2}^{n+\theta})}{\Delta^{n+\theta}} + \left(\frac{|Q|Q}{K^2} \right)_i^{n+\theta} \right\} \frac{\Delta t}{2} (\Delta^n + \Delta^{n+1}) \right] \quad (3.19)$$

where

$$Y_i^{n+\theta} = g A_i^{n+\theta} \quad (3.20)$$

Strelkoff et al (1977) tested the scheme against other schemes developed for comparison purposes while Vasiliev (1970) reported on applications to natural channels.

Fread (1982) proposed a practical, all encompassing dam break model following success with a similar unsteady state model for continuous flow simulation. The model commonly referred to as DAMBRK employs the "weighted four-point" scheme first proposed by Preissmann (1961). The same scheme was successfully implemented by Chaudhry and Contractor (1973), Fread (1974), and others specifically for dam break flood routing. The model and techniques were compared and evaluated by Wurbs (1986) and Land (1980). Fread (1982) used the energy-based shallow water equations which Abbott (1974) and Franz (1977) have criticized. The

model was improved and modified to take river meandering and off-channel flow into consideration and used the following governing equations

$$\frac{\partial(K_c Q)}{\partial x_c} + \frac{\partial(K_\ell Q)}{\partial x_\ell} + \frac{\partial(K_r Q)}{\partial x_r} + \frac{\partial A}{\partial t} - q = 0 \quad (3.21)$$

$$\begin{aligned} \frac{\partial Q}{\partial t} + \frac{\partial}{\partial x_c} \left(\frac{(K_c Q)^2}{A_c} \right) + \frac{\partial}{\partial x_\ell} \left(\frac{(K_\ell Q)^2}{A_\ell} \right) + \frac{\partial}{\partial x_r} \left(\frac{(K_r Q)^2}{A_r} \right) \\ + g A_c \left[\frac{\partial h}{\partial x_c} + S_{fc} + S_e \right] + g A_\ell \left[\frac{\partial h}{\partial x_\ell} + S_{f\ell} \right] \\ + g A_r \left[\frac{\partial h}{\partial x_r} + S_{fr} \right] = 0 \end{aligned} \quad (3.22)$$

where K_c , K_ℓ , K_r are the flow proportions in the channel, left overbank and right overbank respectively. The variables are defined as follows

$$K_c = \frac{1}{1 + k_\ell + k_r} \quad (3.23)$$

$$K_\ell = \frac{k_\ell}{1 + k_c + k_r} \quad (3.24)$$

$$K_r = \frac{k_r}{1 + k_\ell + k_r} \quad (3.25)$$

in which

$$k_\ell = \frac{Q_\ell}{Q_c} = \frac{n_c}{n_\ell} \frac{A_\ell}{A_c} \left[\frac{R_\ell}{R_c} \right]^{2/3} \left[\frac{\Delta x_c}{\Delta x_\ell} \right]^{1/2} \quad (3.26)$$

Similarly k_r

The friction slope is defined for each component by

$$S_{f_c} = \frac{n_c^2 |K_c Q| K_c Q}{C_c A_c^2 R_c^{4/3}} \quad (3.27)$$

and likewise for S_{fr} and S_{ff} . The factor C_c is 1.0 for metric and 2.208 for Imperial Units. Variable 'A' in Equation 3.21 consist of

$$A = A_c + A_f + A_r + A_o \quad (3.28)$$

In the weighted four-point implicit scheme of Figure 3.6, any dependent variable 'f' is defined as

$$f = \theta \left[\frac{f_i^{n+1} + f_{i+1}^{n+1}}{2} \right] + (1 - \theta) \left[\frac{f_i^n + f_{i+1}^n}{2} \right] \quad (3.29)$$

$$\frac{\partial f}{\partial t} = \frac{f_i^{n+1} + f_{i+1}^{n+1} - f_i^n - f_{i+1}^n}{2 \Delta t} \quad (3.30)$$

$$\frac{\partial f}{\partial x} = \theta \left[\frac{f_{i+1}^{n+1} - f_i^{n+1}}{\Delta x} \right] + (1 - \theta) \left[\frac{f_{i+1}^n - f_i^n}{\Delta x} \right] \quad (3.31)$$

Fread (1977) demonstrates the use of the model by applications to field problems such as the simulation of Teton Dam and Buffalo Creek Dam failures. The model in its present form does not have the capability of operating below a weighting factor of 0.6. Other finite difference implicit models are based on similar algorithms, or further improvements by Fread (1984). All these models offer significant field problem oriented features but shed little light on the mathematical and numerical aspects.

Characteristic Method:

Terzidis and Strelkoff (1970) apply the Characteristic Method to the study of surges and shocks in open channel flow. The momentum-based shallow water equations are used. The paper provides a basic treatment in the algebraic formulation of the shock equations. No modelling was done at that time. Strelkoff et al (1977) presented a characteristic method based computational scheme. This scheme was

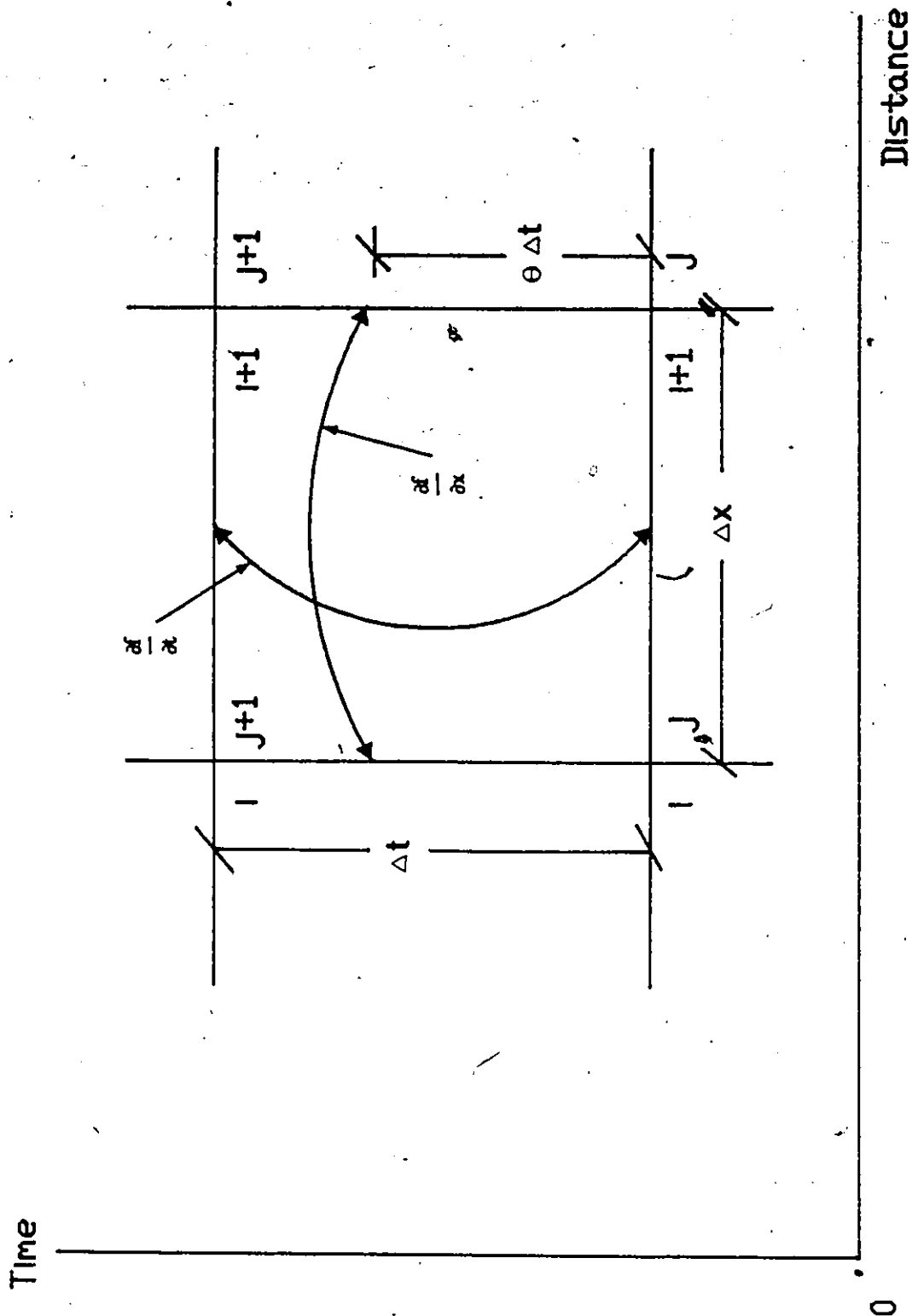


Fig. 3.6 Priesmann's Weighted Four-Point Implicit Scheme.

used as the standard for comparing other four models developed at the University of California, Davis. The paper demonstrates that solutions of the Saint-Venant equations move along the characteristic curves and hence the solution is treated as the one for basis of comparison. The equations employed were of a characteristic form for channels

$$\frac{dV}{dt} \pm \frac{g}{C} \frac{dy}{dt} = g(S_0 - S_f) \mp VC \frac{A_y}{A} \quad (3.32)$$

and

$$\frac{dx}{dt} = V \pm C \quad (3.33)$$

with all the terms as defined before. The resulting four equations solve for the unknowns V and y by an iterative Newton-Raphson method.

Strelkoff et al developed this scheme for studying unsteady flow problems between the advancing discontinuity and the receding negative surge in reservoirs. No applications were presented for field problems and the reported tests are restricted to laboratory flume results.

Chen and Druffel (1977) applied a linked characteristic method and implicit scheme model to simulated dam break problems. The overall model application takes place in two stages. In the stage immediately following dam-break, the Method of Characteristics (MOC) is used for the first few minutes. After the shock has diffused to a certain extent, the linearized implicit model is linked and the computations advanced. The MOC model is based on Equations 3.32 and 3.33 but instead of using a variable grid a fixed space-time grid is employed. The second stage implicit model incorporates a dissipative interface similar to the one proposed by Abbott (1974). The spatial derivatives are fully forward in time and centred in space as follows for any given dependent variable, f .

$$\left. \frac{\partial f}{\partial x} \right|_{i+1/2}^{n+1} = \frac{1}{\Delta x} (f_{i+1}^{n+1} - f_i^{n+1}) \quad (3.34)$$

$$\begin{aligned} \left. \frac{\partial f}{\partial t} \right|_{i+1/2}^{n+1/2} = & \frac{1}{2\Delta t} \left\{ f_i^{n+1} - \left[(1-\alpha)f_i^n + \frac{\alpha}{2}(f_{i+1}^n - f_{i-1}^n) \right] \right. \\ & \left. + f_{i+1}^{n+1} - \left[(1-\alpha)f_{i+1}^n + \frac{\alpha}{2}(f_{i+2}^n - f_i^n) \right] \right\} \end{aligned} \quad (3.35)$$

The authors tested the two models independently in prismatic channel experiments and a rationale was developed on the stage where the two models can be linked. The authors note several advantages and disadvantages in the capabilities and short comings. One of the problems faced by the investigators was the model behaviour when passing through rapidly changing channel geometry.

Chen and Armbruster (1980) improved on the previous work of Chen and Druffel (1977) and furthered the Method of Characteristics. The computational problems associated with rapidly changing geometry was overcome by designating conveyance and off-channel storage zones. The characteristic equations are slightly different from those used earlier by the inclusion of storage width, T_s , as

$$\frac{\partial h}{\partial t} + V \frac{T}{T_s} \frac{\partial h}{\partial x} + \frac{A}{T_s} \frac{\partial V}{\partial x} = \frac{q_L}{T_s} - \frac{V}{T_s} A_x^h \quad (3.36)$$

$$\frac{\partial V}{\partial t} + \frac{\partial V}{\partial x} + g \frac{\partial h}{\partial x} = g(S_o - S_f) \quad (3.37)$$

A linear explicit scheme based on a specified-time interval grid, also known as Hartree's Scheme, was used. The downstream boundary until the time the discontinuity has reached the domain of interest is maintained by the shock equations across the moving front.

As an explicit scheme was employed, a modified Courant conditions developed by Perkins (1968) and adopted by Garrison, et al (1969) was used as follows

$$\Delta t \leq \frac{\Delta x}{|V| + c + \frac{g n^2 |V| \Delta x}{C_c R^{4/3}}} \quad (3.38)$$

where Δt is the time step, Δx is the distance step and other quantities are as defined before. The computer program is based on rewriting the equations in a dimensionless form. The channel geometry was approximated by an asymmetric trapezoid. The model was applied to an actual dam-break case of Laurel Run Reservoir (Chen and Armbruster, 1980). The results were mixed in the sense that the model was capable of handling non prismatic channels while problems related to the attenuated peaks in the discharge hydrographs were noted.

Explicit Methods:

Stoker (1953) and Isaacson et al (1954) used the explicit form of re-derived St. Venant equations to study rapidly varying flows in Ohio-Mississippi River. However, being one of the first applications using digital computers, many simplifying assumptions were made.

Land (1980) carried out an evaluation of four selected dam-break flood-wave models by using field data. Among the four models was an explicit based model developed by Garrison, et al (1969) and maintained by the Hydrological Engineering Centre, U.S. Corps of Engineers. Thomas (1977) has used the same model as part of an investigation by the Corps of Engineers.

The model is called USTFLO or HEC-GVF and employes a leap frog explicit scheme developed by Garrison et al (1969). The space-time grid had the time line going through alternating odd and even computational nodes. The computed values

at the odd nodes were found to be suitable and used for advancing the solutions. The computational grid was spatially uniform. The model is based on the governing equations given by Equations (3.5) and (3.6) and the time step was controlled by Equation (3.38). The computation nodes and grid is depicted in Figure 3.6.

Based on the evaluation carried out and the model documentation provided, it is clear that oscillations are a common problem. Of the three test cases Land (1980) was using, the model failed to provide results for two test cases. It is not known if the reliability of the model was improved when applied to still milder bed slopes. Thomas (1977) applied the model to a slightly larger data set for the Teton Dam failure simulation and reported somewhat erratic behaviour for computed discharges; for example the discharge increased by about 16% some 12 miles downstream of the dam.

Terzidis and Strelkoff (1970) proposed two explicit finite-difference schemes. The momentum based conservation equations are used with the time step controlled by the Courant Condition. The equations representing the discontinuous flow are

$$\frac{\partial q}{\partial x} + \frac{\partial y}{\partial t} = 0 \quad (3.39)$$

$$\frac{\partial q}{\partial t} + \frac{\partial}{\partial x} \left(\frac{q^2}{y} + \frac{gy^2}{2} \right) = gy(S_0 - S_f) \quad (3.40)$$

where q is the discharge per unit width, y the depth of flow and other variables are as defined before. The grids used are presented in Figure 3.8. The discretization procedures for the two methods are as follows

(i) Simple Explicit Scheme

$$y_i^{n+1} = \frac{1}{2} (y_{i-1}^n + y_{i+1}^n) + \frac{\lambda}{2} (q_{i-1}^n - q_{i+1}^n) \quad (3.41)$$

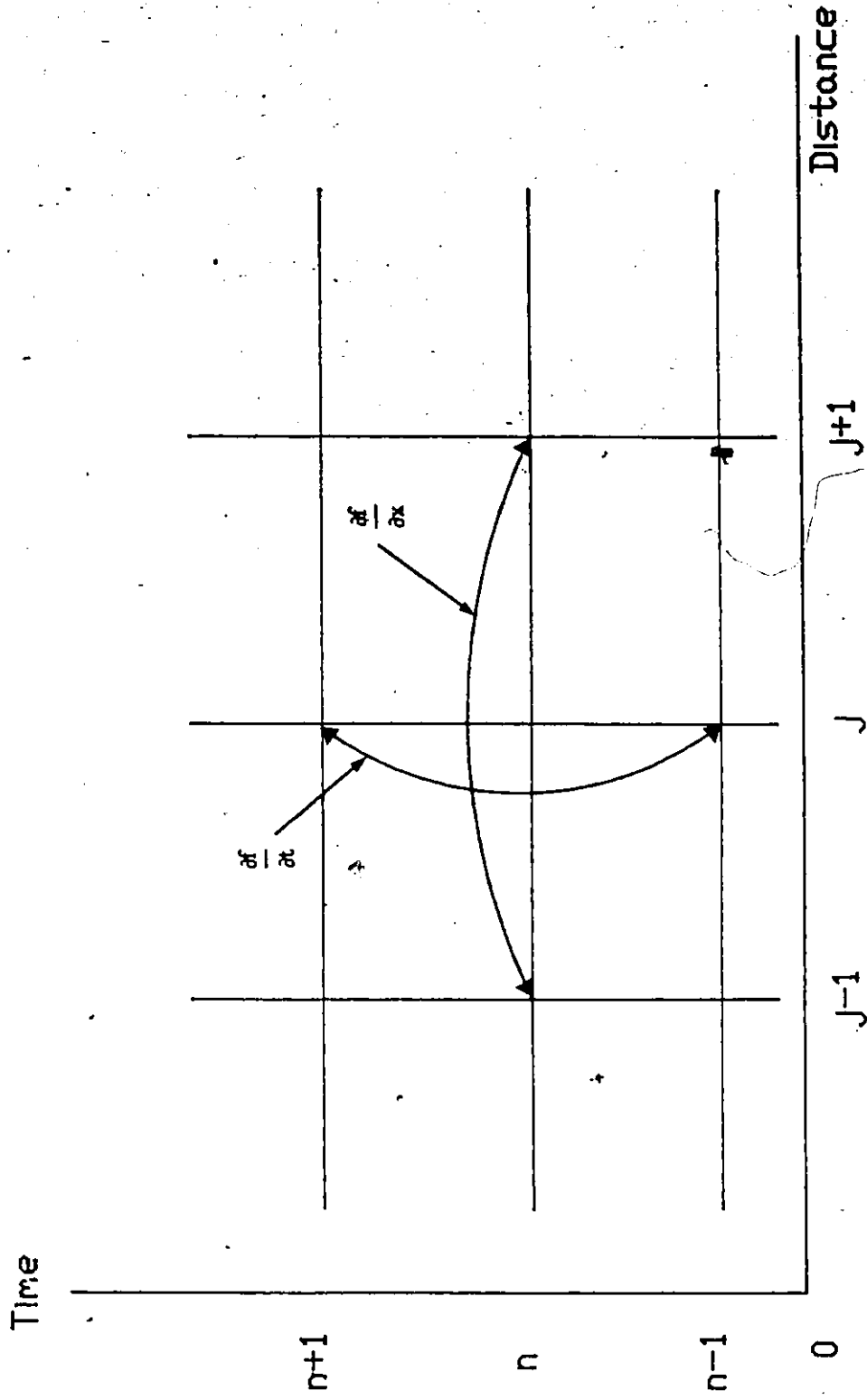
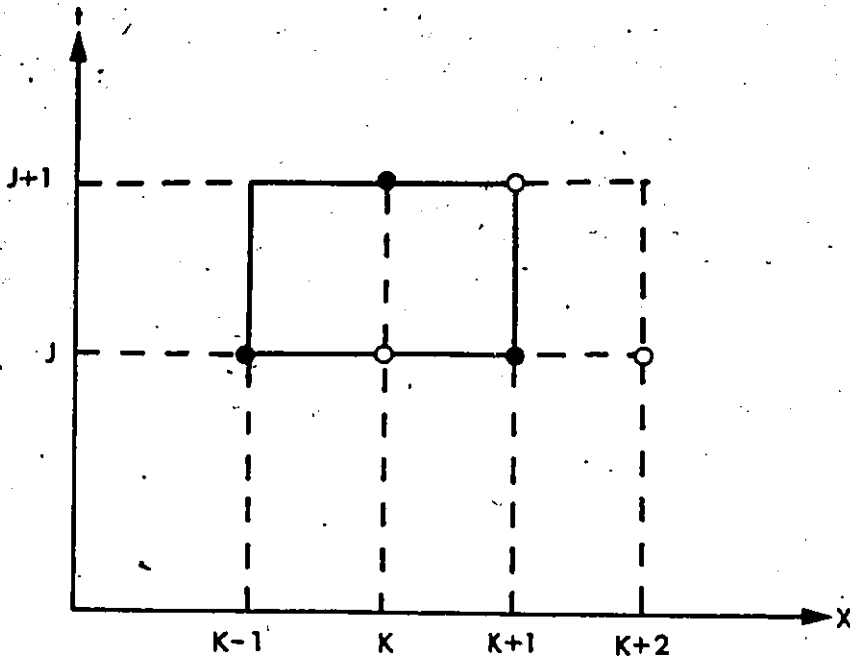
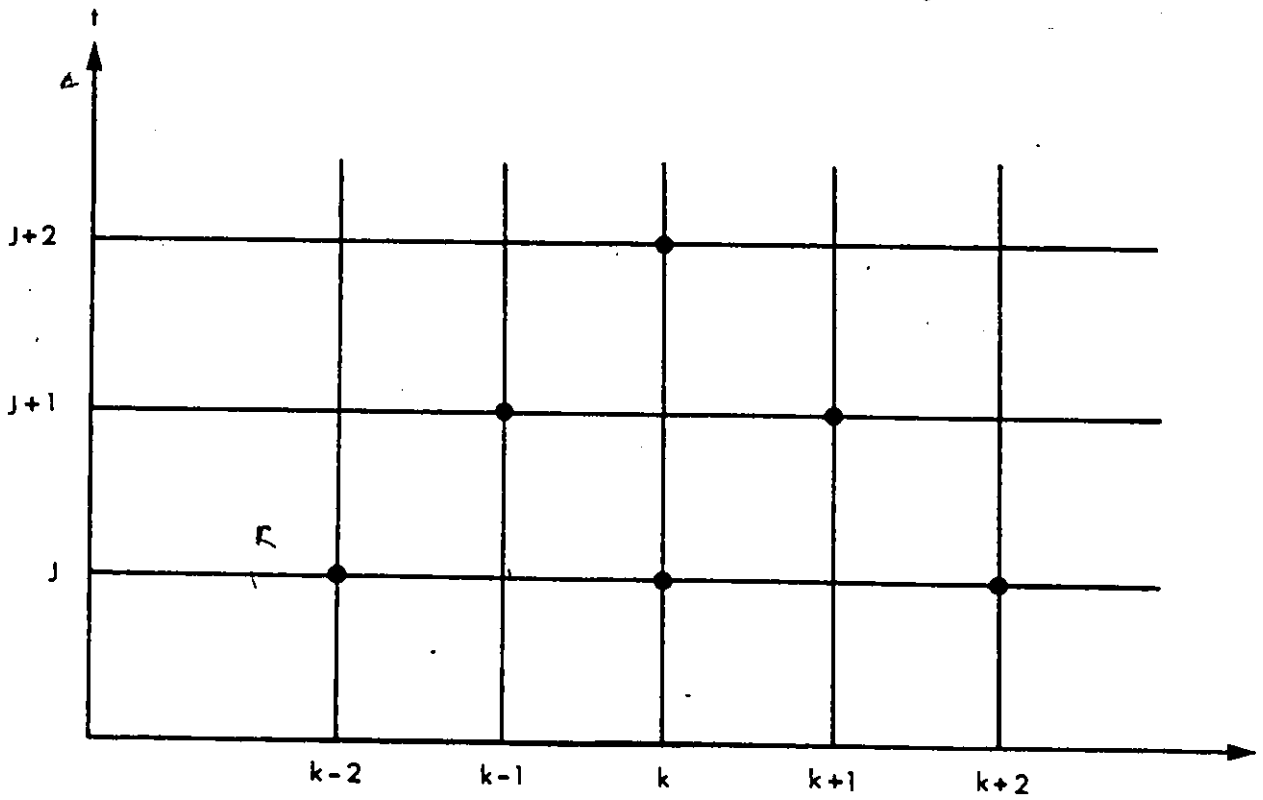


Fig. 3.7 Leap-Frog Explicit Scheme Employed in USTFLO Program.



Simple Explicit Diffusing Scheme



Lax - Wendroff - Richtmyer Two - Step Explicit Scheme

Fig. 3.8 Diffusive One and Two-Steps Explicit Schemes employed by Terzedis and Strelkoff (1970).

$$q_i^{n+1} = \frac{1}{2} (q_{i-1}^n + q_{i+1}^n) + \frac{\lambda}{2} \left[\left(\frac{q^2}{y} + \frac{gy^2}{2} \right)_{i-1}^n - \left(\frac{q^2}{y} + \frac{gy^2}{2} \right)_{i+1}^n \right] + \frac{\Delta t}{2} (\phi_{i-1}^n + \phi_{i+1}^n) \quad (3.42)$$

where

$$\phi = gy (S_o - S_f) \quad (3.43)$$

and the time step Δt is governed by the inequalities

$$\Delta t < \frac{2}{\left| \frac{\partial \phi}{\partial q} \right|} \quad (3.44)$$

and

$$\lambda = \frac{\Delta t}{\Delta x} < \frac{1}{\left| \frac{q}{y} \pm \sqrt{gy} \right|} \quad (3.45)$$

(ii) **The Two-Step Lax-Wendroff-Richtmyer Explicit Scheme**

In the first stage, Equations 3.41 and 3.42 are used in developing intermediate values at time level 'n + 1'. The following equations were used at the second step computation to level 'n + 2'.

$$y_i^{n+2} = y_i^n + \lambda [q_{i-1}^{n+1} - q_{i+1}^{n+1}] \quad (3.46)$$

$$q_i^{n+2} = q_i^n + \lambda \left[\left(\frac{q^2}{y} + \frac{gy^2}{2} \right)_{i-1}^{n+1} - \left(\frac{q^2}{y} + \frac{gy^2}{2} \right)_{i+1}^{n+1} \right] + 2\Delta t \phi_i^{n+1} \quad (3.47)$$

The stability criteria of this scheme is still given by Equations 3.45 and 3.46; however, the accuracy achieved is of a higher order as demonstrated by Richtmyer (1962).

Terzidis and Strelkoff (1970) applied these schemes to several test cases and reported comparable results with other schemes.

3.3.1.2 Finite Element Method

The applications of finite element techniques in open channel flow were introduced by Gunaratnam and Perkins (1970). Cooley and Moin (1976) demonstrated the viability of applying the finite element method for solving the St. Venant equations. King (1976) and Keuning (1976) also used this technique in open channel flow situations.

In the field of open channel hydraulics, the new technique had only a lukewarm reception, with the users of numerical based models clearly favouring finite-difference methods. The problem can be traced to the mathematical basis of the finite element method. Zienkiewicz (1971), Brebbia and Conner (1976) and Pinder and Gray (1972) provide excellent treatment of the finite element method and Galerkin method weighted residuals. Dupont (1973) showed that any Galerkin based technique does not achieve optimal accuracy for hyperbolic problems such as open channel flow in contrast to elliptic and parabolic problems. Katopodes (1984) further argues that "... this was perhaps the serious disadvantage of this otherwise outstanding computational method".

Application of the Galerkin type finite element method usually results in dispersive, non-dissipative behaviour which in turn is responsible for the spurious oscillations. Katopodes (1984) applied a highly selective dissipative interface to the characteristic form of the open channel flow equations. The application demonstrated the capability of the technique to capture a discontinuity without generating oscillations.

Katopodes (1984), following earlier success, developed a dissipative Galerkin scheme for discontinuous flows in open channels. The use is made of a

Petrov-Galerkin type of approximation which the author termed "dissipative Galerkin". The weighting functions for the standard Galerkin and dissipative Galerkin are shown in Figures 3.9 and 3.10. Katopodes used Equations (3.39) and (3.40) with the additional constraint on the momentum equation that the channel is horizontal and frictionless. This makes the right hand side of Equation (3.40) zero. With reference to Figure 3.9, the basis function N_1 and N_2 of the standard Galerkin methods are given as

$$N_1 = \frac{x_{i+1} - x}{x_{i+1} - x_i} \quad (3.48)$$

$$N_2 = \frac{x - x_{i-1}}{x_i - x_{i-1}} \quad (3.49)$$

In contrast, the test function proposed for the dissipative Galerkin approach can be defined as

$$N_1^* = N_1 + \epsilon \frac{\partial N_1}{\partial x} \quad (3.50)$$

$$N_2^* = N_2 + \epsilon \frac{\partial N_2}{\partial x} \quad (3.51)$$

where ϵ is the dissipation parameter which was related to the phase and amplification errors through a Fourier analysis. When the dissipative Galerkin scheme is applied to the continuity and momentum equations, the basis function is not only made orthogonal to the residual error but also to its spatial gradient. After matrix multiplications and other manipulations, Katopodes showed that application of the dissipative method to the continuity and momentum Equations (3.39) and (3.40) is equivalent to applying the standard Galerkin to the following two equations

$$\frac{\partial y}{\partial t} + \frac{\partial q}{\partial x} - \epsilon \left[\frac{\partial^2 q}{\partial x \partial t} + 2u_0 \frac{\partial^2 q}{\partial x^2} + (c_0^2 - u_0^2) \frac{\partial^2 y}{\partial x^2} \right] = 0 \quad (3.52)$$

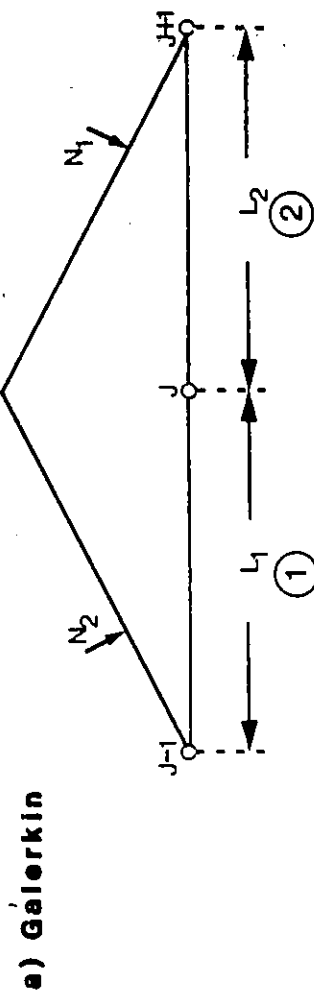


Fig. 3.9 Weighting Function for the Galerkin Scheme

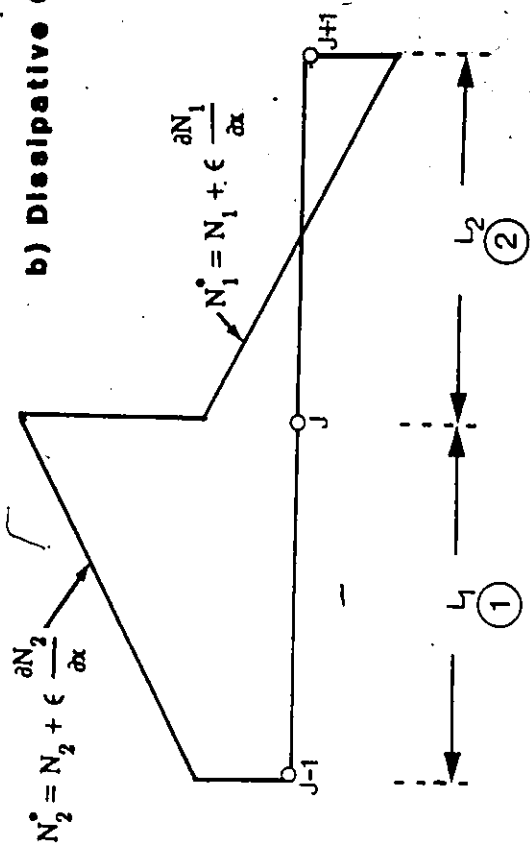


Fig. 3.10 Weighting Function for the Dissipative Galerkin Method.

$$\begin{aligned} \frac{\partial q}{\partial t} + 2u_0 \frac{\partial q}{\partial x} + (c_0^2 - u_0^2) \frac{\partial y}{\partial t} - \epsilon \left[(c_0^2 - u_0^2) \left(\frac{\partial^2 y}{\partial x \partial t} + \frac{\partial^2 q}{\partial x^2} \right) \right. \\ \left. + 2u_0 \left(\frac{\partial^2 q}{\partial x \partial t} + 2u_0 \frac{\partial^2 q}{\partial x^2} + (c_0^2 - u_0^2) \frac{\partial^2 y}{\partial x^2} \right) \right] = 0 \end{aligned} \quad (3.53)$$

where c_0 and u_0 represent the reference celerity and wave velocity respectively. While evaluating, if the mass matrix is diagonalized and ϵ set to Δt , the equations are same as Lax-Wendroff finite-difference method. However, if ϵ is left as a parameter, the resulting equations can be considered as a generalization by providing selective dissipation.

In this regard this was considered as a further generalization of the dissipative interface first proposed by Abbott (1974). By selecting an optimum value of ϵ , the technique was applied to three test runs in frictionless channels of prismatic form. Dramatic improvement over the standard Galerkin method was noted. The author demonstrated that with linear finite elements, the method is no more complicated than a comparable finite-difference method with a much higher accuracy. The selection of ϵ is, however, rather arbitrary and requires much improvement.

In many of the applications two items stood out, a general deterioration of solution with an increase in Courant Number and the presence of a spike at the nose of the surge wave and the development of a shadow wave with increasing dissipation levels. Thus the price of reducing the spike behind the jump is paid by a poorer wave speed and the birth of a shadow wave on the low side of the jump.

3.3.2 Continuous or Gradually Varied Flow Solution:

There has been a considerable thrust in the development of numerical schemes to simulate continuous open channel flows. The conservation of mass and

momentum equations generally used to represent discontinuous flows will provide the basis for the continuous flow solution. It can be proven that the equations where the pressure term is explicitly described, represents the true balance of momentum. Further, it is apparent that when the resistance term dominates the sharp front in a discontinuous flow starts to break down.

With the advancement of the front, the resistance continues to dampen the sharpness to the point that the flow field transforms into a continuous profile. The conservation form of equations that were valid up to this point then are still equally valid. Whereas it is true that momentum equations based on the work-energy concept can no doubt provide correct solution for continuous flows, these fail to balance the momentum on either side of the discontinuity.

The solution of continuous flows can be viewed as the natural progression of a dam-break wave. Various investigators interested in the post failure evaluation of the Teton Dam collapse have agreed on the tremendous attenuation of the wave from approximately 2 million cfs (56,640 m³/s) to 65,000 cfs (1,840 m³/s) some 60 miles (96 km) downstream.

Granted that most of the attenuation took place due to the transition from a canyon to a 50 km wide valley, still the role friction played cannot be overlooked. Thus, any model proposed for computing almost discontinuous flows should also be capable of addressing the continuous flow domain once the friction forces have reduced the wave form considerably. This can be accounted for only by using the divergent form of equations.

The comparisons carried out by Lands (1980) and Wurbs (1986) described several models like DAMBRK, Fread (1982), FLOWSIM1 and FLOWSIM2, USTFLO. Garrison et al (1969) used the non-divergent form of equations. In a Priesmann type

discretization of the partial differential equations into finite-difference forms, there is no error for rectangular-prismatic sections. However, deviations from these combinations could yield unpredictable results due to the errors in preferring a non-divergent scheme for discontinuous flows.

With this preamble and recognizing that a number of excellent comparative studies exist in evaluating different solution schemes for the St. Venant equations, only a small sample is considered and discussed in the following sections.

The criteria subjectively selected are:

- (i) unique solution technique;
- (ii) good documentation;
- and (iii) applications in Canada if possible.

As in the previous section, discussions will be extended to both finite difference and finite element methods.

3.3.2.1 Finite Difference Methods:

There have been several successful applications of the finite-difference solution of the open channel flow equations. Although there have been a significant number of examples in the direct explicit and characteristic methods, direct implicit schemes are most popular despite being most complex and less accurate than characteristic methods. There are a number of reasons for this anomaly.

First consider the characteristic method. This technique, theoretically, provides the most accurate solution. This emanates from the very nature of the hyperbolic equations that any disturbance introduced at the upstream boundary moves along the characteristics. The solution for the prismatic channel is accurate. When this scheme is applied to non-prismatic channels, the results are not predict-

able. One major reason is the change in celerity due to different top widths at adjacent nodes and associated characteristics. Also the explicit characteristic method is restricted by the time step limitations.

Several methods based on the characteristic solution have been proposed since 1960. Lai (1965) provided the step by step details in deriving the governing equations and their solution by the characteristic method. The proposed model was, however, implicit in nature. Others proposing implicit based characteristic models include Amien (1966) and Wylie (1970); whereas explicit characteristic models have been developed by Liggett and Woolhiser (1967), Streeter and Wylie (1967) and Ellis (1970). Characteristic solution grid can be either curvilinear or rectangular in the x-t domain. Abbott (1966) discussed the technique in his book on the characteristic models. Due to the complexities in application of the method to natural channels or to time restrictions, investigators have been discouraged for its use in flood routing. There are no widely used, commercially available computer packages employing this technique.

On the other hand, due to its simplicity, the explicit models gained considerable attention, dating back to the pioneering work of Stoker (1953). There have been a number of reports detailing the method with slight modifications. Liggett and Woolhiser (1967), Martin and DeFazio (1969) and Strelkoff (1970) described the explicit based models. The technique was extended to include estuaries by Dronkers (1969), Ballofett (1969) and Kamphuis (1970). In all these models, there were variations on the type of equations employed, the techniques used for discretizing the equations from the partial differential equations to the finite-difference form. Liggett and Cunge (1975) summarized the different explicit models. One common link which relates all explicit model is the time-step restriction given by Equation (3.38).

Garrison et al (1969) developed an operational model based on the explicit method for flood routing in the Tennessee Valley river and reservoir system. Success was achieved in simulating the movement of disturbances through the system. The model was later adopted by the U.S. Corps of Engineers, Hydrologic Engineering Centre and is maintained and supported by this group. Documented as USTFLO, the model has been used for several studies including dambreak flood routing studies, HEC (1979).

The limitations of the size of time steps imposed for explicit-based methods are largely overcome by discretizing and solving the flow equations by the implicit method. Isaacson et al (1956) presented a concept for the implicit models. Preissmann (1961) and Vasiliev et al (1965) were among the earlier contributors to the implicit method. With the advent and popularity of computers, the implicit based model became very popular in mid 1960s and 1970s. Lai (1965), Baltzer and Lai (1968), Abbott and Ionescu (1967), Dronkers (1969), Kamphuis (1970), Amien and Fang (1970), Contractor and Wiggert (1972), Quinn and Wylie (1972), Fread (1973), Chaudhry and Contractor (1973), Moin (1974), Greco and Panattoni (1975), Amien and Chu (1975), Chen and Simons (1975), Bennett (1975), and Fread (1974) were among the contributors toward the research of implicit based models.

Many of the models described by the workers noted above have been evaluated for stability, accuracy and convergence of the finite-difference forms. Cunge (1966), Abbott and Ionescu (1967), Dronkers (1969), Gunaratnam and Perkins (1970), Fread (1974), Liggett and Cunge (1975) and Ponce and Simons (1977) among others carried out the analysis based on linearized equations. Chaudhry and Contractor (1973), Fread (1974) and Cunge (1975) carried out further analysis of the

effects of large time steps and non linear behaviour and recommended the higher weighting of the terms on the advance time stops.

Basically, the implicit method can be classified in many ways, among others, linear and nonlinear, characteristic form, divergent and non-divergent based momentum equations, six-point and four-point discretization, velocity and flow, depth and stage as dependent variables.

Although several six-point schemes were proposed Vasiliev (1965), Abbott and Ionescu (1967), Moin (1974), the four-point schemes are by far more popular as will be described separately. The six-point scheme requires the nodal spacing to be uniform. Slight increase in computation time occurs when interpolation is required for variables at nodes from irregularly spaced known sections.

Preissmann (1961) proposed a four-point scheme to solve the open channel flow equations. This scheme has since grown to be among the most popular and has been used in numerous studies. The spatial and temporal derivatives of any dependent or derived variable 'f' are given by Equations (3.29) to (3.31). Due to their importance, the equations are repeated here.

$$f = 0.5 \theta (f_i^{n+1} + f_{i+1}^{n+1}) + 0.5 (1 - \theta) f_i^n + f_{i+1}^n \quad (3.29)$$

$$\frac{\partial f}{\partial t} = 0.5 \frac{f_{i+1}^{n+1} - f_{i+1}^n + f_i^{n+1} - f_i^n}{\Delta t} \quad (3.30)$$

$$\frac{\partial f}{\partial x} = \theta \left[\frac{f_{i+1}^{n+1} - f_i^{n+1}}{\Delta x} \right] + (1 - \theta) \left[\frac{f_{i+1}^n - f_i^n}{\Delta x} \right] \quad (3.31)$$

In these equations, when θ is 0.5 it is the classical "box scheme". Investigators soon found that with θ equal to 0.5, large time-steps or rapidly varying hydrographs caused weak or pseudo instability. Fread (1974) and Cunge (1975)

showed that for θ greater than 0.5 and less than 1.0 resulted in smooth solution, albeit at the cost of a dispersive solution. The studies that followed universally adopted θ between 0.55 and 1.0. Recalling that the St. Venant equations when discretized result in non-linear equations, the models that adopted a nonlinear basis generally used θ less than 0.67. The linearized models set θ to be equal to 1.0.

Significant variations exist in the discretization process. For example, Fread (1976) considered averages between nodes exclusively for all variables, others such as Quinn and Wylie (1972) used nodal values; Krishnappen (1981) employed the departures of the dependent variables in the four-point implicit scheme. Walden (1974) and Muir (1976) also adopted variations of this scheme. Price (1974) compared a number of schemes and concluded the weighted four-point implicit scheme to be more versatile and robust when compared to other techniques.

A majority of the models discussed in this section were developed for a specific purpose or were customized for a particular stream. When such models are adopted for other problems, unpredictable results are encountered. Fread (1978, 1982) developed a weighted four-point implicit scheme for natural rivers called Dynamic Wave Operational Model (DWOPER), the model originally developed for flood forecasting in large river systems like the Ohio River and the Mississippi River. Recently the model was adopted successfully on the Saint John River for flood forecasting purposes, MacLaren (1979).

DWOPER has since become one of the most popular implicit based models and a variety of studies testify to its robustness. The model is structured to allow a variety of channel configurations, boundary conditions and several operational features like locks and dams, weir flow over levees, etc. The model was adopted in flood plain management studies to aid in routing flows for mildly sloped streams.

Perks et al (1983) and Moin and Shaw (1984) demonstrated that DWOPER could be used for relatively minor stream systems. DWOPER was developed for the mainframe systems. Patry (1987) reported success in operating the model in a micro computer environment.

3.2.2 Finite Element Method:

When compared to the finite-difference methods, the finite element applications in open channel hydraulics is relatively in its infancy. This coupled with the inherent problems with hyperbolic equations resulted in the finite element method being not a big challenge to the finite difference techniques as was evidenced in fluid mechanics, structural engineering, etc.

One of the earliest applications of the finite element method in open channel hydraulics was by Gunaratnam and Perkins (1970). Calling their technique as an "accurate finite-difference" scheme, Gunaratnam and Perkins applied the method of weighted residuals to the characteristic form of equations. Cooley and Moin (1976) demonstrated that the finite element method can be as effectively applied to the St. Venant equations. King (1976) and Keuning (1976) also furthered the finite element method. Katopodes (1984) developed the Petrov-Galerkin based finite element method specifically for discontinuous flows.

Smith (1979) developed a generalized computer model for river flow simulations. The model developed by Smith named SHP for Stream Hydraulics Package allows for a variety of problems including dambreak problem. Moin (1979) improved on the work of Cooley and Moin (1976) and developed a computerized algorithm for river networks and a dendritic type river system. In all these techniques, the spatial derivatives were discretized by the finite element method

while the time derivative was still approximated by an appropriate finite-difference technique.

All the models described are implicit based and face problems similar to the finite difference methods viz. numerical oscillations for large time steps or rapidly changing boundary conditions. This "problem" is addressed by similar remedies adopted in the finite difference methods. For example Gunaratnam and Perkins (1970) solved linearized equations with the time weighting factor, θ , at 1.0. Cooley and Moin (1976) recommended a value of 0.55 for a predictor-corrector solution.

3.4 On Dissipative and Dispersive Interfaces:

Upon reviewing the material presented in Sections 3.2 and 3.3, we encounter an interesting dichotomy in solving the open channel flow equations. On one hand a purist would like to develop a scheme free from the oscillations, while a practicing engineer is satisfied by an efficient, cost-effective "smooth" solution even if this means sacrificing the accuracy.

The problems associated with high convection in open channel flows, means that forces described by the spatial derivative $\partial/\partial x$ are much greater than the resistive forces defined by the bed roughness. Such problems are similar to those studied by fluid dynamicists for high Peclet Numbers (advection much greater than dispersion). While fluid dynamics problems received significant attention and development of alternative techniques, unfortunately, the same cannot be said about open channel hydraulics.

Abbott (1974) provided the first comprehensive numerical treatment in this field. Strelkoff et al (1977) and Katopodes (1984) also approached the oscillation problem by studying alternate methods and developing new ones. In most other cases

the investigators were satisfied by adopting models from continuous flow situations and modifying them by suitable damping devices. This approach was adopted by Fread (1982) using the same numerical scheme in DWOPER, a continuous flow model, and in DAMBRK a dam-break simulation program. Similar examples can be found in Cunge (1975), Land (1980) and Wurbs (1987).

The problem in solving discontinuous open flows lie in the fact that any finite-difference or finite-element discretization of the differential equation results in a non-dissipative solution. For a frictionless case, then, it means that if a disturbance is introduced, it will continue to propagate without dissipation or dispersion. This is then consistent with the non-dissipative nature of solution. As the resulting finite-difference equations are either non-linear or quasi-linear in behaviour, they would generate nonlinear instabilities or commonly known parasitic waves. The source of this abnormality can be traced to the nonlinear momentum flux (both advection and pressure) terms along with the discrete representation of the solution domain. This combination causes the transfer of "energy" to the shorter wave lengths. This phenomenon is analogous to the one in fluid mechanics where energy transfer occurs from larger eddies to smaller eddies and so on until the Reynolds number is reduced that this mechanical energy is dissipated as heat energy. In a non-dissipative solution scheme, however, this energy cannot be dissipated and gets trapped at the shortest, $2 \Delta x$ length, waves of the numerical solution. This leads to the familiar node to node oscillations.

In natural systems such energy is very easily accounted for by different processes none of which can be easily formulated into the shallow water equations. The node to node oscillations grow to form standing waves which ultimately destroys the true meaning of the solution.

All solution techniques then boil down to devising novel interfaces that are biased towards the short wavelengths. Investigators have used three distinct approaches in overcoming this problem. A précis of these techniques follows.

3.4.1 Isolation of Discontinuity:

In this technique the oscillations are minimized by avoiding the problematic domain, ie. the discontinuity and solving two distinct regimes. These are the shock front satisfied by the Rankine-Hugoniot condition and the gradually varying zones on either side of the discontinuity.

In this method the characteristics of the discontinuities are accounted for by tracing the leading and receding edges by separate equations. Vasiliev (1970) used this approach in tracing the strong discontinuity (leading edge S) and weak discontinuity (receding edge W) by the characteristic equations. The two ends of discontinuities are presented in Figure 3.8. Mathematically, the location of the weak discontinuity, at a distance W, is given by

$$W = (V^- - C^-) \Delta t \quad (3.54)$$

and

$$C^- = \sqrt{g A^- / T^-} \quad (3.55)$$

Where V, C, A and T with negative superscript indicate velocity, celerity, area and effective width on the receding edge side.

The leading edge, on the other hand, requires two pieces of information. The first balances the Rankine-Hugoniot condition across the discontinuity and the second determines the location, S, of the strong discontinuity.

The Rankine-Hugoniot conditions require

$$\left(\frac{P^-}{\rho} - \frac{P^+}{\rho} \right) \left(\frac{1}{A^-} - \frac{1}{A^+} \right) + (V^- - V^+)^2 = 0 \quad (3.56)$$

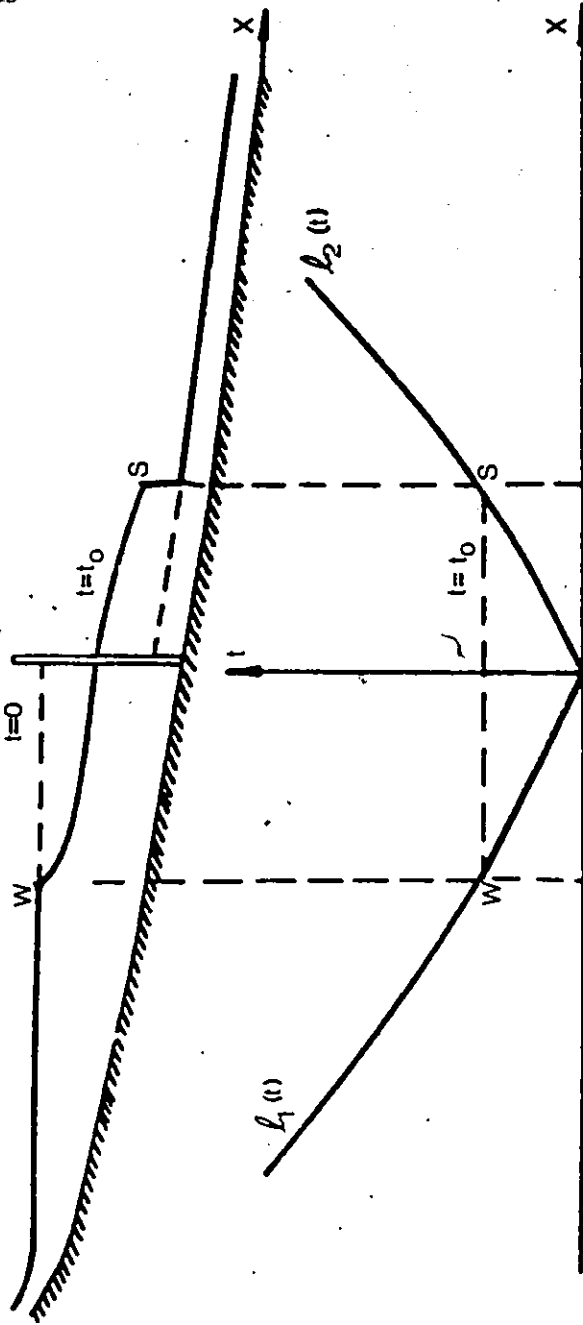


Fig. 3.11 Isolation of Discontinuity by the Characteristic Equations.

$$S = \left\{ v^+ + \sqrt{\frac{A^-}{\rho A^+} \left(\frac{P^- - P^+}{A^- - A^+} \right)} \right\} \Delta t \quad (3.57)$$

where the superscripts "-" and "+" refer to quantities on the left and right side of the discontinuity. P is the first moment of area about the surface.

With this information, the position and height of the discontinuity and the gradually varied flow domain can be computed. There are both advantages and drawbacks in this approach. This approach will be more accurate than a thorough method for a prismatic channel. In a prismatic channel, the tracing of the strong and weak discontinuities is rather straight forward. Also, as only gradually varied flows are analyzed on either side of the discontinuity, most of the shallow water assumptions are valid.

When the analysis is extended to nonprismatic channels, the tracing of the discontinuity becomes difficult depending upon the degree of departure from a prismatic shape. Another complexity arises when there is a possibility of partial reflection of the leading wave at channel geometry changes. In such situations the mathematical computations and wave accounting become extremely tedious.

3.4.2 Dissipative Interfaces and Inconsistent Equations:

By nature all discretization schemes of the St. Venant Equations, be they of finite difference or finite element nature, result in non-dissipative solutions. When these schemes are implemented, especially for rapidly changing boundary conditions or large time steps, node to node, $2 \Delta x$ wave length oscillations develop in the solution. At other times, the nonlinearity of the equations could also lead to similar wiggles.

Thus, the basic objective of incorporating dissipative interfaces is to include, in the solution, a bias towards short wave length oscillations. When a scheme with a dissipative interface is compared without the interface (Figure 3.12), it can be seen that the node to node oscillations have vanished. When the dissipative interface is examined in isolation, it can be reduced usually to higher order terms, which when written in finite-difference and finite-element form lead to oscillations in such a way that the wiggles from the non-dissipative components are neutralized.

Lax-Wendroff (1960) introduced the first of a number of finite-difference and finite element schemes incorporating dissipative interfaces for solving hyperbolic partial differential equations. In most of these cases the provision of interfaces resulted in non-consistent equations. Consistency, here, is defined as when discretization steps are taken to limits, i.e. $\Delta x \rightarrow 0$, $\Delta t \rightarrow 0$, the finite difference formulation should revert back to the partial differential equation. When the resulting equation in limits is different, the finite-difference scheme is said to be non-consistent.

A number of other investigators also used this approach to obtain smooth solutions especially for studying surges. The two schemes of Terzidis and Strelkoff (1970) had their numerical strengths and were discussed in the previous sections. For example, the continuity equation was discretized in an explicit scheme as:

$$y_i^{n+1} = \frac{1}{2} (y_{i-1}^n + y_{i+1}^n) + \frac{\Delta t}{2\Delta x} (q_{i-1}^n - q_{i+1}^n) \quad (3.58)$$

By rearranging the terms, this is equivalent to the partial differential equation

$$\frac{\partial y}{\partial t} + \frac{\partial q}{\partial x} - \frac{(\Delta x)^2}{2\Delta t} \frac{\partial^2 y}{\partial x^2} \quad (3.59)$$

Similar finite-differencing of the momentum equation yield an additional diffusion-like term

Sudden Water Release-Effects Of Dissipation Level

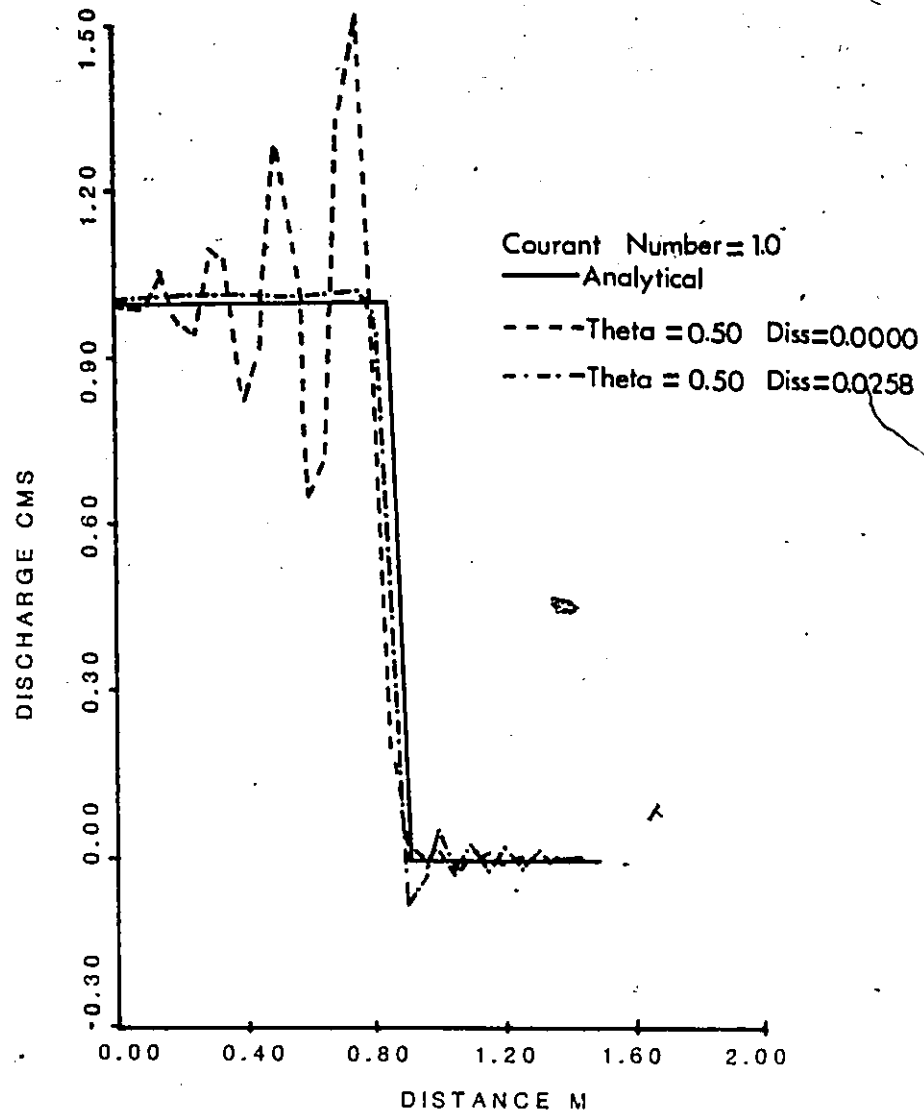


Fig. 3.12

Improvement in a Discontinuous Front solution with a Dissipative Interface. After Katopodes (1984).

$$\frac{(\Delta x)^2}{2\Delta t} \frac{\partial^2 q}{\partial x^2}$$

The very property of this diffusion term is to introduce dispersion, hence the interfaces are sometimes called dispersive.

Abbott (1974) introduced the α algorithm wherein he suggested a dissipative interface in which the value at node 'i' is replaced as

$$f_i^* = \alpha f_{i-1} + (1-2\alpha)f_i + \alpha f_{i+1} \quad (3.60)$$

When employed in the continuity equation, the generalized dissipative term works out to

$$\frac{\alpha(\Delta x)^2}{\Delta t} \frac{\partial^2 y}{\partial x^2}$$

The value of ' α ' can be varied to get the best solution. When α is 0.5, the interface is the same as in Equation 3.55.

Katopodes (1984) employed the Petrov-Galerkin based finite element technique for incorporating a more general dissipative interface which is claimed to be heavily biased towards the $2 \Delta x$ wavelength oscillations. By interpreting the integrated residual equation, Katopodes showed that the use of the Petrov-Galerkin basis function is the same as the Galerkin approximations of the following continuity and momentum partial differential equations:

$$\frac{\partial y}{\partial t} + \frac{\partial q}{\partial x} + \epsilon \left[\frac{\partial^2 q}{\partial x \partial t} + 2u_0 \frac{\partial^2 q}{2x^2} + (c_0^2 - u_0^2) \left(\frac{\partial^2 y}{\partial x^2} \right) \right] = 0 \quad (3.52)$$

$$\begin{aligned} \frac{\partial q}{\partial t} + 2u_0 \frac{\partial q}{\partial x} + (c_0^2 - u_0^2) \frac{\partial q}{\partial x} - \epsilon \left[(c_0^2 - u_0^2) \left(\frac{\partial^2 y}{\partial x \partial t} + \frac{\partial^2 q}{\partial x^2} \right) \right. \\ \left. + 2u_0 \left(\frac{\partial^2 y}{\partial x \partial t} + 2u_0 \frac{\partial^2 q}{\partial x^2} + (c_0^2 - u_0^2) \frac{\partial^2 y}{\partial x^2} \right) \right] = 0 \end{aligned} \quad (3.53)$$

Where u_0 and c_0 are the reference velocity and wave celerity respectively and ϵ is the parameter determining the dissipation level. Although, not fully tested, Katopodes recommended ϵ to be evaluated as

$$\epsilon = \frac{\Delta x}{|u + c| \sqrt{15}} \quad (3.61)$$

The results obtained for three test cases indicate the technique does exhibit a bias by removing the node to node oscillations. There are two points that deserve mention. First, the equations that are solved are not the shallow water equations and second the introduction of ' ϵ ' for achieving the dissipation level reduces the degrees of freedom for solving the problem.

3.4.3 Numerical Damping Devices:

Among the finite difference and finite element methods, one of the most popular techniques used in obtaining a smooth, non-oscillatory solution is the advancing of the temporal weighting parameter. In this approach, the spatial derivatives, instead of being evaluated at mid-point of the time step, are computed at a level closer to the advance time step. Graphically, this is shown in Figure 3.6. It is almost universal to use ' θ ' as the weighting parameter:

In this section, a numerical interpretation of advancing this ' θ ' parameter is provided. The discussion will focus on the popular weighted four-point box scheme, first introduced by Preissmann (1961) and popularized by Cunge (1975) and Fread (1974). Again, for the sake of discussion, reiterating the discretization of a dependent or derived variable, f , and later considering it in the shallow water equation

$$f = 0.5 \theta (f_i^{n+1} + f_{i+1}^{n+1}) + 0.5 (1 - \theta) (f_i^n + f_{i+1}^n) \quad (3.29)$$

$$\frac{\partial f}{\partial x} = 0.5 \frac{f_{i+1}^{n+1} - f_{i+1}^n + f_i^{n+1} - f_i^n}{\Delta t} \quad (3.30)$$

$$\frac{\partial f}{\partial t} = \theta \left[\frac{f_{i+1}^{n+1} - f_i^{n+1}}{\Delta x_i} \right] + (1 - \theta) \left[\frac{f_{i+1}^n - f_i^n}{\Delta x_i} \right] \quad (3.31)$$

This scheme is accurate and results in Crank-Nicolson box scheme for θ equal to 0.5. At this value both spatial and temporal derivatives are second order accurate. Considering only θ values greater than 0.5 the following transformations result:

$$\frac{\partial f}{\partial x} = 0.5 \frac{f_{i+1}^{n+1} - f_i^{n+1}}{\Delta x_i} + 0.5 \frac{f_{i+1}^n - f_i^n}{\Delta x_i} + (\theta - 0.5) \frac{f_{i+1}^{n+1} - f_i^{n+1} - f_{i+1}^n + f_i^n}{\Delta x_i} \quad (3.62)$$

Further evaluation of the third term on the right hand side of Equation (3.62) can be written as

$$(\theta - 0.5) \frac{\Delta t}{\Delta x_i} \left[\frac{\partial f_i}{\partial t} - \frac{\partial f_{i+1}}{\partial t} \right] \quad (3.63)$$

or

$$(\theta - 0.5) \Delta t \frac{\partial^2 f}{\partial x \partial t} \quad (3.64)$$

Substitution of Equation (3.64) in Equation (3.62) gives

$$\frac{\partial f}{\partial x} = \frac{0.5}{\Delta x_i} (f_{i+1}^{n+1} - f_i^{n+1} + f_{i+1}^n - f_i^n) + (\theta - 0.5) \Delta t \frac{\partial^2 f}{\partial x \partial t} \quad (3.65)$$

Similar manipulation of 'f' in Equation (3.30) leads to

$$f = 0.25 (f_{i+1}^{n+1} + f_i^{n+1} + f_{i+1}^n + f_i^n) + \frac{(\theta - 0.5) \Delta t}{0.5} \left[\frac{\partial f}{\partial t} \right] \quad (3.66)$$

The value of $\partial f / \partial t$ is not affected. Substitution of Equations (3.30), (3.65) and (3.66) in the equations of continuity and momentum, lead to the following.

Continuity equation (neglecting lateral flow terms)

$$0.5 \frac{A_{i+1}^{n+1} + A_i^{n+1} - A_{i+1}^n - A_i^n}{\Delta t} + 0.5 \frac{Q_{i+1}^{n+1} - Q_i^{n+1} + Q_{i+1}^n - Q_i^n}{\Delta x_i} + (\theta - 0.5) \Delta t \frac{\partial^2 Q}{\partial x \partial t} = 0 \quad (3.67)$$

Assuming the accurate box scheme to be the starting point, Equation (3.67) is interpreted as

$$\frac{\partial A}{\partial t} + \frac{\partial Q}{\partial x} = (0.5 - \theta) \Delta t \frac{\partial^2 Q}{\partial x \partial t} \quad (3.68)$$

Similarly, the momentum equation is

$$\frac{\partial Q}{\partial t} + \frac{\partial}{\partial x} (Q^2/A) + \frac{\partial}{\partial x} (A \bar{y}) + gA (S_o - S_f) = (0.5 - \theta) \Delta t \left\{ \frac{\partial^2}{\partial x \partial t} (Q^2/A) + \frac{\partial^2}{\partial x \partial t} (A \bar{y}) + \frac{g}{0.5} \left[S_o \frac{\partial A}{\partial t} - \frac{\partial}{\partial t} (A S_f) \right] \right\} \quad (3.69)$$

It is quite obvious from Equations (3.68) and (3.69), that the additional terms on right hand side are implied for θ greater than 0.5. These terms no doubt are dissipative in nature. The finite differences of these terms are less accurate than those on the left hand side making the overall accuracy to be the order of Δx^2 in space and only Δt in time.

Again, at the heart of this numerical interpretation is the fact that the partial differential equations representing the open channel flow are not being solved in their purest form. If Equations (3.68) and (3.69) are compared with, say, Equations (3.59) or (3.61), the parallel properties can be discovered. Thus, there is essentially no difference between dissipative interfaces placed externally or implied by advancing the temporal weighting parameter.

When the six-point discretization is interpreted along the above lines, the results are no different.

3.5 Summary

A literature survey in the fields of convection dominated flows in fluid mechanics and open channel hydraulics of continuous and discontinuous flows have indicated the problem of oscillations in numerical solutions.

Fluid dynamicists have developed several techniques to address problems of oscillatory solutions. These include upwind weighting, reducing distance and time steps, inclusion of dissipative interfaces, flux corrected transport and space-time schemes along the characteristics. Many of the techniques introduced smearing, clipping and distortion of the correct solution. Only the space-time scheme appeared to be provide a reasonable alternative.

Investigators in open channel hydraulics have been generally content to extend the techniques developed for continuous flow situations. A number of shortcomings in handling discontinuous flow analysis was observed. Noteworthy are the use of energy-based momentum equation, including energy like terms to account for losses, incorporating explicit and implied dissipative and dispersive interfaces.

Another area of weakness in the solution of open channel flow equations is the use and misuse of implicit method of solution. A number of researchers did point out that the implicit scheme even though stable for time steps far greater than the Courant conditions, nevertheless, should be restricted to maybe just two times the Courant criteria. This becomes more critical for rapidly varied flow. A number of papers reviewed reported using far greater-time steps disregarding the requirements of resolving the results within the solution domain.

In conclusion, the literature survey identified methodology gaps in the solution of St. Venant equations with respect to alternate techniques for near discontinuous flows. The technique deficiency seemed obvious for schemes that would

not distort or modify the flow equations and at the same time eliminate or significantly reduce the parasitic node to node oscillations. Table 3.1 summarizes the methods reviewed with their strengths and limitations.

Table 3.1

Summary of Reviewed Models and Techniques

Numerical Technique	Strength of Technique	Limitation of Methodology
Finite difference method	Easy to discretize.	Oscillatory solution for sharp fronts.
Finite element method.	Sound and straight forward mathematical basis.	Oscillatory solution. Diffused non-oscillatory solution for Finite Element time integration.
Upwinding finite element method.	Removes node to node oscillations.	Complex basis function. Suppressing more information than oscillations alone..
Advancing temporal weighting.	Selectively removes oscillations. Most popular method.	Dissipated front. Non-consistent equations are resulted.
Dissipative interfaces.	Removes oscillations. Easy to program. Commonly applied.	Non-consistent equations. Ad-hoc basis for selecting dissipation parameter.
Moving finite element method.	Removes oscillations even for sharpest fronts.	Complex basis function. Redundant parameters. Tested for microscale problems.
Petrov-Galerkin based method.	Removes parasitic oscillations. Similar to upwinding.	Non-consistent equations. Extra parameter. Shadow wave develops. Complex basis function.
Lagrangian based method.	Oscillations removed. Integrity of equation preserved.	Tested for one equation case and/or linear problems.

CHAPTER 4

DEVELOPMENT OF METHODOLOGY

4.1 Introduction

The problem defined in Chapter 2 outlined the requirements for simulating discontinuous flows in open channels. Notwithstanding the simplifications and assumptions made in representing the shallow water physics, it was proposed that the technique should be capable of solving St. Venant equations. Further, the scheme should be robust enough to extend the solution to continuous flow situations.

With these constraints, the literature survey identified the problems associated with rapidly varying open channel flows. Almost all schemes required either sacrificing the quality of the solution by artificially introducing dissipative and dispersive interfaces or accepting a more accurate but oscillatory solution

Of the techniques surveyed, a space-time finite element scheme incorporating characteristics for convection dominated flows showed considerable promise. It was decided to develop a solution methodology along similar lines. For reasons that will become evident, the proposed scheme was termed the 'Moving Element Method'.

In this chapter, a detailed description of the technique based on isoparametric space-time elements is presented. The research proposed three numerical integration schemes; these are highlighted and an interpretation provided.

The scheme was developed for a variety of element types to address situations for subcritical and supercritical, direction of flow and boundary conditions.

Initial testing revealed that the idealized moving element method resulted in a non-dissipative solution. Therefore, modifications were provided and these are

discussed in detail. This extension provided a natural interface with a number of interpolation schemes. The proposed technique is further generalized in both temporal and spatial dimensions.

An alternate basis function in the Petrov-Galerkin sense is applied to test the sensitivity of a dissipative parameter. Finally, the methodology is extended to non-prismatic channels including sections with off-channel storage.

The following features of the proposed technique are considered as the contribution of new ideas in open channel hydraulics:

- (1) The space-time finite elements in the Lagrangian frame of reference is the first application of this technique.
- (2) The Eulerian-Lagrangian regridding provides for a natural interface.
- (3) The technique examines alternate forms of upstream boundary elements consisting of a triangular element, a quadrilateral element and a collapsed quadrilateral element.
- (4) Alternate and improved interpolation schemes at the Eulerian step are proposed.
- (5) The technique is generalized in both temporal and spatial sense. These generalizations completely eliminate any spike at the tip of the front.
- (6) The model is flexible to the extent that it could be employed as a finite difference or finite element model.

4.2 Moving Element Solution of St. Venant Open Channel Equations

In view of a number of alternative definitions used throughout this research, it is imperative that a clear meaning of the terms be established. These definitions are further documented in the glossary of terms.

When Varoglu and Finn (1980) generalized the space-time finite element first proposed by Bonnerot and Jamet (1974), it was termed the characteristic method. As the characteristic based methods are deeply rooted in open channel flow equations and do not resemble the proposed technique, an alternate name was required. Space-time finite element technique normally conjures up the rectangular grid in the x-t domain.

Consider the solution by the space-time finite elements at a typical time step as shown in Figure 4.1. For a Eulerian based rectangular grid, the locations X_A and X_D and X_B and X_C are the same. In the proposed technique, the positions X_C and X_D are allowed to move depending upon particle velocity at points A and C. Thus the solution at any given time step is based on a Lagrangian concept. If this process is repeated for a number of time steps, the rays emitting from A and B would eventually move out of the solution domain. From this background, the name 'Moving Element Method' was devised.

As will become evident, alternate forms of this definition are Lagrangian mode or Eulerian-Lagrangian mode solutions. To differentiate the manifestation of solution schemes, consider Figure 4.2 through 4.4.

In Figure 4.2 the Eulerian solution grid is presented. This configuration predestines the locations where the solution will be obtained; in this case, the solution is forced at points A, B, C and D. The discontinuity or a changing boundary is allowed to move across the points of interest. This scenario is similar to that in which the spatial derivatives are discretized by the finite element method and temporal derivative via the finite-difference technique, Cooley and Moin (1976). Moin (1982) in an unpublished report employed space-time finite elements in an Eulerian sense with bilinear elements. This approach breaks down to the same difference equation as

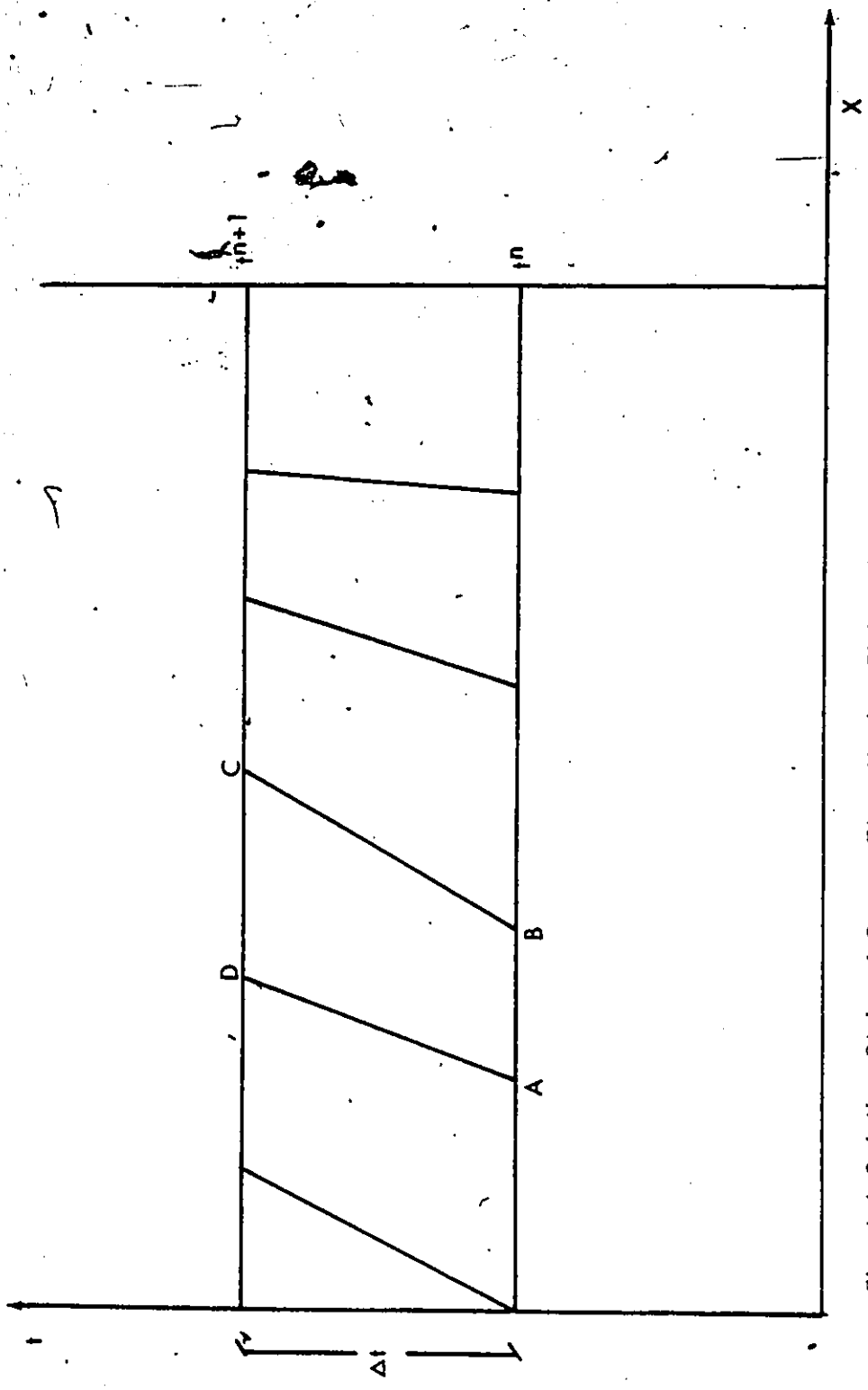


Fig. 4.1 Solution Strip of Space-Time Moving Finite Elements

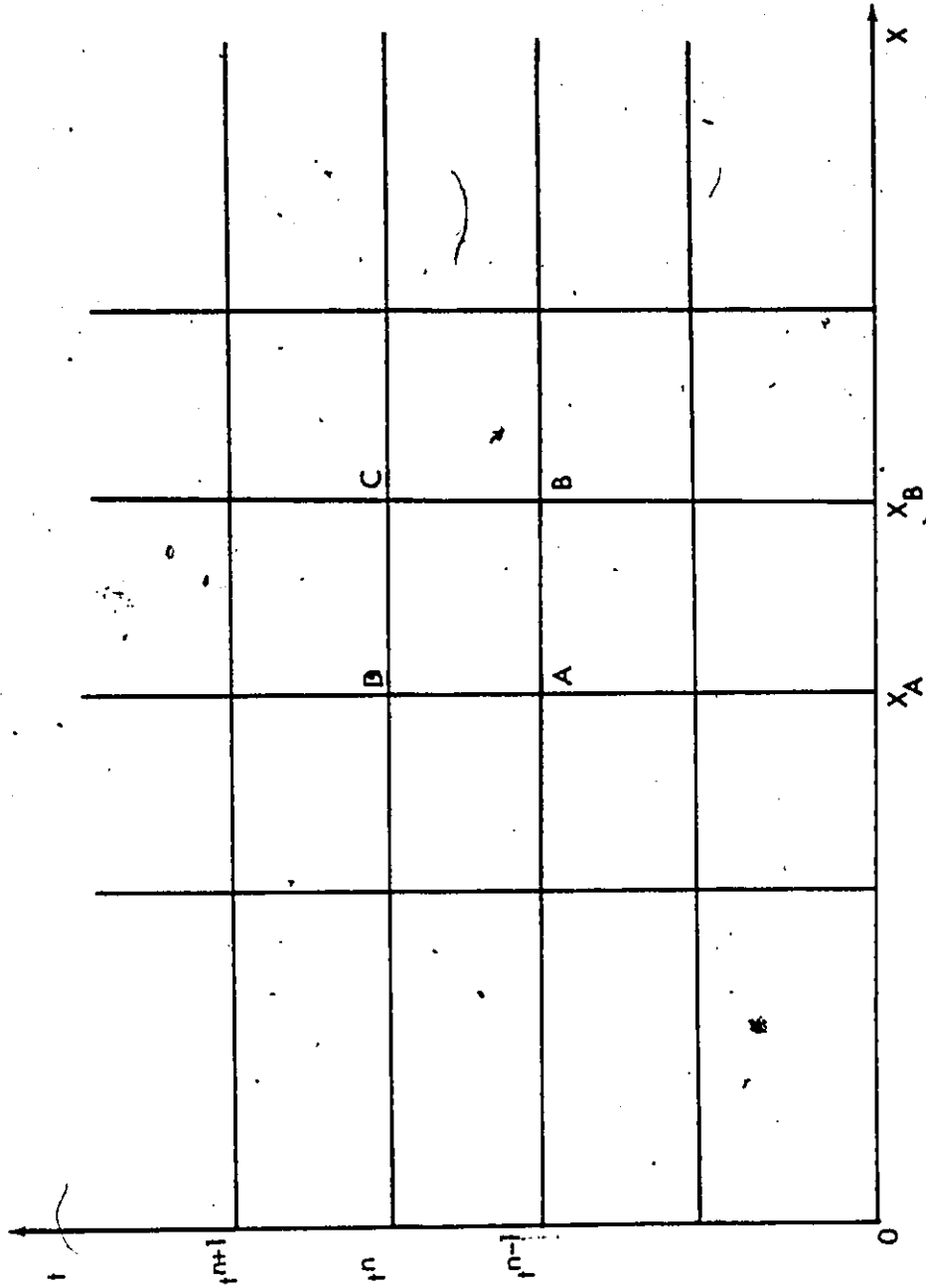


Fig. 4.2 Eulerian Space-Time Grid

described by Cooley and Moin for the temporal weighting parameter θ equalling 0.67. Further, as will be shown later on, this approach produces oscillations for θ equal to 0.5 and smearing for a value of 0.67.

By contrast the Lagrangian solution grid (Figure 4.3) allows points A and B to migrate to D, E and C, F respectively. The relative positions of C and D depend upon the particle velocities at time level t^n . This technique is focussed on in later sections. At the core of this research is the adoption of the Eulerian-Lagrangian concepts and its successful implementation. Figure 4.4 presents the Eulerian-Lagrangian grid as defined within this study context. In this approach, the locations where information is desired are fixed in space at A_0 and B_0 . At any given solution slice between time levels t^{n-1} and t^n , the computation takes place in a Lagrangian sense along ABCD, where points C and D are points A and B displaced by their respective velocities. The moving element scheme computes the dependent variables at points C, D, etc. The values are then interpolated for location A_0 , B_0 , etc. projected at A^1 , B^1 , etc. For example, the values at B^1 are interpolated from the computed flows and depths at C and D. For the next time level, the computations proceed along $A^1B^1C^1D^1$ and the process is repeated.

4.2.1 Governing Equations

There are a multitude of ways of writing the open channel flow equations. The literature surveyed in the last chapter attests to this statement. As noted in Chapter 2, the divergent form of the open channel flow equations will be used in this work.

The divergent form of equations is the only type capable of capturing a surface discontinuity and simultaneously satisfying the Rankine-Hugoniot shock

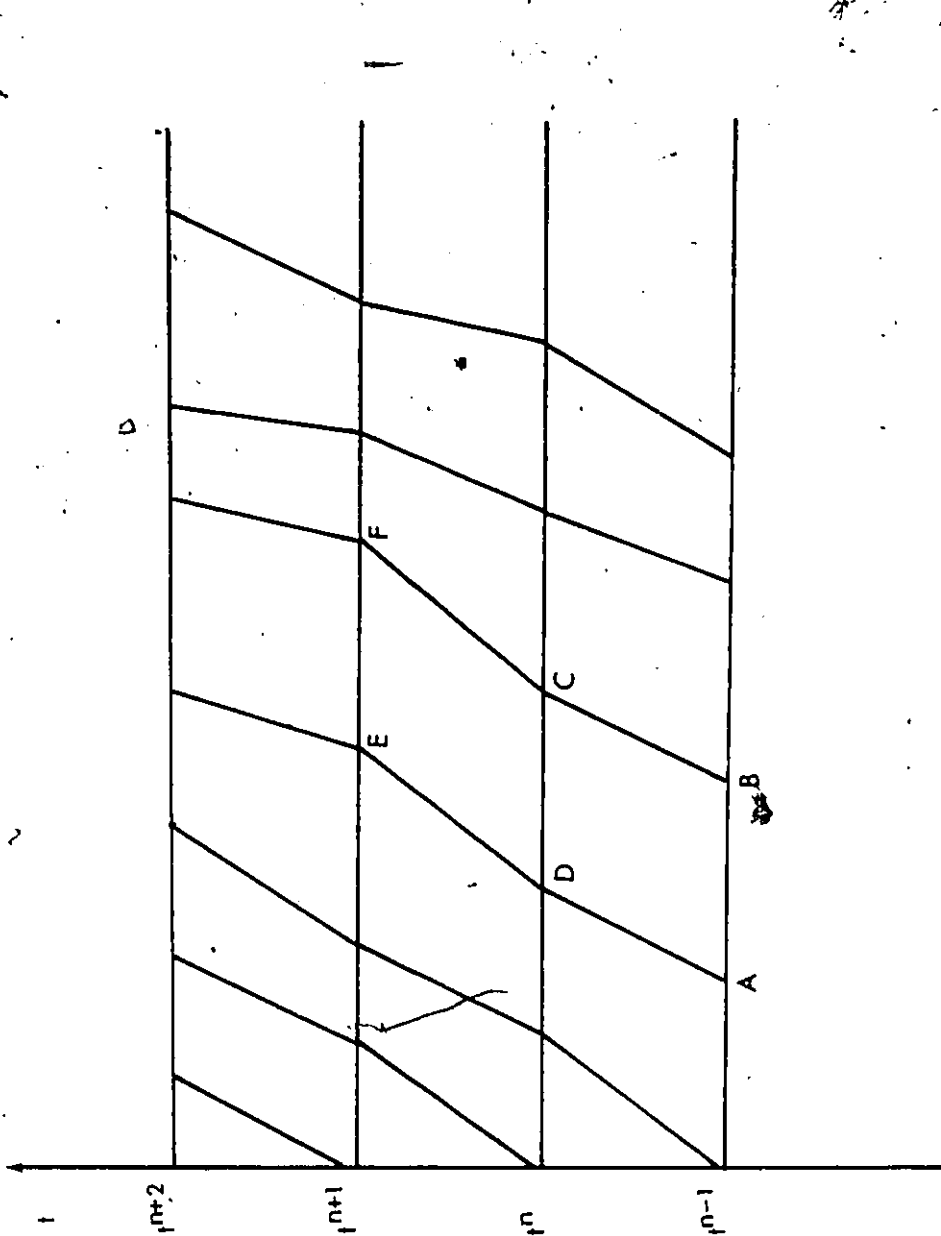


Fig. 4.3 Lagrangian Space-Time Grid

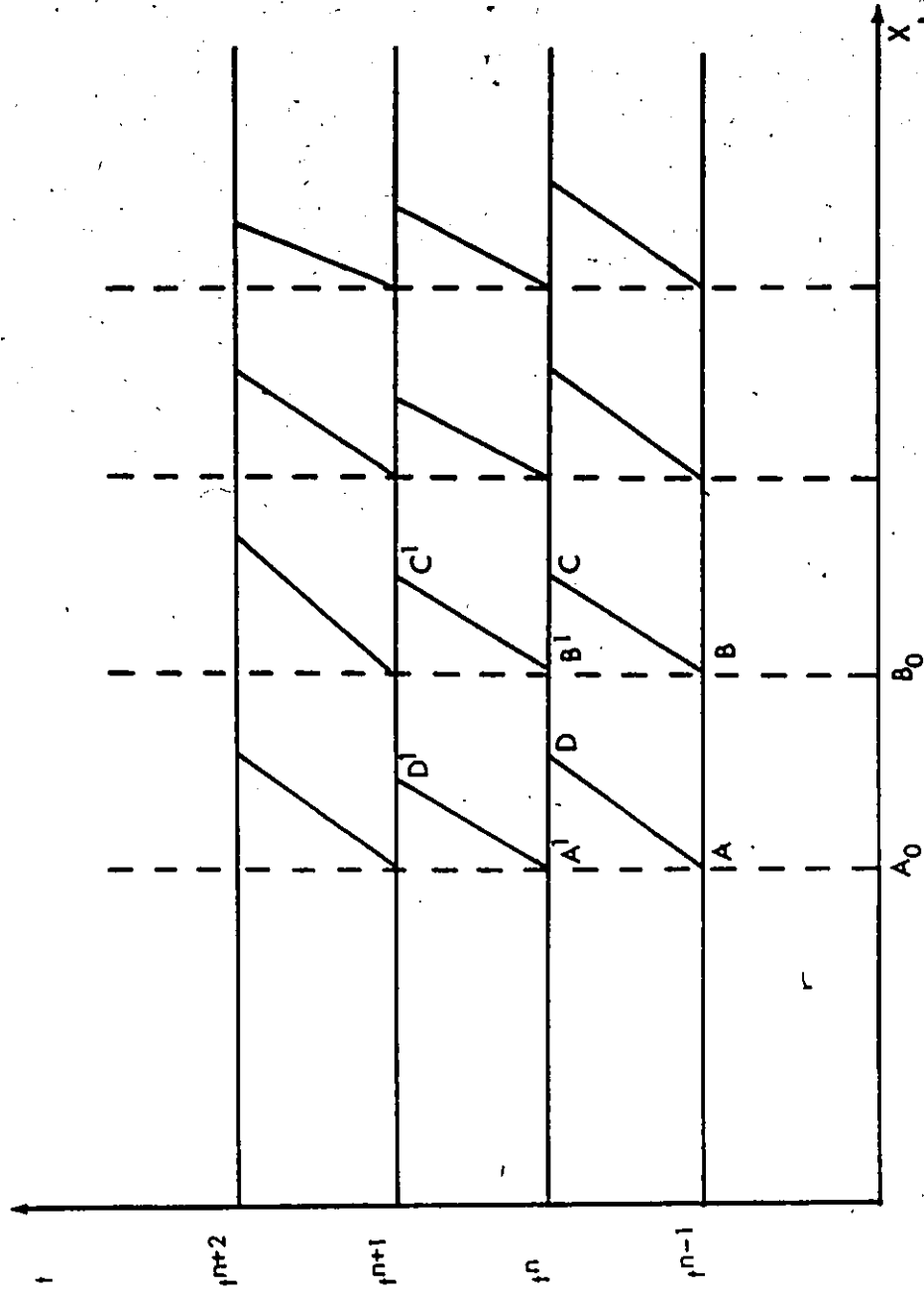


Fig. 4.4 Eulerian-Lagrangian Space-Time Grid

condition. Most of the assumptions used in gradually varied unsteady flows are also in force for studying rapidly varied flow situations. Some of the assumptions may not necessarily be true for rapidly flow conditions, for example the vertical acceleration at the discontinuity may not be small and negligible. Reiterating these assumptions:

1. The vertical acceleration is small or that the pressure distribution along a vertical is hydrostatic. Strictly speaking this condition is violated at the discontinuity.
2. Friction loss approximation are not significantly different from the steady flow conditions.
3. Velocity distribution across the cross-sectional area does not affect the wave motion.
4. The translation of wave is essentially in one direction, ie. the water surface profile across is nearly horizontal.
5. The channel bed slopes are small enough to replace sine of the slope with the value of slope and cosine with unity.

Others like Kuelgen (1946) and Liggett (1975) attempted accommodating the vertical acceleration terms for the completeness of the St. Venant equations by using higher order wave theory.

The divergent form of equations with the flow Q and depth y as the dependent variable are written as:

Conservation of Mass:

$$\frac{\partial A}{\partial t} + \frac{\partial Q}{\partial x} = 0 \quad (4.1)$$

Conservation of Momentum:

$$\frac{\partial Q}{\partial t} + \frac{\partial}{\partial x} (Qu + gA\bar{y}) - gA(S_o - S_f) = 0 \quad (4.2)$$

The definition of the terms is consistent with that in Chapter 2. Equations (4.1) and (4.2) represent unsteady open channel flow in prismatic channels of small slopes and measurable roughness. Other terms usually found in open channel flow analysis like non-prismatic channel forms, lateral flow, etc. are purposely omitted at this point but will be addressed at a later stage.

The solution of Equations (4.1) and (4.2) is not possible without the prescription of the initial and boundary conditions. For subcritical flow condition, the requirements are

Initial Condition:

$$y(x, 0) = f_1(x, Q) \quad (4.3)$$

$$Q(x, 0) = f_2(x, y) \text{ for } x_L \leq x \leq x_R \quad (4.4)$$

Boundary Conditions:

Upstream

$$Q(0, t) = f_3(t) \quad (4.5)$$

or

$$y(0, t) = f_4(t) \quad (4.6)$$

Downstream

$$Q(L, t) = f_5(t) \quad (4.7)$$

or

$$y(L, t) = f_6(t) \quad (4.8)$$

or

$$Q(L, t) = f_7(y(L, t)) \quad (4.9)$$

The requirements for supercritical flow are that both depth, y , and flow, Q , are specified at the upstream boundary and no conditions are required at the down-

stream boundary. The boundary conditions for subcritical flow further require that Equations (4.5) and (4.7) are not simultaneously imposed to avoid trivial solutions.

Following Liggett (1975) in developing second order shallow water equations for depth and flowrate as dependent variables, the resulting momentum equation becomes:

$$\frac{\partial Q}{\partial t} + \frac{\partial(Qu)}{\partial x} + \frac{\partial(gA\bar{y})}{\partial x} - gA(S_0 - S_f) - \frac{1}{3} Ah^2 \left(u \frac{\partial^3 u}{\partial x^3} + \frac{\partial^3 u}{\partial x^2 \partial t} + \frac{\partial u}{\partial x} \cdot \frac{\partial^2 u}{\partial x^2} \right) = 0 \quad (4.10)$$

It can be seen that the much needed higher order terms are present which would help in dissipating the 2 Δx node to node oscillations discussed in the previous chapter. For this research, however, the open channel flow conditions as defined by Saint-Venant in Equations (4.1) and (4.2) along with necessary initial and boundary conditions will be used.

4.2.2 Basis Functions and Isoparametric Elements

A variation of the finite element method is employed, and hence, the method of weighted residuals is used to solve Equations (4.1) to (4.9). Bonnerot and Jamet (1974) employed finite elements in space and time with a variable mesh. Similar notation is used in this work, modified for the two-equation problem, coupled dependent variables and non-linearity of derived variables.

Defining $y(x,t)$ and $Q(x,t)$ as the approximations to the respective solutions of $y(x,t)$ and $Q(x,t)$ of Equations (4.1) to (4.9). Furthermore, let $\phi(x,t)$ be a continuous function in the solution domain in $x \leq x \leq x_R$ and $t_1 \leq t \leq t_2$. The solution at a given time step is depicted in Figure 4.5.

Applying the method of weighted residuals and requiring that the residual with respect to $\phi(x,t)$ vanish

Continuity equation:

$$\int_{t_1}^{t_2} \int_{x_L}^{x_R} \left(\frac{\partial A}{\partial t} + \frac{\partial Q}{\partial x} \right) \phi \, dx \, dt = 0 \quad (4.11)$$

Momentum equation:

$$\int_{t_1}^{t_2} \int_{x_L}^{x_R} \left(\frac{\partial Q}{\partial t} + \frac{\partial (Qu)}{\partial x} + \frac{\partial}{\partial x} (gA\bar{y}) - gAS_o + gAS_r \right) \phi \, dx \, dt = 0 \quad (4.12)$$

for $0 \leq t_1 < t_2$.

Integrating Equations (4.11) and (4.12) by parts and adding lateral flow terms, the conservation of mass and momentum respectively become:

$$\begin{aligned} & \int_{t_1}^{t_2} \int_{x_L}^{x_R} \left(-A \frac{\partial \phi}{\partial t} - Q \frac{\partial \phi}{\partial x} - q\phi \right) dx \, dt \\ & + \int_{x_L}^{x_R} \{A\phi\}_{t_1}^{t_2} dx + \int_{t_1}^{t_2} \{Q\phi\}_{x_L}^{x_R} dt = 0 \end{aligned} \quad (4.13)$$

$$\begin{aligned} & \int_{t_1}^{t_2} \int_{x_L}^{x_R} \left[-Q \frac{\partial \phi}{\partial t} - Qu \frac{\partial \phi}{\partial x} - qA\bar{y} \frac{\partial \phi}{\partial x} - gA(S_o - S_r)\phi - u_x q\phi \right] dx \, dt \\ & + \int_{x_L}^{x_R} \{Q\phi\}_{t_1}^{t_2} dx + \int_{t_1}^{t_2} \{Qu\phi\}_{x_L}^{x_R} dt + g \int_{t_1}^{t_2} \{A\bar{y}\phi\}_{x_L}^{x_R} dt = 0 \end{aligned} \quad (4.14)$$

In order to facilitate the proper interpretation of Equations (4.13) and (4.14), consider the space-time solution strip between time levels t_1 and t_2 and space defined by x_L and x_R . The domain presented in Figure 4.5 also assumes that the flow is moving left to right in such a way that velocities $u(x_L,t)$ and $u(x_R,t)$ are both positive and greater than zero. A more generalized case follows in later sections.

Assuming a generic variable W , the second term in Equations (4.13) and (4.14) implies

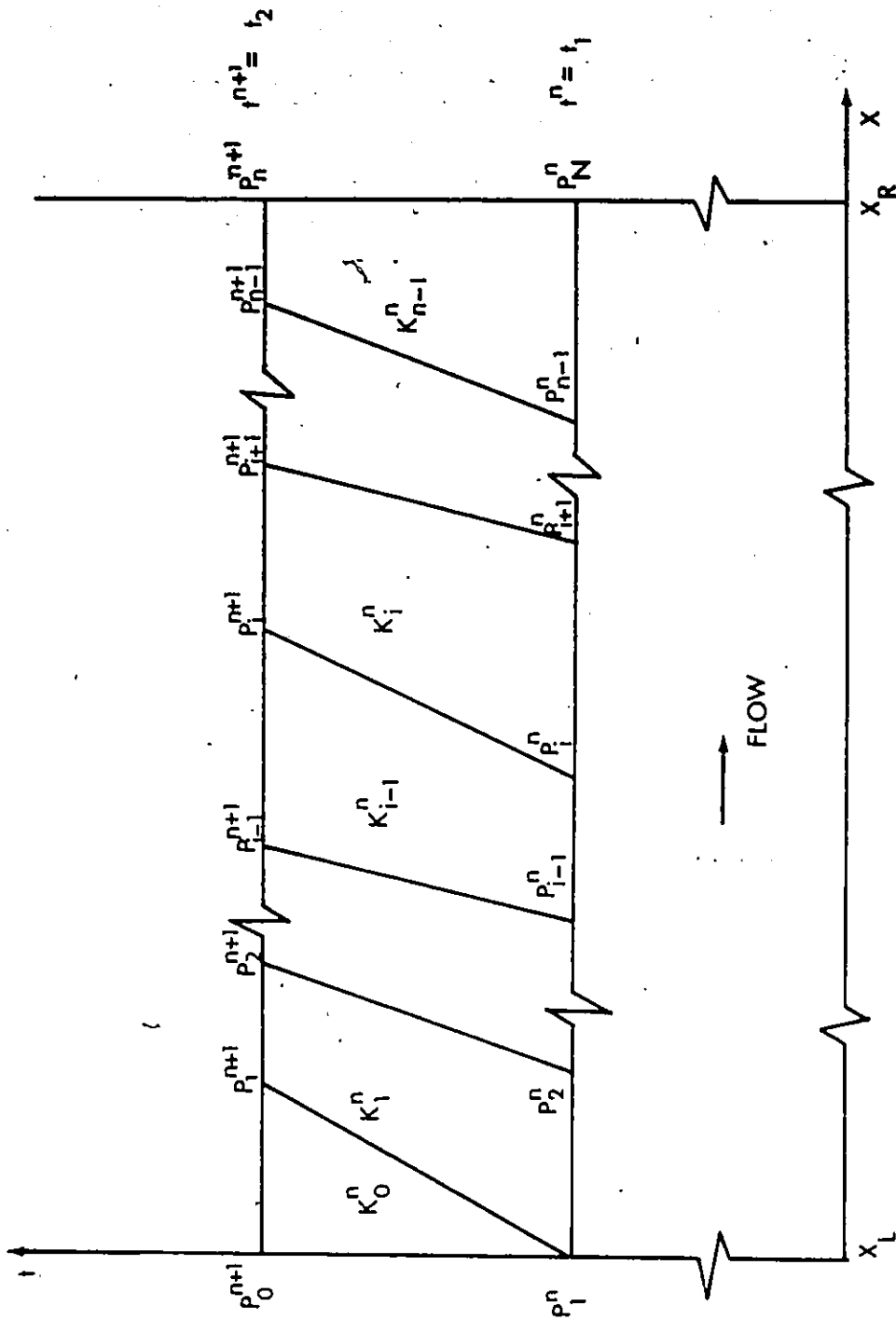


Fig. 4.5 Solution Domain of Space-Time Finite Elements

$$\int_{x_L}^{x_R} -\{W\phi\}_{t_1}^{t_2} dx = \int_{x_L}^{x_R} \{W(x, t^{n+1})\phi\} dx - \int_{x_L}^{x_R} \{W(x, t^n)\phi\} dx \quad (4.15)$$

Similarly, the third term in Equation (4.13) and the third and fourth terms in Equation (4.14) can be interpreted as:

$$\int_{t_1}^{t_2} \{W\phi\}_{x_L}^{x_R} dt = \int_{t_1}^{t_2} \{W(x_R, t)\phi\} dt - \int_{t_1}^{t_2} \{W(x_L, t)\phi\} dt \quad (4.16)$$

Thus both equations compute the line integrals indicating flows across $P_1^n P_N^n$ and $P_0^{n+1} P_N^{n+1}$ by Equation (4.15) and flow volume entering across $P_1^n P_0^{n+1}$ and leaving through $P_N^n P_N^{n+1}$ at x_R . Also, Figure 4.5 indicate but one slice where solution is sought between time levels t^n and t^{n+1} ; the procedure will be the same when extending to advanced time levels. Furthermore, the solution domain defined by $P_1^n P_N^n P_N^{n+1} P_0^{n+1}$ with $x_L < x < x_R$ and $t^n \leq t \leq t^{n+1}$ is discretized by the spatial temporal elements $K_0^n, K_1^n \dots K_{N-1}^n$.

When $t^n = 0$, the values of dependent variables y and Q are known as initial condition and values at point P_0^{n+1} and P_N^{n+1} are either known or related explicitly. As a first step, the solution advances to t^1 . These computed values then become the initial conditions for the next time slice and the procedure is repeated.

At a typical time step, again referring to Figure 4.5, the procedure requires defining two different types of elements. A triangular element defined as K_0^n is required adjoining the left hand boundary to accommodate the "ray" originating at P_1^n . All other elements are trapezoidal in shape.

4.2.2.1 Mathematical Formulation

In the previous section the solution for the depth of flow, $y(x,t)$ and flow rate, $Q(x,t)$ were approximated by function y and Q . Let these approximating

functions be further denoted by y_i^n and Q_i^n representing the values at the node $P_i^n = (x_i^n, t^n)$.

By imposing the conditions that y and Q satisfy the initial conditions given by Equations (4.3) and (4.4), the following equations result:

$$y_i^0 = f_1(x_i, Q_i^0) \quad (4.17)$$

and

$$Q_i^0 = f_2(x_i, y_i^0) \quad (4.18)$$

for $i = 1, 2, \dots, N$.

In applying the finite element approximations to Equations (4.13) and (4.14), the trapezoidal and triangular elements require the transformation of the global $x-t$ coordinate system to an $\eta - \xi$ and $\eta - \xi$ local system. This step allows the approximations and integration on a unit square bounded by $0 \leq \eta \leq 1, 0 \leq \xi \leq 1$, as an example for the trapezoidal element. The trapezoidal element defined by $P_i^n, P_{i+1}^n, P_{i+1}^{n+1}, P_i^{n+1}$ constitute the four vertices and is presented in Figure 4.6 (Page 105).

The procedure developed by Bonnerot and Jamet (1974) is adopted for the two equation system for open channel flow condition. The mapping of a unit square to the typical trapezoidal element is accomplished by co-ordinate transformation. For the element K_i^n as shown in Figure 4.6 can be expressed as

$$t = t^n + \xi(t^{n+1} - t^n) \quad (4.19)$$

$$x = (1 - \eta)(1 - \xi)x_i^n + (1 - \eta)\xi x_{i+1}^{n+1} + \eta(1 - \xi)x_{i+1}^n + \eta\xi x_{i+1}^{n+1} \quad (4.20)$$

Finally, the Jacobian of this transformation derived at a later stage is

$$J_i^n = (t^{n+1} - t^n) \left[(1 - \xi)x_{i+1}^n + \xi x_{i+1}^{n+1} - (1 - \xi)x_i^n - \xi x_i^{n+1} \right] \quad (4.21)$$

By denoting

$$k = t^{n+1} - t^n \quad (4.22)$$

and

$$x_i^{n+\xi} = (1-\xi)x_i^n + \xi x_i^{n+1} \quad (4.23)$$

Equation (4.21) becomes

$$J_i^n = k(x_{i+1}^{n+\xi} - x_i^{n+\xi}) \quad (4.24)$$

Where x_i^n defines the global location of node P_i^n in the $x-t$ plane. Assuming the approximating functions and their derived variables to vary linearly along the side of trapezoid K_i^n , the solution over the element is taken as a polynomial of the form

$$y(\eta, \xi) = (1-\eta)(1-\xi)y_i^n + (1-\eta)\xi y_i^{n+1} + \eta(1-\xi)y_{i+1}^n + \eta\xi y_{i+1}^{n+1} \quad (4.25)$$

$$Q(\eta, \xi) = (1-\eta)(1-\xi)Q_i^n + (1-\eta)\xi Q_i^{n+1} + \eta(1-\xi)Q_{i+1}^n + \eta\xi Q_{i+1}^{n+1} \quad (4.26)$$

A comparison of Equation (4.20) with Equations (4.25) and (4.26) that the same shape functions are used for coordinate transformation, the resulting finite elements have isoparametric properties.

Using similar logic for the triangular element at the left hand boundary, the approximating polynomials for the shape function in local coordinates $\eta - \xi$ are given as

$$x = (1-\eta^1)x_0^{n+1} + (1-\xi)x_1^n + (\eta^1 + \xi - 1)x_1^{n+1} \quad (4.27)$$

$$\bar{y}(\eta^1, \xi) = (1-\eta^1)y_0^{n+1} + (1-\xi)y_1^n + (\eta^1 + \xi - 1)y_1^{n+1} \quad (4.28)$$

$$\bar{Q}(\eta^1, \xi) = (1-\eta^1)Q_0^{n+1} + (1-\xi)Q_1^n + (\eta^1 + \xi - 1)Q_1^{n+1} \quad (4.29)$$

As the nodal values y_i^n and Q_i^n ($i = 1, 2, \dots, N$) are given as initial conditions for $n=0$ and are evaluated and reinitialized for each time steps for $n > 0$ there are $2N+2$ unknowns at the advanced time step. Of these $2N+2$ unknowns, $N+1$ each of 'y' and 'Q', either 'y' or 'Q' is specified at the upstream boundary and either y or Q is specified or y-Q relationship implied at the downstream boundary. This provides two unknowns. There are $N-1$ internal nodes and application of

continuity and momentum equations supply $2N-2$ relationships. As the momentum equations include the continuity equation, this is applied at the boundary nodes along with the boundary conditions. This completes the system of equations.

Recalling Figure 4.5, the solution domain where all the continuous functions are defined on the triangular elements K_0^n by Equations (4.28) and (4.29) and trapezoidal elements

$$K_1^n, K_2^n, \dots, K_{N-1}^n$$

by Equations (4.25) and (4.26). The weighting function ϕ in the solution domain is uniquely established by the nodal values P_i^n ($i = 1, 2, \dots, N$) and P_i^{n+1} ($i = 0, 1, 2, \dots, N$). The function is further defined a priori to vary linearly along the sides of the elements. Following the notation of Varoglu and Finn (1980), defining the function $\phi(x,t)$ for all elements $i = 1, 2, \dots, N-1$ as the function of solutions domain in such a way that

$$\begin{aligned} \phi^{(i)}(P_j^{n+1}) &= 1 && \text{for } i = j \text{ and } i = 1, 2, \dots, N-1, \quad j = 0, 1, \dots, N \\ & && i = 1 \text{ and } j = 0 \\ & && i = N-1 \text{ and } j = N \\ &= 0 && \text{otherwise} \end{aligned} \quad (4.30)$$

$$\begin{aligned} \phi^{(i)}(P_j^n) &= 1 && \text{for } i = j \text{ and } j = 1, 2, \dots, N \\ & && i = N-1 \text{ and } j = N \\ &= 0 && \text{otherwise} \end{aligned} \quad (4.31)$$

Jamet and Bonnerot (1975) used the same weighting functions over the trapezoidal elements successfully for a system of conservation laws. When the discretized weighting function are applied on the individual elements and collected together, $2N+2$ equations in the unknown nodal values of y_i^{n+1} and Q_i^{n+1} are realized with $i = 0, 1, 2, \dots, N$.

The continuity equation becomes

$$\sum_{j=0}^{N-1} \int_{K_j^n} \left(-\bar{A} \frac{\partial \phi^{(i)}}{\partial t} - \bar{Q} \frac{\partial \phi^{(i)}}{\partial x} - q \phi^{(i)} \right) dx dt + \int_{x_L}^{x_R} (\bar{A} \phi^{(i)})_{t^n}^{t^{n+1}} dx - \int_{t^n}^{t^{n+1}} \{ \bar{Q} \phi^{(i)} \}_{x_L}^{x_R} dt = 0 \quad \text{for } i = 1, 2, \dots, N-1 \quad (4.32)$$

The momentum equation takes the form

$$\sum_{j=0}^{N-1} \int_{K_j^n} \left\{ -\bar{Q} \frac{\partial \phi^{(i)}}{\partial t} - \bar{Q} u \frac{\partial \phi^{(i)}}{\partial x} - g \bar{A} \bar{y} \frac{\partial \phi^{(i)}}{\partial x} - g A (S_o - \bar{S}_r) \phi^{(i)} - q (u_x \phi^{(i)}) \right\} dx dt + \int_{x_L}^{x_R} \{ \bar{Q} \phi^{(i)} \}_{t^n}^{t^{n+1}} dx + \int_{t^n}^{t^{n+1}} \{ \bar{Q} u \phi^{(i)} \}_{x_L}^{x_R} dt + g \int_{t^n}^{t^{n+1}} \{ \bar{A} \bar{y} \phi^{(i)} \}_{x_L}^{x_R} dt = 0 \quad (4.33)$$

By definition the weighting function is governed by the equality

$$\sum_{i=1}^{N-1} \phi^{(i)} = 1 \quad \text{for } t^n \leq t \leq t^{n+1} \quad (4.34)$$

$$\text{and } x_L \leq x \leq x_R$$

Examination of Equations (4.32) and (4.33) reveals that when y and Q are satisfied on all elements will also satisfy the following relationships

Mass conservation

$$\int_{t^n}^{t^{n+1}} \int_{x_L}^{x_R} \left[\frac{\partial \bar{A}}{\partial t} + \frac{\partial \bar{Q}}{\partial x} - q \right] dx dt = 0 \quad (4.35)$$

Momentum conservation

$$\int_{t^n}^{t^{n+1}} \int_{x_L}^{x_R} \left[\frac{\partial \bar{Q}}{\partial t} + \frac{\partial}{\partial x} (\bar{Q} u + g \bar{A} \bar{y}) - g \bar{A} (S_o - \bar{S}_r) - u_x q \right] dx dt = 0 \quad (4.36)$$

4.2.3 Numerical Integration

So far the method of weighted residuals has yielded the residuals on the isoparametric elements. In this section the numerical integrations for the basic equation are proposed and implemented.

Recall that the transformations from global coordinates to local coordinates take place according to the relationship.

$$\int_{K_1^n} \phi(x, t) dx dt = \int_A \phi(\eta, \xi) J_1^n(\eta, \xi) d\eta d\xi = \bar{A}_L^{-1}(\phi) \quad (4.37)$$

where J_1^n is the Jacobian of the transformation given by

$$J_1^n = \frac{\partial x}{\partial \eta} \cdot \frac{\partial t}{\partial \xi} - \frac{\partial x}{\partial \xi} \cdot \frac{\partial t}{\partial \eta} \quad (4.38)$$

For any dependent or derived variable defined by S . Following the technique of Bonnerot and Jamet (1974), the integral is evaluated by the Newton-Cotes quadrature formula as

$$\int_A \bar{S}(\eta, \xi) d\eta d\xi = \frac{1}{4} \sum_{s=1}^4 \bar{S}(\bar{P}_s) \quad (4.39)$$

where $P_{s=1,4}$ denotes the four vertices of the unit square mapped by the transformation.

Similarly, the line integral for the element is approximated by the trapezoidal rule as

$$\begin{aligned} \int_{x_i}^{x_{i+1}} \phi(x, t^n) dx &= \frac{x_{i+1}^n - x_i^n}{2} (\phi(x_i^n, t^n) + \phi(x_{i+1}^n, t^n)) \\ &= \bar{L}_{t^n, j}(\phi) \end{aligned} \quad (4.40)$$

When Equations (4.37) and (4.40) are substituted in Equations (4.33) and (4.34), the results are expressed by Equations (4.35) and (4.36). Thus

$$\int_{x_L}^{x_R} \int_{t^n}^{t^{n+1}} \phi(x,t) dx dt = \sum_{i=0}^{N-1} \bar{A}_{L^i}(\phi) \quad (4.41)$$

and

$$\int_{x_L}^{x_R} \phi(x,t) dx = \sum_{i=0}^{N-1} \bar{L}_{t^n, i}(\phi) \quad (4.42)$$

Implementing the above relationships in the continuity equation would result in a system of non-linear equations.

4.2.3.1 Computation of Derivatives

For the sake of brevity, only three typical terms are evaluated, namely a time derivative, a space derivative and a constant. This is accomplished by using an arbitrary function say S given by nodal values as $S_i^n = S_h(P_i^n)$.

(1) Computation of

$$\int_{K_i} \int S_h \frac{\partial \phi^{(i)}}{\partial t} dx dt$$

Noting from Equation (4.30) that $\phi^{(i)}$ is equal to zero on all elements except when $j=i$ and $j=i-1$, therefore

$$\int_{K_i} \int S_h \frac{\partial \phi^{(i)}}{\partial t} dx dt = \bar{A}_{L^i} \left(S_h \frac{\partial \phi^{(i)}}{\partial t} \right) + \bar{A}_{L^{i-1}} \left(S_h \frac{\partial \phi^{(i)}}{\partial t} \right) \quad (4.43)$$

From Equation (4.39) the terms on the right hand side are evaluated by the relationship

$$\bar{A}_{L^i} \left(S_h \frac{\partial \phi^{(i)}}{\partial t} \right) = \frac{1}{4} \sum_{s=1}^4 \bar{S}_h \frac{\partial \phi^{(i)}}{\partial t} J_i^n(P_s) \quad (4.44)$$

The summation is accomplished by evaluating the term at the four vertices of the unit square. First evaluating the value of the Jacobian, from Equations (4.19) and (4.20).

$$\begin{aligned}\frac{\partial x}{\partial \eta} &= (1-\xi)x_{i+1}^n + \xi x_{i+1}^{n+1} - (1-\xi)x_i^n - \xi x_i^{n+1} \\ &= x_{i+1}^{n+\xi} - x_i^{n+\xi}\end{aligned}\quad (4.45)$$

$$\begin{aligned}\frac{\partial x}{\partial \xi} &= (1-\eta)x_i^{n+1} + \eta x_{i+1}^{n+1} - (1-\eta)x_i^n - \eta x_{i+1}^n \\ &= x_{i+\eta}^{n+1} - x_{i+\eta}^n\end{aligned}\quad (4.46)$$

$$\frac{\partial t}{\partial \eta} = 0 \quad (4.47)$$

$$\frac{\partial t}{\partial \xi} = t^{n+1} - t^n = k \quad (4.48)$$

From the above four equations, the value of the Jacobian is

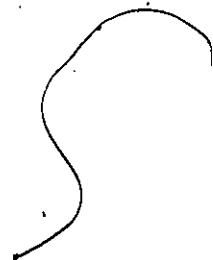
$$J_i^n = k(x_{i+1}^{n+\xi} - x_i^{n+\xi}) \quad (4.24)$$

Similar derivatives are now required for

$$\frac{\partial \phi^{(i)}}{\partial t}$$

First

$$\frac{\partial \phi^{(i)}}{\partial t} = \frac{\partial \phi^{(i)}}{\partial \eta} \frac{\partial \eta}{\partial t} + \frac{\partial \phi^{(i)}}{\partial \xi} \frac{\partial \xi}{\partial t} \quad (4.49)$$



Evaluating from Equations (4.19) and (4.20)

$$\frac{\partial \eta}{\partial x} = \frac{1}{(x_{i+1}^{n+\xi} - x_i^{n+\xi})} \quad (4.50)$$

$$\frac{\partial \eta}{\partial t} = -\frac{1}{k} \frac{(x_{i+\eta}^{n+1} - x_{i+\eta}^n)}{(x_{i+1}^{n+\xi} - x_i^{n+\xi})} \quad (4.51)$$

$$\frac{\partial \xi}{\partial x} = 0 \quad (4.52)$$

$$\frac{\partial \xi}{\partial t} = \frac{1}{k} \quad (4.53)$$

Further, from definition of the basis function $\phi(\eta, \xi) = \phi(x, t)$ is a polynomial of the form

$$\phi(\eta, \xi) = c_0 + c_1 \eta + c_2 \xi + c_3 \eta \xi \quad (4.54)$$

The values of the constants when determined on the vertices as ϕ_i^n etc. yield,

$$\phi(\eta, \xi) = (1-\eta)(1-\xi)\phi_i^n + (1-\eta)\xi\phi_i^{n+1} + \eta(1-\xi)\phi_{i+1}^n + \eta\xi\phi_{i+1}^{n+1} \quad (4.55)$$

Then from Equations (4.30) and (4.31)

$$\frac{\partial \phi^i}{\partial \eta} = \phi_{i+1}^{n+\xi} - \phi_i^{n+\xi} \quad (4.56)$$

$$\begin{aligned} &= -(1-\xi)\phi^i(P_i^n) - \xi\phi^{(i)}(P_i^n) \\ &\quad + (1-\xi)\phi^i(P_{i+1}^n) + \xi\phi^i(P_{i+1}^{n+1}) \\ &= -1 + \xi - \xi = -1 \end{aligned} \quad (4.57)$$

Similarly

$$\frac{\partial \phi^i}{\partial \xi} = \phi_{i+\eta}^{n+1} - \phi_{i+\eta}^n \quad (4.58)$$

$$\begin{aligned} &= -(1-\eta)\phi^i(P_i^n) + (1-\eta)\phi^i(P_i^{n+1}) \\ &\quad - \eta\phi^i(P_{i+1}^n) + \eta\phi^i(P_{i+1}^{n+1}) \\ &= -(1-\eta) + (1-\eta) = 0 \end{aligned} \quad (4.59)$$

Employing Equations (4.51), (4.53), (4.57) and (4.59), the term

$$\frac{\partial \phi^i}{\partial t} = -\frac{\partial \eta}{\partial t} = \frac{1}{k} \frac{(x_{i+\eta}^{n+1} - x_{i+\eta}^n)}{(x_{i+1}^{n+\xi} - x_i^{n+\xi})} \quad (4.60)$$

Substituting Equation (4.60) in Equation (4.44), the area integration becomes

$$\bar{A}_{L^i} \left(S_h \frac{\partial \phi^i}{\partial t} \right) = \frac{1}{4} \sum_{\xi=0}^1 \sum_{\eta=0}^1 S_{i+\eta}^{n+\xi} \frac{\partial \phi^i}{\partial t} \cdot J_i^n \quad (4.61)$$

$$= \frac{1}{4} \sum_{\xi=0}^1 \sum_{\eta=0}^1 S_{i+\eta}^{n+\xi} (x_{i+\eta}^{n+1} - x_{i+\eta}^n) \quad (4.62)$$

Expanding Equation (4.62) results in

$$\bar{A}_{L^i} \left(S_h \frac{\partial \phi^i}{\partial t} \right) = \frac{1}{4} \left\{ (S_i^n + S_i^{n+1})(x_i^{n+1} - x_i^n) + (S_{i+1}^n + S_{i+1}^{n+1})(x_{i+1}^{n+1} - x_{i+1}^n) \right\} \quad (4.63)$$

An examination of the nodal contributions reveals that any one node is connected to no more than two elements. Equation (4.63) describes the contribution to K_i^n element. Following the same logic the contribution to the K_{i-1}^n element

$$\bar{A}_{L^{i-1}} \left(S_h \frac{\partial \phi^i}{\partial t} \right) = -\frac{1}{4} \left\{ (S_i^n + S_i^{n+1})(x_i^{n+1} - x_i^n) + (S_{i-1}^n + S_{i-1}^{n+1})(x_{i-1}^{n+1} - x_{i-1}^n) \right\} \quad (4.64)$$

Adding the contributions from K_i^n and K_{i-1}^n elements the resulting equations is

$$\int_{K_i} \int S_L \frac{\partial \phi}{\partial t} dx dt = \frac{1}{4} \left\{ (S_{i+1}^n + S_{i+1}^{n+1})(x_{i+1}^{n+1} - x_{i+1}^n) - (S_{i-1}^n + S_{i-1}^{n+1})(x_{i-1}^{n+1} - x_{i-1}^n) \right\} \quad (4.65)$$

(2) Computation of

$$\int_{K_i} \int S_L \frac{\partial \phi^{(i)}}{\partial x} dx dt$$

The contributions for this term will be similar to Equation (4.43) as before

$$\frac{\partial \phi^{(i)}}{\partial x} = \frac{\partial \phi^i}{\partial \eta} \cdot \frac{\partial \eta}{\partial x} + \frac{\partial \phi^i}{\partial \xi} \cdot \frac{\partial \xi}{\partial x} \quad (4.66)$$

From Equation (4.57),

$$\frac{\partial \phi^i}{\partial \eta} = -1 \quad (4.57)$$

Equation (4.59) yields

$$\frac{\partial \phi^i}{\partial \xi} = 0 \quad (4.59)$$

and Equation (4.50) gives the value

$$\frac{\partial \eta}{\partial x} = \frac{1}{(x_{i+1}^{n+\xi} - x_i^{n+\xi})} \quad (4.50)$$

From where

$$\frac{\partial \phi^i}{\partial x} = - \frac{1}{(x_{i+1}^{n+\xi} - x_i^{n+\xi})} \quad (4.67)$$

The area integral based on the nodal value is

$$\bar{A}_{L_i} \left(S_h \frac{\partial \phi^{(i)}}{\partial x} \right) = \frac{1}{4} \sum_{s=1}^4 \bar{S}_h \frac{\partial \phi^{(i)}}{\partial x} J_i^n (P_s) \quad (4.68)$$

Substituting Equations (4.24) and (4.67) in Equation (4.68) results in

$$\bar{A}_{L_i} \left(S_h \frac{\partial \phi^i}{\partial x} \right) = \frac{1}{4} \sum_{\xi=0}^1 \sum_{\eta=0}^1 S_{i+\eta}^{n+\xi} \frac{\partial \phi^i}{\partial x} J_i^n \quad (4.69)$$

$$= - \frac{1}{4} \sum_{\xi=0}^1 \sum_{\eta=0}^1 S_{i+\eta}^{n+\xi} k \quad (4.70)$$

Expansion of the above leads to

$$\bar{A}_{L_i} \left(S_h \frac{\partial \phi^i}{\partial x} \right) = - \frac{1}{4} k (S_i^n + S_{i+1}^n + S_i^{n+1} + S_{i+1}^{n+1}) \quad (4.71)$$

Using the same logic employed in the previous computation the contribution for K_{i-1} element is

$$\bar{A}_{L_{i-1}} \left(S_h \frac{\partial \phi^i}{\partial x} \right) = \frac{1}{4} k (S_i^n + S_{i-1}^n + S_i^{n+1} + S_{i-1}^{n+1}) \quad (4.72)$$

Addition of the contributions from K_{i-1} and K_i element results in

$$\int_{K_i} S_h \frac{\partial \phi}{\partial x} dx dt = -\frac{1}{4} k (S_{i+1}^n + S_{i+1}^{n+1} - S_{i-1}^n - S_{i-1}^{n+1}) \quad (4.73)$$

(3) Computation of

$$\int_{K_i} S_h \phi dx dt$$

This is rather straight forward by establishing the relationship

$$\bar{A}_{L_i} = \frac{1}{4} \sum_{\xi=0}^1 \sum_{\eta=0}^1 S_{i+\eta}^{n+\xi} \phi^i(P_{i+\eta}^{n+\xi}) J_i^n \quad (4.74)$$

Substituting for J_i^n from Equation (4.24), noting ϕ^i is equal to 1 when $\eta = 0$ and zero otherwise and expanding the above equation is

$$\bar{A}_{L_i} = \frac{k}{4} \left[S_i^n (x_{i+1}^n - x_i^n) + S_i^{n+1} (x_{i+1}^{n+1} - x_i^{n+1}) \right] \quad (4.75)$$

By adding the contributions from the K_{i-1} element, the resulting equation is

$$\int_{K_i} S \phi dx dt = \frac{k}{4} \left[S_i^n (x_{i+1}^n - x_{i-1}^n) + S_i^{n+1} (x_{i+1}^{n+1} - x_{i-1}^{n+1}) \right] \quad (4.76)$$

4.2.3.2 Computation of Flux Terms

Next the line integrals are evaluated in a similar manner. From Equation (4.40) the line integral was defined as

$$\bar{L}_{t_{i,j}^n}(\phi) = \frac{x_{i+1}^n - x_i^n}{2} \sum_{\eta=0}^1 \left(\phi^i(P_{i+\eta}^n) \right) \quad (4.77)$$

Using this definition the following flux term is evaluated

$$\int_{L_{t_{i,j}^n}} S_h \phi^i dx = \frac{x_{i+1}^n - x_i^n}{2} \sum_{\eta=0}^1 \left(S_{i+\eta}^n \phi^i(P_{i+\eta}^n) \right) \quad (4.78)$$

Noting again ϕ^i is equal to 1 for $n=0$ and zero otherwise leads to

$$\bar{L}_{t_{i,j}^n}(\phi) = \frac{1}{2} (x_{i+1}^n - x_i^n) S_i^n \quad (4.79)$$

Adding contributions of K_{i-1} element results in

$$\int_{L_{t^n}} S_b \phi^i dx = \frac{1}{2} (x_{i+1}^n - x_{i-1}^n) S_i^n \quad (4.80)$$

Similarly,

$$\int_{L_{t^{n+1}}} S_b \phi^i dx = \frac{1}{2} (x_{i+1}^{n+1} - x_{i-1}^{n+1}) S_i^{n+1} \quad (4.81)$$

Lastly, the flux in the time domain at the upstream and downstream boundaries is evaluated in the like manner and defined as follows:

At the upstream boundary

$$\int_{L_{x_L}} S \phi^1 dt = \frac{1}{2} k \sum_{\xi=0}^1 S_{1-\xi}^{n+\xi} \phi^1 (P_{1-\xi}^{n+\xi}) \quad (4.82)$$

In this case ϕ^1 is equal to 1 for both values of ξ . Therefore,

$$\int_{L_{x_L}} S \phi^1 dt = \frac{k}{2} (S_1^n + S_0^{n+1}) \quad (4.83)$$

In a like manner the relationship for the downstream boundary is

$$\int_{L_{x_R}} S \phi^N dt = \frac{k}{2} (S_N^n + S_N^{n+1}) \quad (4.84)$$

It should be noted that the discretized relationship derived in the foregoing section and described by Equations (4.65), (4.73), (4.76), (4.80) and (4.81) is representative of the interior nodes. There are five different type of contributions from the nodes in view of the boundary element influence. Recalling Figure 4.5 the elements are divided as follows:

- | | |
|--------|--|
| Type 1 | for K_0^n contributions and boundary conditions |
| Type 2 | for K_0^n and K_1^n contributions and/or boundary conditions |
| Type 3 | for $K_1^n, K_2^n, \dots, K_{N-1}^n$ contributions |
| Type 4 | for K_{N-2}^n and K_{N-1}^n contributions and/or boundary |
| Type 5 | for K_{N-1}^n contributions and boundary conditions |

The relationships derived so far are valid only for Type 3 elements. Contributions are significantly different for the other types. For brevity, the contributions for Type 2, 4 and 5 will not be derived but will be presented in the final form. Type 1 elements deserve special consideration and are discussed in the following section. The overall contribution framework is established after the boundary conditions are incorporated.

4.3 Boundary Elements

The contributions of the elements at the two extreme boundaries (Type 1 elements) play an important role in the overall harmony of the model. For any six-point implicit scheme, such as the one resulting in this work, handling of the boundary conditions poses a difficult and tricky problem. In this section, new methods are proposed to overcome such difficulties.

As $N + 1$ nodes are in consideration, there are $2N + 2$ equations and $2N + 2$ unknowns. At the two boundary nodes the continuity equation is replaced by the specified flow or depth or flow-depth relationship, the momentum equation is retained. The various terms in the momentum equation do weakly mimic the mass continuity relationship.

In the following sections the derivations of boundary contributions are based on positive velocity at the upstream boundary. When the flow movement is reversed it requires slight modifications in the terms.

4.3.1 Upstream Boundary

When the flood movement is such that it causes positive velocities to occur at the upstream boundary node, then a ray is required at this point. This ray will be

slanted into the solution domain necessitating a triangular element at the upstream boundary. Two approaches were attempted in representing the triangular element. The first and most obvious choice is to treat the element as a triangular element as shown in Figure 4.7(a).

A second alternative was devised in which the triangular element was achieved by collapsing the side at the known time level. This process is shown in Figure 4.7(b).

These two types of elements are next described for each of the subcritical and supercritical flow conditions.

4.3.1.1 Triangular Element

The natural form of element at the upstream boundary is a triangular element. Varoglu and Finn (1980) introduced the concept of mixed triangular and trapezoidal elements. This was modified for a two-equation system and implemented.

As before contributions for any given dependent or derived variables, say, S is obtained. Figure 4.8 depicts a triangular element represented by $P_1^n P_1^{n+1} P_0^{n+1}$ and the element designated as K_0^n .

The time approximation is the same as before in Equation 4.19.

$$t = t^n + \xi(t^{n+1} - t^n) \quad (4.19)$$

However, the shape function ϕ and space approximation now become

$$x = (1 - \xi)x_1^n + \xi x_1^{n+1} + (\eta^1 - 1)(x_1^{n+1} - x_0^{n+1}) \quad (4.85)$$

and

$$\phi^0 = (1 - \xi)\phi^0(P_1^n) + \xi\phi^0(P_1^{n+1}) + (\eta^1 - 1)(\phi^0(P_1^{n+1}) - \phi^0(P_0^{n+1})) \quad (4.86)$$

The Jacobian J_0^n is obtained by definition in Equation (4.38). The individual differentials are

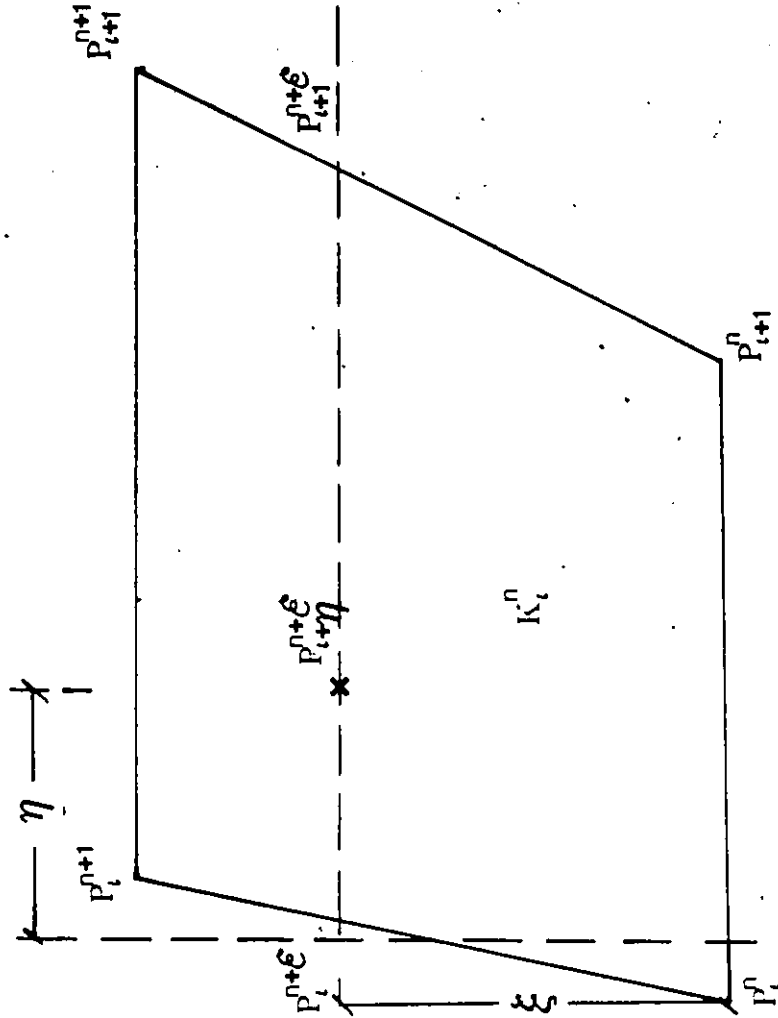


Fig. 4.6 Typical Trapezoidal Element

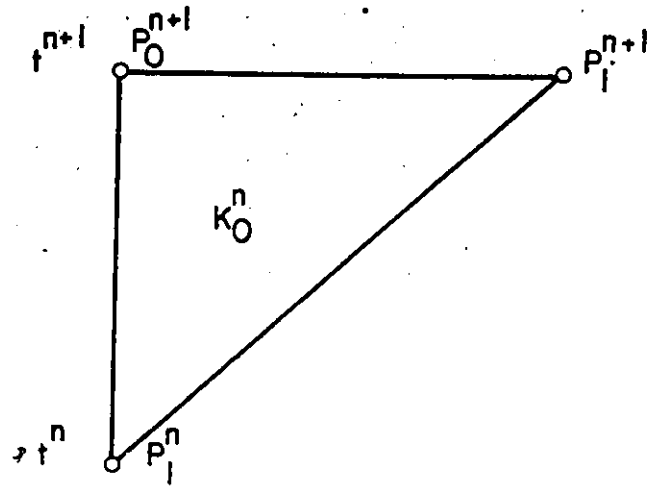


Fig. 4.7(a) Voruglu and Finn's Upstream Boundary Triangular Element

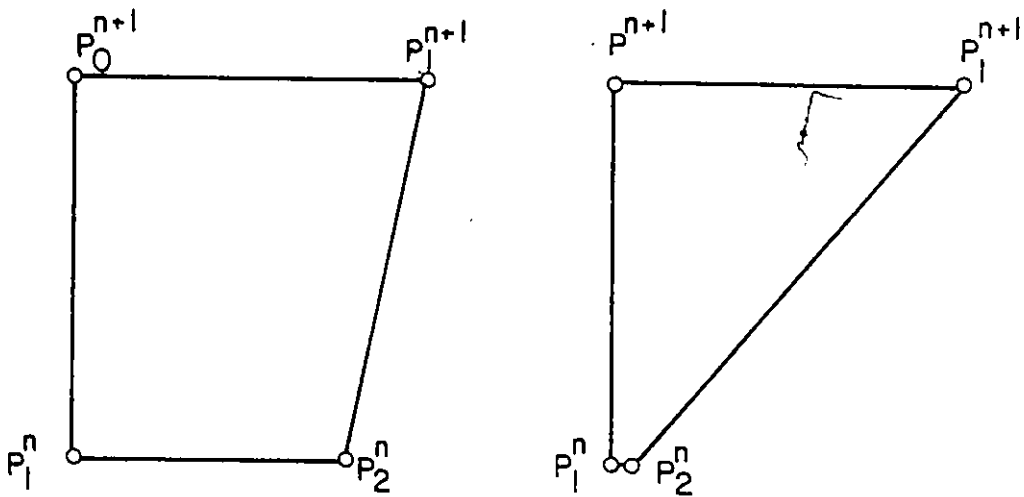


Fig. 4.7(b) Proposed Alternate Form of Upstream Boundary Element

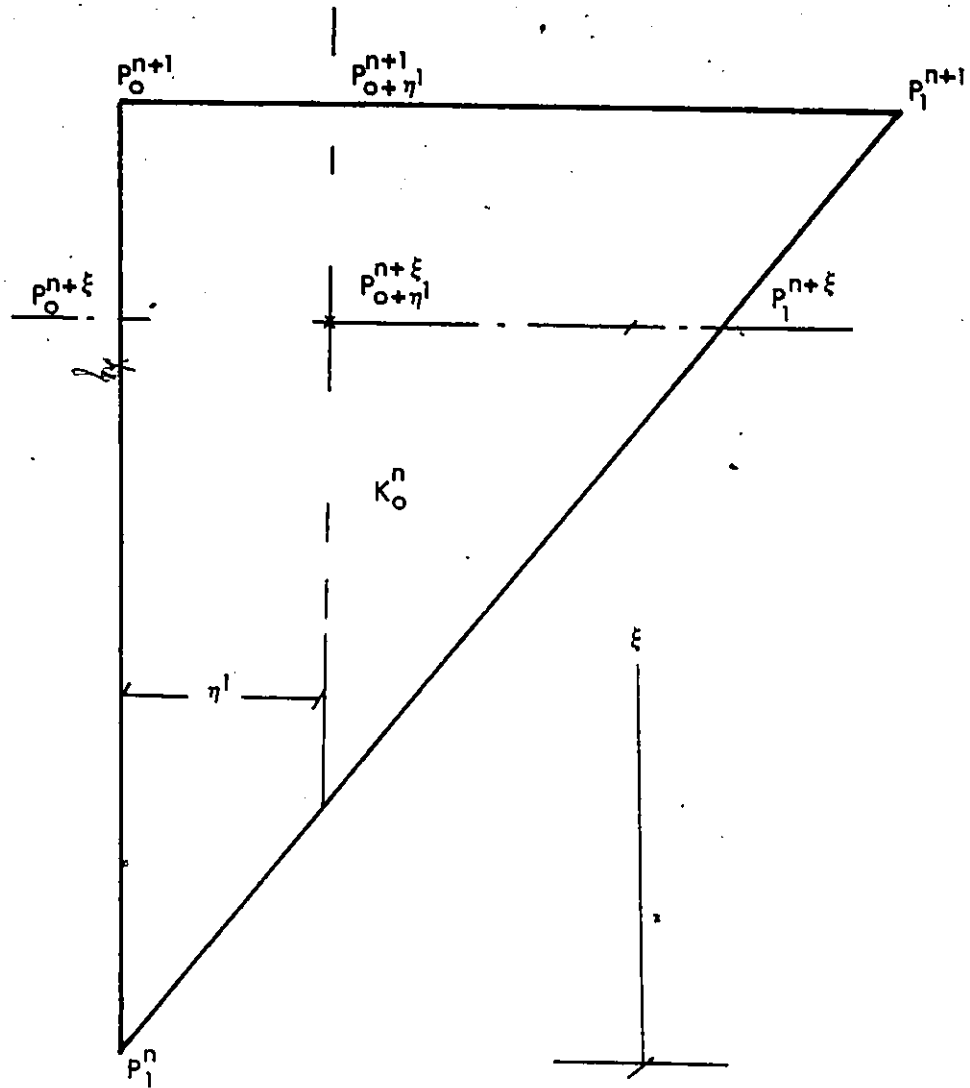


Fig. 4.8 Upstream Triangular Elements

$$\frac{\partial t}{\partial \eta^1} = 0 \quad (4.47)$$

$$\frac{\partial t}{\partial \xi} = k \quad (4.48)$$

$$\frac{\partial x}{\partial \eta^1} = x_1^{n+1} - x_1^n \quad (4.87)$$

$$\frac{\partial x}{\partial \xi} = x_1^{n+1} - x_0^{n+1} \quad (4.88)$$

From above, J_0^n is equated as

$$J_0^n = \frac{\partial t}{\partial \xi} \cdot \frac{\partial x}{\partial \eta^1} - \frac{\partial t}{\partial \eta^1} \cdot \frac{\partial x}{\partial \xi} \quad (4.89)$$

or

$$J_0^n = k(x_1^{n+1} - x_0^{n+1}) \quad (4.90)$$

To obtain the values of other differentials for numerical integration, the results are

$$\frac{\partial \eta^1}{\partial t} = -\frac{1}{k} \frac{(x_1^{n+1} - x_1^n)}{(x_1^{n+1} - x_0^{n+1})} \quad (4.91)$$

$$\frac{\partial \eta^1}{\partial x} = \frac{1}{x_1^{n+1} - x_0^{n+1}} \quad (4.92)$$

(1) Computation of

$$\int_{K_0^n} S_h \frac{\partial \phi^0}{\partial t} dx dt$$

For the upstream boundary node the only element connected with node P_0^{n+1} is K_0^n

where $\phi^0 = 1$ and zero elsewhere. Therefore

$$\int_{K_0^n} S_h \frac{\partial \phi^0}{\partial t} dx dt = \bar{A}_{L_0} \left(S_h \frac{\partial \phi^0}{\partial t} \right) \quad (4.93)$$

For the triangular element, the numerical integration for area is approximated as

$$\int_{K_0^n} \psi dx dt = \frac{1}{6} k (x_1^{n+1} - x_0^{n+1}) (\psi(P_1^n) + \psi(P_1^{n+1}) + \psi(P_0^{n+1})) \quad (4.94)$$

Consideration of Equation (4.86)

$$\frac{\partial \phi^0}{\partial t} = \frac{\partial \phi^0}{\partial \xi} \cdot \frac{\partial \xi}{\partial t} + \frac{\partial \phi^0}{\partial \eta^1} \cdot \frac{\partial \eta^1}{\partial t} \quad (4.95)$$

Also

$$\frac{\partial \xi}{\partial x} = 0 \quad (4.52)$$

and

$$\frac{\partial \xi}{\partial t} = \frac{1}{k} \quad (4.53)$$

The other terms in Equation (4.95) are derived from Equation (4.86).

$$\frac{\partial \phi^0}{\partial \xi} = -\phi^0(P_1^n) + \phi^0(P_1^{n+1}) = 0 \quad (4.96)$$

$$\frac{\partial \phi^0}{\partial \eta^1} = \phi^0(P_1^{n+1}) - \phi^0(P_0^{n+1}) = -1 \quad (4.97)$$

From which

$$\frac{\partial \phi^0}{\partial t} = \frac{1}{k} \frac{(x_1^{n+1} - x_1^n)}{(x_1^{n+1} - x_0^n)} \quad (4.98)$$

and

$$\bar{A}_{L^0} \left(S_n \frac{\partial \phi^0}{\partial t} \right) = \frac{1}{6} \sum_{\eta^1=0}^1 \sum_{\xi=0}^1 S_1^{n+\xi} (x_1^{n+1} - x_1^n) \quad (4.99)$$

Expanding and substituting Equation (4.99) in Equation (4.93), the integral becomes

$$\int_{K_0^n} S_n \frac{\partial \phi^0}{\partial x} dx dt = \frac{1}{6} (x_1^{n+1} - x_1^n) (S_1^n + S_1^{n+1} - S_0^{n+1}) \quad (4.100)$$

(2) Computation of

$$\int_{K_0^n} S_h \frac{\partial \phi^0}{\partial x} dx dt$$

Similar to Equation (4.93) the integral is

$$\int_{K_0^n} S_h \frac{\partial \phi^0}{\partial x} dx dt = \bar{A}_{L^0} \left(S_n \frac{\partial \phi^0}{\partial x} \right) \quad (4.101)$$

Again considering Equation (4.86) and expanding it to yield

$$\frac{\partial \phi^0}{\partial x} = \frac{\partial \phi^0}{\partial \xi} \frac{\partial \xi}{\partial x} + \frac{\partial \phi^0}{\partial \eta^1} \frac{\partial \eta^1}{\partial x} \quad (4.102)$$

Noting contributions of the various terms, the value is

$$\frac{\partial \phi^0}{\partial x} = \frac{-1}{(x_1^{n+1} - x_0^{n+1})} \quad (4.103)$$

Taking the Jacobian in Equation (4.90)

$$\bar{A}_{L^0} \left(S_n \frac{\partial \phi^0}{\partial x} \right) = \frac{1}{6} \sum_{\eta^1=0}^1 \sum_{\xi=0}^1 S_n^{\eta^1+\xi} \left(\frac{-1}{(x_1^{n+1} - x_0^{n+1})} \right) J_0^n \quad (4.104)$$

The expansion of Equation (4.104) leads to

$$\int_{K_0^n} S_h \frac{\partial \phi^0}{\partial x} = -\frac{1}{6} k (S_1^n + S_1^{n+1} + S_0^{n+1}) \quad (4.105)$$

A visual examination of Equation (4.94) results in

$$\int_{K_0^n} S_h \phi dx dt = \frac{1}{6} k (x_1^{n+1} - x_0^{n+1}) (S_1^n + S_1^{n+1} + S_0^{n+1}) \quad (4.106)$$

A comparison with Equations (4.80) and (4.81) would result in the calculation of flux as

$$\int_{L^n} S_h \phi^0 dx = 0 \quad (4.107)$$

$$\int_{L^{n+1}} S_h \phi^0 dx = \frac{1}{2} (x_1^{n+1} - x_0^{n+1}) S_0^{n+1} \quad (4.108)$$

The above terms are used in the mass and momentum conservation equations for subcritical flow conditions. When supercritical flow persists the requirements of boundary conditions change such that both dependent variables depth, y , and discharge, Q , are specified at node P_0^{n+1} . These specifications replace both the equations and the flow and depth continuity is then captured at the nodal point P_1^{n+1} . The contributions for the supercritical flow regime are presented in Appendix B.

4.3.1.2 Trapezoidal Element

The earlier work of Bannerot and Jamet (1975) presented a trapezoidal element at the upstream boundary. This element had a finite base length. There was no provision in that technique to introduce a ray emitting from nodal point P_1^n .

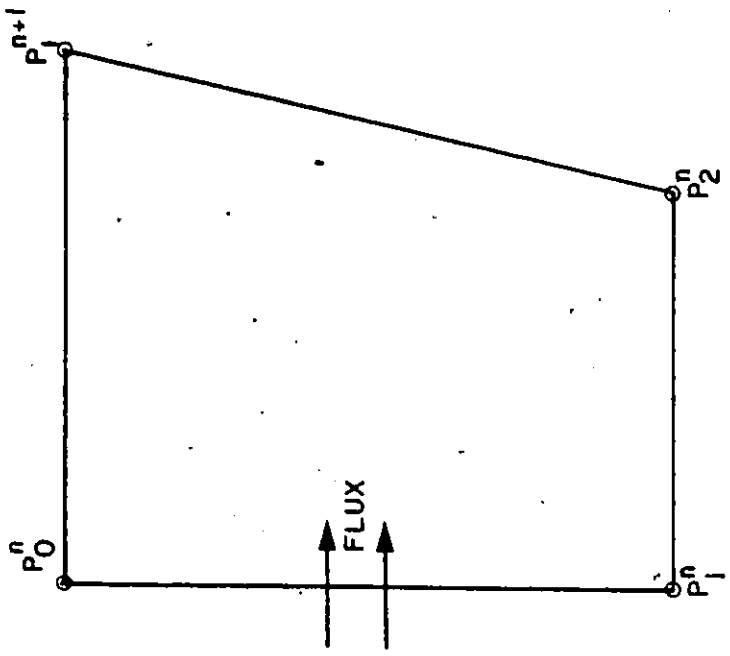
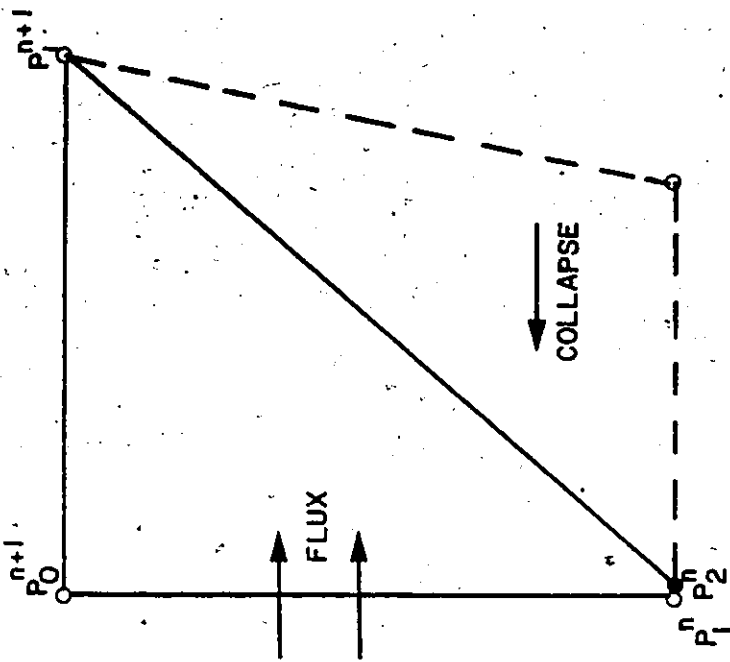
This deficiency was overcome by allowing for a quadrilateral element at the upstream boundary and collapsing the base length between P_1^n and P_2^n to zero. This is presented in Figure 4.9. The contributions of various terms are very similar to those derived for the K_1^n element with allowance for the no-displacement of side at the upstream boundary, i.e.

$$x_0^{n+1} - x_1^n = 0$$

The various contributions are summarized below based on the derivations in Equations (4.63), (4.71) and (4.75).

$$\int_{K_0^n} \int S_h \frac{\partial \phi^0}{\partial t} dx dt = \frac{1}{4} (S_1^{n+1} + S_2^n) (x_1^{n+1} - x_2^n) \quad (4.109)$$

$$\int_{K_0^n} \int S_h \frac{\partial \phi^0}{\partial x} dx dt = -\frac{1}{4} k (S_1^n + S_2^n + S_0^{n+1} + S_1^{n+1}) \quad (4.110)$$



Bonnerot and Jamez's Upstream Boundary Element

Proposed Collapsed Quadrilateral

Fig. 4.9 Upstream Boundary Trapezoidal Element

$$\int_{\bar{x}_0^n} S_h \phi^0 dx dt = \frac{k}{4} S_0^{n+1} (x_1^{n+1} - x_0^{n+1}) \quad (4.111)$$

The estimation of flux across the boundaries is given by Equations (4.83), (4.107) and (4.108):

The nodal contributions for supercritical flow conditions are presented in Appendix B. The tests carried out by employing the triangular and the collapsed quadrilateral elements yielded almost identical results. For this reason, from a programming convenience, the results in the following chapters are based on collapsed quadrilateral.

4.3.2 Downstream Boundary:

The downstream boundary does not play as important a role as the upstream boundary. Nevertheless, an ill-conditioned downstream boundary becomes equally important when corrupted signals move up and destroy the validity of the interior, otherwise good, solution. When the mass of water leaves the domain, the velocity at the boundary is positive and this in turn necessitates a trapezoidal element.

It is to be noted that negative flows and hence negative velocities at the downstream boundary implies the need of a ray and triangular element at this point. A typical trapezoidal element for positive velocities is depicted in Figure 4.10.

Giving due consideration to the fact that $x_N^{n+1} = x_N^n = x_R$, the following typical integrations of the dependent or derived variable S are similar to Equations (4.64), (4.72) and (4.76) as:

$$\int_{K_{N-1}} S_h \frac{\partial \phi^N}{\partial t} dx dt = -\frac{1}{4} (S_{N-1}^{n+1} + S_{N-1}^n) (x_{N-1}^{n+1} - x_{N-1}^n) \quad (4.112)$$

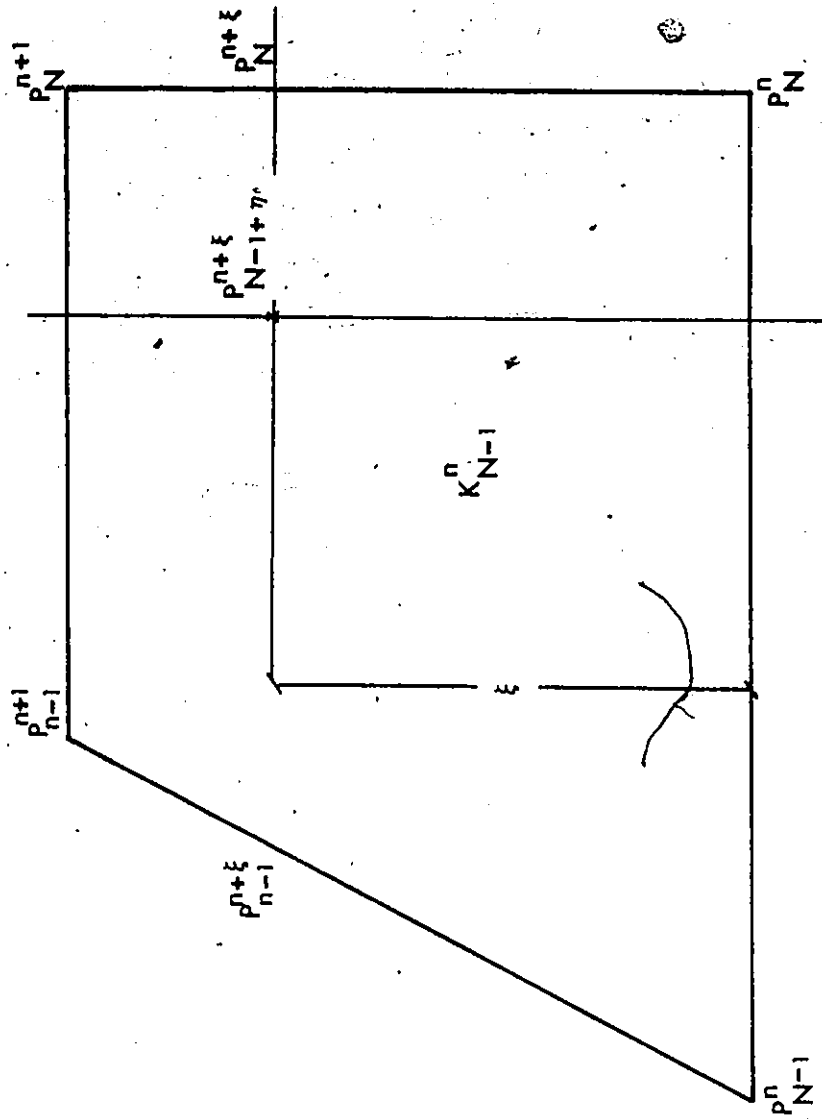


Fig. 4.10 Downstream Boundary Trapezoidal Element

$$\int_{K_{N-1}} S_h \frac{\partial \phi^N}{\partial x} dx dt = \frac{1}{4} k (S_N^n + S_N^{n+1} + S_{N-1}^n + S_{N-1}^{n+1}) \quad (4.113)$$

$$\int_{K_{N-1}} S_h \phi^N dx dt = \frac{k}{4} \{ (S_N^{n+1} (x_N^{n+1} - x_{N-1}^{n+1}) + S_N^n (x_N^n - x_{N-1}^n)) \} \quad (4.114)$$

The boundary flux are again derived along the same lines as for the upstream boundary with the resulting equalities as:

$$\int_{L_{t^n}} S_h \phi^N dx = \frac{1}{2} (x_N^n - x_{N-1}^n) S_N^n \quad (4.115)$$

and

$$\int_{L_{t^{n+1}}} S_h \phi^N dx = \frac{1}{2} (x_N^{n+1} - x_{N-1}^{n+1}) S_N^{n+1} \quad (4.116)$$

The volume of mass leaving the domain is computed as:

$$\int_{L_R} S \phi^N dt = \frac{k}{2} (S_N^n + S_N^{n+1}) \quad (4.84)$$

4.4 Discretized Form of Difference Equation

In Sections 4.2 and 4.3 differentials with respect to time and space were numerically integrated for any given dependent or derived variable, S. These terms were next implemented in Equations (4.32) and (4.33). The substitution then resulted in five different types of equations depending upon the location of the element.

The contributions from the elements are grouped and presented as five types of elements.

Type 1 elements for $i=0$ in $\phi^{(i)}$ shape functions

Conservation of Mass:

$$\begin{aligned} & \frac{k}{6} (Q_1^n + Q_0^{n+1} + Q_1^{n+1}) - \frac{1}{6} (x_1^{n+1} - x_1^n) (A_1^n + A_0^{n+1} + A_1^{n+1}) \\ & - \frac{k}{6} (x_1^{n+1} - x_0^{n+1}) (q_1^n + q_0^{n+1} + q_1^{n+1}) \\ & - \frac{k}{2} (Q_0^{n+1} + Q_1^n) + \frac{1}{2} (x_1^{n+1} - x_0^{n+1}) A_0^{n+1} = 0 \end{aligned} \quad (4.117)$$

Conservation of Momentum:

$$\begin{aligned} & -\frac{1}{6} (x_1^{n+1} - x_1^n) (Q_1^n + Q_0^{n+1} + Q_1^{n+1}) + \frac{k}{6} (Q_1^n u_1^n + Q_0^{n+1} u_0^{n+1} + Q_1^{n+1} u_1^{n+1}) \\ & + \frac{kg}{6} (A_1^n \bar{y}_1^n + A_0^{n+1} \bar{y}_0^{n+1} + A_1^{n+1} \bar{y}_1^{n+1}) - \frac{kg}{6} (x_1^{n+1} - x_0^{n+1}) \\ & (A_1^n S_{g_1}^n + A_0^{n+1} S_{g_0}^{n+1} + A_1^{n+1} S_{g_1}^{n+1}) - \frac{k}{2} [Q_1^n u_1^n + Q_0^{n+1} u_0^{n+1} \\ & + g(A_1^n \bar{y}_1^n + A_0^{n+1} \bar{y}_0^{n+1})] + \frac{1}{2} (x_1^{n+1} - x_0^{n+1}) Q_0^{n+1} = 0 \end{aligned} \quad (4.118)$$

Type 2 elements for $i=1$ in $\phi^{(i)}$ shape functions:

Conservations of Mass:

$$\begin{aligned} & \frac{k}{4} (Q_1^n + Q_1^{n+1} + Q_2^n + Q_2^{n+1}) - \frac{k}{6} (Q_1^n + Q_0^{n+1} + Q_1^{n+1}) \\ & - \frac{1}{4} [(A_1^n + A_1^{n+1})(x_1^{n+1} - x_1^n) + (A_2^n + A_2^{n+1})(x_2^{n+1} - x_2^n)] \\ & + \frac{1}{6} (x_1^{n+1} - x_1^n) (A_1^n + A_0^{n+1} + A_1^{n+1}) - \frac{k}{4} [q_1^n (x_2^n - x_1^n) \\ & + q_1^{n+1} (x_2^{n+1} - x_1^{n+1})] - \frac{k}{6} (x_1^{n+1} - x_0^{n+1}) (q_1^n + q_0^{n+1} + q_1^{n+1}) \\ & + \frac{1}{2} [(x_2^{n+1} - x_0^{n+1}) A_1^{n+1} - (x_2^n - x_1^n) A_1^n] = 0 \end{aligned} \quad (4.119)$$

Conservation of Momentum:

$$\begin{aligned}
& -\frac{1}{4} [(Q_1^n + Q_1^{n+1})(x_1^{n+1} - x_1^n) + (Q_2^n + Q_2^{n+1})(x_2^{n+1} - x_2^n)] \\
& + \frac{1}{6} (x_1^{n+1} - x_1^n)(Q_1^n + Q_0^{n+1} + Q_1^{n+1}) + \frac{k}{4} (Q_1^n u_1^n + Q_2^n u_2^n \\
& + Q_1^{n+1} u_1^{n+1} + Q_2^{n+1} u_2^{n+1}) - \frac{k}{6} (Q_1^n u_1^n + Q_0^{n+1} u_0^{n+1} + Q_1^{n+1} u_1^{n+1}) \\
& + \frac{kg}{4} (A_1^n \bar{y}_1^n + A_2^n \bar{y}_2^n + A_1^{n+1} \bar{y}_1^{n+1} + A_2^{n+1} \bar{y}_2^{n+1}) \\
& - \frac{kg}{6} (A_1^n \bar{y}_1^n + A_0^{n+1} \bar{y}_0^{n+1} + A_1^{n+1} \bar{y}_1^{n+1}) - \frac{kg}{4} [A_1^n S_{g_1}^n (x_2^n - x_1^n) \\
& + A_1^{n+1} S_{g_1}^{n+1} (x_2^{n+1} - x_1^{n+1})] \\
& - \frac{kg}{6} (x_1^{n+1} - x_0^{n+1})(A_1^n S_{g_1}^n + A_0^{n+1} S_{g_0}^{n+1} + A_1^{n+1} S_{g_1}^{n+1}) \\
& + \frac{1}{2} [(x_2^{n+1} - x_0^{n+1})Q_1^{n+1} - (x_2^n - x_1^n)Q_1^n] = 0 \tag{4.120}
\end{aligned}$$

Type 3 elements for $\bar{\Gamma} = 2, 3, \dots, N-2$ in $\phi^{(i)}$ shape functions.

Conservation of Mass:

$$\begin{aligned}
& \frac{k}{4} (Q_{i+1}^n + Q_{i+1}^{n+1} - Q_{i-1}^n - Q_{i-1}^{n+1}) - \frac{1}{4} [(A_{i+1}^{n+1} + A_{i+1}^n) \\
& (x_{i+1}^{n+1} - x_{i+1}^n) - (A_{i-1}^{n+1} + A_{i-1}^n)(x_{i-1}^{n+1} - x_{i-1}^n)] \\
& - \frac{k}{4} [q_i^n (x_{i+1}^n - x_{i-1}^n) + q_i^{n+1} (x_{i+1}^{n+1} - x_{i-1}^{n+1})] \\
& + \frac{1}{2} [(x_{i+1}^{n+1} - x_{i-1}^{n+1})A_i^{n+1} - (x_{i+1}^n - x_{i-1}^n)A_i^n] = 0 \tag{4.121}
\end{aligned}$$

Conservation of Momentum:

$$\begin{aligned}
 & -\frac{1}{4} [(Q_{i+1}^{n+1} + Q_{i+1}^n)(x_{i+1}^{n+1} - x_{i+1}^n) - (Q_{i-1}^{n+1} + Q_{i-1}^n)(x_{i-1}^{n+1} - x_{i-1}^n)] \\
 & + \frac{k}{4} (Q_{i+1}^n u_{i+1}^n + Q_{i+1}^{n+1} u_{i+1}^{n+1} - Q_{i-1}^n u_{i-1}^n - Q_{i-1}^{n+1} u_{i-1}^{n+1}) \\
 & - \frac{kg}{4} (A_{i+1}^n \bar{y}_{i+1}^n + A_{i+1}^{n+1} \bar{y}_{i+1}^{n+1} - A_{i-1}^n \bar{y}_{i-1}^n - A_{i-1}^{n+1} \bar{y}_{i-1}^{n+1}) \\
 & - \frac{kg}{4} [A_i^n S_i^n (x_{i+1}^n - x_{i-1}^n) + A_i^{n+1} S_i^{n+1} (x_{i+1}^{n+1} - x_{i-1}^{n+1})] \\
 & + \frac{1}{2} [Q_i^{n+1} (x_{i+1}^{n+1} - x_{i-1}^{n+1}) - Q_i^n (x_{i+1}^n - x_{i-1}^n)] = 0 \tag{4.122}
 \end{aligned}$$

Type 4 elements for $i = N - 1$ in $\phi^{(i)}$ shape functions:-

Conservation of Mass:

$$\begin{aligned}
 & \frac{k}{4} (Q_N^n + Q_N^{n+1} - Q_{N-1}^n - Q_{N-1}^{n+1}) + \frac{1}{4} (A_{N-2}^{n+1} + A_{N-2}^n) \\
 & (x_{N-2}^{n+1} - x_{N-2}^n) - \frac{k}{4} [q_{N-1}^n (x_N^n - x_{N-2}^n) + \\
 & q_{N-1}^{n+1} (x_N^{n+1} - x_{N-2}^{n+1})] + \frac{1}{2} [A_{N-1}^{n+1} (x_N^{n+1} - x_{N-2}^{n+1}) - \\
 & A_{N-1}^n (x_N^n - x_{N-2}^n)] = 0 \tag{4.123}
 \end{aligned}$$

Conservation of Momentum:

$$\begin{aligned}
& \frac{1}{4} (Q_{N-2}^{n+1} + Q_{N-2}^n) (x_{N-2}^{n+1} - x_{N-2}^n) + \frac{k}{4} (Q_N^n u_N^n + Q_N^{n+1} u_N^{n+1} \\
& - Q_{N-2}^n u_{N-2}^n - Q_{N-2}^{n+1} u_{N-2}^{n+1}) + \frac{kg}{4} (A_N^n \bar{y}_N^n + A_N^{n+1} \bar{y}_N^{n+1} \\
& - A_{N-2}^n \bar{y}_{N-2}^n - A_{N-2}^{n+1} \bar{y}_{N-2}^{n+1}) - \frac{kg}{4} [A_{N-1}^n S_{N-1}^n (x_N^n - x_{N-2}^n) \\
& + A_{N-1}^{n+1} S_{N-1}^{n+1} (x_N^{n+1} - x_{N-2}^{n+1})] + \frac{1}{2} [Q_{N-1}^{n+1} (x_N^{n+1} - x_{N-2}^{n+1}) \\
& - Q_{N-1}^n (x_N^n - x_{N-2}^n)] = 0
\end{aligned} \tag{4.124}$$

Type 5 elements for $i = N$ in $\phi^{(i)}$ shape function

Conservation of Mass:

$$\begin{aligned}
& -\frac{k}{4} (Q_{N-1}^n + Q_{N-1}^{n+1} + Q_N^n + Q_N^{n+1}) + \frac{1}{4} (A_{N-1}^{n+1} + A_{N-1}^n) (x_{N-1}^{n+1} - x_{N-1}^n) \\
& - \frac{k}{4} [q_N^n (x_N^n - x_{N-1}^n) + q_N^{n+1} (x_N^{n+1} - x_{N-1}^{n+1})] \\
& + \frac{1}{2} [A_N^{n+1} (x_N^{n+1} - x_{N-1}^{n+1}) - A_N^n (x_N^n - x_{N-1}^n)] \\
& + \frac{k}{2} (Q_N^{n+1} + Q_N^n) = 0
\end{aligned} \tag{4.125}$$

Conservation of Momentum:

$$\begin{aligned}
& \frac{1}{4} (Q_{N-1}^n + Q_{N-1}^{n+1})(x_{N-1}^{n+1} - x_{N-1}^n) - \frac{k}{4} (Q_{N-1}^n u_{N-1}^n + Q_{N-1}^{n+1} u_{N-1}^{n+1} \\
& + Q_N^n u_N^n + Q_N^{n+1} u_N^{n+1}) - \frac{kg}{4} (A_{N-1}^n \bar{y}_{N-1}^n + A_{N-1}^{n+1} \bar{y}_{N-1}^{n+1} + A_N^n \bar{y}_N^n \\
& + A_N^{n+1} \bar{y}_N^{n+1}) - \frac{kg}{4} [A_N^n S_{g_N}^n (x_N^n - x_{N-1}^n) + A_N^{n+1} S_{g_N}^{n+1} (x_N^{n+1} - x_{N-1}^{n+1})] \\
& + \frac{1}{2} [Q_N^{n+1} (x_N^{n+1} - x_{N-1}^{n+1}) - Q_N^n (x_N^n - x_{N-1}^n)] \\
& + \frac{k}{2} [Q_N^n u_N^n + Q_N^{n+1} u_N^{n+1} + g (A_N^{n+1} \bar{y}_N^{n+1} + A_N^n \bar{y}_N^n)] = 0 \tag{4.126}
\end{aligned}$$

In the foregoing the following substitutions and assumptions were made:

- (i) The term S_g defines the difference of bedslope and friction slope i.e.

$$S_g = S_0 - S_f$$
- (ii) For the sake of brevity the term defining momentum contributions of the lateral flow were not included in the momentum equation. These contributions are, however, listed in Appendix C.
- (iii) The derivations of continuity and momentum equations were made with a triangular element at the upstream boundary. As significant model testing was carried out employing the collapsed quadrilateral, these equations which impact only the first two types of elements are presented in Appendix D.

Equations (4.117) to (4.126) were presented without consideration to the boundary conditions at the two extremities. In a previous section it was noted that the momentum equation weakly mimics the continuity of mass as well. This was later confirmed by numerical experimentation, and for this reason the mass continuity equations at the two boundaries were replaced by the imposed conditions.

These replacements required the handling of flux terms or line integrals through Type 2 and 4 elements. The incorporation of boundary conditions necessitates the changes in Equations (4.117), (4.119), (4.123) and (4.125) respectively as:

$$y_0^{n+1} = y_u(t) \quad (4.127)$$

or

$$Q_0^{n+1} = Q_u(t) \quad (4.128)$$

Equation (4.119) is replaced by:

$$\begin{aligned} & \frac{k}{4} (Q_1^n + Q_1^{n+1} + Q_2^n + Q_2^{n+1}) - \frac{1}{4} [(A_1^n + A_1^{n+1})(x_1^{n+1} - x_1^n) \\ & + (A_2^n + A_2^{n+1})(x_2^{n+1} - x_2^n)] - \frac{k}{4} [q_1^n(x_2^n - x_1^n) + q_1^{n+1}(x_2^{n+1} - x_1^{n+1})] \\ & - \frac{k}{6} (x_1^{n+1} - x_0^{n+1})(q_1^n + q_0^{n+1} + q_1^{n+1}) + \frac{1}{2} [A_1^{n+1}(x_2^{n+1} - x_0^{n+1}) \\ & - A_1^n(x_2^n - x_1^n)] + \frac{1}{2} A_0^{n+1}(x_1^{n+1} - x_0^{n+1}) - \frac{k}{2} (Q_0^{n+1} + Q_1^n) = 0 \end{aligned} \quad (4.129)$$

A similar flux handling transforms Equation (4.123) into

$$\begin{aligned} & - \frac{k}{4} (Q_{N-2}^n + Q_{N-2}^{n+1} + Q_{N-1}^n + Q_{N-1}^{n+1}) - \frac{1}{4} [(A_{N-2}^n + A_{N-2}^{n+1})(x_{N-2}^{n+1} - x_{N-2}^n) \\ & + (A_{N-1}^n + A_{N-1}^{n+1})(x_{N-1}^{n+1} + x_{N-1}^n)] + \frac{k}{4} [q_{N-1}^n(x_N^n - x_{N-2}^n) \\ & + q_{N-1}^{n+1}(x_N^{n+1} - x_{N-2}^{n+1})] - \frac{k}{4} [q_N^n(x_N^n - x_{N-1}^n) + q_N^{n+1}(x_N^{n+1} - x_{N-1}^{n+1})] \\ & + \frac{1}{2} [A_{N-1}^{n+1}(x_N^{n+1} - x_{N-2}^{n+1}) - A_{N-1}^n(x_N^n - x_{N-2}^n)] \\ & + \frac{1}{2} [A_N^{n+1}(x_N^{n+1} - x_{N-1}^{n+1}) - A_N^n(x_N^n - x_{N-1}^n)] \\ & + \frac{k}{2} (Q_N^{n+1} + Q_N^n) = 0 \end{aligned} \quad (4.130)$$

Imposing the boundary condition Equation (4.125) is replaced by

$$y_N^{n+1} = y_d(t) \quad (4.131)$$

or

$$Q_N^{n+1} = Q_d(t) \quad (4.132)$$

or

$$Q_N^{n+1} + F(y_N^{n+1}) = 0 \quad (4.133)$$

Equation (4.133) implies a unique stage-discharge relationship. If y_N^{n+1} is the critical depth for a flow Q_N^{n+1} then the boundary condition is of non-reflective type or else there is a possibility of wave reflections. This aspect is addressed in the following chapters. To avoid trivial solutions Equations (4.128) and (4.132) are not prescribed simultaneously.

In the previous sections while developing the finite element formulations, no restrictions were placed on the orientation of the rays and hence the sides $P_i^n P_i^{n+1}$ for $i = 1, 2, \dots, N-1$.

In this work the orientation of the rays is restricted to follow the condition imposed by

$$x_i^{n+1} = x_i^n + u_i^n k \quad (4.134)$$

The interpretation of Eqn. 4.134 implies that the new position of a particle previously at x_i^n is determined by the mean velocity at the point and the time interval, k . It will be shown in the next section that in the limiting case of $k \rightarrow 0$ the system of equations of the moving element schemes reduces to the central-difference technique. This is consistent with the findings of Bonnerot and Jamet (1974), Varoglu and Finn (1980) and Lam and Simpson (1976).

4.5 Solution Procedure:

In the previous section the discretized equations for the five types of element contributions were derived. A closer examination of the equations reveal two important characteristics.

- (i) The equations involve only two different levels of dependent variables 'y' and 'Q', namely at levels 'n' and 'n + 1'. For $n = 0$ the state is that of initial condition when both y and Q are prescribed. When $n > 0$, the values obtained for y and Q at the current solution step become the initial conditions and known values. Thus at all levels of solution, dependent and derived variables at level 'n' are known. These values can then be transferred to the right hand side of the equation, leaving unknowns at level $n + 1$ to be solved on the left hand side.
- (ii) For any equation there are no more than three unknowns in depth and discharge, y and Q respectively. A further comparison of the subscripts indicate that the same nodes repeat for both mass conservation and momentum conservation equations. This results in the bi-tridiagonal set of equations which can be solved efficiently by any stable double-sweep technique.

The transformed equations can be written as:

Conservation of Mass:

$$a_1 y_{i-1}^{n+1} + a_2 Q_{i-1}^{n+1} + b_1 y_i^{n+1} + b_2 Q_i^{n+1} + c_1 y_{i+1}^{n+1} + c_2 Q_{i+1}^{n+1} = d_1 \quad (4.135)$$

Conservation of Momentum:

$$a_3 y_{i-1}^{n+1} + a_4 Q_{i-1}^{n+1} + b_3 y_i^{n+1} + b_4 Q_i^{n+1} + c_3 y_{i+1}^{n+1} + c_4 Q_{i+1}^{n+1} = d_2 \quad (4.136)$$

where a_1, a_2 etc can be obtained by comparing Equations (4.135) and (4.136) with Equations (4.117) to (4.126). A further inspection also reveals that the resulting equations from Equations (4.135) and (4.136) are nonlinear in nature and would require solution by an iterative technique.

Following the double sweep technique adapted by Cooley and Moin (1976), the non-linear equations are solved by the Newton-Raphson Method. The following steps summarize the procedure adopted. Appendix E provides the coefficients a_1, a_2 , etc.

For $i=0$ Equations (4.135) and (4.136) become

$$b_1 y_0^{n+1} + b_2 Q_0^{n+1} = d_u \quad (4.137)$$

$$b_3 y_0^{n+1} + b_4 Q_0^{n+1} + c_3 y_1^{n+1} + c_4 Q_1^{n+1} = d_2 \quad (4.138)$$

For $i = 1, 2, \dots, N-1$

$$a_1 y_{i-1}^{n+1} + a_2 Q_{i-1}^{n+1} + b_1 y_i^{n+1} + b_2 Q_i^{n+1} + c_1 y_{i+1}^{n+1} + c_2 Q_{i+1}^{n+1} = d_1 \quad (4.135)$$

$$a_3 y_{i-1}^{n+1} + a_4 Q_{i-1}^{n+1} + b_3 y_i^{n+1} + b_4 Q_i^{n+1} + c_3 y_{i+1}^{n+1} + c_4 Q_{i+1}^{n+1} = d_2 \quad (4.136)$$

For $i = N$

$$a_1 y_{N-1}^{n+1} + a_2 Q_{N-1}^{n+1} + b_1 y_N^{n+1} + b_2 Q_N^{n+1} = d_1 \quad (4.139)$$

$$b_3 y_N^{n+1} + b_4 Q_N^{n+1} = d_d \quad (4.140)$$

Where in Equation (4.137) either $b_1 = 1$ and $b_2 = 0$ or $b_1 = 0$ and $b_2 = 1$ and d_u given as

$$d_u = b_1 y_u(t) + b_2 Q_u(t) \quad (4.141)$$

A similar relationship exists for Equation (4.140). The coefficients for the dependent variables are established by:

$$a_1 = \frac{\partial F}{\partial y_{i-1}^{n+1}} \quad (4.142)$$

$$a_2 = \frac{\partial F}{\partial Q_{i-1}^{n+1}} \quad (4.143)$$

$$b_1 = \frac{\partial F}{\partial y_i^{n+1}} \quad (4.144)$$

$$b_2 = \frac{\partial F}{\partial Q_i^{n+1}} \quad (4.145)$$

$$c_1 = \frac{\partial F}{\partial y_{i+1}^{n+1}} \quad (4.146)$$

$$c_2 = \frac{\partial F}{\partial Q_{i+1}^{n+1}} \quad (4.147)$$

$$d_1 = -F \quad (4.148)$$

$$a_3 = \frac{\partial G}{\partial y_{i-1}^{n+1}} \quad (4.149)$$

$$a_4 = \frac{\partial G}{\partial Q_{i-1}^{n+1}} \quad (4.150)$$

$$b_3 = \frac{\partial G}{\partial y_i^{n+1}} \quad (4.151)$$

$$b_4 = \frac{\partial G}{\partial Q_i^{n+1}} \quad (4.152)$$

$$c_3 = \frac{\partial G}{\partial y_{i+1}^{n+1}} \quad (4.153)$$

$$c_4 = \frac{\partial G}{\partial Q_{i+1}^{n+1}} \quad (4.154)$$

$$d_2 = -G \quad (4.155)$$

where F and G are associated with mass and momentum equations respectively and given by Equations (4.117) to (4.126). At the first iteration step in the Newton-Raphson technique, the values of y_i^{n+1} and Q_i^{n+1} for $i = 0, 1, \dots, N$ are assumed and then corrected for residual errors.

The coefficients for successive elimination are first computed as:

$$\beta_1 = b_1 - a_1 a_{1j-1} - a_2 a_{3j-1} \quad (4.156)$$

$$\beta_2 = b_2 - a_1 a_{2j-1} - a_2 a_{4j-1} \quad (4.157)$$

$$\beta_3 = b_3 - a_3 a_{1j-1} - a_4 a_{3j-1} \quad (4.158)$$

$$\beta_4 = b_4 - a_3 a_{2j-1} - a_4 a_{4j-1} \quad (4.159)$$

$$\delta_1 = d_1 - a_1 Y_{1j-1} - a_2 Y_{2j-1} \quad (4.160)$$

$$\delta_2 = d_2 - a_3 Y_{1j-1} - a_4 Y_{2j-1} \quad (4.161)$$

$$\text{for } j = 1, 2, 3, \dots, N$$

$$\beta_i = b_i \quad \text{for } i = 1, 2, 3, 4 \quad (4.162)$$

$$\delta_i = d_i \quad \text{for } i = 1, 2 \quad (4.163)$$

$$\text{for } j = 0.$$

At the next step β and δ provide the forward substitution as follows:

$$u = \beta_1 \beta_4 - \beta_2 \beta_3 \quad (4.164)$$

$$\alpha_{1j} = (\beta_4 c_1 - \beta_2 c_3) / u \quad (4.165)$$

$$\alpha_{2j} = (\beta_4 c_2 - \beta_2 c_4) / u \quad (4.166)$$

$$\alpha_{3j} = (\beta_1 c_3 - \beta_3 c_1) / u \quad (4.167)$$

$$\alpha_{4j} = (\beta_1 c_4 - \beta_3 c_2) / u \quad (4.168)$$

$$\gamma_{1j} = (\beta_4 \delta_1 - \beta_2 \delta_2) / u \quad (4.169)$$

$$\gamma_{2j} = (\beta_1 \delta_2 - \beta_3 \delta_1) / u \quad (4.170)$$

The values of α and γ are stored and used in the backsweep steps. The residuals for depth and discharge are computed as:

$$\Delta y_N = \gamma_{1,N} \quad (4.171)$$

$$\Delta Q_N = \gamma_{2,N} \quad (4.172)$$

For interior points, the recursive equations yield

$$\Delta y_i = \gamma_{1,i} - \alpha_{1,i} \Delta y_{i+1} - \alpha_{2,i} \Delta Q_{i+1} \quad (4.173)$$

$$\Delta Q_i = \gamma_{2,i} - \alpha_{3,i} \Delta y_{i+1} - \alpha_{4,i} \Delta Q_{i+1} \quad (4.174)$$

$$y_{i,\ell+1}^{n+1} = y_{i,\ell}^{n+1} + \Delta y_{i,\ell} \quad (4.175)$$

and

$$Q_{i,\ell+1}^{n+1} = Q_{i,\ell}^{n+1} + \Delta Q_{i,\ell} \quad (4.176)$$

where ℓ is the iteration level.

4.6 Extension to Eularian-Lagrangian Concept

So far the computations have been aimed at a Lagrangian solution grid presented earlier in Fig. 4.3. In this Section a variation to the pure Lagrangian scheme is presented. It should be recognized that at any given time step the solution procedure is valid for both Lagrangian and Eularian-Lagrangian scheme.

The Eularian-Lagrangian concept was qualitatively described in Section 4.2. In the following paragraphs, the computational aspects are explained. Recalling the proposed technique between time steps 'n' and 'n+1' as shown in Fig. 4.11, the solution is carried out by the equations defined in Sections 4.3, 4.4 and 4.5.

When the solution progresses from time level t_n for points A,B,C, etc. along rays AD, BE, CF, etc. the solution is obtained at points D,E,F, etc. In the Lagrangian scheme, points D,E,F, etc. then become the initial conditions to advance the solution further. For the Eularian-Lagrangian scheme the solution at D, E, F, etc. is adjusted back to the Eularian grid points A',B',C', etc. Here various interpolation schemes are presented.

4.6.1 Two Point Linear Interpolation:

The method is also known as the Lagrange Two Point Interpolation Formula. This scheme was the first to be implemented. When initial testing was carried out for discontinuous flows, the interpolation was responsible for clipping the wave front and retarding the advancement.

Referring to Fig. 4.11, the computed values at D and E for example were used to estimate the initial values of depth and flow at B'. This estimate was in turn used for advancing the solution. Mathematically, the relationships are:

$$y_{B'} = (1 - p)y_D + py_E + R_1 \quad (4.177)$$

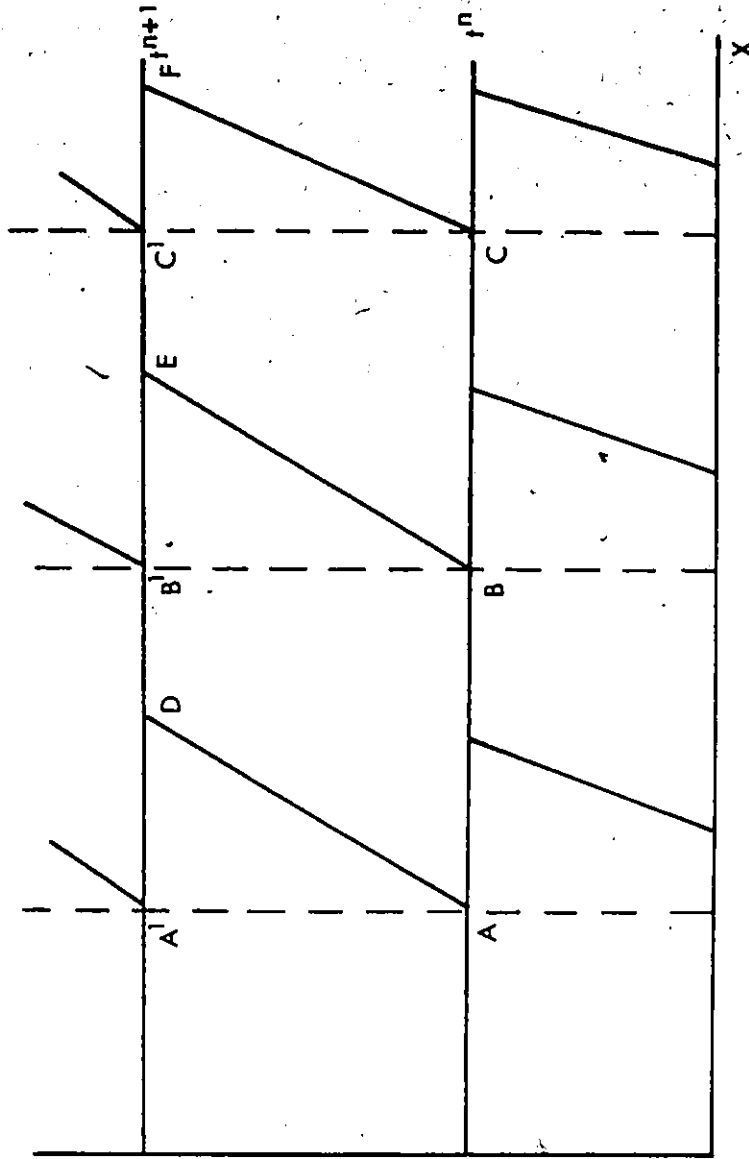


Fig. 4.11 Eulerian-Lagrangian Time Step

where

$$p = (x_B - x_D) / (x_E - x_D) \quad (4.178)$$

and R_1 is the remainder of second order estimated as

$$R_1 \approx 0.125 \Delta^2 \quad (4.179)$$

A similar relationship exists for computing discharge at point B'.

The results of the sensitivity analysis using this scheme are discussed at length in the next chapter. The interpolation scheme gives good estimates in regions where the depth and flow are relatively smooth. Even with extreme non-linearity, large time-step, which result in weak oscillations, the linear interpolation provides an excellent natural dissipation interface.

The scheme provides poor discontinuous front capturing properties and resulted in mass continuity errors. To avoid these problems, a nose tracking algorithm was developed. Initially, the scheme appeared promising with the location of front predicted accurately. Other problems with pseudo waves and oscillations were discovered for some sharply rising hydrographs. This alternative was then discarded for a better three point formula.

4.6.2 Three Point Lagrangian Interpolation

The Lagrangian Three Point Interpolation formula is suitable for estimating intermediate values close to the tip of discontinuity. This becomes evident when this interpolation is compared with the two point formula explained in the previous section as shown in Fig. 4.12.

On a much exaggerated scale the improvements of a three point formula over a two point scheme are quite evident. It is also clear that outside of the front capturing properties, both methods provide almost identical interpolation. The three-point formula, as will be shown in the next chapter, is quite faithful in not only

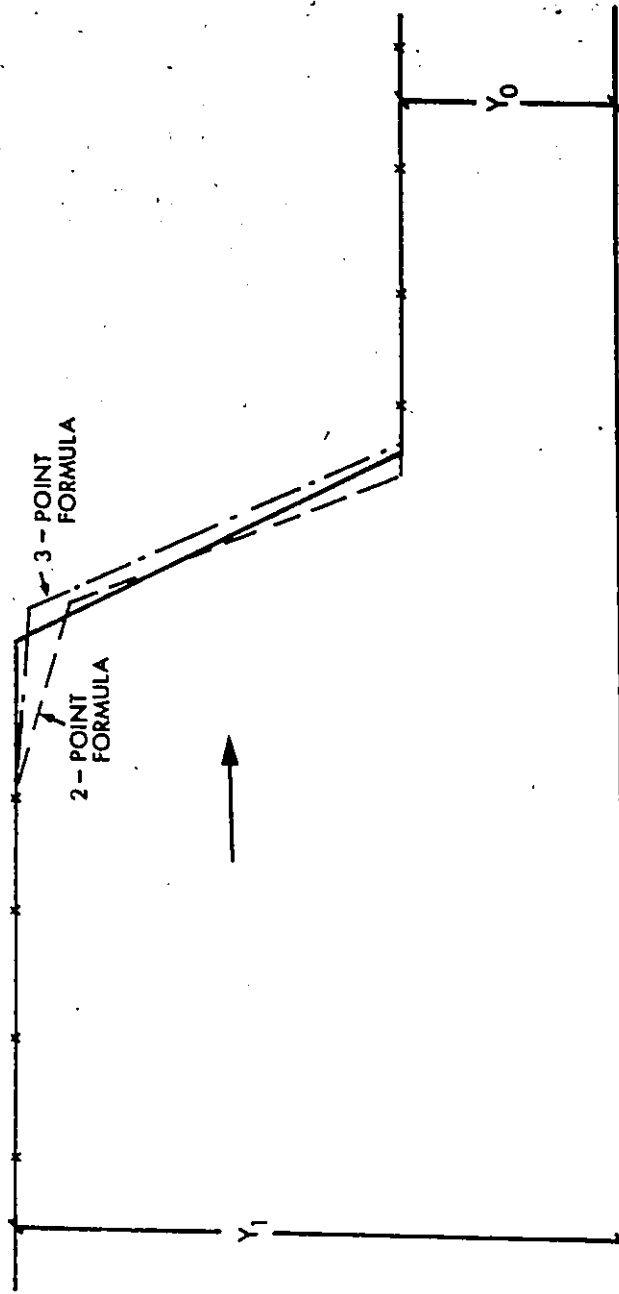


FIG. 4.12 Two and Three Point Lagrange Interpolation Schemes

capturing the discontinuity but also reproducing any oscillatory tendencies due to an ill-defined grid.

Again referring to Figure 4.11, the values of depth and discharge at computed points D,E,F are employed to interpolate the values at either B' or E' depending upon their locations with respect to the front and nodal points D or E.

The relationships employed are, for depth

$$y_{C'} = \frac{p(p-1)}{2} y_D + (1-p^2) y_E + \frac{p(p+1)}{2} y_F + R_2 \quad (4.180)$$

where

$$p = (x_{C'} - x_E) / (x_F - x_E) \quad (4.181)$$

and the third order remainder term is

$$R_2 = 0.065 \Delta^3 \text{ and } |p| \leq 1 \quad (4.182)$$

Strictly speaking the three point formula gives good results when points D,E,F, etc. are evenly spaced. For a discontinuous front, the velocities at the originating nodes A,B,C, etc. capturing the front are quite different necessitating an uneven computational grid. In order to overcome this disparity, different weighting schemes were tried but these proved to be unhelpful in further improving the results. Furthermore, as the second order values of 'p' are used in weighting, the results are highly biased to the location of E' to C and contributions of other nodes are then minimal. In view of these factors the interpolation with Equations (4.180) and (4.181) was retained.

4.6.3 Mixed Linear-Lagrangian Interpolation

In the foregoing sections the strengths and weaknesses of both the two point and three point interpolation formulas were discussed. A third alternative was tested and retained in the model combining the two techniques.

In this scheme the two point interpolation formula is used in regions where the flow is relatively smooth, whereas the three point formula is employed in the vicinity of discontinuity.

To implement this mixed interpolation scheme the location of discontinuity is first established. This is achieved by computing either the node with maximum velocity or the element with the highest water surface gradient. Once the discontinuity is established, a three to five node set back is provided. Within the discontinuity the interpolation for the Eularian regridding is carried out using Equations (4.180) and (4.181). In other regions the linear interpolation formula described by Equations (4.177) and (4.178) is employed.

It may be argued that the three point formula being of a higher order accuracy should be used. In response, it may be recalled that the basic assumption of the moving element scheme was the linear interpolation of the dependent variables between nodes. For regions away from the front this assumption is valid. On the other hand, in rapidly varying flows and depths, the water surface slope could be better interpolated by a non-linear surface represented by the second-order interpolation formula.

4.6.4 Choice of Eularian-Lagrangian Scheme Over Lagrangian Scheme:

The solution of open channel flow equations presented in Equations (4.117) to (4.126) is still non-dissipative in character. This means that if any error or oscillation is introduced in the solution domain, there are no mechanisms present to either suppress or dissipate them. In this aspect the method is no different than any other non-dissipative finite-difference and finite element techniques.

S

When the convection dominated flows in fluid mechanics are solved by similar Lagrangian based techniques, the resulting solution is significantly improved. Why, then, are similar improvements not realized in open channel flows? The answer is not a straight forward one.

- (1) The mechanisms governing open channel flows are quite different than, say, a concentration front. Open channel flows are governed by the simultaneous balance of mass and momentum.
- (2) In open channel flow equations, there is cross-coupling of terms between mass and momentum relationships. Burger's equation, for example, on the other hand, has only one variable.

Consider the conservation of mass equation written in slightly different form as

$$\frac{\partial A}{\partial t} + \frac{\partial(uA)}{\partial x} = 0 \quad (4.183)$$

This equation implies that the variable cross-section area is transported with a velocity 'u'. However, both variables u and A appear again in momentum term.

- (3) The open channel flow equations assume a number of conditions that are being met like streamlines not crossing, occurrence of gradually varied flow, absence of vertical acceleration terms, etc. These assumptions for most part are valid except at the discontinuity, where all of the above conditions are violated.
- (4) In the Lagrangian mode solution the aspect ratios of the elements after a number of time steps, become large causing the solution to degenerate.
- (5) When the discontinuity is moving in otherwise still water condition, there are a large number of rays that cross-over affecting the solution algorithm.

- (6) In the literature of fluid mechanics most of results presented in the Lagrangian mode used a very fine grid size and the presence of at least a token dissipative term, Varoglu and Finn (1981). Such fine discretization was not attempted here because the practical and field applications of the model were part of the study objectives.
- (7) As only momentum is conserved across the discontinuity, there are no mechanisms present in the solution that would account for the dissipation of energy. Being a non-dissipative solution, this energy moves toward the tip of the discontinuity, forms a spike and causes undulations behind the surge. In this way, the solution mimics what is happening in the prototype. However, the flow equations are not representing this phenomenon.
- (8) It was found that the Eulerian-Lagrangian concept provides an excellent and natural dissipative interface. This interface is free from external variables and does not violate the basic assumption except in a small region near the tip of the discontinuity.

4.7 Generalization of the Solution Procedure:

The basic technique developed in Section 4.2 provides the framework for generalizing the procedure. Before attempting this generalization, an examination of the properties of the discretized equations is made. For this purpose only elements of Type 3 are evaluated.

Rewriting Equations (4.121) and (4.122)

Conservation of Mass:

$$\begin{aligned} & \frac{k}{4} (Q_{i+1}^n + Q_{i+1}^{n+1} - Q_{i-1}^n - Q_{i-1}^{n+1}) - \frac{1}{4} [(A_{i+1}^{n+1} + A_{i+1}^n) \delta_{i+1} \\ & - (A_{i-1}^{n+1} + A_{i-1}^n) \delta_{i-1}] - \frac{k}{4} (q_i^n \Delta^n + q_i^{n+1} \Delta^{n+1}) \\ & + \frac{1}{2} [A_i^{n+1} \Delta^{n+1} - A_i^n \Delta^n] = 0 \end{aligned} \quad (4.184)$$

Conservation of Momentum:

$$\begin{aligned} & - \frac{1}{4} [(Q_{i+1}^{n+1} + Q_{i+1}^n) \delta_{i+1} - (Q_{i-1}^{n+1} + Q_{i-1}^n) \delta_{i-1}] \\ & + \frac{k}{4} [(Qu)_{i+1}^{n+1} + (Qu)_{i+1}^n - (Qu)_{i-1}^{n+1} - (Qu)_{i-1}^n] \\ & + \frac{kg}{4} [(Ay)_{i+1}^{n+1} + (Ay)_{i+1}^n - (Ay)_{i-1}^{n+1} - (Ay)_{i-1}^n] \\ & - \frac{kg}{4} (A_i^n S_i^n \Delta^n + A_i^{n+1} S_i^{n+1} \Delta^{n+1}) \\ & + \frac{1}{2} (Q_i^{n+1} \Delta^{n+1} - Q_i^n \Delta^n) = 0 \end{aligned} \quad (4.185)$$

where

$$\delta_{i+1} = x_{i+1}^{n+1} - x_{i+1}^n \quad (4.186)$$

$$\delta_{i-1} = x_{i-1}^{n+1} - x_{i-1}^n \quad (4.187)$$

$$\Delta^n = x_{i+1}^n - x_{i-1}^n \quad (4.188)$$

$$\Delta^{n+1} = x_{i+1}^{n+1} - x_{i-1}^{n+1} \quad (4.189)$$

By definition,

$$\delta_i = u_i^n k \quad (4.190)$$

Also, defining other terms as follows:

$$A_i^{n+1/2} = \frac{1}{2} (A_i^{n+1} + A_i^n) \quad (4.191)$$

$$\begin{aligned} \Delta^{n+1/2} &= \frac{1}{2} (\Delta^{n+1} + \Delta^n) = \Delta^n + \frac{1}{2} (u_{i+1}^n - u_{i-1}^n) k \\ &= \Delta^{n+1} - \frac{1}{2} (u_{i+1}^n - u_{i-1}^n) k \end{aligned} \quad (4.192)$$

For now, concentrating only on Equation (4.184), dividing by $1/2 k \Delta^{n+1/2}$ will result

$$\begin{aligned} &\left(\frac{Q_{i+1}^{n+1/2} - Q_{i-1}^{n+1/2}}{\Delta^{n+1/2}} \right) - \left(\frac{A_{i+1}^{n+1/2} u_{i+1}^n - A_{i-1}^{n+1/2} u_{i-1}^n}{\Delta^{n+1/2}} \right) \\ &- \frac{1}{2} \left[\frac{q_i^n \Delta^n + q_i^{n+1} \Delta^{n+1}}{\Delta^{n+1/2}} \right] \\ &+ \left[\frac{A_i^{n+1} - A_i^n}{k} + A_i^{n+1/2} \left(\frac{u_{i+1}^n - u_{i-1}^n}{\Delta^{n+1/2}} \right) \right] = 0 \end{aligned} \quad (4.193)$$

This is basically the centred, Crank-Nicholson scheme where the spatial and temporal derivatives are taken along a moving grid. The partial differential equation of which Equation (4.193) is the difference equation, is:

$$\frac{\partial Q}{\partial x} + \frac{\partial A}{\partial t} - q = \frac{\partial(Au^n)}{\partial x} - A \frac{\partial u^n}{\partial x} \quad (4.194)$$

where

$$q = \frac{1}{2} \left[\frac{q_i^n \Delta^n + q_i^{n+1} \Delta^{n+1}}{\Delta^{n+1/2}} \right] \quad (4.195)$$

The terms on the right hand side of Equation (4.194) account for orienting the grid along the rays. Thus the moving element method becomes a general case of finite-differencing in a Lagrangian sense. This can be also verified by considering the special case of Eulerian grid. In other words,

$$\Delta^{n+1} = \Delta^n = \Delta^{n+1/2} = \Delta \quad (4.196)$$

and

$$\delta_i = \delta_{i+1} = \delta_{i-1} = 0 \quad (4.197)$$

Substitutions of Equations (4.196) and Equations (4.197) in (4.184) and (4.185) lead to the classical central difference scheme, second order accurate given as

$$\frac{Q_{i+1}^{n+1/2} - Q_{i-1}^{n+1/2}}{\Delta} + \frac{A_i^{n+1} - A_i^n}{k} - q_i^{n+1/2} = 0 \quad (4.198)$$

$$\frac{Q_i^{n+1} - Q_i^n}{k} + \frac{(Qu)_{i+1}^{n+1/2} - (Qu)_{i-1}^{n+1/2}}{\Delta} + g \frac{(Ay)_{i+1}^{n+1/2} - (Ay)_{i-1}^{n+1/2}}{\Delta} - g(A S_i)^{n+1/2} = 0 \quad (4.199)$$

Thus establishing roots of the moving element method, effort is now directed at generalizing the procedure. Two different types of generalization were proposed, tested and implemented. These are described in the following sections.

4.7.1 Temporal Generalization:

The scheme presented earlier is centered in time such that an equal weight of 0.25 is placed on the four values at each of the nodes of the trapezoidal elements. This is also consistent with the second-order accuracy of the scheme.

A first step in making the scheme generic is to relax the constraint of the four-point Newton-Cotes quadrature formula. Such relaxation always carries a price in sacrificing the overall accuracy of the scheme. In this method the second order accuracy is reduced to the first order.

Three different types of terms are evaluated by a modified integration formula. Recalling Equation (4.43) the equality is:

$$\int_{K_i} \int S_h \frac{\partial \phi^i}{\partial t} dx dt = A_{L_i} \left(S_h \frac{\partial \phi^{(i)}}{\partial t} \right) + A_{L_{i-1}} \left(S_h \frac{\partial \phi^{(i)}}{\partial t} \right) \quad (4.43)$$

It is proposed that the terms on the right hand side be evaluated as:

$$A_{L_i} \left(S_h \frac{\partial \phi^{(i)}}{\partial t} \right) = \frac{1}{4} \sum_{\xi=0}^1 \sum_{\eta=0}^1 (\theta S_{i+\eta}^{n+1} + (1-\theta) S_{i+\eta}^n) (x_{i+\eta}^{n+1} - x_{i+\eta}^n) \quad (4.200)$$

where $0.5 \leq \theta \leq 1.0$.

The following equivalency is implied:

$$S_{i+\eta}^{n+\xi} = \theta S_{i+\eta}^{n+1} + (1-\theta) S_{i+\eta}^n \quad (4.201)$$

When the contributions from K_{i-1} element are added and Equation (4.200) expanded, the value of the area integral is:

$$\int_{K_i} S_h \frac{\partial \phi^i}{\partial t} dx dt = \frac{1}{2} \left\{ [\theta S_{i+1}^{n+1} + (1-\theta) S_{i+1}^n] (x_{i+1}^{n+1} - x_{i+1}^n) - [\theta S_{i-1}^{n+1} + (1-\theta) S_{i-1}^n] (x_{i-1}^{n+1} - x_{i-1}^n) \right\} \quad (4.202)$$

Using similar substitutions of Equation (4.201), the spatial derivative in Equation (4.73) becomes:

$$\int_{K_i} S_h \frac{\partial \phi^i}{\partial x} dx dt = \frac{k}{2} [\theta (S_{i+1}^{n+1} - S_{i-1}^{n+1}) + (1-\theta) (S_{i+1}^n - S_{i-1}^n)] \quad (4.203)$$

Completing the numerical integration by drawing parallel with Equation (4.73).

$$\int_{K_i} S_h \phi^i dx dt = \frac{k}{2} [\theta S_i^{n+1} (x_{i+1}^{n+1} - x_{i-1}^n) + (1-\theta) S_i^n (x_{i+1}^n - x_{i-1}^n)] \quad (4.204)$$

At the next step the numerical integrations for Equations (4.202) to (4.204) are substituted for various terms in Equations (4.32) and (4.33). Here the terms for type 3 element are presented. For other types similar arguments may be forwarded and equations developed.

Conservation of Mass:

$$\begin{aligned} & \frac{k}{2} [\theta (Q_{i+1}^{n+1} - Q_{i-1}^{n+1}) + (1-\theta) (Q_{i+1}^n - Q_{i-1}^n)] \\ & - \frac{1}{2} \left\{ [\theta A_{i+1}^{n+1} + (1-\theta) A_{i+1}^n] \delta_{i+1} - [\theta A_{i-1}^{n+1} + (1-\theta) A_{i-1}^n] \delta_{i-1} \right\} \\ & - \frac{k}{2} [\theta q_i^{n+1} \Delta^{n+1} + (1-\theta) q_i^n \Delta^n] + \frac{1}{2} [A_i^{n+1} \Delta^{n+1} - A_i^n \Delta^n] = 0 \end{aligned} \quad (4.205)$$

Conservation of Momentum:

$$\begin{aligned}
 & - \frac{1}{2} \left\{ [\theta (Q_{i+1}^{n+1} + (1-\theta) Q_{i+1}^n) \delta_{i+1} - [\theta Q_{i-1}^{n+1} + (1-\theta) Q_{i-1}^n] \delta_{i-1}] \right\} \\
 & + \frac{k}{2} \left\{ \theta [(Qu)_{i+1}^{n+1} - (Qu)_{i-1}^{n+1}] + (1-\theta) [(Qu)_{i+1}^n - (Qu)_{i-1}^n] \right\} \\
 & + \frac{kg}{2} \left\{ \theta [(A\bar{y})_{i+1}^{n+1} - (A\bar{y})_{i-1}^{n+1}] + (1-\theta) [(A\bar{y})_{i+1}^n - (A\bar{y})_{i-1}^n] \right\} \\
 & - \frac{kg}{2} [(AS_g)_{i+1}^{n+1} \Delta^{n+1} - (1-\theta) (AS_g)_i^n \Delta^n] \\
 & + \frac{1}{2} (Q_i^{n+1} \Delta^{n+1} - Q_i^n \Delta^n) = 0 \tag{4.206}
 \end{aligned}$$

It is evident from the above two equations that for $\theta = 0.5$ the difference forms revert back to Equations (4.184) and (4.185). When the moving element scheme was implemented with a variable input in θ , the oscillations present in Lagrangian mode solution are suppressed for $\theta > 0.5$. The price is paid in a slight dispersion of the front.

A number of tests were carried out to study the variation of θ and discussed in the next chapter under sensitivity analysis.

4.7.2 Spatial Generalization

The spatial generalization can be made in two ways. In the first approach the steps taken in the temporal generalization are followed at the numerical integration of the area integral defined in Equation (4.43). This approach, however, was not implemented, but merits further investigation.

The second method, which was employed in model formulation consists of assigning different weights for line integrals. This in turn effects the computation of flux terms across the time plane. Recalling the line integral for the flux terms.

$$\int_{L_{t_i^n}} S_h \phi^i dx = \frac{x_{i+1}^n - x_i^n}{2} \sum_{\eta=0}^1 S_{i+\eta}^n \phi^i(P_{i+\eta}^n) \quad (4.78)$$

In this equation the variable S is approximated as:

$$S_{i+\eta}^n = \beta S_i^n + (1-\beta) S_{i+1}^n \quad (4.207)$$

where $0.5 \leq \beta \leq 1.0$.

Substitution of Equation (4.207) in Equation (4.78) the result is:

$$\int_{L_{t_i^n}} S_h \phi^i dx = \frac{1}{2} (x_{i+1}^n - x_i^n) (\beta S_i^n + (1-\beta) S_{i+1}^n) \quad (4.208)$$

Adding contributions from element K_{i-1} the flux entering the solution domain is adjusted to:

$$\int_{L_{t_i^n}} S_h \phi^i dx = \frac{1}{2} \left[(x_i^n - x_{i-1}^n) (1-\beta) S_{i-1}^n + (x_{i+1}^n - x_i^n) \beta S_i^n + (x_{i+1}^n - x_i^n) (1-\beta) S_{i+1}^n \right] \quad (4.209)$$

In a like manner the flux leaving the solution domain is computed as

$$\int_{L_{t_i^{n+1}}} S_h \phi^i dx = \frac{1}{2} \left[(x_i^{n+1} - x_{i-1}^{n+1}) (1-\beta) S_{i-1}^{n+1} + (x_{i+1}^{n+1} - x_i^{n+1}) \beta S_i^{n+1} + (x_{i+1}^{n+1} - x_i^{n+1}) (1-\beta) S_{i+1}^{n+1} \right] \quad (4.210)$$

When flux terms at time level t^n , i.e. Equation (4.209) are implemented and no adjustments for flux leaving the domain at the time level t^{n+1} are made, i.e. β in Equation (4.210) is set to 1.0. This scenario is equivalent to the α -algorithm proposed by Abbot (1974) with one difference that all nodal values are for a Lagrangian grid. Although not tested, this approach may provide yet another dissipative interface.

Retaining the temporal generalization terms in Equations (4.205) and (4.206), the discretized flow equations become, following the definitions of

$$\Delta_{i-1/2}^n = x_i^n - x_{i-1}^n \quad (4.211)^a$$

$$\Delta_{i+1/2}^{n+1} = x_{i+1}^{n+1} - x_i^{n+1} \quad (4.212)$$

Conservation of Mass:

$$\begin{aligned} & \frac{k}{2} [\theta (Q_{i+1}^{n+1} - Q_{i-1}^{n+1}) + (1-\theta)(Q_{i+1}^n - Q_{i-1}^n)] \\ & - \frac{1}{2} \left\{ [\theta A_{i+1}^{n+1} + (1-\theta)A_{i+1}^n] \delta_{i+1} - [\theta A_{i-1}^{n+1} + (1-\theta)A_{i-1}^n] \delta_{i-1} \right\} \\ & - \frac{k}{2} [\theta q_i^{n+1} \Delta^{n+1} - (1-\theta)q_i^n \Delta^n] \\ & + \frac{1}{2} [(1-\beta)\Delta_{i-1/2}^{n+1} A_{i-1}^{n+1} + \beta \Delta^{n+1} A_i^{n+1} + (1-\beta)\Delta_{i+1/2}^{n+1} A_{i+1}^{n+1} \\ & - (1-\beta)\Delta_{i-1/2}^n A_{i-1}^n - \beta \Delta^n A_i^n - (1-\beta)\Delta_{i+1/2}^n A_{i+1}^n] = 0 \quad (4.213) \end{aligned}$$

Conservation of Momentum:

$$\begin{aligned} & - \frac{1}{2} \left\{ [\theta Q_{i+1}^{n+1} + (1-\theta)Q_{i+1}^n] \delta_{i+1} - [\theta Q_{i-1}^{n+1} + (1-\theta)Q_{i-1}^n] \delta_{i-1} \right\} \\ & + \frac{k}{2} \left\{ \theta [(Qu)_{i+1}^{n+1} - (Qu)_{i-1}^{n+1}] + (1-\theta)[(Qu)_{i+1}^n - (Qu)_{i-1}^n] \right\} \\ & + \frac{kg}{2} \left\{ \theta [(A\bar{y})_{i+1}^{n+1} - (A\bar{y})_{i-1}^{n+1}] + (1-\theta)[(A\bar{y})_{i+1}^n - (A\bar{y})_{i-1}^n] \right\} \\ & - \frac{kg}{2} [\theta (AS_g)_{i+1}^{n+1} \Delta^{n+1} + (1-\theta)(AS_g)_i^n \Delta^n] \\ & + \frac{1}{2} [(1-\beta)\Delta_{i-1/2}^{n+1} Q_{i-1}^{n+1} + \beta \Delta^{n+1} Q_i^{n+1} + (1-\beta)\Delta_{i+1/2}^{n+1} Q_{i+1}^{n+1} \\ & - (1-\beta)\Delta_{i-1/2}^n Q_{i-1}^n - \beta \Delta^n Q_i^n - (1-\beta)\Delta_{i+1/2}^n Q_{i+1}^n] = 0 \quad (4.214) \end{aligned}$$

A comparison with Equations (4.184) and (4.185) shows that the discretized Equations (4.213) and (4.214) are generalized forms of the basic equations. When θ is equal to 0.5 and β is equal to 1.0 the basic form is retained.

A further examination of the last term associated with spatial or generalization indicates that this process causes the difference equation to take a consistent mass matrix against lumped mass for the basic equations. Finally, when the value of β is set to 2/3 and computation made along an Eulerian grid the equations are same with respect to weighting in the basic finite element scheme developed by Cooley and Moin (1976). Thus the generalization developed in Equations (4.213) and (4.214) is the finite element version along the Lagrangian grid when $\beta = 2/3$.

The sensitivity of this parameter is discussed in the next chapter.

4.8 Employment of Petrov-Galerkin Basis Function:

During the initial testing of the Lagrangian mode solution, the non-dissipative behaviour resulted in oscillatory solution. To overcome the problem by means of external dissipation mechanisms alternate forms of basis functions were investigated. One of the techniques employed resembled an alternate basis function with reported success by Katopodes (1984).

In the Petrov-Galerkin approach of the method of weighted residuals the residuals are not only minimized against the basis function but also the slope of the basis function. Similar techniques have had success in the field of fluid mechanics.

Using the definitions used in developing the moving element method in Section 4.2.2 and applying the method of weighted residuals with the requirement that the residual with respect to $\phi(x, t) + \epsilon(\partial/\partial x)\phi(x, t)$ vanish.

Conservation of Mass:

$$\int_{t_1}^{t_2} \int_{x_L}^{x_R} \left(\frac{\partial A}{\partial t} + \frac{\partial Q}{\partial x} - q \right) \left(\phi + \epsilon \frac{\partial \phi}{\partial x} \right) dx dt = 0 \quad (4.215)$$

Conservation of Momentum:

$$\int_{t_1}^{t_2} \int_{x_L}^{x_R} \left[\frac{\partial Q}{\partial t} + \frac{\partial}{\partial x} (Qu) + g \frac{\partial}{\partial x} (A \bar{y}) - gA (S_0 - S_f) \right] \left(\phi + \epsilon \frac{\partial \phi}{\partial x} \right) dx dt = 0 \quad (4.216)$$

where ϵ defines the dissipation level.

It is clear from the above equations that the solution consist of two parts: the first part with weighting parameter ϕ obviously leads to the moving element scheme and is not repeated here. In this section, the second part of the integral is derived for the three terms of continuity equation given by Equations (4.65), (4.73) and (4.76). Only terms for Type 3 elements are presented.

Considering the continuity equation:

$$\epsilon \int_{t_1}^{t_2} \int_{x_L}^{x_R} \left[\frac{\partial Q}{\partial x} + \frac{\partial A}{\partial t} - q \right] \frac{\partial \phi}{\partial x} dx dt \quad / \quad (4.217)$$

Only the first two terms require derivation as the others have been derived earlier.

(1) Evaluation of

$$\epsilon \int \int_{K_i} \frac{\partial Q}{\partial x} \frac{\partial \phi}{\partial x} dx dt$$

From Equation 4.67 the value of $\partial \phi / \partial x$ is

$$\frac{\partial \phi^i}{\partial x} = - \frac{1}{(x_{i+1}^{n+\xi} - x_i^{n+\xi})} \quad (4.67)$$

In the same fashion

$$\frac{\partial Q}{\partial x} = \left(\frac{Q_{i+1}^{n+\xi} - Q_i^{n+\xi}}{x_{i+1}^{n+\xi} - x_i^{n+\xi}} \right) \quad (4.218)$$

From Newton-Cotes integration for K_i contribution

$$A_i \left(\frac{\partial Q}{\partial x} \frac{\partial \phi^i}{\partial x} \right) = \frac{\epsilon}{4} \sum_{\eta=0}^1 \sum_{\xi=0}^1 \frac{\partial Q}{\partial x} \cdot \frac{\partial \phi^i}{\partial x} \cdot J_i^n \quad (4.219)$$

Expanding by substituting Equations (4.24), (4.67) and (4.218) in (4.219)

$$A_i \left(\frac{\partial Q}{\partial x} \frac{\partial \phi^i}{\partial x} \right) = - \frac{k\epsilon}{4} \left[\frac{Q_{i+1}^{n+1} - Q_i^{n+1}}{x_{i+1}^{n+1} - x_i^{n+1}} + \frac{Q_{i+1}^n - Q_i^n}{x_{i+1}^n - x_i^n} \right] \quad (4.220)$$

Adding contributions from element K_{i-1} the integral leads to:

$$\epsilon \int_{K_i} \left(\frac{\partial Q}{\partial x} \frac{\partial \phi^i}{\partial x} \right) dx dt = - \frac{k\epsilon}{2} \left[\frac{Q_{i+1}^{n+1} - Q_i^{n+1}}{\Delta_{i+1/2}^{n+1}} + \frac{Q_{i+1}^n - Q_i^n}{\Delta_{i+1/2}^n} \right. \\ \left. - \frac{Q_i^{n+1} - Q_{i-1}^{n+1}}{\Delta_{i-1/2}^{n+1}} - \frac{Q_i^n - Q_{i-1}^n}{\Delta_{i-1/2}^n} \right] \quad (4.221)$$

where the values of were defined in Equations (4.211) and (4.212).

(ii) Evaluation of

$$\epsilon \int_{K_i} \frac{\partial A}{\partial t} \frac{\partial \phi}{\partial x} dx dt$$

As a first step evaluating

$$\frac{\partial A}{\partial t} = \frac{\partial A}{\partial \xi} \frac{\partial \xi}{\partial t} + \frac{\partial A}{\partial \eta} \frac{\partial \eta}{\partial t} \quad (4.222)$$

From the definition of 'A'

$$\frac{\partial A}{\partial \xi} = (A_{i+\eta}^{n+1} - A_{i+\eta}^n) \quad (4.223)$$

and

$$\frac{\partial A}{\partial \eta} = (A_{i+1}^{n+\xi} - A_i^{n+\xi}) \quad (4.224)$$

Substituting Equations (4.51), (4.53), (4.223) and (4.224) in (4.22) yield

$$\frac{\partial A}{\partial t} = \frac{1}{k} (A_{i+\eta}^{n+1} - A_{i+\eta}^n) - \frac{1}{k} \frac{(A_{i+1}^{n+\xi} - A_i^{n+\xi})}{(x_{i+1}^{n+\xi} - x_i^{n+\xi})} (x_{i+\eta}^{n+1} - x_{i+\eta}^n) \quad (4.225)$$

From the known value of the Jacobian, the contribution from element K_i is

$$A_{L_i} \left(\frac{\partial A}{\partial t} \frac{\partial \phi^i}{\partial x} \right) = - \frac{\epsilon}{4} \sum_{\eta=0}^1 \sum_{\xi=0}^1 \left[(A_{i+\eta}^{n+1} - A_{i+\eta}^n) \right. \\ \left. - (A_{i+1}^{n+\xi} - A_i^{n+\xi}) \frac{(x_{i+\eta}^{n+1} - x_{i+\eta}^n)}{(x_{i+1}^{n+\xi} - x_i^{n+\xi})} \right] \quad (4.226)$$

Expansion of Equation (4.226) and addition of the contribution from element K_{i-1}

evaluate the integral as

$$\begin{aligned}
\epsilon \int_{K_i} \left[\frac{\partial A}{\partial t} \cdot \frac{\partial \phi^i}{\partial x} \right] dx dt = & \frac{\epsilon}{4} \left\{ (\delta_{i+1} + \delta_i) \left[\frac{(A_{i+1}^n - A_i^n)}{\Delta_{i+1/2}^n} + \frac{(A_{i+1}^{n+1} - A_i^{n+1})}{\Delta_{i+1/2}^{n+1}} \right] \right. \\
& \left. - (\delta_i + \delta_{i-1}) \left[\frac{(A_i^n - A_{i-1}^n)}{\Delta_{i-1/2}^n} + \frac{(A_i^{n+1} - A_{i-1}^{n+1})}{\Delta_{i-1/2}^{n+1}} \right] \right\} \\
& - \frac{\epsilon}{2} (A_{i+1}^{n+1} - A_{i+1}^n - A_{i-1}^{n+1} + A_{i-1}^n)
\end{aligned} \tag{4.227}$$

Thus the extra terms in the continuity equation for Type 3 elements alone are the sum total of the contributions of the three terms as:

$$\begin{aligned}
& - \frac{k\epsilon}{2} \left[\frac{(Q_{i+1}^{n+1} - Q_i^{n+1})}{\Delta_{i+1/2}^{n+1}} + \frac{(Q_{i+1}^n - Q_i^n)}{\Delta_{i+1/2}^n} - \frac{(Q_i^{n+1} - Q_{i-1}^{n+1})}{\Delta_{i-1/2}^{n+1}} \right. \\
& \left. - \frac{(Q_i^n - Q_{i-1}^n)}{\Delta_{i-1/2}^n} \right] + \frac{\epsilon}{4} \left\{ (\delta_{i+1} + \delta_i) \left[\frac{(A_{i+1}^n - A_i^n)}{\Delta_{i+1/2}^n} + \frac{(A_{i+1}^{n+1} - A_i^{n+1})}{\Delta_{i+1/2}^{n+1}} \right] \right. \\
& \left. - (\delta_i + \delta_{i-1}) \left[\frac{(A_i^n - A_{i-1}^n)}{\Delta_{i-1/2}^n} + \frac{(A_i^{n+1} - A_{i-1}^{n+1})}{\Delta_{i-1/2}^{n+1}} \right] \right\} \\
& - \frac{\epsilon}{2} (A_{i+1}^{n+1} - A_{i+1}^n - A_{i-1}^{n+1} + A_{i-1}^n) \\
& + \frac{k\epsilon}{4} (q_{i+1}^n + q_{i+1}^{n+1} - q_{i-1}^n - q_{i-1}^{n+1})
\end{aligned} \tag{4.228}$$

For the momentum equation various terms for the equations are similarly developed. The two equations were then modelled into a separate computer program. The results form part of discussion in the next chapter.

4.9 Extension of Methodology to Nonprismatic Channels

The equations describing the open channel flow in Equations (4.1) and (4.2) are restricted. The equations are valid for prismatic channels with no contribution of

lateral flow to momentum. The first restriction is a serious one in that near-discontinuous flow simulation in natural channels will be in error:

To overcome this drawback the momentum equation was expanded to address the pressure forces due to form changes in nonprismatic channels. This is described in Section 4.9.1.

The second modification was made to allow off-channel storage to be analyzed separately. In natural channels there are zones where the flood waters are stored during the rising limb, the flow in several zones in the direction of main flow (i.e. 'x' direction) is negligible and stored waters are released during the recession part of the hydrograph. The adjustments were required and made to the mass conservation equation. The extra terms and their contributions are discussed in Section 4.9.2.

4.9.1 Convective Acceleration and Pressure Terms:

There are a number of studies reporting the adjustments in the convective acceleration or pressure terms. Studies where the energy form of momentum equation is used, usually resort to adding a term to the convective acceleration component. On the other hand, when the conservative or divergent form of momentum equation is used, the pressure term is expressed explicitly as the first moment of area. In situations like these, adjustments are made to the pressure term to account for the non-prismatic form. In the literature search conducted, no instances were found in which adjustments were made to both convective acceleration and pressure terms. Further, the reports indicate unsatisfactory handling of nonprismatic channels when only one of the two adjustments are made.

A closer examination of the divergent form of momentum equation indicate that both convective acceleration and pressure terms require to be addressed for the

changes in channel shapes. Recalling the momentum equation,

$$\frac{\partial Q}{\partial t} + \frac{\partial}{\partial x} (Qu) + g \frac{\partial (A \bar{y})}{\partial x} - gA (S_o - S_f) = 0 \quad (4.2)$$

Considering the second term in this equation, which accounts for the convective acceleration, replacing the velocity 'U' by Q/A and expanding

$$\frac{\partial (Qu)}{\partial x} = 2u \frac{\partial Q}{\partial x} - u^2 \frac{\partial A}{\partial x} \quad (4.229)$$

To account for the nonprismatic form, the second term on the right hand side is expanded as

$$\frac{\partial (Qu)}{\partial x} = 2u \frac{\partial Q}{\partial x} - u^2 \frac{\partial A}{\partial y} \cdot \frac{\partial y}{\partial x} - u^2 \frac{\partial A}{\partial x} \Big|_{y=\text{constant}} \quad (4.230)$$

The last term in the above expansion is interpreted as the rate of change of area with respect to channel length for a given depth of flow. Numerically it is the equivalent of the measure of departure from a prismatic shape. Obviously the third term vanishes for prismatic channels.

Next, consider the third term in Equation (4.2) describing the pressure term. This term is incomplete for nonprismatic channel and requires an additional term to account for the force exerted, by the difference in area between two sections, on the body of water. Mathematically the complete term is given as:

$$\frac{\partial}{\partial x} (g A \bar{y}) + g \int_0^y (y - \epsilon) \frac{\partial b(\epsilon)}{\partial x} \cdot d\epsilon \quad (4.231)$$

where $b(\epsilon)$ is the width of cross-section at any depth ϵ . Again, the integral in the above equation can be interpreted as the rate of change of the first moment of area for a given depth of flow.

By taking into account the momentum contribution of lateral flows and the terms derived above, the momentum equation as used in this work becomes:

$$\frac{\partial Q}{\partial t} + \frac{\partial(Qu)}{\partial x} + g \frac{\partial(A\bar{y})}{\partial x} - gA(S_0 - S_f) - u_x q + \int_0^y g(y-\epsilon) \frac{\partial b(\epsilon)}{\partial x} d\epsilon - u^2 \frac{\partial A}{\partial x} \Big|_{y=\text{constant}} = 0 \quad (4.232)$$

The sensitivity of the above additions when analysing rapidly varying flows is presented in Chapter 5.

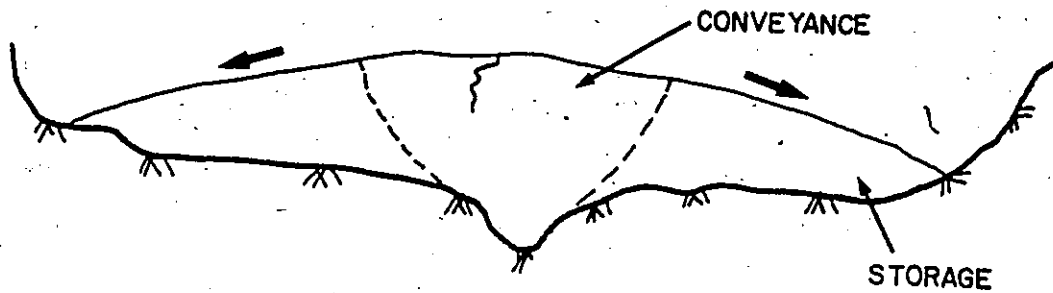
4.9.2 Off-Channel Storage:

In natural channels it is a quite common occurrence that the bulk of flow is carried by the main channel and its immediate confines. In adjacent areas the water may be moving extremely slowly or not at all. It has been reported that for natural conditions, the main channel with about 15% of the cross-section area carried an estimated 85% of the total flow.

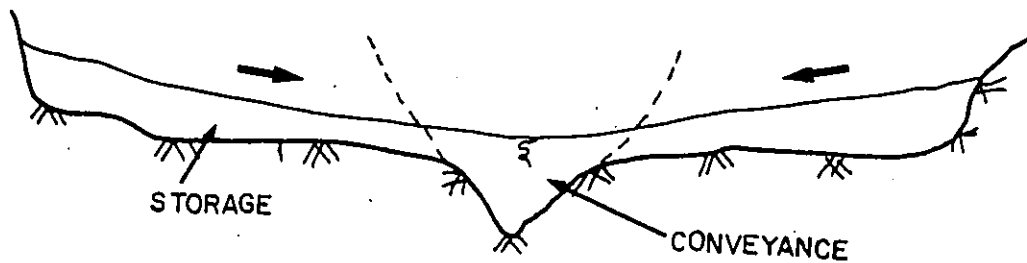
Thus the presence of off-channel storage requires that the mass continuity be properly preserved. Also, as the storage is assumed to have no flow properties, the conveyance requirements explained by the momentum equation are waived. The off-channel storage term, therefore, appears only in the mass-continuity equation.

Technically, the off channel storage problem involves a two-dimensional problem. As shown in Fig. 4-13, the flow occurs in a transverse direction from the main channel to storage during the rising limb of hydrograph and a gradient is, therefore, present to explain this. The process reverses during the recession limb of hydrograph. For modelling purposes, however, it is assumed that the water level in the main channel and storage rises simultaneously and are at the same elevation as shown in Fig. 4-14.

A number of workers have addressed the off-channel storage question adequately by modifying the mass continuity equation as:



Flow from Conveyance to Storage During Rising Limb of Hydrograph



Flow from Storage to Conveyance During Recession Limb of Hydrograph

Fig. 4.13 Main Channel and Storage Flow Dynamics

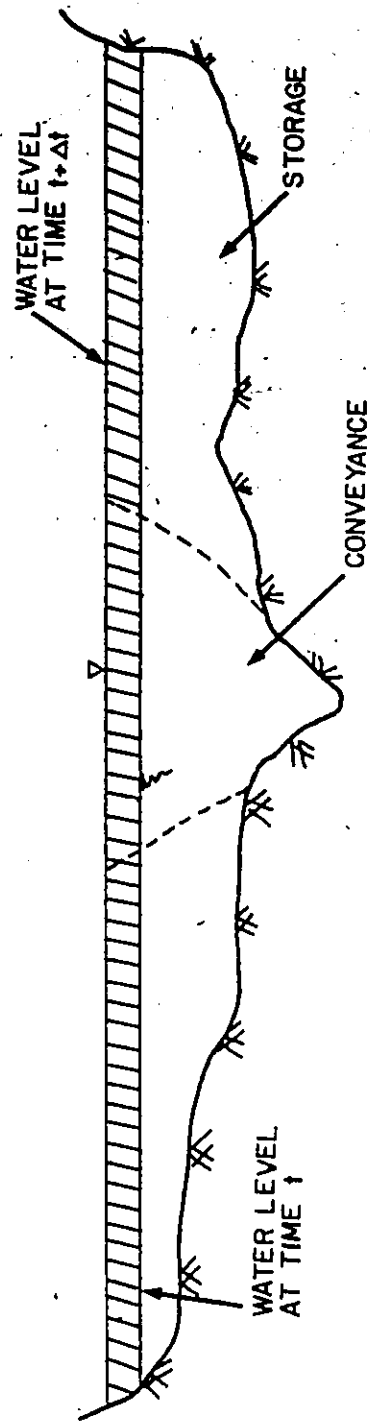


Fig. 4.14 Approximation of Conveyance and Storage Flow Interchange

$$\frac{\partial Q}{\partial x} + \frac{\partial A}{\partial t} + \frac{\partial A_o}{\partial t} - q = 0 \quad (4.233)$$

where A_o represents the cross-sectional area in the off-channel storage zone. The third term of the equation is handled separately and in the same way as the area term is handled. The off-channel storage option was implemented for testing in natural streams.

It should be noted that the division between the main and off-channel is arbitrary at best. Improper division would result in differences in computed elevations.

4.10 Summary

In this chapter the description of a generalized moving element model was provided. The methodology was highlighted with assumptions, model formulation and limitations. The basic model incorporates a Lagrangian mode solution of the divergent form of open channel flow equations.

The model consists of mixed triangular and isoparametric trapezoidal elements. The triangular element is required at the upstream boundary. The trapezoidal element sides are oriented such that their slopes are proportional to nodal velocities. The model is capable of handling both subcritical and supercritical flows. The discretized form of equations are solved by an efficient double sweep technique.

The Lagrangian mode solution is non-dissipative in character. In this regard, the technique suffers, to a lesser extent, with the problems of other non-dissipative schemes. This problem was largely overcome by developing an alternate form of solution domain, termed Eulerian-Lagrangian linked grid. The scheme provides for a natural dissipative interface. The basic moving element method was generalized in both temporal and spatial sense. This was achieved by redefining the

numerical integration methods. The dissipative interface was improved by employing a higher order interpolation formula to reduce clipping errors and for a better representation of the front.

An area not fully pursued was an alternate form of Lagrangian mode solution by the Petrov-Galerkin scheme. The method requires that the residual vanish with respect to a modified basis function. The basis function consist of a normal function and first-order spatial derivative of the normal function. Other areas of improvement of the model were in a complete description of the rapidly varying open channel flow equations to account for nonprismatic form of conveying and off-channel storage zones.

CHAPTER 5

NUMERICAL EXPERIMENTS

5.1 Introduction

In order to prove that the model developed is not a futile exercise in calculus and numerical analysis, it is essential that the model be subject to some benchmark tests. There are no uniform or universal standards against which unsteady flow models can be tested.

The best alternative would be compare the model results against observations in real life from either data collected during and after a dambreak or flashflood. At such times, sensibly, the authorities are more concerned about saving lives and reducing the potential of flood damages than the trivialities of data collection. Hence, any data from a real life scenario would be the survey of the highest flood level profile following the flood event, and stage hydrographs of a few stream gauges if they survived. Even when a stage hydrograph is preserved, the associated discharges are uncertain at best because the observed stages are likely to be well beyond any recorded or measured flows and the gauge rating table. Also, there are other factors that influence both flow and elevation, most important of them being infiltration losses in a dry valley, mud flow, erosion of stream bed, etc. In such situations matching the profiles or hydrograph is an exercise in curve fitting, and the more parameters one has, the better the fit is.

The information obtained in an experimental set up of physical models thus becomes even more important. Experimental data provided by Faure (1935), Terzidis (1968) and those reported by Vasiliev et al (1965) provide good benchmarks for model

testing. These benchmarks, however, do not indicate the numerical behaviour of the scheme, or the strengths or weaknesses and limitations of the model. Limited verifications of this type are described Chapter 7.

In order to study the performance of the moving element scheme, a battery of numerical experiments were designed. These experiments are described in this chapter. The next step in model testing is sensitivity analysis. Such analysis usually highlights the variables which most influence the model output.

As the model is being purported to be better than or equal to other available methods, limited comparative test results with finite difference and finite element method are presented. Most of the testing and comparisons are with the Eulerian-Lagrangian based moving element models. Therefore, results are also shown for Lagrangian and Petrov-Galerkin based schemes. Finally, extensive testing for nonprismatic channels is reported as this forms the basis for application to natural streams.

5.2 Design of Experiments:

With mathematical models, such as the one developed in this work, it is quite common to evaluate the behaviour by designing suitable experiments. Such experiments are devised with the end use of model as the basic objective. For example, when Vasiliev et al (1965) described the two-stage predictor-corrector method, the numerical experiment consisted of routing a supercritical wave in a frictionless, horizontal channel 200 m wide. Subsequent applications were in natural streams. On the other hand, Katopodes (1984) concentrated on the numerical efficiency and the model tests reflected this focus of the Petrov-Galerkin scheme.

There are numerous combinations, that one can think of, to carry out these tests. A large number of tests were designed and carried out; space limitations, however, preclude inclusion of and discussion of all the tests. Only the basic tests which highlighted the strengths and pointed out the shortcomings are noted. In order to preserve the identification of runs the following classification was used:

Test A: Supercritical surge moving downstream

Test B: Subcritical surge moving downstream

Test C: Subcritical surge moving upstream

Test D: Continuous flow simulation

Test E1: Surge through choke - horizontal constriction

Test E2: Surge over hump - vertical constriction

These experiments are discussed in the following sections.

5.2.1. Test A - Supercritical Surge Moving Downstream

This test was first designed and reported by Vasiliev et al (1965) and a two-stage implicit predictor-corrector method was used. The test was modified by Terzides and Strelkoff (1970) and a basic explicit and an improved Lax-Wendroff type explicit methods were employed. The experiment adopted here is the same as that reported by Terzides and Strelkoff. The experiment is defined by the following particulars.

Physical Description:

The channel is 200 m wide and 1500 m long and rectangular in cross-section. The bed is horizontal, that is to say the normal depth for any flow is of infinite value. The channel roughness is described by the Manning's equation and is assumed to be zero. In other words, the channel is frictionless.

Initial and Boundary Conditions

The initial conditions in the channel consisted of a level pool 2 m deep with no flow. The boundary conditions imposed were a flow increase from zero m^3/s to 28,000 m^3/s in 0.5 sec while the upstream depth is fixed at 10.1 m. These conditions are maintained at the upstream boundary for the duration of the experiment. The discharge and depth combination produces a velocity of 13.86 m/s which is greater than the critical velocity for this depth, hence the flow regime upstream of the discontinuity is supercritical. On the other hand, subcritical flow conditions exist downstream of the front.

With these requirements, both flowrate and depth of flow are required at the upstream boundary, while the downstream node is maintained as no flux or zero flow boundary.

Discretization and Solution Procedure:

Following the results reported by Vasiliev et al (1965) and Terzides and Strelkoff (1970), the solution domain was divided into 150 elements each 10 m long. For this element size, the Courant condition is

$$\Delta t \leq \frac{\Delta x}{|u + c|} \quad (5.1)$$

where $u = 13.86 \text{ m/s}$ $c = \text{celerity} = \sqrt{gy}$
 $= 9.95 \text{ m/s}$

from where the time step is given as 0.41 second. Also the Courant Number is defined as

$$C_r = (c + \sqrt{gy}) \Delta t / \Delta x \quad (5.1a)$$

The Courant condition requires $C_r \leq 1.0$.

However, the computations were carried out at a time step of 0.5 s. The Courant Number was 1.2.

The supercritical surge was allowed to progress for 60 seconds and the stage profile captured at that time is presented in Fig. 5.1. The profile is based on the Eulerian-Lagrangian scheme with the interpolation by the Three Point Lagrangian Formula. Since it was intended that this serve as a solution comparison for other runs the numerical scheme, was set as pure centered, that is, the temporal weighting was set at 0.5 and spatial weighting at 1.0.

The theoretical wave speed and thus the location of the wave front after a specified elapsed time is known. With the problem as posed above, the wave travels at a speed of 17.3 m/s. In other words, the wave front after 60 s should travel 1037 m respectively.

It is evident from the results in Fig. 5.1 that both the wave profile and the speed are computed in an acceptable manner. The only noticeable difference is at the tip of the front where a spike or piling of water is observed immediately behind the nose of the front. Excluding the spike region, the maximum difference is less than 1% of the height of the wave. Furthermore, the entire frontal wave is captured within 20 metres. A comparison with the results of the investigations by Vasiliev et al (1965) and by Terzides and Strelkoff (1970) reveals improved wave capturing properties. The existence of the spike is discussed separately as a common problem in other schemes.

5.2.2 Test B - Subcritical Surge Moving Downstream

This test was specifically designed for this study. The experiment was later employed in other tests. Just as a matter of comparison, the temporal rate of rise adopted in this

EULARIAN-LAGRANGIAN SOLUTION

Profiles at Time = 60 Sec. TEST "A"

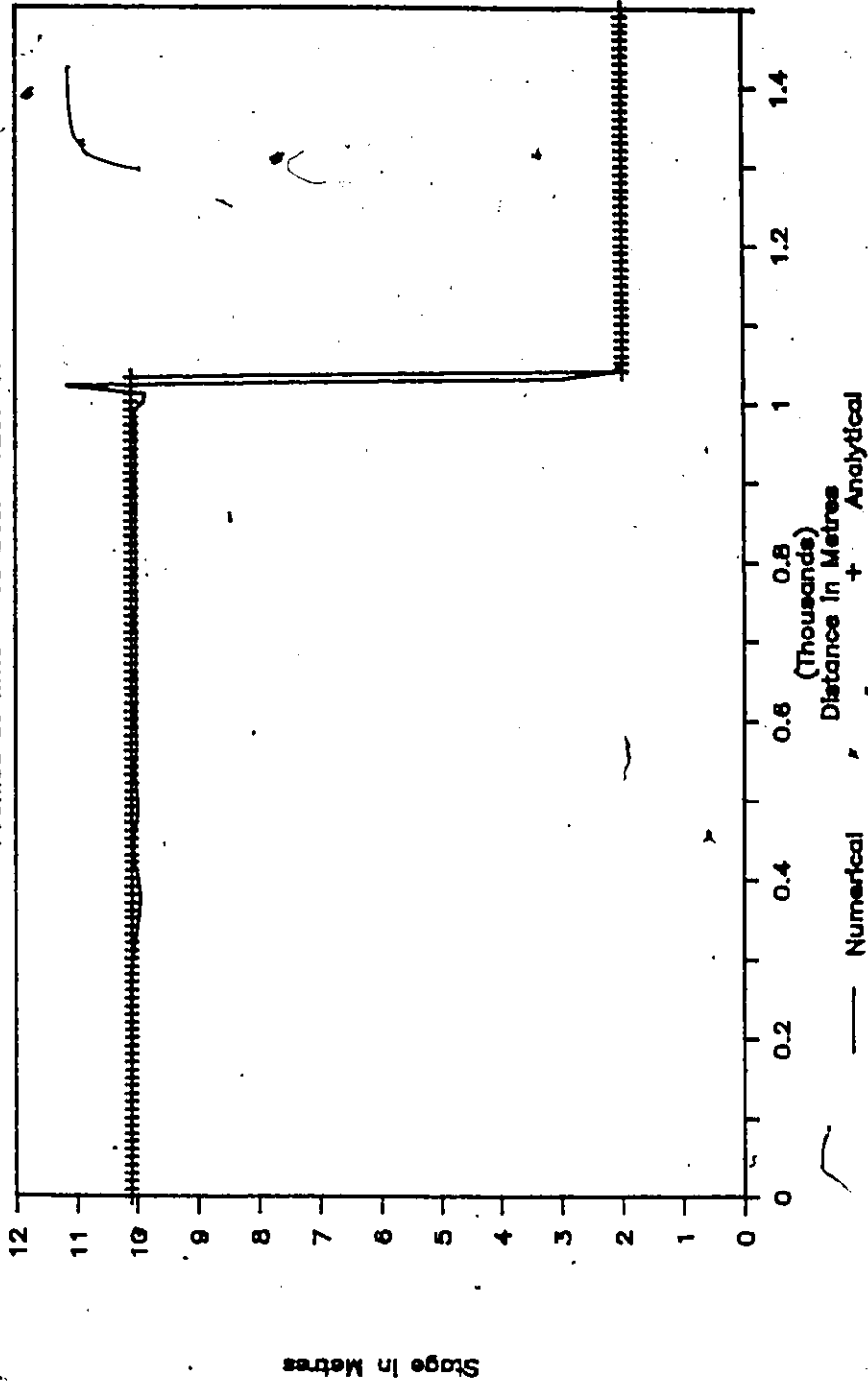


Fig. 5.1 Water Surface Profiles for Test 'A' - Supercritical Surge in Frictionless Channel.

Stage in Metres

(Thousands)

Distance in Metres

— Numerical - - - Analytical

experiment ranged from 500 to 2000 times the reported temporal acceleration of the Teton Dam-Break flood. The following particulars were adopted.

Physical Description:

The rectangular channel of 100 m width is 1000 m long with a horizontal bed. The channel roughness is described by the Manning's equation and as in Test A is assumed to be zero for the basic run. Other runs included a real world situation with a channel roughness of 0.015.

Initial and Boundary Conditions:

The initial conditions consisted of a level pool 2 m deep and no flow. The boundary condition at the upstream end required the flow to increase from zero to 2000 m³/s in 1.0 sec. This combination results in a subcritical flow condition. Hence only the flow was specified at the upstream boundary. It is assumed that unlimited supply is available as this flow is maintained for the duration of experiment.

For subcritical flow conditions throughout the solution domain, the downstream boundary is required. Single-stage rating curve was, therefore, prescribed. This was equivalent to imposing a zero flow condition.

Discretization and Solution Procedure:

As a basis of comparison, it was decided to obtain a solution at a Courant Number slightly greater than 1.0. For this purpose, the analytical solution was first obtained by computing the wave characteristics by using the following basic equations.

$$V_w = \frac{Q_1 - Q_0}{A_1 - A_0} \quad (5.2)$$

and

$$V_w = \frac{(Q_1 u_1 - Q_0 u_0) + g(A_1 \bar{y}_1 - A_0 \bar{y}_0)}{Q_1 - Q_0} \quad (5.3)$$

where V_w is the velocity of wave. The variables with zero subscript refer to quantities at initial flow conditions, while with those a subscript of one are associated with surge flow. In Equations (5.2) and (5.3) the two unknowns are V_w and y_1 . By eliminating V_w between the equations, a value was obtained of $y = 4.41$ m with a wave velocity of 8.3 m/s.

For these flow conditions and an element 10 m long, a Courant Number of 1.0 is associated with a time step of 0.9 sec. For the basic run, therefore, a time step of 1.0 sec or 1.1 times the Courant condition was used.

The subcritical surge was allowed to progress for 90 sec with profiles captured at intermediate times. The solution based on the Eulerian-Lagrangian moving element scheme is presented in Fig. 5.2. The stage hydrographs at the quarter, mid and three quarter points of the channel for the same run is shown in Fig. 5.3. The other parameters for this run included the interpolation by the Three Point Lagrangian formula, using a temporal weighting of 0.5 and spatial centering.

As with the supercritical flow simulation, the locations and shapes of surge at different times are well produced. Again, as in the previous test, a spike appears at the tip of the front. Except for the spike, the height of the wave is practically the same as the theoretical wave height. The wave is captured within two elements or 20 m which indicates excellent profile capturing properties.

The impact of channel roughness was studied by introducing a Manning's value of 0.015. The moving element scheme was operated with conditions identical to

EULARIAN - LAGRANGIAN SOLUTION

Profiles at 60 & 120 Sec. TEST 'B'

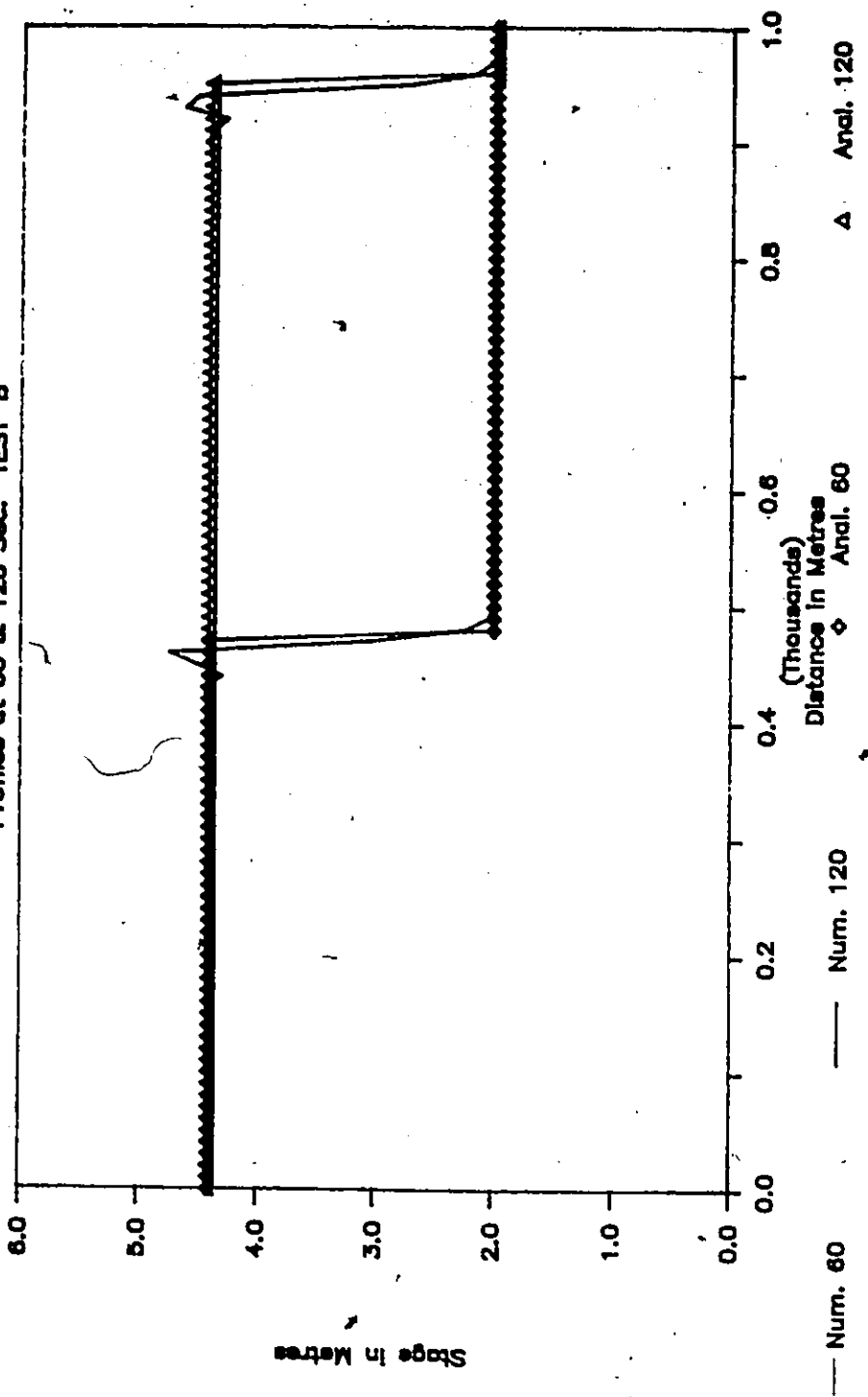


Fig. 5.2 Water Surface Profiles for Test 'B' - Subcritical Surge in Frictionless Channel.

— Num. 60

— Num. 120

◇ Ancl. 60

△ Ancl. 120

EULARIAN -- LAGRANGIAN SOLUTION

Hydrographs at 250 500 & 750 M TEST 'B'

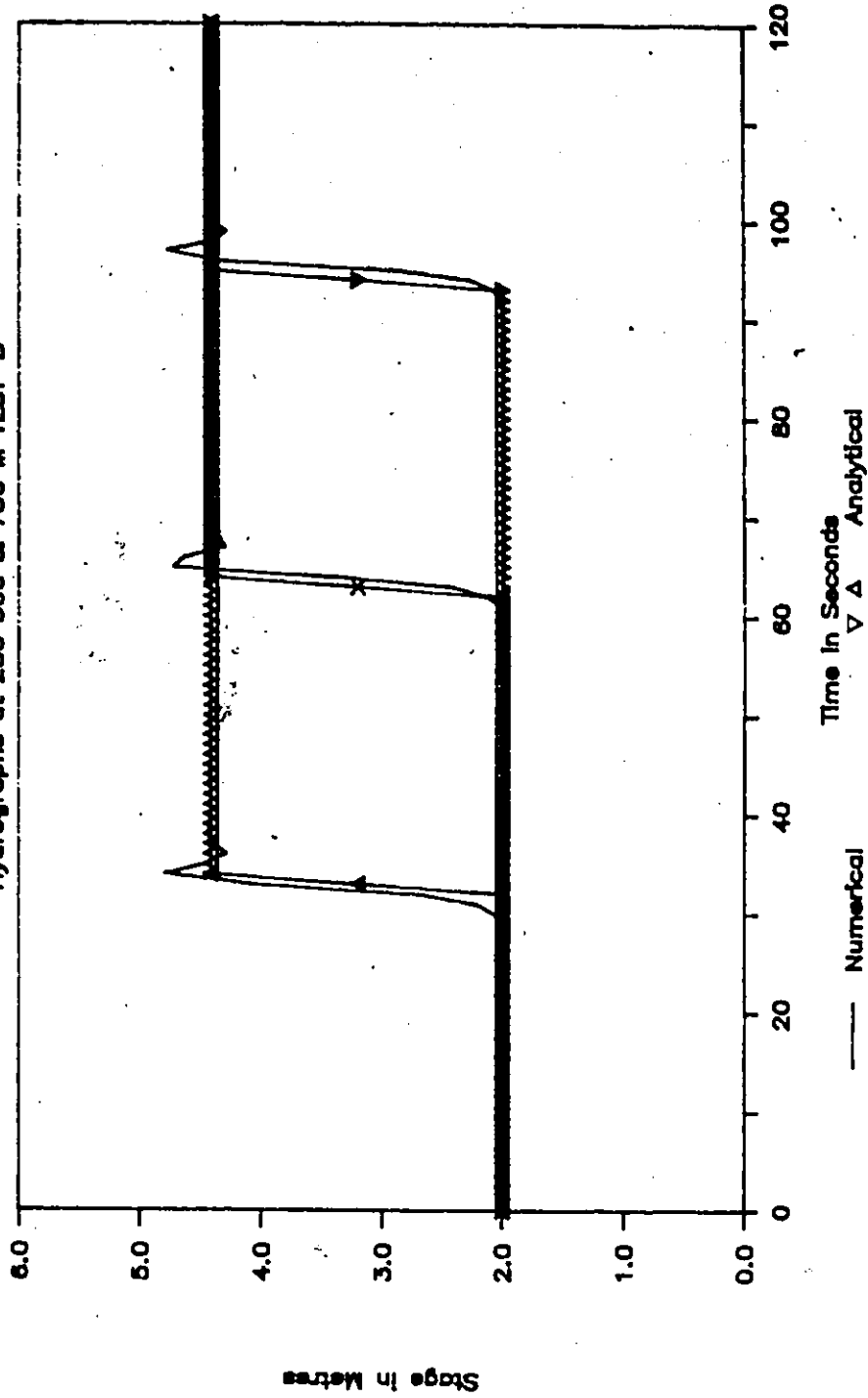


Fig. 5.3 Flow Hydrograph at Channel Mid-Point for Test 'B'.
Subcritical Surge in Frictionless Channel.

those presented above. The results are shown in Fig. 5.4. The retardation in both wave properties, height and speed is clearly visible when comparing with the frictionless case.

5.2.3 Test C - Subcritical Surge Moving Upstream:

A numerical test with a description similar to the one adopted here was reported by Cunge (1975). It was intended to repeat this experiment with the moving element scheme. Upon a closer examination, of the above noted test of Cunge several discrepancies were noted between the description of the experiment and channel geometry. Instead of designing an entirely different experiment, this adopted test is largely what was reported by Cunge. The following particulars formed the experiment.

Physical Description:

The channel for this test is trapezoidal in shape with 1V:1H side slopes. The channel base is 100 m wide. The length of channel simulated was 2 km. The channel bed slopes at a rate of 0.00002 m/m or 2 cm/km which is extremely mild even for the proposed discharges. The channel roughness is equivalent to a Manning coefficient of 0.0125. These values are representative of the tail race channels of the Rhone Valley in France.

Initial and Boundary Conditions:

The channel carries an initial flow of 2694.5 m³/s at a depth 14 m. At the downstream boundary, the flow is reduced from 2694.5 to 250 m³/s in 15 sec. This is

EFFECT OF ROUGHNESS ON SURGE LOCATION

Profiles at Time = 60 & 120 S TEST "B"

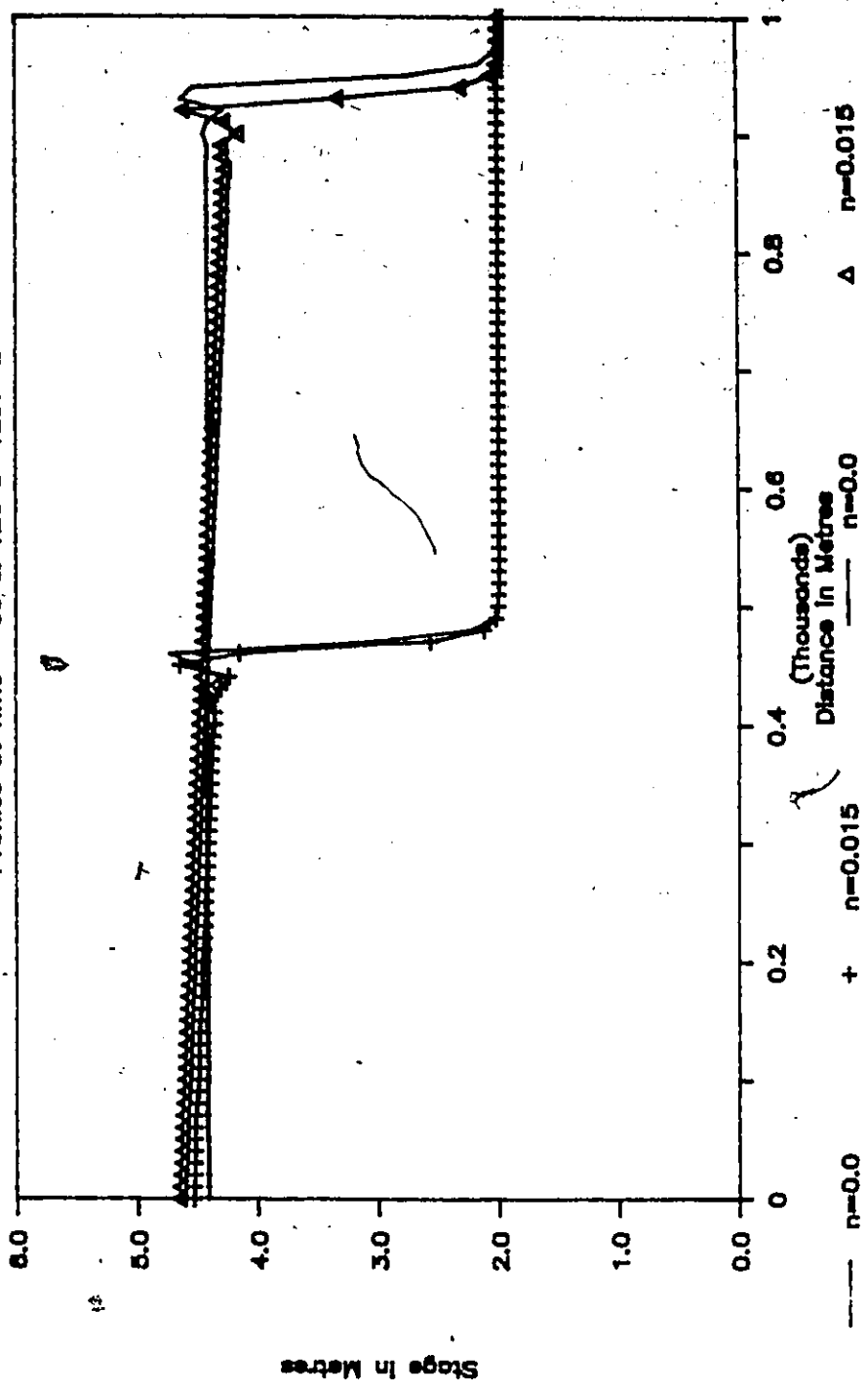


Fig. 6.4 Influence of Channel Roughness on Water Surface Profiles for Test 'B'.

equivalent to turbine rejection which results in a positive surge moving upstream. At the upstream boundary, the depth of flow throughout the experiment is held at 14 m.

Discretization and Solution Procedure:

The same basic grid size was employed as the one reported by Cunge (1975). The channel was divided into 80 elements each 25 m long. A time step of 3 sec. was employed which corresponds to a Courant Number of 1.3.

The resulting surge is subcritical in nature and moves upstream with a speed of 9.16 m/s. The corresponding water depth is 16.05 m which represents a wave height of 2.05 m above the initial depth. The test was simulated for 180 sec. with the profiles captured at intermediate steps.

The solution is based on the Eulerian-Lagrangian moving element scheme with interpolation provided by the Three Point Lagrangian formula. The temporal and spatial weightings were centred, that is, $\theta = 0.5$ and $\beta = 1.0$. The simulated profiles at 90 sec. and 180 sec. are presented in Fig. 5.5. Immediately noticeable in this experiment is the presence of the oscillatory waves in the computed profiles. The nature and the reasons for their occurrence are discussed in detail in Section 5.2.7. In general the height of the computed and analytical surge behind the front, locations after 90 and 180secs. of calculations and hence the wave speed compared well. Similarly, mass-balance computations show that the volumetric mass was conserved within one percent.

5.2.4 Test D - Continuous Flow Simulation:

One of the objectives of this research was to develop a robust model not only capable of handling near discontinuities but also gradually varied flows. For this

EULARIAN - LAGRANGIAN SOLUTION

Profiles at Time = 90 & 180 S TEST 'C'

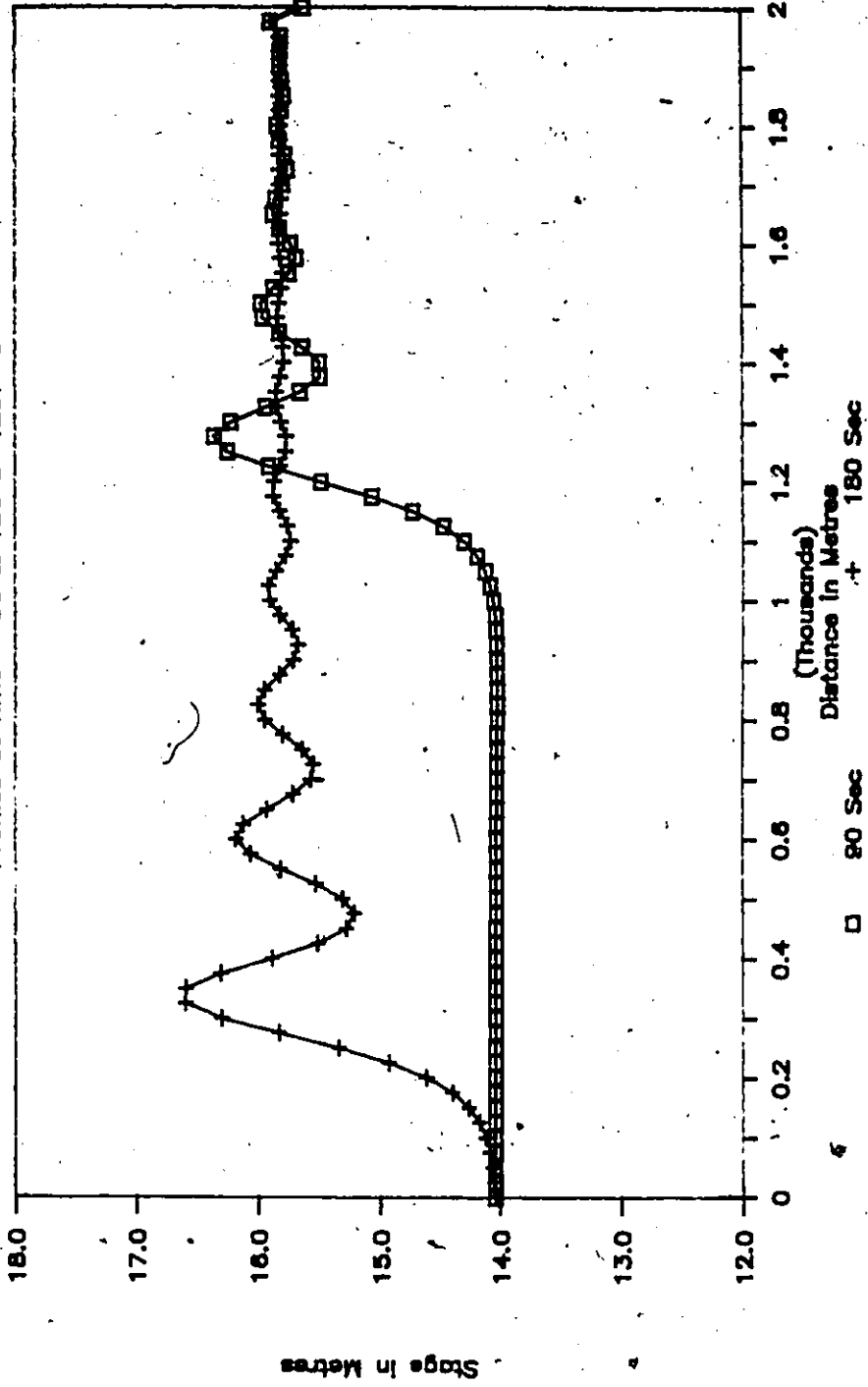


Fig. 5.5 Water Surface Profiles for Test 'C' - Subcritical Sutage Moving Upstream in Trapezoidal Channel.

purpose, a comparison was made with a test reported by Viesmann et al (1970) and Cooley and Moin (1976) was used. The details of the experiment are as follows:

Physical Description:

The channel for this test is rectangular in section and 20 ft wide. The length of channel studied is 2 miles and slopes at a rate of 0.0015 ft/ft. Channel roughness is approximated by the Manning Coefficient of 0.02.

Initial and Boundary Conditions:

The channel carries an initial flow of 833.94 cfs at a depth of 6 ft. The downstream boundary is defined by a single value rating curve based on the Manning equation and assuming channel control (i.e. normal depth). At the upstream boundary the flow is increased from 833.94 cfs to 2000 cfs in 20 min. The flow is then reduced back to 833.94 cfs in the next 40 min.

Discretization and Solution Procedure:

The grid size adopted for this test is the same as that reported in the earlier studies, namely, the 2 mile reach was divided into 20 elements of 528 ft each. Viesmann et al (1970) employed an explicit scheme with a time step of 2 sec.; using a predictor-corrector implicit scheme Cooley and Moin (1976) solved the problem with a 60 sec. time step. In this study, the basic run was also made with a time step of 60 sec.

The flow conditions remain subcritical throughout the one-hour simulation. The solution is based on the Eulerian-Lagrangian moving element scheme. The interpolation between steps is by the Three Point Lagrangian interpolation formula. The temporal and spatial weighting factors were set at 0.5 and 1.0 respectively. For

this test, instead of recording profiles at different times, hydrographs for a number of nodes are captured. The hydrographs for the mid-point and the downstream boundary are depicted in Fig 5.6. The solution by Viesmann et al is not plotted as the results were same as those of the moving element model. Again for this test the mass was conserved within 0.03 percent. Other simulations by the Lagrangian scheme conserved the mass completely.

5.2.5 Text E1 - Surge Through Choke - Horizontal Constriction:

In order to test the moving element scheme's capabilities for handling nonprismatic channel sections, two experiments were devised. The first test studied the passage of a surge through a constriction; a second test is described in Section 5.2.6. As is expected, when a constriction is placed in the passage of a surge, partial wave reflection takes place. In this test, as a second objective, the study of wave reflection was included. This was accomplished by studying wave reflections at the constriction and also by placing a reflective boundary at the downstream limit.

Physical Description:

In this test the rectangular channel is 100 m wide, 1000 m long and slopes at a rate of 0.0001 m/m or 0.1 m/km. The constriction is symmetrical and is represented by a converging inlet 100 m long starting at 350 m from the upstream boundary wherein the channel narrows from 100 m to 50 m width. This 50 m throat width is maintained for the next 100 m. The channel expands again to the 100 m width in the subsequent 100 m. Graphically, the channel layout in plan is shown in Fig 5.7.

EULARIAN - LAGRANGIAN SOLUTION

Hydrographs at 0, 1 & 2 Miles TEST 'D'

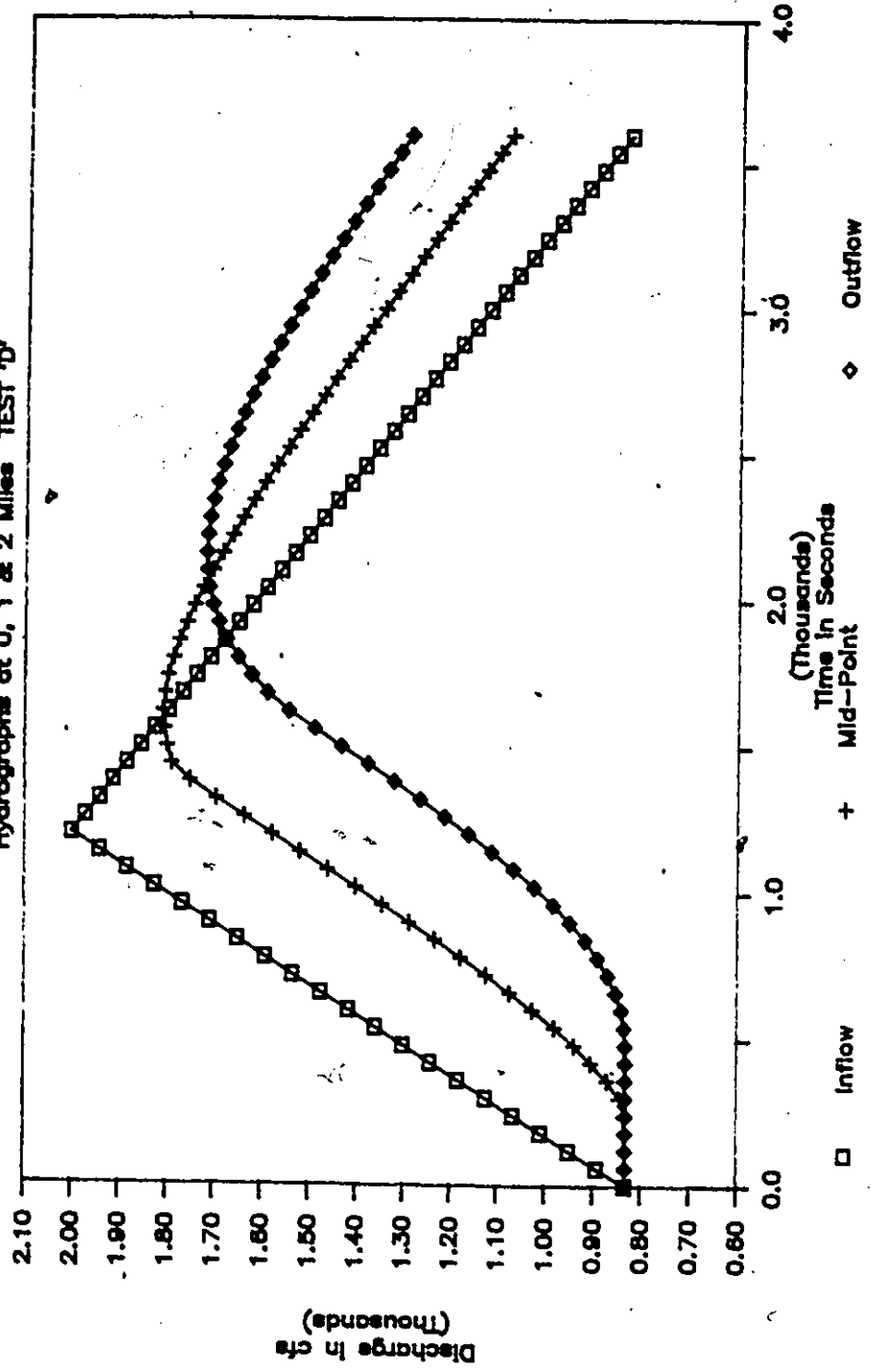


Fig. 5.6 Flow Hydrographs at Upstream and Downstream Boundaries and Channel Mid-Point for Test 'D' - Continuous Flow Simulation.

FLOW THROUGH A CHOKE

Plan Layout

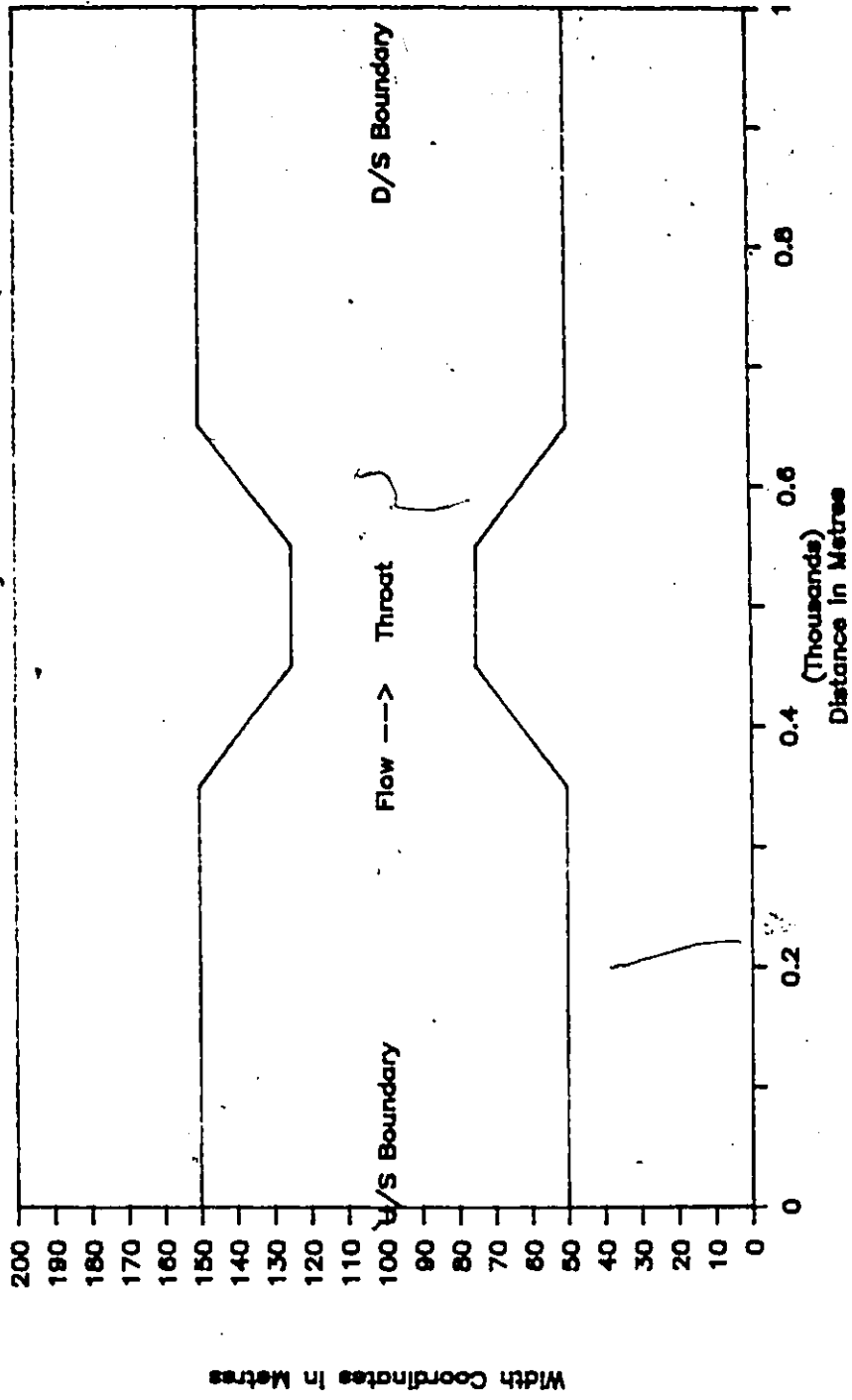


Fig. 5.7 Plan Layout for Test 'E1' - Flow Through a Choke.

The channel roughness is represented by the Manning equation and equal to 0.015.

Initially, the depth of flow is 2 m with a flow of 206.1 m³/s. These conditions, however, exist beyond the influence of the Choke; steady gradually varied flow exists within the domain of Choke. The boundary condition at the upstream node required the flow to increase from the initial steady value of 206.1 m³/s flow to 2000 m³/s in a time span of 30 sec. This increased discharge is maintained during the 1200 sec. simulation run. The downstream boundary is represented by the depth-discharge relationship given by the uniform flow equation:

$$Q = \frac{K}{n} A R^{2/3} S_0^{1/2} \quad (5.4)$$

where K is a constant = 1.0 for SI units

= 1.486 for Imperial units.

S_0 is the bedslope at the downstream boundary node.

This provides for a reflective boundary due to the low bed slope.

Discretization and Solution Procedure:

As the initial and boundary conditions were similar to Test 'B', the same grid sizes of 10 m-long elements and 1 sec. time steps were employed. The transitions and choke each occupied 10 elements. For such a discretization, the Courant Number was greater than one.

The subcritical surge was allowed to progress through the choke for a period of 1200 sec. During this duration, the following phenomena were noted.

- (i) Upon reaching the Choke, part of the incident surge was transmitted through and part was reflected.

- (ii) The flow in the throat section went through the critical depth into the supercritical regime and in the expansion transition formed a hydraulic jump and regained the subcritical flow properties.
- (iii) When this subcritical surge reached the downstream boundary, partial reflection took place and a positive wave started to travel upstream.
- (iv) Reflected waves from the downstream boundary eventually drowned out the control in the Choke and by 1200 sec. a quasi-steady state condition was obtained.

For reasons explained in Section 5.2.7, it was decided to carry out the test at a temporal weighting of $\theta = 0.6$. The spatial weighting was set to 1.0. The profiles were captured at a number of time steps which are shown in Figs. 5.8 and 5.9. Similarly, the flow hydrographs for a number of points through the choke and downstream boundary were captured. These are presented in Fig. 5.10.

The above solution is based on the Eulerian-Lagrangian linked moving element scheme. The intermediate interpolations are by the Three Point Lagrangian formula.

5.2.8 Test E2 - Surge over Hump - Vertical Constriction

This test in many ways is similar to the previous experiment, Test E1. Instead of a horizontal constriction, the surge is forced first over an adverse slope then travels on a hump, an overly broad-crested weir, and shoots down a chute. Like the previous experiment which attempted simulating the surge through constrictions such as bridges, this experiment was aimed to duplicate the flow over obstructions.

FLOW THRU CONSTRICTION -- PROFILES

DX=20 DT=3S THETA=0.6 DTRISE=30S

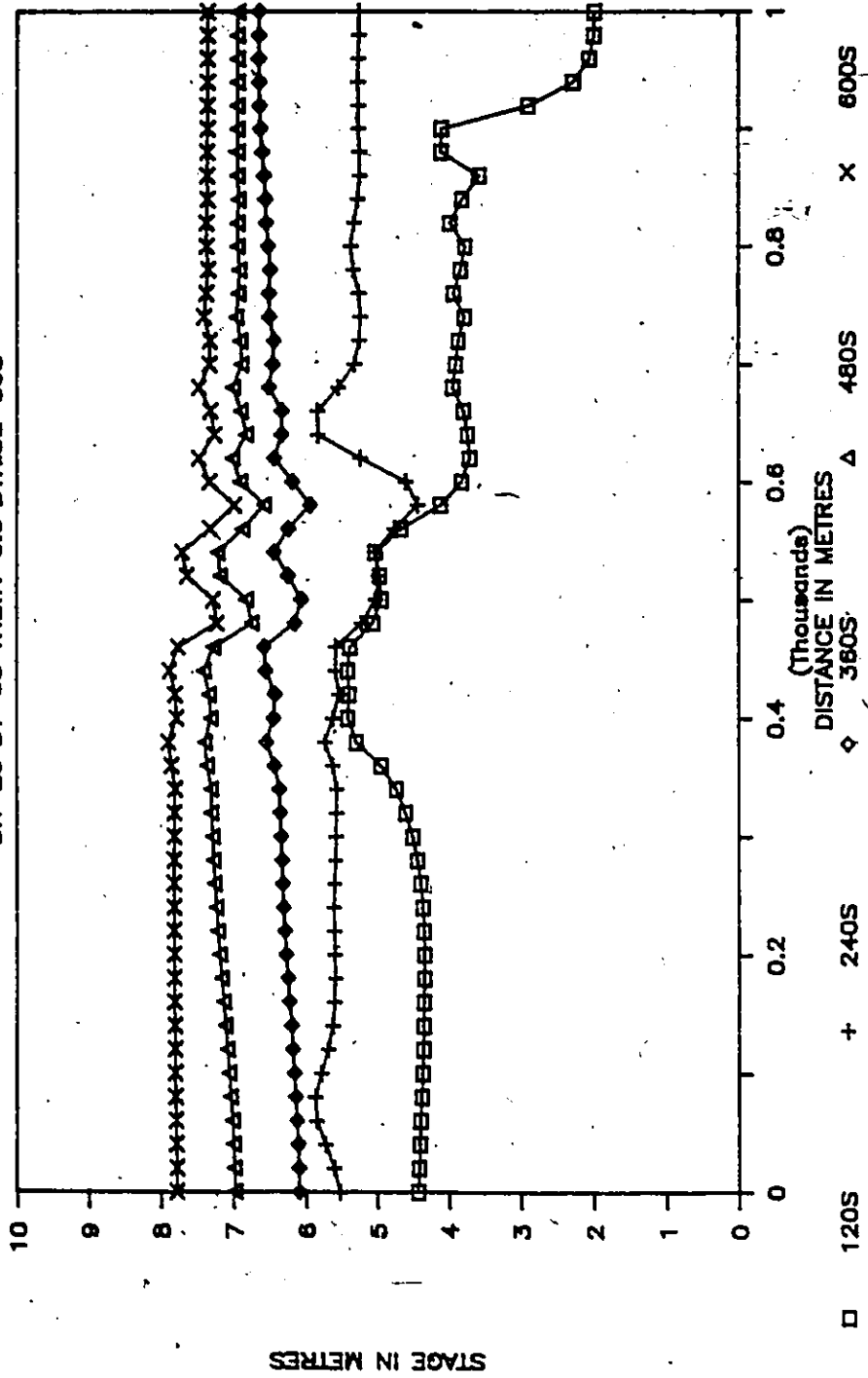


Fig. 5.8 Water Surface Profiles for Test 'E1' - Flow Through a Choke.

FLOW THRU CONSTRUCTION -- PROFILES

DX=20 DT=3S THETA=0.6 DTRISE=30S

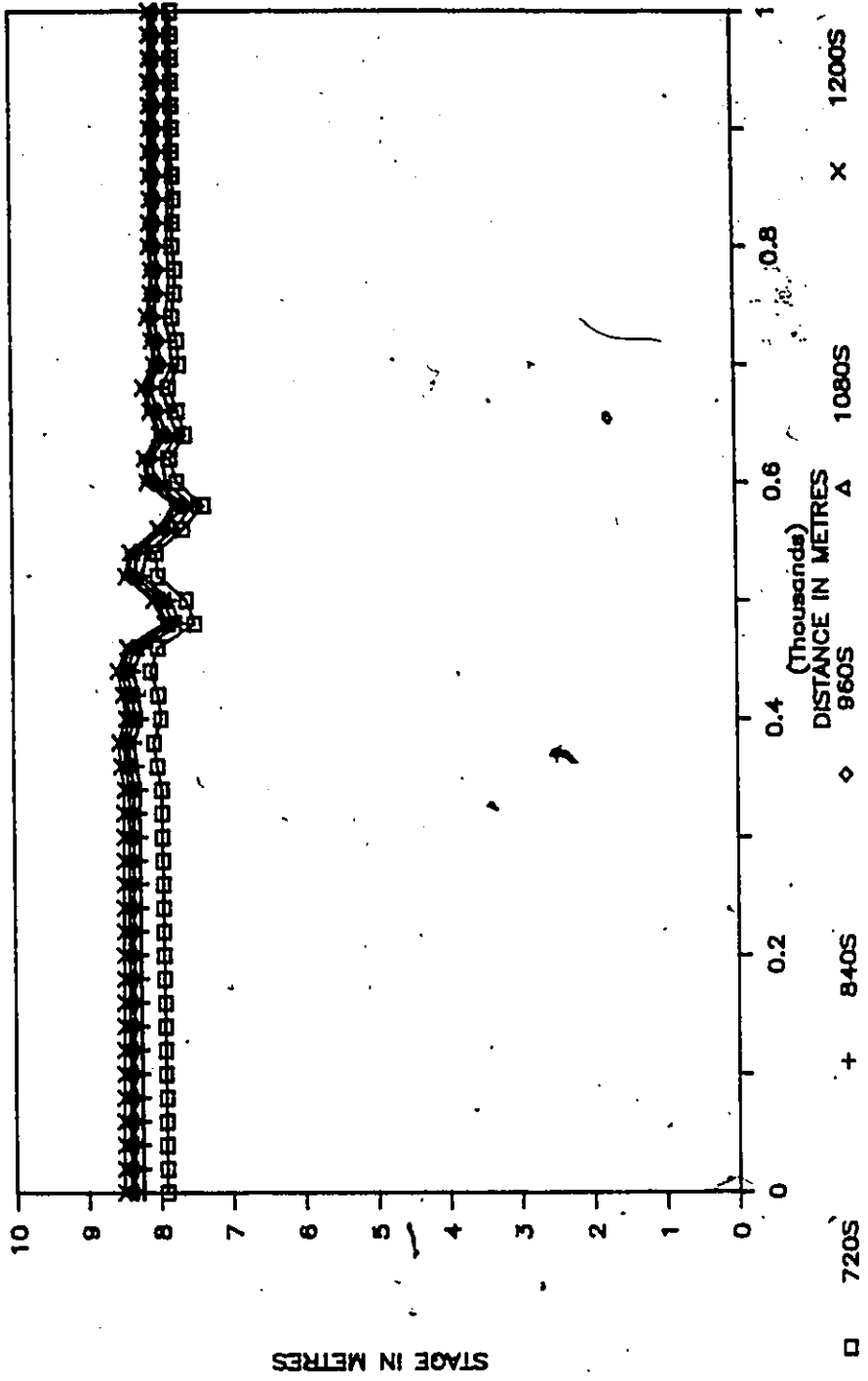


Fig. 5.9 Water Surface Profiles for Test 'E1' - Flow Through a Choke.

FLOW THRU CONSTRICTION

DX=20 DT=3 THETA=0.6 DTRISE=30S

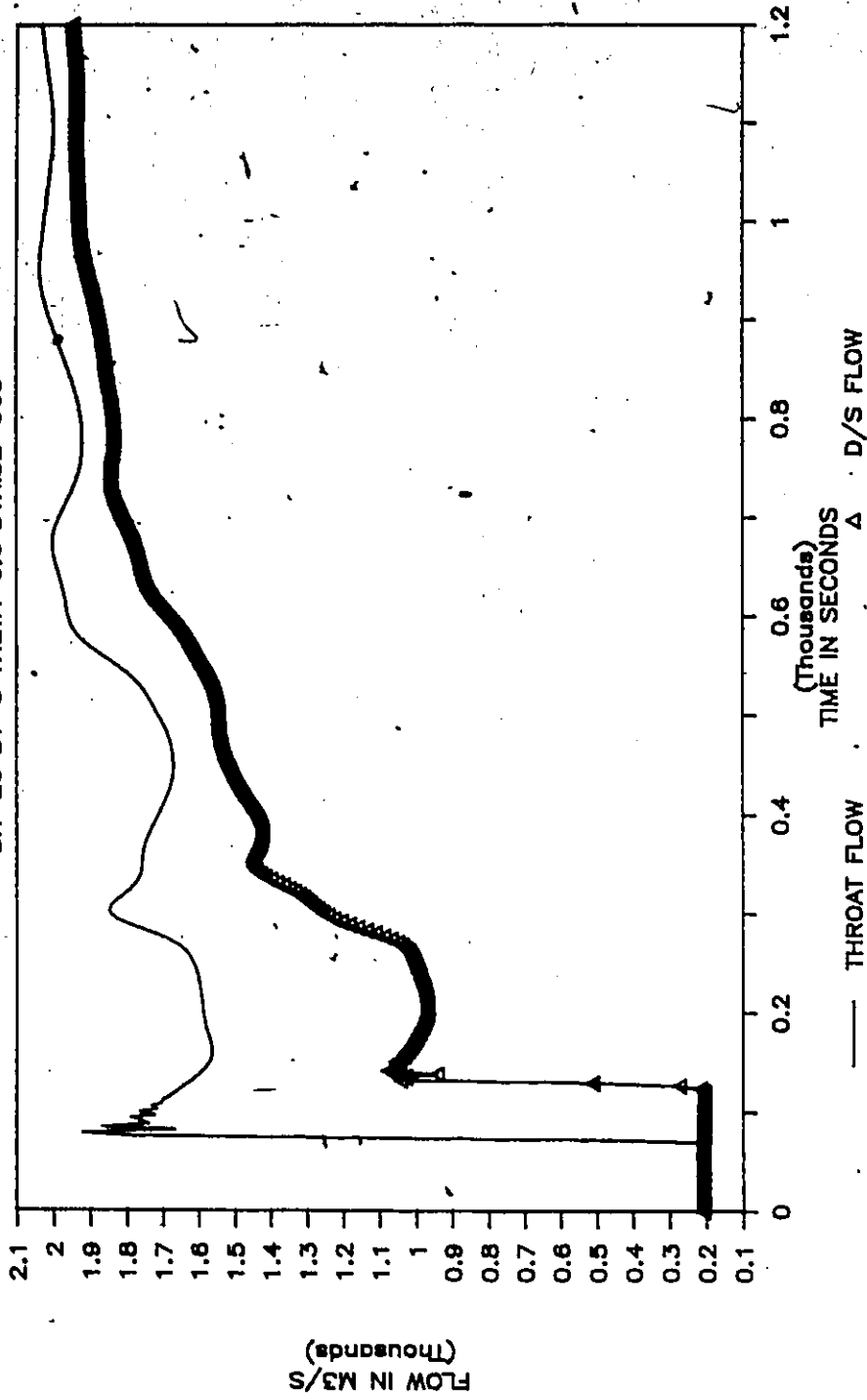


Fig. 5.10 Flow Hydrographs for Flow Through a Choke - Test 'E1'

Physical Description:

As in Test E1, the rectangular channel is 100 m wide, 1000 m long and slopes at 0.1 m/km. The Hump is represented, first by an adverse slope of -1% starting at 350 m followed by a broad crested section which is represented by an almost level section 100 m long. The chute is represented by a 100 m long section sloping at 1% ending at 650 m.

The frictional losses are governed by the Manning equation and set equal to 0.015. A longitudinal profile of the channel invert is shown in Fig. 5.11.

Initial and Boundary Conditions:

The initial conditions consist of a depth of flow of 2 m and a flowrate of 206.1 m³/s. These conditions were influenced by the gradually varied flow conditions near the transitions. The upstream boundary consisted of a flow hydrograph rising from 206.1 m³/s to 2000 m³/s in 30 sec. and maintained at this rate for the duration of this experiment. The downstream boundary was implemented using Equation (5.4) to describe the stage-flow relation.

Discretization and Solution Procedure:

For this experiment the grid size of Tests 'B' and 'E1' are adopted. These amount to 100 elements each 10 m long and time steps of 1 sec. The adverse slope, the crest reach and the chute each occupy 10 elements. The Courant Number for such discretization is greater than 1.0.

The resulting subcritical surge was allowed to progress for 240 sec. The profiles of the surge were saved for different time steps and these are presented in Fig. 5.12. Similarly, hydrographs around the hump are shown in Fig. 5.13.

FLOW OVER A HUMP - TEST 'E2'

Sectional Profile - Level Pool

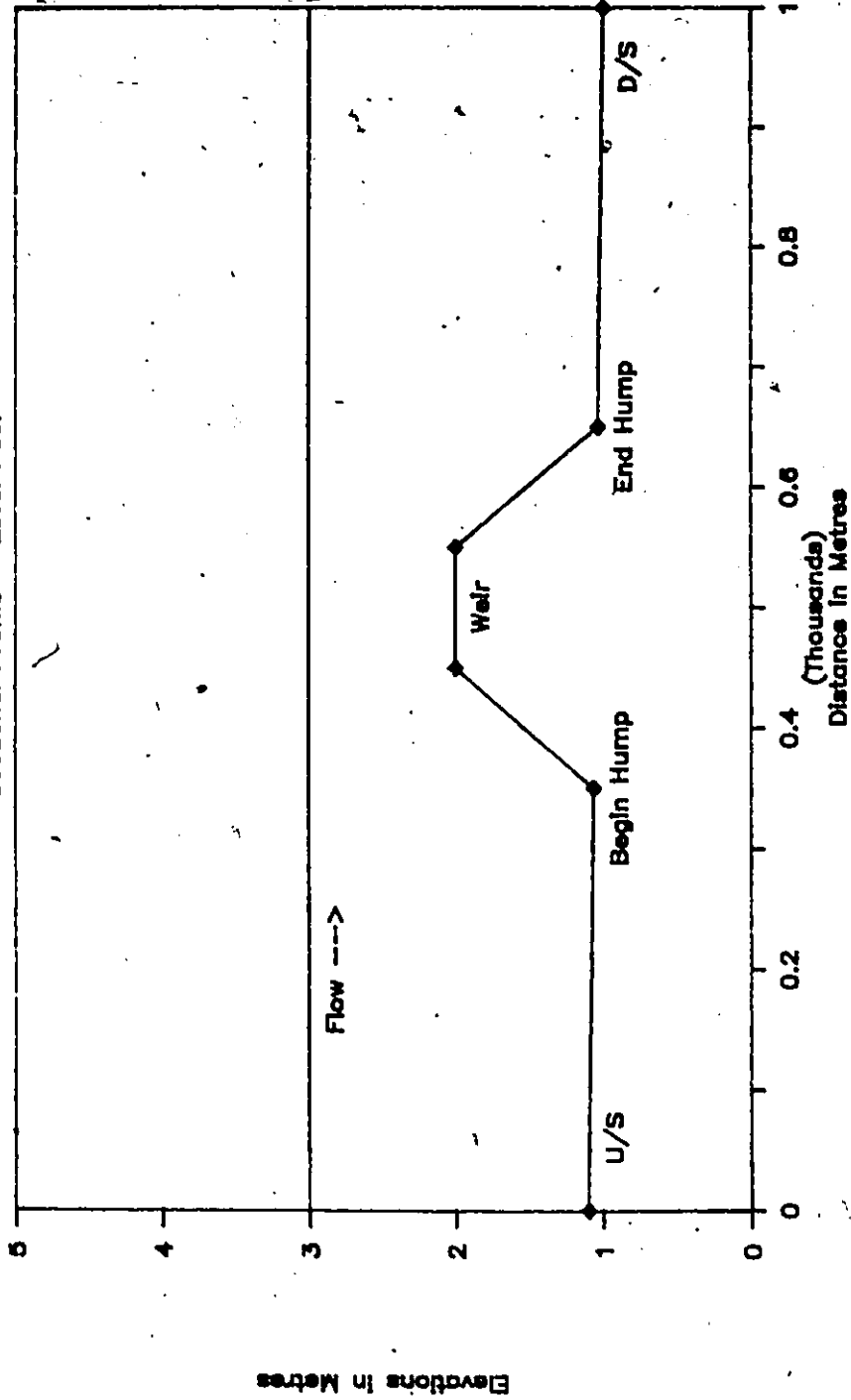


Fig. 5.11 Cross-Sectional Profile of an Obstruction (Hump) in a Channel for Test 'E2'.

Subcritical Surge Over Hump

Stage Profile at 120 s TEST 'E2'

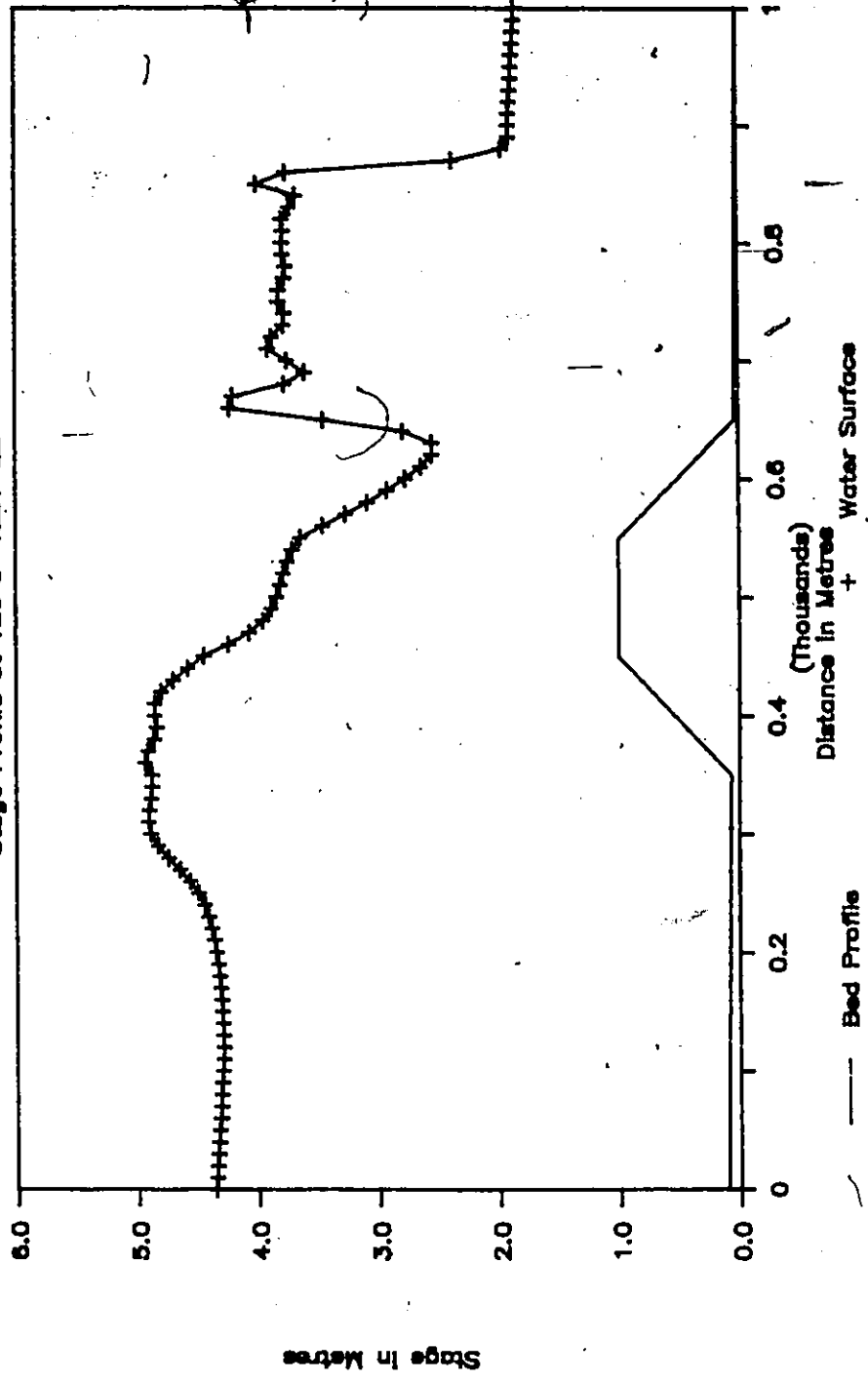


Fig. 5.12 Water Surface Profiles for Test 'E2' - Flow over a Hump.

Subcritical Surge Over Hump

Stage Hydrographs at Hump TEST 'E2'

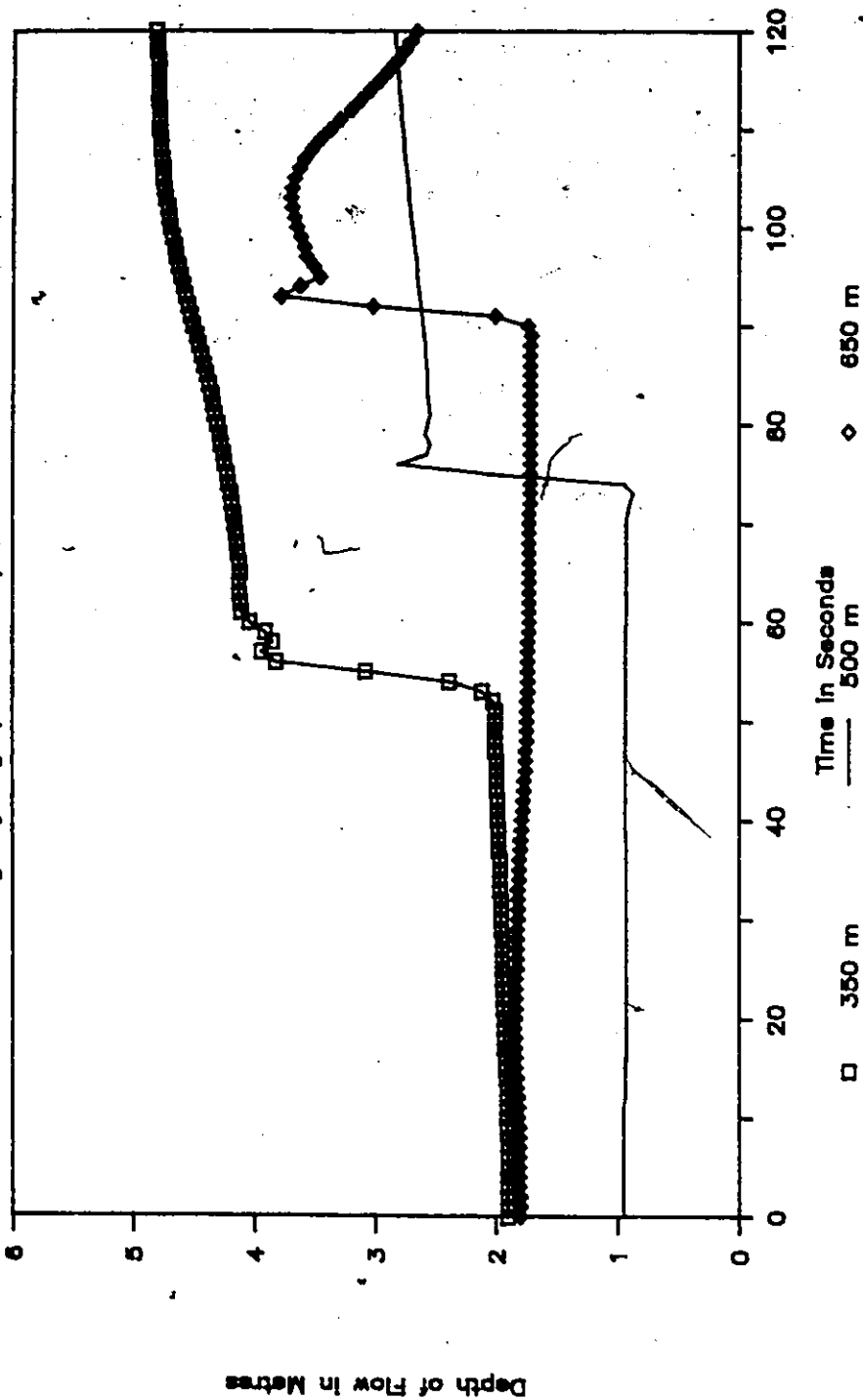


Fig. 5.13 Flow Hydrographs at Hump for Test 'E2'.

The solution for this experiment is based on the Eulerian-Lagrangian linked moving element scheme and employing Three Point Lagrangian interpolation formula.

5.2.7 Discussion of Results:

In the previous sections the results from the six experiments were presented. As there are a number of common features, the present discussion is directed at all the tests. The translation of a surge along the channel and its numerical solution can be gauged by considering the degree of success in simulating the following features:

- (i) Shape of the front
- (ii) Speed of the wave
- (iii) Conservation of mass
- (iv) Steepness of the front
- (v) Handling of nonprismatic sections
- (vi) Direction of front

These points are discussed below:

5.2.7.1 Shape of the Front:

One of the most visible and important simulation capabilities of any scheme is how well the general shape of the moving surge is predicted. As is evident from various figures, especially so, for the surge moving downstream, the general shape is preserved through the entire profile. Leaving the discussion on surges moving upstream to a later section, the comments here apply to tests A, B and E2.

The profiles in all three cases developed a spike at the tip of the front. The timing of the first appearance of the spike was related to the maturing of the front. That is, the front initially would be sloping, however, the points with greater depth would move faster causing a general steepening of the front; when the front steepens enough and occupies only one or two elements, the spike begins to form.

The reasons why the spike forms and persists are closely related to the non-dissipative nature of the solution at each time step. Also, there are violations of basic assumptions by neglecting vertical acceleration terms in the vicinity of the front.

In general, it was found that the overall shape of the front was produced very well. Usually the maximum deviations from analytical solutions except for the spike were approximately 0.1% of the wave height.

5.2.7.2 Speed of the Wave:

In terms of importance, the criteria next calls for the scheme to faithfully reproduce the speed of the wave. This key factor is directly linked with the mass conservation requirements. If the speed of the surge is in error then so is the mass conservation. For test cases A, B and C the height of the wave and hence its speed can be calculated analytically. This is specially valid for Tests A and B in view of the frictionless channel scenario; that is, the presence of friction tends to slow down the wave by an undetermined amount.

Again, as noticed in the profiles for these tests, the speed of the wave is truly portrayed. This matching was a result of a judicious selection of the grid size. If the time step selected for a given element size is not near the optimum value there is a possibility of clipping errors introduced during interpolation at the Eulerian step. It is inferred from the above that in order to simulate the speed, hence, its location and,

by extension, the mass conservation, there exist a band of element length-time step, that is grid size, combination or grid size as feet ratio which provides optimum results.

Based on numerous experiments with time step-element size combinations, it was found, for near discontinuities, that if the node at the advanced time step is displaced by approximately half the element length the clipping errors at the tip of the front are minimized. In other words if the sides of the elements are inclined at about 60° angle for the isoparametric elements, the time-step / element size combination is near optimal.

5.2.7.3 Conservation of Mass:

Mass conservation, as noted earlier, is closely linked with the time step used for a given element size. Problems with mass conservation usually arise for three reasons. First, the handling of the mass continuity relationship at the boundary nodes may influence the overall solution. Second, the numerical approximations may lead to mass continuity errors. The third and most important factor is the interpolation that takes place between time steps.

From all the numerical experiments carried out the mass continuity was evaluated for each of the experiments. In general, for the tests reported the maximum error in mass conservation was less than 1.8%. Although the literature does not provide the capabilities of other similar models, it is generally believed that for near discontinuous flows, errors in excess of 5% are quite common.

It is noteworthy that for Test D, the continuous flow experiment, the mass continuity errors were less than 0.03%.

In order to isolate the source of this minor discrepancy, a number of variations were tested out. A comparison was made with the fully Lagrangian

solution to evaluate the impact of Eulerian interpolation. The Lagrangian solution conserved the mass. This indicates that the source of error is indeed at the interpolation stage, which is pronounced only at the tip of the front. At the nose of this discontinuity even the three point interpolation formula would be inadequate, resulting in a slight clipping of the front. Subsequent experiments of slanting the element proportional to the celerity only worsened the solution.

From the above evaluation, if a weakness in an otherwise novel and robust scheme is to be found, it is the mass conservation at the interpolation stage. In all the experiments, whenever a mass conservation error is noted, the net flow through the domain exceeded the net change in storage. This again points to clipping errors.

5.2.7.4 Steepness of Front

For any numerical technique integrating the solution of the open channel flow equations, that is, treating the discontinuity as a surface gradient, it is important that the proper shape of the front be preserved. Other factors being same, the schemes which employ artificial damping mechanisms tend to diffuse the front over a number of element reaches.

The steepness of the wave obviously depends largely on the spatial discretization of the solution domain. In all the test cases reported in the previous sections the front was captured within two elements or three nodes. Thus, if the elements are 10 m long, the wave front is captured within 20 m and if the reach length was 25 m, then the wave occupied 50 m.

For Test A, a comparison of the steepness results that Terzidis and Strelkoff (1970) provide, the explicit scheme captured the front in 60 m while Vasiliev et al (1965) reported a highly diffused front over a 200 m strip. For the same spatial

discretization, moving element scheme captured the wave within 20 m; a ten fold improvement over Vasiliev and three fold over Terzidis and Strelkoff.

5.2.7.5 Handling of Non-prismatic Cross-Sections:

The numerical schemes are normally developed for idealized conditions. It is not uncommon to report basic results for either channels of infinite width eliminating the channel width in the equations or rectangular cross-sections and prismatic channels. The real test of any numerical scheme, however, lies in its ability to handle non-prismatic cross-sections. This is essential for the application for the simulation of real world problems.

In order to test results for the moving element scheme with established models like Dynamic Wave Operational Model (DWOPER), Fread (1978) and Dambreak model (DAMBRK), Fread (1982), were employed which are capable of handling non-prismatic cross-sections. Even when the data employed for Tests E1 and E2 were modified for the two models, the execution of the models resulted in either a non-convergent solution or a program termination. In the absence of this comparison, a general discussion on the capability is left until the applications with recorded field problems are reported.

From Tests E1 and E2, it is evident that the moving element scheme handles non-prismatic cross-sections in an acceptable manner. The constriction imposed in Test E1 is a severe one and the model responds with realistic partial reflection. Another feature of Test E1 was the formation of supercritical flow in the throat of the choke, hydraulic jump in the expansion and a subsequent change to a subcritical surge. From the profiles in Figs. 5.8 and 5.9 it is evident that this feature is reproduced to an acceptable degree. The scheme faithfully handles the series of

reflections by variations in flows and by the drowning of the control point formed in the throat of the Choke.

A point worth noting for this experiment was the testing of terms required to simulate nonprismatic cross-sections. Based on this evaluation, both convective acceleration and pressure terms in the momentum equations required corrective terms for the nonprismatic shapes.

5.2.7.6 Direction of Front:

From Figs. 5.2 and 5.5 which respectively represent the downstream and upstream moving fronts, the quality of simulation is obvious. The results for the downstream moving are clearly superior to those of upstream moving. The reason for this disparity lies in the very concept of the moving element method. The moving element method relies on the particle velocity behind the front. For the downstream moving surge, there is no difficulty as the elements slant adequately to employ all the features of the scheme. This is, however, not the case for the upstream moving problem; velocity behind the surge in most cases is very small when compared to the upstream side of the front. In these cases, the moving element schemes reduce to a conventional finite element scheme and its inherent oscillatory, non-dissipative results. This is evident in the saw-tooth solution for Test C. Still, as will be shown later, the moving element scheme solution is better than the conventional finite difference and finite element schemes.

This was also evident for the Choke and Hump problems, Tests E1 and E2, where there is a sudden reduction of velocity due to either upstream moving reflected wave or a standing hydraulic jump. These problems in a practical sense are adequately addressed by slightly increasing the temporal weighting factor, θ . For

example, the results for Test E1 are presented for $\theta = 0.6$. This achievement in a more or less smooth solution is, however, not without a price. There is a slight increase in the dispersion of the solution which spreads out the surge over a number of elements.

A summary of the model performance in the six categories is presented in Table 5.0.

5.3 Sensitivity Analysis

The purpose of any sensitivity analysis is to isolate and identify parameters which influence the solution. This process assists greatly in any application exercise where adjustment of parameters can help during the calibration phase and subsequent simulation. Sensitivity analysis is a requirement in situations such as these, where a numerical model cannot be easily tested in a real life situation.

With the foregoing as the basis, six different parameters were varied to carry out the sensitivity analysis while holding the other parameters to the basic test values. These parameters are time-step, element size, temporal weighting factor θ , spatial weighting factor, β , channel roughness, and rate of change of inflow hydrograph ($\partial Q/\partial t$) at the boundaries.

It is emphasized here that, although, the sensitivity analysis carried out is quite extensive, it is, however, far from exhaustive. Due to the nature and scope of numerical experiments, no attempt was made to address, for example, simultaneous variation of channel roughness and time step. Therefore, no guidelines could be developed in relating the time step size with the channel roughness and element size. Other observations, similarly, can be made with respect to other model parameters.

Table 5.0

Summary of Numerical Experiments

Criteria	Performance of Moving Element Method
1. Shape of Front	Overall shape produced very well. Maximum deviations less than 1% of wave height. Only drawback: presence of spike.
2. Speed of Wave	Speed of wave truly portrayed. Computed location within 1% of analytical results.
3. Conservation of Mass	Generally mass conserved within 1.5%. Mass conservation dependent on optimum time step. Wave clipping occurs for too small a time step.
4. Steepness of Front	Steepness of wave dependent on element length. Wave front captured within two elements. Three fold improvement over explicit scheme of Terzidis and Strelkoff (1970) and 20 fold over Vasiliev's (1965).
5. Handling of Non-prismatic Cross-sections	Proper simulation of wave reflections chocking at constriction, drowning of control, etc.
6. Direction of Front	Surge moving downstream handled better than moving upstream. Acceptable results for upstream moving surge by advancing temporal weighting parameter.

5.3.1 Variation of Time-step

For a given element size, a variation of time step results in different Courant Numbers. Theoretically, the resulting numerical scheme for the moving element scheme is implicit in nature, however, to obtain reliable results the Courant Number should not vary greatly from 1.0. This is particularly important for rapidly varying flow situations. In order to study the behaviour of the time step variation, three numerical experiments were employed; these were Tests B, C, and D. These are discussed separately.

Test B - The variations for this experiment from the basis of comparison (BOC) case are noted in Table 5.1. For this analysis, an element size of 25 m was used. The base case for the Courant Number close to 1.0 was set at a time step of 3.0 sec. Thus two time steps were chosen to examine the effects, one at 1.0 sec (Courant Number $\approx 1/3$) and the other at 10 sec (Courant Number ≈ 3). The results from the three computer runs are presented in Figure 5.14.

The impact of time step is evident in the general shape of the stage profiles. The overall front is captured with varying degrees of advancement. The heights of the surge away from the front for all time steps are computed to be the same indicating good momentum balance. For a time step of 10 seconds, however, long waves start to appear which merge with a much larger spike at the tip of the surge.

The height of spikes for the 1.0 and 3.0 second time steps are about the same; whereas, for a time step of 10 seconds, the spike is over 0.6 m in height. The location of the front is best predicted with a 3.0 second time step. The locations of the tip, represented by the spike, for other time steps lag by one element size; such lags are indicative of clipping errors and evident in the overall mass balance. Further, for the 10 second time step run, the front exhibits a faintly dispersive nature.

TABLE 5.1
Sensitivity Analysis of Varying Computation Time Step

Name of Numerical Experiment	Type of Numerical Solution	Element Length (delx)	Time Step (delt)	Temporal Weighting Parameter (Theta)	Spatial Weighting Parameter (Beta)	Manning's Channel Roughness (n)	Temporal Accl. at U/S Boundary (dQ/dt)
** Test 'B'							
Test 'B'	Eularian - Lagrangian	25.00	1.00	0.50	1.00	0.0150	66.67
Test 'B'	Eularian - Lagrangian	25.00	3.00	0.50	1.00	0.0150	66.67
Test 'B'	Eularian - Lagrangian	25.00	10.00	0.50	1.00	0.0150	66.67
** Test 'C'							
Test 'C'	Eularian - Lagrangian	25.00	1.00	0.50	1.00	0.0125	162.67
Test 'C'	Eularian - Lagrangian	25.00	2.00	0.50	1.00	0.0125	162.67
Test 'C'	Eularian - Lagrangian	25.00	3.00	0.50	1.00	0.0125	162.67
Test 'C'	Eularian - Lagrangian	25.00	5.00	0.50	1.00	0.0125	162.67
** Test 'D'							
Test 'D'	Eularian - Lagrangian	528.00	15.00	0.50	1.00	0.0200	0.97
Test 'D'	Eularian - Lagrangian	528.00	30.00	0.50	1.00	0.0200	0.97
Test 'D'	Eularian - Lagrangian	528.00	60.00	0.50	1.00	0.0200	0.97
Test 'D'	Eularian - Lagrangian	528.00	120.00	0.50	1.00	0.0200	0.97
Test 'D'	Eularian - Lagrangian	528.00	300.00	0.50	1.00	0.0200	0.97

TIME STEP SENSITIVITY ANALYSIS

Profiles at Time = 120 sec TEST "B"

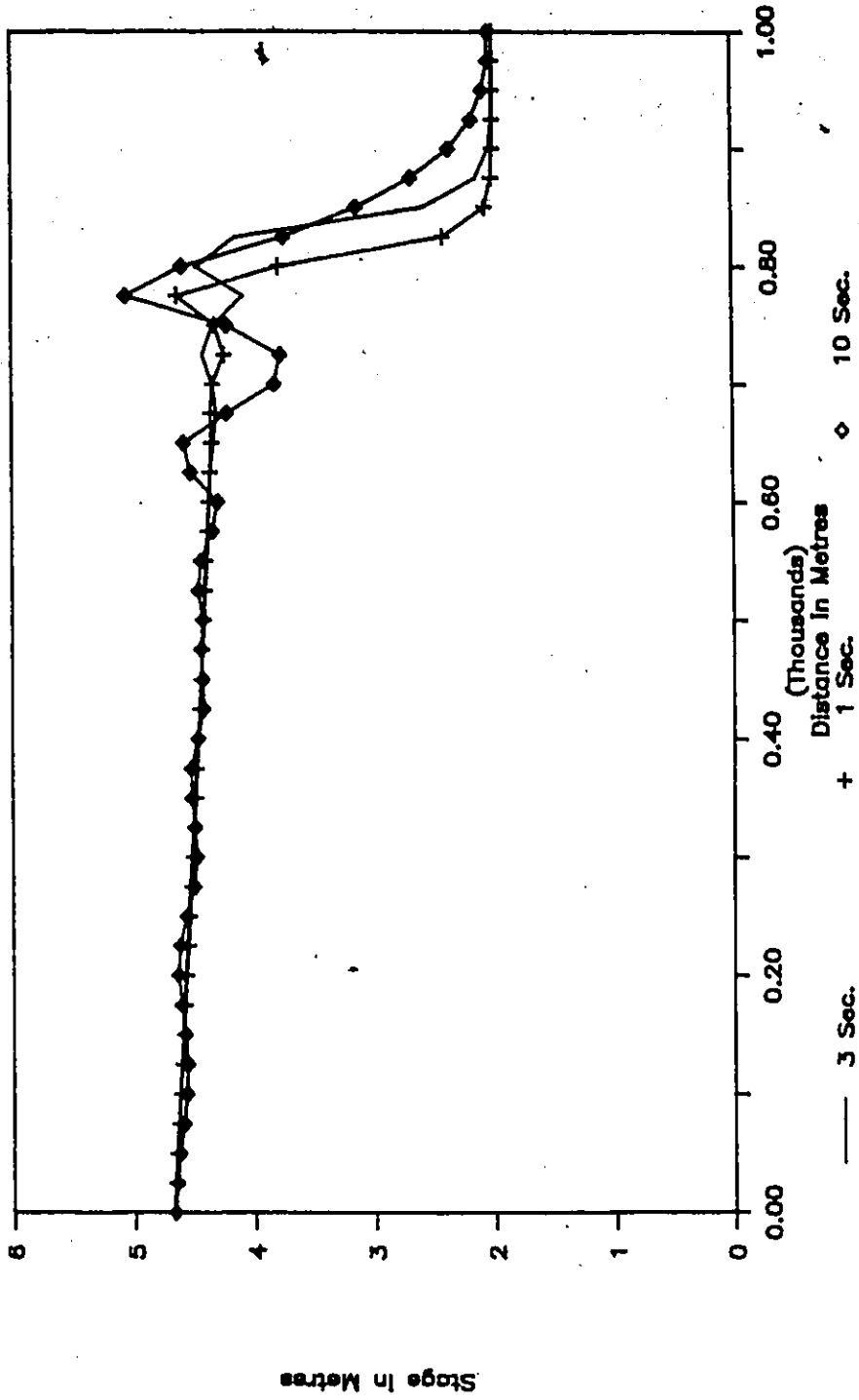


Fig. 5.14 Time Step Sensitivity for Test 'B' - Subcritical Surge Moving Downstream.

Test C - Table 5.1 shows the model parameters used for BOC case and the variation of time steps. It may be recalled that, Test 'C' involved the propagation of a positive surge in the upstream direction.

As in the previous experiment, the BOC scenario allowed a grid size 25 m long and 3 second time step. A two-second time step, however, corresponds closely to a Courant Number of 1.0. Therefore, time steps of 1.0, 2.0 and 5.0 seconds were tested. The stage profiles at 180 seconds were compared. These profiles at 180 seconds are shown in Figure 5.15.

Except for the stage profile for a time step of 5.0 seconds, all other profiles exhibit almost identical results. There is a gradual sharpening with smaller time steps. Another notable feature is the location of the front which is the same for all time steps. The size of the undulations at the front were larger for the smaller time steps and vice versa.

A phase shifting of undulations was evident for the 5.0 second time step computer run when compared to the other three experiments. The total lengths to which these undulations persisted were limited to between 400 and 500 metres.

Test D - As in the previous two tests, the parameters used in this continuous flow test are listed in Table 5.1. The results for this test were reported by Viesmann, et al (1973) using an explicit finite difference scheme with a time step of 2.0 seconds. For the same grid length, the BOC case employed a time step of 60 seconds.

In order to test the robustness of the model for the case of continuous flow simulation, four different time steps were used. Time steps of 15 and 30 seconds were employed as one-half and one-quarter of BOC scenario. On the other hand time-steps of 120 seconds and 300 seconds or twice and five times the BOC time-step. The

TIME-STEP SENSITIVITY ANALYSIS

Profiles at Time = 180 Sec. TEST "C"

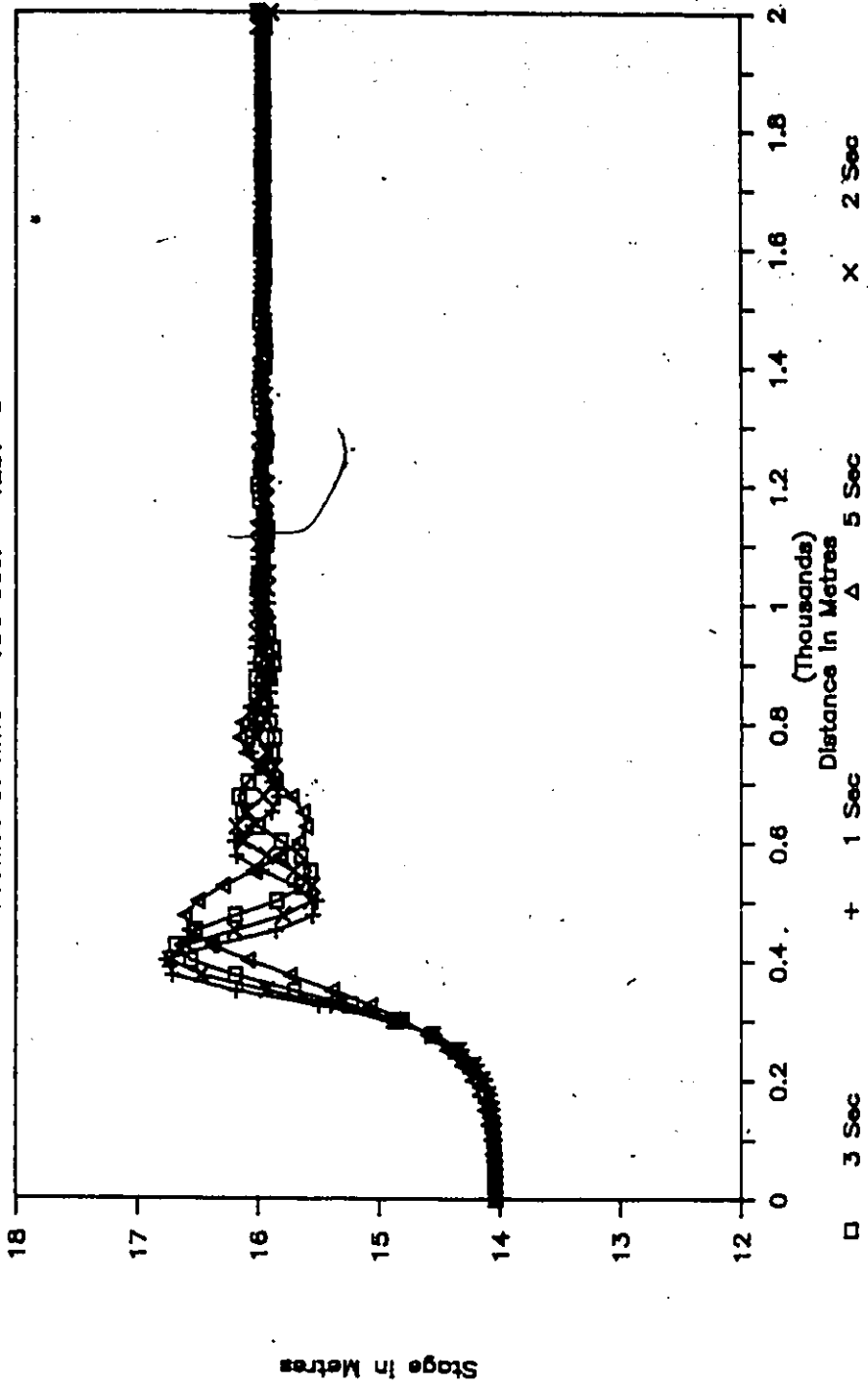


Fig. 5.15 Time Step Sensitivity for Test 'C' - Subcritical Surge Moving Upstream.

results, in the form of the upstream input hydrograph and the downstream routed hydrographs are presented in Figs. 5.16 and 5.17.

It is evident from the computer runs, that the model results were exceptionally close to the BOC simulation. For time steps up to 120 seconds, the hydrographs are virtually the same, with the differences only in the first or second decimal places. The exception was the run with a 300 second time step. The reason can be attributed to the ill-conditioned downstream boundary element with the element lengths at the old and new time levels separated by a factor of six or more.

From this sensitivity analysis, it can be deduced that for the simulation of continuous flow problems, the restriction does not come from the Courant criteria but rather is related to the conditioning of the elements. As a corollary, it can be further noted that the Courant criteria limitation noted for the passage of surges on initially still water as base flow can be relaxed to a certain extent if the base flow is moving at a reasonable velocity.

5.3.2 Variation of Element Length

The impact of varying the element length is similar to the time step variation. That is to say that a different element length implies a change in the Courant Number. This particular sensitivity test also allowed studying the effects of discretization. Table 5.2 lists the parameters employed and their variation. Similar arguments with respect to Courant Number and time steps were made as described in Section 5.3.1.

For studying this behaviour Test 'B' was employed. Instead of establishing a BOC case, three element sizes were chosen for the same time step of 1.0 second. The

TIME STEP SENSITIVITY ANALYSIS

Hydrographs at D/S Boundary TEST "D"

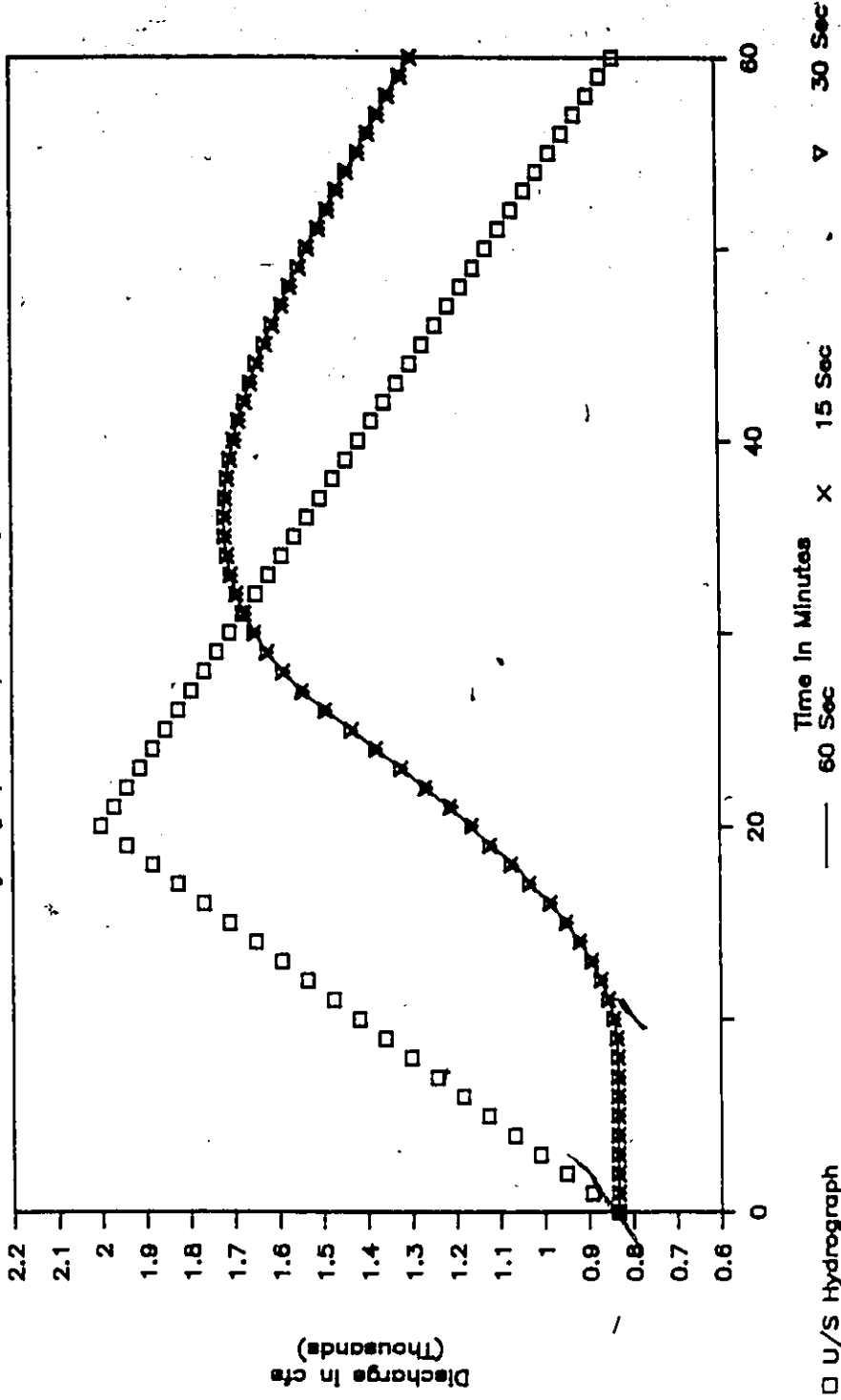


Fig. 5.16 Time Step Sensitivity for Test 'D' - Continuous Flow Simulation.

TIME STEP SENSITIVITY ANALYSIS

Hydrographs at D/S Boundary TEST "D"

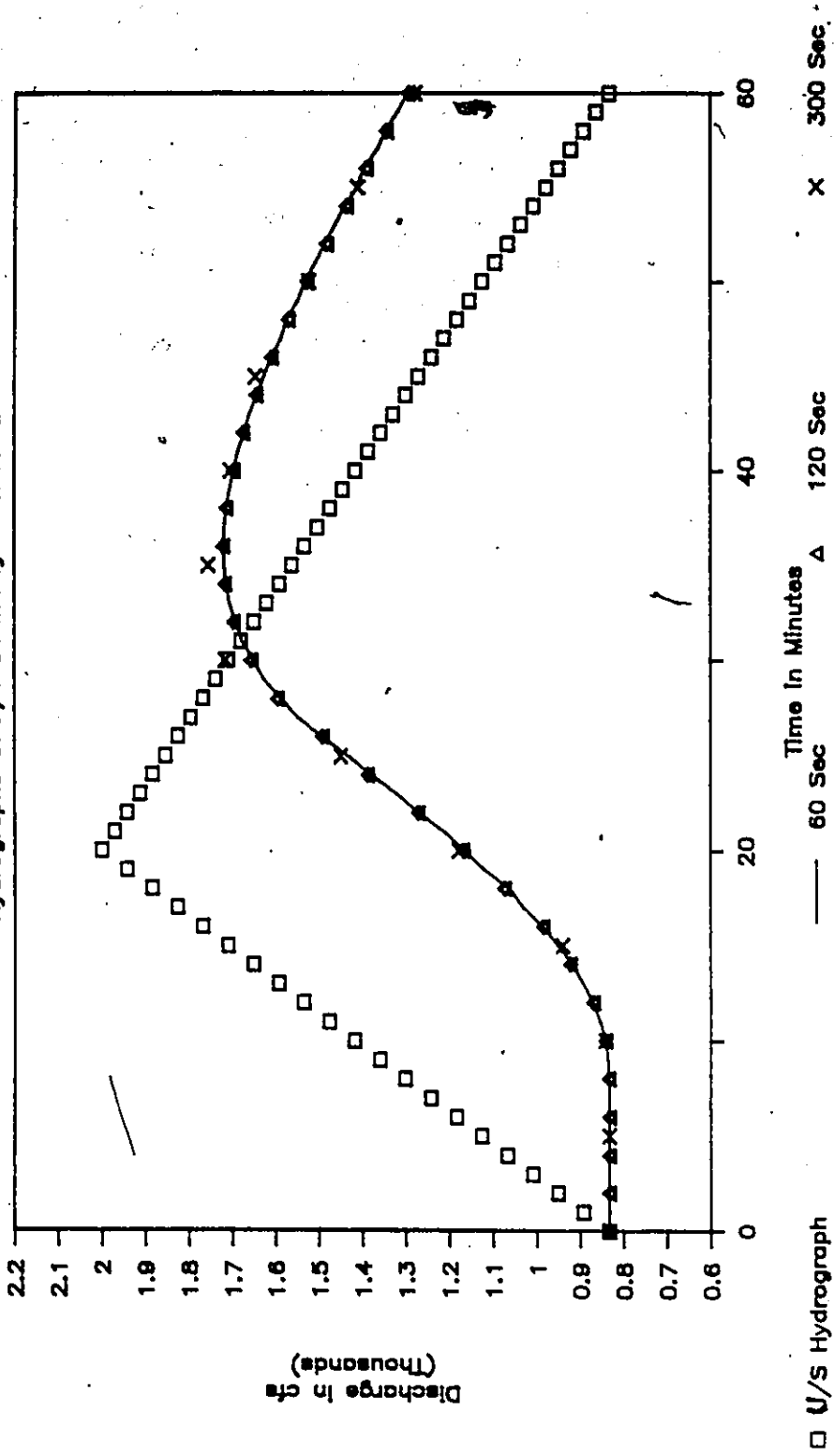


Fig. 6.17 Time Step Sensitivity for Test 'D' - Continuous Flow Simulation.

TABLE 5.2
Sensitivity Analysis of Varying Element Length

Name of Numerical Experiment	Type of Numerical Solution	Element Length (delx)	Time Step Weighting Parameter (Theta)	Spatial Weighting Parameter (Beta)	Manning's Channel Roughness (n)	Temporal Accel. at U/S Boundary (dQ/dt)
** Test 'B'						
Test 'B'	Eularian - Lagrangian	10.00	1.00	1.00	0.0150	66.67
Test 'B'	Eularian - Lagrangian	20.00	1.00	1.00	0.0150	66.67
Test 'B'	Eularian - Lagrangian	50.00	1.00	1.00	0.0150	66.67

element sizes were 10, 20 and 50 metres. The stage profiles captured time equal to 120 sec are presented in Figure 5.18.

The results, qualitatively speaking, are not different from Figure 5.14. Similar observations include the overall shapes of the front are maintained. The front is captured within two elements regardless of the element size, thereby flattening or spreading the front from 20 m for the 10 m element size to 100 m for the 50 m elements.

The height of surge is computed to be the same for all three grid sizes indicating that the momentum balance is achieved across the discontinuity. The spike is of the same height for all three element lengths. The spike for the smallest grid size, (i.e. the highest Courant No.) is however, the most pronounced. For the 50 m element length, the spike is flattened over three nodes, indicating a gradual increase in height which is about eight percent of the surge size.

As the element sizes of 20 and 50 m resulted in the Courant Numbers of less than one, no long waves were encountered. If on the other hand, element sizes of one or two metres, the possibility of long waves exist based on Section 5.3.1 results.

5.3.3 Variation of Temporal Weighting Factor

In Chapter 4 it was shown that the addition of the temporal weighting parameter, θ , introduces a dispersive agent in the solution of open channel flow equations. Work done in the finite difference and finite element solutions in fluid mechanics in general and open channel flow in particular point to the success of incorporating the temporal weighting parameter. To assess the impact of varying this parameter, sensitivity analysis was carried out for Tests A, B and C. For Tests A and C, Eulerian-Lagrangian solution was sought. The Lagrangian solution was obtained

ELEMENT LENGTH SENSITIVITY ANALYSIS

Profiles at Time = 120 Sec. TEST "B"

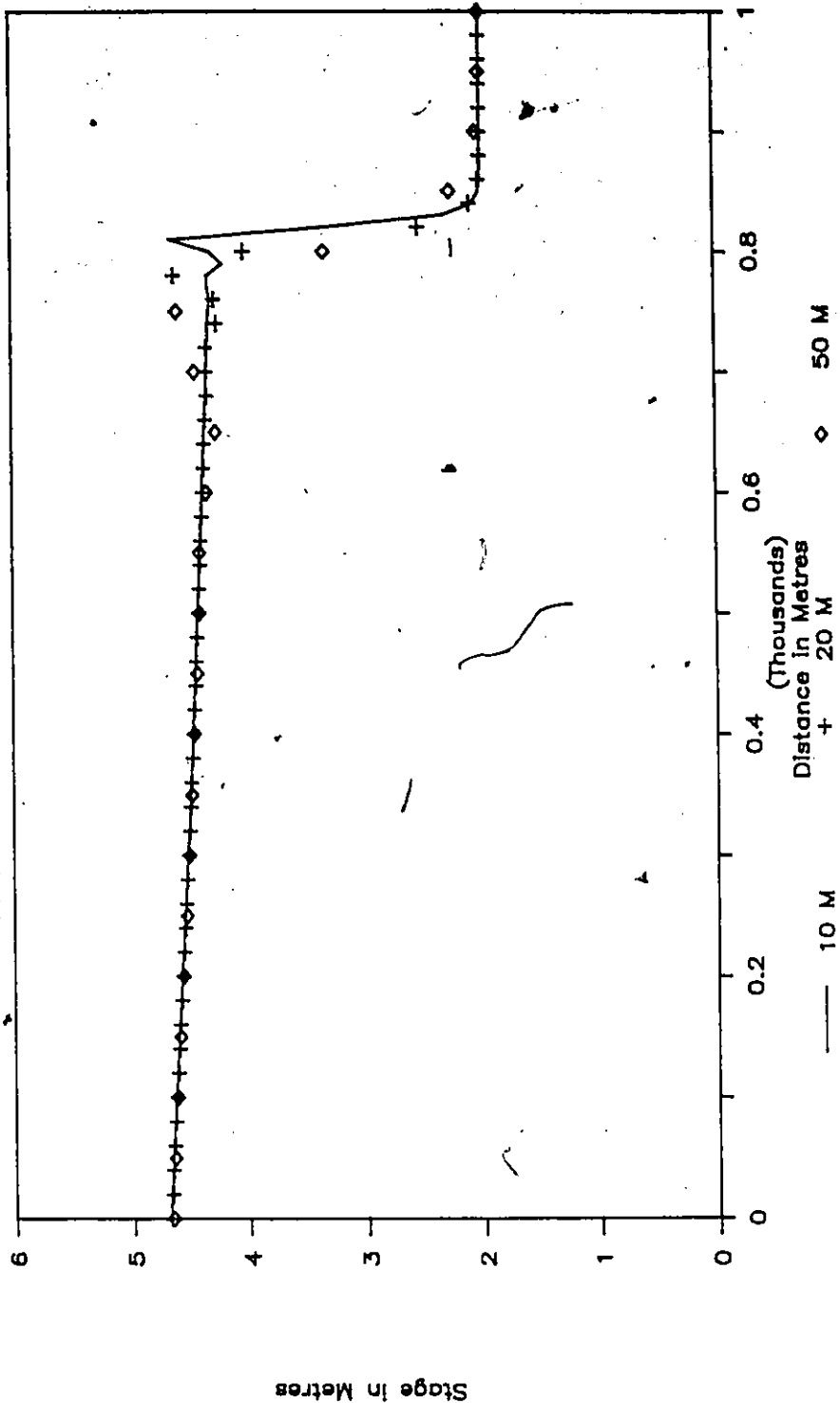


Fig. 5.18 Element Length Sensitivity for Test 'B' - Subcritical Surge Moving Downstream.

for Test B and is reported in Section 5.4.5. The parameters used in this analysis are reported in Table 5.3. These tests are discussed separately.

Test A - In evaluating the impact of varying the temporal weighting factor, three different values were used. These were 0.5, 0.6 and 0.67. A value of 0.5 reflects the basic centered Crank-Nicholson scheme and serves as the basis for the moving element scheme. Several finite-difference models simulating rapidly varying flows use a parameter value of 0.6 as minimum. For this reason a value of 0.6 was tested. Also, as finite element integration of the time derivative leads to a weighting of 0.67, this value was included in the sensitivity analysis. The other model parameter values are listed in Table 5.3.

The stage profiles at 60 seconds for the three weighting factors are presented in Figure 5.19. All three profiles exhibit excellent wave capturing characteristics. As in other tests, the only difference in the three model results is in the vicinity of the sharp discontinuity. The spike exhibited for $\theta = 0.5$ is better controlled than for the other two runs. The location of the front for values of 0.6 and 0.67 is slightly advanced when compared to the basic run. This is an indication that some dispersion is present when the weighting advances beyond 0.5. The height of the supercritical surge is preserved in all three model runs and the front is captured within 20 m or two element lengths.

Test C - In this sensitivity analysis the temporal weighting factor was allowed to change from 0.5, the basic element to 1.0 a fully implicit scheme, with intermediate values of 0.6 and 0.75. The values of other model parameters are presented in Table 5.3.

The stage profiles for the positive surge moving upstream were captured at 120 seconds and are presented in Figure 5.20. In contrast to Test A where little

TABLE 5.3

Sensitivity Analysis of Varying Temporal Weighting Parameter, Theta

Name of Numerical Experiment	Type of Numerical Solution	Element Length (delx)	Time Step (delt)	Temporal Weighting Parameter (Theta)	Spatial Weighting Parameter (Beta)	Manning's Channel Roughness (n)	Temporal Accl. at U/S Boundary (dQ/dt)
** Test 'A'							
Test 'A'	Eularian - Lagrangian	10.00	0.50	0.50	1.00	0.0000	56000.00
Test 'A'	Eularian - Lagrangian	10.00	0.50	0.60	1.00	0.0000	56000.00
Test 'A'	Eularian - Lagrangian	10.00	0.50	0.67	1.00	0.0000	56000.00
** Test 'C'							
Test 'C'	Eularian - Lagrangian	25.00	3.00	0.50	1.00	0.0125	162.67
Test 'C'	Eularian - Lagrangian	25.00	3.00	0.60	1.00	0.0125	162.67
Test 'C'	Eularian - Lagrangian	25.00	3.00	0.75	1.00	0.0125	162.67
Test 'C'	Eularian - Lagrangian	25.00	3.00	1.00	1.00	0.0125	162.67

THETA VARIATION SENSITIVITY ANALYSIS

Profiles at Time = 60 sec. TEST "A"

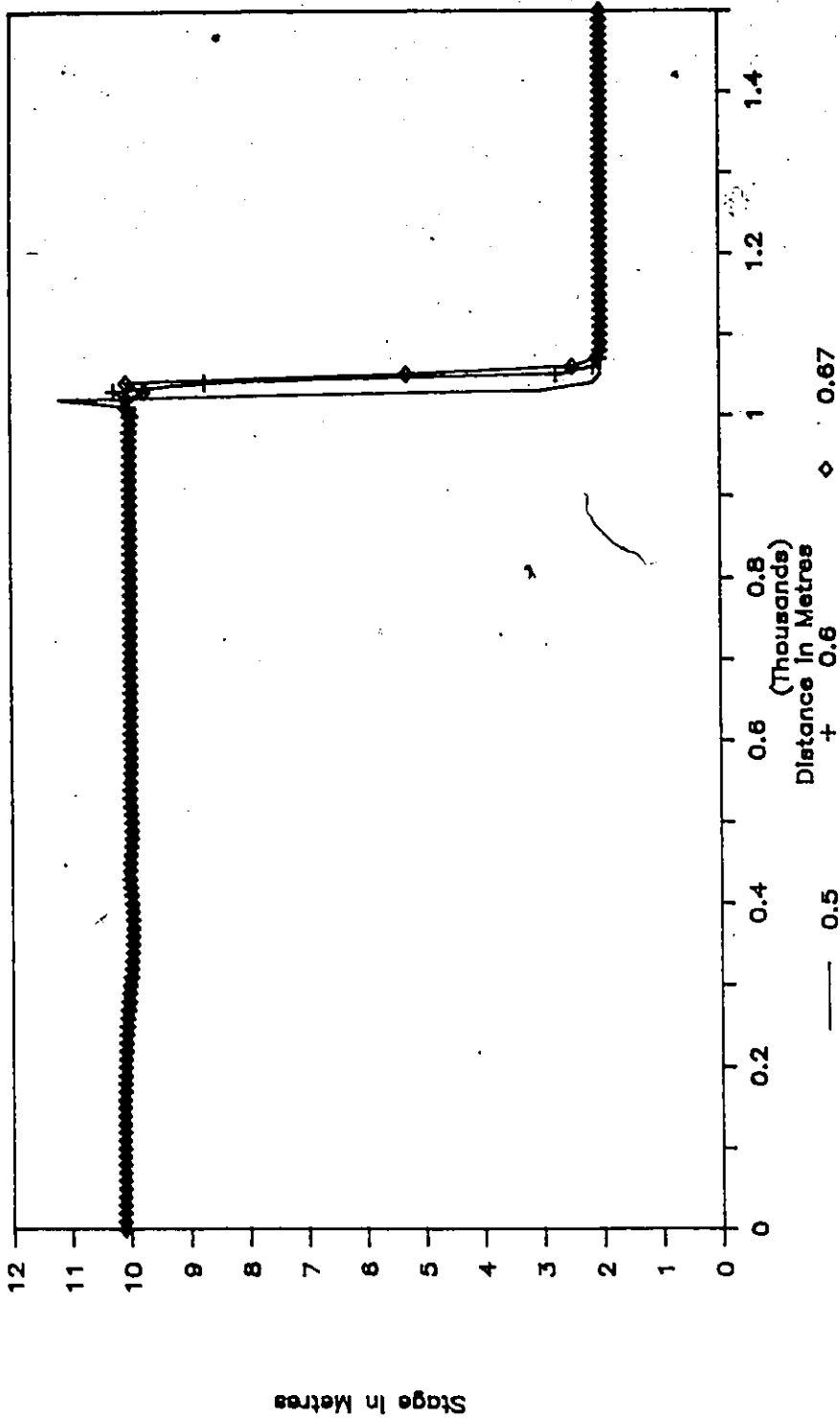


Fig. 5.19 Sensitivity of Varying Temporal Weighting Parameter, θ , for Test 'A' - Supercritical Surge in Frictionless Channel.

THETA VARIATION SENSITIVITY ANALYSIS

Profiles at Time = 120 Sec. TEST "C"

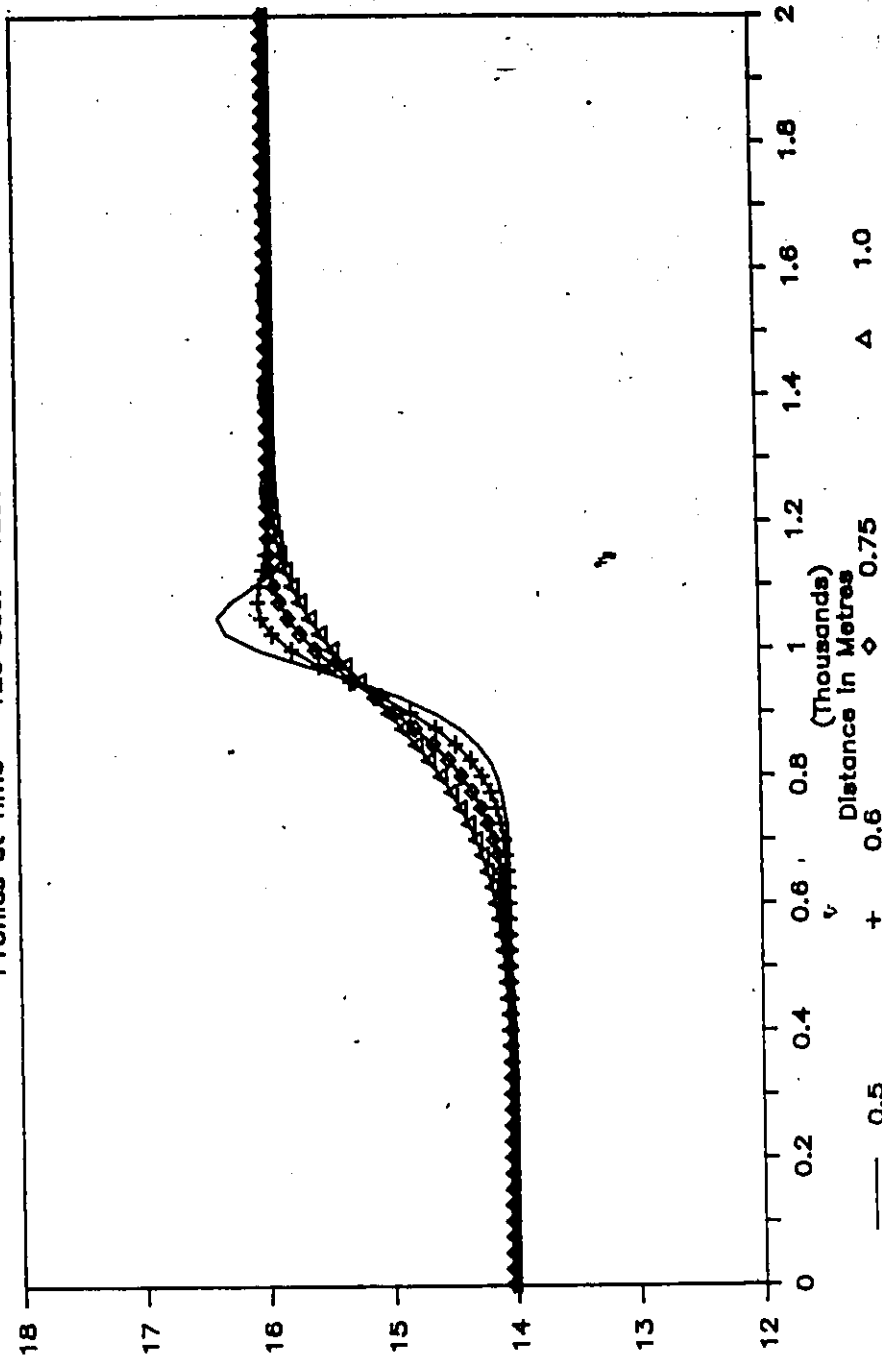


Fig. 5.20 Sensitivity of Varying Temporal Weighting Parameter, θ , for Test 'C' - Subcritical Surge Moving Upstream.

Stage in Metres

Distance in Metres (Thousands)

improvement over the centered scheme was achieved, better oscillation damping properties are observed. The basic Test C resulted in an oscillatory solution for reasons noted in the previous section. A temporal weighting of 0.6 was able to selectively remove the oscillations. The price paid for the smooth solution was a dispersive wave front. With increasing values of θ , the front is increasingly dispersed.

From these runs it can be concluded that for cases where oscillatory solutions result, an acceptable practical alternative for maintaining a discontinuous front and a smooth profile would be to use a temporal weighting factor between 0.55 and 0.6. It is emphasized that oscillations in the moving element solution occur when the time step chosen is too large or when a positive surge moves upstream. In the latter case, the moving element scheme is closer to a centered difference scheme.

5.3.4 Variation of Spatial Weighting Factor

The property of the spatial weighting parameter, β , is to convert the lumped mass matrix of the moving element scheme to a consistent mass matrix. This difference is similar to the mass matrices of a centred finite difference and finite element methods. While developing the concept of the spatial weighting parameter, testing carried out to study the impact of β variation showed promising results. These results for Test B are reported in this section.

Table 5.4 lists the parameters used in these tests. Four values of β were used besides the BOC case of 1.0 for the basic moving element scheme. These values are 0.8, 0.67, 0.6 and 0.5. (These correspond to values of 0, 0.1, 0.167, 0.2 and 0.25 respectively in the legend of the figures.) A value of 0.67 was used to mimic the mass matrix of the finite element technique while 0.5 refers to the mass matrix of a box finite difference scheme.

TABLE 5.4

Sensitivity Analysis of Varying Spatial Weighting Parameter, Beta

Name of Numerical Experiment	Type of Numerical Solution	Element Length (delx)	Time Step (delt)	Temporal Weighting Parameter (Theta)	Spatial Weighting Parameter (Beta)	Manning's Channel Roughness (n)	Temporal Accel. at U/S Boundary (dQ/dt)
** Test 'B'	Eularian - Lagrangian	25.00	5.00	0.50	1.00	0.0150	66.67
Test 'B'	Eularian - Lagrangian	25.00	5.00	0.50	0.80	0.0150	66.67
Test 'B'	Eularian - Lagrangian	25.00	5.00	0.50	0.67	0.0150	66.67
Test 'B'	Eularian - Lagrangian	25.00	5.00	0.50	0.60	0.0150	66.67
Test 'B'	Eularian - Lagrangian	25.00	5.00	0.50	0.50	0.0150	66.67

BETA VARIATION SENSITIVITY ANALYSIS

Profiles at Time = 120 Sec. TEST "B"

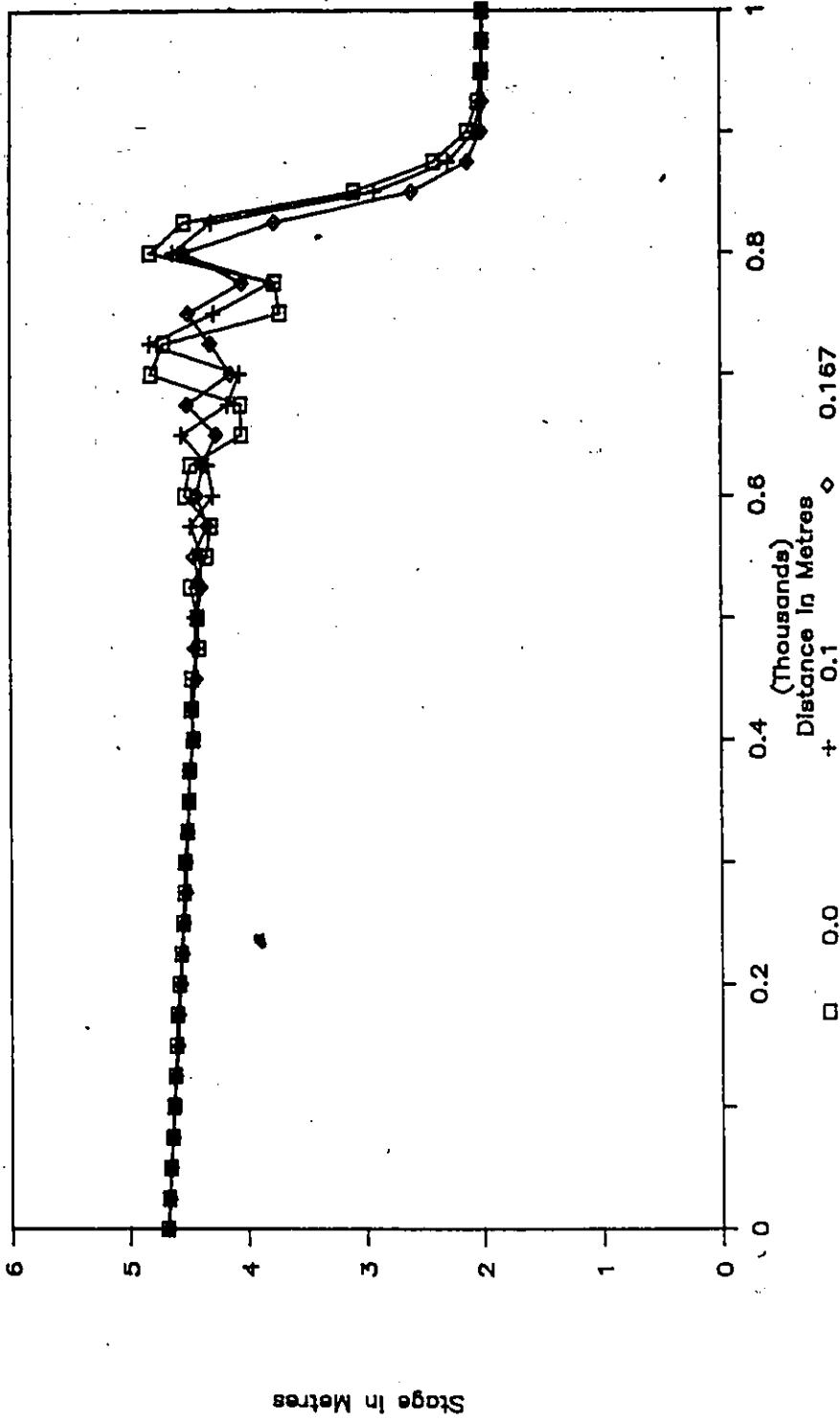


Fig. 5.21 Sensitivity of Varying Spatial Weighting Parameter, β , for Test 'B' - Subcritical Surge Moving Downstream.

BETA VARIATION SENSITIVITY ANALYSIS

Profiles at Time = 120 Sec. TEST "B"

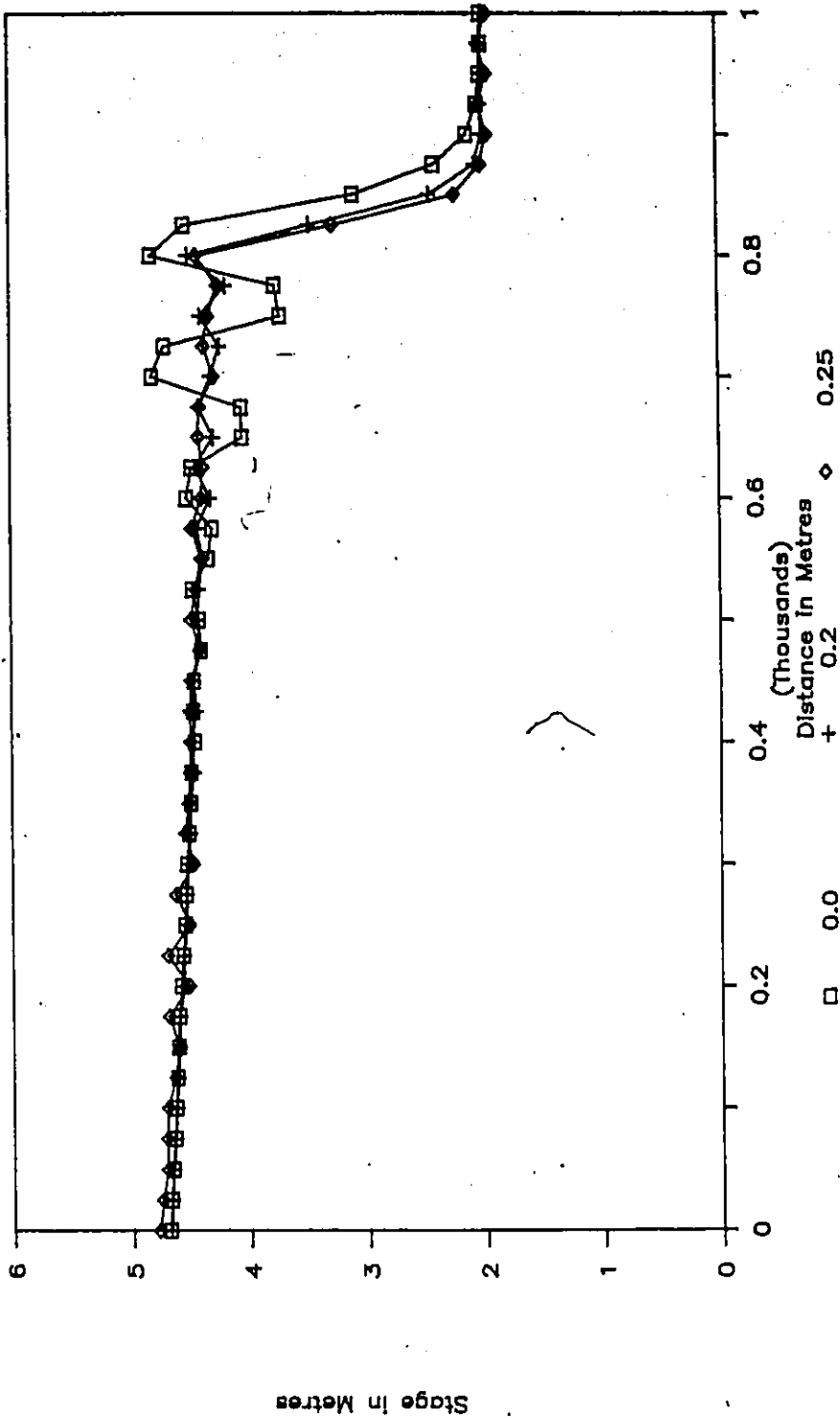


Fig. 5.22 Sensitivity of Varying Spatial Weighting Parameter, β , for Test 'B' - Subcritical Surge Moving Downstream.

The stage profiles at 120 seconds were captured and presented in Figs. 5.21 and 5.22. A time step of 5 seconds was purposely chosen to introduce oscillations at the nose of the surge and extending backwards over several nodes. Figures 5.21 and 5.22 indicate a start of phase shifting of oscillations for β less than 1.0. The height of the undulatory waves is reduced and the peaks shifted forwards with lower values of β . The location of the wave front is not effected for lower values of the weighting factor, while, clipping and wave retardation are evident for lower values of β . With β set to 0.5, secondary parasitic node to node oscillations develop away from the wave front.

All factors considered, the best improvement is achieved when β was equal to 0.6. The height of surge is the same as for BOC case with the oscillations reduced by over 80%. Based on the sensitivity analysis carried out, it can be concluded that the spatial weighting parameter can be of use in solving oscillation problems under restricted conditions for practical and field problems. Although tested, the impact of simultaneous variations of the temporal and spatial parameters are not shown here; these are presented in Appendix F. As a guideline, the value of β could best be set during a calibration process, which may be influenced by a variety of field variables.

5.3.5 Variation of Channel Roughness

It is well known that an increase in channel roughness causes a steeper gradient to discharge the same flow. All conditions being same at a downstream section, the stage for a given flow rate at the upstream section is higher for a rougher channel bed. Channel roughness play a more important role in near discontinuous flow study than, say, in continuous flow situations. The bed roughness has a

pronounced effect on the resulting shapes of stage and flow profiles, a wrong interpretation of which could lead to significant errors.

In order to study the impact of channel roughness, a sensitivity analysis was carried out for Test B. The bed forces acting on the body of water are represented by the Manning's flow equation. Five values of channel roughness were selected ranging from no friction case to extremely rough bed surface with three intermediate values.

Numerically, Manning's n ranged from zero to 0.10, with intermediate values of 0.01, 0.03 and 0.05. A secondary objective of this analysis was to simulate the surge behaviour under field conditions. Table 5.5 lists the parameter values for the model simulations.

The stage and flow profiles were captured at 120 seconds and are respectively presented in Figures 5.23 and 5.24. Immediately noticeable is the difference in profiles from any of the previous sensitivity runs. The stage profiles provide the variation from near horizontal front to an almost continuous variation from the upstream boundary to the tip of the surge front. The depth of flow at the upstream boundary is sensitive to the roughness coefficient and so is the location of the front. Between Manning's n of 0.05 and 0.10, the surge loses the definite form which is noticeable for lower roughness values.

From Figure 5.24, the retardation of flows for increasing Manning's n is evident. The flow, for example, is almost half at a point about 600 m from the upstream end when the roughness changes from 0.01 to 0.03. Thus, consideration of mass balance at a point midway in the solution domain for two different roughness conditions could lead to interesting observations. For roughness values of 0.01 and 0.03, the change in storage is lower and the difference in inflow and outflow lower for

TABLE 5.5
Sensitivity Analysis of Varying Manning's Roughness Coefficient, n

Name of Numerical Experiment	Type of Numerical Solution	Element Length (delx)	Time Step (delt)	Temporal Weighting Parameter (Theta)	Spatial Weighting Parameter (Beta)	Manning's Channel Roughness (n)	Temporal Accel. at U/S Boundary (dQ/dt)
** Test 'B'							
Test 'B'	Eularian - Lagrangian	25.00	3.00	0.50	1.00	0.0000	66.67
Test 'B'	Eularian - Lagrangian	25.00	3.00	0.50	1.00	0.0100	66.67
Test 'B'	Eularian - Lagrangian	25.00	3.00	0.50	1.00	0.0300	66.67
Test 'B'	Eularian - Lagrangian	25.00	3.00	0.50	1.00	0.0500	66.67
Test 'B'	Eularian - Lagrangian	25.00	3.00	0.50	1.00	0.1000	66.67

27

ROUGHNESS CHANGE SENSITIVITY ANALYSIS

Profiles at Time = 120 Sec. TEST "B"

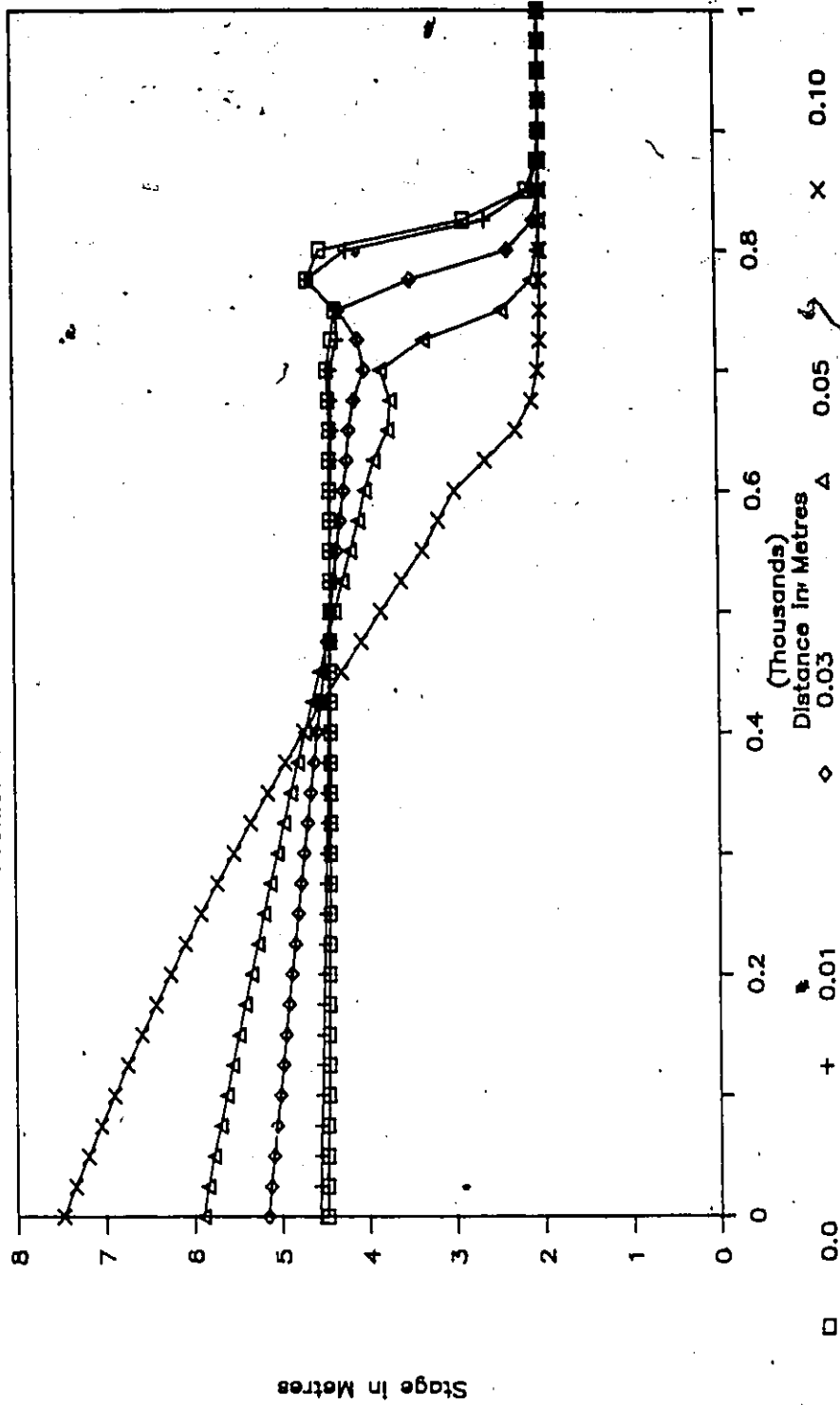


Fig. 5.23 Sensitivity of Varying Channel Roughness Coefficient, n , for Test 'B' - Stage Profiles at Time = 120 Sec.

ROUGHNESS CHANGE SENSITIVITY ANALYSIS

Profiles at Time = 120 Sec. TEST "B"

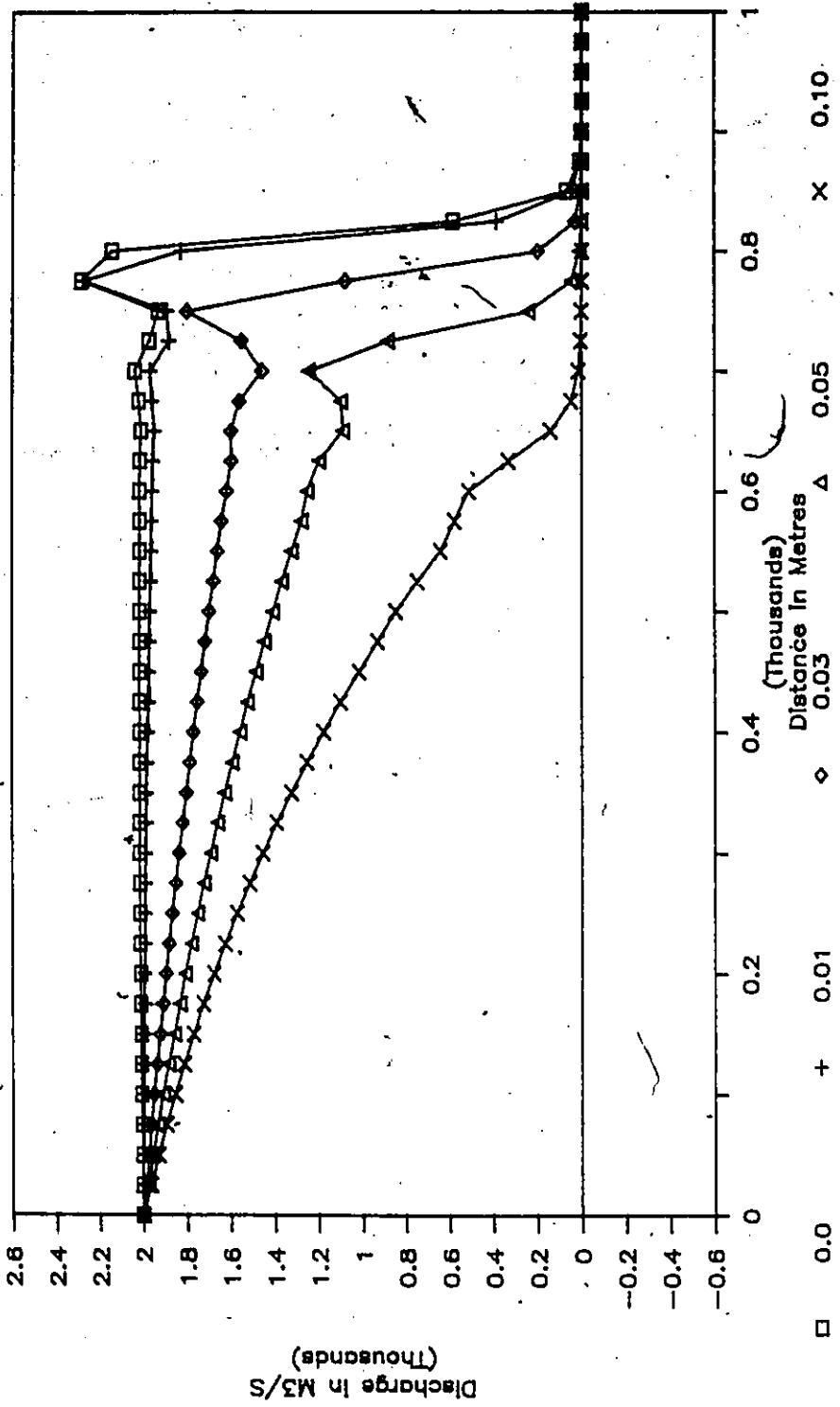


Fig. 5.24 Sensitivity of Varying Channel Roughness Coefficient, n, for Test 'B' - Flow Profiles at Time = 120 Sec.

6

lower roughness and vice versa for higher Manning's n . Figure 5.23 bears testimony to this assertion as the water piles up higher for large 'n' values.

Another noteworthy point from this analysis is the fate of the surge when only a token roughness is added. Referring to the stage and flow profiles for Manning's n value of 0.01, it is observed that under these conditions the model mimics frictionless scenario.

5.3.6 Variation of Temporal Acceleration

For the purpose of this study, the term temporal acceleration is defined as the temporal rate of change of flow rate at the boundaries. Mathematically, if the flow at the boundary changes from Q_1 to Q_2 in a time interval t_1 to t_2 , then the temporal acceleration is $(Q_2 - Q_1)/(t_2 - t_1)$. The dimension of this term is L^3T^{-2} .

The location of the front and shape of the wave is strongly dependent on the temporal acceleration. To study the behaviour of varying the rate of change of flow rate, numerical experiments were designed for Tests 'B' and 'C'. These are now discussed.

Test 'B' - The variations for this experiment from the basis of comparison case are noted in Table 5.6. For this analysis, a frictionless scenario is considered with an element size of 10 m. The time step was fixed at 1.0 second. With a time step of 1.0 second, all temporal accelerations had to be slower than the base case of 2000 m^3/s^2 . In other words, the flow at the upstream boundary changes from no flow to 2000 m^3/s in 1, 10, 30 and 60 seconds respectively. These values may be compared to the estimated temporal accelerations rates of 4.0 to 10.0 m^3/s for the Teton Dam-Break flood with a comparable channel size.

TABLE 5.6

Sensitivity Analysis of Varying Temporal Acceleration, dQ/dt

Name of Numerical Experiment	Type of Numerical Solution	Element Length (delx)	Time Step (deltat)	Temporal Weighting Parameter (Theta)	Spatial Manning's Channel Roughness (Beta)	Temporal Accel. at U/S Boundary (dQ/dt)
** Test 'B'						
Test 'B'	Eularian - Lagrangian	10.00	1.00	0.50	1.00	2000.00
Test 'B'	Eularian - Lagrangian	10.00	1.00	0.50	1.00	200.00
Test 'B'	Eularian - Lagrangian	10.00	1.00	0.50	1.00	66.67
Test 'B'	Eularian - Lagrangian	10.00	1.00	0.50	1.00	33.33
** Test 'C'						
Test 'C'	Eularian - Lagrangian	25.00	3.00	0.50	1.00	81.33
Test 'C'	Eularian - Lagrangian	25.00	3.00	0.50	1.00	40.67
Test 'C'	Eularian - Lagrangian	25.00	3.00	0.50	1.00	20.33

The results for the four cases are presented in Figure 5.25. These profiles were captured at 120 seconds, well after a steady flow rate is established at the upstream boundary. Except for the slightly different spike sizes, the obvious difference is the location of the front. As expected, the highest temporal acceleration rate corresponds to the most advanced front and vice versa. There were marginal differences in the height of discontinuities. A matured discontinuity for a frictionless case, such as the one being investigated, assumes a horizontal surface. This is evident for acceleration of $2000 \text{ m}^3/\text{s}^2$ and $200 \text{ m}^3/\text{s}^2$. For lower rates, there is a minimal surface gradient to offset the spatial and temporal flow accelerations. For this purpose, the four profiles were windowed and plotted at a more suitable scale as shown in Figure 5.26. The above discussion is clearly demonstrated in the figure.

Test 'C' - Table 5.6 presents the model parameters that were used for the basis of comparison and those varied for this analysis. The grid size and time steps were fixed at 25 m and 3.0 seconds respectively and roughness defined by a Manning's roughness coefficient of 0.0125. The temporal accelerations corresponded to reducing flows from $2694.5 \text{ m}^3/\text{s}$ to $250 \text{ m}^3/\text{s}$ in 30, 60 and 120 seconds. The profiles were captured at 180 seconds and presented in Figure 5.27.

This experiment exhibited the development of undulations with maturing of the wave front. For a temporal acceleration corresponding to 120 seconds, no oscillations are present, a gradual formation is next seen for 60 seconds while the undulations take a permanent form for a distance of 300 to 400 m, consistent with other experiments for Test 'C'. Also, similar to Test 'B' the locations of the front were directly linked with the rate of temporal accelerations.

5.3.7 Summary of Sensitivity

TEMPORAL ACCL. SENSITIVITY ANALYSIS

Profiles at Time = 120 Sec. TEST 'B'

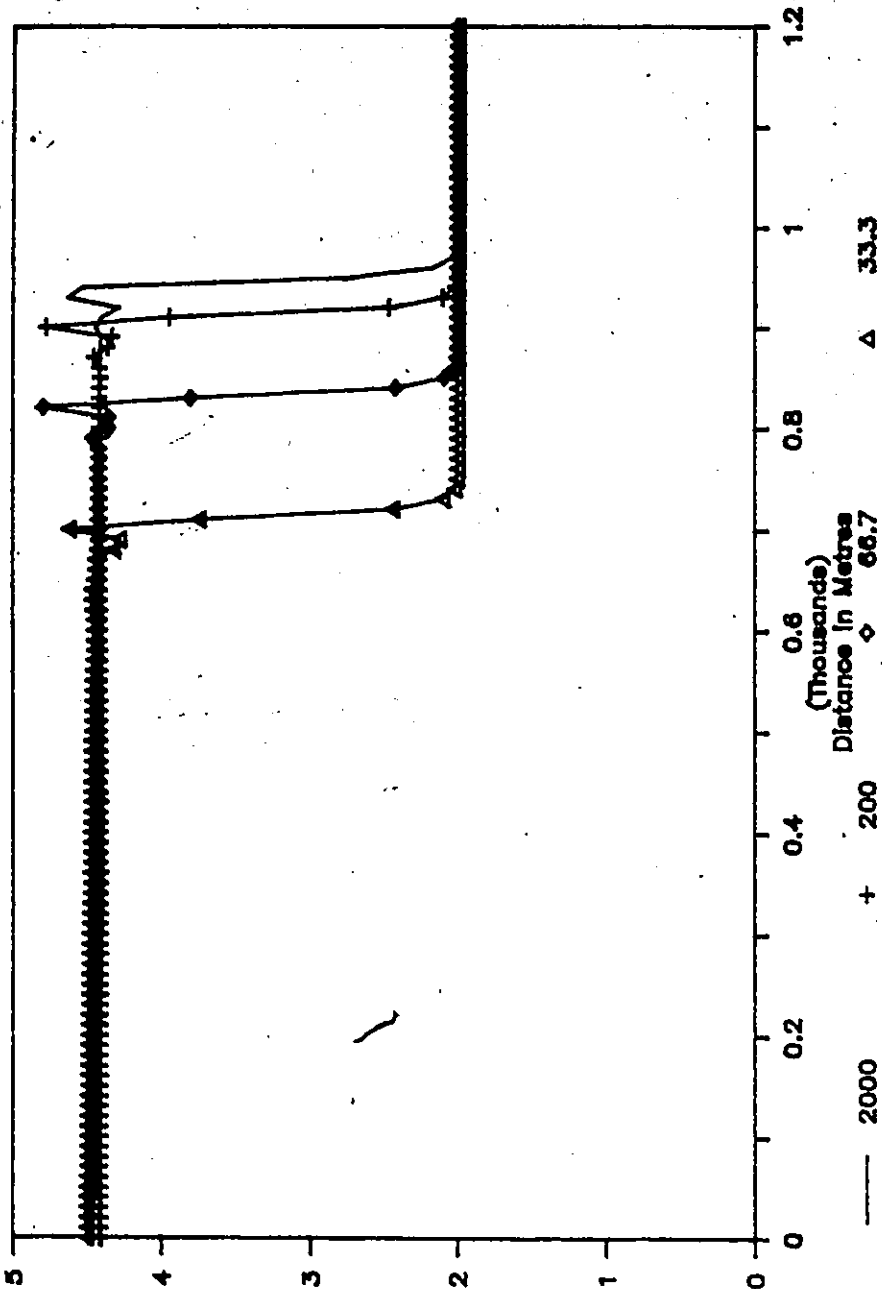


Fig. 5.25 Sensitivity of Varying Temporal Acceleration at Upstream Boundary for Test 'B'.

Stage in Metres

(Thousands)
Distance in Metres

— 2000 + 200 ◊ 66.7 Δ 33.3

TEMPORAL ACCL. SENSITIVITY ANALYSIS

Profiles at Time = 120 Sec. TEST "B"

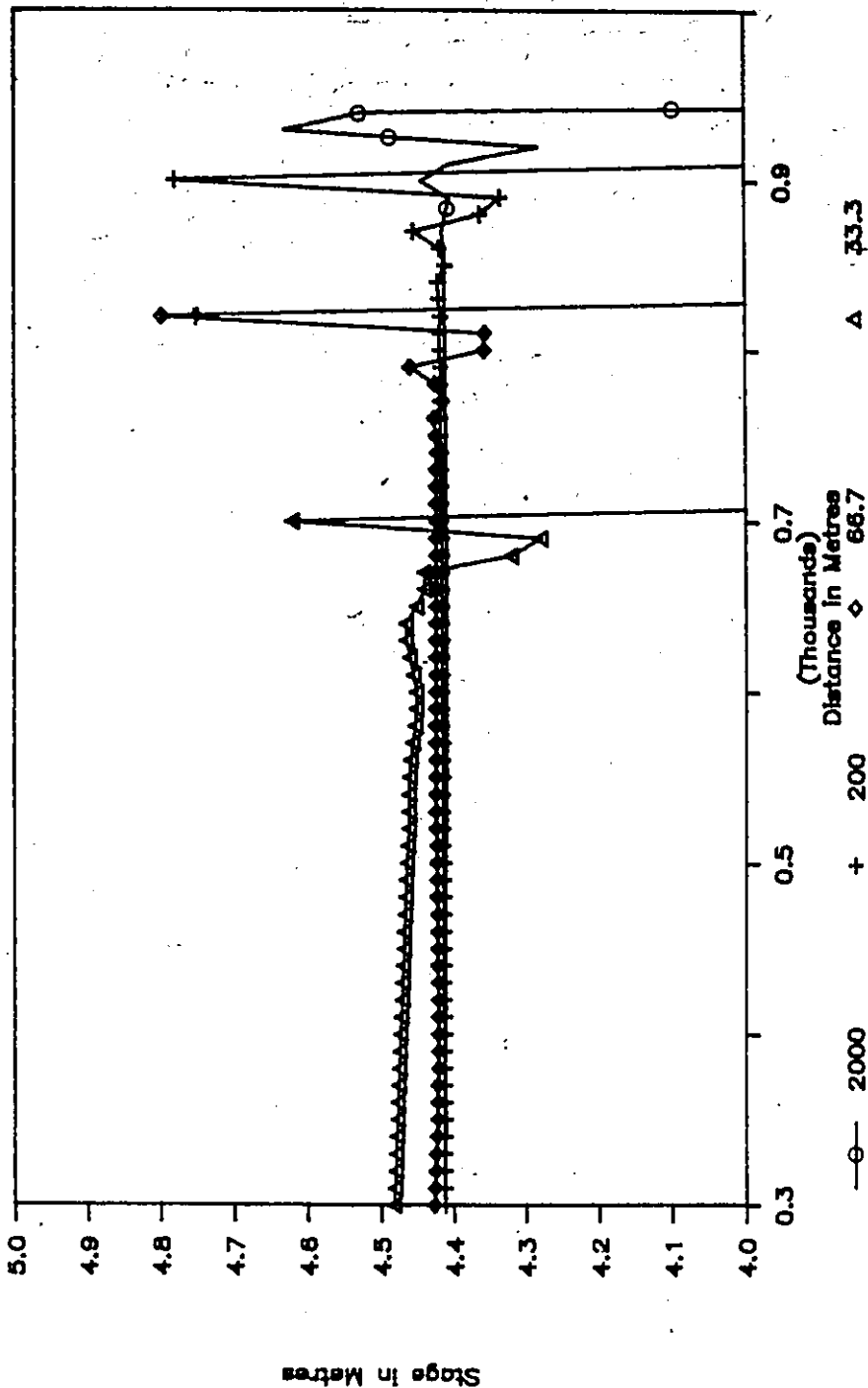


Fig. 5.26 Exploded Window with Exaggerated Vertical Scales From 5.25.

TEMPORAL ACCLN. SENSITIVITY ANALYSIS

Profiles at Time = 180 Sec. TEST "C"

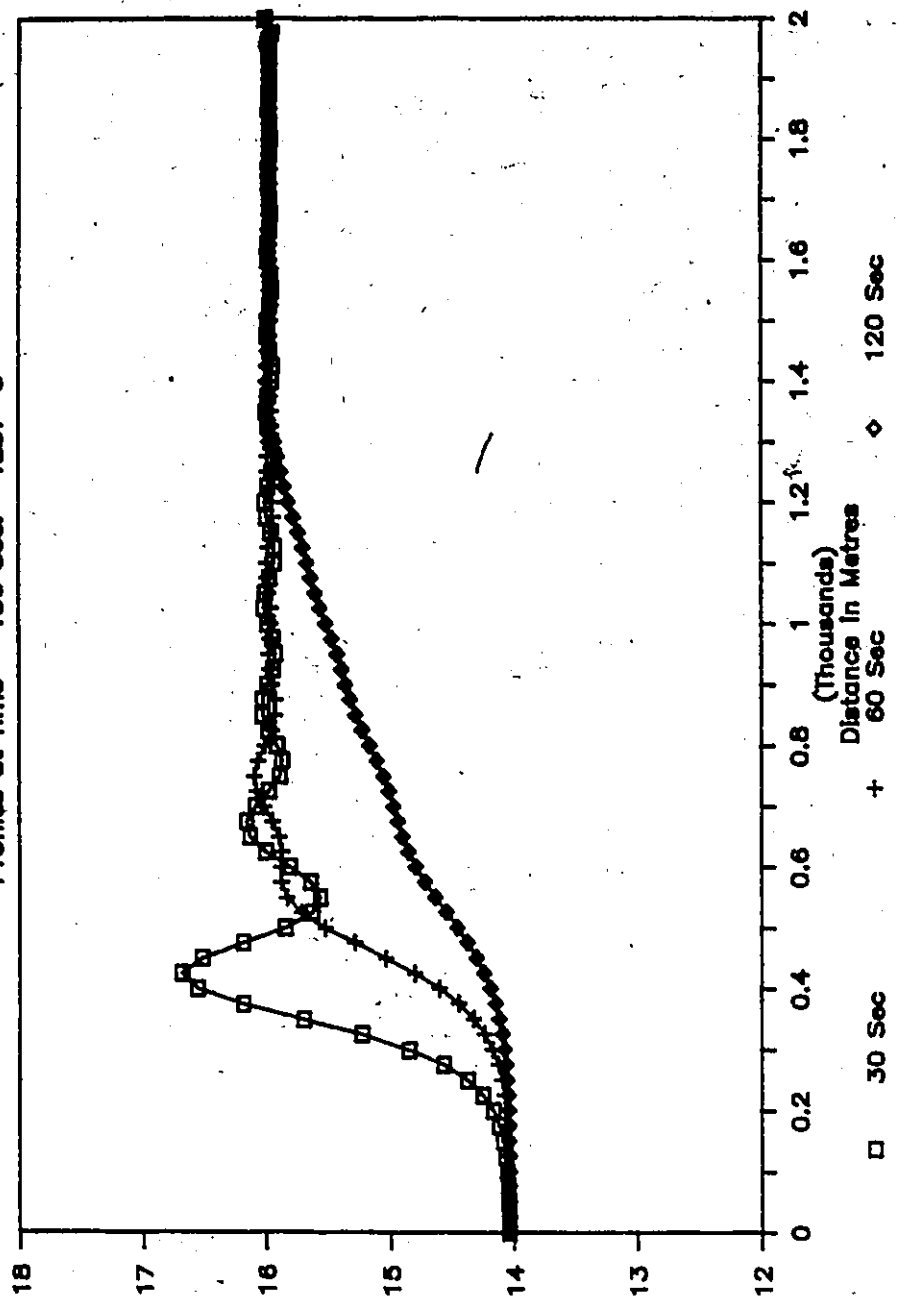


Fig. 5.27 Sensitivity of Varying Temporal Acceleration at Downstream Boundary for Test 'C'.

Stage in Metres

Based on the sensitivity analyses carried out, a number of parameters showed significant changes in results. These parameters are listed in the order of their sensitiveness to the numerical schemes performance in Table 5.6(a). Another factor which greatly influences the shape of the hydrograph is the lateral flow term. This is of even more importance for natural streams where non-point flows influence the shape of the hydrograph. This was not tested.

5.4 Comparison With Other Techniques

The best judge of a different algorithm, an improved technique, or a newer model is the performance of the methodology against real world data. In the absence of such data which are not existant, save for a few controlled laboratory experiments, a secondary level of testing can be carried out using other available techniques. In this section comparisons with finite difference and finite element methods were carried out and the superiority of the proposed technique demonstrated.

Limited testing was also carried out for the Petrov-Galerkin based space-time finite element scheme and the pure Lagrangian model described in the previous chapter. These tests were compared with the Eularian-Lagrangian mode solution and conclusions are drawn. These are also described.

5.4.1 Selection of Finite Difference and Finite Element Models

The first task in carrying out meaningful comparisons is the selection of an established model or a technique capable of handling near discontinuous flows. Other factors that were imposed in the model selection included addressing frictionless channels, a variable temporal weighting parameter which can be set at 0.5 for the true Crank-Nicholson case, zero flow, horizontal water and channel bed conditions.

Table 5.6(a)

Summary of Sensitivity Analysis

Sensitivity Parameter Performance Indicators

- | | | |
|----|----------------------------------|---|
| 1. | Time Step | Controls the Courant number, hence the success of the scheme. Resolves correct location of surge, minimizes mass conservation errors. Most important sensitivity parameter. |
| 2. | Element Length | Controls the shape and steepness of front. Indirectly responsible for Courant number. |
| 3. | Roughness Factor | Controls the overall shape, location, height and steepness of front. Parameter best fixed through calibration. |
| 4. | Temporal weighting factor | Controls the spike at the tip of front. Provides a smooth profile. Relaxes the time step to certain extent. Solution is dissipative. |
| 5. | Spatial weighting factor | Controls the spike for a given value of theta. Provides for a consistent mass matrix. |
| 6. | Temporal acceleration | Determines the location of the surge. Shape of the surge is influenced. Least sensitive parameter. |

The imposition of the above criteria eliminated almost all the available finite difference and finite element models. The only model that met some of the conditions was DAMBRK developed by Fread, 1978. Test 'B' was used for studying the model behaviour. The model, however, failed to operate even for an advanced temporal weighting parameter and a retarded temporal acceleration rate. At this stage, DAMBRK was dropped from any further testing.

Next, effort was directed at developing alternate models that would allow the testing. During this experimentation stage another strength of the moving element scheme was noted. By simply constraining the elements to prevent distortion between time steps and manipulating the temporal and spatial weighting parameters the model can be made to yield to various forms of finite difference and finite element schemes. In a sense, therefore, the moving element scheme is a very generalized form of other, less versatile models.

In the scenario, when the nodes are not allowed to migrate, a temporal weighting of 0.5 and a spatial weighting of 1.0 result in a central difference finite difference scheme. This is demonstrated by simply considering the conservation of mass equation given by Equation (4.213).

$$\begin{aligned}
 & \frac{k}{2} [\theta (Q_{i+1}^{n+1} - Q_{i-1}^{n+1}) + (1-\theta)(Q_{i+1}^n - Q_{i-1}^n)] \\
 & - \frac{1}{2} \left\{ [\theta A_{i+1}^{n+1} + (1-\theta)A_{i+1}^n] \delta_{i+1} - [\theta A_{i-1}^{n+1} + (1-\theta)A_{i-1}^n] \delta_{i-1} \right\} \\
 & - \frac{k}{2} [\theta q_i^{n+1} \Delta^{n+1} - (1-\theta)q_i^n \Delta^n] \\
 & + \frac{1}{2} [(1-\beta)\Delta_{i-1/2}^{n+1} A_{i-1}^{n+1} + \beta \Delta_{i-1/2}^{n+1} A_i^{n+1} + (1-\beta)\Delta_{i+1/2}^{n+1} A_{i+1}^{n+1} \\
 & - (1-\beta)\Delta_{i-1/2}^n A_{i-1}^n - \beta \Delta_{i-1/2}^n A_i^n - (1-\beta)\Delta_{i+1/2}^n A_{i+1}^n] = 0
 \end{aligned} \tag{4.213}$$

By setting

$$\Delta^n = \Delta^{n+1} = \Delta$$

$$\delta_{i+1} = \delta_{i-1} = 0$$

$$\theta = 0.5$$

$$\beta = 1.0$$

and dividing the equation by $1/2 k\Delta$ results in

$$0.5 \left\{ \frac{Q_{i+1}^{n+1} - Q_{i-1}^{n+1}}{\Delta} + \frac{Q_{i+1}^n - Q_{i-1}^n}{\Delta} \right\} + \frac{A_i^{n+1} - A_i^n}{k} - 0.5 (q_i^{n+1} + q_i^n) = 0 \quad (5-5)$$

This equation is the same as the central difference scheme and similar to one employed by Vasiliev et al (1967).

Similarly, by employing Equation (4.213), and imposing δ equal to zero, θ to 0.5 and β to 2/3, the classical equation, with finite element in space and finite difference in time, results. Using the same procedure as before leads to

$$0.5 \left\{ \frac{Q_{i+1}^{n+1} - Q_{i-1}^{n+1}}{\Delta} + \frac{Q_{i+1}^n - Q_{i-1}^n}{\Delta} \right\} + \frac{1}{6} \frac{A_{i-1}^{n+1} - A_{i-1}^n}{k} + \frac{2}{3} \frac{A_i^{n+1} - A_i^n}{k} + \frac{1}{6} \frac{A_{i+1}^{n+1} - A_{i+1}^n}{k} - 0.5 (q_i^{n+1} + q_i^n) = 0 \quad (5-6)$$

The resulting equation is the one used by Cooley and Moin (1976).

Based on the foregoing two different models were set up by fixing the parameters that results in the finite element and finite difference models. The results are discussed next.

5.4.2 Finite Difference Methods

A truer comparison between the moving element and finite difference method would have entailed employment of a variety of finite difference forms like the six point or four point schemes. The circumstances, however, prevented such analysis and limited to only the central difference scheme. For this comparison, Tests 'A' and 'B' were selected. The parameters used in these experiments are noted in Table 5.7. In all the tests carried out, the Eulerian-Lagrangian linked moving element model was used.

Test 'A' - This supercritical test presented a gruelling problem to the technique. The frictionless scenario provided for the added dimension of the true dissipation requirements. The finite difference model used is based on the divergent form of equations and allow like for like comparison. As noted in Table 5.6, both methods were evaluated at a temporal weighting of 0.5.

The results for the moving element and finite difference methods are presented in Figure 5.28. The finite difference method produces a highly oscillatory solution. These oscillations exist through out the zone of front travel with the amplitude gradually diminishing towards the upstream boundary.

When compared to the theoretical travel time, the wave front has advanced an extra 50 to 60 metres. The advancement could be attributed to higher particle velocities associated with nodes with higher depths and flows. The maximum deviations for depth from the theoretically correct value of 10.1 metre were +3.3 metre and -7.3 metres. Although the experiment was not continued beyond obtaining the profile at 60 seconds, it appears that the oscillations would continue to grow, eventually terminating the calculations when the depth of flow approaches zero or a negative value.

TABLE 5.7
 Comparison of Moving Element Method with Finite Difference Method

Name of Numerical Experiment Solution	Type of Numerical Solution	Element Length (delx)	Time Step (delt)	Temporal Weighting Parameter (Theta)	Spatial Weighting Parameter (Beta)	Manning's Channel Roughness (n)	Temporal Accl. at U/S Boundary (dQ/dt)
** Test 'A'	Eularian - Lagrangian	10.00	0.50	0.50	1.00	0.0000	56000.00
Test 'A'	Finite Difference	10.00	0.50	0.50	1.00	0.0000	56000.00
** Test 'B'	Eularian - Lagrangian	25.00	3.00	0.50	1.00	0.0150	66.67
Test 'B'	Finite Difference	25.00	3.00	0.50	1.00	0.0150	66.67

MOVING ELEMENT VS FINITE DIFF. METHOD

Profiles at Time = 60 Sec. TEST "A"

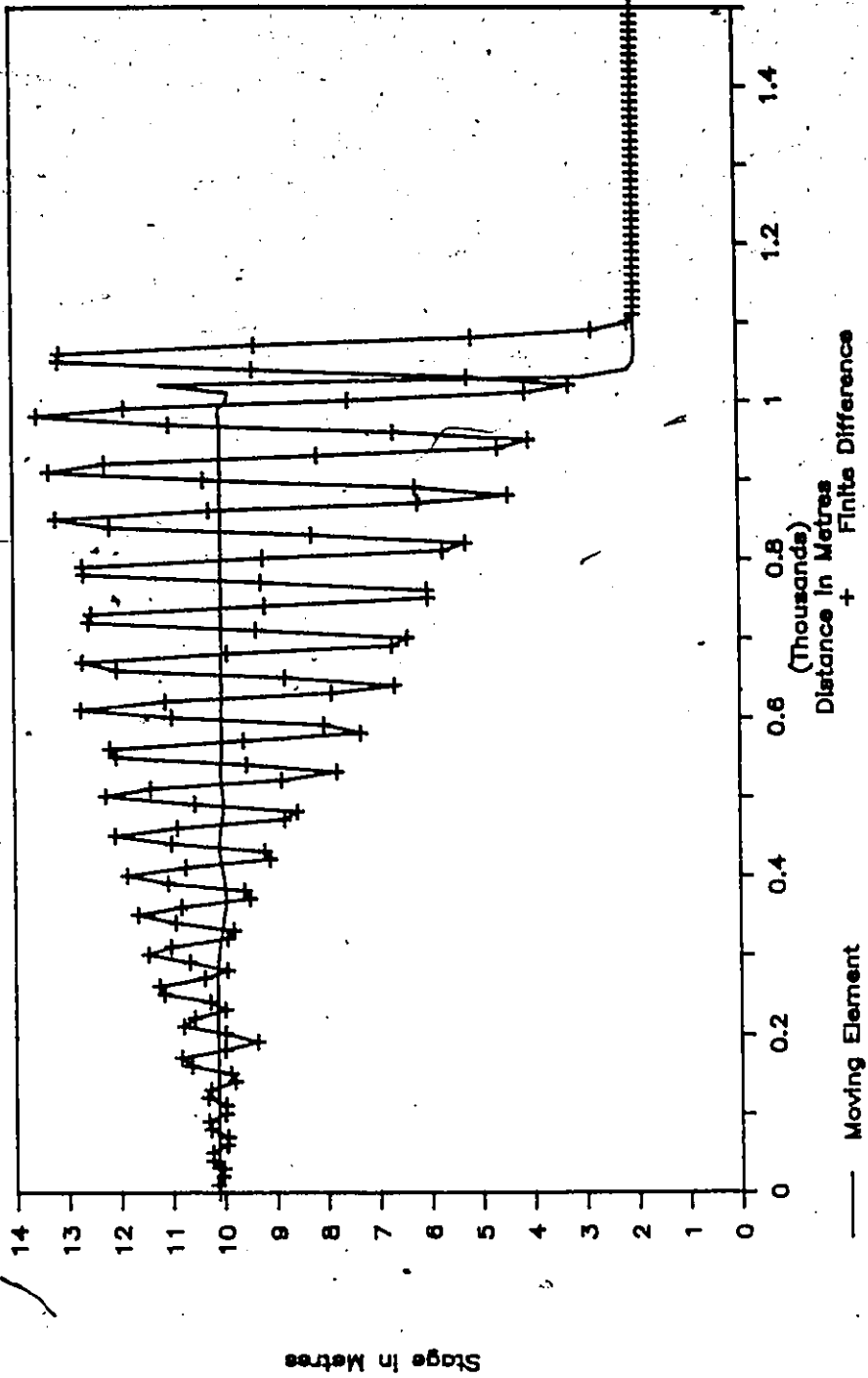


Fig. 5.28 Comparison of Moving Element Method with Finite Difference Method for Test 'A'

In contrast, the moving element solution exhibits none of the oscillations that dominate the finite difference solution. Except for the presence of a spike at the nose of the front, the deviations at any point do not exceed ± 0.1 m.

The only positive note for the finite difference method was the property of mass conservation, the mass being perfectly conserved. For the moving element method, due to interpolation and clipping errors, there was a mass conservation error of about 0.7%.

Test 'B' - To test the generality of the moving element method against the finite difference technique, the comparison was next carried out for Test 'B'. As in Test 'A' both models were evaluated at a temporal weighting of 0.5. The results in this comparison are same as for Test 'A'. The results are presented in Fig. 5.29. The superiority of the moving element scheme is clearly evident.

5.4.3 Finite Element Method

As for the finite difference method, two comparisons were carried out with the finite element technique. These were also for Tests 'A' and 'B'. The model parameters used in the two tests are noted in Table 5.8. Both, finite element and moving element models were evaluated at a temporal weighting of 0.5. For the moving element model, the Eulerian-Lagrangian mode solution was employed.

Test 'A' - The results for the finite element and moving element methods are presented in Figure 5.30. Like the finite difference method, the finite element solution is dominated by the parasitic oscillations. Unlike the finite difference method, however, the finite element exhibits a somewhat tighter band in the amplitude of oscillations. The finite element solution also indicates a higher rate of node to node oscillations. For the finite difference method, there are four nodes

MOVING ELEMENT VS FINITE DIF. METHODS

Profiles at Time = 120 ■ TEST 'B'

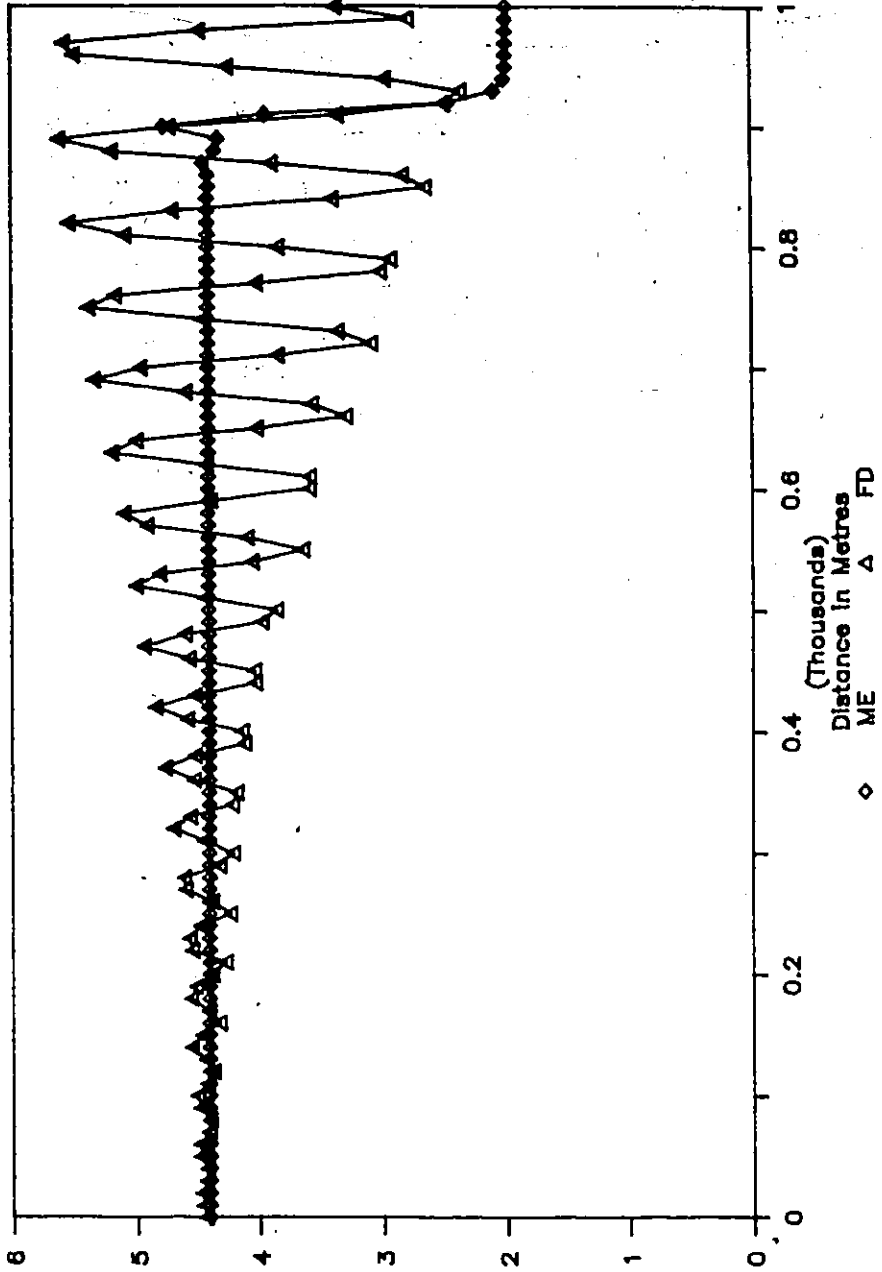


Fig. 5.29 Comparison of Moving Element Method with Finite Difference Method for Test 'B'.

Stage in Metres

(Thousands)
Distance in Metres

◇ ME
△ FD

TABLE 5.8

Comparison of Moving Element Method with Finite Element Method

Name of Numerical Experiment	Type of Solution	Element Length (delx)	Time Step (delt)	Temporal Weighting Parameter (Theta)	Spatial Weighting Parameter (Beta)	Manning's Channel Roughness (n)	Temporal Accl. at U/S Boundary (dQ/dt)
** Test 'A'							
Test 'A'	Eularian - Lagrangian	10.00	0.50	0.50	1.00	0.0000	56000.00
Test 'A'	Finite Element	10.00	0.50	0.50	0.67	0.0000	56000.00
** Test 'B'							
Test 'B'	Eularian - Lagrangian	25.00	3.00	0.50	1.00	0.0150	66.67
Test 'B'	Finite Element	25.00	3.00	0.50	0.67	0.0150	66.67

MOVING ELEMENT VS FINITE ELEMENT METHOD

Profiles at Time = 60 Sec. TEST 'A'

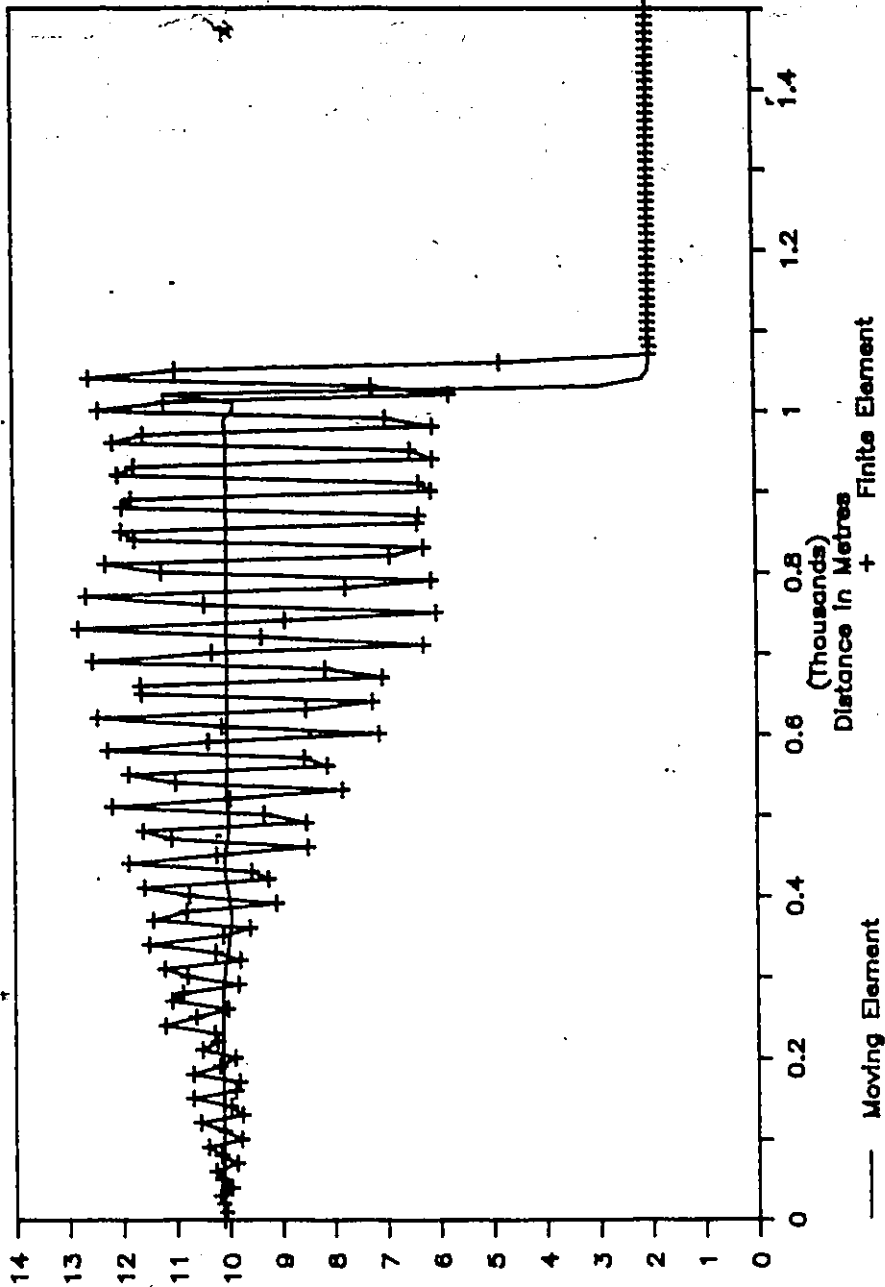


Fig. 5.30 Comparison of Moving Element Method with Finite Element Method for Test 'A'.

Stage In Metres

MOVING ELEMENT VS FINITE ELEMENT METHOD

Profiles at Time = 120 Sec. TEST "B"

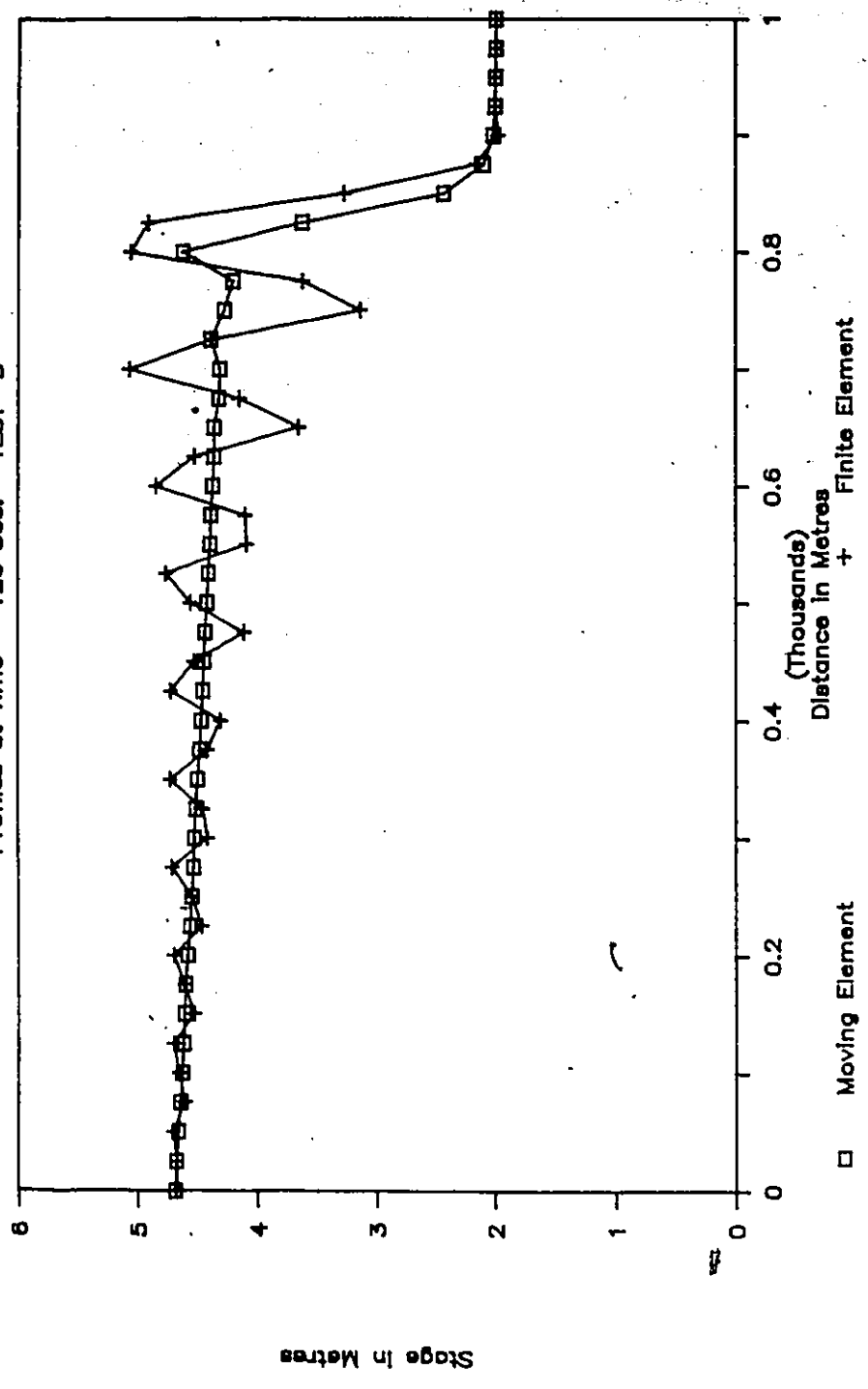


Fig. 5.31 Comparison of Moving Element Method with Finite Element Method for Test 'B'.

occupying one cycle of oscillations, while five to six nodes describe an oscillation cycle in the finite element technique.

The oscillations show similar properties as exhibited by the finite difference method. The amplitude variations about the analytical solution were +2.8 m and -4.2 m. Thus the size of the oscillations is smaller. The difference in the shape and size of the oscillations can be attributed to the consistent mass matrix of the finite element method against the lumped mass matrix of the finite difference solution.

Test 'B' - Again this comparison of the moving element with the finite element method demonstrated the superiority of the former. The results are presented in Figure 5.31. The observation made with respect to the comparison with the finite difference method apply here as well.

The two foregoing sections have described the behaviour of the moving element in its basic form, that is with a temporal weighting of 0.5 and a spatial weighting of 1.0. There are, however, a number of possible combinations that would allow comparisons. A number of experiments for Tests 'A' 'B' and 'C' were carried out and compared with various forms of finite element and finite difference solutions. The results are presented in Appendix F.

5.4.4 Petrov-Galerkin Based Method

In Chapter 4, an alternate form of the basis function was used, orthogonalized and solution obtained. This alternate form, termed Petrov-Galerkin based method, required orthogonality not only with the basis function, but also with its spatial derivative. Such a requirement led to the development of a separate model, twice as big in terms of computer code as the basic moving element method.

TABLE 5.9

Comparison of Moving Element Method with Petrov - Galerkin Method

Name of Numerical Experiment	Type of Solution	Element Length (delx)	Time Step (delt)	Temporal Weighting Parameter (Thets)	Spatial Weighting Parameter (Beta)	Manning's Channel Roughness (n)	Temporal Accel. at U/S Boundary (dq/dt)
** Test 'B'	Eularian - Lagrangian	25.00	5.00	0.50	1.00	0.0150	66.67
Test 'B'	Petrov - Galerkin	25.00	5.00	0.50	1.00	0.0150	66.67
Test 'B'	Petrov - Galerkin	25.00	3.00	0.50	1.00	0.0150	66.67
Test 'B'	Petrov - Galerkin	25.00	3.00	0.50	1.00	0.0150	66.67
Test 'B'	Petrov - Galerkin	25.00	3.00	0.50	1.00	0.0150	66.67
Test 'B'	Eularian - Lagrangian	25.00	3.00	0.50	1.00	0.0150	166.67
Test 'B'	Petrov - Galerkin	25.00	3.00	0.50	1.00	0.0150	166.67

PETROV-GALERKIN MOVING ELEMENT SOLUTION

Profiles at Time = 120 Sec. TEST "B"

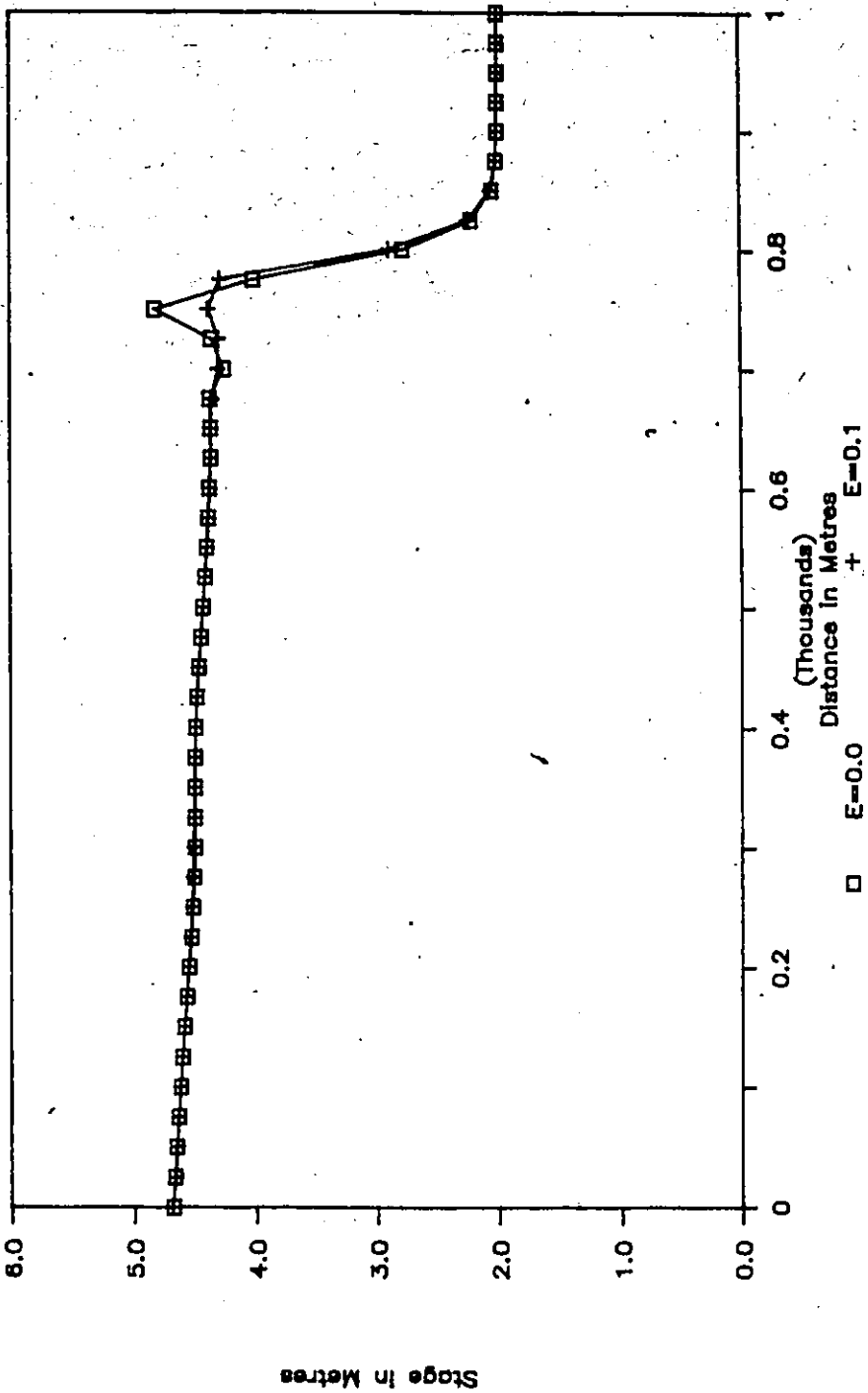


Fig. 5.32 Comparison of Basic Moving Element Method with Petrov-Galerkin Based Moving Element for Test 'B' - Dissipation Level, $\epsilon = 0.1$.

PETROV-GALERKIN MOVING ELEMENT SOLUTION

Profiles at Time = 120 Sec. TEST "B"

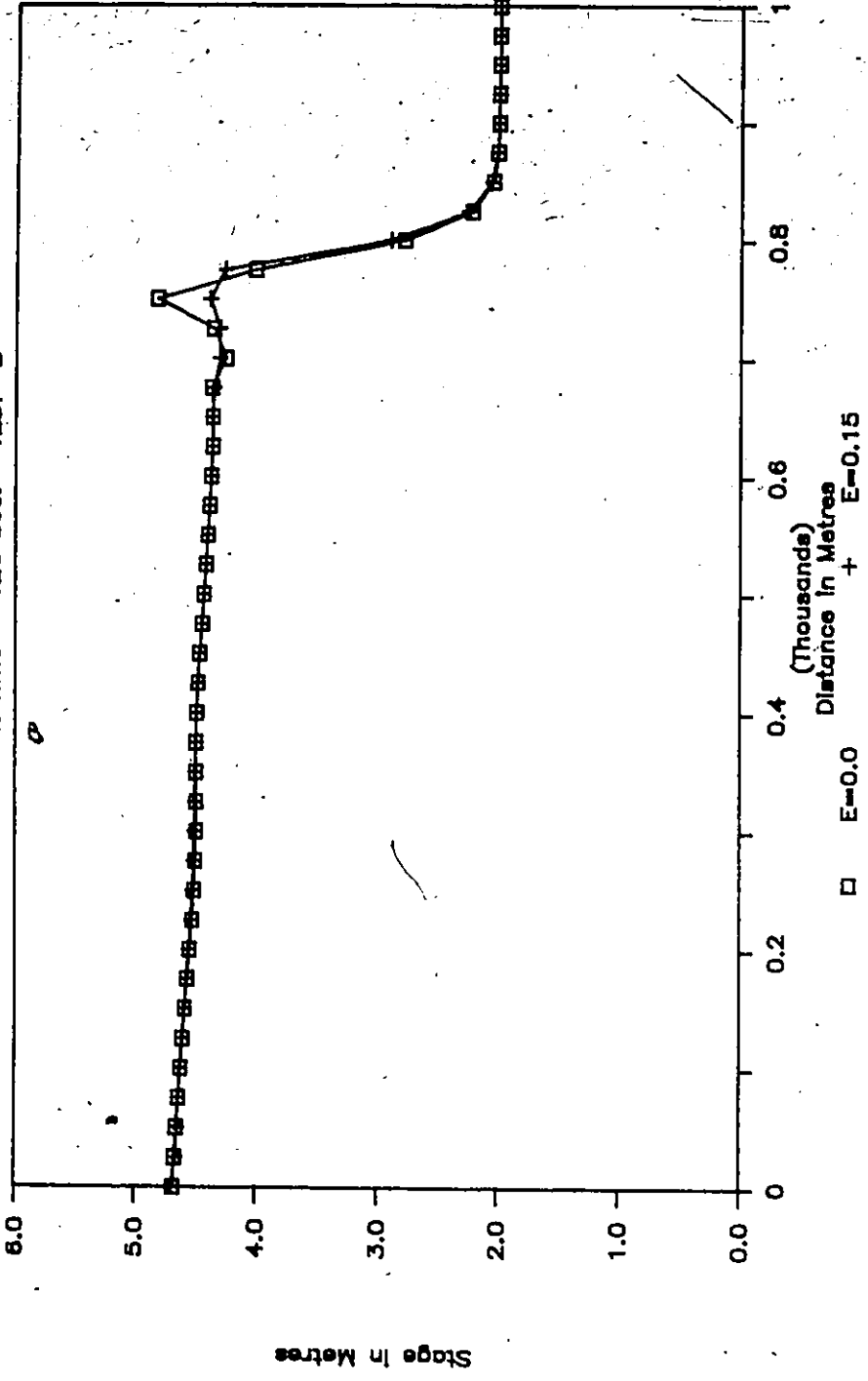


Fig. 5.33 Comparison of Basic Moving Element Method with Petrov-Galerkin Based Moving Element for Test 'B' - Dissipation Level, $\epsilon = 0.15$.

PETROV-GALERKIN MOVING ELEMENT SOLUTION

Profiles at Time = 120 Sec. TEST "B"

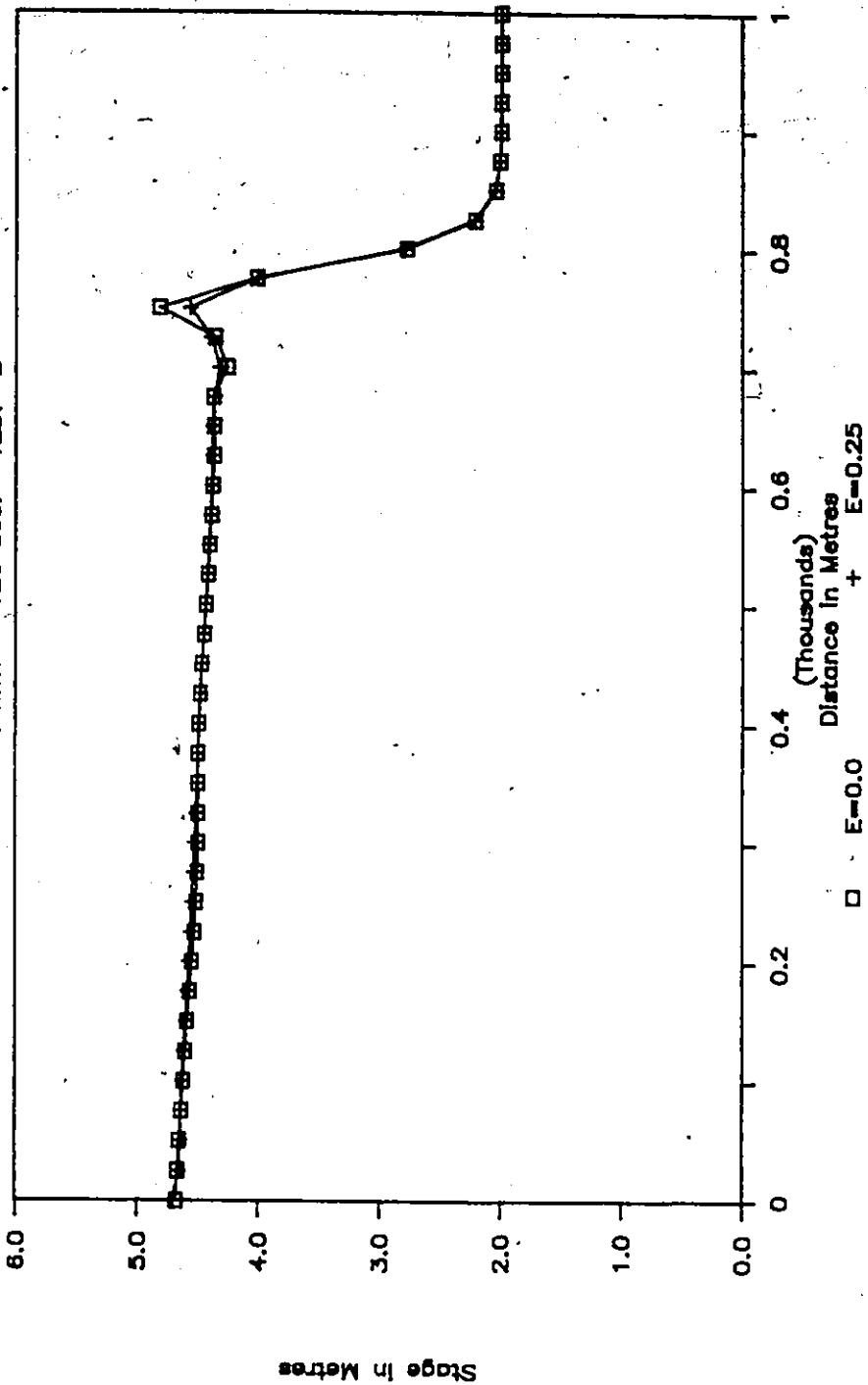


Fig. 5.34 Comparison of Basic Moving Element Method with Petrov-Galerkin Based Moving Element for Test 'B'. Dissipation Level, $\epsilon = 0.25$.

PETROV-GALERKIN MOVING ELEMENT SOLUTION

Profiles at Time = 120 Sec. TEST "B"

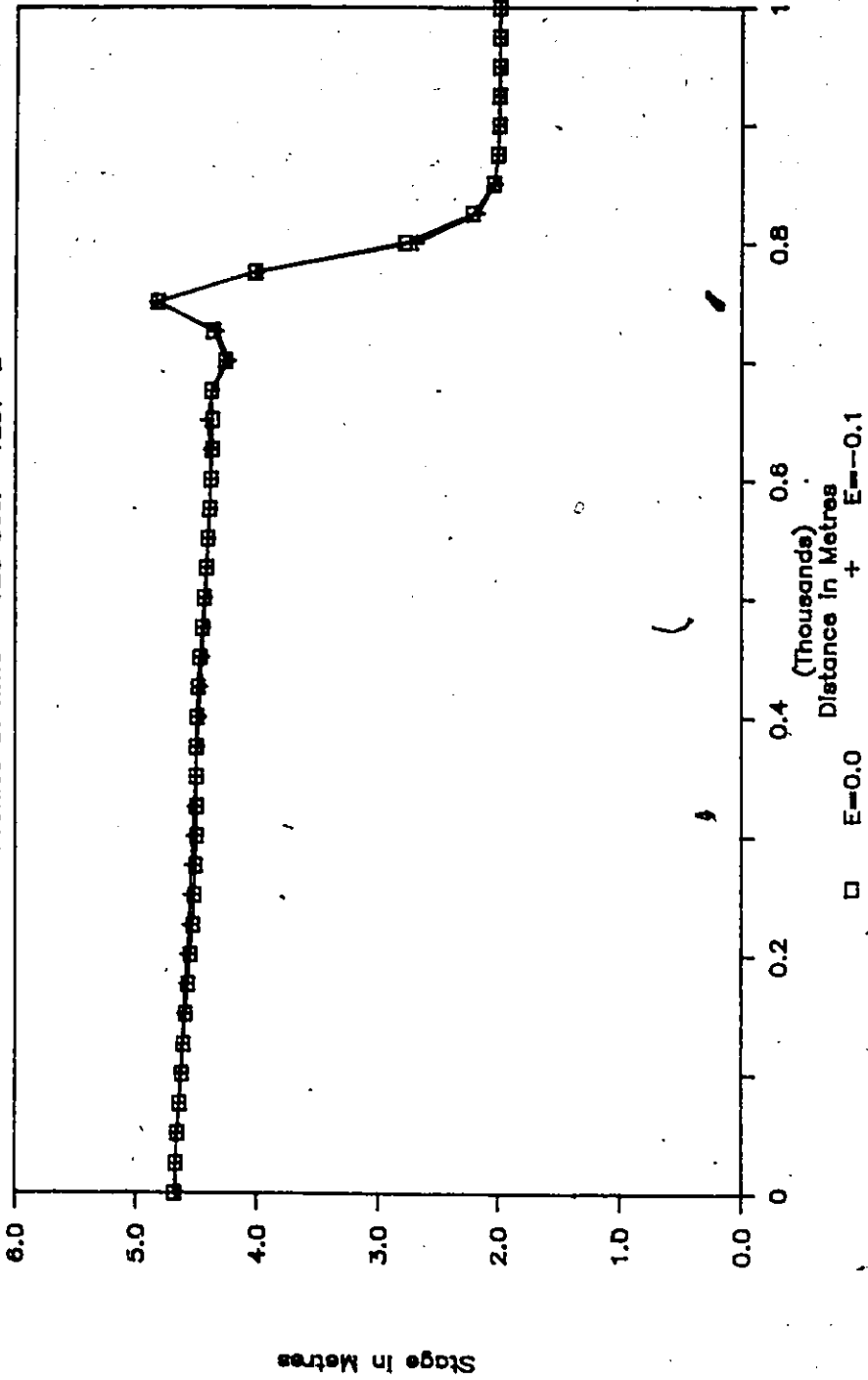


Fig. 5.35 Comparison of Basic Moving Element Method with Petrov-Galerkin Based Moving Element for Test 'B' - Dissipation Level, $\epsilon = -0.1$.

PETROV-GALERKIN MOVING ELEMENT SOLUTION

Profiles at Time = 120 Sec. TEST "B"

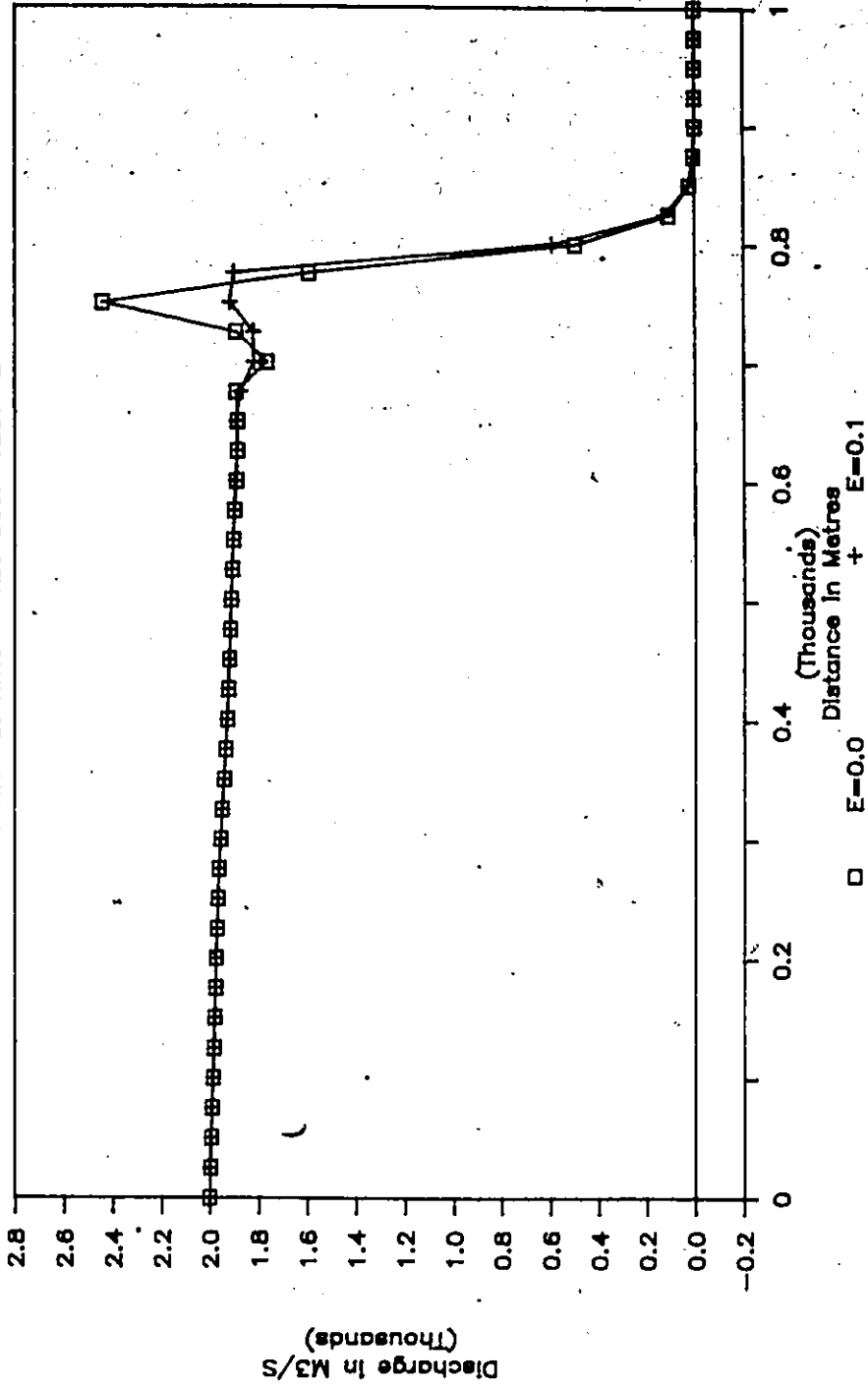


Fig. 5:36 Comparison of Basic Moving Element Method with Petrov-Galerkin Based Moving Element for Test 'B'. Flow Profiles for Dissipation Level, $\epsilon = 0.1$.

A limited amount of testing was carried out employing Test 'B' as the test case. The solution was next compared with the moving element scheme. For both the techniques, comparisons were made for the solutions obtained via the Eulerian-Lagrangian linked algorithm. The model parameters are listed in Table 5.9. The Petrov-Galerkin based method required a selective dissipation parameter which was varied.

The test results are shown in Figures 5.32 to 5.38. Figures 5.32 to 5.35 show the behaviour of the Petrov-Galerkin scheme by varying the dissipation parameter, depicted ' ϵ ' in the figures. A value of ϵ equal to zero corresponds to the basic moving element scheme. It is evident from these figures that a value of $\epsilon = 0.1$ and 0.15 provided the required resolution in reducing the size of the spike. The spike, however, reappears for a higher value of 0.25 , (Figure 5.34) whereas a negative value of -0.1 neither helps nor destroys the quality of results (Figure 5.35). A more dramatic feature of Petrov-Galerkin scheme is shown in Figure 5.36 where discharge profiles are plotted. The success of the scheme for a dissipation parameter of 0.1 is evident.

Figure 5.37 presents the stage profiles for a steeper wave front. Here the improvement over the basic method is marginal at best. An exploded window shows the relative improvement provided by the Petrov-Galerkin scheme. The maintenance of discontinuity with a sharp front is evident (Fig. 5.38).

It is seen that the Petrov-Galerkin scheme provides for marginal improvements near the face of discontinuity as most of the oscillations are removed by the basic moving element method. The price for reducing this irritant is the loss of a degree of freedom for evaluation. Katopodes (1984), showed the improvements for frictionless cases. The interrelation of the dissipation parameter with channel rough-

PETROV-GALERKIN MOVING ELEMENT SOLUTION

Profiles at Time = 120 Sec. TEST "B1"

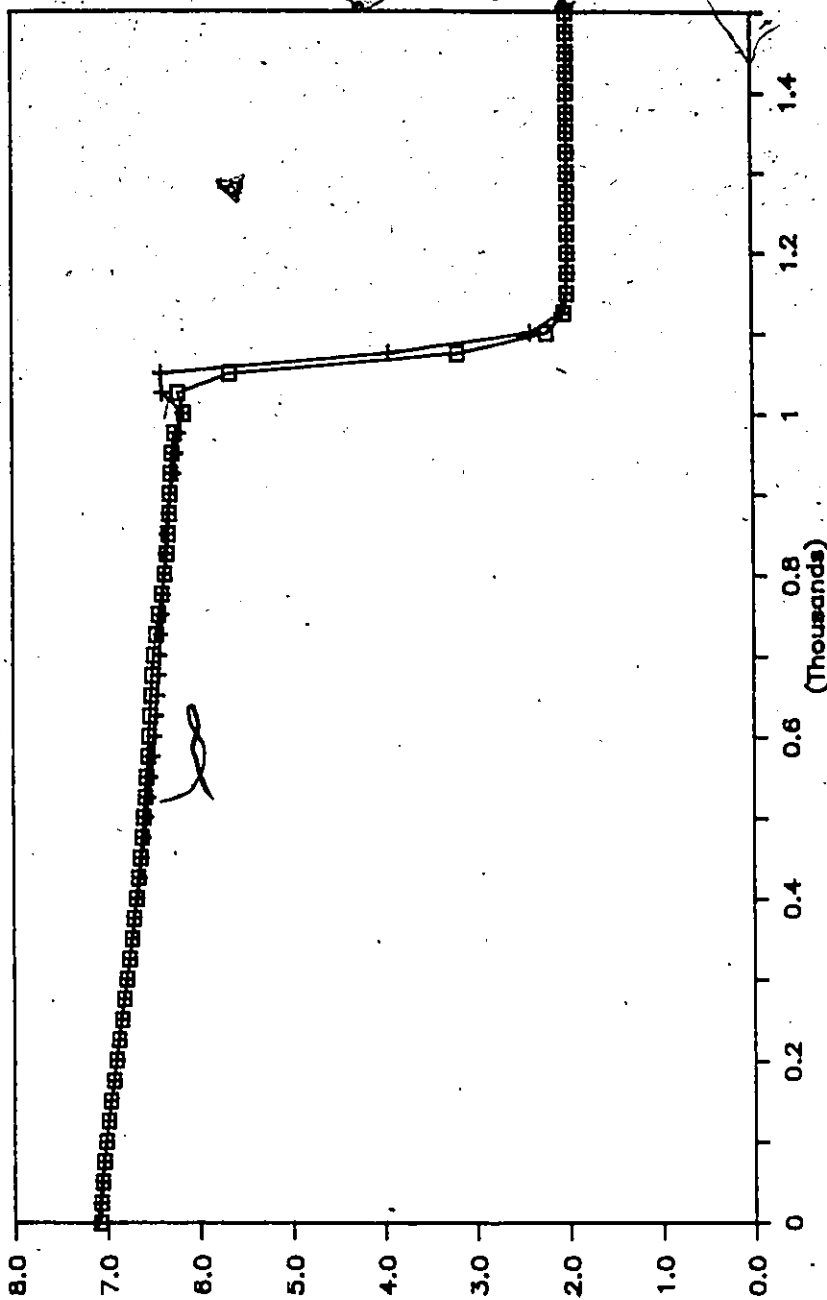


Fig. 5.37 Comparison of Basic Moving Element Method with Petrov-Galerkin Based Moving Element for Test 'B' - Stage Profiles for Dissipation Level, $\epsilon = 0.1$ and Temporal Acceleration at U/S Boundary of $162.67 \text{ m}^3/\text{s}$.

Stage in Metres

Distance in Metres (Thousands)

□ E=0.0

— E=0.10

PETROV-GALERKIN MOVING ELEMENT SOLUTION

Profiles at Time = 120 Sec. TEST "B"

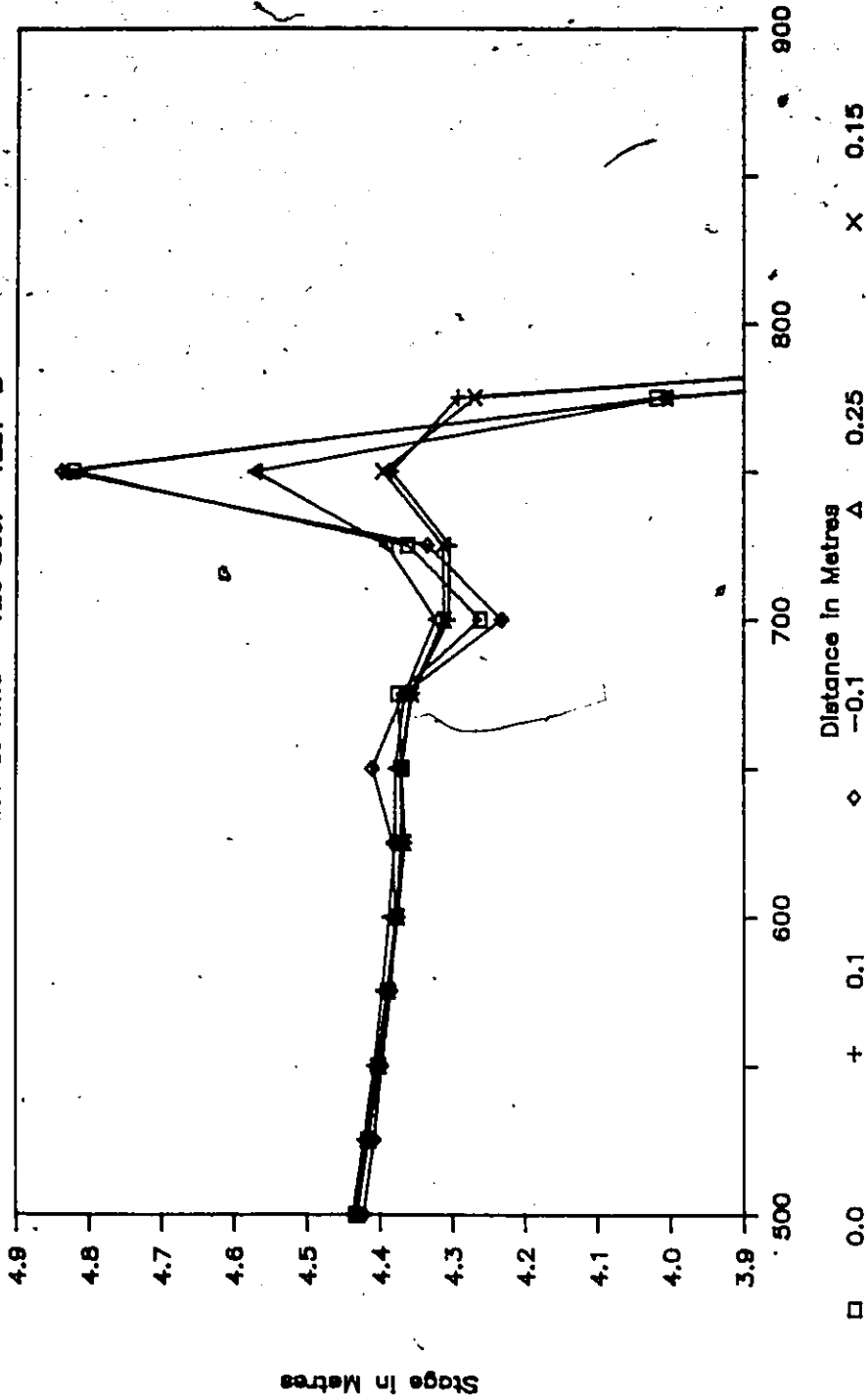


Fig. 5.38 Exploded Window with Exaggerated Vertical Scale for Controlling Spikes in 5.32 to 5.35.

ness is not well known or fully understood. Until the limited testing carried out here is supplemented with exhaustive evaluation along with a procedure to establish the dissipation parameter, no verdict can be passed concerning the Petrov-Galerkin scheme.

It should be noted that the Petrov-Galerkin scheme is driven by the moving element method. Similar techniques in the Eulerian frame of reference yield a smooth but dissipative surface.

5.4.5 Lagrangian Based Method

When the research for this study was initiated, it was conceived that a Lagrangian based space-time finite element scheme might overcome the problems of oscillatory solutions. The final configuration of the Lagrangian scheme, however, remained non-dissipative in nature. The situation was exacerbated by extremely high aspect ratios of the elements, especially near the discontinuity. The problem was rectified by resorting to an Eulerian-Lagrangian scheme with a natural non-dissipative interface.

The Lagrangian based method still provides excellent results for situations where the initial conditions permit finite velocities that would allow maintenance of adequate element aspect ratios. It was also found, as will be described in this section, that by advancing the temporal weighting parameter for situations with a horizontal bed, no friction and zero flow initial condition, it is possible to employ the Lagrangian model with no restriction.

TABLE 5.10
 Comparison of Eulerian - Lagrangian Method with Lagrangian Method

Name of Numerical Experiment Solution	Type of Numerical Solution	Element Length (delx)	Time Step (delt)	Temporal Weighting Parameter (Theta)	Spatial Weighting Parameter (Beta)	Manning's Channel Roughness (n)	Temporal Accel. at U/S Boundary (dQ/dt)
** Test 'B'	Eulerian - Lagrangian	10.00	1.00	0.50	1.00	0.0000	2000.00
Test 'B'	Lagrangian	10.00	1.00	0.50	1.00	0.0000	2000.00
Test 'B'	Lagrangian	10.00	1.00	0.60	1.00	0.0000	2000.00
Test 'B'	Lagrangian	10.00	1.00	0.75	1.00	0.0000	2000.00
Test 'B'	Lagrangian	10.00	1.00	1.00	1.00	0.0000	2000.00
Test 'B'	Eulerian - Lagrangian	10.00	1.25	0.50	1.00	0.0000	2000.00
Test 'B'	Eulerian - Lagrangian	10.00	1.33	0.50	1.00	0.0000	2000.00
** Test 'D'	Lagrangian	528.00	30.00	0.50	1.00	0.0200	0.97
Test 'D'	Lagrangian	528.00	60.00	0.50	1.00	0.0200	0.97
Test 'D'	Lagrangian	528.00	120.00	0.50	1.00	0.0200	0.97
Test 'D'	Lagrangian	528.00	300.00	0.50	1.00	0.0200	0.97
Test 'D'	Lagrangian	528.00	600.00	0.50	1.00	0.0150	0.97

COMPARISON OF MOVING ELEMENT METHODS

Profiles at Time = 60 Sec. TEST 'B'

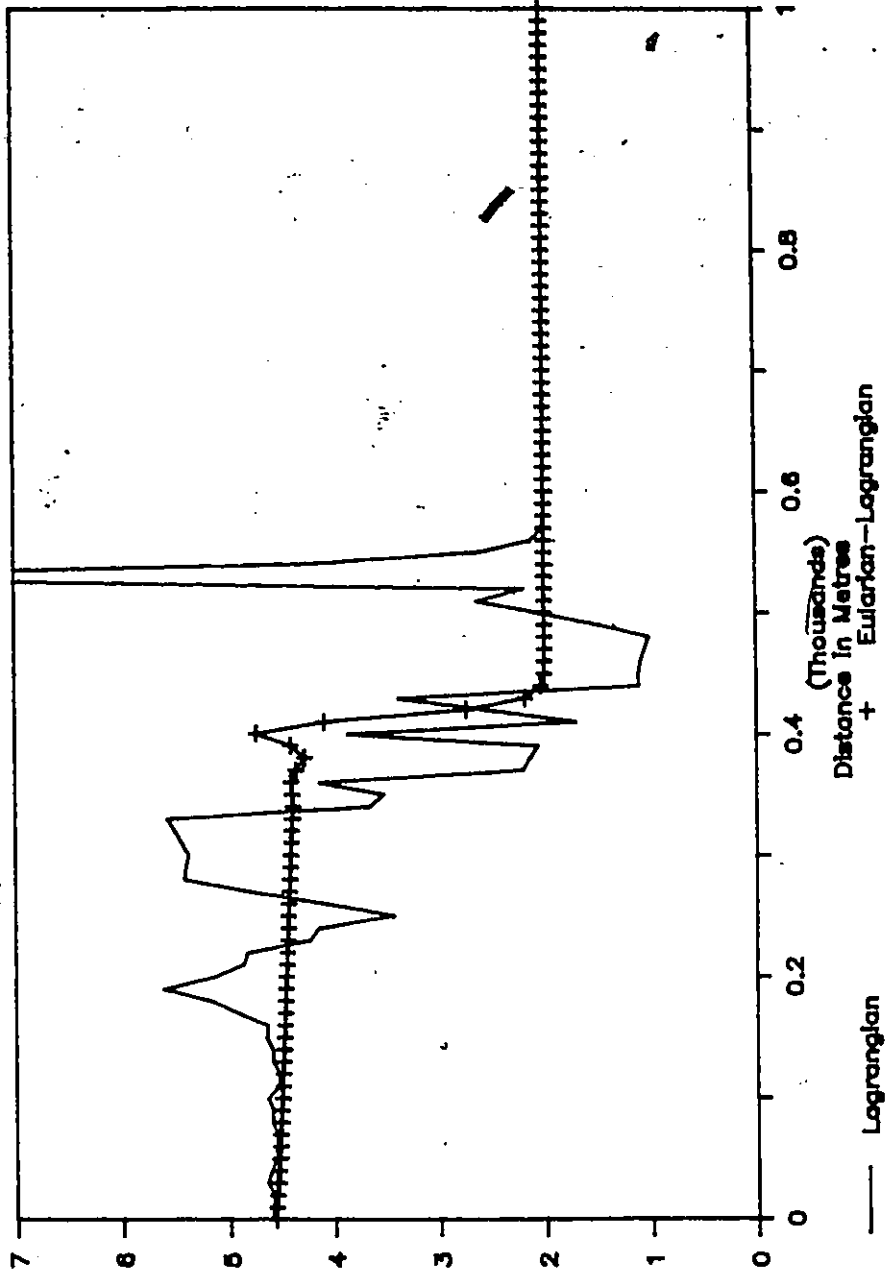


Fig. 5.39 Comparison of Eulerian - Lagrangian Linked Algorithm with Lagrangian Solution for Test 'B'. Temporal Weighting Factor = 0.5.

Stage in Metres

Distance in Metres (Thousands)

— Lagrangian

+ Eulerian-Lagrangian

To evaluate the behaviour of the Lagrangian moving element scheme two experiments were setup for Tests 'B' and 'D'. The parameters used in these experiments are noted in Table 5.10.

Test 'B' - This test was carried out on a finer grid size of 10 m element length and 1.0 second time step. The basic comparison at a temporal weighting of 0.5 is presented in Figure 5.39 for the Lagrangian and Eulerian-Lagrangian moving element schemes. It is clear from this comparison, that the Lagrangian solution is destroyed and no meaningful information can be deduced. Further, if the computations are continued, the computations are terminated when non-sensical negative depths are calculated. In comparison, the Eulerian-Lagrangian model exhibits an acceptable solution albeit with the spike.

As a next step, the temporal weighting parameter was varied. The advancement of this parameter paid immediate dividends and acceptable wave capturing properties resulted. Four different weighting parameters 0.5, 0.6, 0.75 and 1.0 were employed and plotted in Figure 5.40. The non-dissipative oscillations are still present for 0.6 while these are completely eliminated for 1.0. The profiles show sharpness for a value up to 0.75, whereas, dispersion of the wave front was in evidence for a value of 1.0. The mass was completely conserved for 0.5 while very small errors of less than 0.2% were noted, which increased with the advancement of the weighting parameter.

Finally, a comparison was made between the Lagrangian model at a temporal weighting of 0.75 and the Eulerian-Lagrangian model for the centred weighting. The results are provided in Figure 5.41 at 60 seconds and 120 seconds. This comparison clearly demonstrates the validity of employing the Lagrangian model with an advanced temporal weighting. Another improvement over the

THETA VARIATION SENSITIVITY ANALYSIS

Profiles at Time = 60 Sec. TEST 'B'

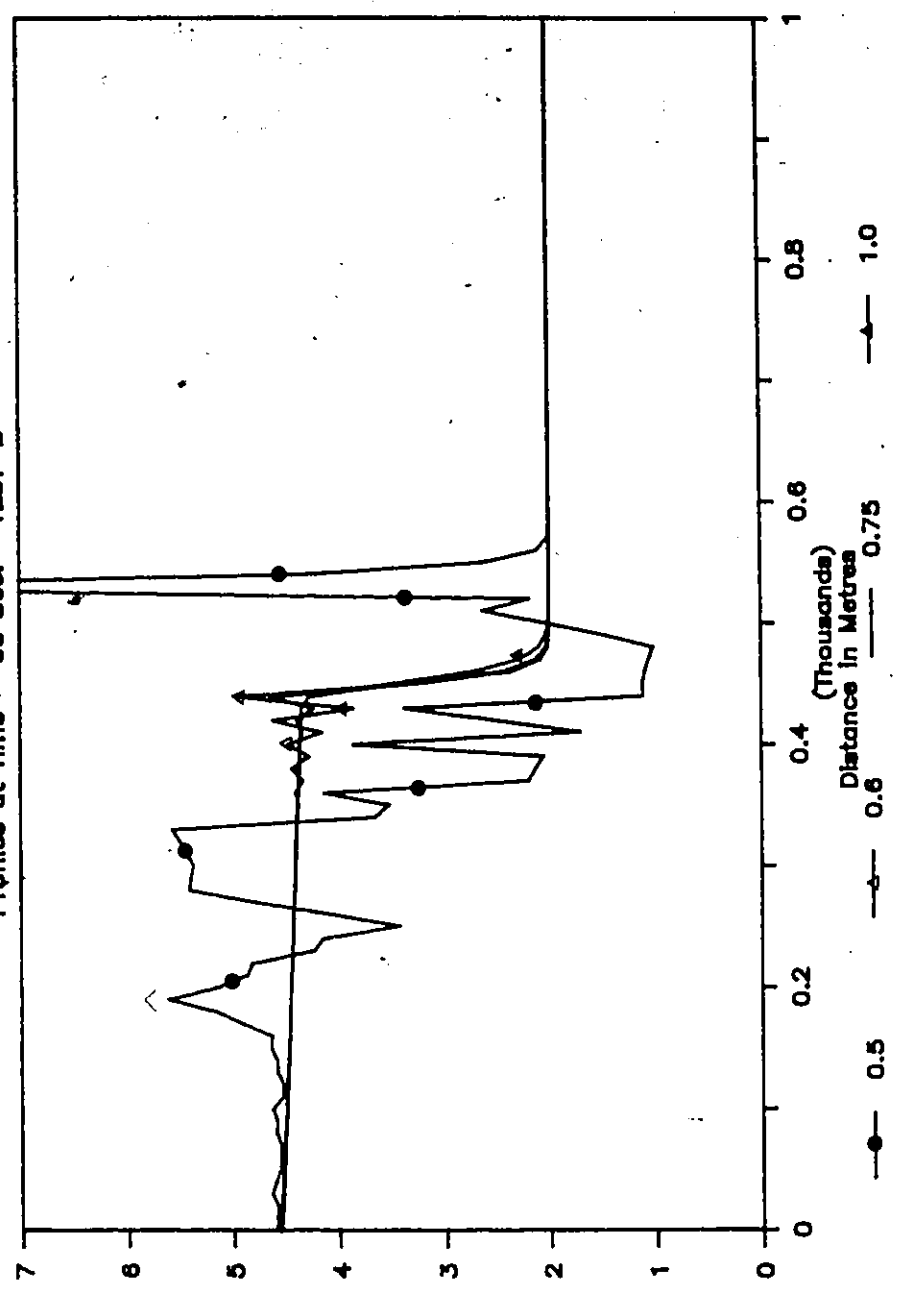


Fig. 5.40 Influence of Temporal Weighting Parameter on Lagrangian Solution for Test 'B'.

Stage In Metres

COMPARISON OF MOVING ELEMENT METHODS

Profiles at 60 & 120 Sec. TEST 'B'

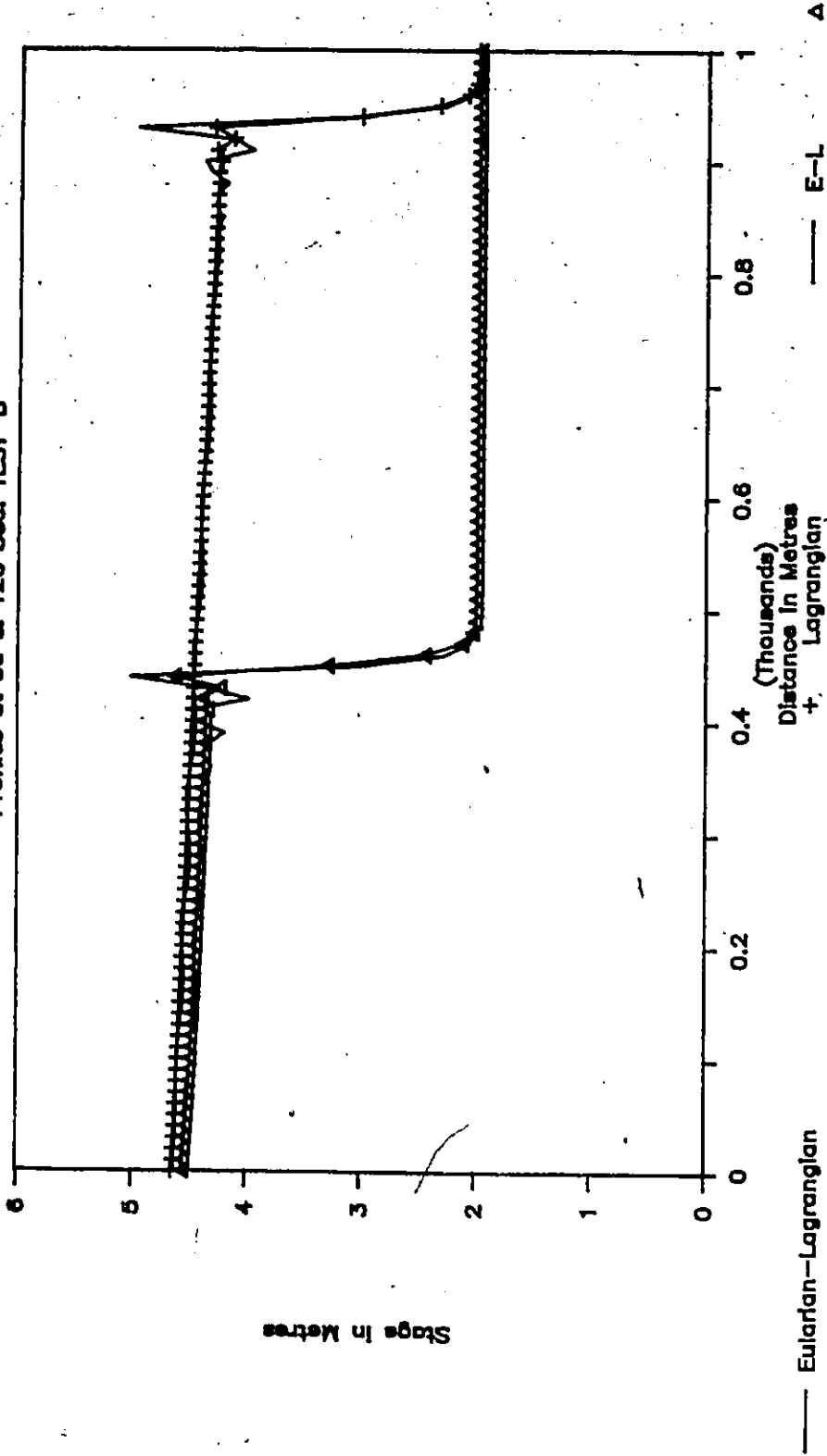


Fig. 5.41 Comparison of Eulerian - Lagrangian Linked Algorithm with Lagrangian Solution for Test 'B' - Temporal Weighting Factor = 0.75.

Eularian-Lagrangian model was the size of spike at the nose became almost non-existent. The front for the Lagrangian model was as sharp as the other while maintaining a smaller mass conservation error.

Further controlled testing may establish this as an alternate to the Eularian-Lagrangian model.

Test 'D' - When a finite initial velocity is present, as will most likely be the case in natural situations the Lagrangian model can be employed for much higher Courant numbers even with a centred weighting parameter. The problem presented by Viesmann et al. and portrayed as Test 'D' was solved using time steps of 30, 60, 120, 300 and 600 seconds. These are much higher than the time step of 2.0 sec. used by Viesmann et al (1973) as restricted by the Courant-Lewy-Feidrichs' condition.

Initially, the element size was kept at 528 ft. By its very nature, the model generates its own grid size at future time steps. The contrast is dramatic, for example with a time step of 30 seconds, the grid size varies between 210 and 310 feet at initial flow and peak flow rates respectively, while with a time step of 600 seconds the element size varied from 4100 ft to 6000 ft for initial and peak flow rates.

The results shown in Figures 5.42 to 5.45 bears testimony to the robustness of the technique. The hydrographs at the downstream boundary demonstrates a slightly erratic behaviour. The reason for this is obvious. The downstream condition imposed was a single value rating curve. Such a requirement forces the model to simultaneously satisfy the full momentum equation and uniform flow condition for the boundary node. The comparative solutions with the 2.0 second time step are not plotted as these are the same as the one with the moving element solution.

Simulation in Lagrangian Mode

Time_step=30 s. Theta=0.5

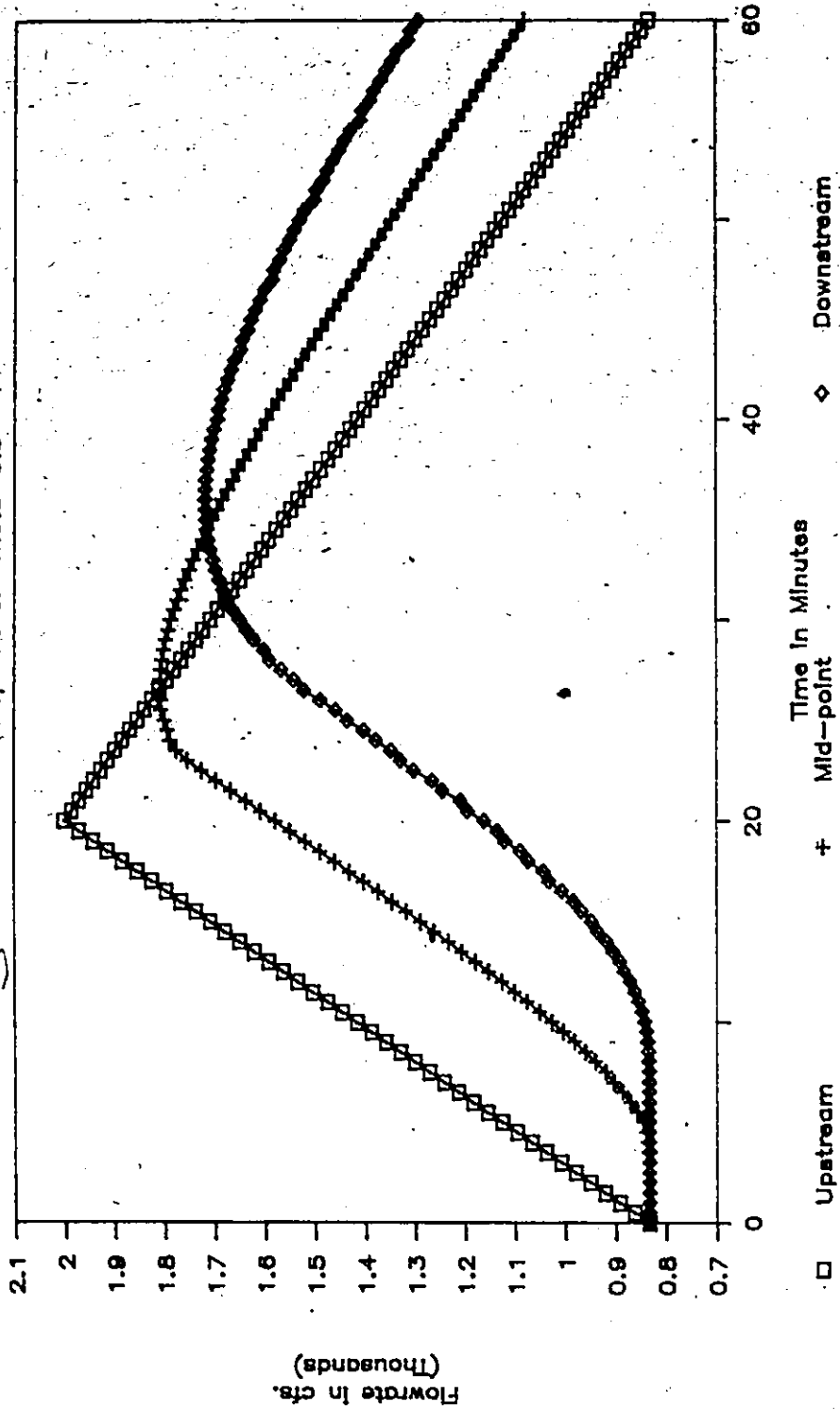


Fig. 5.42 Lagrangian Mode Solution of Test 'D'; Time Step = 30 Sec.

Simulation in Lagrangian Mode

Time-steps of 60 & 600 s, Theta=0.5

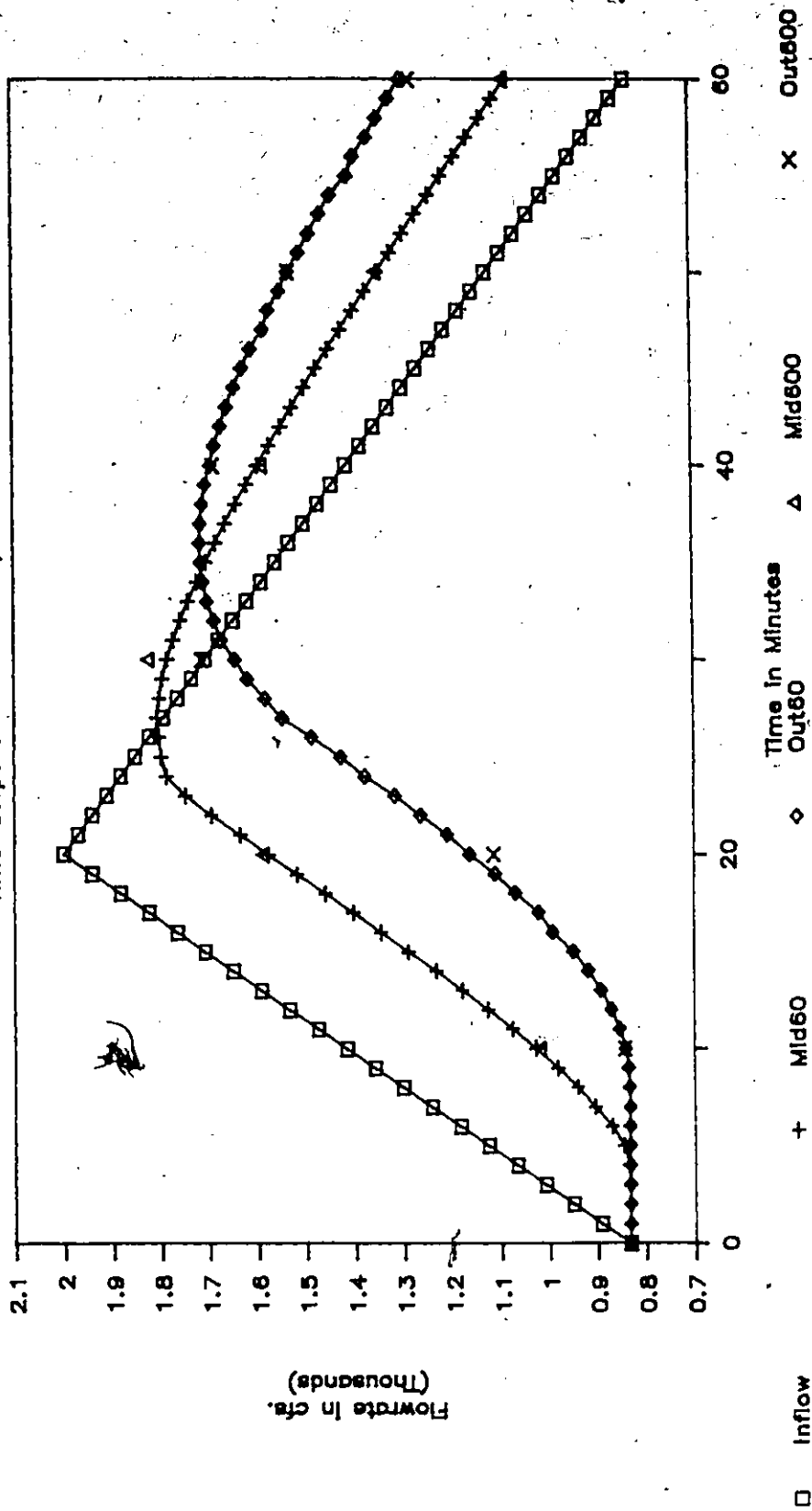


Fig. 5.43 Lagrangian Mode Solution of Test 'D' - Time Step = 60 and 600 Sec.

Hydrographs for Lagrangian Mode

Time step=120 s. Theta=0.5

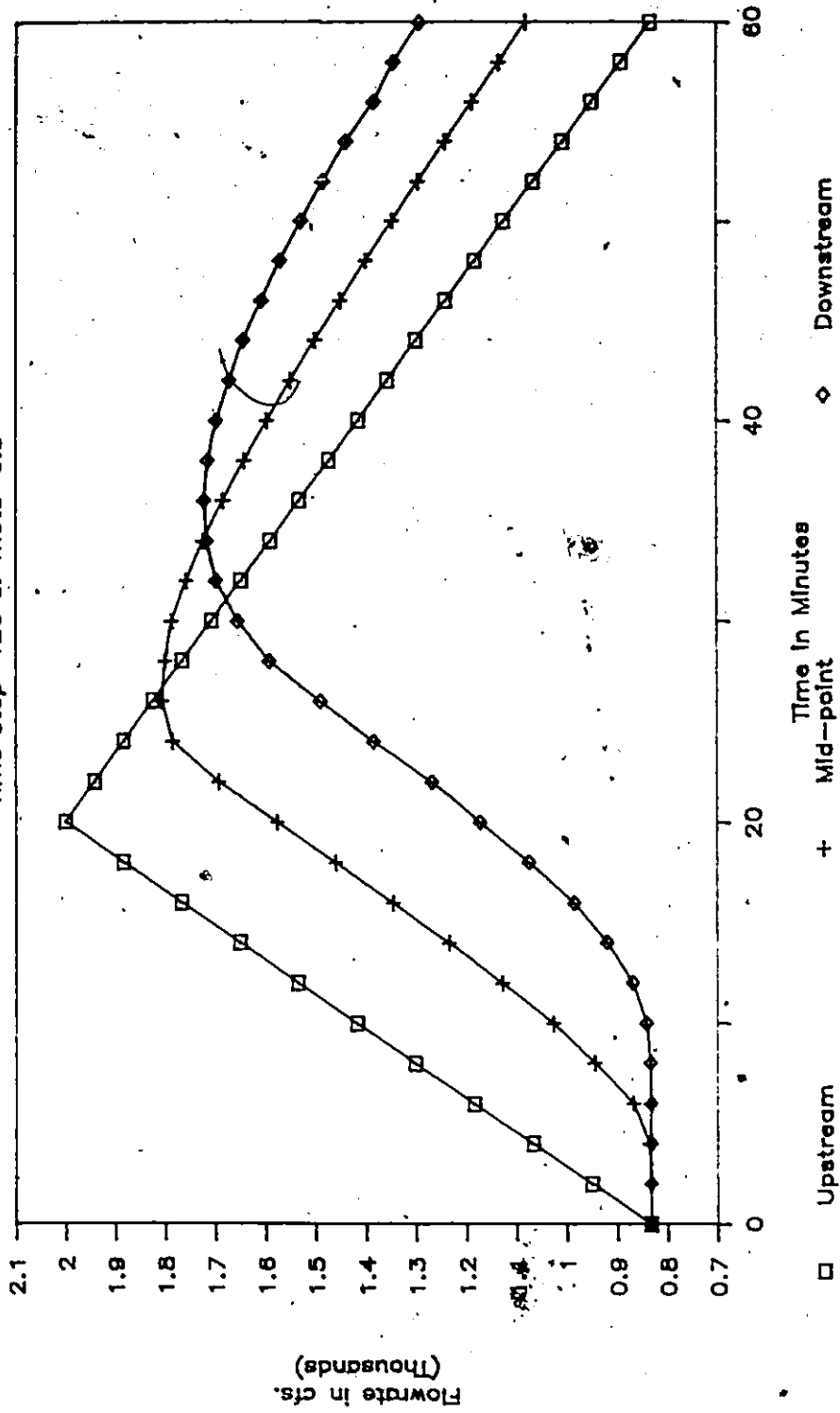


Fig. 5.44 Lagrangian Mode Solution of Test 'D' - Time Step = 120 Sec.

Simulation in Lagrangian Mode

Time step 300 • Theta=0.5

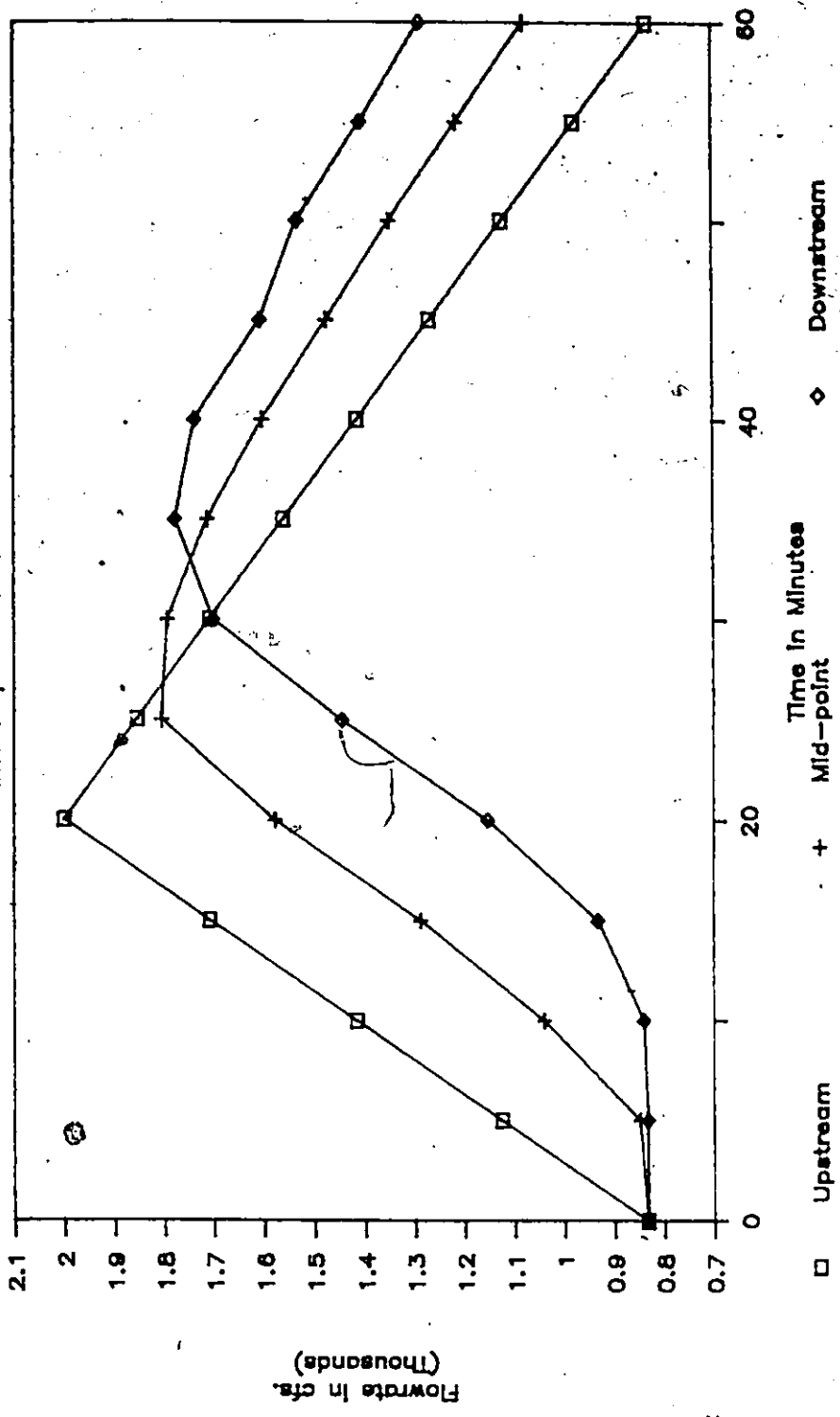


Fig. 5.45 Lagrangian Mode Solution of Test 'D' - Time Step = 300 Sec.

5.4.6 Summary of Comparisons:

In the previous sections, the superiority of the moving element model was evident when the numerical scheme was compared with established techniques like the finite difference and finite element methods. Furthermore, limited evaluation of other moving element based schemes like the pure Lagrangian mode model and the Petrov-Galerkin based model exhibited much promise. More testing is, however, required before drawing definite conclusions. A summary of the comparisons is presented in Table 5.11.

5.5 Tests on Non-prismatic Channels

One of the primary objectives in developing any fully dynamic model, such as the one proposed here, is its capability of handling a variety of scenarios. These may include but not be limited to addressing continuous and near discontinuous flows, prismatic and non-prismatic or natural channel boundaries, etc. Before studying non-prismatic channels in natural settings, controlled numerical experiments were carried out. These experiments were aimed at studying the impact of roughness, degree of non-linearity, etc.

In this section, two different types of non-prismatic channels were studied namely a diverging channel and a converging channel section. For the converging channel, the rectangular section reduced from 200 m wide to 100 m in a distance of 1000 m, while it was the opposite for the diverging channel. The channel bed is horizontal and a Manning's roughness of 0.02 is assumed. The downstream boundary consist of a single value rating curve. The initial flow conditions were a depth of flow of 2.0 m and zero flow rate. At the upstream boundary the flow was forced to increase from zero to 2000 m³/s in 30 seconds. The flow was then held at that rate for the

Table 5.11

**Comparison of Moving Element Method
with Other Numerical Techniques**

Performance Indicator	Other Techniques	Moving Element Method
Shape of Surge	FD: Oscillatory solution varies +37% to -73% of Analytical solution. FE: Oscillatory solution varies +28% to -40%. Lag: Oscillations for $\theta = 0.5$, smooth solution for $\theta > 0.6$. PG: Same as for ME for $\epsilon = 0.0$, spike removed for $\epsilon = 0.15$.	No oscillations except for spike. Surge height within 1% for supercritical flow and 0.2% for subcritical.
Location and speed	FD and FE: Advanced when compared with analytical. Advanced for $\theta = 0.5$ and exact for $\theta > 0.6$. PG: Same as for ME.	Location exact with optimal time step. Trails the analytical solution for other time steps. Correct speed predicted.
Mass conservation	FD, FE and Lag: Mass exactly conserved. PG: Same as ME.	Mass conserved to within 0.1% for optimal time step.
Direction of front	FD and FE: No difference in solution. Lag: Handled downstream moving surge better than upstream moving. PG: Not tested.	Downstream moving surge handled better than upstream moving for $\theta = 0.5$ and same for $\theta > 0.6$.

FD = Finite Difference Method, FE = Finite Element Method
 ME = Moving Element Method, Lag = Lagrangian based ME Method
 PG = ME based Petrov-Galerkin Method
 θ = Temporal weighting factor

duration of experiment. The profiles were captured at 120 seconds. The two non prismatic channel cases are discussed separately below.

5.5.1 Diverging Channel

As a first step, the model was set for a frictionless case and the two profiles are plotted in Figure 5.46. The behaviour of the two profiles are normal even for an abnormally high non prismatic form (the rate of change of width is 0.1 m/m). As expected, even for the frictionless case the height of surge continues to fall to accommodate the expanding cross-section. The velocity at the tip of the surge is significantly less than at upstream boundary and again this is to be expected.

Next, the sensitivity of the surge to the degree of non-prismatic form was investigated. The initial and boundary conditions remained the same. The width at the downstream boundary was varied from 100 m (that is, the prismatic form) to 200 m in steps of 25 m. The stage and floor profiles for the five relative degrees of non prismatic form are plotted in Figures 5.47 and 5.48 respectively.

The stage profiles exhibit the phenomenon as expected viz, the front in the prismatic channel (corresponding to 0% difference in upstream and downstream width) is most advanced while it is retarded for a 100% change in width. The flow profiles, however, indicate an interesting feature. The flow reduces slightly for the prismatic form to accommodate channel roughness of 0.02 from node to node. When compared to the flow profile for the highly non-prismatic channel (corresponding to 100% width change), the flow remains at 2000 m³/s as if there is no channel resistance. In other words, the flow conditions behind the front for a prismatic channel with no friction are approximated by a non-prismatic channel with a

NON-PRISMATIC CHANNEL ROUTING

Profiles at Time = 120 Sec. TEST "F"

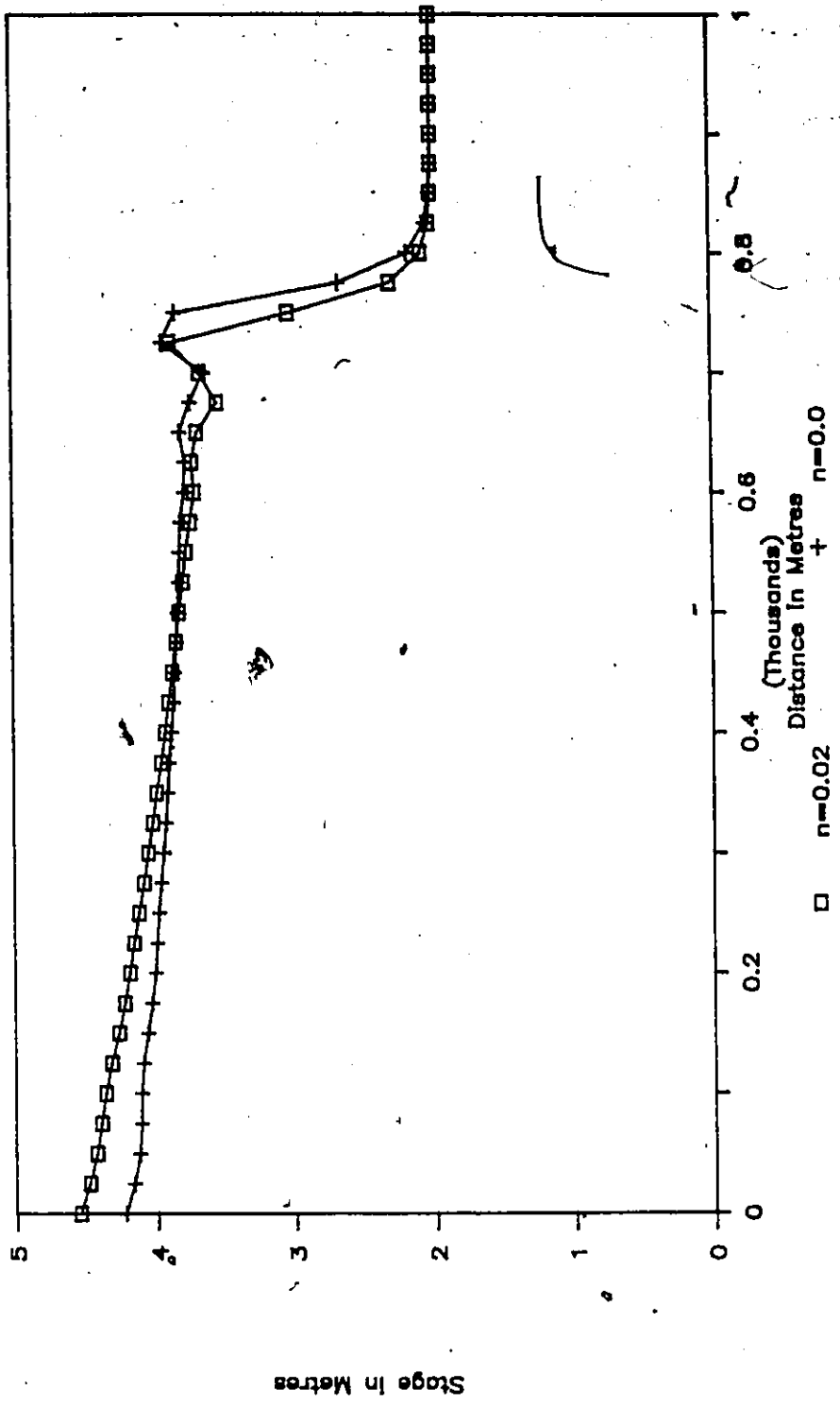


Fig. 5.46 Surge Movement in Non-Prismatic Diverging Channel - Influence of Channel Roughness.

roughness of 0.02. It appears the channel expansion has an opposite effect to that of channel roughness.

5.5.2 Converging Channel

The same computer runs were made with the converging channel as for the diverging channel. Figure 5.49 presents the results when a comparison is made between no channel resistance and a friction of 0.02. In this figure, the stage profile for frictionless case gradually builds up head to forge ahead in a converging channel while for the case with friction, the surface is almost horizontal. Again, like the previous analysis, this experiment provides some interesting insights in the mechanics of this solution algorithm.

If the total energies (both potential and kinetic) at two points, say the upstream boundary and a point behind the surge front, are compared, then the energy at the downstream point will be greater than the upstream point. This appears to be an abnormal behaviour. There is, however, a very logical explanation. The basic equation that is being solved guarantees conservation of mass and momentum, while energy is not conserved. The energy travels moving towards the tip of the near discontinuity and is expended across the surge. In retrospect, the presence of the spike behind the front could be explained through this logic.

As in the case of the diverging channel the sensitivity of the surge to channel width variation was carried out. In this case, the channel width at the downstream boundary was fixed at 100 m, while the upstream was varied between 200 m (100% wider) to 100 m (0% wider, prismatic channel) with steps of 25 m. The stage and flow profiles are shown in Figures 5.50 and 5.51. The degrees of choking provided by the converging channels are reflected in the relative advancement of the

WIDTH VARIATION SENSITIVITY ANALYSIS

Profiles at Time = 120 Sec. TEST "F"

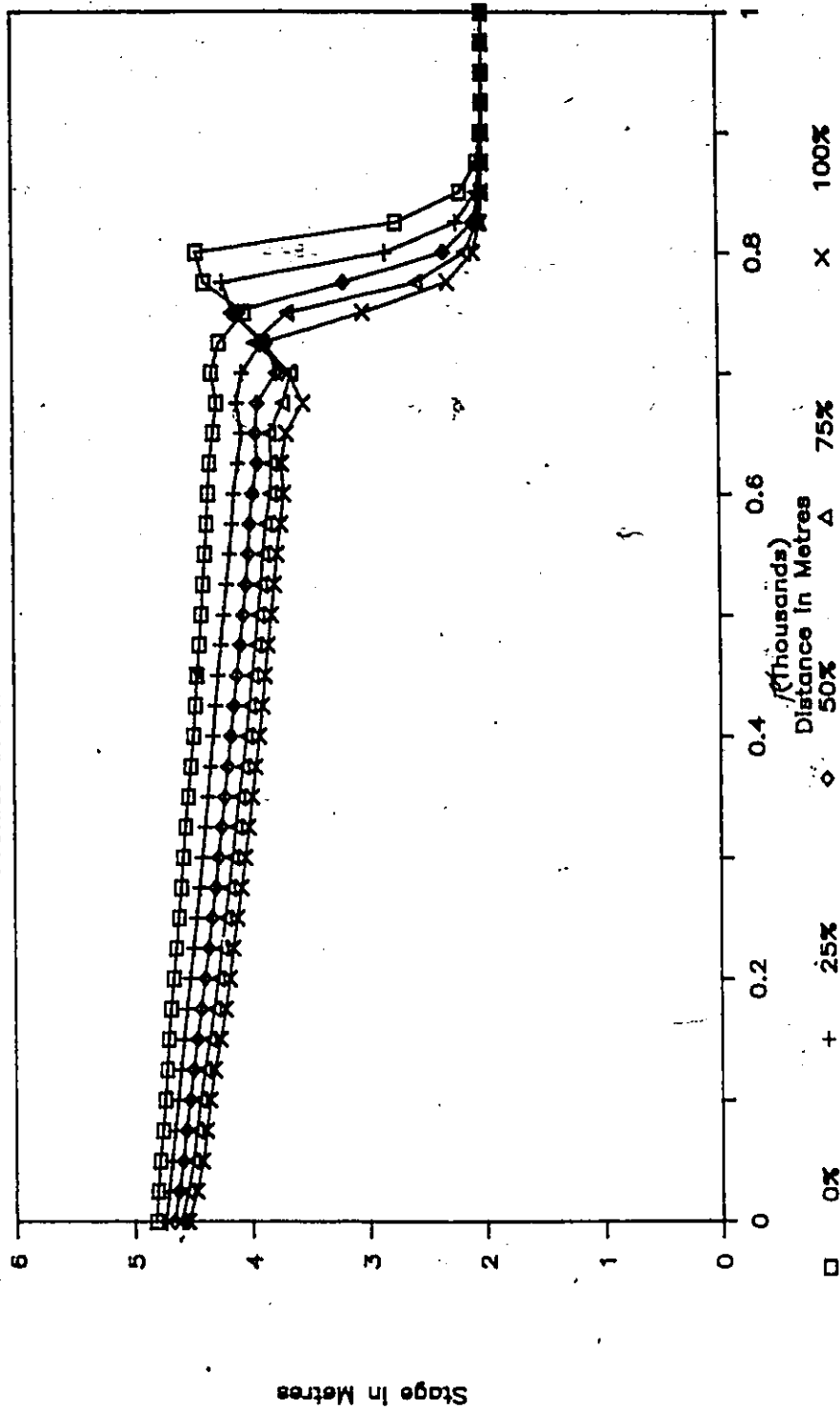


Fig. 5.47 Stage Profile Sensitivity for Degree of Non-Prismatic Channel Form - Diverging Channels.

WIDTH VARIATION SENSITIVITY ANALYSIS

Profiles at Time = 120 Sec. TEST "F"

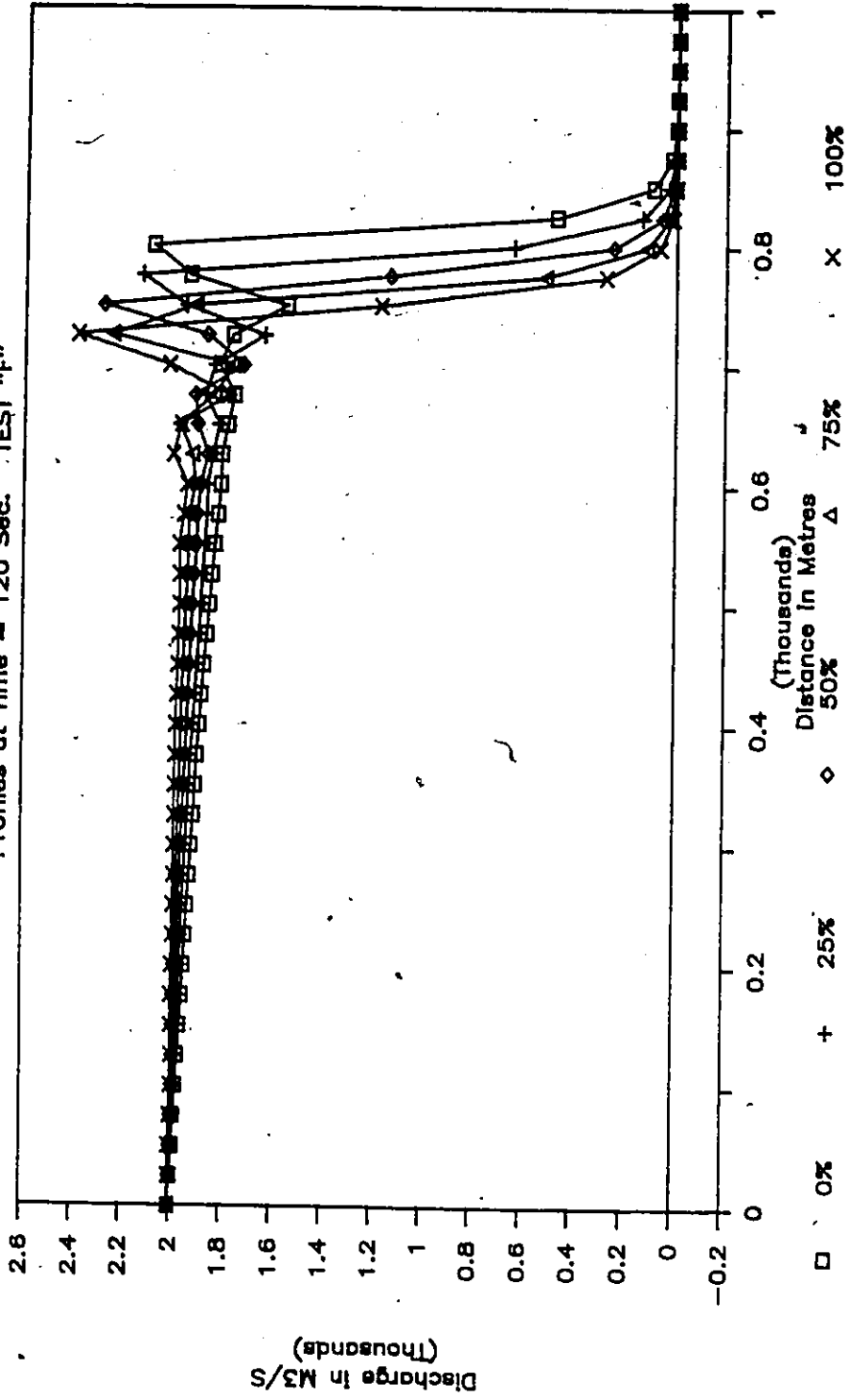


Fig. 5.48 Flow Profile Sensitivity for Degree of Non-Prismatic Channel Form - Diverging Channels.

NON-PRISMATIC CHANNEL ROUTING

Profiles at Time = 120 Sec. TEST "G"

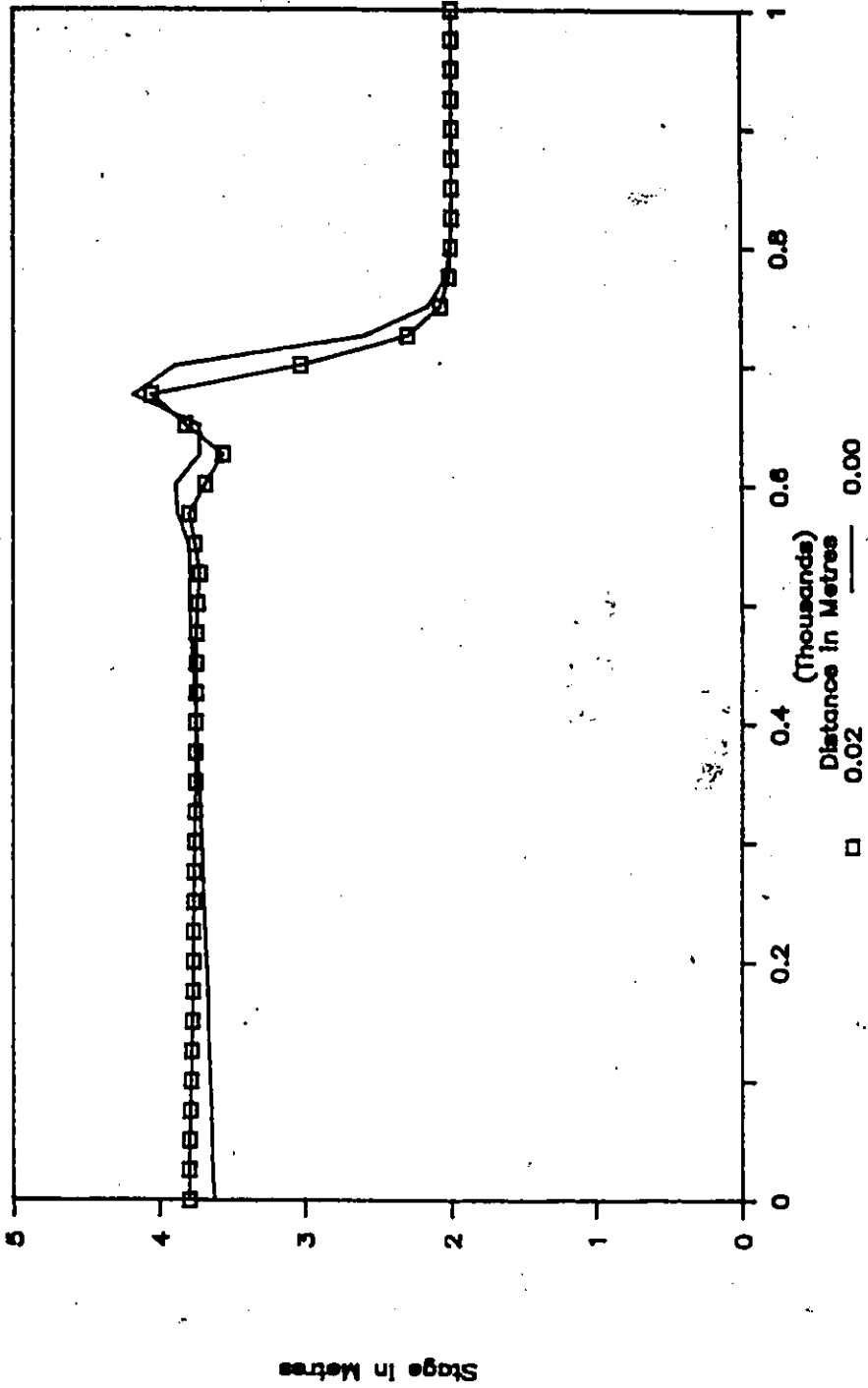


Fig. 5.49 Surge Movement in Non-Prismatic Converging Channel - Influence of Channel Roughness.

WIDTH VARIATION SENSITIVITY ANALYSIS

Profiles at Time = 120 Sec. TEST "G"

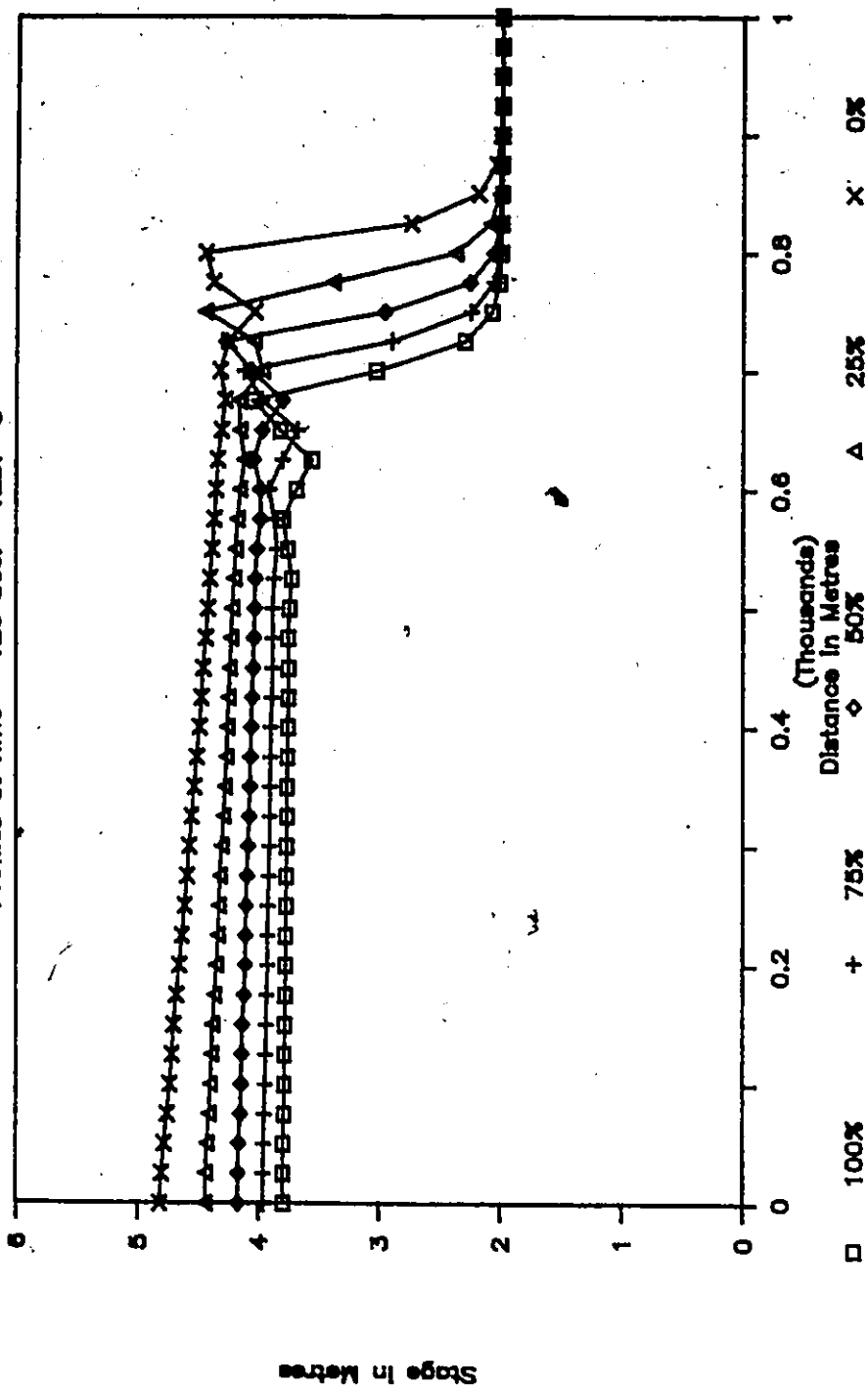


Fig. 5.50 Stage Profile Sensitivity for Degree of Non-Prismatic Channel Form - Converging Channels.

WIDTH VARIATION SENSITIVITY ANALYSIS

Profiles at Time = 120 Sec. TEST "G"

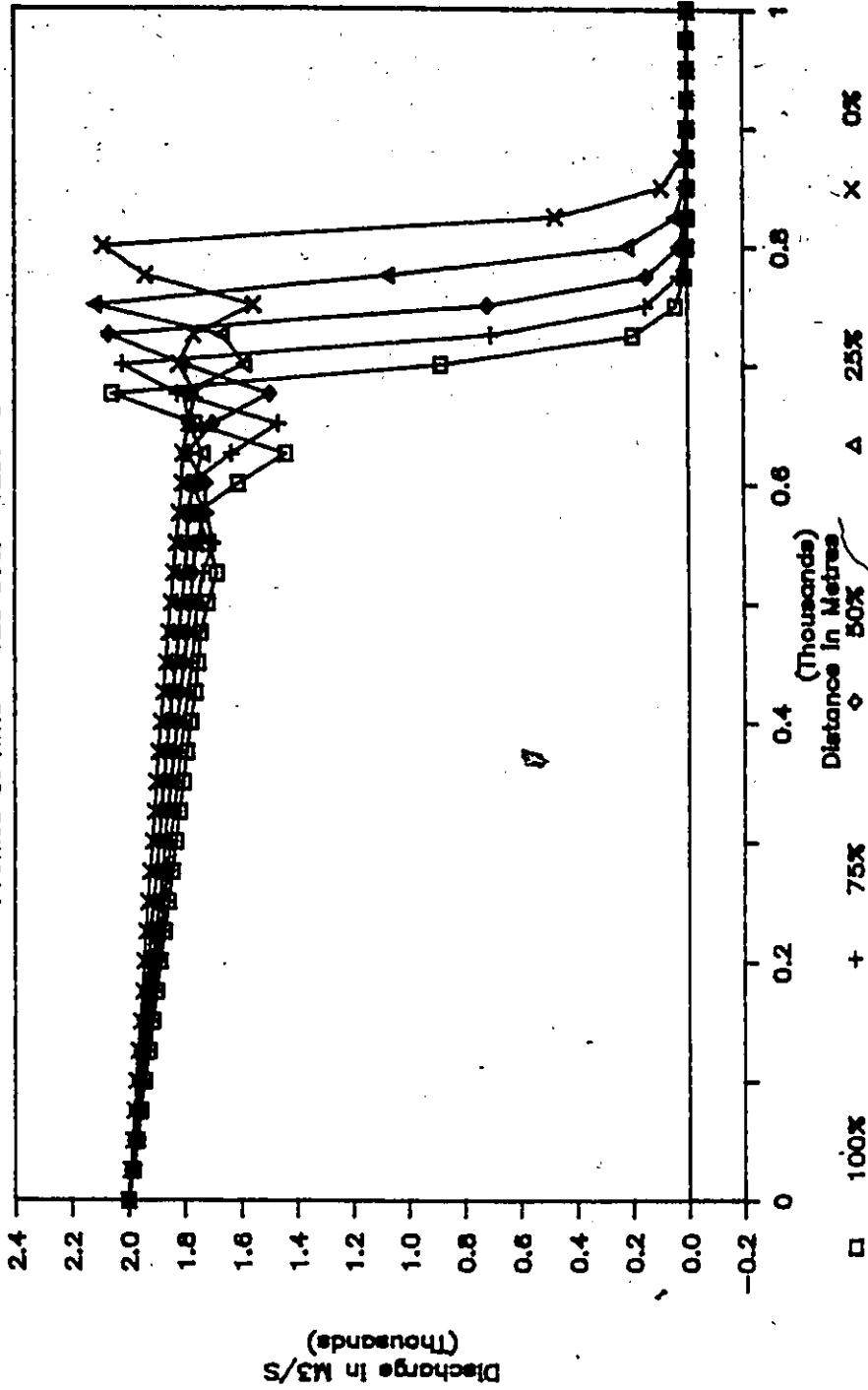


Fig. 5.51 Flow Profile Sensitivity for Degree of Non-Prismatic Channel Form - Converging Channels.

wave fronts. For example, the surge in prismatic channels advances most whereas that with 100% difference in width is retarded to the maximum limit. Unlike the diverging channel, the flow rate is also reduced to indicate increased resistance from the converging section. Also, unlike the diverging channel case, it is the stage profile for the 100% variation that mimics a frictionless case in a prismatic channel with an almost horizontal surface.

5.6 Miscellaneous Experiments

In previous sections a series of structured experiments were reported. These experiments explored and highlighted various aspects of the solution algorithm. A number of other experiments were designed and executed. The objective each time was to better understand the model behaviour, strengths, weaknesses, applicability to field problems, emulating real life situations, etc. The following experiments were implemented:

- i) mass conservation error and time step;
- ii) mass conservation error and interpolation
- iii) wave steepening
- iv) emulation of a bridge by channel constriction; and
- v) emulation of a lake by channel expansion.

These aspects are briefly discussed.

5.6.1 Mass Conservation and Time Step

Any numerical model should be capable of conserving volume or, strictly speaking mass. Although the Lagrangian model was excellent in conserving mass, it had problems operating at Crank-Nicholson's centred weighting. The Eulerian-

Lagrangian model, because of the interpolation between time steps, exhibited some mass conservation error. A comparison was carried out between the Lagrangian model at temporal weighting factors of 0.6, 0.75 and 1.0 and the Eulerian-Lagrangian model at a centred weightings.

Test 'B' was chosen for the basis of comparison with a grid size of 10 m and 1.0 second. The upstream boundary flow rate, changed from zero at a level pool of 2.0 m to 2000 m³/s in 1.0 second. The results of the four computer runs are shown in Figure 5.52. The figure was purposely blown-up to exaggerate the mass conservation error. Based on a criteria of shape and mass error, the Lagrangian model results for a weighting of 0.6 appear the best.

Next, the Eulerian-Lagrangian model was executed with a variety of time steps using the same configuration as above time steps of 1.0, 1.25, 1.33 and 1.5 seconds. The results are presented in Figure 5.53. These profiles at 120 seconds are again exaggerated in a window and indicate that a time step of 1.33 seconds produces the best results from minimizing mass conservation error considerations. In comparing results from Figures 5.52 and 5.53, it becomes apparent that the results for Lagrangian model at 1.0 second time step and 0.75 temporal weighting are almost identical to Eulerian-Lagrangian model at 1.33 second time step and centred weighting. From this observation, conclusion to the effect, that liberal time steps are permitted for Eulerian-Lagrangian model, should not be reached.

5.6.2 Mass Conservation and Interpolation Scheme

In the previous sections, it was recounted that the evolution of Eulerian-Lagrangian moving element scheme required the development, testing and implementation of a variety of interpolation schemes. This procedure is necessary in

MASS CONSERVATION ERROR WITH TIME STEP

Profile Window at Time = 120 • TEST 'B'

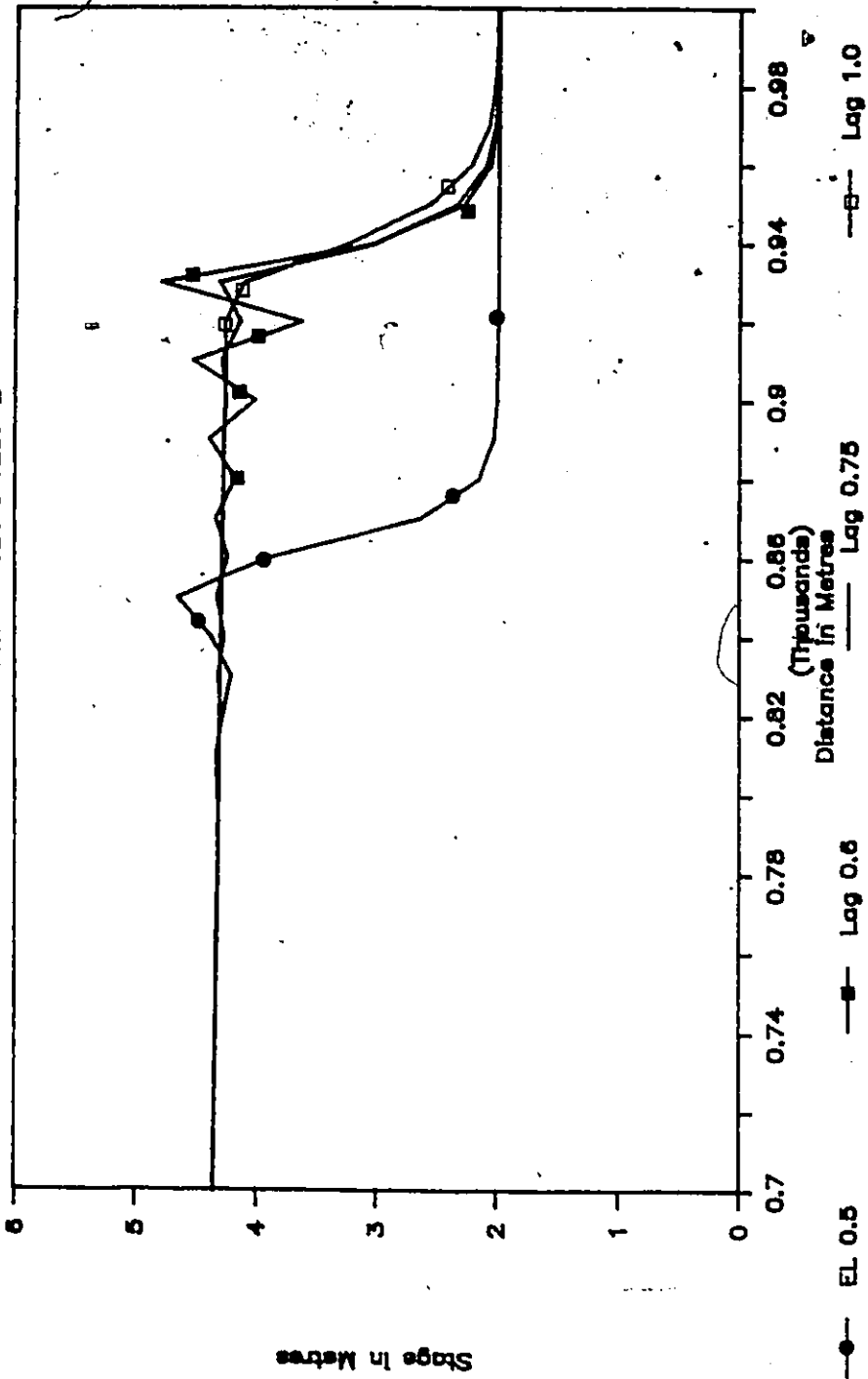


Fig. 5.52 Comparison of Mass Conservation Characteristics of Eulerian-Lagrangian and Lagrangian Models.

TIME STEP EFFECT ON MASS CONSERVATION

Profile Window at Time = 120s. TEST 'B'

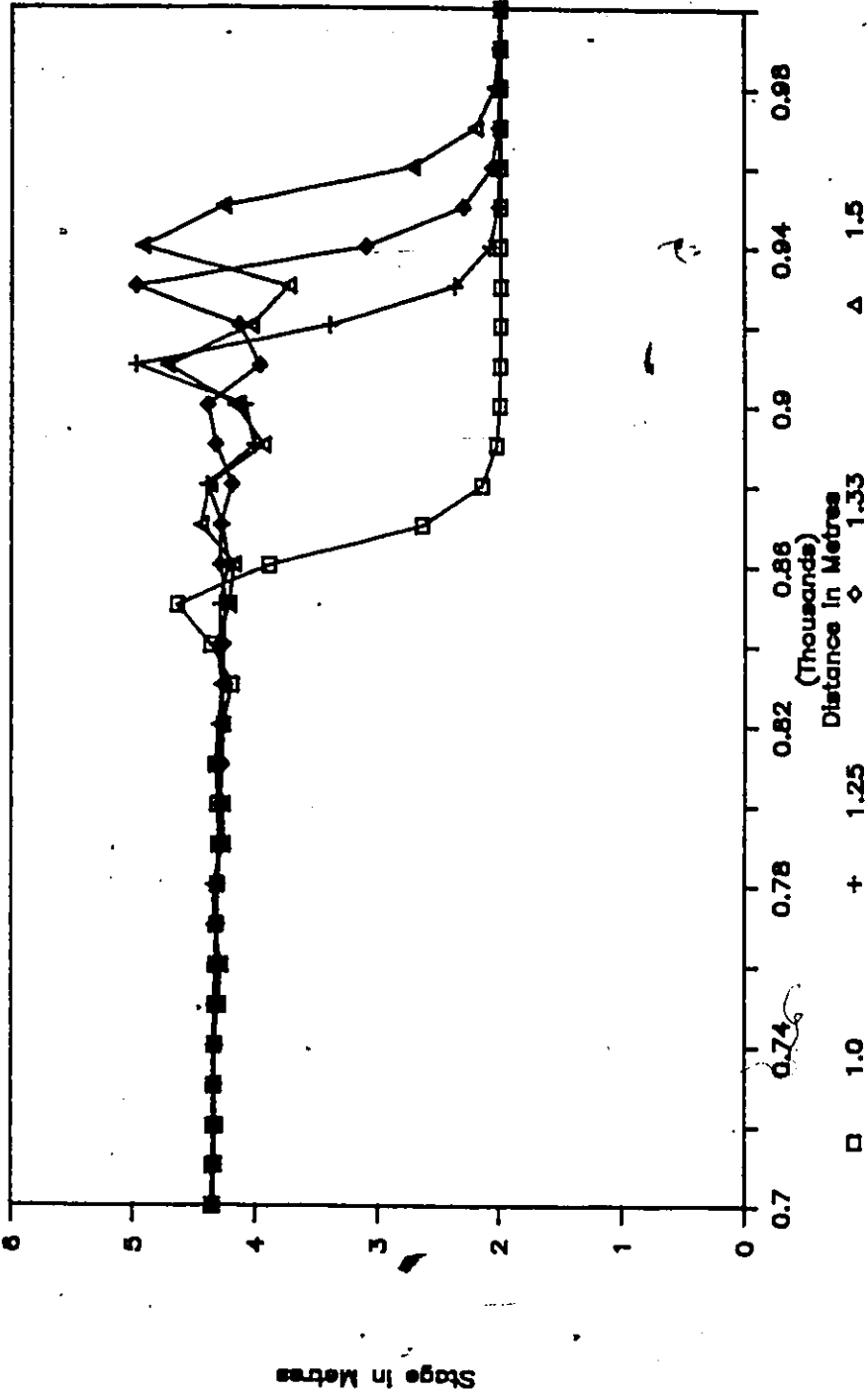


Fig. 5.53 Effect on Mass Conservation with Time Step for Test 'B'

order to tie the solution obtained in the Lagrangian mode to the Eulerian grid. This is also the step where, if care is not exercised, mass conservation errors can creep in due primarily to clipping of the wave front. As was noted earlier a number of interpolation schemes were considered; four of these were evaluated and three finally implemented in the model. The objective at this stage was to minimize errors in mass conservation, especially at the wave front. In this regard three experiments were designed, two with Test 'A' and one with Test 'B'. These interpolations schemes have been discussed at length in Chapter 4. Briefly the schemes are:

1. 2-point linear;
2. 3-point Lagrangian or non-linear;
3. 2-point linear with front tracking; and
4. mixed 2-point and 3-point.

In the first experiment, the first three schemes were employed and compared against the analytical solution. The results are plotted in Fig. 5.54. The relative position of the computed front with respect to the analytical result define the degree of mass conservation error. Scheme 3 overshoots the theoretical locations while Scheme 2 indicates minor clipping errors of less than 1%. Scheme 1, on the other hand, showed significant clipping errors (about 5-7%) as is indicated by a retarded wave front. The results were exaggerated twelve fold vertically and plotted in Figure 5.55. This graph brings the problems with Scheme 3 to the fore. Also, it proves that the 3-point non-linear scheme had the least error.

Scheme 3 was dropped in favour of a mixed linear/non-linear scheme. This scheme along with linear and non-linear interpolation are shown in Figure 5.56.

Test 'B' was used to demonstrate the growth of clipping error with time. This becomes quite clear when the results for the linear and non-linear interpolation

Interpolation Comparison; Supercritical

Profile @ 60s, dt=0.5s, theta=0.5

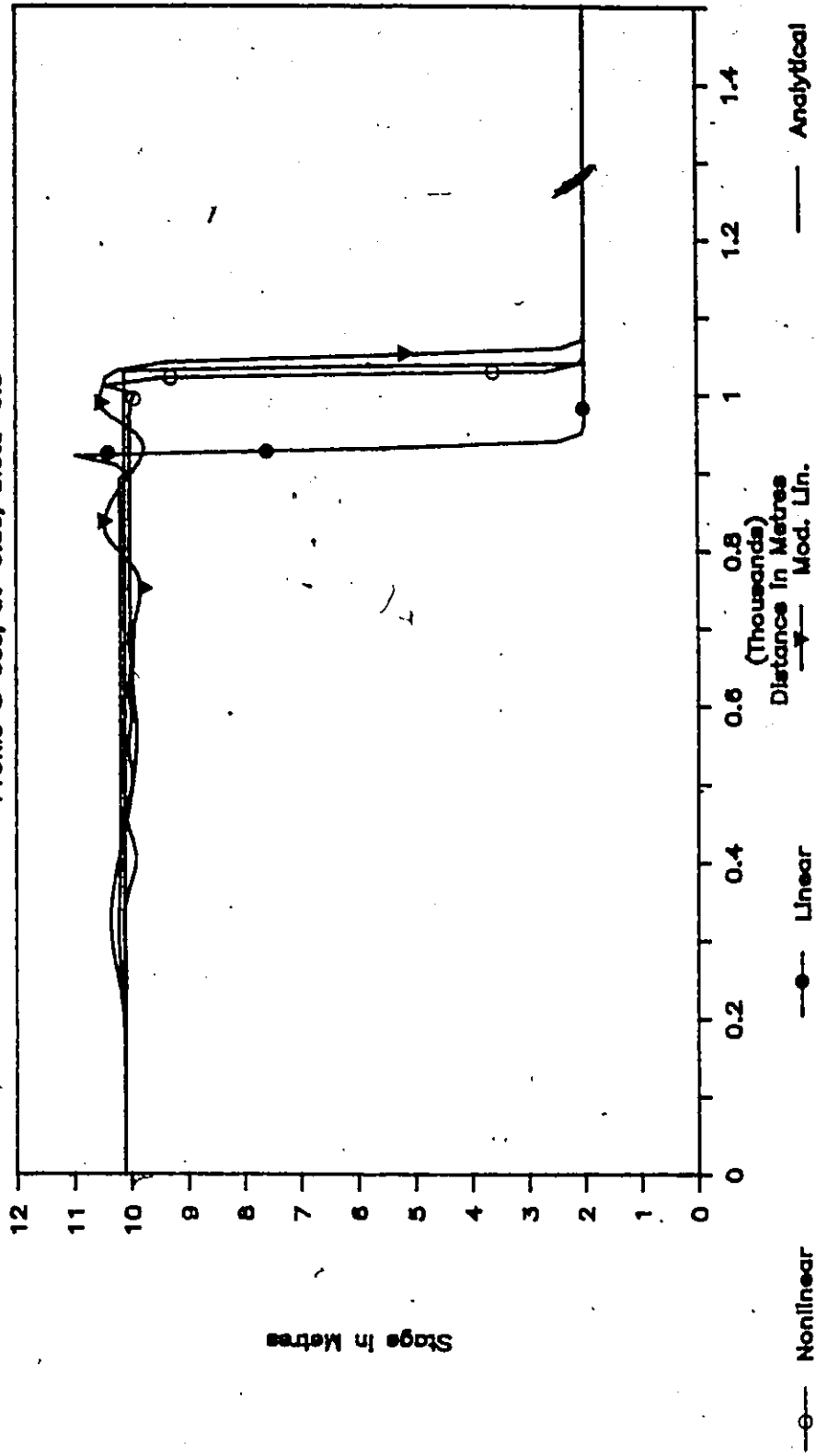


Fig. 5.54 Comparison of Interpolation Schemes at Eulerian Step for Test 'A'.

Interpolation Comparison..Supercritical

Profiles at 60 Sec., $dt=0.5s$, $\theta=0.5$

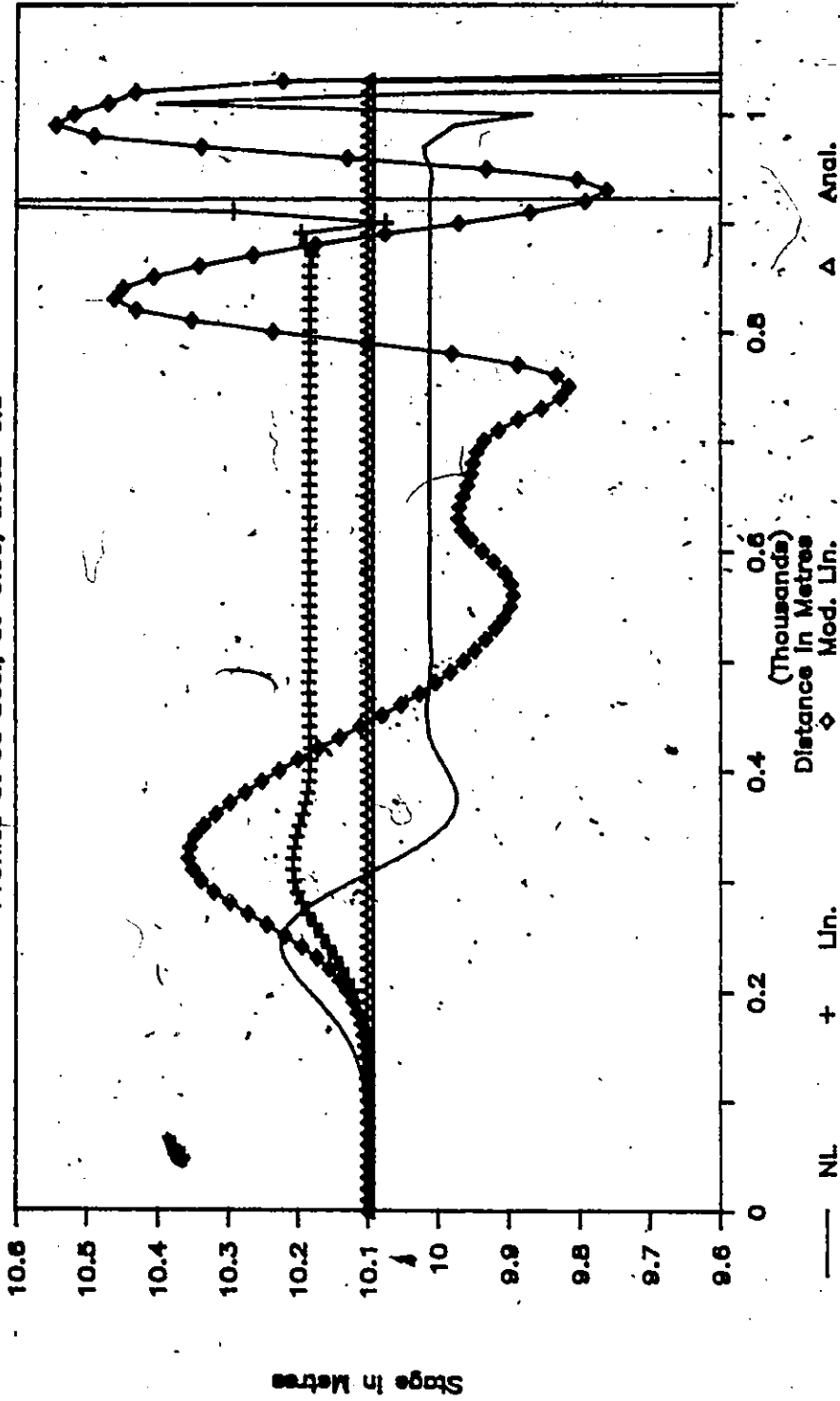


Fig. 5.55 Exploded Window Showing Influence of Interpolation Schemes for Test 'A'.

COMPARISON OF INTERPOLATION SCHEMES

Profiles at Time = 60 Sec. TEST "A"

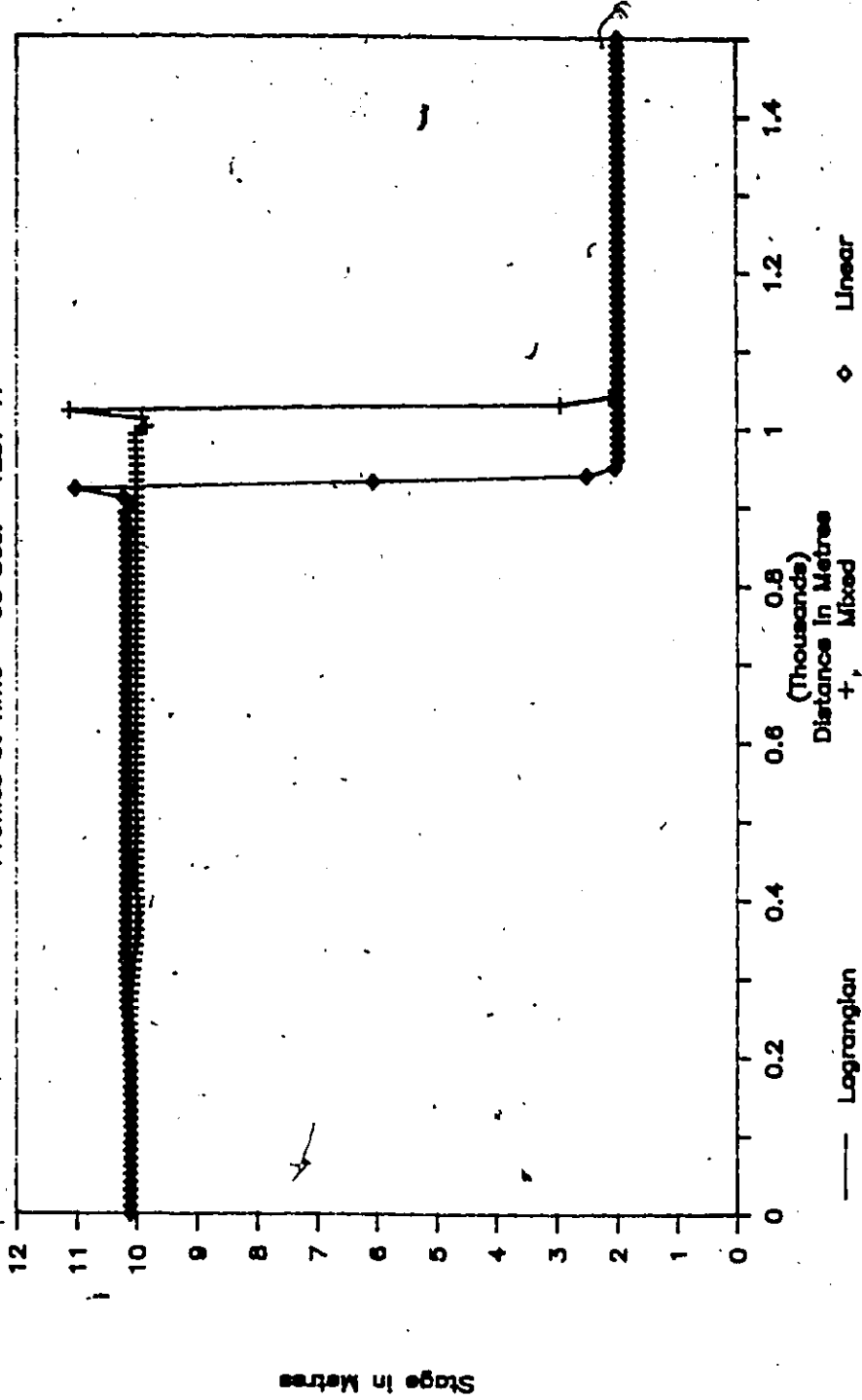


Fig. 5.56 Comparison of Interpolation Schemes at Eulerian Step for Test 'B'.

Linear and Nonlinear Interpolations

TimeStep=3s, Theta=0.5 @ 60s & 120s

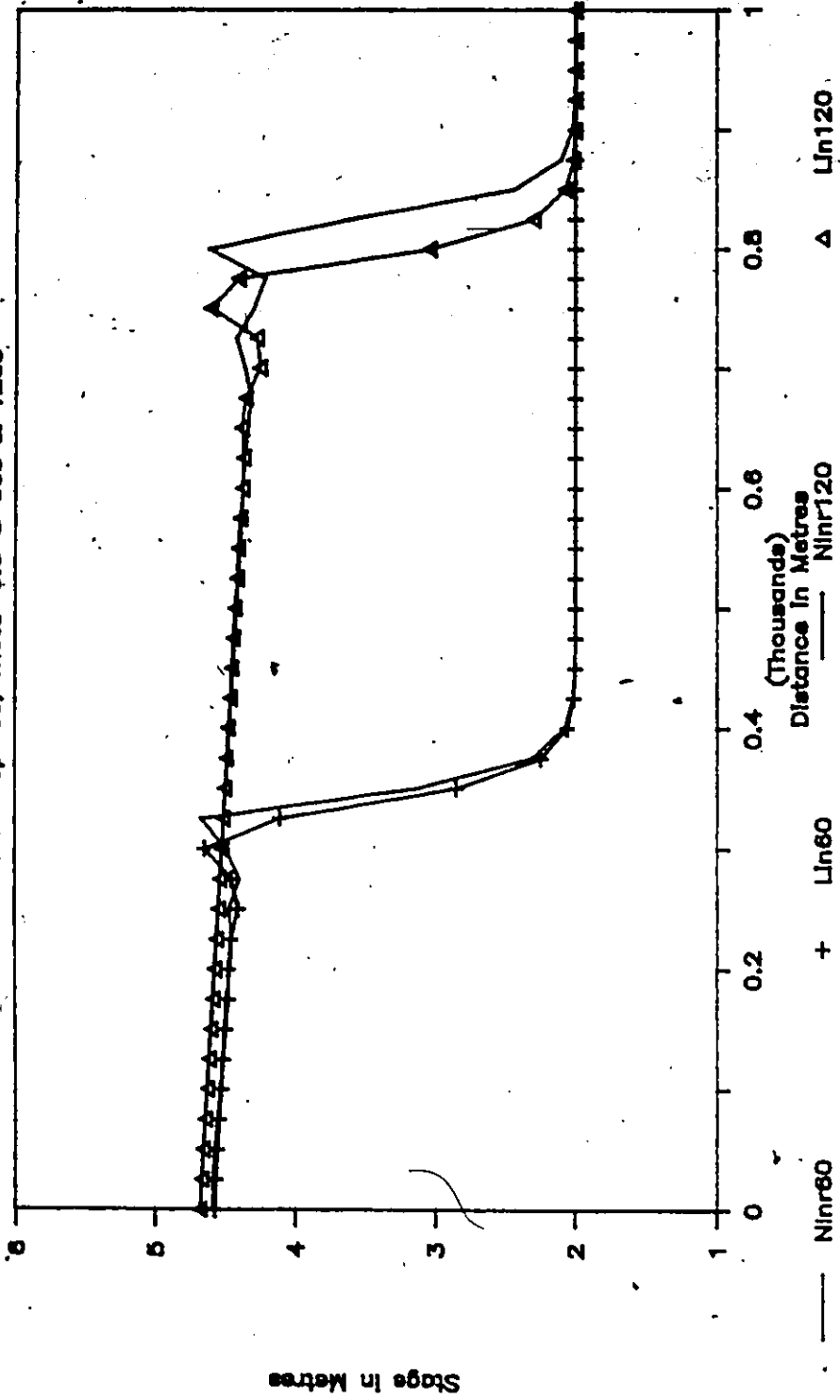


Fig. 5.57 Introduction of Clipping Errors in Time with Interpolation Schemes.

schemes are plotted in Figure 5.57. In this case, the mass-conservation error grew from about 1% at time 60 seconds to 5% at time 120 seconds. It should not be concluded from these two items of information that the growth of error is exponential. In this case the time to reach the maximum flow rate was 30 seconds and hence it required some more time steps for the front to mature. Prior to the formation of a near discontinuity, linear and non-linear interpolations provide similar results.

5.6.3 Wave Steepening

In all the test runs reported so far, the discontinuity was introduced at the upstream or downstream boundary to study the wave steepening behaviour, that is, the phenomenon of waves at greater depths travelling at higher speeds and overtaking flows at shallower depths. Employing Test B for this purpose, a discontinuity was placed in the solution domain and model behaviour studied for a number of time steps.

Fig. 5.58 depicts and demonstrates the handling of this dynamic flow problem. Initially, the wave is spread over a great number of elements. Subsequently, the wave occupies fewer and fewer nodes by strengthening wave fronts. The emergence of a spike is closely tied with the maturing of wave.

5.6.4 Emulation of Bridges and Reservoirs

In carrying out the numerical experiments, the impact of placing a choke in the path of a surge was studied as Test 'E1'.

A bridge can be considered as a constriction within the channel. The constriction imposed in Test 'E1' resulted in 50% and 75% blockage of area; these

WAVE STEEPENING & BREAKING

$dx=10m, dt=1s, sf0=1.2\%, theta=0.5$

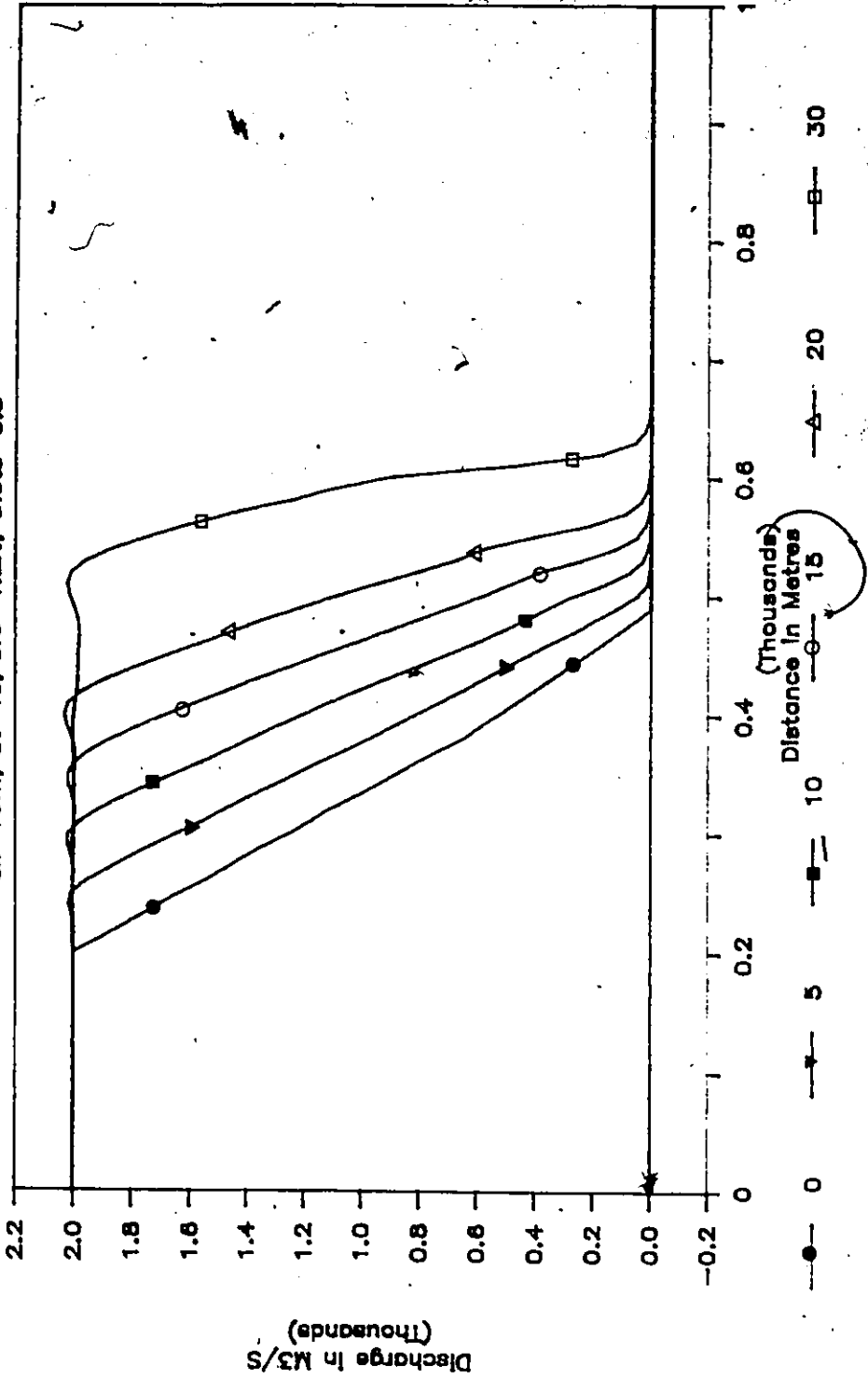


Fig. 5.58 Dynamic Effects of Wave Steepening, Maturing and Breaking.

encroachments provide severe choking effects although the transitions were each 100 m long.

A number of scenarios were tested for this purpose, a significant amount of results were presented earlier and the rest are shown in Appendix F. All this information points to the robustness of the moving element method.

Similar to the bridge problem, presence of a lake or reservoir within the solution domain can be easily explained by an expansion, followed by a wide channel section describing the reservoir topography and finally a constriction to describe the outlet conditions. Other areas where this emulation can be invoked include the study of turbine rejection and its absorption within the surge acceptance chambers. These surge chambers are usually an expansion in the channel.

To study this behavior, a numerical experiment was designed with the following particulars:

Physical Description:

In this test the rectangular channel is 100 m wide, 1000 m long and slopes at a rate of 0.0001 m/m or 0.1 m/km. The reservoir is represented by a diverging zone 100 m long starting at 350 m from the upstream boundary wherein the channel widens from 100 m to 200 m width. This 200 m expansion is maintained for the next 100 m. The channel narrows again to the 100 m width in the subsequent 100 m. The channel roughness is represented by the Manning equation with a coefficient of 0.015.

Initially, the depth of flow is 2 m with a flow of 206.1 m³/s. These conditions, however, exist beyond the influence of the expansion; steady gradually varied flow exists within the domain of transitions. The boundary condition at the upstream node required the flow to increase from the steady initial flow to 2000 m³/s

in a time span of 30 sec. This condition is maintained during the 240 s simulation run.

At the downstream boundary, the depth-discharge relationship exhibited by the uniform flow equation is given.

Discretization and Solution Procedure:

As the initial and boundary conditions were similar to Test 'B', the same grid sizes of 10 m long elements and 1 sec. time steps were employed. The transitions and reservoir each occupied 10 elements. For such a discretization, the Courant Number was greater than one.

The subcritical surge was allowed to progress through the expansion for a period of 240 s. The results in the form of stage and flow profiles at different times and hydrographs at predetermined points are presented in Appendix F.

5.7 Summary

For a new technique to be universal and fit for field application, it should be robust, versatile and modular. These aspects were subjected to extensive numerical tests. These tests emulated most of the circumstances that might arise in field situations.

The Eulerian-Lagrangian linked moving element method proved to be a competent tool for analyzing near discontinuous and continuous flow situations. This claim is based on the wave capturing properties, suppression of $2 \Delta x$ length node to node oscillations, minimal mass conservation error, handling of partial and total wave reflection, horizontal and adverse slope, non-prismatic channel sections, etc. Separate numerical experiments were set up to study each of the properties noted earlier.

Comparisons were carried out with other established numerical models based on the finite difference and finite element techniques. This again demonstrated the superiority of the Eulerian-Lagrangian and Lagrangian based models over the current Eulerian based techniques. Limited testing for prismatic channels employing Lagrangian based models and an alternate form based on the Petrov-Galerkin formulation in an Eulerian-Lagrangian grid proved these schemes to be worthy of further consideration.

Finally, sensitivity analysis involving a number of model parameters such as grid size, roughness coefficient, temporal acceleration rate at boundaries, temporal and spatial weighting proved normal model behaviour. Model versatility was also demonstrated in solving continuous and discontinuous flow situations.

CHAPTER 6

DESCRIPTION OF COMPUTER PROGRAM

6.1 Introduction

Success in implementing any mathematical algorithm and associated numerical schemes is closely related to the physical equations which are adapted and the method employed for casting them into efficient computer programs. The crystalization of the moving finite element method paralleled the development of the computer program logic.

This chapter describes the development, testing and implementation of a series of computer programs to address different situations in rapidly and gradually varied flows. Further, the subsequent amalgamation of several models into a single computer program is highlighted.

A poorly designed computer program will exhibit problems when transported to other operating systems. In order to evaluate the portability of the moving element model, the computer program was tested on two mainframes and several microcomputers. The model was further tested by devising experiments and subjecting the microcomputer's central processor and numeric co-processors to numerically intensive calculations. These experiments are described.

Finally, for a model to be practical and operationally effective, it is desirable to have a minimum of input, internal efficiency, and brief and meaningful output. The model input requirements and a sample of program output are presented and discussed.

6.2 Development on Mainframe Computers

The initial development of the computer program was on the CDC Cyber 171 mainframe computer at the Canada Centre for Inland Waters (CCIW). At this stage a series of computers programs were developed. These included different models for (1) supercritical flow, (2) subcritical flows, (3) surge moving in upstream direction, (4) surge moving in downstream direction, (5) Lagrangian mode solution, (6) Eulerian-Lagrangian mode solution, (7) upstream boundary represented by triangular elements, and (8) upstream boundary represented by collapsed quadrilateral elements. Separate models were developed to solve finite difference, finite element and Petrov-Galerkin schemes.

As a next step, the first six versions were gradually amalgamated into one single program. This activity was most easily carried out by modularization of the program requiring a number of subroutines and a program. To allow the user to choose the proper mode of operation, a series of switching or logical variables were added to allow for branching. In the final form the model consisted of the following modules.

Main Program: The main program reads the first half of the data set which consist essentially of control variables to set the mode of simulation. These variables are echoed with explanation. The control is then transferred to subroutine `MOVEL`.

Subroutine `MOVEL`: This is the main or 'shell' subroutine which controls the program operation. The remaining data are read consisting of channel geometry, layout, boundary and initial conditions. All other subroutines are called from this routine.

All computations in terms of Lagrangian grid set up, calculations of matrix coefficients, matrix solution by the double-sweep technique and printing of profiles at predetermined times are performed by this subroutine. Other output comes from specific subroutines.

Even in a skeletal form, this subroutine comprises close to 1,000 lines of code excluding comment statements. At this stage, there was no need for further modularization by the creation of additional subroutines. Several sections could, however, be easily encapsulated to compute the Lagrangian the grid, matrix coefficient set up and the solution.

Subroutine PROPS: This subroutine computes the channel geometric and hydraulic properties for a given depth of flow. The channel properties are exchanged between subroutines through labelled common blocks.

For a given depth the computed channel properties include cross-section area, wetted perimeter, topwidth of conveyance and off-channel zones, off-channel area, and first moment of area about the free surface. The channel roughness is computed as varying with depth. Channel representation and the stage-channel roughness relationship is described and discussed in a later section.

Subroutine INTERP: When the Lagrangian step is implemented, points at the advanced time level are offset with respect to the spatial Eulerian grid. The channel properties for the spatially fixed points do not change; however, for the Lagrangian points the channel properties need to be interpolated. This interpolation takes place in this subroutine. The subroutine interpolates channel invert, hence the bed slopes, channel roughness and off-channel characteristics, etc.

Subroutine INITIAL: This subroutine was added to the program to calculate initial steady flow conditions based on backwater computations given the flows at all points and the starting downstream elevation. The computation require balancing of momentum terms between adjoining sections. At the time of writing, the momentum balance procedures are simplistic. For example, the non-prismatic channel form terms for pressure forces are not included. This approach has, however, proved to be quite successful and the results showed no erratic behaviour. This success is contrary to the problems reported by Kowen (1984) and Wurbs (1986) in establishing initial flow conditions.

Subroutine LAGPRNT: This subroutine is invoked when computation in the main program are carried out in the Lagrangian mode. The depth of flow, discharge, stage and velocity are interpolated at regular predetermined points from the irregularly spaced Lagrangian grid.

Subroutine HYDPRNT: The hydrographs at predetermined locations are printed by the subroutine. The time frequency of printing the flow rate, depth and stage is controlled by a variable defined in the main program.

Subroutine ENVELOP: This subroutine is called from the MOVEL subroutine at the end of computations and prints out the most important information on the maximum value of stage, depth and flow rates. The envelope of stage defines the limit of the flood plain. Also, two other informative items are printed in terms of the times at which maximum flow rate and maximum depth of flow occur. Also computed and

printed are the top widths associated with the maximum flow depths. The average width between any two stations multiplied by the distance yields an approximate value of the area of flooding.

Subroutine PRTOTA: A tabular output of various input and output variables is printed by this subroutine.

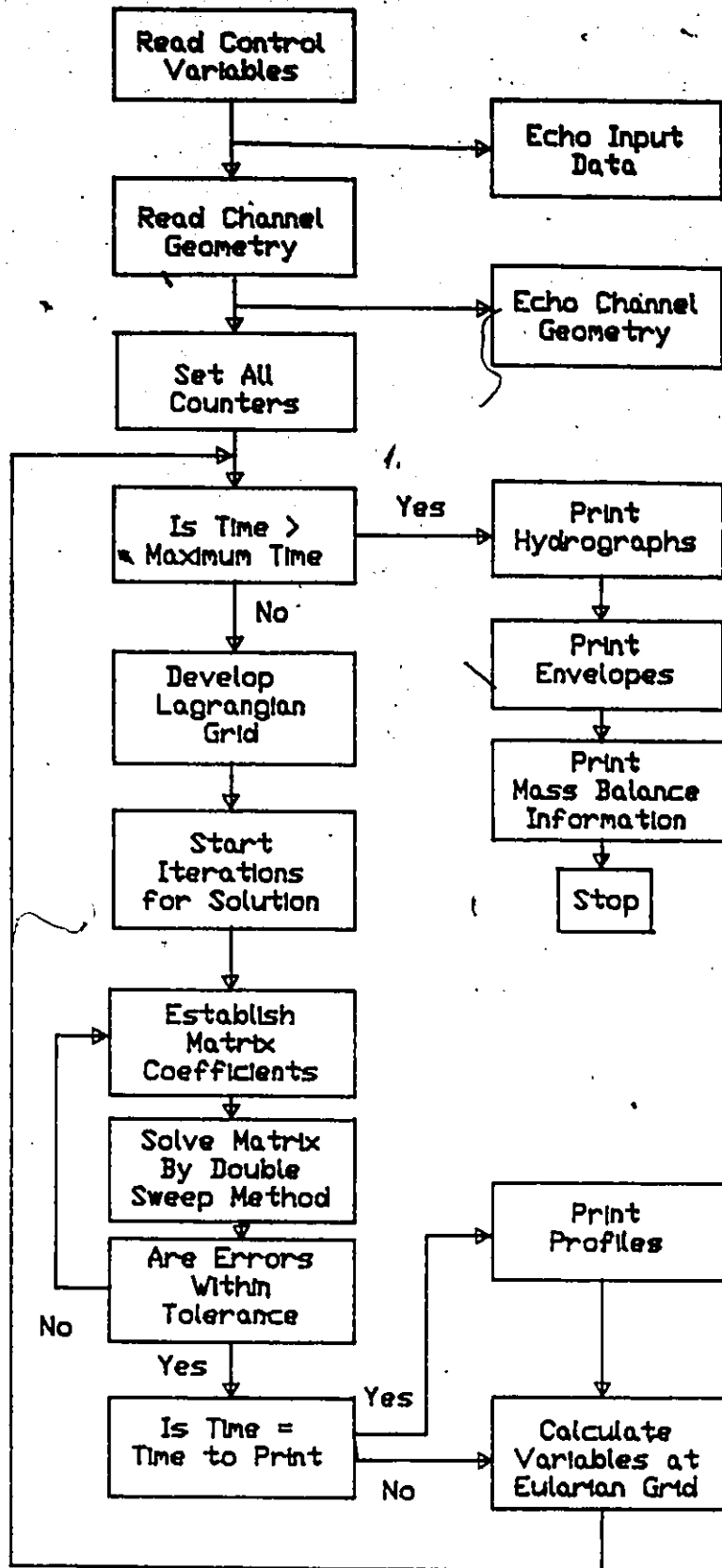
Subroutine CNVRT: The spatial and temporal variables are converted to the units in which the output is made.

A simplified flow chart of the computer program is presented in Figure 6.1. Many of the subroutines described above evolved out of necessity for proper representation of channel geometry, roughness coefficients and their variations, etc. These adaptations are described next.

Representation of Area: The most important parameter to describe mathematically is the variation of cross-sectional area with the depth of flow. If a reasonable approximation can be determined for this variable all other properties follow suit. Initially, the model was capable of handling only trapezoidal channels (note that rectangular or triangular cross-section are special cases of the generalized trapezoidal cross-section), with inclusions for the non-prismatic cross-sections and off-channel storage, the following relationships define the channel properties with reference to Figure 6.2.

Using the following definitions:

y_d = Thalweg (i.e. the locus of lowest cross-sectional points) elevation of channel



6.1 Simplified Flow Chart of Moving Element Model.

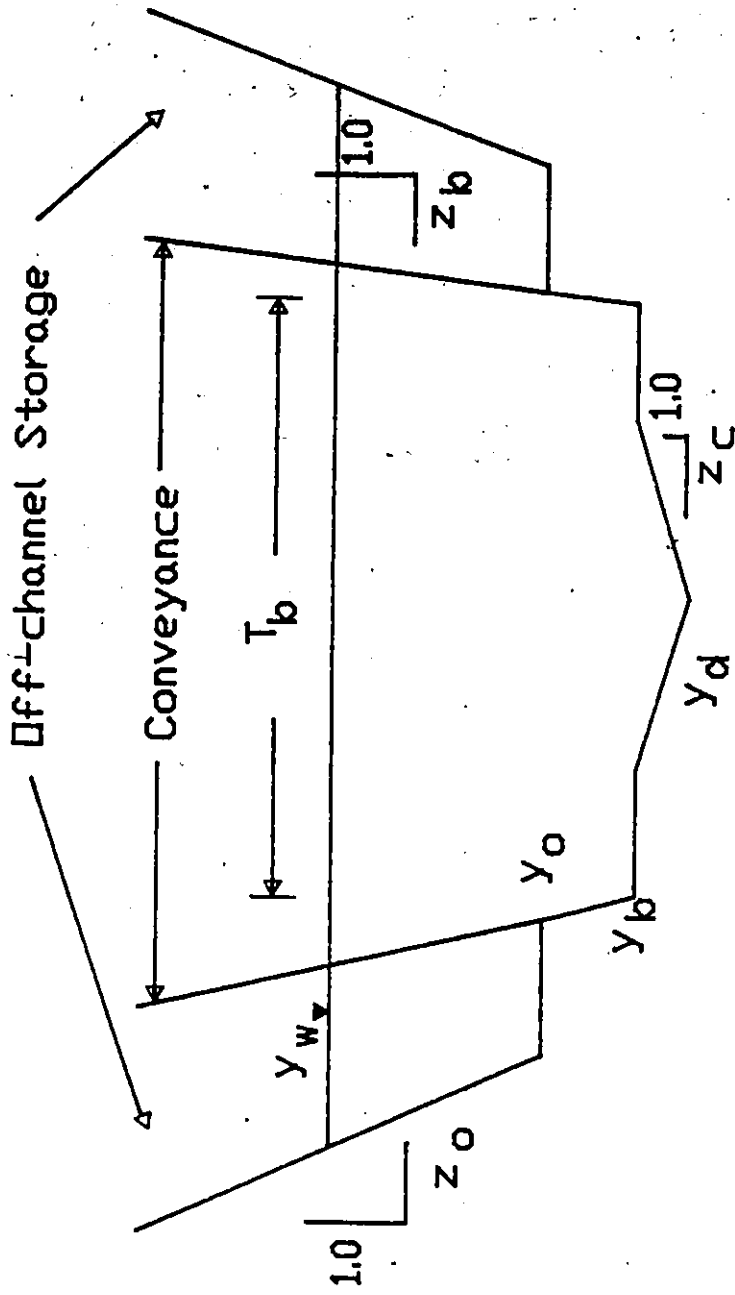


Fig. 6.2 Channel Cross-section
Definition in Moving Element Model

- y_b = Bank full elevation
 y_o = Elevation at which off-channel storage occurs
 y_w = Water surface elevation
 z_c = Channel side slopes for low flow channel
 z_b = Assumed slope for conveyance section
 z_o = Off-channel storage lateral slope
 T_b = Channel width at bank full flow conditions
 $y = y_w - y_d$ = Depth of flow

Dependent variables:

- A = Cross-sectional area
 T_c = Top width of conveyance section
 T_o = Top width of off-channel section
 WP = Wetted perimeter
 G = First moment of area about the water surface
 A_o = Off channel storage area

Case 1 when $y_w < y_b$

$$A = z_c y^2 \quad (6.1)$$

$$T_c = 2 z_c y \quad (6.2)$$

$$T_o = 0 \quad (6.3)$$

$$WP = 2 y \sqrt{1 + z_c^2} \quad (6.4)$$

$$G = \frac{1}{3} z_c y^3 \quad (6.5)$$

Case 2 when $y_b < y_w < y_o$

$$A = z_c (y_b - y_d)^2 + T_b (y_w - y_b) + z_b (y_w - y_b)^2 \quad (6.6)$$

$$T_o = 0.0 \quad (6.3)$$

$$T_c = T_b + 2 z_b (y_w - y_b) \quad (6.7)$$

$$WP = 2 (y_b - y_d) \sqrt{1 + z_c^2} + 2 (y_w - y_b) \sqrt{1 + z_b^2} \quad (6.8)$$

$$G = z_c (y_b - y_d)^2 (y_w - \frac{2}{3} y_b - \frac{1}{3} y_d) + \frac{1}{2} T_b (y_w - y_b)^2 + \frac{1}{6} z_b (y_w - y_b)^3 \quad (6.9)$$

Case 3 when $y_w > y_o$

$$A = z_c (y_b - y_d)^2 + T_b (y_w - y_b) + z_b (y_w - y_b)^2 \quad (6.6)$$

$$A_o = z_o (y_w - y_o)^2 \quad (6.10)$$

$$T_c = T_b + 2 z_b (y_w - y_b) \quad (6.7)$$

$$T_o = 2 z_o (y_w - y_o) \quad (6.11)$$

$$WP = 2 (y_b - y_d) \sqrt{1 + z_c^2} + 2 (y_w - y_b) \sqrt{1 + z_b^2} \quad (6.8)$$

$$G = z_c (y_b - y_d)^2 (y_w - \frac{2}{3} y_b - \frac{1}{3} y_d) + \frac{1}{2} T_b (y_w - y_b)^2 + \frac{1}{6} z_b (y_w - y_b)^3 \quad (6.9)$$

With the above equations most of the field channel cross-sections were adequately described. The channel roughness was allowed to vary with depth

according to the following relationship.

$$n_w = n_b \{1 + k(y_w - y_t)\} \quad (6.12)$$

for $y_w > y_t$

else $n_w = n_b$

where

n_w = Manning's roughness coefficient at water level

y_t = elevation above which the roughness changes base value of the roughness coefficient

k = rate at which the roughness changes

The parameter "k" can take either positive or negative values to allow an increase or decrease in roughness respectively. Adequate checks are built into the computer program to ensure that roughness coefficients are not assigned unreasonable values.

For natural channels with off-channel storage it is usual to reduce the roughness for increasing stages to account for the efficient boundaries between the conveying and non conveying sections. On the other hand if no off-channel storage is considered the roughness may increase or decrease depending upon the bed material of the conveying and flood-plain sections.

Once the program was operational on the Cyber computer, it was transferred to the VAX-8600 research computer at McMaster University. Due to different word sizes for Cyber (64 bit words) and VAX (32 bit words) a number of variables require declaration at double precision level. Most of these variables were associated with energy slopes, matrix inversion coefficients, etc.

Of the two mainframe computers, the VAX 8600 proved to be faster in light of the dedicated virtual memory mode operations. There were significant differences

in the execution times using identical data inputs. This apparent anomaly was attributed to the different word accuracies at the matrix inversion and convergence check stages. As the results were printed to three decimal places no differences were noted in the computed values.

6.3 Tests on Personal Computers

The availability of increasingly powerful personal computers (PCs) has accelerated the trend of modifying programs originally developed for large mainframe machines for implementation on these PCs. In particular, many finite difference and finite element models in water resources requiring extensive memory and sophisticated integration procedures have been converted to run on personal computers.

Programs like HEC-2, United States Army Corps of Engineers (1973), Mobile Bed Hydraulics (MOBED), Krishnappen (1977), DWOPER, Fread (1984) are a few examples of programs in the fields of water resources engineering which have been posted to PCs.

In view of the foregoing, two objectives were set for downloading the computationally intensive moving element scheme. The first objective involved compiling and operating the program developed on the Cyber and VAX mainframe machines on the personal computers. Secondly, it was required to carry out a series of tests to identify any limitations imposed by the computationally intensive schemes required to solve such problems.

For the microcomputers environment, all the PCs were equipped with the Intel's 8086/8088/80286 family of the central processing units (CPU). All these computers, further, operated under MS/PC-DOS commands. The FORTRAN

compilers for the comparisons consist of MicroSoft (Version 3.30), WATFOR77 and WATFOR87 (Version 1.0).

The first objective was fulfilled without much difficulty. No changes in program logic were required when transferring programs from mainframe to PC environment. As in the transfer from Cyber to VAX machines, it was found that a further number of variables had to be computed at double precision to avoid problems with underflow and overflows. Upon reconciliation, the computer programs for PC and VAX machines became identical.

As the second objective involved the testing of certain computational aspects on the PCs, input/output requirements were minimized. This constraint evolved from the 8-bit input/output channels for writing to files if output is required versus 16-bit for computations and 80-bit numeric co-processors. For input, the channel geometry, time and distance steps, initial flow and stages, stage or discharge hydrograph, reach length, duration of simulation, etc. were required. The water surface or depth profiles at desired times, the stage/discharge hydrographs at prescribed points and overall mass balance measurements were written to a file.

For testing purposes three different numerical experiments were designed and implemented. Basically, these experiments were only slight variations of Tests A, B, and C described in Chapter 5. The various combinations of hardware/software along with the results are presented in the following sections.

6.3.1 Hardware/Software Description

The experiments, as two separate computer programs for supercritical and subcritical regimes, were first implemented on a CDC Cyber 171 mainframe facility at the Canada Centre for Inland Waters, Burlington. To test the programs in a PC

Table 6.1

Hardware Configurations of Micro-Computers

No.	Central Processing Unit	Numeric Data Coprocessor	Clock Speed (MHz)
1	8088	None	5.0
2	8086	None	8.0
3	8088	8087	.4.77
4	8086	8087-2	8.0
5	80826	None	8.0
6	80826	80827	8.0

Table 6.2

Comparison of Execution Time for Different PC Configurations
relative to CDC Cyber Performance

CPU(s)	Clock Speed (MHz)	Microsoft Fortran (V 3.30)			Watcom WATFOR77 WATFOR87
		MATH	8087	ALTMATH	
8088	5.0	220	n/a*	56.3	116
8086	8.0	100	n/a	25.7	50.3
8088 +8087	4.77	10.5	10.5	n/a	24.6
8086 +8087	8.0	6.1	6.1	n/a	15.2
80286 +80287	8.0	8.8	8.8	n/a	n/t‡

* n/a not applicable

‡ n/t not tested

environment, a number of different machines were employed, running at different clock speeds and with and without numeric co-processors. The range of hardware configurations tested is summarized in Table 6.1.

Another factor of some importance in implementing a PC version of the computer program, is the choice of a compiler and options employed when using it. In addition to the CDC Fortran 77 used for the mainframe, the PC versions were executed using MicroSoft Fortran (version 3.30) and Watcom's WATFOR77. The MicroSoft compiler offers a number of alternative options with respect to run-time libraries (e.g. MATH.LIB, 8087.LIB or ALTMATH.LIB.) and (although not tested) metacommands such as the \$NOFLOATCALLS option. Each of these features significantly affected execution speed and made comprehensive bench-marking a very complex issue, highly sensitive to the characteristics of the executing program in terms of Input/Output, data accessing and arithmetic operations. Not all of the possible permutations were able to be tested but the matrix of Table 6.2 gives some insight into the results.

6.3.2 Comparison of Operating Environments

In comparing mainframe and PC results it should be noted that for all three experiments, the resulting profiles and flow values obtained using MicroSoft Fortran on the PCs were identical. These are collectively termed the 'PC results'. Minor differences were noted between these and results obtained using the WATFOR77 compiler on the micros and the Cyber 171. Newer versions of various PC compilers have, however reconciled the differences. The results from the different machines are compared first with respect to accuracy and consistency and secondly in terms of execution time.

Accuracy

Because of the significantly larger word size in the Cyber, the results of the mainframe computation were arbitrarily taken to be the basis against which all other results were compared. When compared to the mainframe results, the computations on PCs do indicate some round off error. This is more pronounced in Test 'A' due to the intensity of computational requirements. The results are identical at 20 seconds but about 1% difference in the profiles become evident at 60 seconds.

As noted previously that a number of variables required double precision accuracy when converting from mainframe to PC. These changes were implemented on a trial and error basis. Therefore, the differences in the results between the mainframe and PC could be minimized by selectively choosing the parameters that really influence. An attempt was made to make all variables at double precision. The computer memory requirements, however, exceeded the available storage and precluded further work in this area.

Another point of interest is that the results generated by WATFOR77 and MS-FORTRAN are slightly different for Test 'A'. This could be attributed to the differences in the compilers and rounding off techniques, especially when accessing only 8088 processor.

Execution Time

By their very nature, Tests 'B' and 'C' were computationally less demanding than Test 'A'. It was found that the relative execution time for the three tests was very similar for all of the PC/MicroSoft Fortran configurations with slight differences for the Cyber and PC/WATFOR77 cases. Table 6.3 gives an impression of

Table 6.3

Relative Execution Time for Test Cases
using Different Hardware/Software Configurations

Test Case	A	B	C
Statements executed (Millions) (Normalized).	5.80 (3.84)	1.98 (1.31)	1.51 (1)
CDC Cyber 171	2.28	1.51	1
PC/Microsoft Fortran*	2.27	1.57	1
PC/WATFOR77	2.86	1.35	1

* Averaged over various Intel/MS configurations

the relative run-time for the different configurations. It was not clear to the reason why the PC/WATFOR77 results exhibited abnormal behaviour. The Cyber execution time is, however, influenced by the provision of a roll-out queue when a number of programs are executing concurrently.

Table 6.2 is a matrix which describes the different combinations of hardware and software options which may be employed with the available micro-computers. The values given represent the factor by which execution time exceeds that for the CDC Cyber. The rows are arranged in order of increasing execution time using MicroSoft Fortran with the FORTRAN and MATH default run-time libraries. These produce slightly larger (6 to 10K bytes) executable code which will address the 8087 or 80287 if present or emulate it if not. Clearly, the emulation of the 8087 accuracy carried an overhead in execution time.

By using the alternate ALTMATH library, both the size and execution time of the code were reduced. Of course, in the presence of an 8087, the use of the 8087.LIB library further reduced the size of executable code. The \$NOFLOATCALLS metaccommand available in MSFORTRAN allows the programmer further control on the tradeoff between accuracy and speed of execution. This causes the floating point operations to be processed by calls to library routines. In view of the stringent accuracy requirements of the moving element scheme, this option was not tested.

The most dramatic statistic is the excellent performance of the 8086 and 8088 CPU with the 8087 co-processor. The performance of the 8086 system benefits not only from the higher clock speed but also from the full 16-bit data path which halves the data access time. The benefit would normally be realizable since the compiler always sets the address of numeric data arrays at even byte (i.e. full word) addresses.

The performance of the 80286 configurations alone (which were not tested) would be impressive but as is now well recognized, the addition of the 80287 does not yield anything like the improvement that the 8087 brought to the older CPU. The reasons for this behaviour are very well described by Fried (1985).

The WATFOR77 compiler, although produced chiefly as an educational tool, performed very well, especially the version which can address the 8087. This compiler, which was on its first release, would see better test results when later versions would allow linking and generation of object code modules.

6.3.3 Other Testing on Microcomputers

Development of the computer program in a microcomputer environment facilitated testing of several ideas. Following the experience gained in implementation of the computer program, the model was compiled and executed using Ryan-MacFarland Professional Fortran and Lahey Fortran. The programs performed without any problem.

The graphics capabilities offered by the PCs were also utilized. To provide transportability among various graphics boards, HALOF by Media Cybernetics was selected to translate the numeric data into visual information. Several sub-routines were developed to display water surface profiles in a quasi animated mode. This allowed the results to be inspected at each time step or as desired. This provided considerable insight to the development of the spike and steepening of the wave profile.

6.3.4 Summary

Based on the extensive testing and development of the moving element model on the microcomputers provided the comparison of results retrieval times with the mainframe computers. It was found that the retrieval time from 8086, 8088 real time processors and WATFOR77 compilers is excessive from the viewpoint of operations requirements.

The Intel 8087, 80287 or equivalent numeric data processors make execution PC environment comparable with the mainframe computers. Differences noted in the results between the mainframe and PCs could be attributed to the larger word size for CYBER 171 mainframe computer. The difference noted between the results of MS-FORTRAN and WATFOR77 for Test 'A' may be the result of rounding off technique. More testing by similar computationally intensive programs are, however, required to ascertain the reasons.

6.4 Input Requirements

The flexibility of computer program use, the transportability among various operating environments and robustness is directly associated with the input requirements of the model. An otherwise efficient program would lose its efficiency if the input requirements are excessive, too sparse, obscure or site dependent.

Based on the experience gained in transposing the moving element from a powerful numerical algorithm into an efficient, site independent, practical computer program, the input requirements for the model were optimized. This does not, however, preclude further improvements in input setup when the moving element technique is generalized into an operational tool for flow forecasting and simulation.

In the present computer program development phase, data are read in two stages. At the first stage in the main program various control parameters are read in. These include the number of nodes, grid size, interval of printing results, temporal and spatial weighting parameters, convergence limits, etc. The remaining input data comprises the channel geometry information, upstream hydrograph, downstream flow condition and initial flow conditions.

Appendix G describes the input requirements and type of data for simulating the Teton Dam - Break Flood. For executing some of the prismatic channel model runs, a minimum of thirteen lines of data would suffice the input requirements. On the other hand, for simulating floods in the Grand River, described in the next chapter, 51 lines of data were sufficient. A sample of input files for computer runs simulating various experiments are included on the diskette.

6.5 Output Description

The efficiency of a computerized model, such as the moving element method, is not properly realized unless the program outputs meaningful information. With the foregoing as the background, objectives were set in printing output in an efficient manner.

Following the example of a number of existing models, it was decided to echo the input variables along with the variable name and its function. This minimizes the need of a user manual for interpreting the output. Another objective required the printing of profiles in such a manner that the output can readily be employed in displaying the results graphically. In fact most of the results reported in Chapters 5 and 7 were developed directly from the computer output.

The output can be divided into six major components. These are:

- (1) **Echo of input:** In this section the input is echoed along with a description of the variable. This consists of all control variables, channel geometry, etc. A sample of this part of the output is shown in Appendix H.
- (2) **Initial conditions:** In the moving element model the initial conditions can be specified in three different ways. For prismatic channels with steady uniform flow, the depth and flow can be specified at the upstream boundary. The depth and flow at other points are simply reflected from the upstream values. This was used more out of convenience due to horizontal bed and pool conditions for many of the computer runs. Strictly speaking, this technique should only be used for supercritical initial flow conditions. The initial conditions may also be indicated by specifying the depth of flow and flow rate at the furthest downstream points. The depth and flow at other points are computed in the backwater subroutine employing a momentum balance criteria. Finally, the depth of flow and flowrate can be specified at each computation node of the initial grid configuration. This information is printed in the section.
- (3) In the third group, the flow profile is printed at predetermined fixed time intervals. The interval for printing is specified in the B input card. The variables that are printed include node location, discharge, stage, depth of flow, velocity and top-width. Most of the graphs produced for the numerical experiments were extracted from this group.
- (4) The hydrographs for a specified number of nodes are saved and printed in the fourth group of output data. The information consists of node location, time since computation started, flow rate, depth of flow and stage.

- (5) The quality of interpolation, of time step, etc. are reflected in the mass conservation or, strictly speaking, volume conservation calculations. Information is printed for volume of water entering the domain, volume leaving, and the change in storage between initial and final time-steps and the error introduced. For Lagrangian mode solution, it was not uncommon to have perfect mass balance if the initial conditions are specified correctly.
- (6) The sixth group of output data was added when computer simulations of the Teton Dam break and the Grand River flood were carried out. It is rare to find continuous temporal information at a number of points on the river. The most readily obtained information is the highest elevations that are recorded along the stream. To reflect this, the program was enhanced to store the highest computed elevations and maximum discharge. As the highest elevation and maximum discharge are reached at different times, these times are also stored. The envelope of maximum elevation and discharge and associated times are printed. A sample from the Grand River output for the 1974 flood is displayed in Appendix I.

6.8 Summary

In this chapter, the transition of the moving element model from a numerical algorithm to a practical forecasting tool was highlighted. While it is important for the research to be captured and represented by a computer program, the advantage of the technique cannot be realized until it can be demonstrated that the computer program indeed is a viable tool for operational flash flood forecasting. This was achieved in this section.

The course of the model development was charted along with the extensive tests the various versions were subjected. The postability of the model was established by first evaluating the program coding on two mainframe computers. Subsequently, the program was posted to a number of microcomputers.

CHAPTER 7

APPLICATIONS

7.1 Introduction

The extensive and controlled numerical testing reported in Chapter 5 provided the backdrop for extending the application of model to solve field problems. The computer program described in Chapter 6 required only slight modification when applying the model to different problems. This will be described in detail and this requirement of modifications should not be interpreted as being very site specific. The need arose from describing a particular feature which then could easily be generalized.

In this chapter, five applications and two laboratory experiment verifications are described. Of the applications, only two are with real field data and observed flood events. One other application examines the impact of mild slopes and channel expansions on flood characteristics. Another application is in a controlled channel section with an observed flood hydrograph; in this study comparisons between other dambreak models by Wurbs (1986) are extended. Finally, the fifth application explores the flooding characteristics when a hypothetical dambreak flood is imposed on a calibrated continuous flow model. The experience in simulating laboratory experiments is described in Section 7.7.

This somewhat makeshift approach to the demonstration of the model became necessary for several reasons. Among them are:

- (1) The general lack of field data in terms of continuous or near-continuous stage hydrographs at a number of locations throughout study reach;

- (2) Only few control points exist that would allow conversion of depth of flow to discharge to study flow attenuation properties;
- (3) No information is available on the variation of roughness with depth; and
- (4) Overall lack of data for near discontinuous flow situation.

In the absence of such vital information, the model becomes, more or less, a black box between the upstream boundary usually controlled (either physically or by information), and the downstream control point.

Three of the applications are related to the flood event following the failure of the Teton Dam flooding and two applications deal with flooding in the lower reaches of the Grand River. These are further broken down as follows

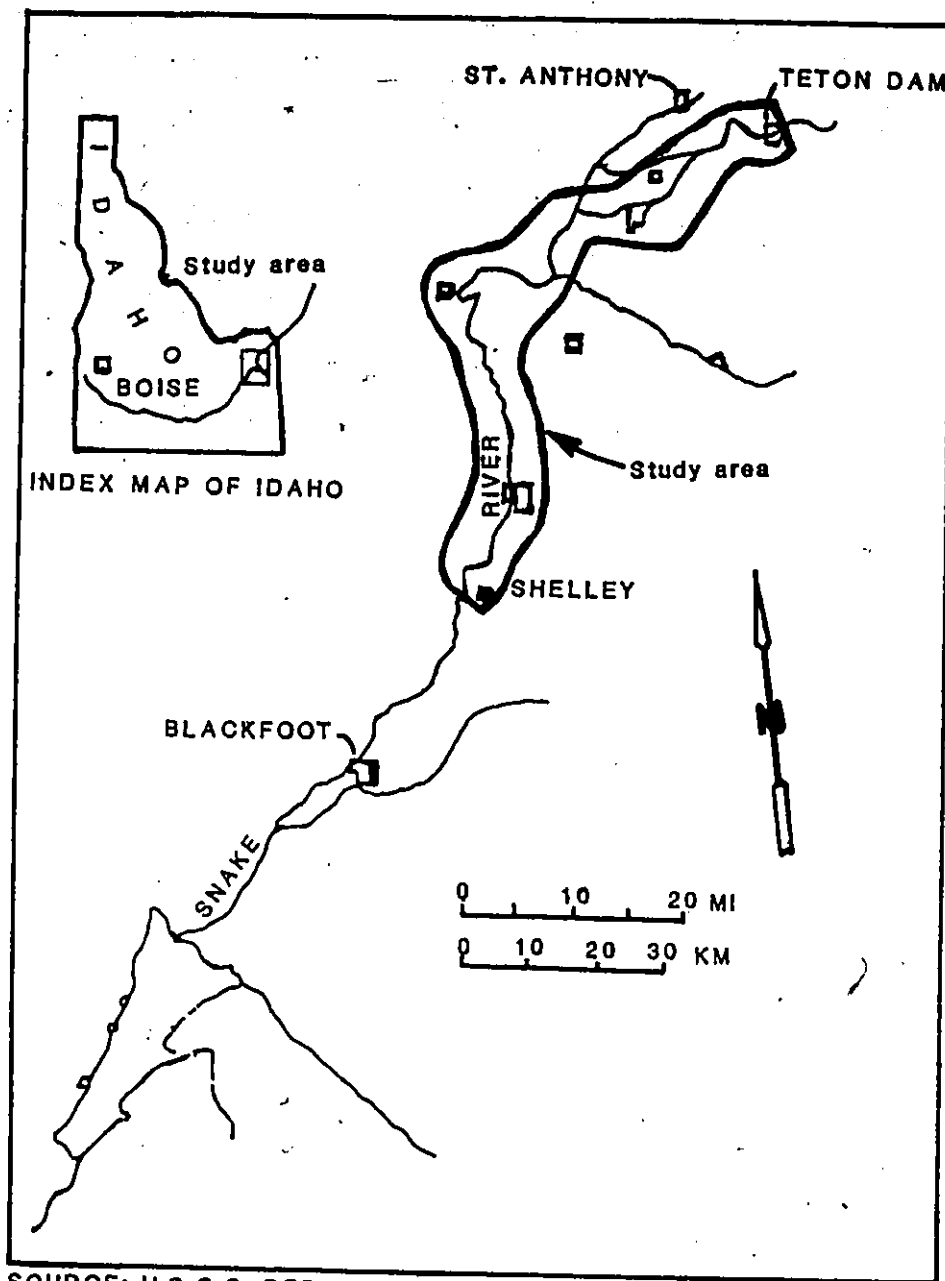
- (1) Teton Dam failure simulation;
- (2) Teton Dam failure simulation with prismatic channel;
- (3) Teton Dam failure simulation on mild sloped channel;
- (4) Grand River flood simulation; and,
- (5) Grand River flood simulation with hypothetical dambreak hydrograph.

The details of these applications are described in the following sections.

7.2 Teton Dam Failure Simulation

The Teton Dam is located near Rexburg in south-eastern Idaho, U.S.A. The dam, straddling across the Teton River, was designed as a zoned earthfill embankment with a maximum height of 305 feet above the river bed. The dam was experiencing the first fill after construction in 1976, when the failure due to piping occurred on June 5. The location map of the Teton Dam is shown in Figure 7.1.

The hydraulic events surrounding the failure have been recorded and reported by a number of agencies. Noteworthy reports were prepared by Gundlack



SOURCE: U.S.G.S. REPORT 77-785

Fig. 7.1 Location Map of Teton Dam Break Flood Study

and Smith (1977) and Fread (1982). A variety of scenarios have been postulated in support of developing inflow hydrographs and subsequent hydraulic routing. For the purpose of this study, the hydrograph generated by the U.S. National Weather Service Model DAMBRK developed by Fread (1978) was employed.

The information in this section is arranged as follows:

- (1) description of the physical geometry, channel properties, etc.;
- (2) initial flow and boundary conditions;
- (3) model set up; and,
- (4) discussion of results.

7.2.1 Physical Description

For modelling purpose, the information was obtained by reducing the data supplied with the DAMBRK computer model. The reach length modelled was 59.5 miles, starting at the Teton Dam and ending at Shelly Gaging station. The channel flows through three quite distinct reaches. For the first five miles the river flows in a steep walled canyon and empties into a very wide shallow valley. This valley is approximately 36 miles long; in the final reach the river once again traverses a well defined section, through the City of Idaho Falls, for the remaining distance of 18.5 miles.

The channel cross-section data supplied with DAMBRK consist of a table of elevations and top widths for the conveyance section with a similar arrangement for the over-bank storage, available at 12 locations where the channel geometry was representative of the reach. Manning's roughness coefficients were also obtained at these points. DAMBRK also provides a table of the coefficient of roughness as a function of depth.

The moving element model was not equipped for the computation of section properties like DWOPER, therefore, the stage-top width information was converted into an exponential power relationship. A typical cross-section defined by the moving element model is shown in Figure 7.2. In the model the channel properties are defined as a function of the depth of flow.

The functional form is defined as follows:

$$A = C_1(y_b - y_d)^{2/2} + T_1(y_s - y_b) + (y_s - y_b)^{2/2} \quad (7-1)$$

$$T = T_1 + C_2(y_s - y_b)^5 \quad (7-2)$$

If the flow is below the bank then

$$A = C_1(y_s - y_d)^{2/2} \quad (7-3)$$

$$T = C_1(y_s - y_d) \quad (7-4)$$

where,

A = area of cross-section

T = top width

C₁ = channel side slopes below bank

C₂ = channel side slopes above bank

T₁ = channel top width at bank level

y_d = thalweg elevation

y_b = bank elevation

y_s = water surface elevation

Similar relationships were used in calculating the wetted parameter and the first moment of area about the water surface. Table 7.1 reflects the constants used for describing conveying and non-conveying section properties. A constant Manning's

CHANNEL CROSS-SECTION DEFINITIONS Implemented in Moving Element Model

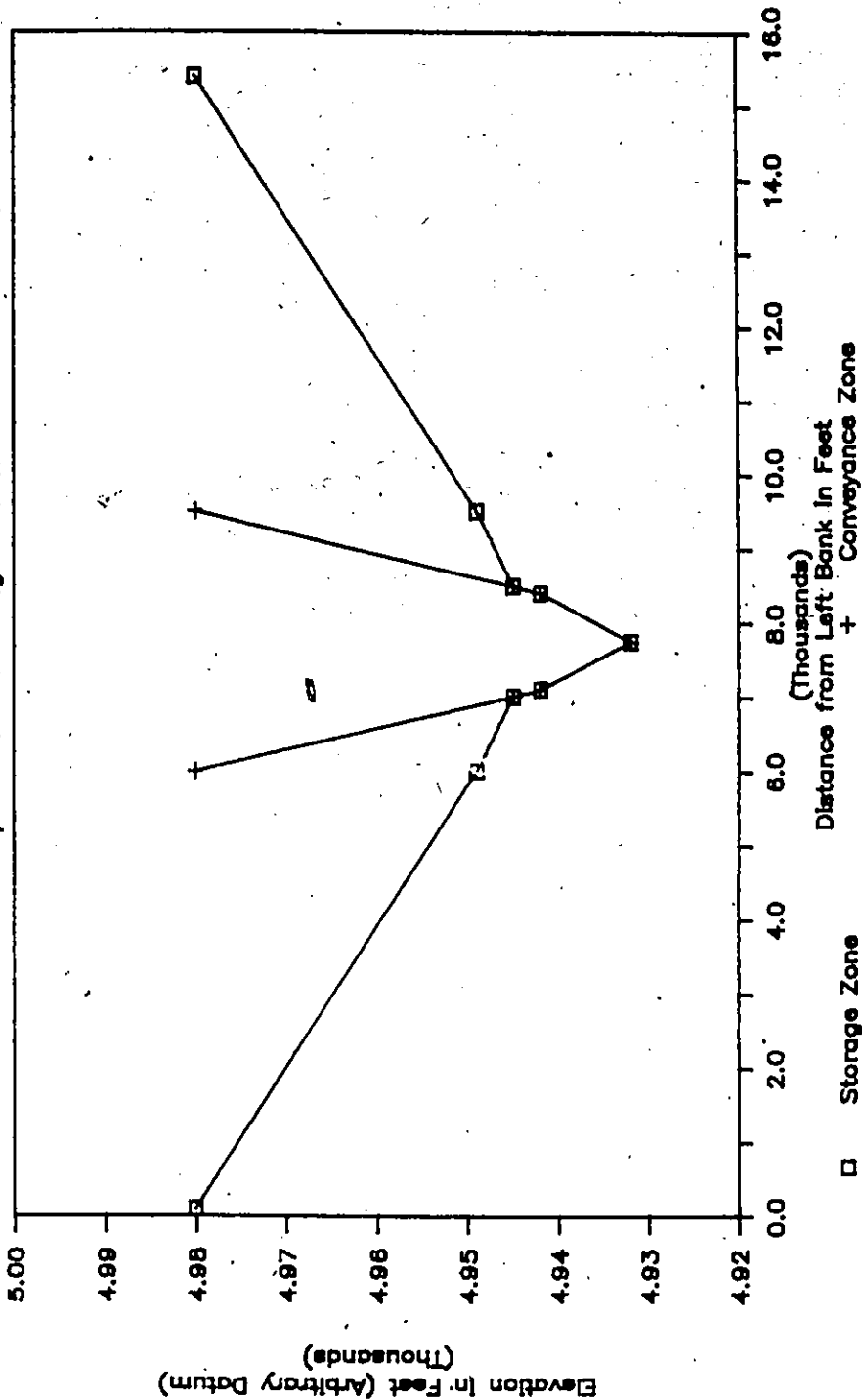


Fig. 7.2 Typical Channel Cross-section with Conveying and Storage Zones
Adopted for Moving Element Model

Table 7.1

Channel Properties for the Teton Dam Break Flood Model Teton Dam to Shelly Gauge Reach
Data Adopted from DAMBRK Model, Fread (1982)

No.	Location D/S of Teton Dam (Miles)	Thalweg Elevation (Feet)	Bank Elevation (Feet)	Storage Elevation (Feet)	Bank Topwidth (Feet)	Channel Side Slope	Overbank Side Slope	Storage Side Slope	Manning's Roughness Coeff.
1	0.0	5027.0	5050.0	5050.0	460.0	20.0	2.0	0.0	0.080
2	5.0	4965.0	4980.0	4980.0	420.0	28.0	4.5	53.0	0.050
3	8.5	4920.0	4930.0	4942.0	400.0	40.0	250.0	360.0	0.040
4	16.0	4837.0	4847.0	4847.0	440.0	44.0	420.0	500.0	0.034
5	22.5	4805.0	4814.0	4814.0	603.0	67.0	460.0	250.0	0.038
6	27.5	4788.0	4797.0	4802.0	144.0	36.0	300.0	310.0	0.037
7	32.5	4762.0	4774.0	4774.0	180.0	15.0	800.0	1090.0	0.034
8	37.5	4752.0	4763.0	4763.0	220.0	20.0	285.0	400.0	0.034
9	41.0	4741.0	4756.0	4756.0	270.0	13.5	195.0	195.0	0.034
10	43.0	4737.0	4749.0	4749.0	290.0	14.5	70.0	100.0	0.036
11	51.5	4654.0	4663.0	4663.0	175.0	12.5	2.3	0.0	0.036
12	59.5	4601.0	4612.0	4612.0	480.0	22.0	2.5	0.0	0.036

roughness coefficient was used at each section, these ranged from 0.08 in the canyon immediately downstream of the dam to 0.034 in the valley.

There was only one cross-section which caused some problem. This section was located at Mile 16.0 (that is, 16.0 miles below the dam). The thalweg elevation at this point differed by 20 feet between the data from DAMBRK and one reported by Gundlach and Smith (1977). This difference could be attributed to using two different forks of the stream in the valley. The moving element model was set up and run in both modes; this is reported in the following sections.

7.2.2 Initial and Boundary Conditions

Proper initial conditions are necessary to ensure that the numerical computations proceed as smoothly as possible. Similarly, the boundary conditions have to be formulated in such a way that trivial solutions are not obtained.

For this problem the Shelly Gaging station was assumed to have a single value stage-discharge relationship. This was a departure from the conditions used by DAMBRK where a looped rating curve was employed. The initial flow was assumed to be 13,000 cfs at all points. A depth of flow corresponding to 13,000 cfs was provided at the downstream boundary.

To calculate the initial flow depths, the backwater computation routine was invoked. This routine was referred to in Chapter 6.

The inflow hydrograph at the upstream boundary consisted of a table of time versus flow rate generated by a subroutine in the DAMBRK model. The inflow hydrograph rose sharply from 13,000 cfs to 1,684,000 cfs within 1.25 hours followed by an exponential decay over a period of 9.0 hours before a base flow of 13,000 cfs was restored. Despite the fact that the inflow hydrograph was of about 11 hours duration,

the computations were carried out for 50 hours to account for the passage of the peak flow through the system.

7.2.3 Model Set up

To simulate the Teton Dam failure hydrographs, the moving element model was initially set up for three different element sizes. These were 0.25, 0.5 and 1.0 mile. The model with 1.0 mile element size was too coarse and resulted in convergence problems due to highly nonlinear channel geometry variation. With the other two element sizes, the model operated reasonably; the time step requirements, however, for the 0.25 mile element size forced the execution times to be more than four times that for 0.5 mile element size and this element size was therefore abandoned. After establishing an element size of 0.5 mile, 120 nodes and 119 elements were required for the 59.5 mile reach.

Two different time steps were employed to route the hydrograph for the 50-hour period. During the first 10 hours, when the hydrograph is changing quite rapidly and velocities sufficiently large to violate the suggested criteria for the moving element scheme; consequently, a time step of 450 seconds was used. After 10 hours, the wave characteristics are reduced to that of a continuous flow problem, and the time step was doubled to 900 seconds without causing any convergence problem.

The model was executed at centered spatial and temporal weightings. The interpolation at the Eulerian regridding was obtained by the Three Point Lagrangian formula. When applying a numerical model to problems such as these, there are always several minor studies within the overall study to investigate certain aspects of the flow in exaggerated detail. In this study several items were considered, some were

not pursued and no discussion ensued, whereas others required further analysis and these discussions are presented in the next section.

For example, the model was initially set up with no division between the conveying and the non-conveying over bank section. Although the model worked, the timing of peak flow, peak flow rate and depth were not consistent with the observed values. This aspect of modelling is therefore not reported.

7.2.4 Discussion of Results

Following the passage of the flood, damage to natural features provided evidence of the peak stage achieved by the wave in the form of high water marks along the trees, buildings, bridge piers, etc. This information was subsequently surveyed and related to the geodetic bench marks. These data along with indirect establishment of hydrographs provided a basis of comparison. Initially, this was considered more than adequate. As the results were gradually analyzed, however, it was found that the field information could be duplicated by varying a number of different parameters due to uncertainties in data.

Some of these features are now discussed.

- a) Transition from canyon to valley: Although the moving element model produced no abnormal results, the sudden change in flow behavior in the valley may be an indicator of a control section at the canyon outlet. This is evident from the maximum flow envelope shown in Figure 7.3. If the grid is made finer by employing smaller element sizes and time steps, the results showed considerable improvements. This is discussed further in the next application.

TETON DAM FAILURE SIMULATION

Maximum Discharge Envelope

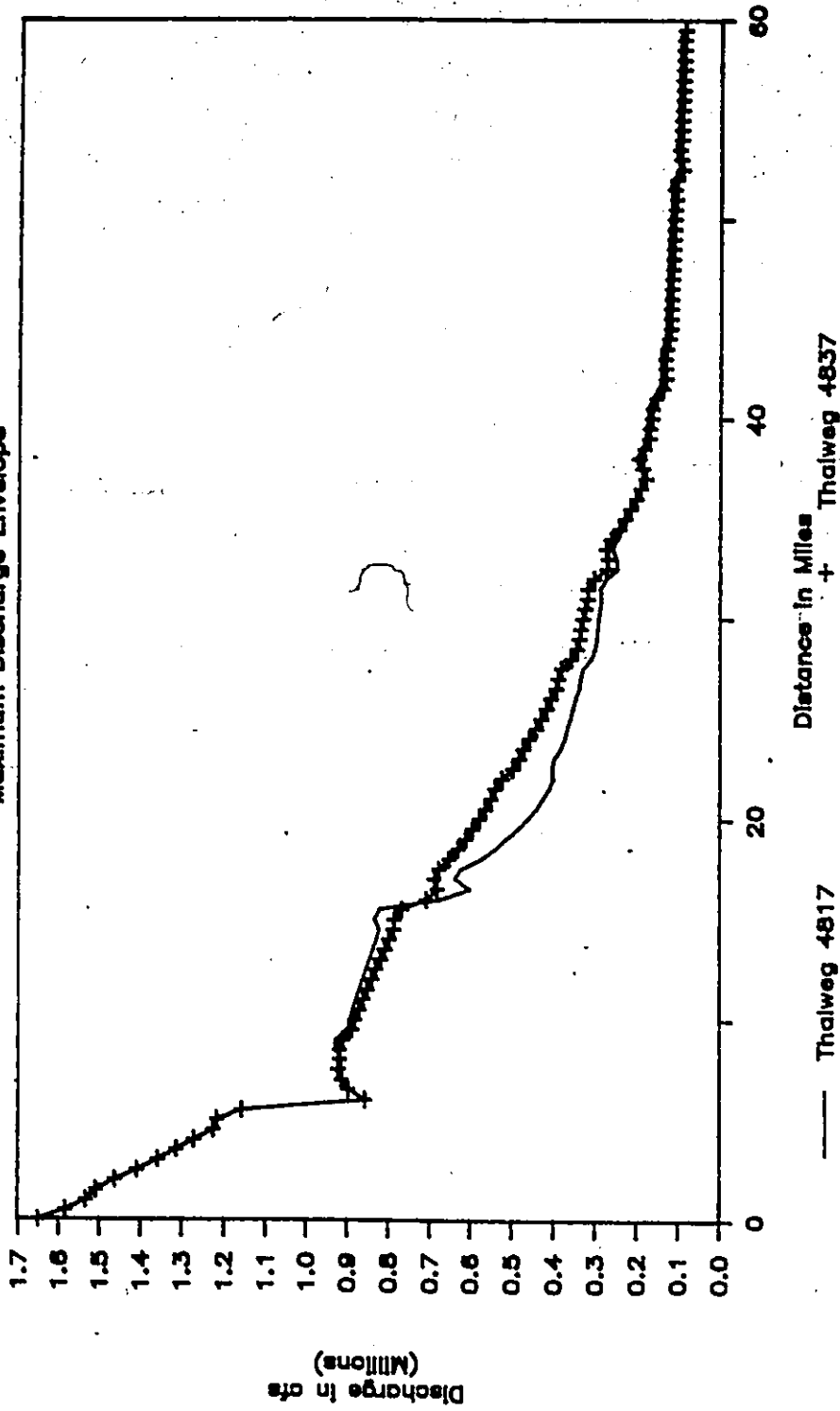


Fig. 7.3 Envelopes of Maximum Flows for Teton Dam Break Flood with Bed Elevations of 4817 and 4837 ft at Mile 16.0

- b) **Slope change at Mile 16.0:** As in the problem of the channel expansion, a sudden change in slope caused similar model performance. The logical reasoning for this behavior would be the same as for the previous case. To illustrate the problem, 3.5 miles of reach length was isolated and plotted along with the initial water surface profile and the state reached by operating the model at the initial flow rate of 13,000 cfs for 40 hours. The minor difference in profiles can be attributed to the fact that for computing the initial flow profile, the forces on the water body due to form changes are not included. This information is presented in Figure 7.4. It appears that the choking effect of the backwater stretching into the steeper reach extend about 0.5 mile into this steep sloped section.

This influence is evident in Figure 7.3 where the impact of slope changes due to alternate thalweg elevations of 4817 and 4837 ft are investigated. In this comparison, the flow does not 'dip' at the point of slope change for the higher thalweg at Mile 16.0. The results improve when a smaller space-time grid is utilized near the break in slopes.

- c) **Two dimensional flow in valley:** This is actually two problems in one. The first case of a pure two-dimensional flow nature is easily explained. There is considerable lateral water slope along with the natural longitudinal slope. Usually the impact of such lateral slope is not of great significance; in this case, however, the observed and surveyed elevations on the two banks differed by as much as 30 ft. Differences of such magnitudes in cross-elevations violates the basic assumptions of one-dimensional flow. In general, the existence of lateral flow components slows down the wave and affects the hydrograph in the lower reaches, the wave characteristics and

Profiles for Teton Dam Simulation

Break in Slope at 16 mile

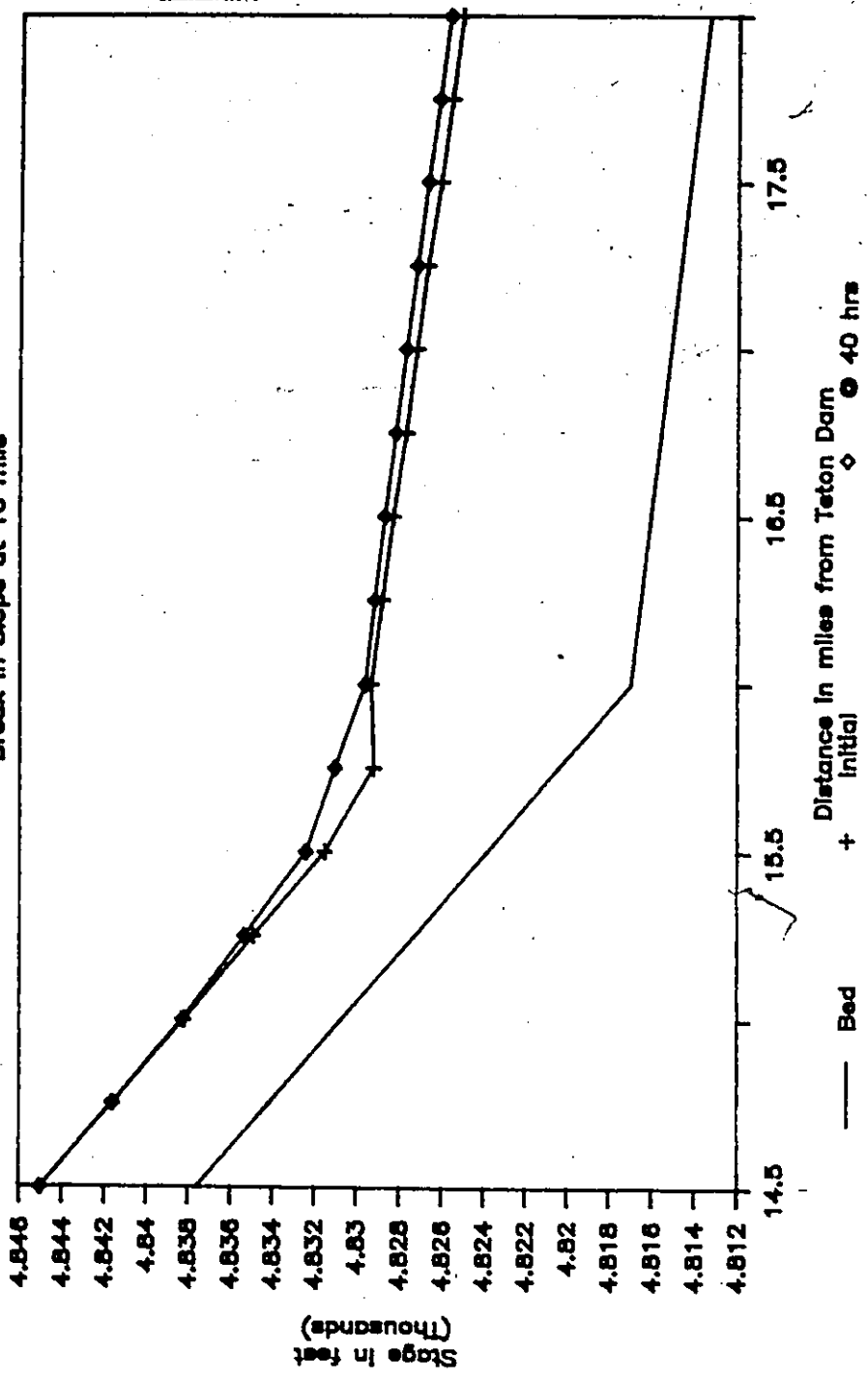


Fig. 7.4 Choking Provided by Steep to Mild Slope Change at Mile 16.0
- Steady State Profile

the hydrograph shape. All these unknowns are usually incorporated into the channel roughness coefficient.

The second aspect consists of lateral sloshing of water from one over-bank to other. This phenomenon is clearly noted in Table 7.2. The elevation differences, at the same site, between the left and right water edges varied between 10 to 30 ft.

- d) **Water loss due to infiltration:** When the flood waters start to inundate the dry valley bed, there is significant recharge into the groundwater system. With increased depths, the pressure head and consequently the infiltration rates are increased. Fread (1976) reported a value of 0.3 cfs/ft length of the valley. This estimate was arrived at by a trial and error process to match the indirectly measured discharges along the stream.
- e) **Definition of conveying and non-conveying off-channel storage areas:** This is yet another modelling activity which is best described by field observation of active flow and storage zones. The models are usually sensitive to the way conveyance area is defined in terms of peak flow rate, timing, stage or in other words, the entire shape of the hydrograph.

As noted earlier, all the data used were derived from Fread's DAMBRK model except by using two alternate thalweg elevations at Mile 16.0. The envelopes of maximum elevations along with the range of observations at various points are presented in Figures 7.5 and 7.6 for the two configurations. The comparisons between computed and observed values indicate an acceptable level of model performance.

The predicted depths of flow envelopes for the study are plotted in Figure 7.7 and demarcate the flow zones. For example, the canyon depths change rapidly until the wave emerges into the valley at Mile 5.0. The flow in the valley continues to

Table 7.2

Two-Dimensional Flow Aspects Following the Teton Dam Break
All Elevations in Feet Above Mean Sea Level

Location Number	Location D/S of Teton Dam (Miles)	Observed Elevation Right Bank	Observed Elevation Left Bank	Computed by Moving Element Model
1	5.5	5018.8	5013.3	5000.7
2	6.8	4983.5	4971.2	4977.4
3	8.1	4961.2	4963.7	4956.1
4	12.5	4903.7	4906.0	4901.5
5	13.6	4865.0	4895.0	4889.7
6	14.5	4845.0	4887.0	4878.1
7	17.2	4838.0	4860.0	4857.2
8	17.9	4837.5	4855.0	4851.7
9	19.6	4834.2	4847.0	4843.5
10	21.8	4825.0	4828.2	4830.7

TETON DAM FAILURE SIMULATION

Max. Stage Envelope, El 4817 at M16.0

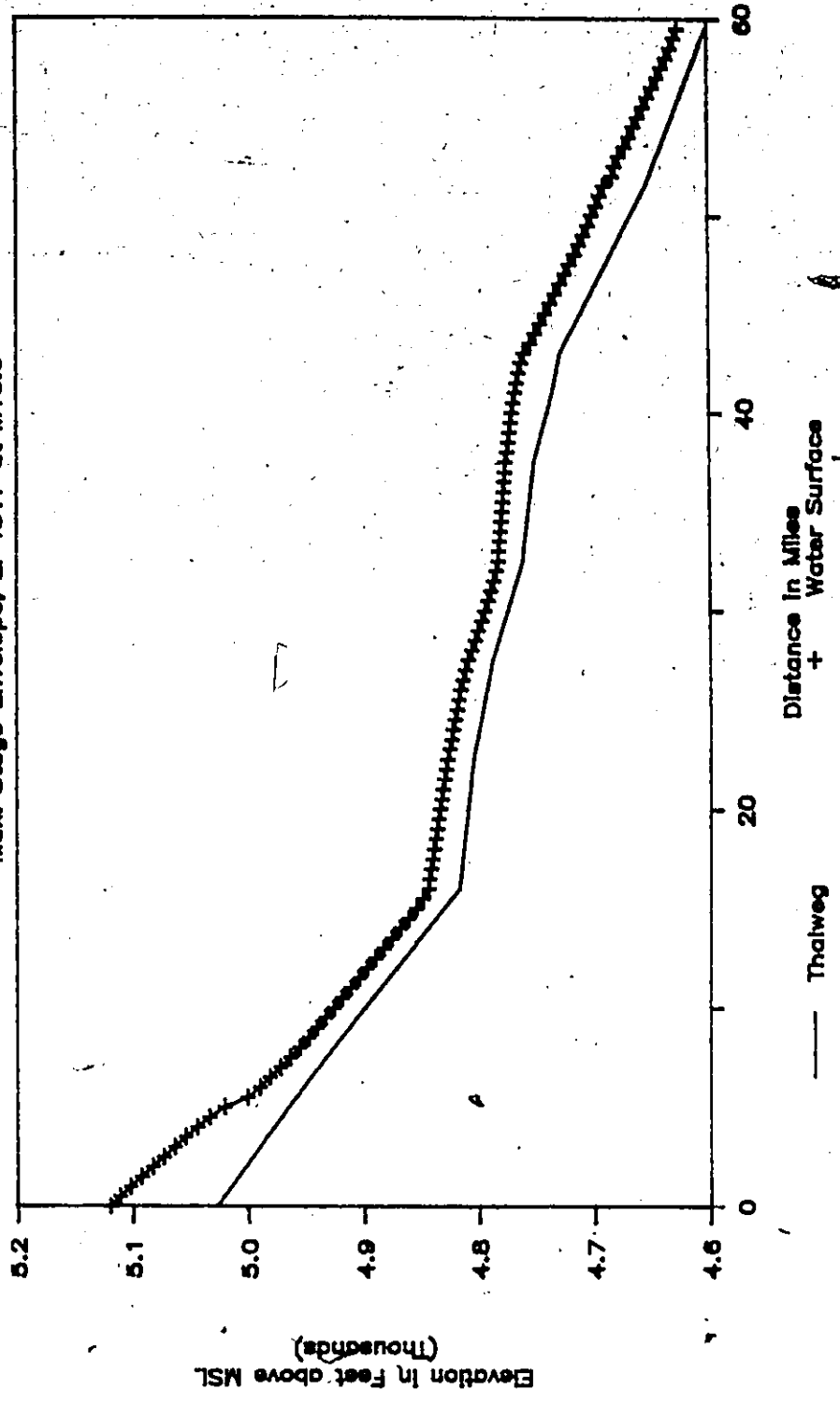


Fig. 7.5 Envelope of Maximum Elevations for Teton Dam Break Flood with Bed Elevation of 4817 ft at Mile 16.0

TETON DAM FAILURE SIMULATION

Max. Stage Envelope, El 4837 at M16.0

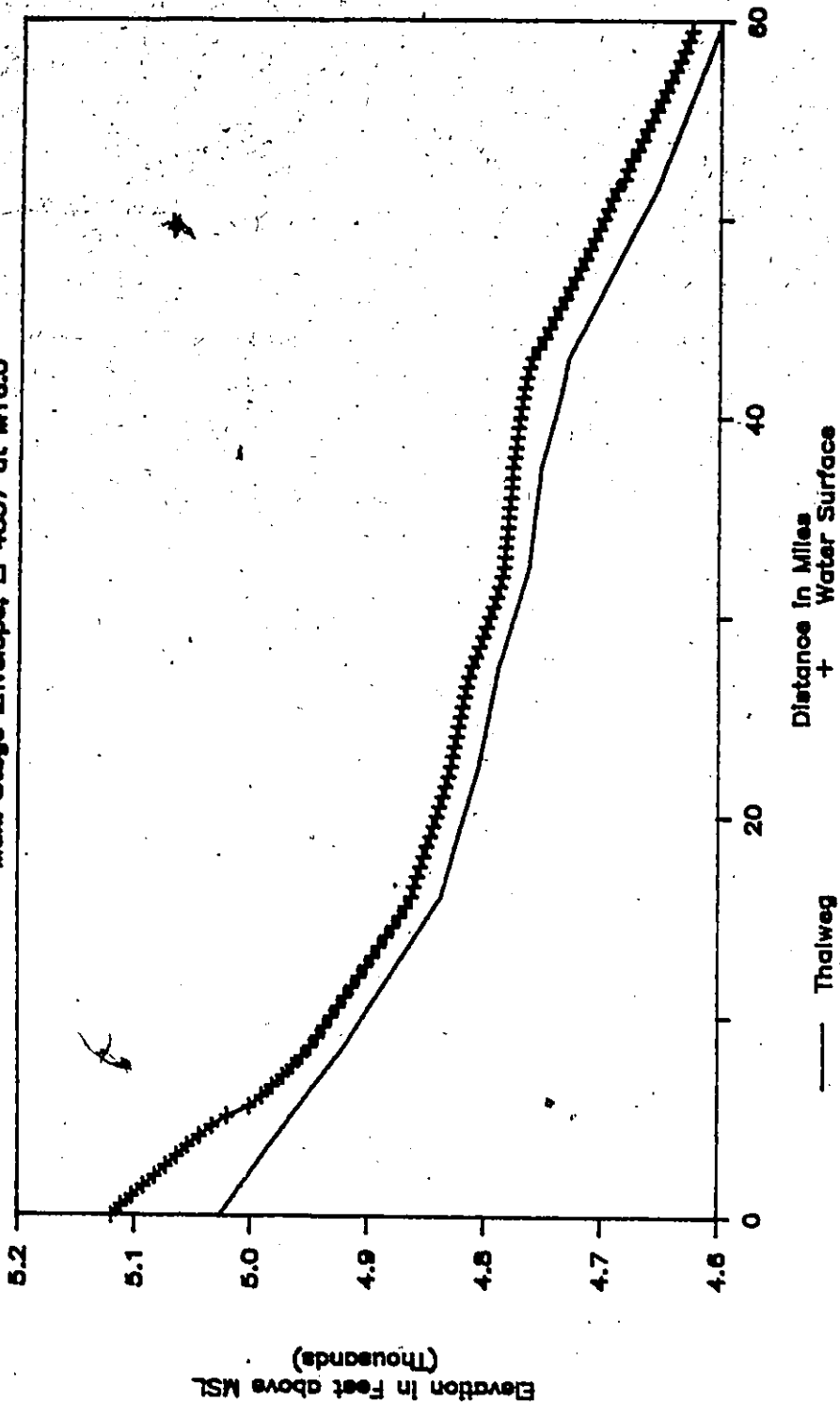


Fig. 7.6 Envelope of Maximum Elevations for Teton Dam Break Flood with Bed Elevation of 4837 ft at Mile 16.0

TETON DAM FAILURE SIMULATION

Maximum Depth Envelope

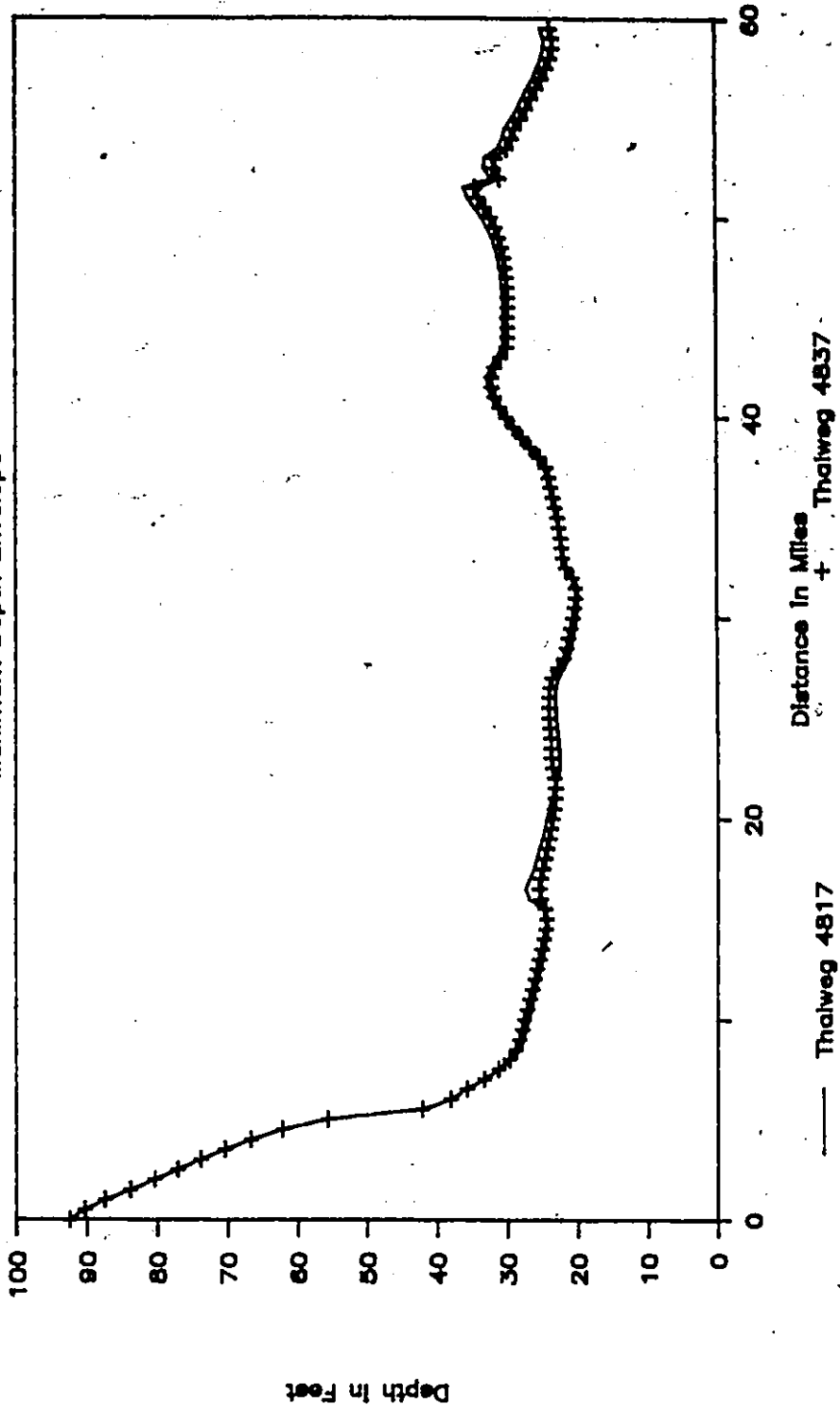


Fig. 7.7 Envelopes of Maximum Flow Depths for Teton Dam Break Flood with Bed Elevations of 4817 and 4837 ft at Mile 16.0

approximately Mile 40.0 beyond which the flood wave is again contained in the valley. This is represented by an increase in flow depth from Mile 40.0 to 59.5.

Figure 7.8 depicts the time of occurrence of peak depth at points along the river reach. These two curves refer to different thalweg elevations at Mile 16.0. As expected, the wave is slower when an elevation of 4817 ft is used at Mile 16.0. Similarly, the times to peak for discharge and depth are presented in Figure 7.9 for a thalweg elevation of 4817 ft. Here, again, the model predictions support field observations, not only in timings but also in algorithm behavior. Observations for mild sloped streams show a looped rating or hysteresis effect. That is, during the rising limb of a hydrograph, a smaller depth is required than on the recession limb for the same flow rate. This can be easily verified by analyzing the momentum terms. For the steep sloped portions of canyon and valley, the time of peak flow and depth do not differ sufficiently to allow visible separation at the scales at which these graphs are plotted. Once the wave enters the mild slopes beyond Mile 16.0 the differences become discernable. However, again at the downstream point the maximum depth and flow occur at the same time due to the forced condition of uniform flow at the downstream boundary.

The flow attenuation and lag characteristics of the model along with dispersion due to channel roughness were studied. This involved plotting flow hydrographs and stage graphs at 11 points along the solution domain. The flow hydrographs are shown in Figures 7.10 and 7.11, while Figures 7.12 and 7.13 present the stage graphs. For example, the flow rate is reduced by more than 50% within 8.5 miles of the dam or upstream boundary whereas by Mile 32.5, the dam-break flood more or less resembles a conventional flood hydrograph. The dispersive of channel roughness is obvious. The time to peak flow is only 1.25 hour at the upstream

TETON DAM FAILURE SIMULATION

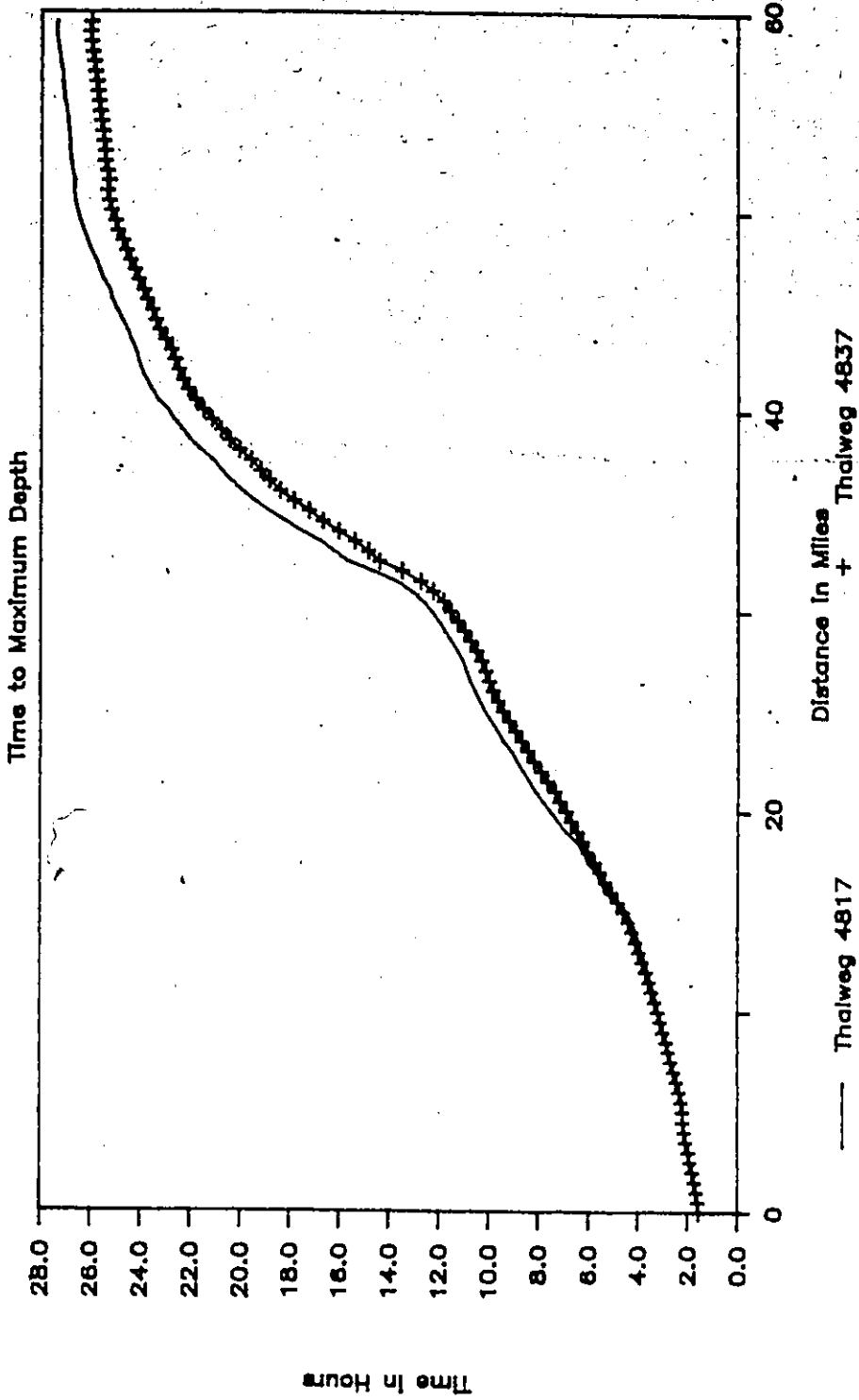


Fig. 7.8 Times of Maximum Elevation for Teton Dam Break Flood with Bed Elevations of 4817 and 4837 ft at Mile 16.0

TETON DAM FAILURE SIMULATION

Time to Max. Depth/Flow, El 4817 at M16

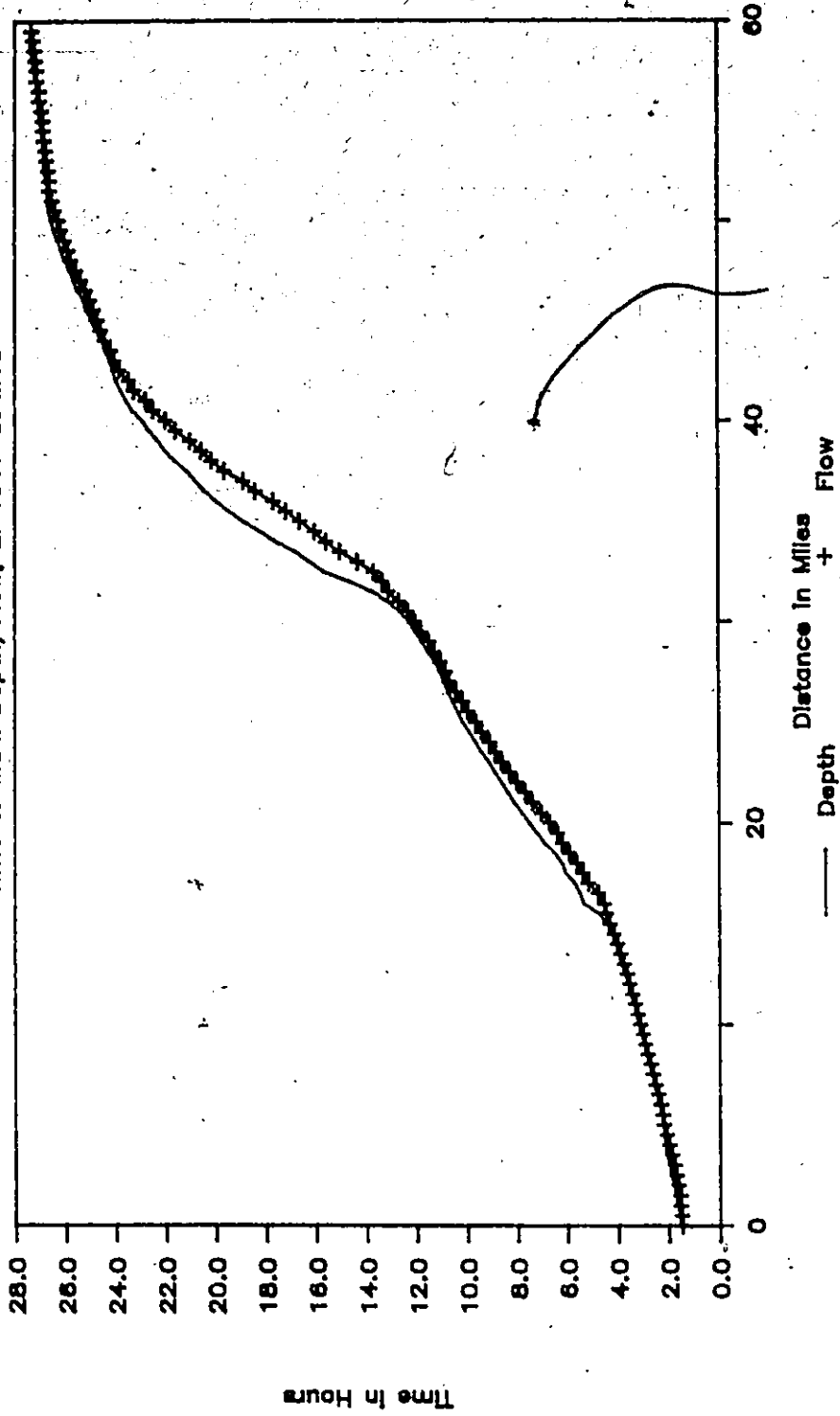


Fig. 7.9 Times for Maximum Elevation and Discharge for Teton Dam Break Flood

TETON DAMBREAK SIMULATION - HYDROGRAPHS

$\Delta x = 0.5$ Mile, $\Delta t = 450$ s, $\theta = 0.5$

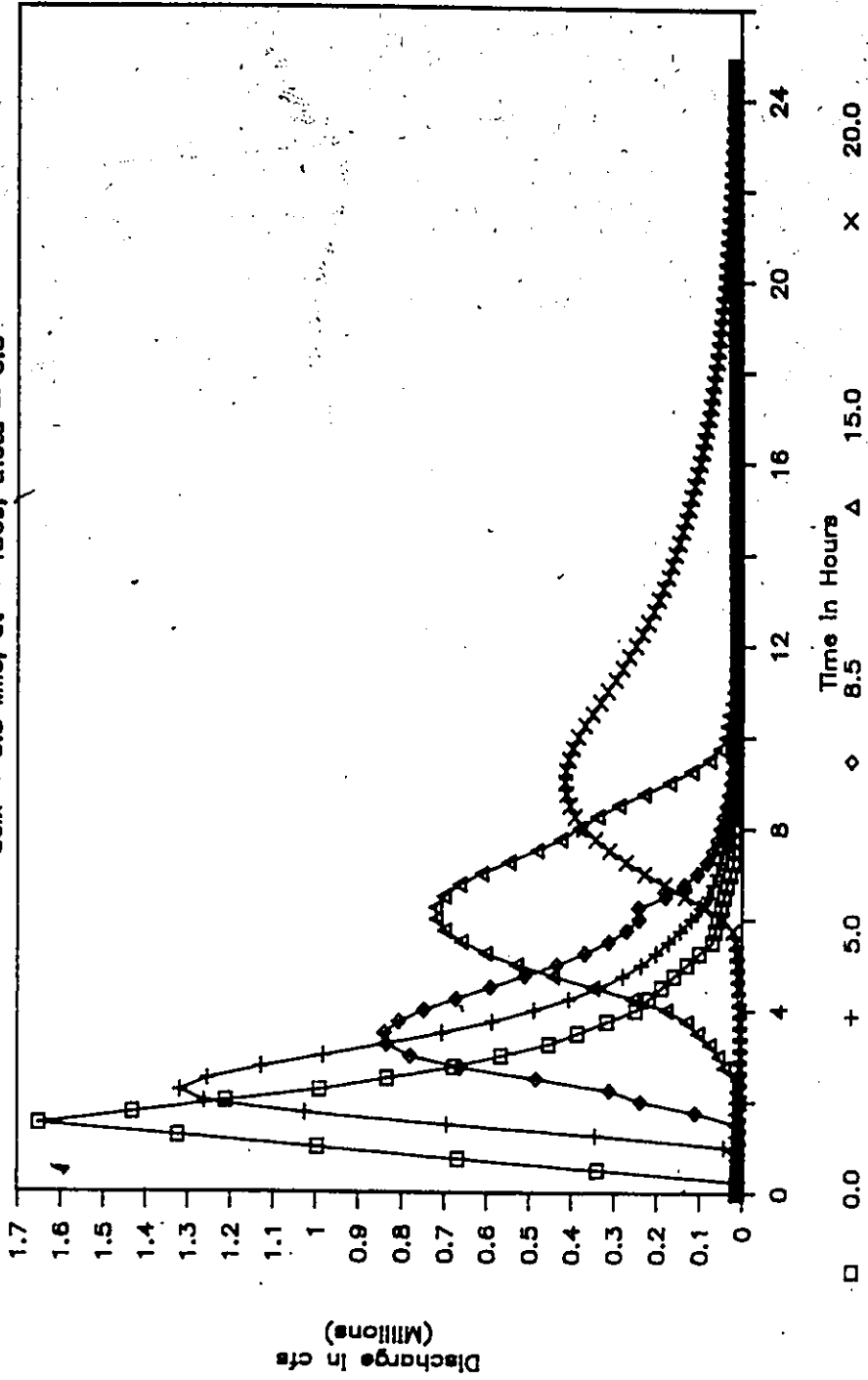


Fig. 7.10 Flow Attenuation and Lag for Teton Dam Break Flood - Mile 0.0 to 20.0

TETON DAMBREAK SIMULATION — HYDROGRAPHS

$dx = 0.5$ Mile, $dt = 900$ s, $\theta = 0.5$

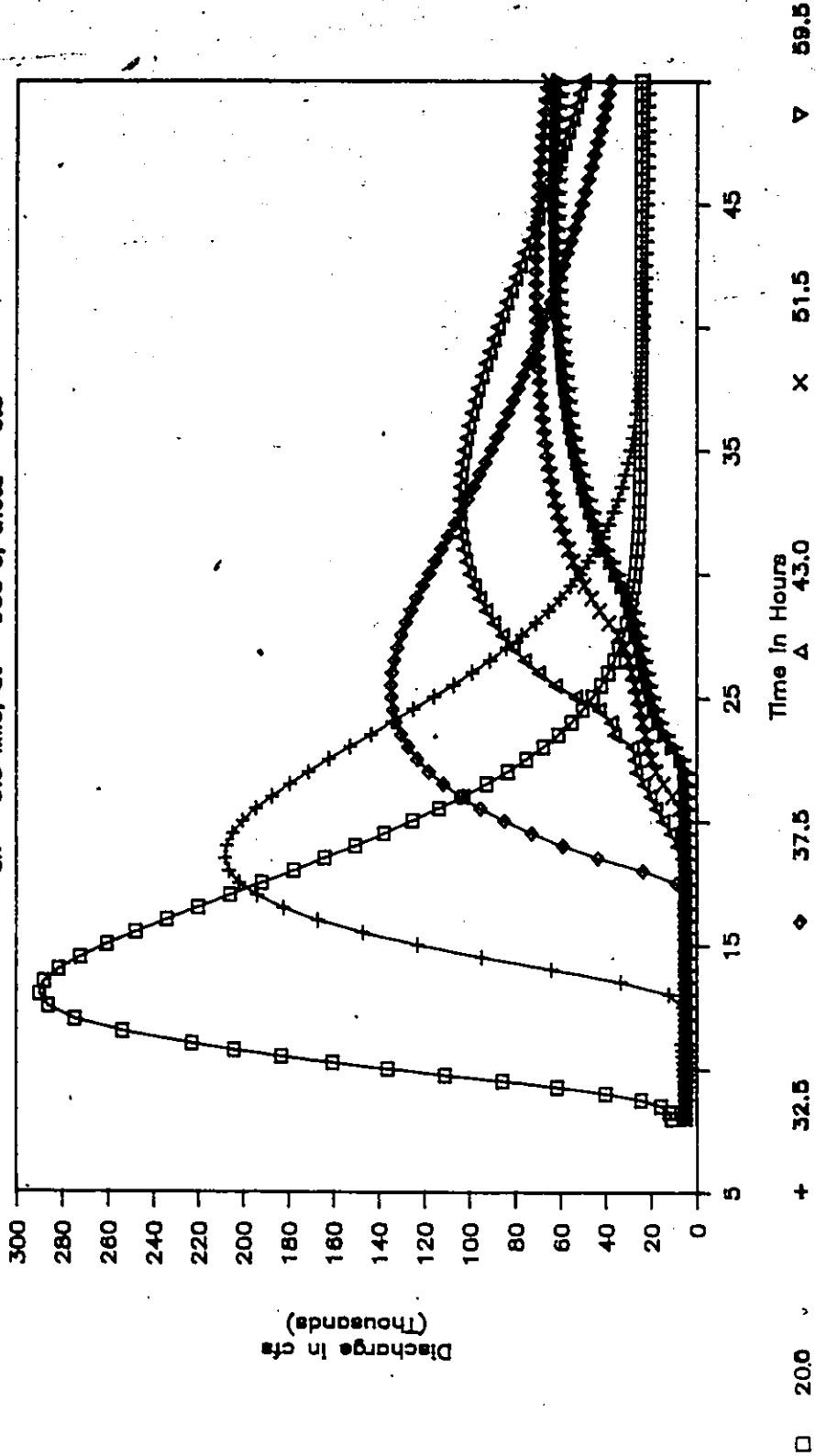


Fig. 7.11 Flow Attenuation and Lag for Teton Dam Break Flood - Mile 20.0 to 59.5

TETON DAMBREAK SIMULATION -- STAGEGRAPHS

delx = 0.5 Mile, dt = 450s, theta = 0.5

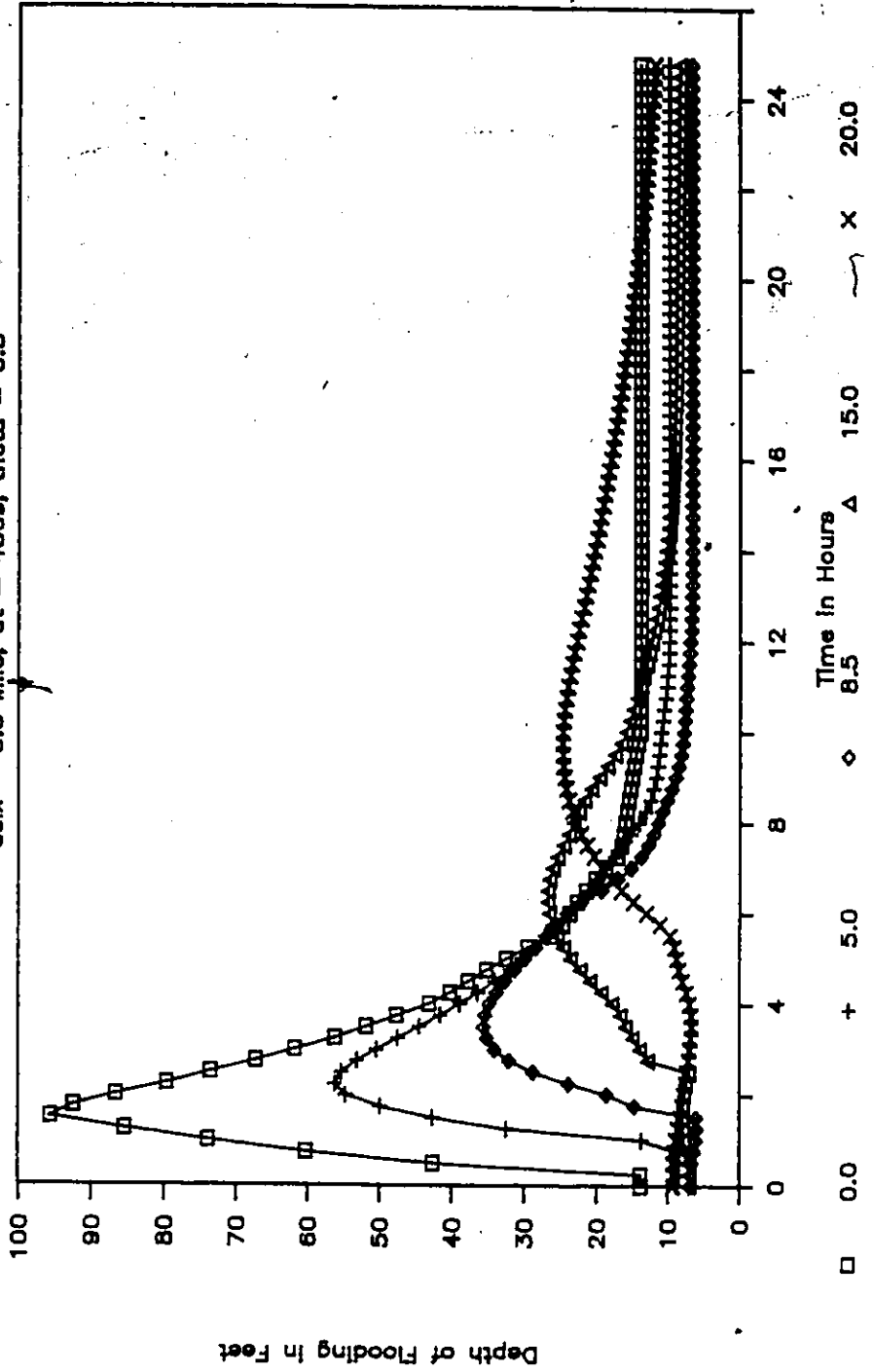


Fig. 7.12 Stage Hydrographs for Teton Dam Break Flood Mile 0.0 to 20.0

TETON DAMBREAK SIMULATION - STAGEGRAPHS

$dx = 0.5$ Mile, $dt = 900$ s, $\theta = 0.5$

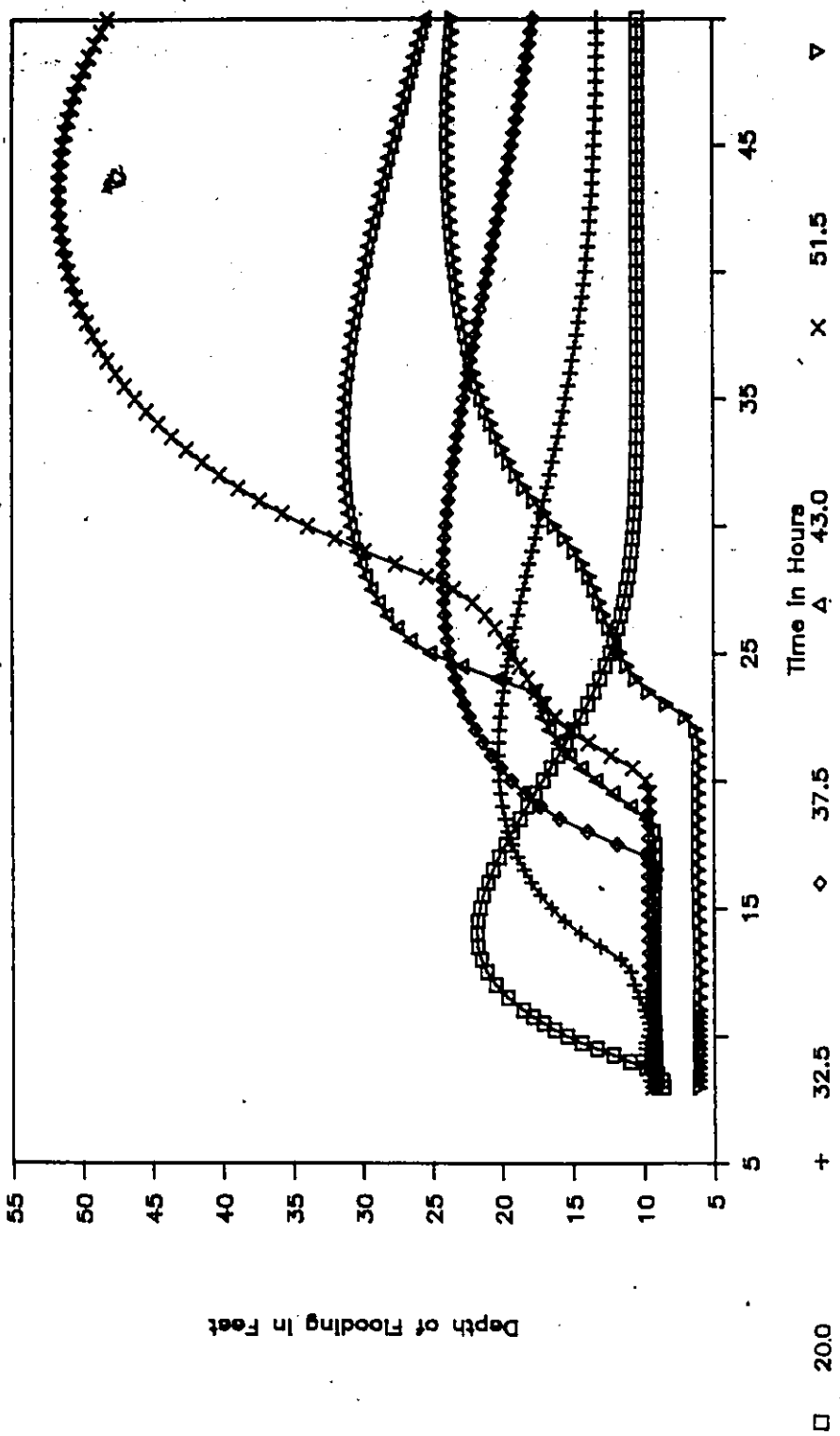


Fig. 7.13 Stage Hydrographs for Teton Dam Break Flood Mile 20.0 to 59.5

boundary but this grows to over 7.0 hours after travelling only 32.5 miles. The changes are not as dramatic for the stage hydrographs, although the depth of flooding characteristics remain uniform. The water depths in the canyon near the source of dambreak are in excess of 80 ft while in the valley region, these exhibit normal flooding behaviour with changes of 15 to 20 ft.

7.3 Teton Dam Failure Flood Simulation with Prismatic Channel

An extensive evaluation of available dambreak flood routing models was carried out by Wurbs (1986). While comparing the model results employing different programs with observed and indirectly measured data, this deficiency of like to like evaluations was evident. This precipitated from the need of modifying the field data to operate a given model. In order to make a better judgement on the model performance, Wurbs designed a hypothetical problem around the Teton Dam failure hydrograph. The same model was adopted for the present study and performance was compared with results reported by Wurbs.

7.3.1 Channel Description

Wurbs employed two reaches of prismatic channels as shown in Figures 7.14 and 7.15. The upstream prismatic section reach is five miles long and is generally representative of the canyon below the Teton Dam. The downstream prismatic section reach is 40 miles long and is connected to the upstream reach a five-mile long transition reach. The channel has a uniform bed slope of 10 ft/mile which is the same as for the upper reaches below the Teton Dam.

Thus, the only part which bears any resemblance to the field conditions are the first five miles of the model: the wide valleys were replaced by a much narrower

TETON FLOOD IN PRISMATIC CHANNEL

Channel Cross--Section Mile 0.0 to 5.0

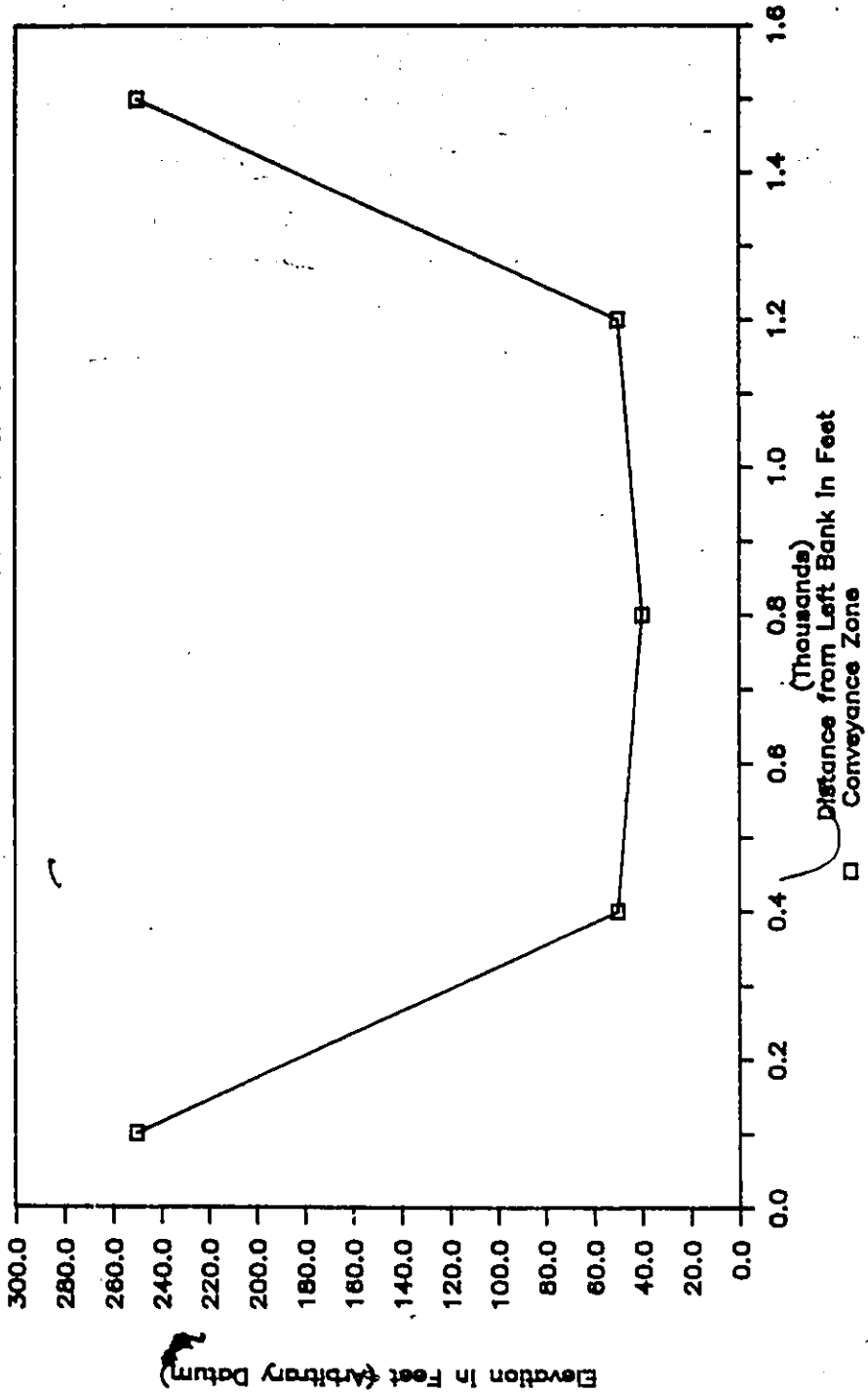


Fig. 7.14 Prismatic Channel Cross-section with Teton Dam Break Flood
- Mile 0.0 to 5.0

TETON FLOOD IN PRISMATIC CHANNEL

Channel Cross-Section Mile 10.0 to 50.0

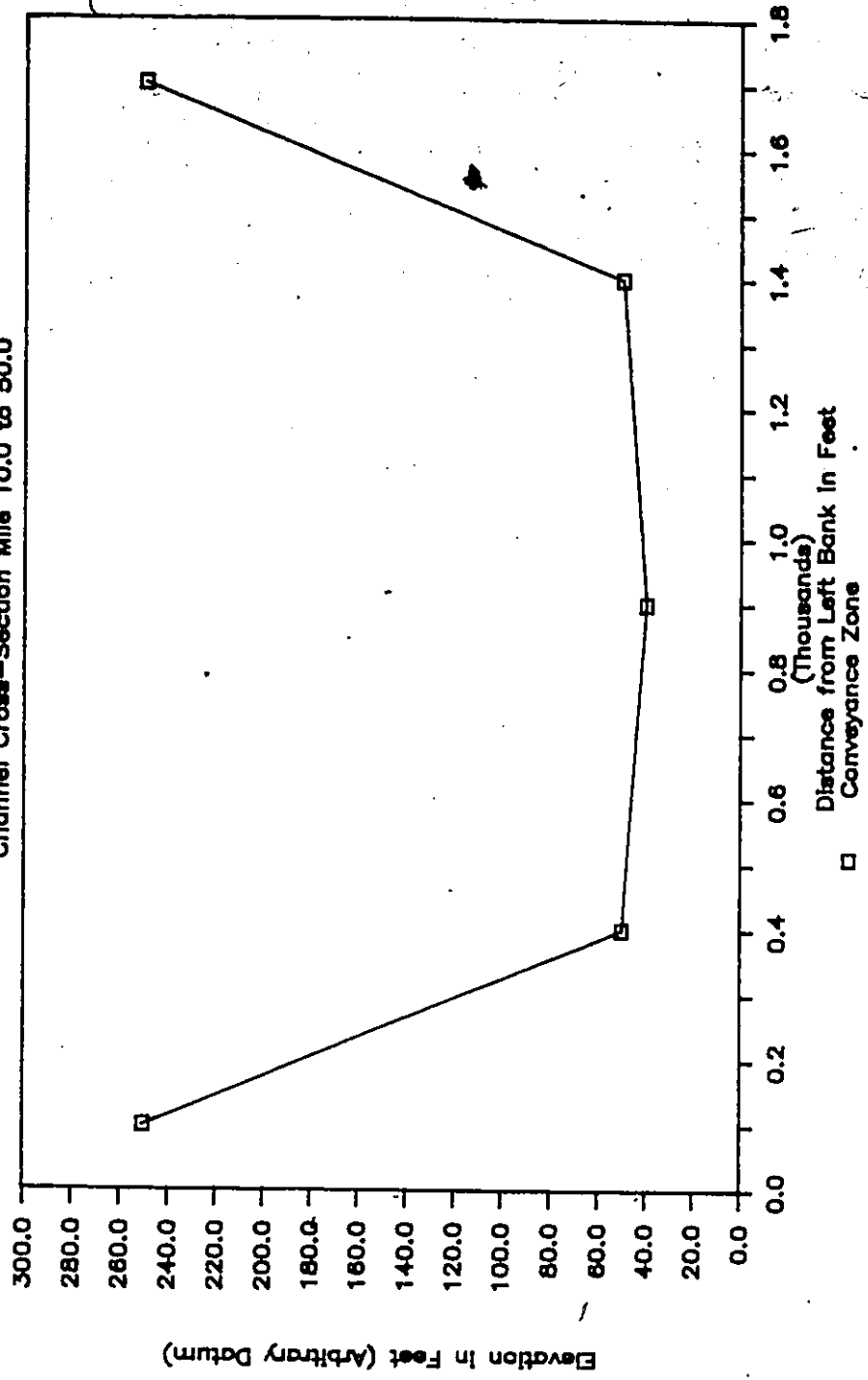


Fig 7.15 Prismatic Channel Cross-section with Teton Dam Break Flood - Mile 10.0 to 50.0

section. The Manning's roughness coefficient was assumed to be constant and equal to 0.04.

7.3.2 Initial and Boundary Conditions

The initial conditions are based on a uniform flow of 13,000 cfs throughout the study reach. The downstream boundary was defined by a single value uniform flow boundary.

The upstream boundary condition is defined by a discharge hydrograph based on a synthesized Teton Dam failure estimates. This hydrograph is significantly larger and steeper than the one employed in Section 7.2. The peak flow rate, for instance, is 3,841,000 cfs and attained in one hour. The flow reduces back to 13,000 cfs exponentially in the next five hours. This flow was maintained for a further four hours to facilitate the routing of the flood wave through the study reach.

7.3.3 Model Set-up

The model was discretized into 100 elements each 0.5 mile long and two different time steps were used. For the first five hours, a time step of 180 seconds was employed while for the remainder of simulation time, the time step was doubled to 360 seconds.

The moving element model was operated in the Eulerian-Lagrangian mode. For this test case an alternate form of momentum equation was implemented based on the non-divergent form of the equation. This provided some insight into the sensitivity of the results to employing the non-divergent form of equations and resulting difference in computed elevations.

7.3.4 Discussion of Results

As noted in the previous section, employment of the two moving element models, namely, for the divergent and non-divergent based equations, provided two sets of results. These results were compared with the prediction from other tests carried out by Wurbs (1986). Wurbs reported the results at seven salient points consisting of flow depth, flow rate and the time for peak depth. Of a number of models evaluated, the results for DAMBRK, the finite difference based model and SMPDBK, a storage routing based model are compared in this section.

The maximum depth envelopes are plotted in Figure 7.16 for the divergent model (depicted as MED) and the non-divergent model (MEND). There is a difference of almost eight feet between the divergent and non-divergent schemes with the former registering the greater depths.

Similarly, Figure 7.17 presents the envelopes for maximum flows. The non-divergent scheme shows greater attenuation than the divergent model. For example for the divergent model, the flow attenuates from 3.841 million cfs at the upstream boundary to 2.57 million cfs at a distance of 50 miles downstream whereas for the non-divergent scheme the flow reduces to 2.29 million cfs. The latter compares favorably with the simple dambreak model; the depths and flows predicted by the DAMBRK model are considerably lower.

As the flow attenuates faster for the non-divergent model, the flood waves travel at similar speeds for the two schemes. The time to peak depths are plotted in Figure 7.18 and compared with other models. The predictions of the moving element model indicate results similar to those obtained using the finite difference models.

COMPARISON FOR PRISMATIC TEST CASE

Prismatic (Teton X-Section) Channel

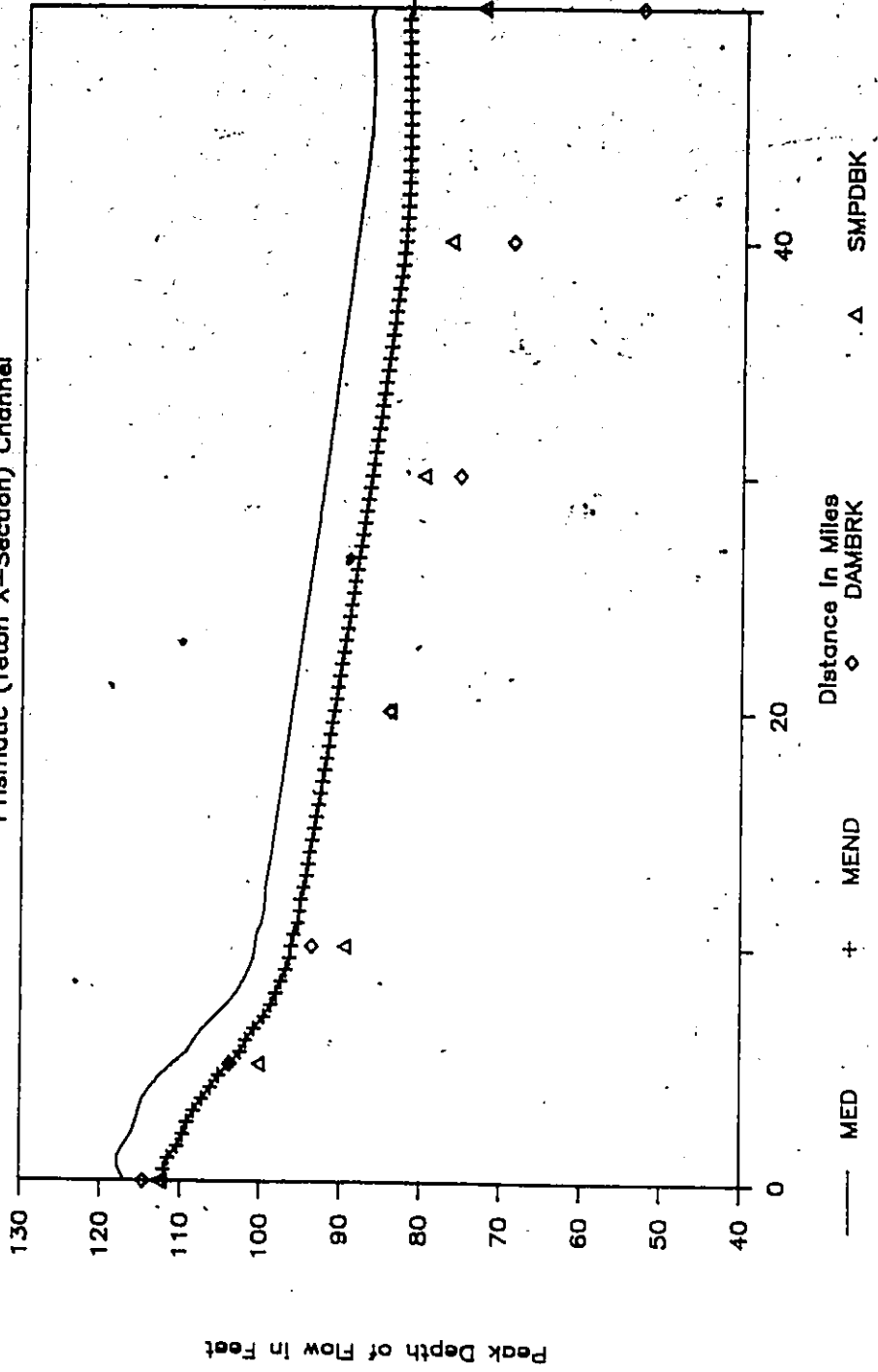


Fig. 7.16 Comparison of Moving Element Models (Divergent and Non-Divergent) with DAMBRK and SMPDBK for Maximum Depths

COMPARISON FOR PRISMATIC TEST CASE

Prismatic (Teton X-Section) Channel

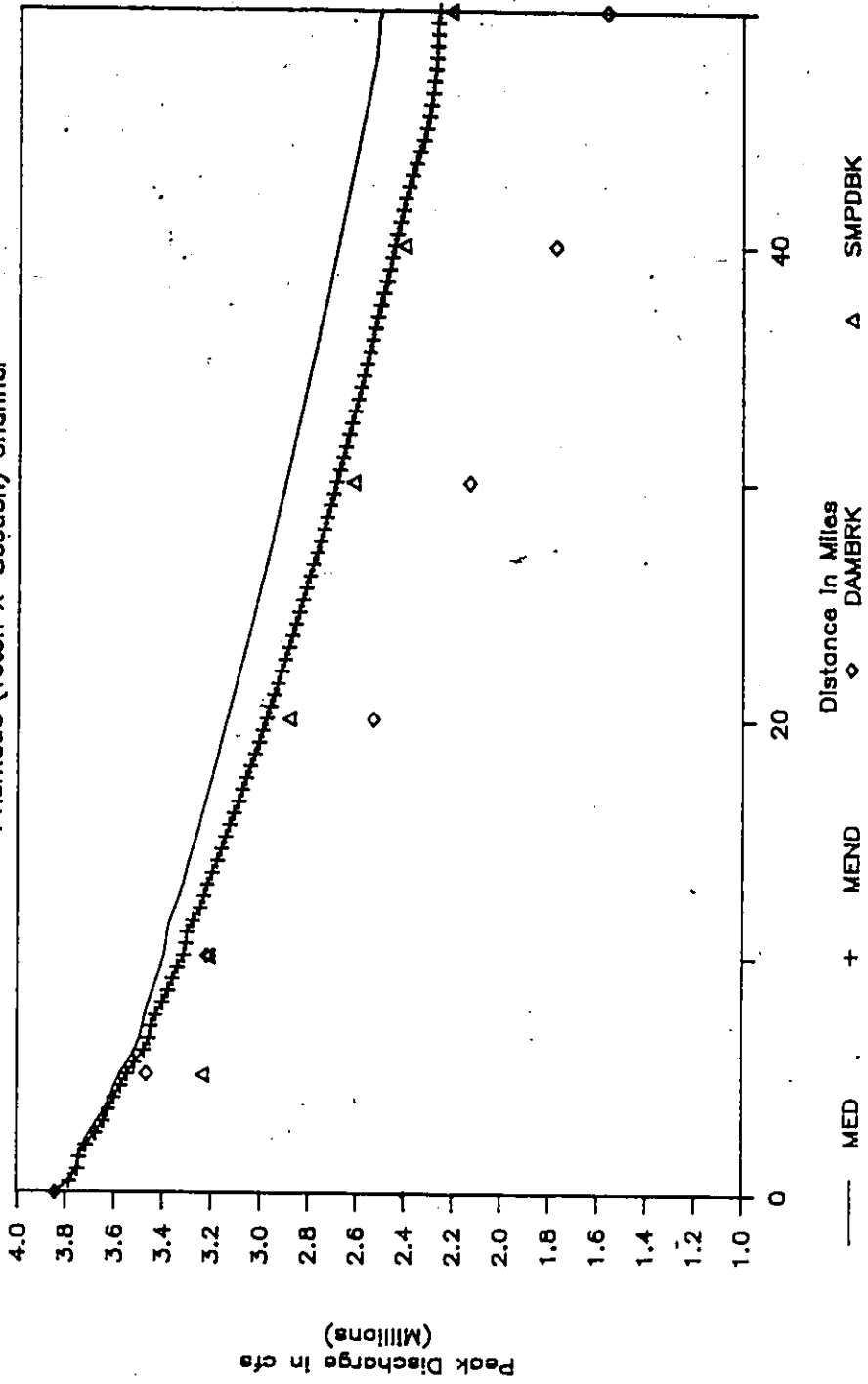


Fig. 7.17 Comparison of Moving Element Models (Divergent and Non-Divergent) with DAMBRK and SMPDBK for Maximum Discharges

COMPARISON FOR PRISMATIC TEST CASE

Prismatic (Teton X-Section) Channel

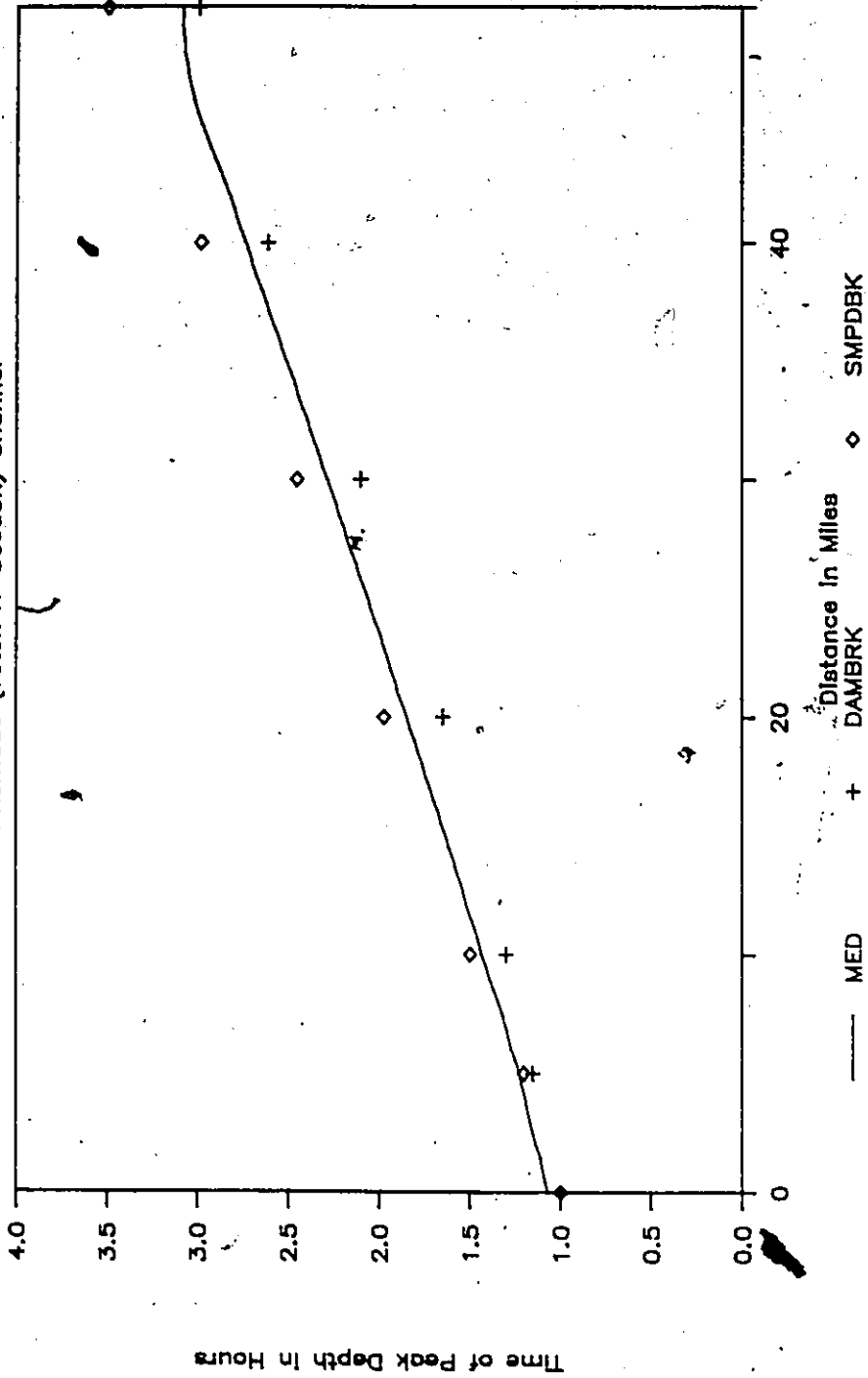


Fig. 7.18 Comparison of Moving Element Model with DAMBRK and SMPDBK for Times to Maximum Depth

7.4 Teton Dam Failure Hydrograph on Mild Sloped Non-Prismatic Channel:

When the Teton Dam failure simulation was carried out, the channel exhibited a variety of slopes ranging from about 12 ft/mile to 6 ft/mile. There were no sections which were flat enough to adequately test the moving element model's behavior in presence of highly non-prismatic cross-sections such as those of the Teton Valley. Wurbs (1986) addressed this problem by studying a hypothetical dam failure for the Stillhouse Hollow Dam in central Texas. The channel below this dam, however, was well-defined with gently varying valley topography with an average bed slope of 5.4 feet/mile (0.001).

To allow a broad range of conditions to be studied, even the Stillhouse Hollow Dam's (hypothetical) failure does not present features which are sufficiently demanding for model testing. These data were therefore not used. As a hypothetical dam-break event was desired for modelling, it was decided to impose a more severe test to evaluate the model results. This testing also allowed some sensitivity analysis to be used along with comparison with earlier studies.

7.4.1 Channel Description

As the objective of this exercise was to study the flood wave movement over a highly non-prismatic channel with very mild bed slope, a hypothetical model was set up with real topographical data. The measured part of data for the model consist of channel cross-sections from the Teton Dam failure simulation while the assumed part required the bed slope of the channel to be maintained at nearly flat 1.0 ft/mile (0.000189).

With this information, the model was set for the first sixteen miles and using the four cross-sections at Mile 0.0, 5.0, 8.5 and 16.0. A Manning's roughness coefficient of 0.04 was used for the first two sections and 0.034 for the remaining two. The active channel and off-channel storage areas were divided in a similar fashion to the Teton Dam failure study and cross-sections presented in Appendix I.

The above configuration allowed a study to be made of the impact of lateral expansion on a mild sloped channel, namely, the sudden expansion of the canyon into the wide valley. Further, as only hypothetical floods were to be simulated, it allowed testing of a variety of conditions and limited sensitivity analysis.

7.4.2 Initial and Boundary Conditions:

The initial conditions consist of a base flow of 13,000 cfs at all points. The depths corresponding to these flows were computed by the backwater routine. At the downstream boundary the depth reflected the uniform flow conditions.

The upstream boundary was a flow hydrograph identical to the one described in Section 7.2. Also as before, a single flow rating curve was employed at the downstream boundary. The hydrograph duration was 20 hours.

7.4.3 Model Set-up

As the modelling length was only 16 miles, this permitted a variety of element lengths to be studied. Three different sizes of 0.125 mile, 0.25 mile and 0.5 mile were employed. These three element sizes require respectively 129, 65 and 33 nodes. Two different time steps of 45 and 90 seconds were used in the simulations. The former was utilized for all three element lengths while the larger time step was used with 0.25 and 0.5 mile time step.

The moving element model with the above configuration was operated in the Eulerian-Lagrangian mode. Flow hydrographs were captured at six points. Furthermore, separate stage and flow hydrographs were computed at Mile 15.0. This permitted comparison with steep slope model for the Teton Dam failure at the same location.

7.4.4 Discussion of Results

Results for all the above variations provide interesting insights into the flow mechanics at the channel expansion at Mile 5.0. Comparisons of the maximum stage envelopes for the three element sizes and two time steps are presented in Figures 7.19 to 7.21. It is quite obvious that in a general sense a coarse grid model yields which results are inferior to those from the fine grid model. This difference is critical at the point where the canyon expands into the wide valley.

At the expansion the water surface profile has a slope of approximately 20 ft/mile (0.0038) compared to only 1.0 ft/mile (0.000189) for the channel bed. As expected, the profile for the finer grid model is relatively smoother than for the other models. From a practical and operational standpoint, the results from the finer element size (Figure 7.19) compare adequately with the model of 0.25 mile element size, Figure 7.20.

More dramatic in presentation are the maximum flow envelopes for the stage profiles discussed above. These are shown in Figures 7.22 to 7.24. For the coarse grid model, presented in Figure 7.24, the results indicate a rather abnormal model performance which gradually subsides as the grid is made finer. Again, this erratic behavior is more pronounced just downstream of the channel expansion. An improvement in results with the employments of finer grids supports the argument

TETON X-SECN, SLOPE=1/5280, EXPANSION

DELX=0.125 M, DELT=45 S, THETA=0.5

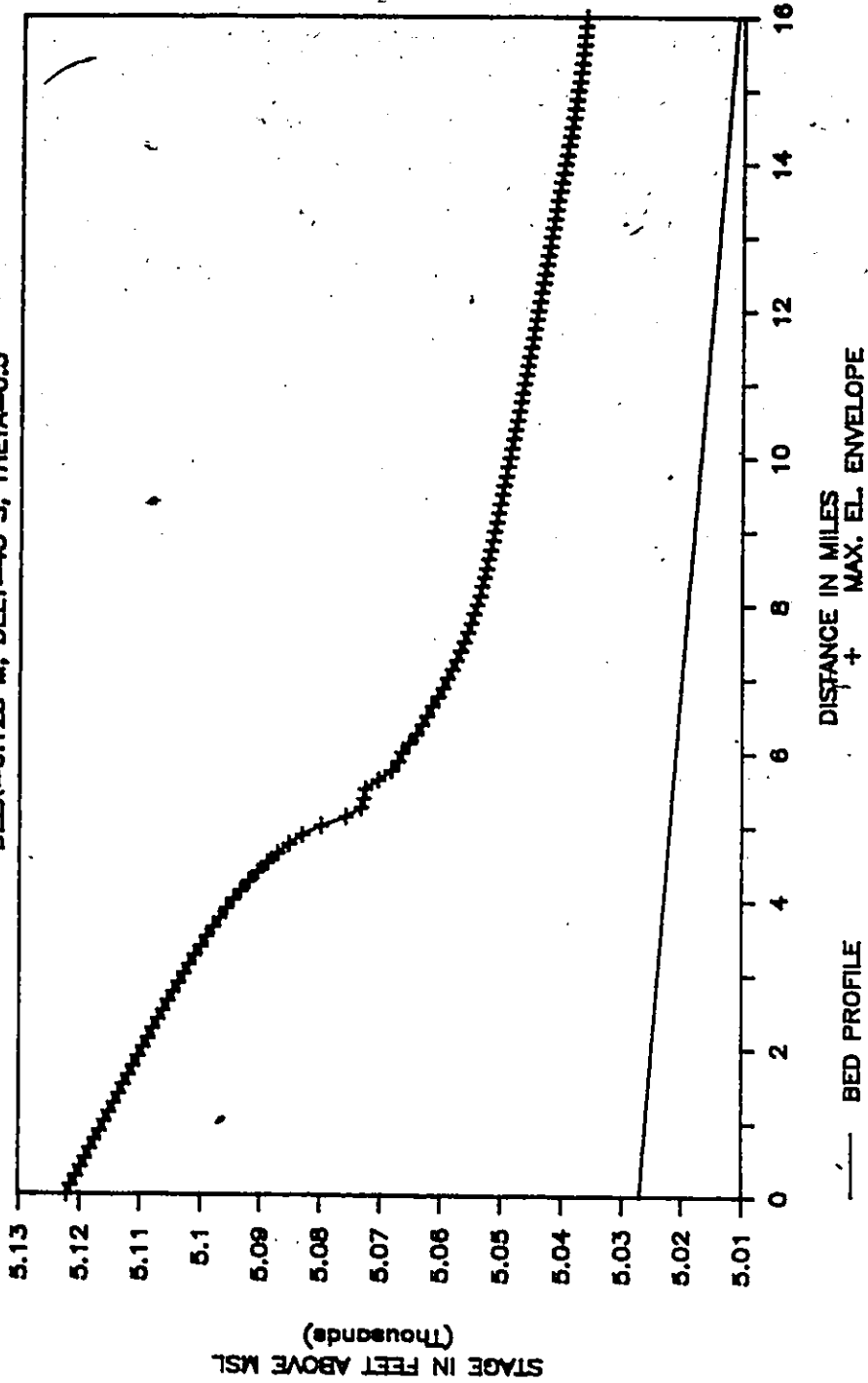


Fig. 7.19 Envelope of Maximum Elevation for Teton River Channel Cross-section and Dam Break Hydrographs on a Mild Sloped Channel

TETON X-SECN, SLOPE=1/5280, EXPANSION

DELX=0.25 M, DELT=45 & 90 S, THETA=0.5

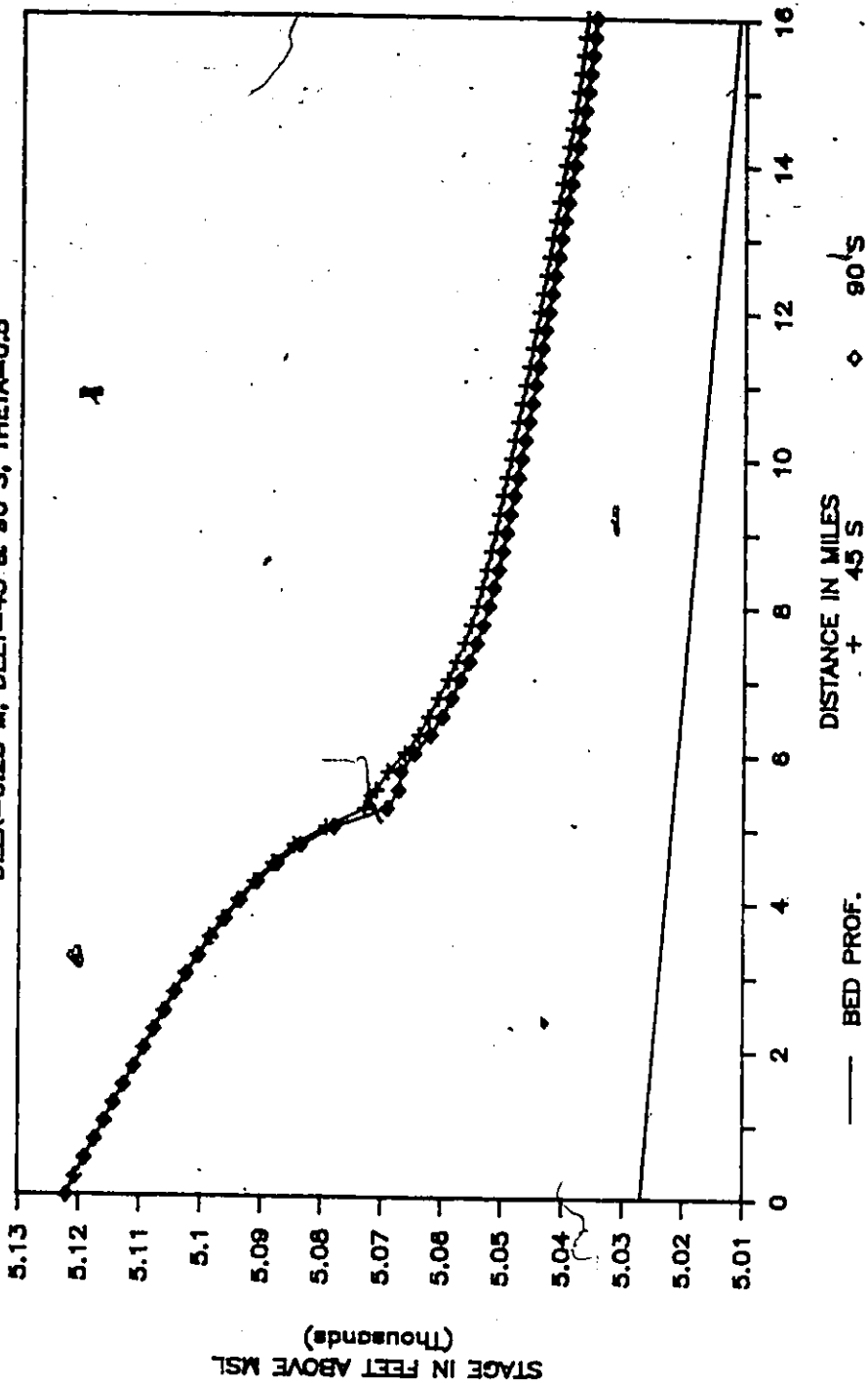


Fig. 7.20 Envelope of Maximum Elevation for Teton River Channel Cross-section and Dam Break Hydrographs on a Mild Sloped Channel

TETON X-SECN, SLOPE=1/5280, EXPANSION
 DELX=0.5 M, DELT=45 & 90 S, THETA=0.5

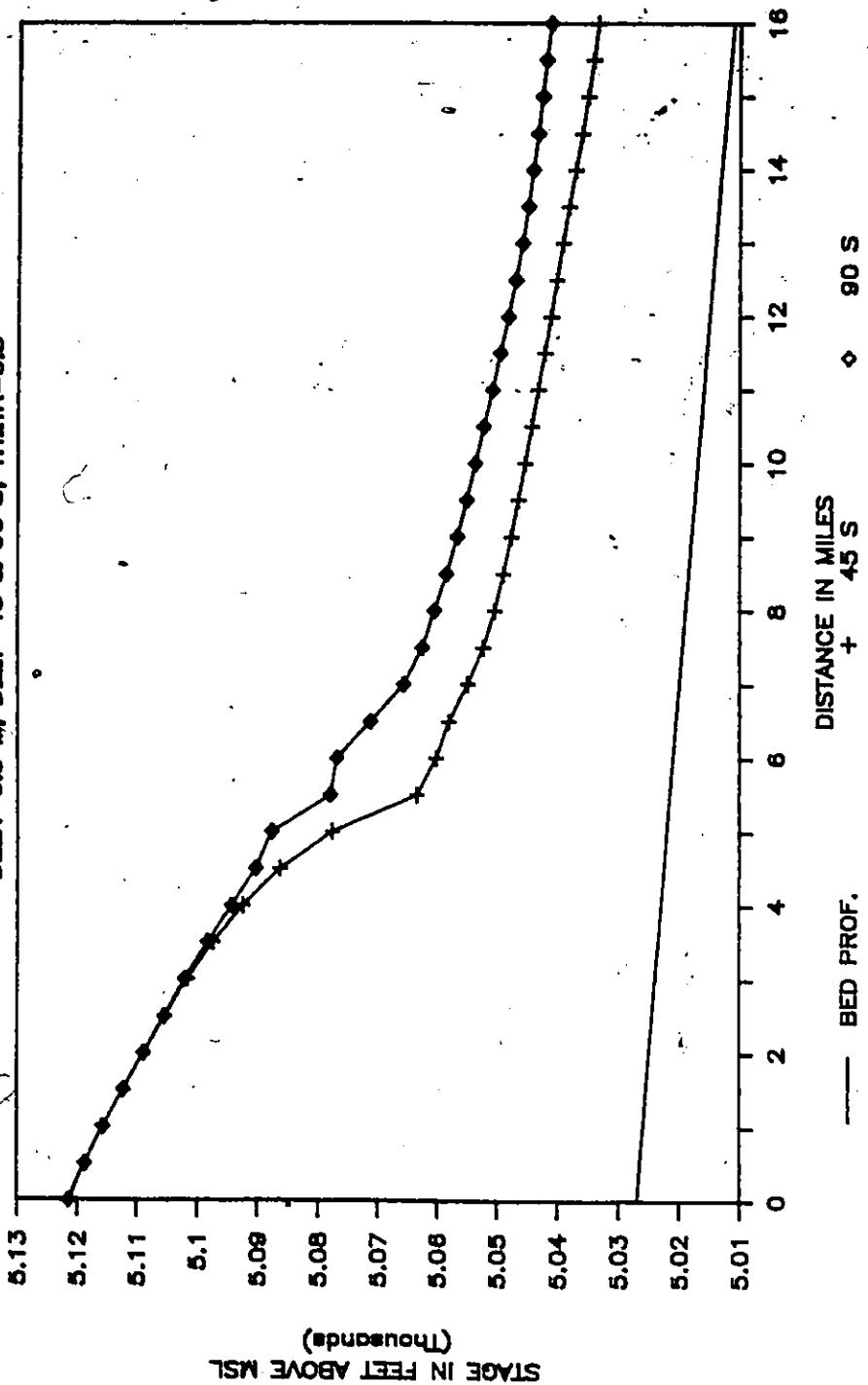


Fig. 7.21 Envelope of Maximum Elevation for Teton River Channel Cross-section and Dam Break Hydrographs on a Mild Sloped Channel

TETON X-SECN, SLOPE=1/5280, EXPANSION DELTA=0.125 M, DELT=45 S, THETA=0.5

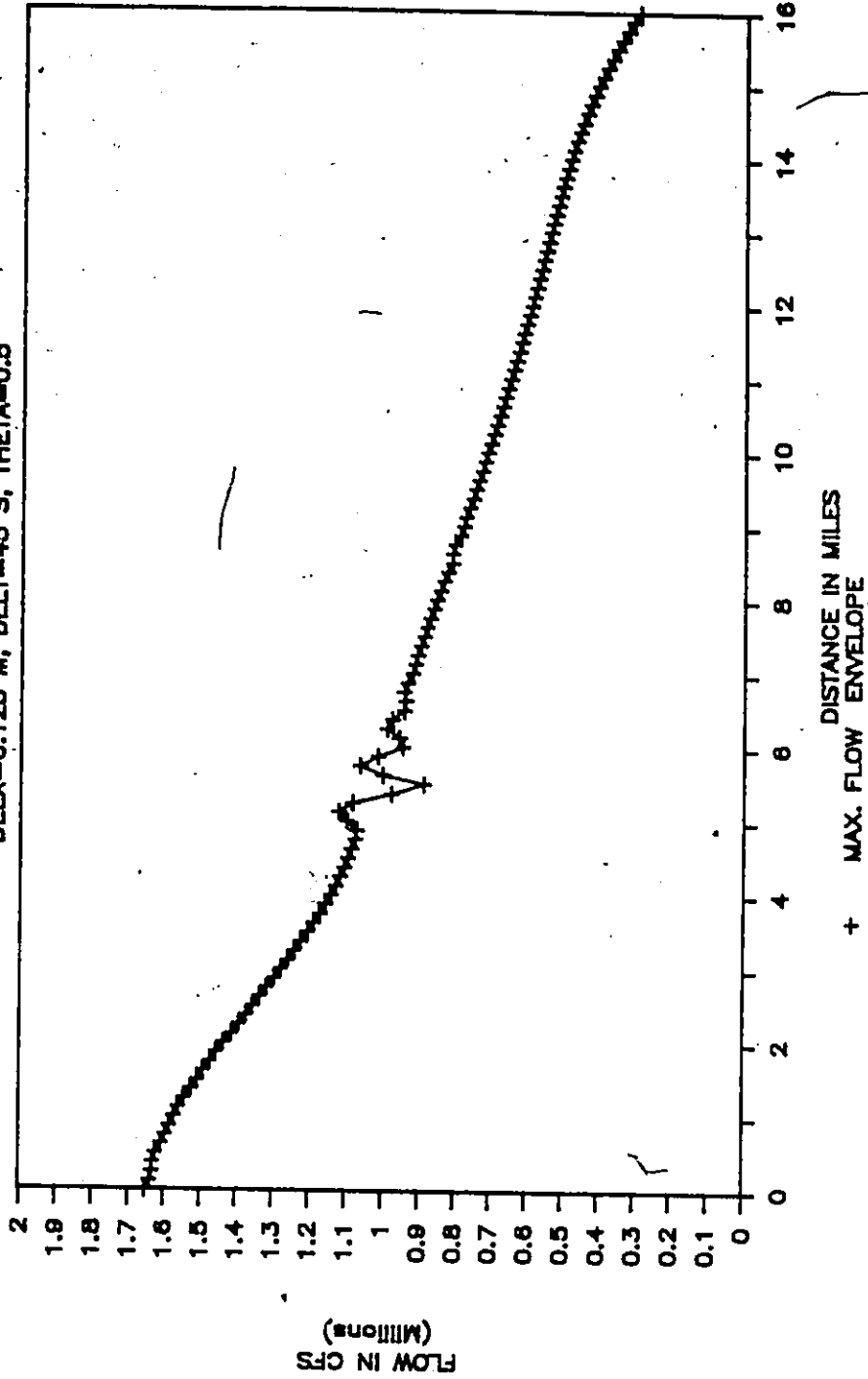


Fig. 7.22 Envelope of Maximum Discharge for Teton River Channel Cross-section and Dam Break Hydrographs on a Mild Sloped Channel

TETON X-SECN, SLOPE=1/5280, EXPANSION

DELX=0.25 M, DELT=45 & 90 S, THETA=0.5

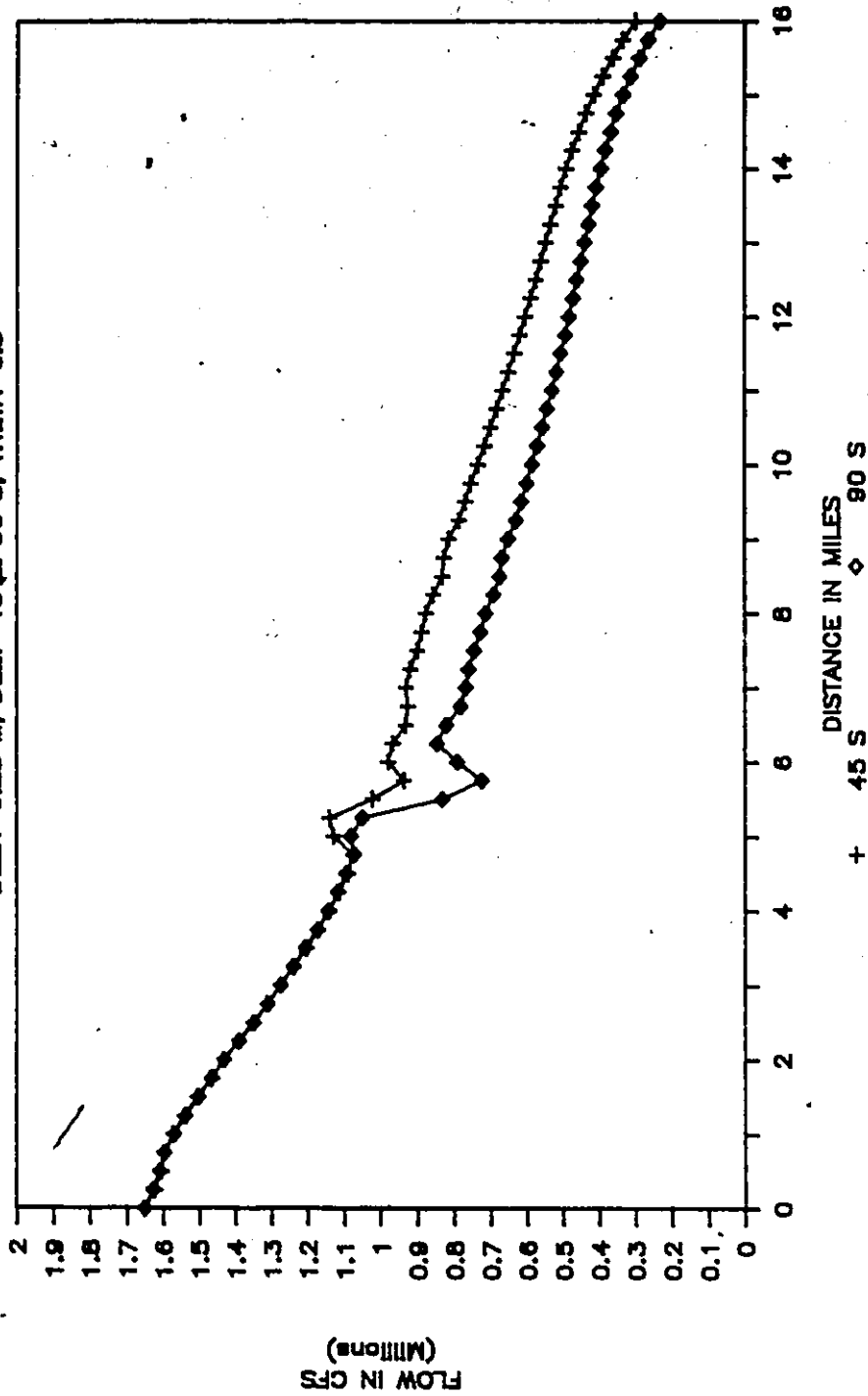


Fig. 7.23 Envelope of Maximum Discharge for Teton River Channel Cross-section and Dam Break Hydrographs on a Mild Sloped Channel

TETON X-SECN, SLOPE=1/5280, EXPANSION

DELX=0.5 M, DELT=45 & 90 S, THETA=0.5

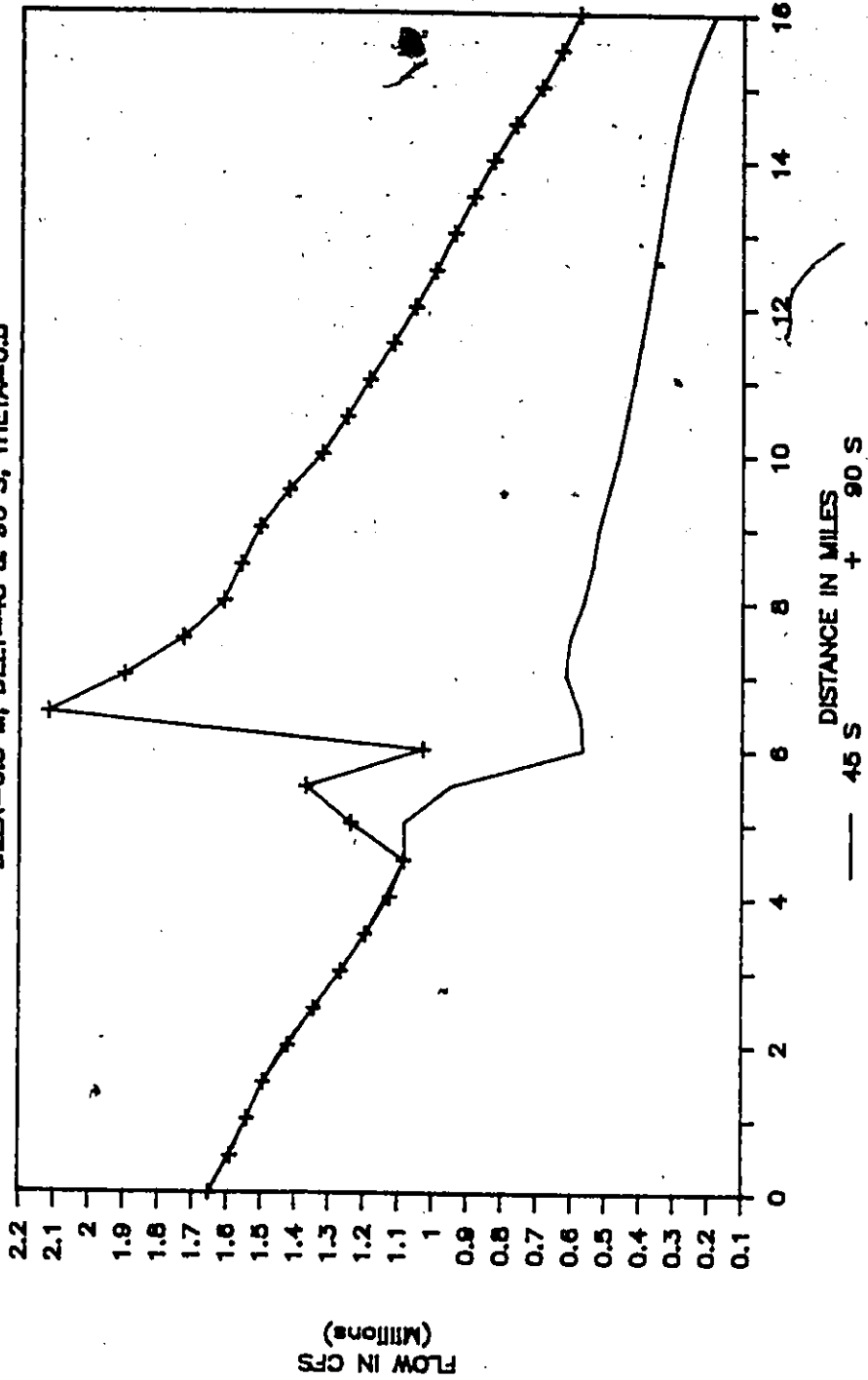


Fig. 7.24 Envelope of Maximum Discharge for Teton River Channel Cross-section and Dam Break Hydrographs on a Mild Sloped Channel

that a large proportion of problems can be directly addressed by refining the model resolution.

Figures 7.25 and 7.26 demonstrate the model behavior in the areas of wave attenuation and translation. The mild slope shows much higher rates of wave attenuation. For example, the flow is reduced by a factor of six within 16 miles for the mild channel; the same attenuation was reached only after 32 miles for the Teton Dam failure described in Section 7.2. Similar observations can be made with respect to the stage hydrographs in Figure 7.26.

A direct comparison was made between the steep-bed model with results from this exercise. Recall that the channel bed profile for the Teton Dam failure (Section 7.2) has a slope of approximately 10 ft/mile (0.00189). Also as noted previously, flow and depth hydrographs were captured at Mile 15.0 for the two models and plotted respectively in Figures 7.27 and 7.28. In order to obtain a feel for the flow attenuation and wave translation, the upstream inflow hydrograph is also presented in Figure 7.27. Some of the observations relevant to this comparison between the mild slope (MS) and steep slope (SS) models are as follows.

1. The flow attenuation is much greater for the MS model when compared to SS model. Flow for MS channel is only 40% of SS model (Figure 7.27).
2. The wave front arrives about an hour later for the MS model. The peak flow rate however, occurs more or less at the same time for the two models. The recession is sharply defined establishing the base flow after 12 hours for the SS model, whereas the recession for the MS channel is prolonged and the base flow value is not re-established even after 20 hours of simulation.

HYDROGRAPHS FOR MILD SLOPE CHANNEL

Teton X-Section, Slope = 1/5280

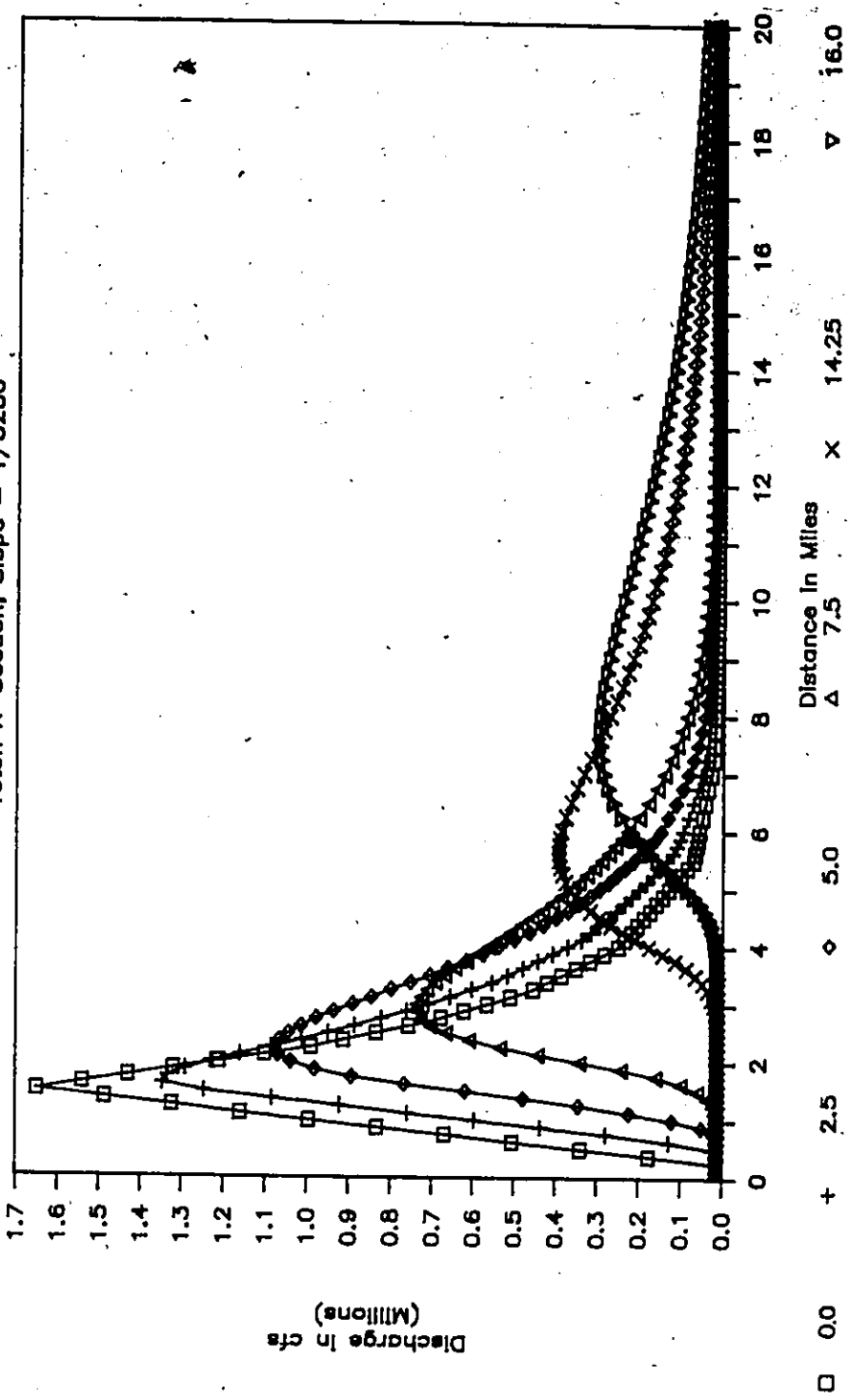


Fig. 7.25 Flow Attenuation and Lag for Teton Dam Break Hydrograph on a Mild Sloped Channel

STAGEGRAPHS FOR MILD SLOPE CHANNEL

Teton X-Section, Slope = 1/5280

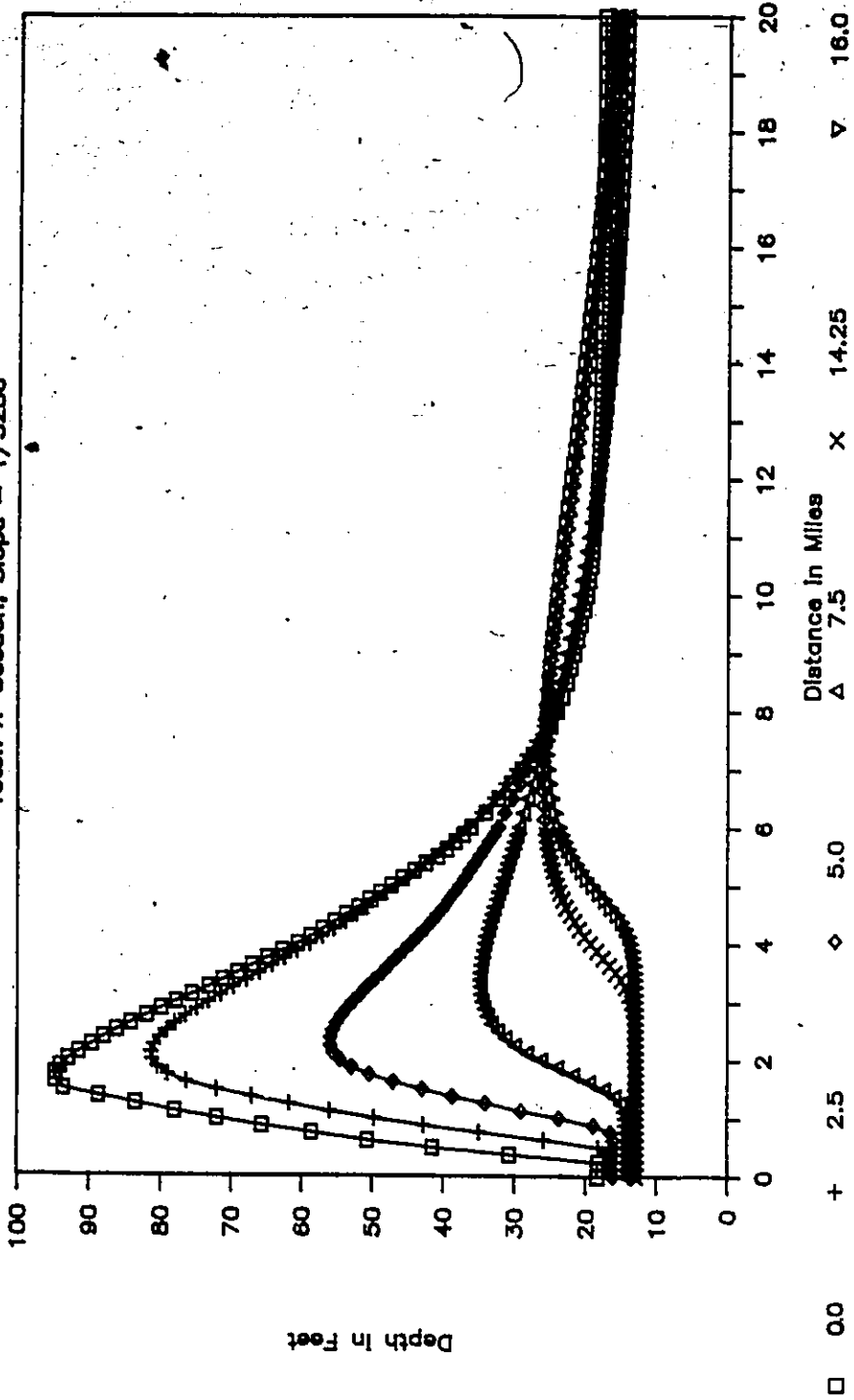


Fig. 7.26 Stage Hydrographs for Teton Dam Break Flood on a Mild Sloped Channel

SLOPE CHANGE IMPACT AT MILE 15.0

Teton X-Section, Slopes ft/m → 10 ft/m

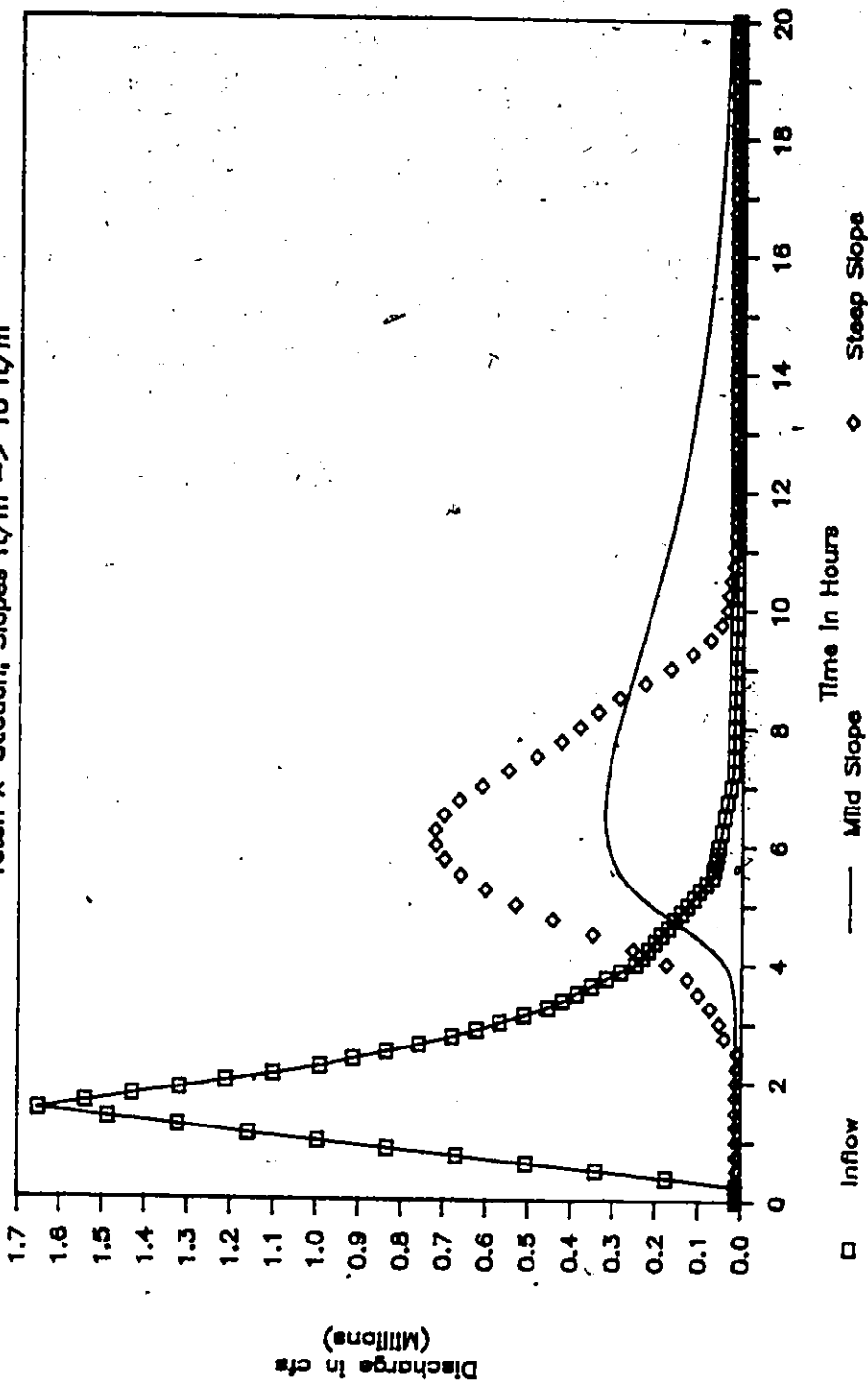


Fig. 7.27 Comparison of Steep and Mild River Models for Discharge Hydrographs at Mile 15.0

3. Figure 7.28 compares the depth of flow hydrographs for the MS and SS models. The first difference which is quite obvious and easily explained is the initial depth of flow. The MS model computes a depth of 13.0 feet to support 13,000 cfs while a depth of 7.0 feet sufficient for the SS model. All factors being the same, the discharge is a product of channel conveyance and the square root of bed slopes. So, if bed slope decreases, the conveyance has to increase to compensate and results in a greater depth of flow.
4. Surprisingly the rate of change of depth for the two models was same, although the recession limb was drawn out. Another important feature is the maximum depth of flow for the two models, which was almost the same (26.7 feet for SS versus 25.4 feet for MS model). The backwater effects corresponding to the MS model are quite noticeable.

The final measure of sensitivity for this test was to study the impact of changing the roughness coefficient at the upstream boundary node only. A Manning's coefficient of 0.08 was used and the maximum stage and flow profiles are plotted in Figures 7.29 and 7.30 respectively. For comparison the base case coefficient of 0.04 simulation results are also plotted. As expected, the larger roughness causes the maximum depth to be higher by over 12 feet at the upstream boundary. This difference gradually diminishes and the profiles become identical after five miles. The difference in the maximum flow envelopes, however, are not appreciable.

This exercise goes a long way in explaining some of the practical aspects of model calibration. Given the observed elevation, a combination of suitable roughness coefficients are likely to match it. Care is required however, to take account of the flow conditions, as any adjustment in roughness is likely to impact significantly on flow attenuation and translation properties.

SLOPE CHANGE IMPACT AT MILE 15.0

Teton X-Section, Slopes ft/m → 10 ft/m

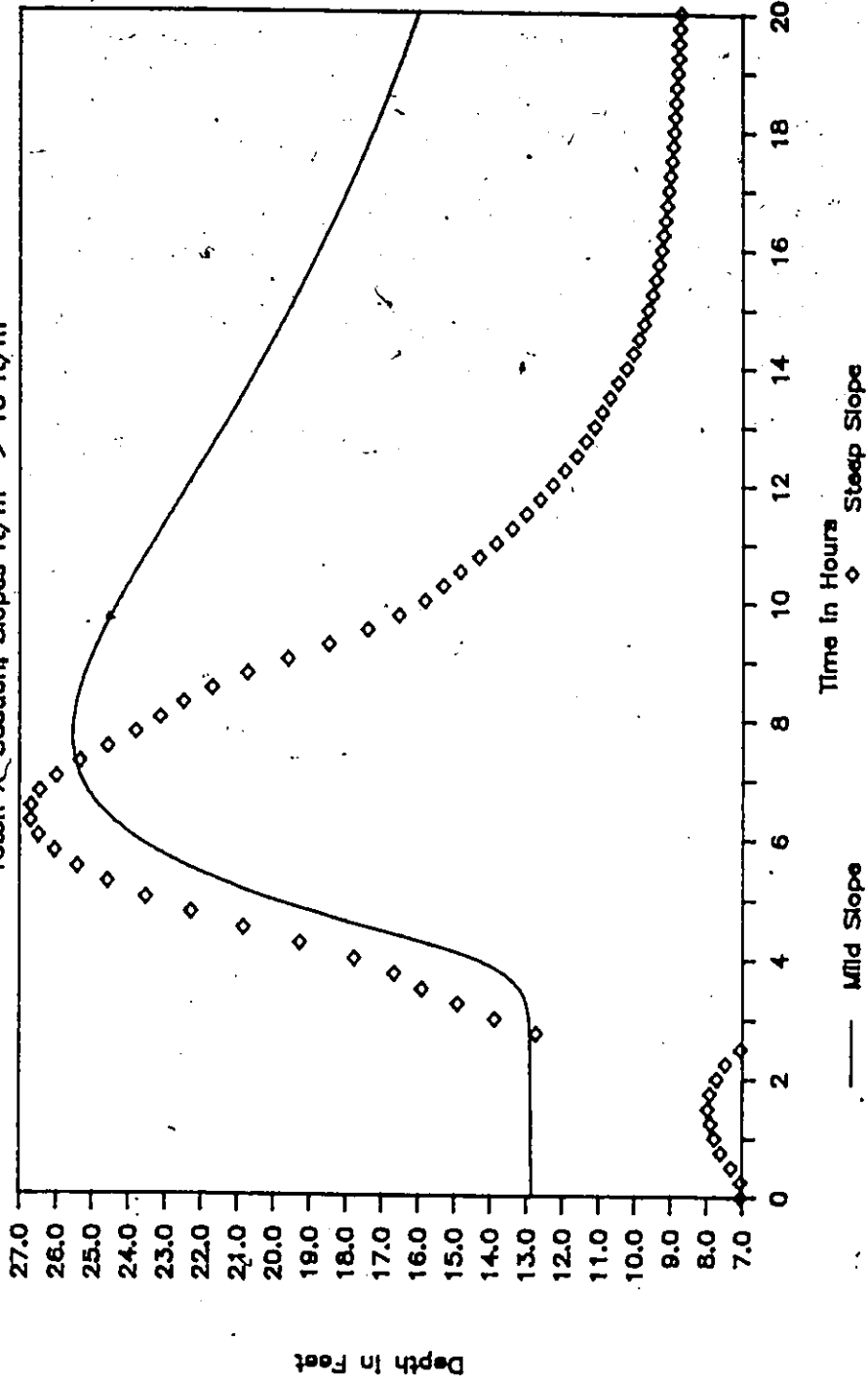


Fig. 7.28 Comparison of Steep and Mild River Models for Stage Hydrographs at Mile 15.0

Effect of Roughness Change at Node 1

Teton X-Section, Slope 1/5280

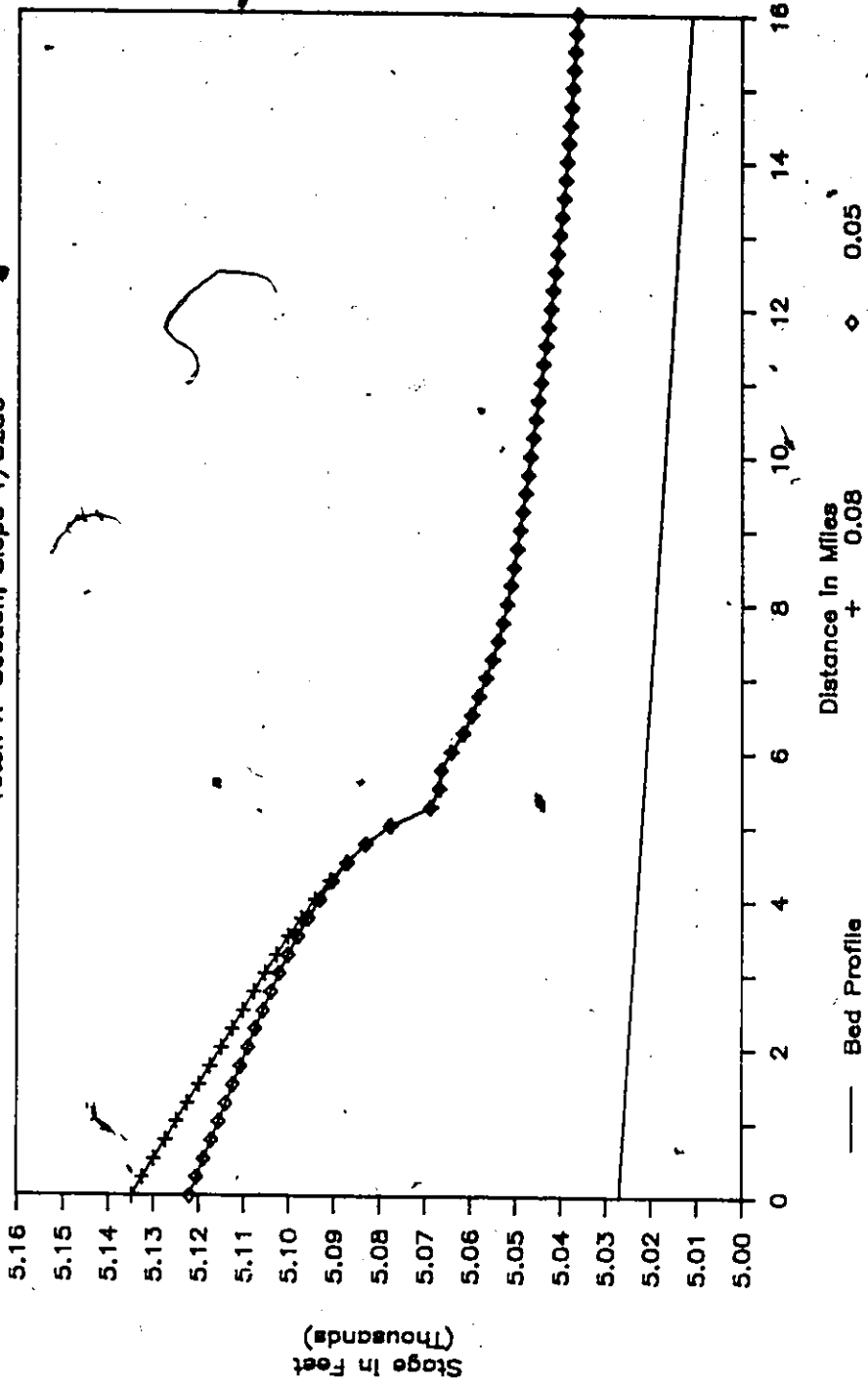


Fig. 7.29 Sensitivity of Channel Roughness Change at Mile 0.0 - Maximum Stage Envelopes for Mild Slope Model

Effect of Roughness Change at Node 1 Teton X--Section, Slope 1/5280

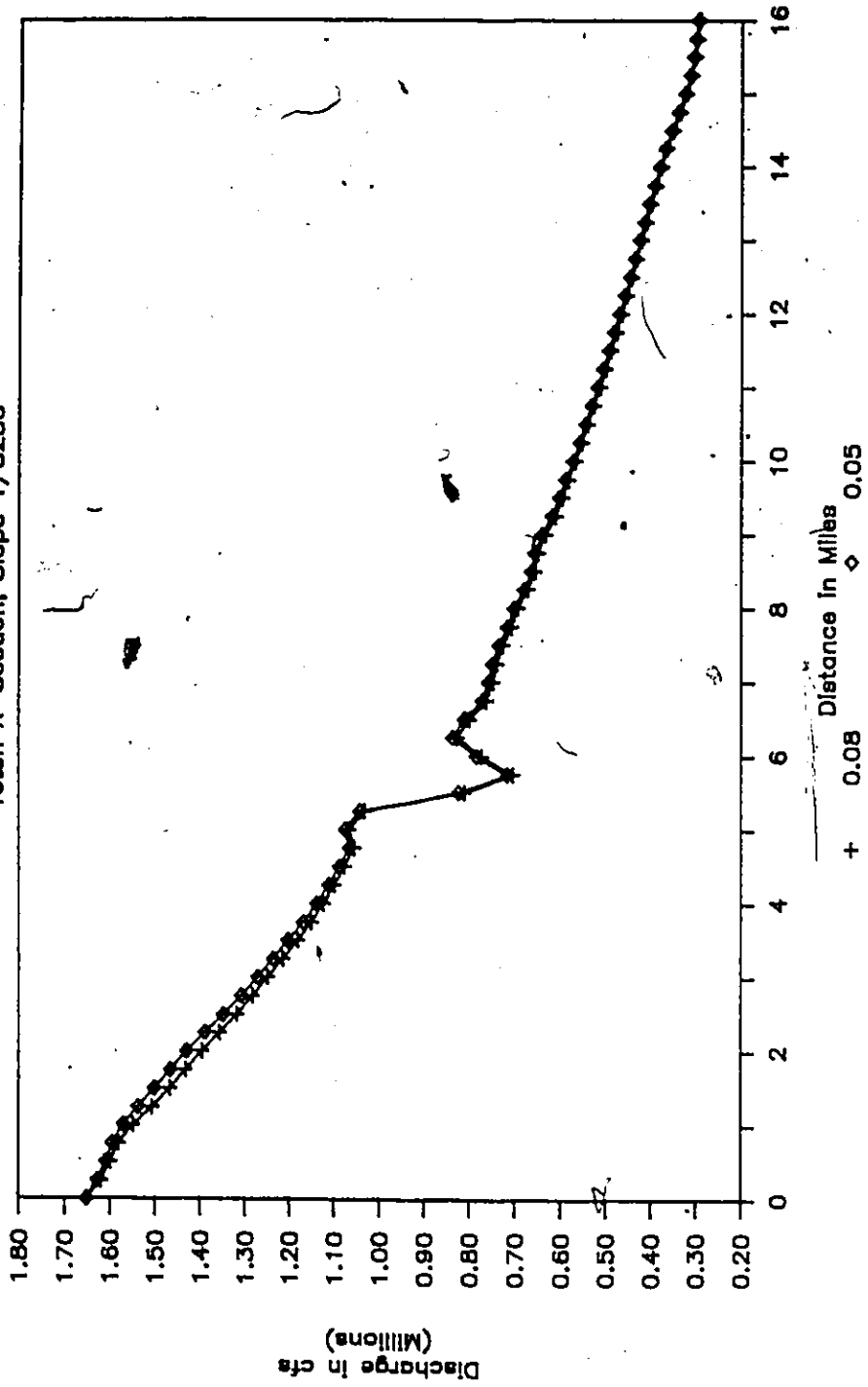


Fig. 7.30 Sensitivity of Channel Roughness Change at Mile 0.0 - Maximum Discharge Envelopes for Mild Slope Model

7.5 Grand River Flood Routing - Continuous Flow Modelling

One of the objectives in developing the moving element model was to extend the procedures from simulating the near discontinuous flows to continuous flow routing. To achieve this objective modelling exercise was developed to simulate flood routing in the lower reaches of the Grand River in Southern Ontario.

The location of the modelling reach is shown in Figure 7.31. The river reach studied is 60 miles long with an average slope of 0.00029. This river was selected in view of the extremely mild bed slope and the availability of a good data base. The Grand River is managed by the Grand River Conservation Authority. The Authority carried out a hydraulic analysis in 1977-78 and collected extensive field data in terms of channel cross-sections and made estimates of the Manning's roughness coefficients. The river reach is monitored by two streamflow gauges at Brantford, at the upstream end, and at York 35 miles downstream. The downstream boundary coincides with Lake Erie. Water levels for Lake Erie are collected at numerous points on its perimeter.

The data collected by the Conservation Authority for the water surface profile computation was too detailed for the nature of this study. Initially, every twentieth cross-section was selected for establishing the moving element model. The degree of channel non-linearity, for the element sizes used here however, proved to be critical for the model and reasons are described later on; hence approximately every fortieth section was adopted. This provided the necessary stability. The use of all sections would have required the employment of much smaller element size so as not to violate the assumption of linear variation of the channel properties.

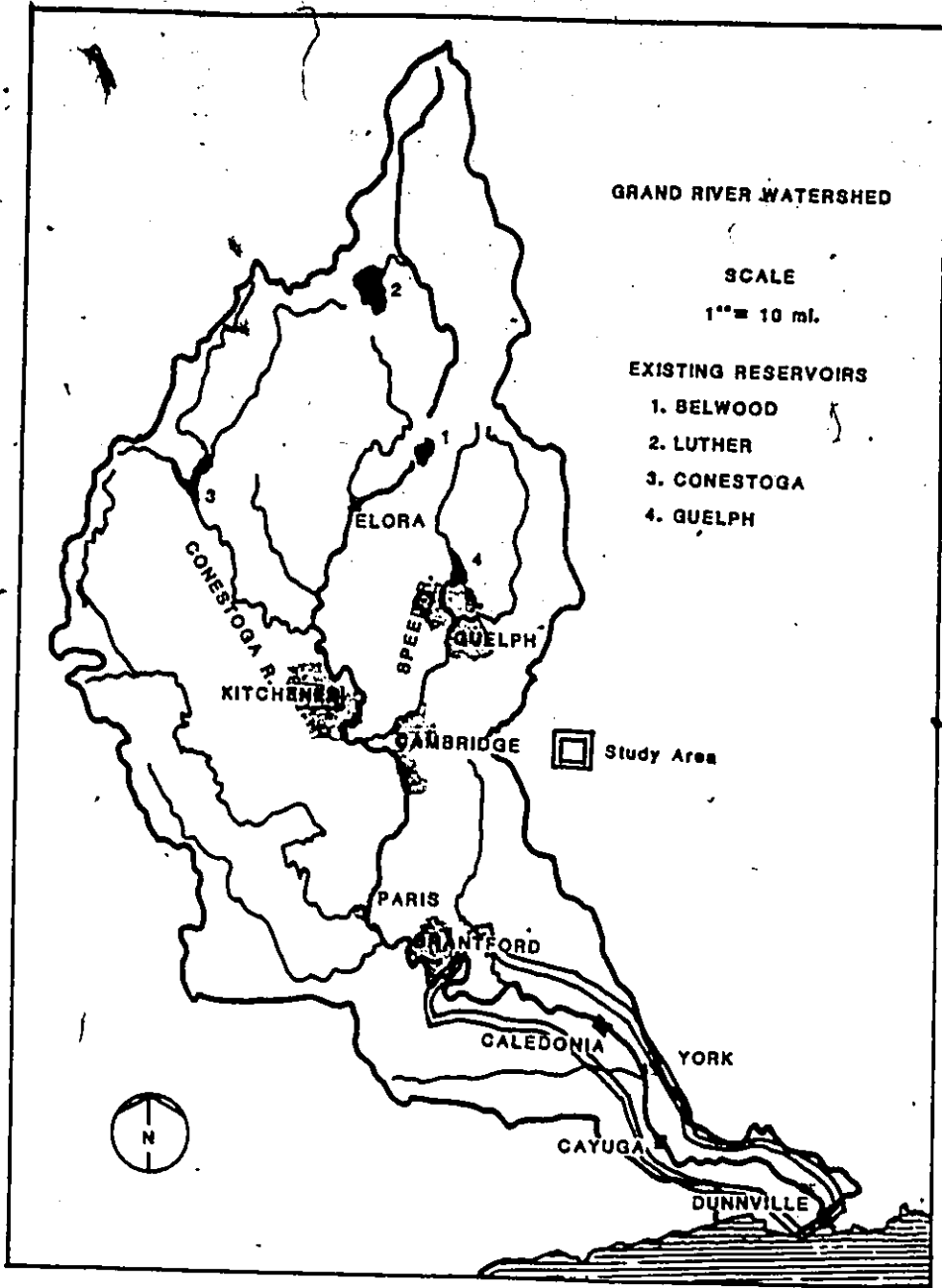


Fig. 7.31 Location Map of Grand River Flood Routing Model Study ,Brantford to Lake Erie Reach

Table 7.3

Channel Properties for the Grand River Flood Routing Model Brantford to Lake Erie Reach
Data Provided by Grand River Conservation Authority (1987)

No. D/S of Brantford	Location Elevation (Miles)	Thalweg Elevation (Feet)	Bank Elevation (Feet)	Storage Elevation (Feet)	Bank Topwidth (Feet)	Channel		Overbank		Storage Side Slope	Manning's Roughness Coeff.
						Side Slope	Side Slope				
1	0.0	621.0	625.0	625.0	296.0	37.0	1.3	0.0	0.045		
2	8.0	610.0	633.1	633.1	538.8	11.7	24.0	0.0	0.045		
3	16.0	610.0	640.2	640.2	1178.6	19.5	16.4	0.0	0.045		
4	24.0	609.0	630.4	630.4	953.2	22.3	29.7	0.0	0.045		
5	28.0	606.0	620.6	620.6	722.5	24.7	39.9	0.0	0.045		
6	35.0	587.5	600.9	600.9	909.1	33.8	32.1	0.0	0.045		
7	38.5	573.6	584.2	584.2	820.1	38.3	58.1	0.0	0.045		
8	45.0	561.2	588.1	588.1	1166.2	21.7	5.6	0.0	0.045		
9	53.0	561.5	569.4	569.4	516.7	32.7	43.9	0.0	0.045		
10	60.0	546.4	560.4	560.4	396.4	12.8	22.1	0.0	0.045		

Table 7.4

Simulation Characteristics for Grand River Flood Routing
Brantford to Lake Erie Reach

Run No.	Initial Flow (cfs)	Starting Elevation (Feet)	Initial Time Step (Seconds)	Final Time Step (Seconds)	Duration of Run (Hours)
1974	3530	572.87	450.0	900.0	153.0
1975	4200	570.80	450.0	900.0	172.0
1979	3850	571.00	450.0	900.0	153.0

7.5.1 Channel Description

Kowen (1984) carried out a study employing the DWOPER (Fread, 1982) and MOBED (Krishnappen, 1981) models for the same river reach. Much of the data used here were adapted from that report. The 60 mile reach was modelled by representative cross-sections located at regular intervals. The channel properties in terms of equations relating area, top width, wetted perimeter and first moment of area are given in Table 7.2. The equations are defined as Eqns. 7.1 to 7.4 and graphically presented in Appendix J.

Two different models were selected for defining the channel roughness. In the first model, constant average roughness values as noted in Table 7.3 were used at these representative cross-sections, while in the other model the roughness was allowed to vary with the depth of flow. In the latter scenario, a higher roughness was assumed at a lower flow rate; this was reduced at a uniform rate using Equation 6.12, until this value was one half of the base value. This approach was not dissimilar to Kowen's proposal.

Between the two bench mark gauges there are several minor and two major tributaries that discharge laterally into the Grand River. It is next to impossible to accurately predict their influence on hydrograph at York. Kowen completely ignored the influence of the lateral inflow. After the initial runs it was decided to retain the lateral flow contributions from the Fairchild Creek, which empties into the Grand River about two miles upstream of the York gauge.

Although the lower reaches near the Lake Erie exhibit wide floodplain no over-bank non-conveying sections were employed, in order to maintain consistency with the earlier study.

7.5.2 Initial and Boundary Conditions

The initial conditions in the river consist of the flow preceding the flood hydrographs for the three events the initial flows and the starting downstream elevations are noted in Table 7.2. The lateral flows were not included in the computation of the initial depth. This was corrected at the first time step of unsteady flow calculations.

Kowen (1984) reported considerable difficulty in establishing initial flow conditions for both DWOPER and MOBED. The experience with the backwater routine in the moving element model was, however, different. Except for the five miles from the lake which were highly influenced by the lake elevations, all other sections were computed without any convergence problems.

The lateral flow rates were set rather arbitrarily without knowledge of hourly flow rates at the mouth of Fairchild Creek. The lateral flow was dispersed over a length of 2.5 miles and the values were adjusted to match the stages in the early part of hydrographs at York.

The upstream boundary consisted of inflow hydrographs at Brantford reported on hourly basis for all three events modelled. At the downstream boundary a constant depth of flow condition was imposed by the lake. As the point of interest was at York, not much consideration was given to the lake elevation in view of the change in slope at about Mile 54.0. This prevented the influence of the lake level at the gauge.

7.5.3 Model Set-up

The moving element model was employed in the Eulerian-Lagrangian mode. The reach of 60 miles was divided into 120 elements each one-half mile long.

Two different time steps were used in each of the three runs modelled for the flood events of 1974, 1975 and 1979. For the first 100 hours of simulation a time step of 450 seconds was used and for the rest of the simulation, it was doubled to 900 seconds.

For the 1974 and 1979 floods the simulation was carried for a period of 152 hours but for the 1975 event, 172 hours was used. As in all other simulations, a number of intermediate results were captured to study properties like attenuation, translation, hysteresis or looping effects at Brantford and York.

7.5.4 Discussion of Results

Reflecting the nature of the study, the results are discussed separately addressing various facets of the simulation. These are discussed considering all three events of the 1974, 1975 and 1979 floods. Also, the 1974 event was considered as the calibration event wherein adjustments to the roughness coefficient, time step and lateral flow rate were made to simulate stages at the York Gauge. No further adjustments were then allowed for the other two validation computer runs, other than the lateral flow from the Fairchild Creek.

7.5.4.1 Simulation of Stage Hydrograph at York

The streamflow gauge at York is located 35 miles downstream of the upstream boundary at York. The bed slope in the vicinity of gauge is 10 ft/mile (0.00189). The information for the site was supplied in the form of bristol charts from the water level recorder which were then reduced to the stage hydrographs by adding the gauge datum to the recorded elevation.

Figure 7.32 presents a comparison of the observed hydrograph with the simulation by the moving element model for the 1974 flood. The model results are

GRAND RIVER FLOOD ROUTING - MAY 1974

Brantford to Lake Erie Reach

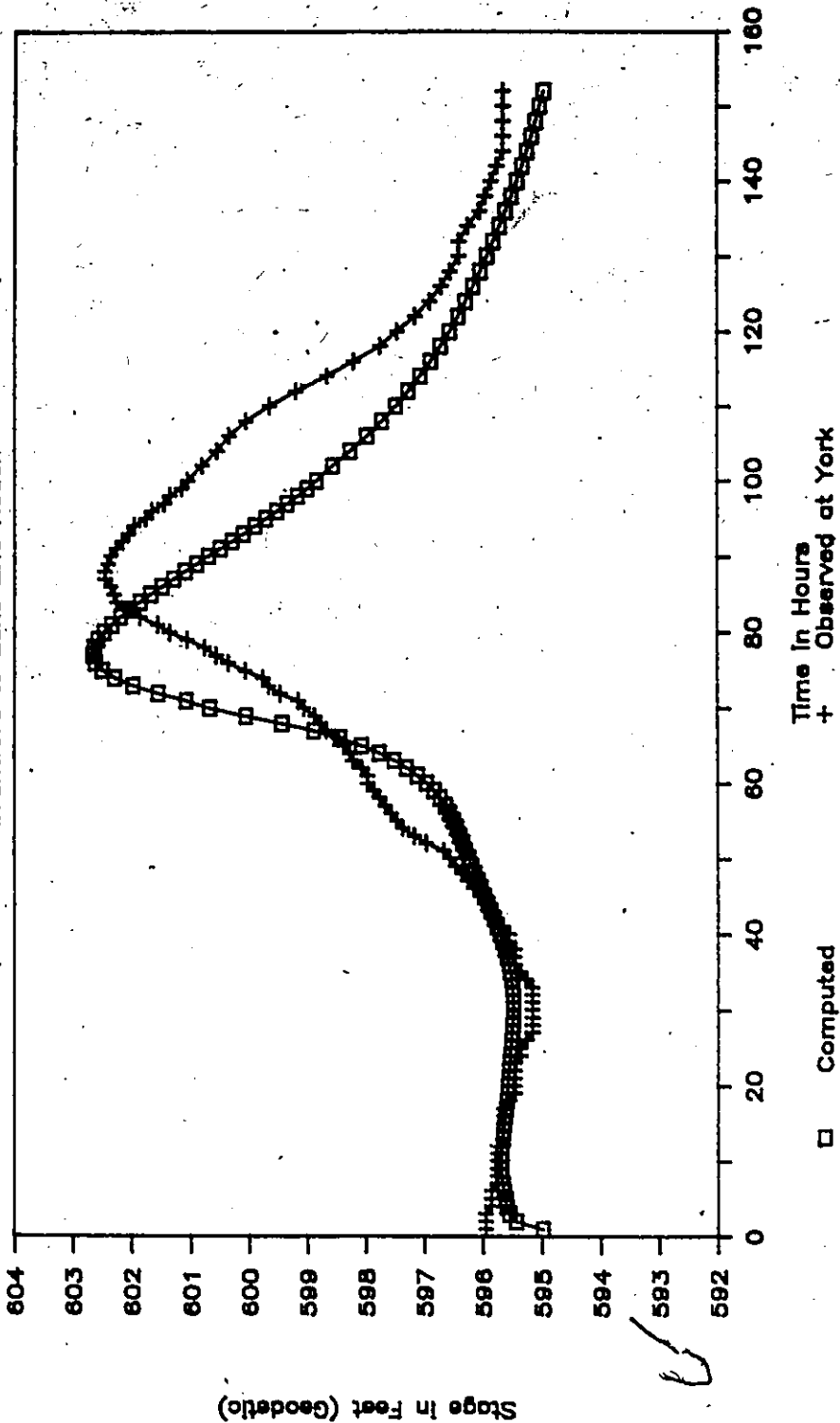


Fig. 7.32 Comparison of Observed and Computed Stage Hydrographs at York Gauge for Flood of May 1974

acceptable in areas of peak depth and the general shape of the stage hydrograph. The starting elevation and the hydrograph recession duplicate the observed values. The rate of rising limb and the timing of the peak were not simulated satisfactorily. The model predicted a steeper rate of rise and consequently an earlier peak. A number of parameters were varied to match the time to peak and slow down on the rising limb but with no avail. Figures 7.33 and 7.34 show the routed stage graph for the 1975 and 1979 events. A two day discontinuity in collected data occurred in the observed stages for the 1975 flood. A comparison of simulated and observed events for the 1979 event is self evident. One reason for the different rate of rise for the hydrographs is the peak flow timing of the Fairchild Creek. Obviously, the contribution from this tributary will be most likely, as a single peak hydrograph. The moving element model, however, provides for a single uniform rate of lateral inflow.

To evaluate the impact of the lateral flow rate on stages at York, the flows from Fairchild Creek were set at 0.0. The 1974 event along with the calibrated simulation are shown in Figure 7.35. A comparison of lateral and no lateral inflow cases points immediately to the importance of the lateral flow. A difference of about two feet exist without the lateral flow for the first 40 hours. The contribution of lateral flow is, however, not in evidence during the crest of the wave. Thus, at the lower flow, the influence of lateral flow rate is more prominent than at the peak flow conditions. The overall shape of the hydrograph is very sensitive the lateral flow rate.

7.5.4.2 Attenuation and Translation of Flood Wave

On a mild sloped channel, such as the Grand River, with a long reach and minor lateral flows, the major hydraulic features of a flood hydrographs are attenuation and translation. Attenuation in this context is defined as the reduction in

GRAND RIVER, FLOOD ROUTING - APRIL 1975

deltx = 0.5 mile, delt = 450 & 900 sec.

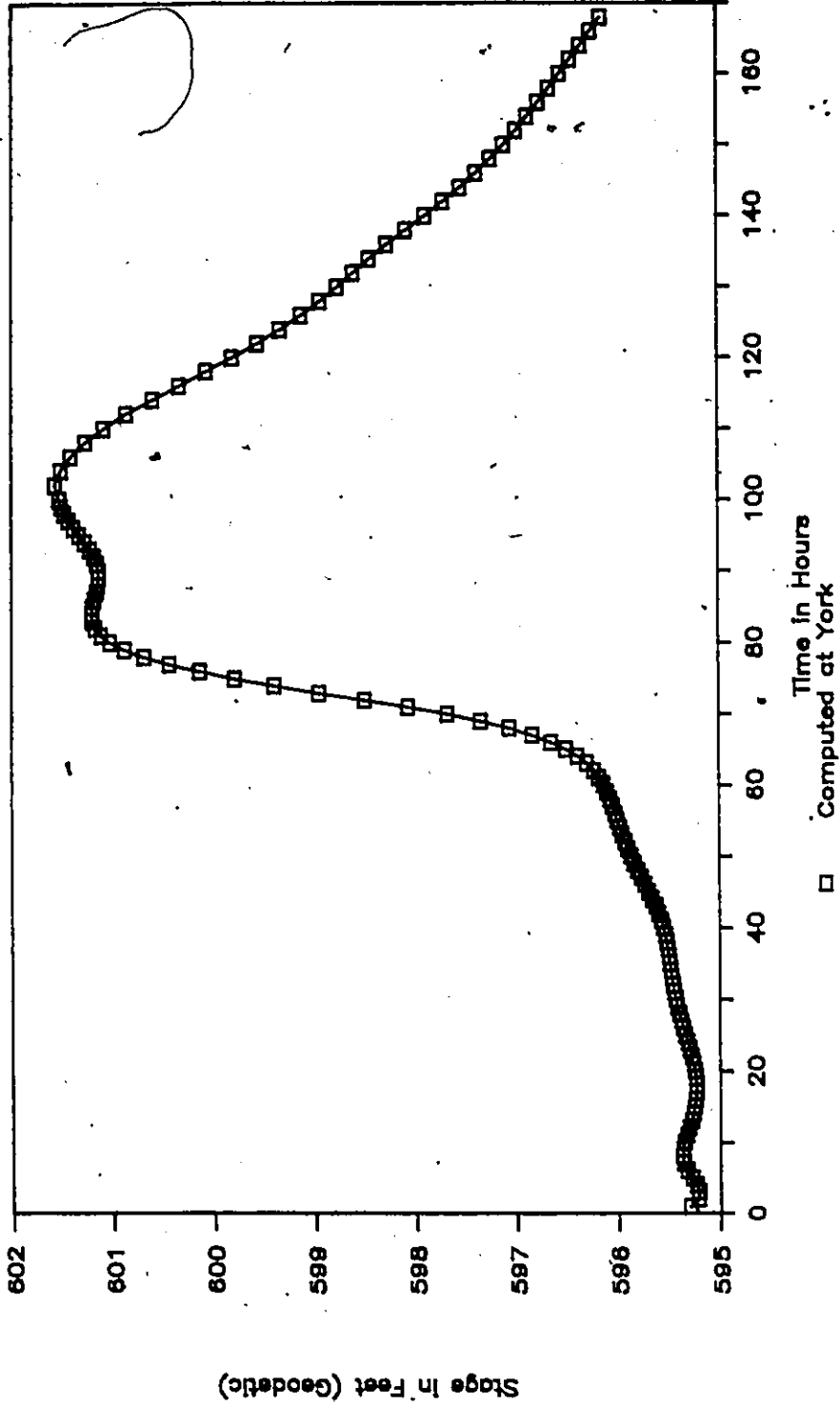


Fig. 7.33 Simulated Stage Hydrograph at York Gauge for Flood of April 1975

Grand River Flood - April 1979

delx = 0.5 mlie delt = 450 & 900 sec

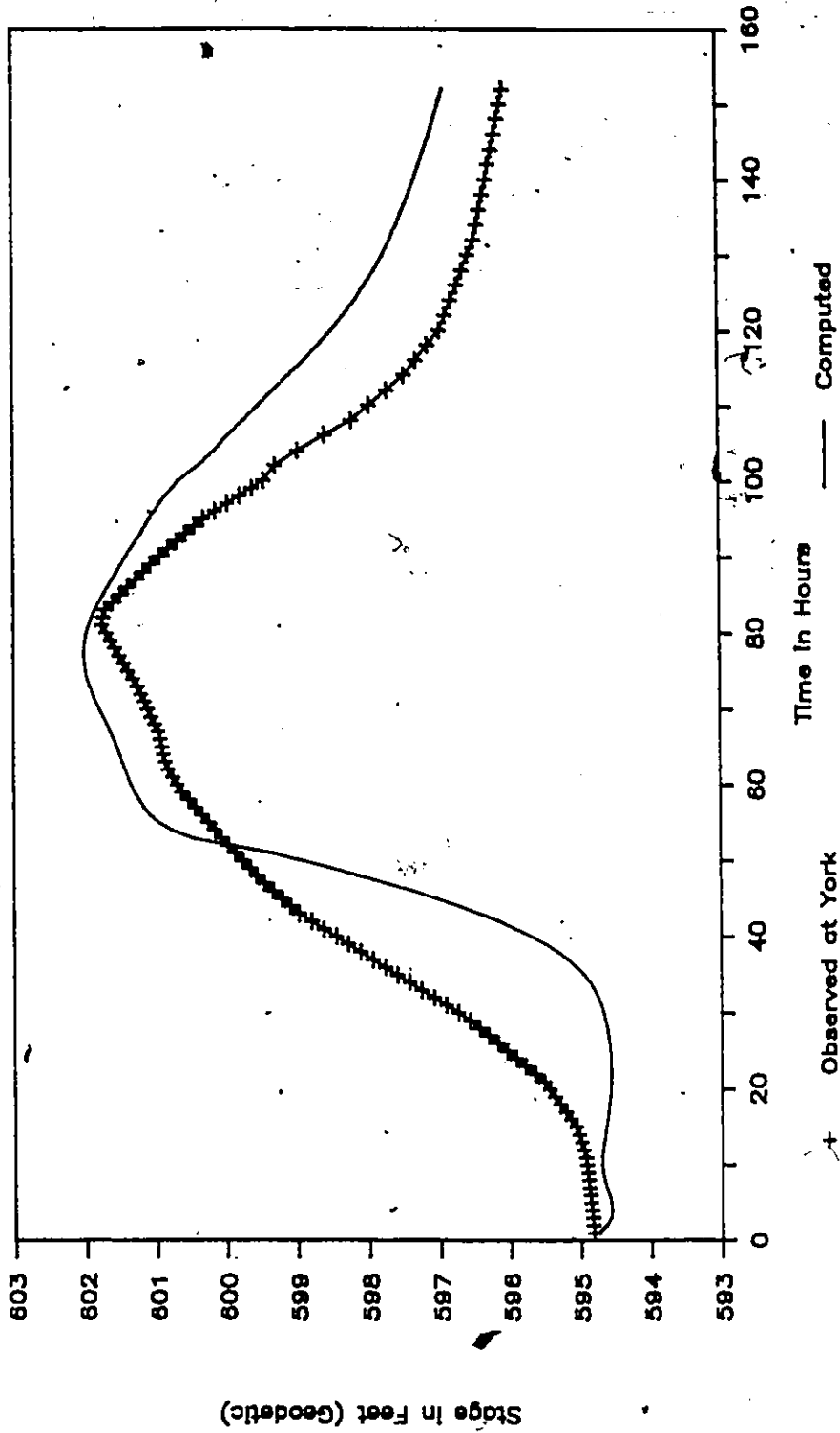


Fig. 7:34 Comparison of Observed and Computed Stage Hydrographs at York Gauge for Flood of April 1979

GRAND RIVER FLOOD ROUTING - MAY 1974

Brantford to Lake Erie Reach

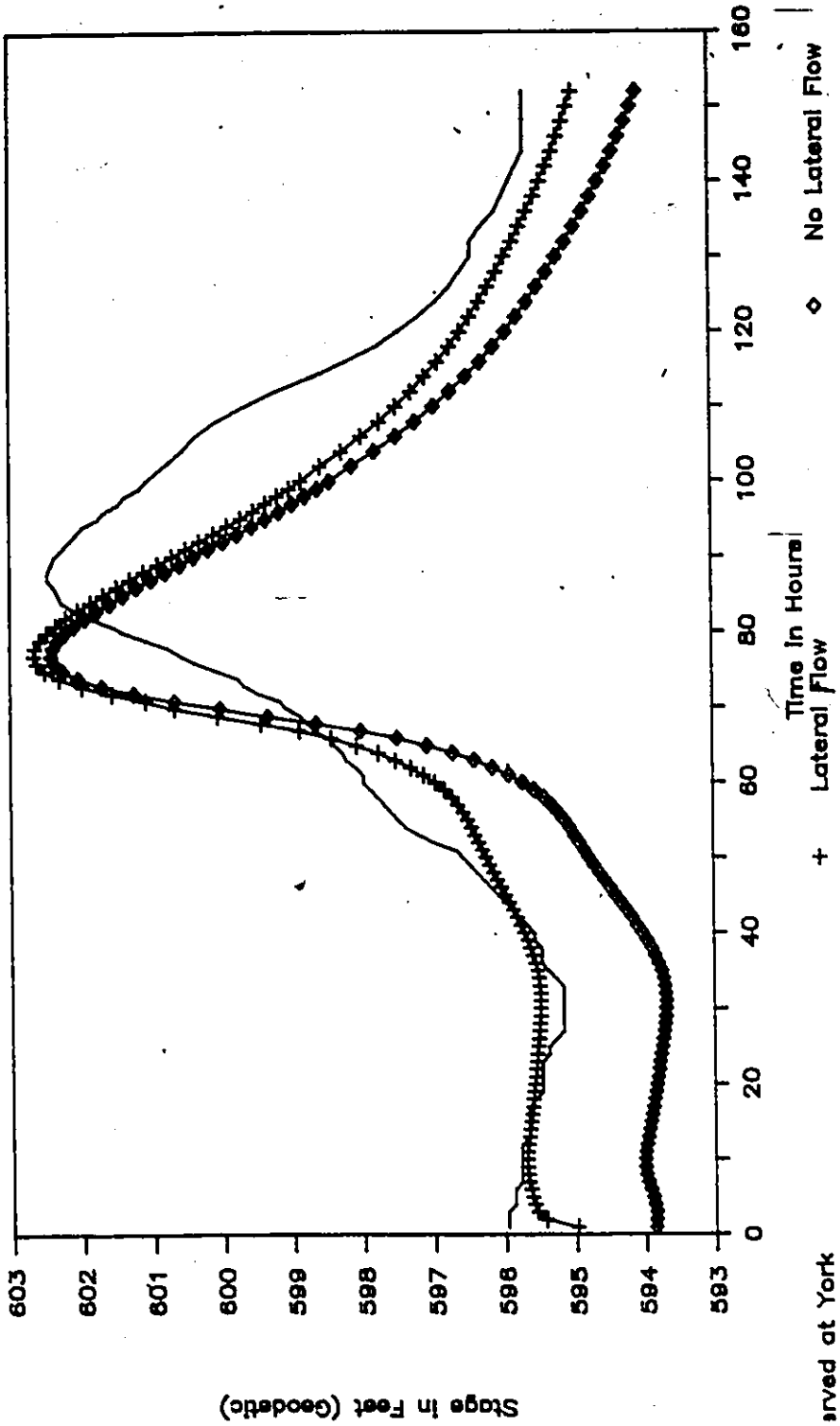


Fig. 7.36 Influence of Lateral Flow on Stage Hydrographs at York Gauge for Flood of May 1974

peak flow, while translation is the temporal delay in peak between the upstream and downstream points.

Discharge hydrographs at Brantford and York were compared for all three flood events studied. These are presented in Figures 7.36, 7.37 and 7.38 for the 1974, 1975 and 1979 events respectively. In all three cases the hydrographs at York Gauge show an early rise when compared with charts. Also, the peak occurs four to six hours earlier than the observed peak. A possible explanation for this consistent error in the estimation of peak timing is the removal of bridges in the modelling exercise, thus eliminating constrictions which would hold back and retard flood wave. The most important factor for this peak shifting is flow retardation at the Caledonia Dam upstream of the Gauge; this was not modelled. Figure 7.36 shows an attenuation in the peak by approximately 34% while the peak flow is shifted by 16 hours. Similar observations are made with respect to the other flood events.

The moving element model in this regard behaves in a reasonable fashion to reflect hydraulic characteristics of flood waves including multi-peak events such as that of 1975. The satisfactory behavior of the model with a temporal weighting of 0.5 represents a major improvement in open channel hydraulic modelling.

7.5.4.3 Hysteresis or Looping Effect

It is well known that in the presence of mild slopes, the dynamic or momentum conservation equation is capable of developing the stage-discharge rating curve. In these situations, the rating curve exhibits a looping behavior. The stage for a given flow is generally lower on the rising limb than on the recession side for the same flow. A similar interpretation can be made by examining the signs of individual terms of the momentum equation during the rising and recession limbs.

GRAND RIVER FLOOD ROUTING — MAY 1974

Brantford to Lake Erie Reach

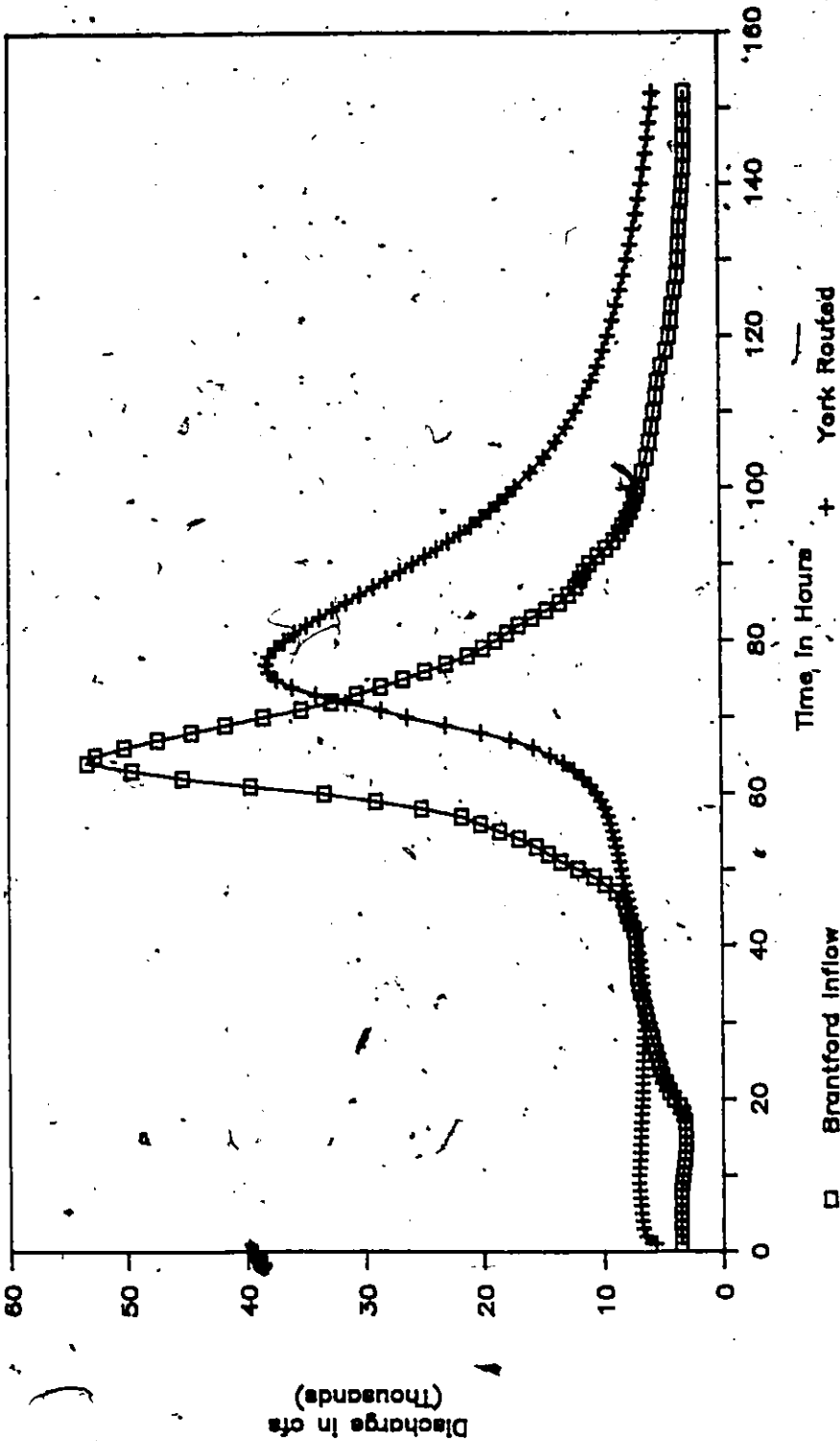


Fig. 7.36 Flow Attenuation and Lag for Grand River Flood of May 1974 Between Brantford and York Gauge

GRAND RIVER FLOOD ROUTING - APRIL 1975

delx = 0.5 mile, delt = 450 & 900 sec.

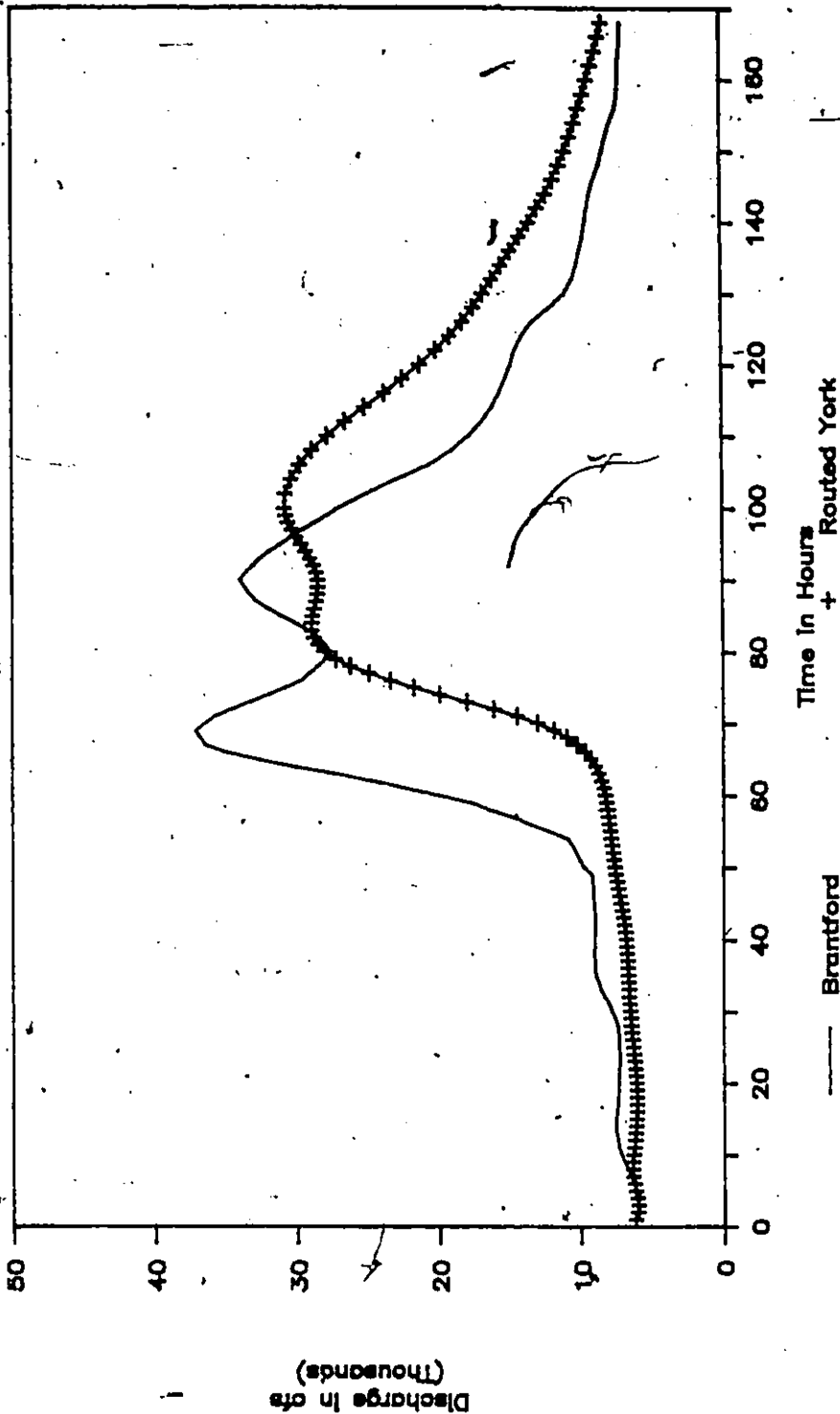


Fig. 7.37 Flow Attenuation and Lag for Grand River Flood of April 1975 Between Brantford and York Gauge

Grand River Flood - April 1979

delta x = 0.5 mile delta t = 450 & 900 sec

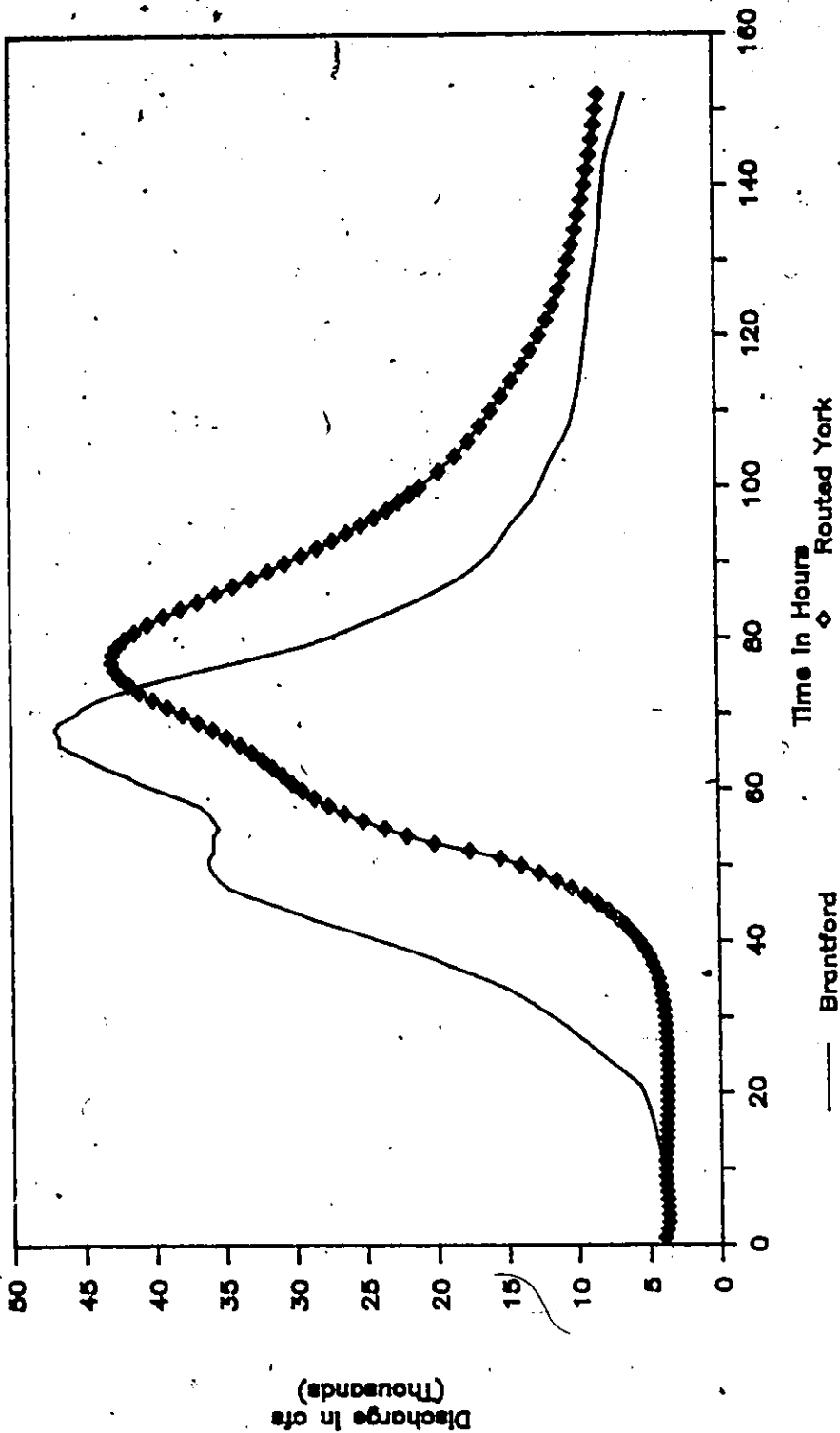


Fig. 7.38 Flow Attenuation and Lag for Grand River Flood of April 1974 Between Brantford and York Gauge

In order to study this phenomenon stage-discharge curves were developed for Brantford and York. These two points are located in mild and steep grades respectively. The rating curves for Brantford and York are shown in Figures 7.39 and 7.40. A comparison of the two figures show some interesting features. First, the degree of hysteresis at Brantford is significantly more pronounced than at York where the stage-discharge relation is single valued. This is consistent with the momentum equation which indicates a smaller significance of the downstream conditions for steep channel slope and vice versa.

From this comparison, it is obvious that the location of the gauge at York is excellent as it provides a unique discharge for a given stage. This is then an ideal situation for the gauge placement.

7.5.4.4 Water Surface Profile

As in other applications described in the previous sections, water surface profile corresponding to the maximum elevations were plotted. The envelope for the 1974 event is presented in Figure 7.41. It shows that the approximate drop in water surface is very similar to the bed profile. There are significant differences in the maximum depths in the flatter reaches and steeper slopes around York. This varied from about 14 feet at Mile 35.0 to over 35 feet at Mile 10.0.

The maximum observed elevation at York is also plotted to provide a comparison with the simulated profile.

GRAND RIVER FLOOD ROUTING - MAY 1974

Hysteresis Effects at Brantford

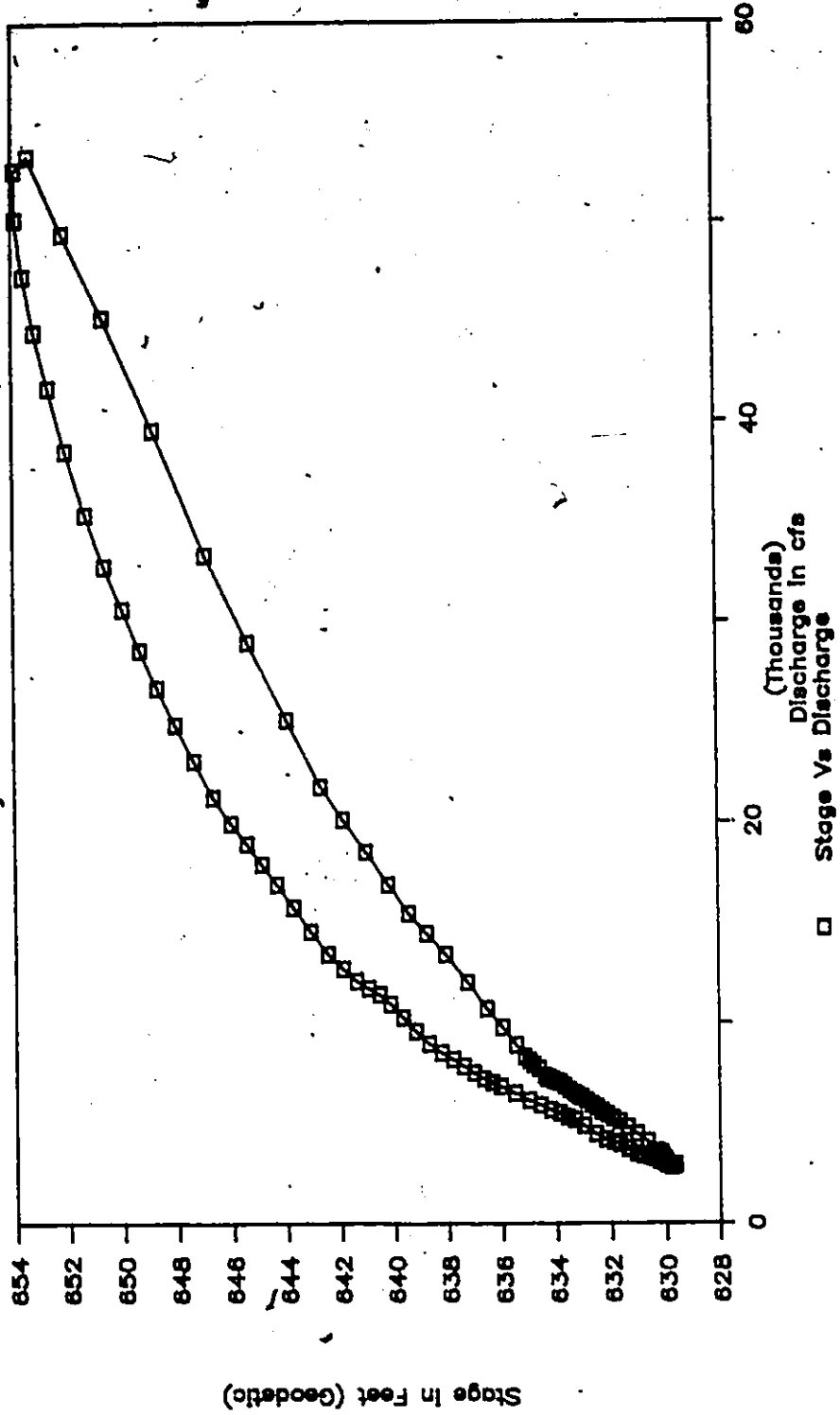


Fig. 7.39 Hysteresis Effects at Brantford Gauge for the Stage versus Discharge Relationship

GRAND RIVER FLOOD ROUTING - MAY 1974

Hysteresis Effects at York Gauge

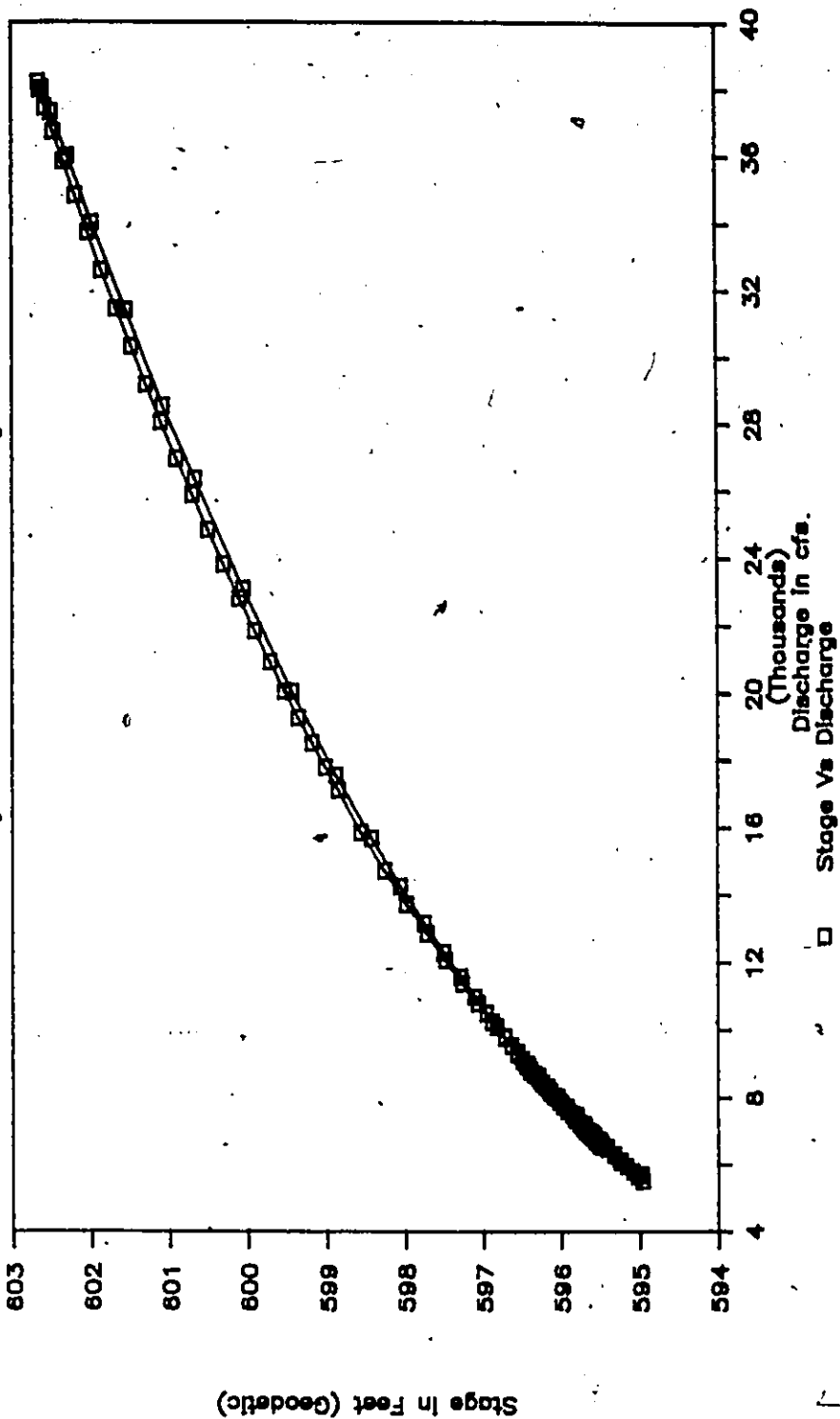


Fig. 7.40 Hysteresis Effects at York Gauge for the Stage versus Discharge Relationship

GRAND RIVER FLOOD PROFILE - MAY 1974

Envelope - Brantford to Lake Erie

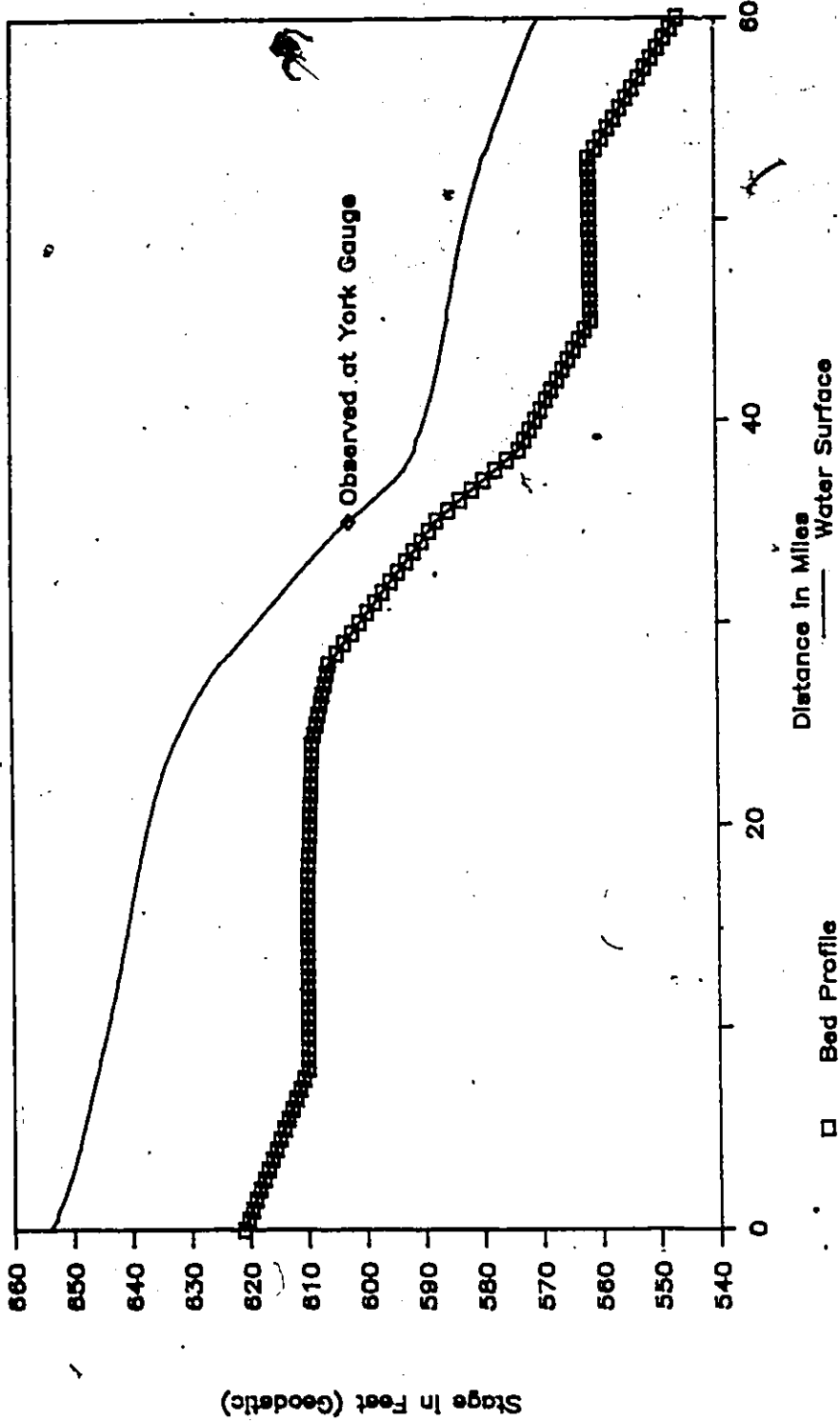


Fig. 7.41 Maximum Stage Envelope for Grand River Flood of May 1974

7.6 Grand River Flood Simulation with Hypothetical Dam Break Hydrograph.

As an addendum to the continuous flow simulation described in the previous section, a sharply rising hypothetical hydrograph was introduced at the upstream boundary and routed through the system. Briefly, the findings consist of studying the attenuation effects and the maximum elevation profile.

There are three major dams upstream of Brantford that provide flood protection to a number of communities. Even their simultaneous failure will not cause the flow magnitudes equal to the hypothetical hydrograph designed at the upstream end of the study reach. The hypothetical discharge is assumed to increase from about 3,500 cfs to 600,000 cfs in two hours and reduced back linearly after another six hours. This flow is then maintained for another 32 hours. This forty-hour hydrograph was routed with no lateral flow influence due to the Fairchild Creek.

The channel description and model set up have already been described in the previous section. Two different time steps of 90 seconds for the first twenty hours and 450 seconds for the remaining duration were employed. The moving element model in the Eulerian-Lagrangian mode was used with a centered Crank-Nicholson weighting scheme.

Wave attenuation characteristics were representative of the channel slopes and are presented in Figure 7.42. If the peak flow rates are followed, the typical exponential decay of peak rate is evident. A uniform decay is noted for the first 25 miles, however, negligible attenuation is noted in the next 10 miles. The reason for this is directly linked to the increase in the bed slopes in this reach.

Figure 7.43 show the envelope of maximum elevation. When comparison is made with similar profiles for lower flow values, the higher depths in the 43.0 to 54.0

ATTENUATION & LAG..SURGE IN GRAND RIVER

Brantford to Lake Erie Reach

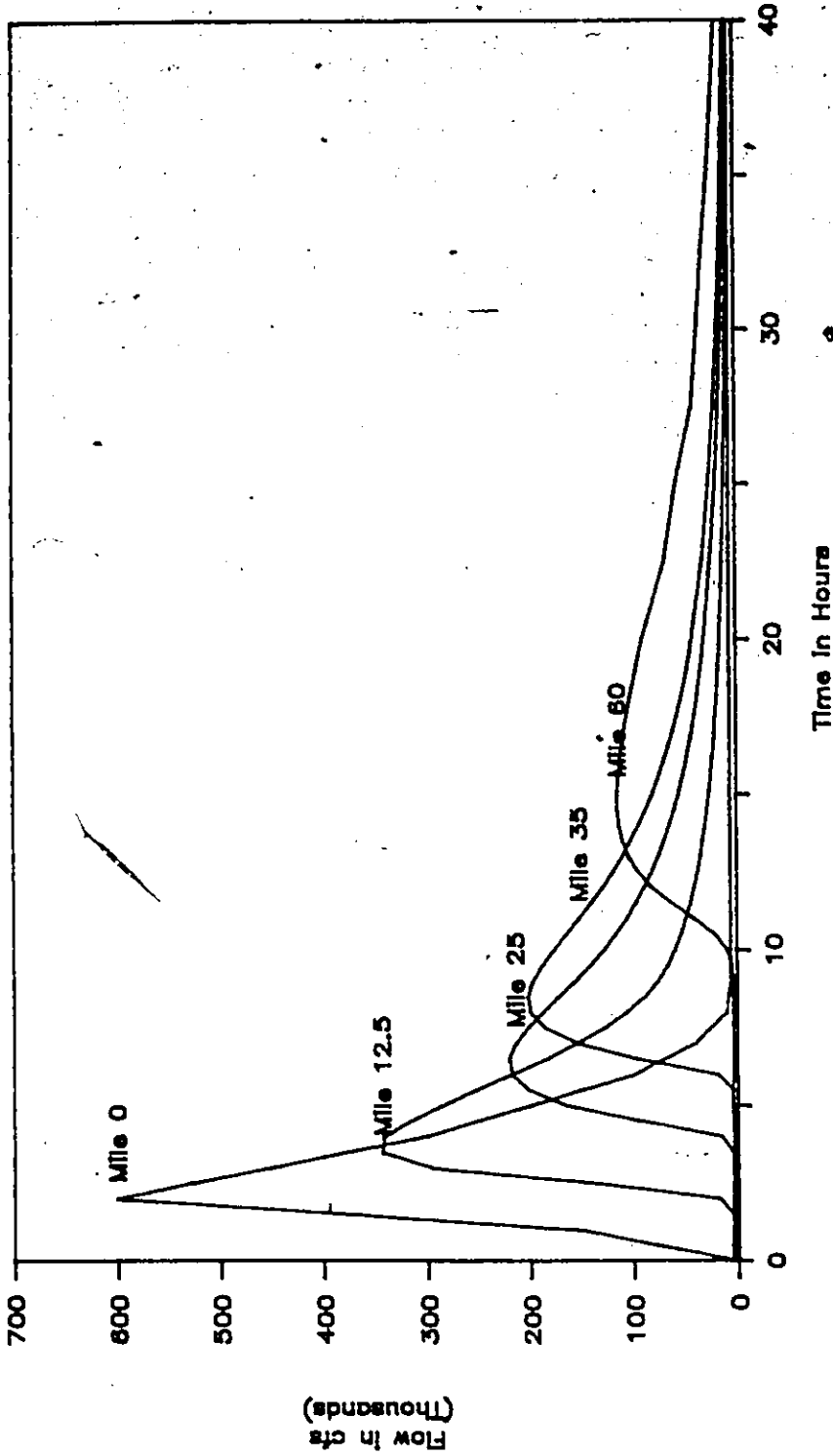


Fig. 7.42 Flow Attenuation and Lag for Grand River Hypothetical Flood Between Brantford and York Gauge

GRAND RIVER SURGE ROUTING - ENVELOPE

Brantford to Lake Erie Reach

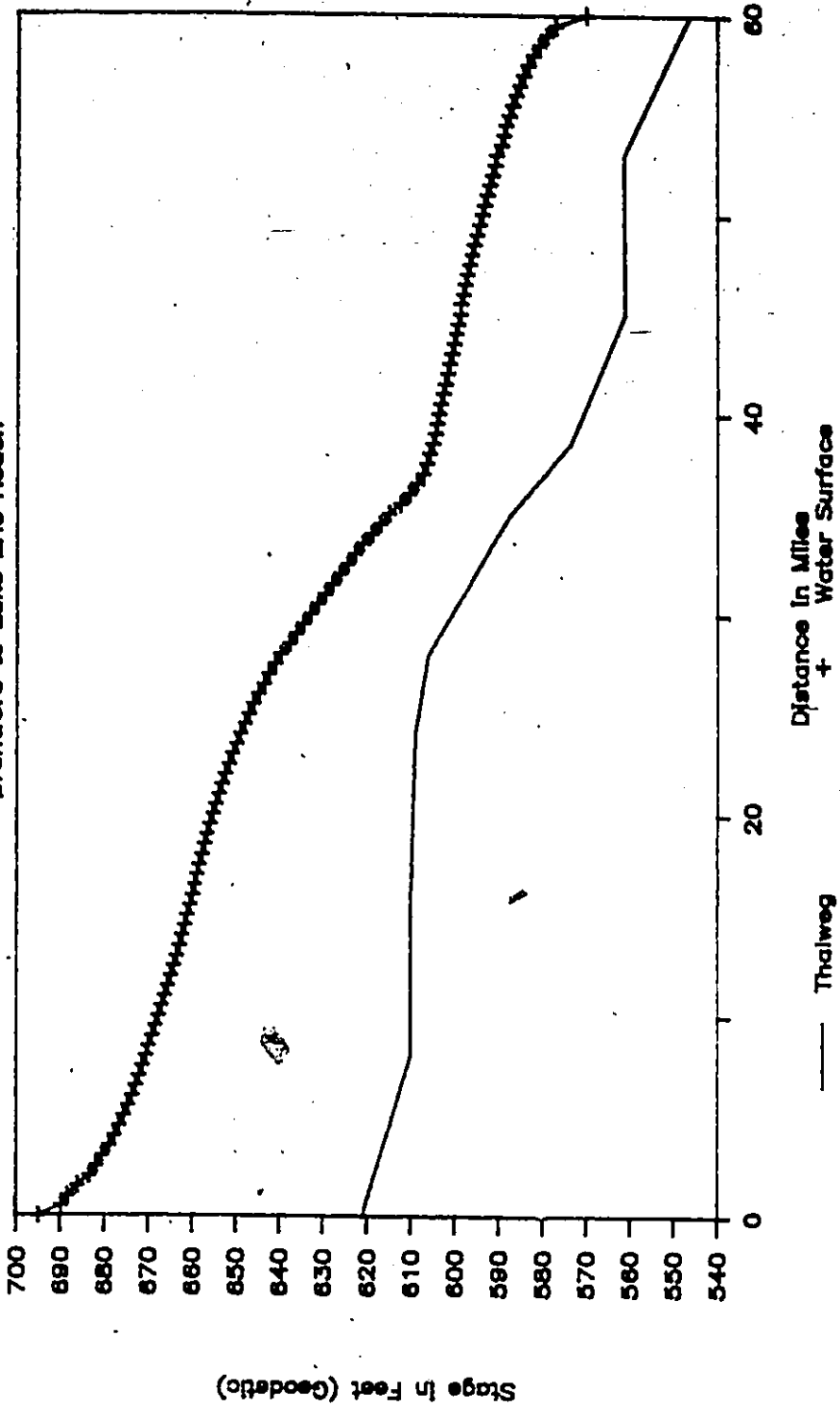
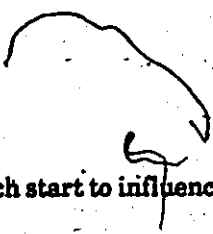


Fig. 7.43 Maximum Stage Envelope for Grand River Hypothetical Flood



mile reach start to influence the profile in the steeper slope reach between Mile 28.0 to Mile 43.0. In order to evaluate this impact, the rating curve of stage versus flow at the York Gauge was developed and plotted in Figure 7.44. The loop in the rating curve becomes obvious. This is a clear indication of backwater effect during the passage of a flood wave. A comparison with Figure 7.40 show the degree of influence caused by backwater at higher flow rates.

The change in the rating curve for a higher flow rate brings into focus certain practical aspects of locating and establishing a stream flow gauge. The gauge point may exhibit an unique single value rating curve for lower flows. This curve would lead to erroneous results if it is extended without regard to submergence or backwater effects.

7.7 Laboratory Experiment Verifications

In Chapter 5 it was noted that the moving element model would be tested against observed data from laboratory experiments. In this section, the moving element method is compared against the experiments carried out by Egiazarov (1937) and Faure (1935) and reported by Vasiliev et al. (1965) and Terzedis and Strelkoff (1970). These are now discussed separately.

7.7.1 Egiazarov's Experiment

Egiazarov (1937) published results of the experiments he carried out on unsteady wave motion in long pools. The following particulars govern the experimental set-up.

GRAND RIVER SURGE SIMULATION

Backwater Effects at York Gauge

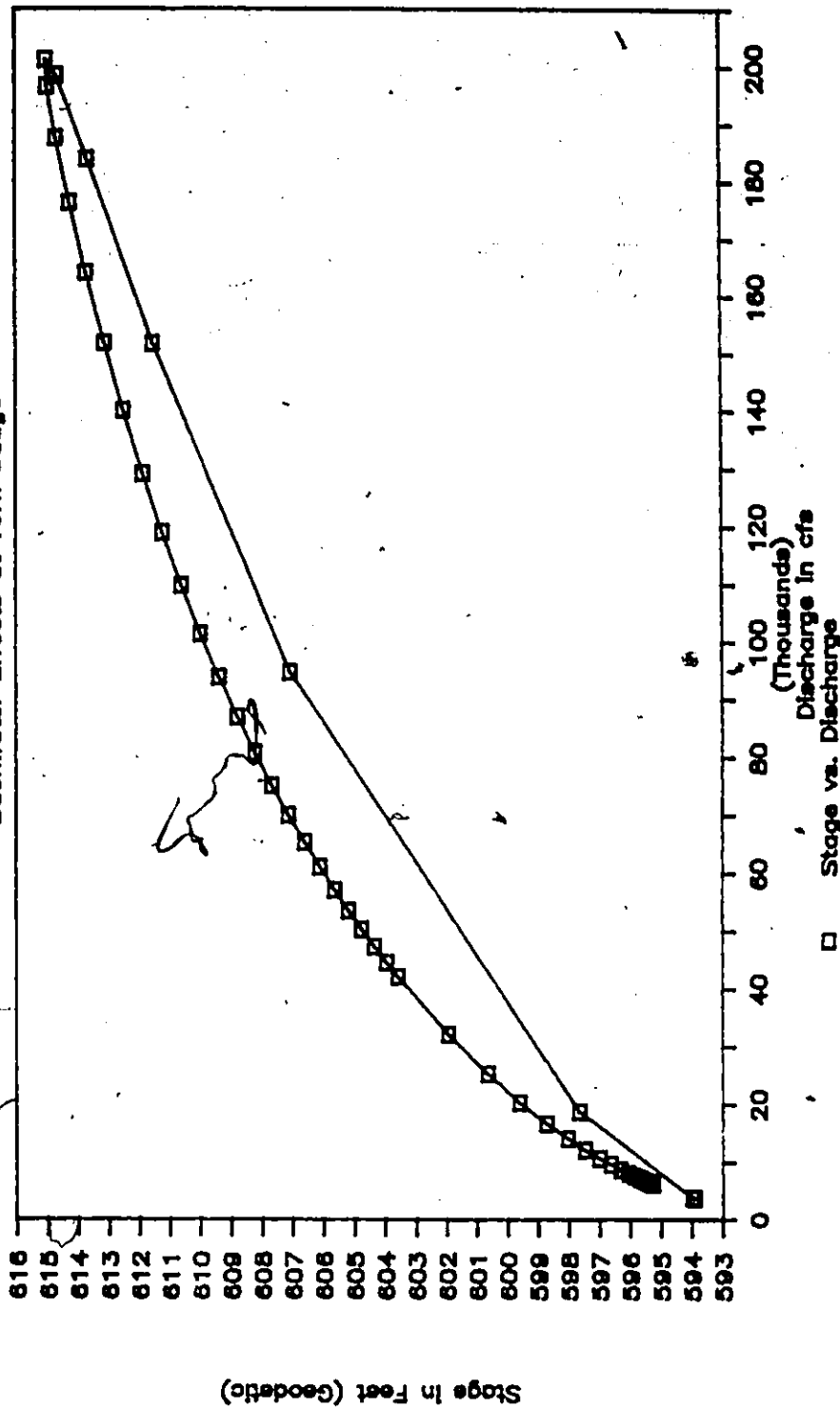


Fig. 7.44 Influence of Higher Flow on Hysteresis Effects at York Gauge for the Stage versus Discharge Relationship

Physical Description:

The prismatic flume used was rectangular in cross-section and 0.4 m wide. The channel sloped at 0.005 m/m or 5 mm per m with a length of 75 m. The author provided a relationship between the channel roughness and depth of flow. Vasiliev (1965) employed a Chezy's equivalent of $40 \text{ m}^{1/2}/\text{s}$, while Terzidis and Strelkoff (1970) used a Manning's roughness coefficient of 0.09. However, in the present study, computations based on the uniform initial flow conditions, yielded a value of 0.0225, and this value was employed for all computer runs in this exercise.

Initial and Boundary Conditions:

The initial conditions in the flume consisted of a flow of 26.3 l/s with a depth of 0.12 m. In the lower section of the flume there was a slight backwater. For the current simulations, however, a depth of 0.12 m was used for the entire reach.

At the upstream end the flow is maintained at a rate of 26.3 l/s, while the flow at the downstream boundary is shut-off within 0.5 s. This condition is maintained for the 45 s of the experiment reported.

Discretization and Solution Procedure:

Vasiliev et al. (1965) presented results based on a reach length of 0.75 m and time step of 0.5 s, while Terzidis and Strelkoff (1970) employed 1.0 m by 0.5 s grid. For the moving element model, an element size of 1.0 m was used with a time step of 0.5 s. Thus there are 76 nodes and 75 elements and the computations were carried out for 90 time steps.

The solution was based on the Eulerian-Lagrangian based moving element model. The interpolation at the Eulerian step was carried out by the Three Point

Lagrangian formula. For reason that the surge is moving upstream, (explained in Chapter 5) the temporal weighting factor was set at 0.75 and the spatial weighting was centered.

The profiles were captured at 5, 15, 30 and 45 s after initiating the experiment. The computed profiles are plotted in Fig. 7.45 along with the observed data points provided by Vasiliev et al. An examination of the observed and computed elevations indicate good predictions in both the depth of flow and advancement of wave front. These profiles also provided the basis for comparisons with the work of other investigators.

The depths of flow and discharges at the four time levels noted previously are presented in Figures 7.46 and 7.47 respectively. These two graphs provide an understanding of the advancement of the wave front with time and the influence of bed slope on the shape of the front. As the bed slope is significant at 0.5%, most of the momentum is consumed in establishing a level pool behind the front, reflecting the no flow condition at the downstream boundary. Fig. 7.46 supports the general absence of a sharp front examined in Test 'C', where the wave front proceeded upstream.

Also, the choking on the discharge takes place within a few elements as indicative of a discontinuous front property and is evident in Fig. 7.47. The volume was conserved within 0.2% of the difference between inflow and outflow volumes.

7.7.2 Faure's Experiment

This experiment was also reported by Vasiliev et al. (1965) and Terzedis and Strelkoff (1970). The results of the laboratory experiments carried out by Faure (1935) forms the basis of observations at five points and hydrographs at several other locations. To provide consistency with the results of other investigators, information

EGIAZAROV'S EXPERIMENT PROFILES

Time = 5, 15, 30 & 45 Sec Theta = 0.75

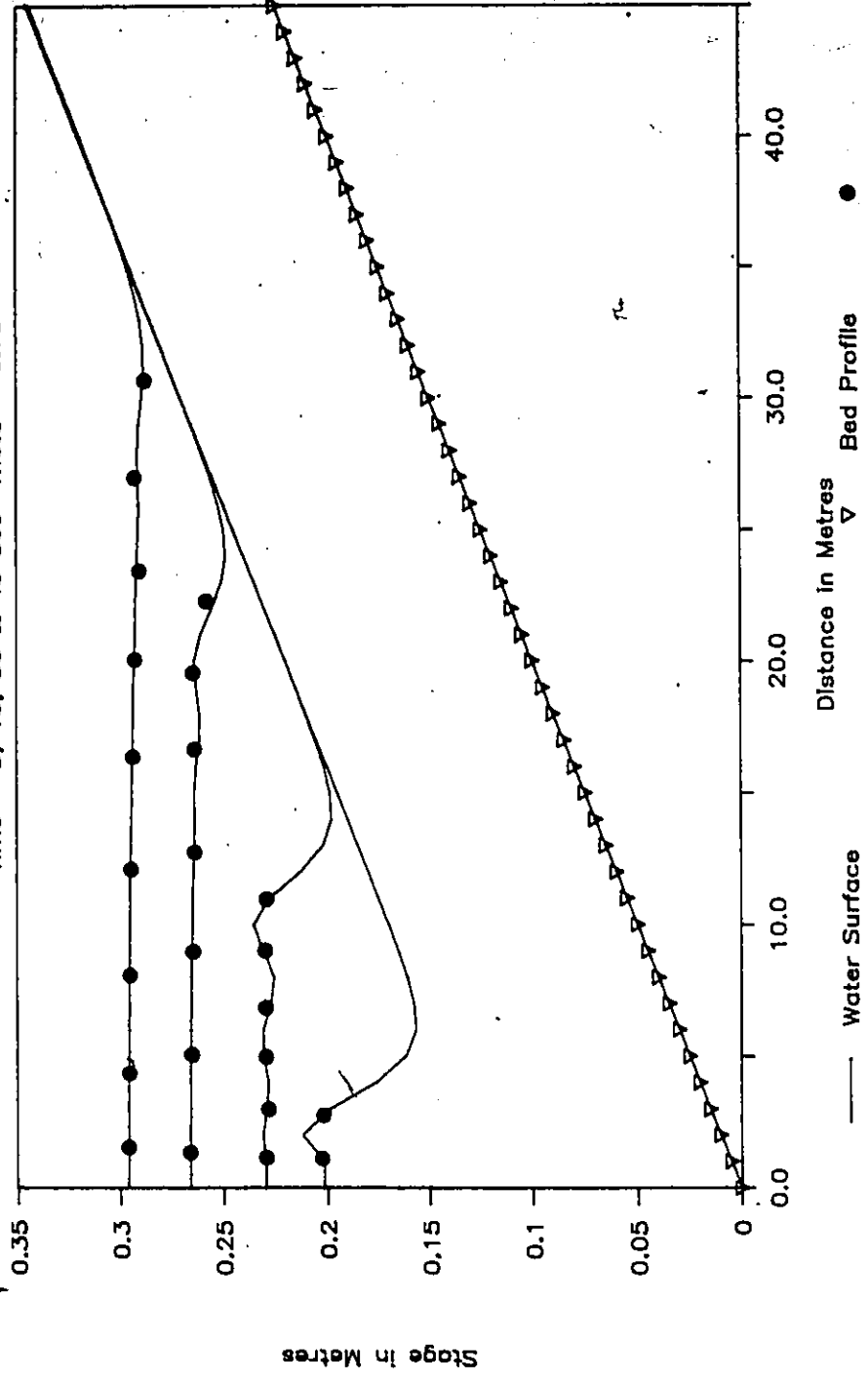


Fig. 7.45 Comparison of Stage Profiles at 5, 15, 30 and 45 Sec. - Egiazarov's Experiment



EGIAZAROV'S EXPERIMENT

Water Depth Progression, Theta = 0.75

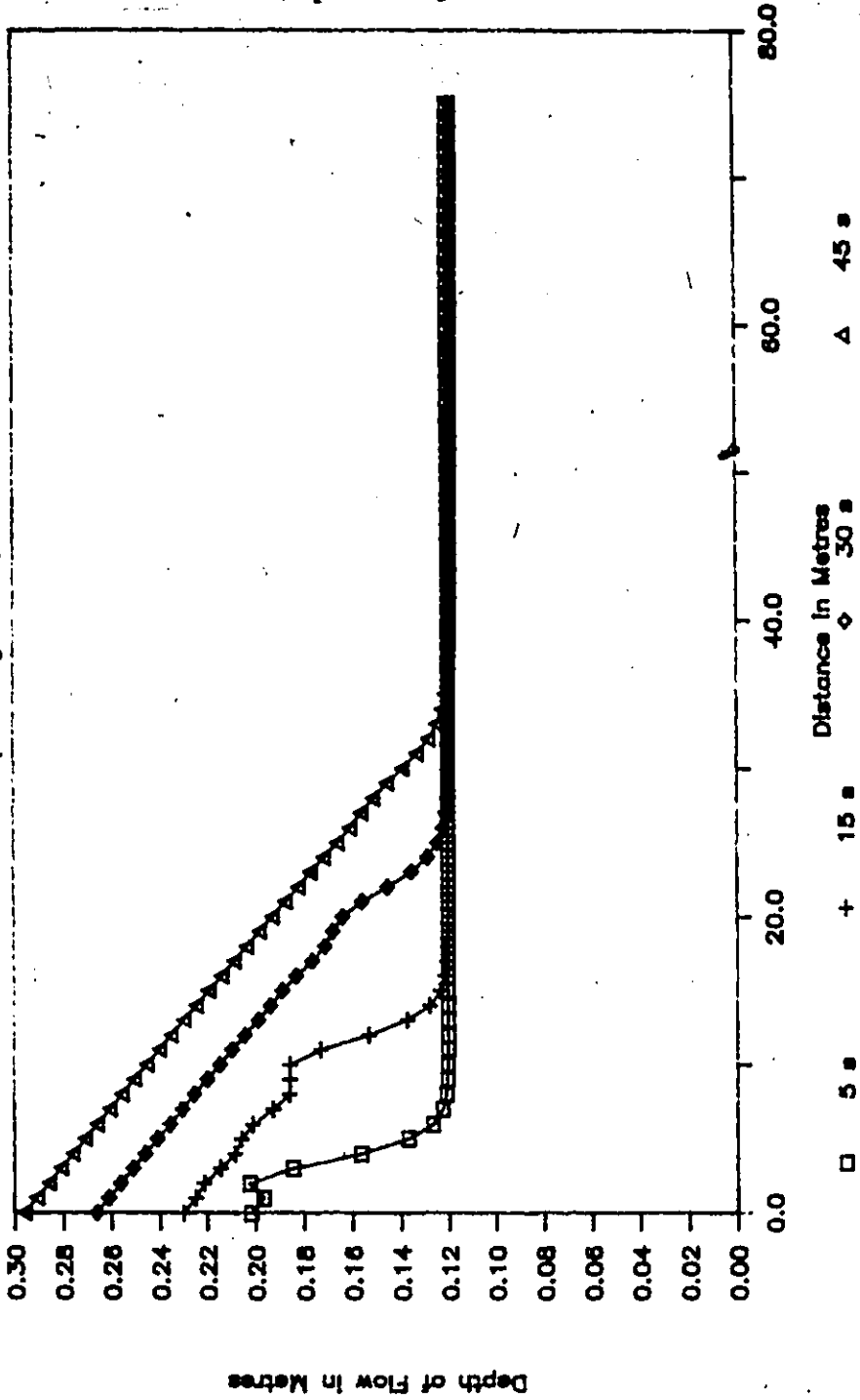


Fig. 7.46 Advancement of Surge in Time for Depth of Flow - Egiazarov's Experiment

EGIAZAROV'S EXPERIMENT

Wave (Flow) Progression, Theta = 0.75

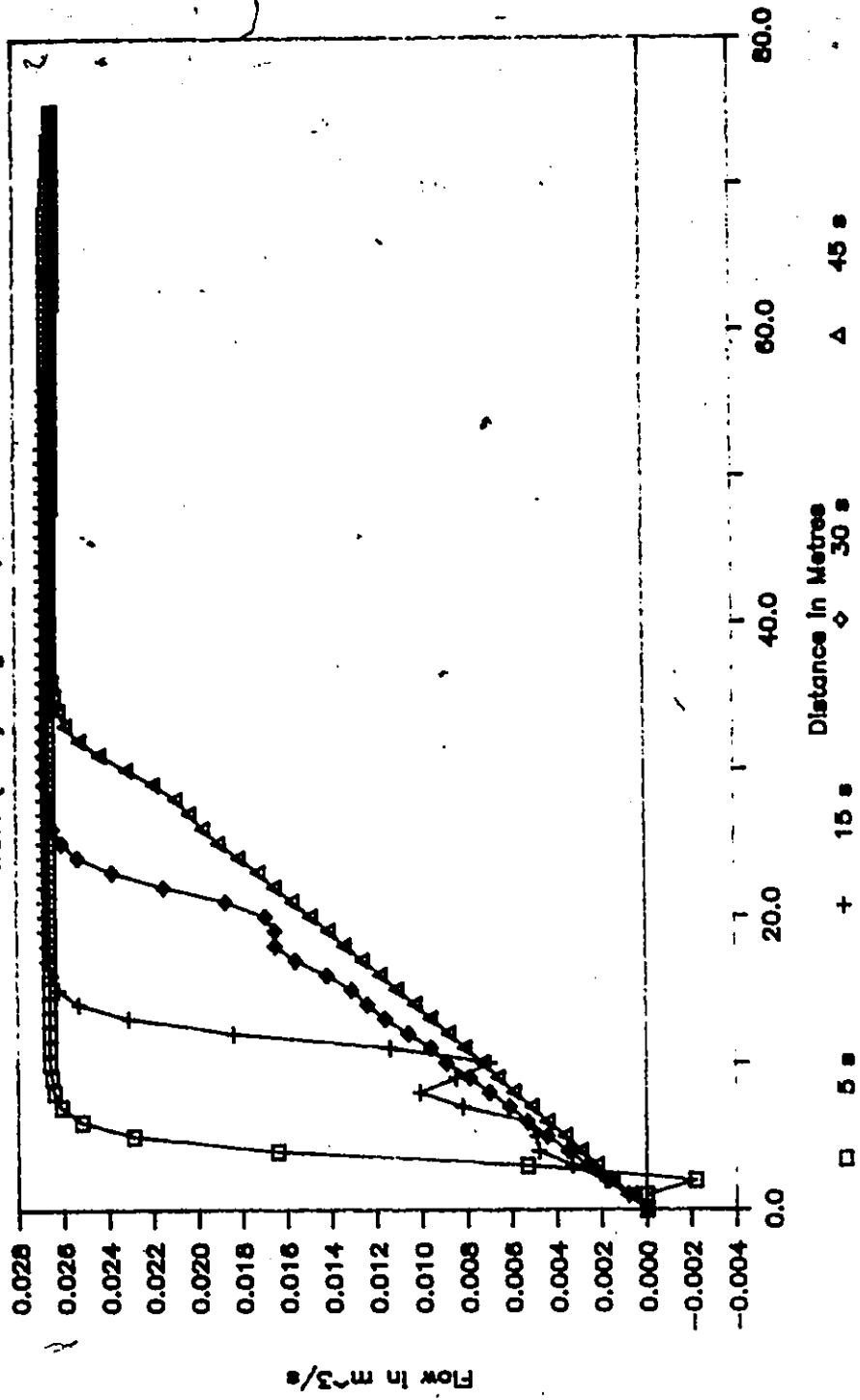


Fig. 7.47 Advancement of Surge in Time for Discharge - Egiazarov's Experiment

for the moving element model was gathered at the same time levels and at the same points as reported by the above workers. The experimental details are as follows:

Physical description:

The prismatic flume employed for the experiment was 0.42 m wide, rectangular in cross-section and 75 m in length. The channel bed was horizontal. The channel roughness was approximated by the Manning coefficient and set equal to 0.01.

Initial and Boundary Conditions:

Initial conditions for the experiment consisted of a level pool of 0.205 m depth with zero velocity.

At the upstream end, the flow is increased to 28 l/s within 0.2 s and is maintained for the 40 s of the experiment. At the downstream boundary, no flow condition is imposed. The resulting surge is subcritical in nature and therefore it is sufficient to supply one boundary condition at each end.

Discretization and Solution Procedure:

Both, Vasiliev et al. (1965) and Terzedis and Strelkoff (1970) employed a grid size of 0.75 m. They used time steps of 0.2 s and 0.4 s respectively. For the simulation with the moving element model, the reach length of 75 m was divided into 101 nodes and 100 elements each 0.75 m long. A time step of 0.2 s was selected for the computer run.

The solution is based on the Eulerian-Lagrangian based moving element model. The interpolation is based on the Three Point Lagrangian formula. Initially, a

temporal weighting of 0.5 was selected. The resulting surge which was only 0.041 m in height caused unacceptable undulations behind the wave front. The reason for this performance appears to stem from the fact that the initial and final wave celerities were not very different (0.135 m/s). To verify that the initial and final celerities do influence the results, second computer run was made by reducing the initial depth of flow to 0.0205 m (from 0.205 m) and executing the program with a temporal weighting factor of 0.5. Other than the spike at the tip of the front, the model exhibited excellent surge capturing properties. Based on this observation and inference drawn from the results, the temporal weighting for reproducing the experiment was increased to 0.75. The spatial weighting was centered.

The water surface profiles are captured at 20 s and 40s time levels, while the hydrographs are recorded at 31.5 m, 43.5 m and 55.5 m from the upstream boundary. The depth of flow profiles are presented in Fig. 7.48 along with the observed values (two points at 20s and five points at 40 s). The profiles indicate excellent reproduction in the height, speed and location of the front. When compared with the successive stage profiles provided by Terzedis and Strelkoff (1970), the wave front by the moving element method is captured in fewer elements. This is indicative that the wave front is relatively sharper than other techniques.

Figures 7.49 to 7.51 show the stage hydrographs at the locations noted above. The measured times of surge arrival are also displayed in the figures. Again, a comparison with the other finite difference based methods demonstrate the superior predictions of the finite element model.

FAURE'S EXPERIMENT

Profiles at 0, 20 & 40 s, Theta=0.75

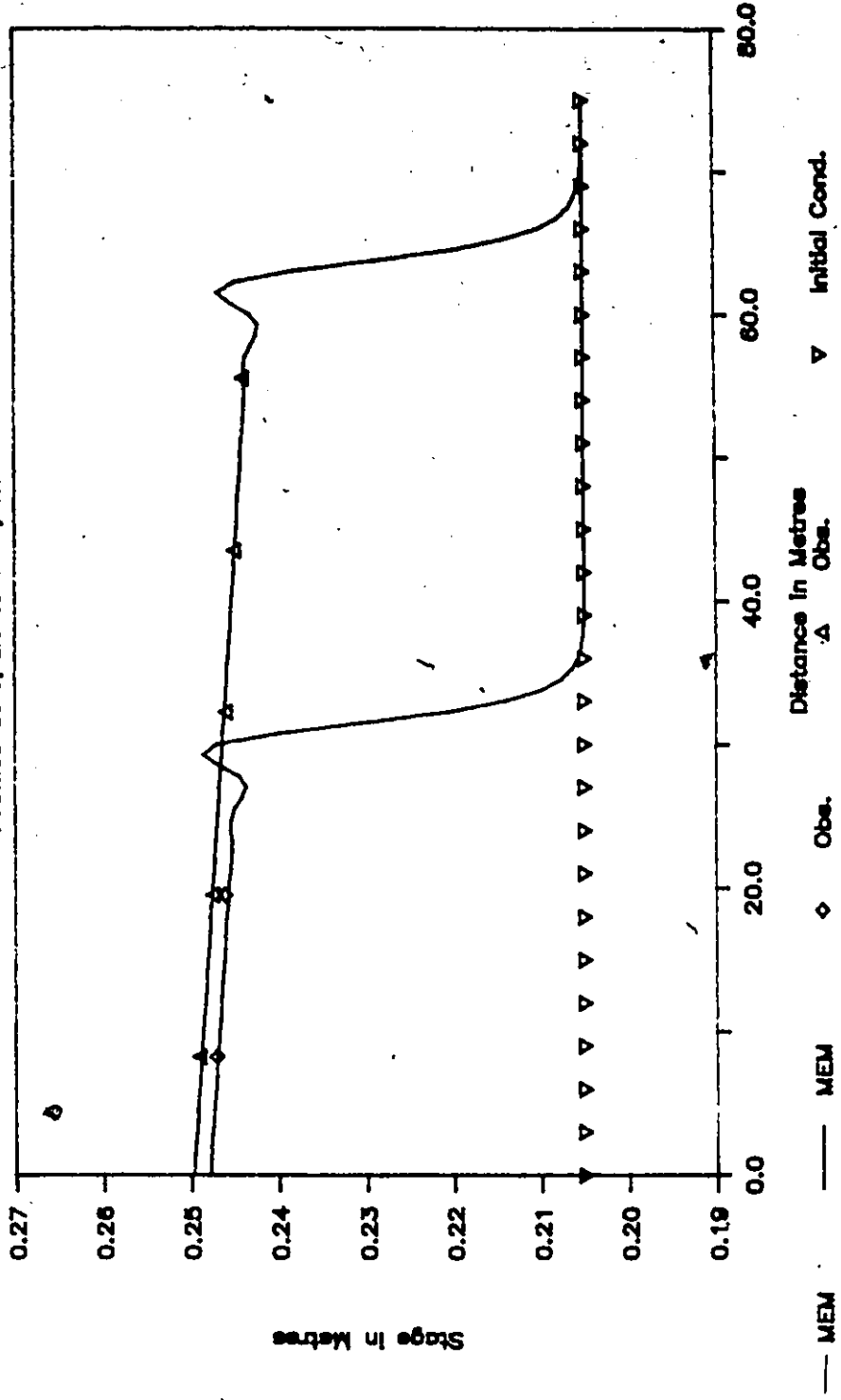


Fig. 7.48 Comparison of Stage Profiles at 20 and 40 Sec. for Faure's Experiment

FAURE'S EXPERIMENT

Stage Hydrograph at 31.5 m, Theta=0.75

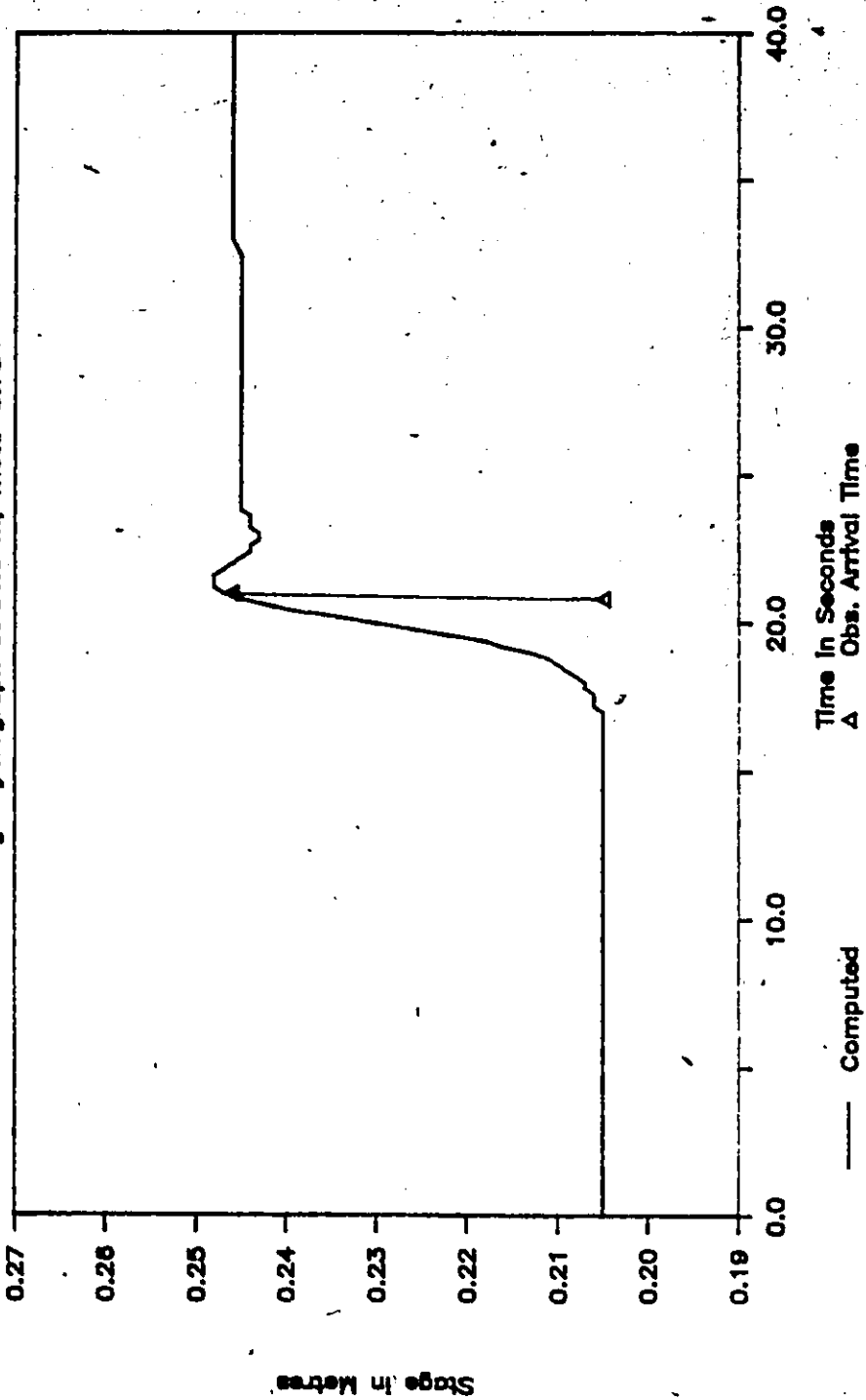


Fig. 7.49 Comparison of Surge Arrival Times Between Observed and Computed Discharge Hydrograph for Faure's Experiment at 31.5 M

FAURE'S EXPERIMENT

Stage Hydrograph at 43.5 m, Theta=0.75

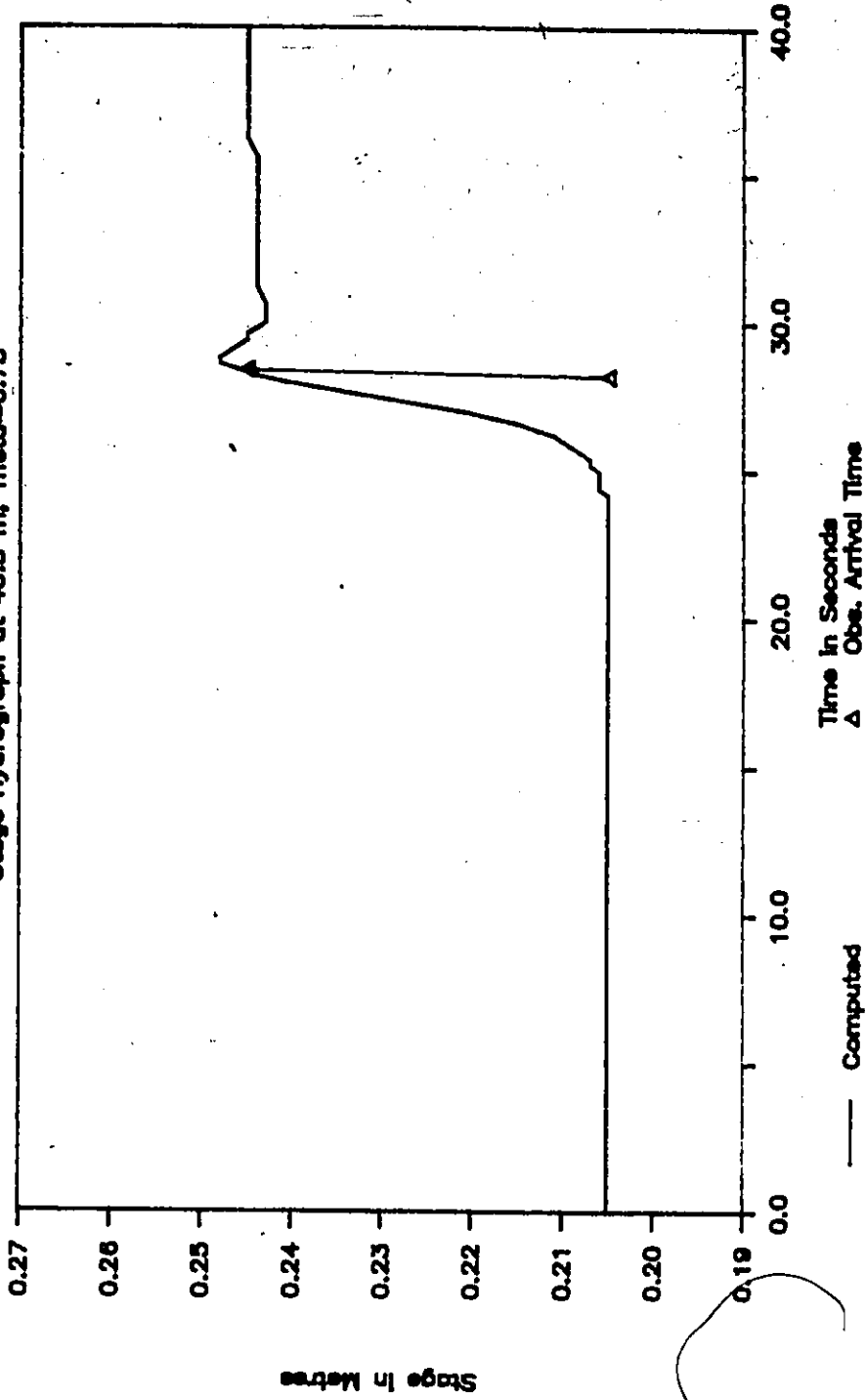


Fig. 7.50 Comparison of Surge Arrival Times Between Observed and Computed Discharge Hydrograph for Faure's Experiment at 43.5 M

FAURE'S EXPERIMENT

Stage Hydrograph at 55.5 m, $\Theta = 0.75$

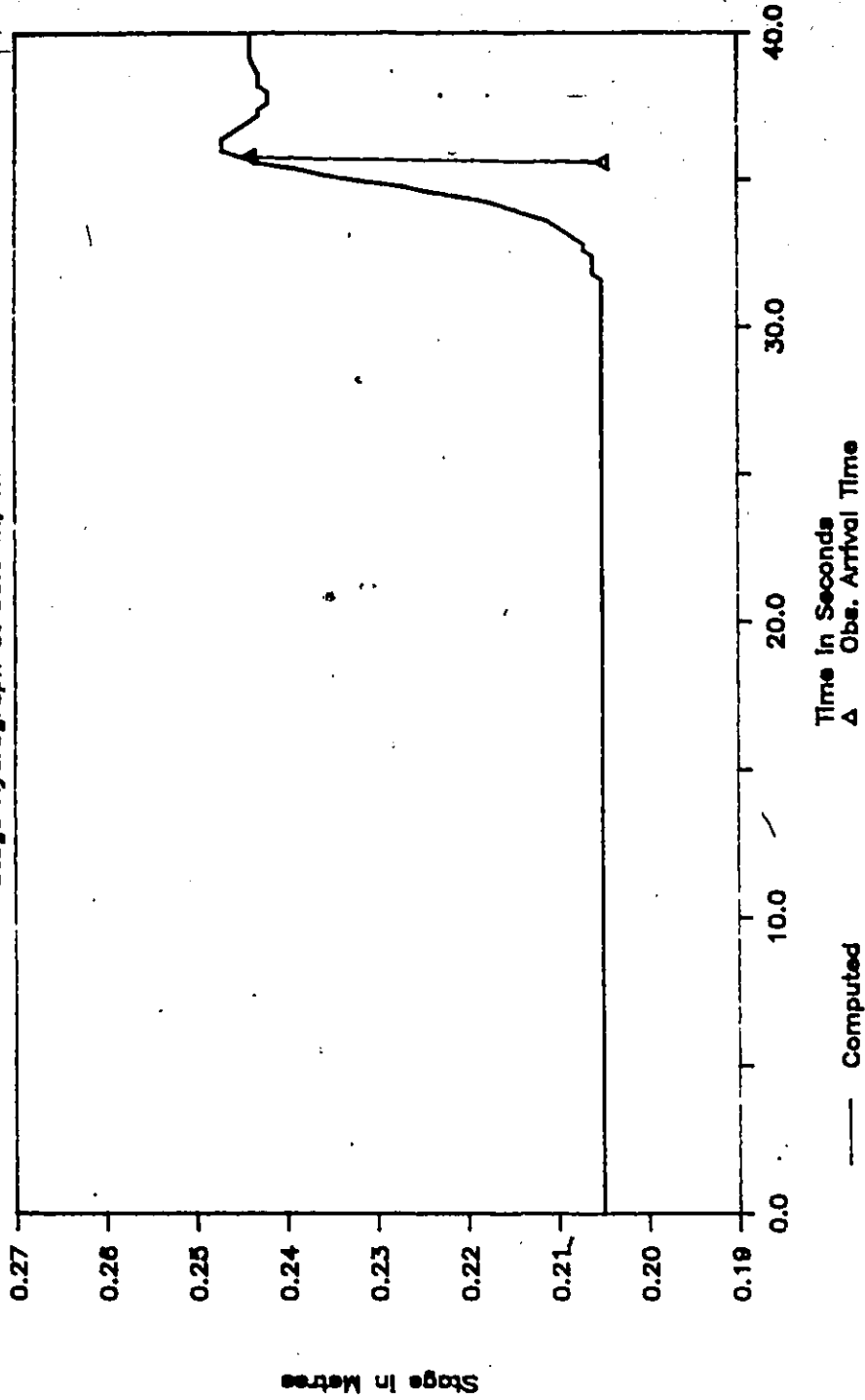


Fig. 7.51 Comparison of Surge Arrival Times Between Observed and Computed Discharge Hydrograph for Faure's Experiment at 55.5 M

7.8 Summary

The Eulerian-Lagrangian linked moving element model was applied to two real flood events. One involved the Teton dam failure and the other related to three high floods in the Grand River. The verification of two laboratory experiments was also carried out. Besides, three other hypothetical scenarios with either real field information or real hydrograph were simulated. All the tests conclusively point at the robust nature of the moving element algorithm at the central core of the model.

The model required several changes to address and improve the presentation of the results. In all changes, the central matrix and its inversion were not touched except when off-channel storage was introduced. Other areas where improvements to the model were successfully implemented include (1) handling of complex channel geometry, (2) lateral inflow and losses due to infiltration handled as lateral outflow, (3) changes in Manning's roughness with increasing stages, (4) calculation of maximum depth and flow envelopes, (5) initial steady state depth and flow, etc.

The moving element scheme proved to be consistent, convergent and stable even in the presence of highly non-linear channel geometry, rapidly and slowly changing boundaries, etc. The model did not exhibit any oscillatory behavior for a temporal weighting factor of 0.5. For the laboratory verifications, however, a value of 0.75 was required. The scheme was operated at 10 to 12 times the time steps than those dictated by the Courant-Lewy-Friedreich's condition. A different kind of limitation was, however, noted relating to cross-sectionally averaged velocity and the shape of the space-time grid. Optimum results were obtained when the spatial displacements at the advanced time level were approximately half the element size. This time-step was further constrained by the degree of departure from prismatic channel shape.

The results exhibited sensitivity similar to that reported by other investigators when model parameters were varied within reason. Further, in the presence of expansions from canyon to valley the model's performance was reasonable considering that no 'sedatives' were added to the model. The results at channel transitions improved with the refining of grid size.

The moving element scheme was subjected to extremes of channel slopes with a highly non-linear, non-prismatic channel shape, namely 1.0 ft/mile (0.000189) with the Teton River cross-sections to over 10 ft/mile (0.000189). The results could again be rationalized. There are no reports of similar model performance especially for the milder slopes even when advanced temporal weightings, energy and form losses are taken into consideration.

CHAPTER 8

SUMMARY, CONCLUSIONS AND RECOMMENDATIONS

In this chapter, a summary of research methodology and accompanying results are presented. Conclusions drawn from the extensive numerical experiments and limited testing in natural channels and laboratory setting are developed. Finally, recommendations emanating from these conclusions and preceding research are highlighted.

8.1 Summary

The research reported herein was carried out in five steps. At the outset, a detailed literature review was carried out to properly define the current techniques employed in the fields of fluid mechanics and open channel hydraulics. Emphasis in the fluid mechanics area was placed in the convection dominated flows while dam break flood simulation techniques were pursued in the field of open channel hydraulics. This survey concluded that most methods whether solving Burger's equation in fluid mechanics or the St. Venant equations for open channel flow employed either an internal or an external dissipation mechanism to handle otherwise non-dissipative solution schemes.

The second part of the work concentrated on the development of a study methodology where the divergent form of open channel flow equations was solved. The unsteady flow hydraulics is defined by a pair of nonlinear hyperbolic equations and their associated initial and boundary conditions. These are solved by a novel Eulerian-Lagrangian linked algorithm. This technique relies on the powerful

Lagrangian based solution and yet maintain the flexibility of computing flows at known Eulerian locations.

The Eulerian-Lagrangian model is capable of capturing near discontinuous flows at a temporal weighting consistent with the Crank-Nicholson scheme. The solution is free of any node to node oscillations found in other numerically accurate finite difference and finite element methods at Crank - Nicholson weighting.

The basic Lagrangian scheme in itself provides a non-dissipative solution. This, therefore, requires the advancement of temporal weightings for the discontinuous flow solution only. This technique, in contrast to other numerical methods, maintained a steep front which is resolved usually within two elements.

In a limiting sense, the model permits the motion of the wave front or discontinuity as a vertical wall by piling up water behind the nose of the front and forming a stable spike. Extensive numerical testing provided an insight to the impact a variety of model parameters such as time step, element size, temporal and spatial weighting parameters, roughness coefficient.

In part three, the model was tested with numerous continuous and discontinuous flow problems as part of the numerical experiment. This exercise demonstrated another feature of the technique, namely time-step control to retain and resolve the information within the solution domain. The time-step, however, is not restricted to the Courant conditions. The algorithm was successful in simulating a variety of flow situations including supercritical and subcritical flows, downstream and upstream moving surges, etc. The solution algorithm was tested successfully against two laboratory experiments reported in the literature.

An important step in the fourth stage of the research was to move the model from the stage of numerical experiment to the simulation of actual dam-break floods

in natural channel. The model was modified to reflect topographical and geometrical features, off-channel storage and variation of roughness. A lack of adequate field data precluded exhaustive testing and the establishment of the model limitations. Rapidly varying flows for the Teton Dam break flood and gradually varying Grand River floods were simulated in an acceptable manner.

Finally, the numerical model was successfully implemented in a variety of computer hardware. The program was originally developed in a mainframe computer environment and later ported to personal computers. A variety of hardware/software combinations were tested.

8.2 Conclusions

From the five part research summarized in the previous section, the following conclusions are drawn.

1. The Eulerian-Lagrangian linked algorithm employing space-time isoparametric finite elements proved to be a novel and powerful method for solving the equations of open channel flow.
2. The method of weighted residuals applied to the divergent form of St. Venant unsteady flow equations gave a difference scheme which had $(\Delta x)^2$ and $(\Delta t)^2$ accuracy and was free of oscillatory solutions in the Eulerian-Lagrangian mode.
3. The moving (finite) element model was found to handle a variety of problems from near discontinuous flow hydrographs to gradually varied flow.

4. It was found that discontinuous or rapidly varying flows can be modelled without sacrificing accuracy or prejudicing the integrity of the governing equations.
5. The model is capable of predicting the shape, size, location and timing of wave front in an exceptional manner. Unlike other models, negative flows or shadow waves accompanying depression ahead of the front were not developed.
6. The Eularian-Lagrangian scheme provides for a natural time step control to maintain the solution resolved within the domain. This time step can be relaxed if the initial base flow is at non-zero positive velocity.
7. The technique with the numerical quadrature integration formula provided a Crank-Nicholson's centered temporal weighting of 0.5. The generalized model allows for variable spatial and temporal weighting parameters.
8. The sensitivity analysis concluded that the time step can be increased by advancing the temporal weighting or by dispersing the mass matrix via assignment of non-zero spatial weightings.
9. It was found that the Lagrangian scheme in itself provides for a non-dissipative solution. The natural dissipative interface is provided by the Eularian regridding.
10. The model was successfully adaptated from the controlled numerical experiment stage to dam-break and flood routing field problems.
11. The robustness of the model was demonstrated by employing the same model with different data sets for the Teton Dam failure and the Grand River floods.

12. The scheme was found to resolve the complex flow behaviour found in the vicinity of natural features such as bridges and weir flows. The wave reflections at dead ends and partial reflections at constrictions appear to be properly accounted for.
13. The model performance for surges moving upstream with slowly moving waters behind the front was only marginally better than that obtained by finite element and finite difference methods in current use (see page 186).
14. The model performance of the Eularian-Lagrangian scheme for rapidly varying flows is far superior to any other numerical scheme reported in the literature.
15. The model has all the necessary capabilities to form the central core of a flood forecasting model for rapidly varying flows associated with dam break.

8.3 Recommendations

With the development of any new technique, such as the Eularian-Lagrangian linked algorithm in this research, avenues open up for postulating numerous alternatives to further research. Some of these recommendations are described briefly as follows:

1. Considerable potential exists for further testing and development of the pure Lagrangian mode solution for rapidly varying flows by advancing the temporal weighting and continuous flow problems as a centred Crank-Nicholson scheme.
2. An attempt was made to carry out the Fourier analysis to investigate the behaviour of $2\Delta x$ length waves. Due to complex nonlinear behavior and

cross-coupling of terms, it was not further pursued. It is felt that a Fourier analysis of the linearized scheme will indicate that $2\Delta x$ oscillations for pure Lagrangian scheme will be preserved. This area, however, merits more attention.

3. When the numerical algorithm was modified and adopted for natural channels, the physical geometry was represented by a rather simplistic relationship. The model features can be enhanced to allow alternate representation of cross-section geometry.
4. The model has proved to be an equally powerful tool for the study of both rapidly and gradually varied flows. This feature will allow the model to act as a central core for a generalized open channel flow simulation tool in the same fashion as the Finite Element River Network Simulator FERNS (Moin, 1982) and Dynamic Wave Operational Model DWOPER (Fread, 1978).
5. The development of the Petrov-Galerkin scheme was carried to the point where extensive testing is required first to establish its validity and adaptability to field problems and secondly to develop relationships for the dissipation parameter.

APPENDIX A

Nomenclature and Glossary of Terms

Part 1 - Nomenclature

English Letters

- A -- Channel cross-sectional area
Area integral (with subscript L)
Area in channel, left over-bank and right over-bank (with subscripts c, l and r respectively)
Rate of departure from prismatic form (with subscript x and superscript y)
Off-channel storage area (with subscript o)
- B -- Channel top-width
- C -- Celerity of wave
Manning's equation constant (with subscript c)
- D -- Hydraulic depth
- F -- Froude No. (with subscript r)
Known functions (with numerical subscripts)
Boundary friction
- G -- First moment of area
Known functions (with numerical subscripts)
- H -- Known functions (with numerical subscripts)
- J -- Jacobian

- K -- Manning's equation constant**
 Conveyance in channel, left over-bank and right over-bank (with subscripts c, l and r respectively)
- L -- Line integral (with subscripts n and n + 1)**
- P -- Pressure (when divided by RHO)**
 Peclet no. (with subscript e)
 Wetted Perimeter
- Q -- Discharge or flow rate**
- R -- Hydraulic radius**
- S -- Location of leading edge of front channel bed slope (with subscript o)**
 friction slope (with subscript f) difference of bed & friction slopes (with subscript g)
- T -- Top-width of channel**
 Top-width in channel and over-bank (with subscripts c and o respectively)
- V -- Mean velocity**
- W -- Location of receding front**
- WP -- Wetted perimeter**
- X -- Boundary friction**
- a -- Bi-tri diagonal matrix coefficient (with numerical subscripts)**
- b -- Bi-tri diagonal matrix coefficient (with numerical subscripts)**
 Channel width as a function of depth
- c -- Bi-tri diagonal matrix coefficient (with numerical subscripts)**
 Celerity of wave
 Celerity of a reference flow (with subscript o)

- d -- Bi-tri diagonal matrix coefficient (with numerical subscripts)
- f -- Functional relationship (with numerical subscripts)
- Flux level
- g -- Acceleration due to gravity
- Functional relationship (with numerical subscripts)
- h -- Functional relationship (with numerical subscripts)
- Depth of flow
- Depth of centroid from surface (with a bar)
- k -- Ratio of conveyance in left and right over-banks (with subscripts l and r)
- Time step
- n -- Manning's roughness coefficient
- Roughness coefficient in channel, left over-bank and right over-bank (with subscripts c, l & r respectively)
- Variable roughness (with subscript w)
- Base roughness (with subscript b)
- p -- Source and sink terms in mass continuity
- Ratio in interpolation scheme
- q -- Lateral flow rate
- Source and sink terms in momentum conservation
- s -- Distance along the stream
- t -- Time units
- Time level (with numerical subscripts)
- u -- Average velocity
- Velocity of a reference flow (with subscript o)

- Velocity of lateral flow (with subscript x)
- Constant in bi-tri diagonal matrix solution
- x -- Distance units
- Distance along channel, left over-bank and right over-bank (with subscripts c, l and r respectively)
- U/S boundary chainage (with subscript L)
- D/S boundary chainage (with subscript R)
- y -- Water surface elevation above a reference datum
- Thalweg elevation (with subscript d)
- Bank elevation (with subscript b)
- Off-channel storage elevation (with subscript o)
- Water surface elevation (with subscript w)
- z -- Thalweg elevation
- Channel lateral slope (with subscript c)
- Conveyance lateral slope (with subscript b)
- Off-channel storage lateral slope (with subscript o)

Greek Letters

- α -- Dissipation parameter
- Bi-tri diagonal matrix solution constants
- β -- Spatial weighting parameter
- Bi-tri diagonal matrix solution constants
- γ -- First moment of area
- Bi-tri diagonal matrix solution constants

- δ -- Nodal displacement at Lagrangian step
 Bi-tri diagonal matrix solution constants
- Δ -- Order of error
 Increments of time and distance
- ϕ -- Basis function
- ∂ -- Partial derivative function
- θ -- Temporal weighting parameter
- ε -- Dissipation parameter
- ρ -- Density of water
- ξ -- Area integral weighting factor
- η -- Area integral weighting factor

Subscripts

- d -- Downstream boundary values
- i -- Space increment identifier
- l -- Newton-Raphson iteration level
- n -- Time level identifier
- o -- Initial time level
- u -- Upstream boundary values
- L -- Left boundary
- N -- Last element
- R -- Right boundary
- 0 -- First element

Superscripts

n -- Time level identifier

Part 2**Glossary of Terms**

Gradually Varied Flow (GVF) - Nonuniform flow condition where the depth and flow change rather slowly.

Rapidly Varied Flow (RVF) - Nonuniform flow where the temporal and spatial gradients are excessive.

Froude Number (F_r) - Classification number to indicate the type of flow. It is the ratio of inertial to gravitational forces. If F_r is less than 1.0, the flow is subcritical, if greater than 1.0, then the flow is supercritical.

Prismatic Section - A channel with both a constant cross sectional shape and bottom slope. Channel that depart from this criteria are nonprismatic.

Conveyance Section - Part of channel cross-section carrying the flood waters.

Off-Channel Storage - Part of channel cross-section where the flood waters are either moving very slowly or not moving at all.

Choke - A constriction in area by encroaching the channel reducing the area to pass the flow...**Hump** - An obstruction in the path of flow by providing sharp adverse slope, a short level reach followed by sharp drop.

Finite Difference Method - Finite difference methods are discrete numerical techniques wherein the domain of interest is represented by a set of points or nodes and information between these points employing Taylor series expansions.

Finite Element Method - Finite element method is a numerical technique wherein the domain of interest is represented by a set of nodes and employs piecewise continuous polynomials to interpolate between these points.

Lagrangian Solution - A solution based on tracking the movement of a particle. The spatial points where the solution is sought change between time steps.

Eulerian Solution - A solution based on a fixed space-time grid. The information moves across the points of interest.

APPENDIX B

Nodal Contributions at the Upstream Boundary for Supercritical Flow Conditions

For supercritical flow, the upstream boundary conditions require the specification of both the depth of flow and discharge. The momentum equation is replaced by this specification and therefore makes it necessary to adjust the continuity and momentum equations for the first two types of elements. These are provided for both the triangular and collapsed quadrilateral boundary elements.

1. Triangular Element

Type 1 element contribution

$$Y_0^{n+1} - Y_u(t) = 0 \quad (B-1)$$

$$Q_0^{n+1} - Q_u(t) = 0 \quad (B-2)$$

Type 2 element contributions. Mass continuity is given by Equation 4.129.

Momentum Conservation:

$$\begin{aligned} & -\frac{1}{4} [Q_1^n + Q_1^{n+1}](x_1^{n+1} - x_1^n) + (Q_2^n + Q_2^{n+1})(x_2^{n+1} - x_2^n) \\ & + \frac{k}{4} [(Qu)_1^n + (Qu)_1^{n+1} + (Qu)_2 + (Qu)_2^{n+1}] \\ & + \frac{kg}{4} [(A\bar{y})_1^n + (A\bar{y})_1^{n+1} + (A\bar{y})_2^n + (A\bar{y})_2^{n+1}] \\ & - \frac{kg}{4} [A_1^{n+1} Sg_1^{n+1} (x_2^{n+1} - x_1^{n+1}) + A_1^n Sg_1^n (x_2^n - x_1^n)] \\ & - \frac{kg}{6} (x_1^{n+1} - x_0^{n+1}) (A_1^n Sg_1^n + A_1^{n+1} Sg_1^{n+1} + A_0^{n+1} Sg_0^{n+1}) \\ & + \frac{1}{2} [Q_1^{n+1} (x_2^{n+1} - x_0^{n+1}) - Q_1^n (x_2^n - x_1^n)] \\ & + \frac{1}{2} Q_0^{n+1} (x_1^{n+1} - x_0^{n+1}) - \frac{k}{2} [(Qu)_0^{n+1} + (Qu)_1^n] \\ & - \frac{kg}{2} [(A\bar{y})_0^{n+1} + (A\bar{y})_1^n] = 0. \end{aligned} \quad (B-3)$$

2. Collapsed Quadrilateral Element

Equations B-1 and B-2 describe Type 1 element contribution.

Type 2 element contribution

Mass Continuity:

The only terms effected are those involving lateral flow terms. In Equation 4-129, the third and fourth terms are replaced by

$$\begin{aligned}
 & - \frac{k}{4} [q_1^n (x_2^n - x_1^n) + q_1^{n+1} (x_2^{n+1} - x_0^{n+1}) \\
 & \quad + q_0^{n+1} (x_1^{n+1} - x_0^{n+1})]
 \end{aligned}
 \tag{B-4}$$

Momentum Conservation:

Similar to the mass continuity equatoin only terms without a spatial or temporal derivative are affected. In Equation B-3 above, the fourth and fifth terms are written as

$$\begin{aligned}
 & - \frac{k}{4} [A_1^n Sg_1^n (x_2^n - x_1^n) + A_1^{n+1} Sg_1^{n+1} (x_2^{n+1} - x_0^{n+1}) \\
 & \quad + A_0^{n+1} Sg_0^{n+1} (x_1^{n+1} - x_0^{n+1})]
 \end{aligned}
 \tag{B-5}$$

APPENDIX C

Nodal Contributions of the Lateral Flow Component in the Momentum Conservation Equation

The lateral flow contributions for the five types of elements are given below. These terms are to be added to the respective momentum conservation equations.

Type 1 element (terms added to Equation 4.118)

$$-\frac{k}{6} (x_1^{n+1} - x_0^{n+1}) (u_{x_1}^n q_1^n + u_{x_1}^{n+1} q_1^{n+1} + u_{x_0}^{n+1} q_0^{n+1}) \quad (C-1)$$

Type 2 element (terms added to Equation 4.120)

$$-\frac{k}{6} (x_1^{n+1} - x_0^{n+1}) (u_{x_1}^n q_1^n + u_{x_1}^{n+1} q_1^{n+1} + u_{x_0}^{n+1} q_0^{n+1})$$

$$-\frac{k}{4} [u_{x_1}^n q_1^n (x_2^n - x_1^n) + u_{x_1}^{n+1} q_1^{n+1} (x_2^{n+1} - x_1^{n+1})] \quad (C-2)$$

Type 3 element (terms added to Equation 4.122)

$$-\frac{k}{4} [u_{x_i}^n q_i^n (x_{i+1}^n - x_{i-1}^n) + u_{x_i}^{n+1} q_i^{n+1} (x_{i+1}^{n+1} - x_{i-1}^{n+1})] \quad (C-3)$$

Type 4 element (terms added to Equation 4.124)

$$-\frac{k}{4} [u_{x_{N-1}}^n q_{N-1}^n (x_N^n - x_{N-2}^n) + u_{x_{N-1}}^{n+1} q_{N-1}^{n+1} (x_N^{n+1} - x_{N-2}^{n+1})] \quad (C-4)$$

Type 5 element (terms added to Equation 4.126)

$$-\frac{k}{4} [u_{x_N}^n q_N^n (x_N^n - x_{N-1}^n) + u_{x_N}^{n+1} q_N^{n+1} (x_N^{n+1} - x_{N-1}^{n+1})] \quad (C-5)$$

APPENDIX D

Nodal Contributions for Collapsed Quadrilateral Elements

Employment of the collapsed quadrilateral elements require changes only in the first two types of elements. In the model, Equations 4.117 to 4.120 are replaced by the following relationships.

Type 1 elements for $i = 0$

Conservation of Mass:

$$\begin{aligned} & \frac{k}{4} (Q_1^n + Q_0^{n+1} + Q_2^n + Q_1^{n+1}) - \frac{1}{4} (x_1^{n+1} - x_2^n) (A_1^{n+1} + A_2^n) \\ & - \frac{k}{4} (x_1^{n+1} - x_0^{n+1}) Q_0^{n+1} + \frac{1}{2} A_0^{n+1} (x_1^{n+1} - x_0^{n+1}) \\ & - \frac{k}{2} (Q_0^{n+1} + Q_1^n) = 0 \end{aligned} \tag{D-1}$$

Conservation of Momentum:

$$\begin{aligned} & - \frac{1}{4} (x_1^{n+1} - x_2^n) (Q_1^{n+1} + Q_2^n) + \frac{k}{4} [(Qu)_1^n + (Qu)_0^{n+1}] \\ & + (Qu)_2^n + (Qu)_1^{n+1}] + \frac{kg}{4} [(A\bar{y})_1^n + (A\bar{y})_0^{n+1} \\ & + (A\bar{y})_2^n + (A\bar{y})_1^{n+1}] - \frac{kg}{4} (x_1^{n+1} - x_0^{n+1}) A_0^{n+1} Sg_0^{n+1} \\ & + \frac{1}{2} Q_0^{n+1} (x_1^{n+1} - x_0^{n+1}) - \frac{k}{2} [(Qu)_0^{n+1} + (Qu)_1^n] \\ & - \frac{kg}{2} [(A\bar{y})_0^{n+1} + (A\bar{y})_1^n] = 0 \end{aligned} \tag{D-2}$$

Type 2 elements for $i = 1$

Conservation of Mass:

$$\begin{aligned}
& \frac{k}{4} (Q_2^{n+1} - Q_0^{n+1} + Q_3^n - Q_1^n) - \frac{1}{4} (x_2^{n+1} - x_3^n) (A_2^{n+1} + A_3^n) \\
& - \frac{k}{4} [q_1^{n+1} (x_2^{n+1} - x_0^{n+1}) + q_1^n (x_3^n - x_1^n)] \\
& + \frac{1}{2} [A_1^{n+1} (x_0^{n+1} - x_3^n) - A_1^n (x_3^n - x_1^n)] = 0
\end{aligned} \tag{D-3}$$

Conservation of Momentum:

$$\begin{aligned}
& - \frac{1}{4} (x_2^{n+1} - x_3^n) (Q_2^{n+1} + Q_3^n) + \frac{k}{4} [(Qu)_2^{n+1} - (Qu)_0^{n+1} \\
& + (Qu)_3^n + (Qu)_1^n] + \frac{kg}{4} [(Ay)_2^{n+1} - (Ay)_0^{n+1} \\
& + (Ay)_3^n - (Ay)_1^n] - \frac{kg}{4} [A_1^{n+1} Sg_1^{n+1} (x_2^{n+1} - x_0^{n+1}) \\
& + A_1^n Sg_1^n (x_3^n - x_1^n)] + \frac{1}{2} [Q_1^{n+1} (x_2^{n+1} - x_0^{n+1}) \\
& - Q_1^n (x_3^n - x_1^n)] = 0
\end{aligned} \tag{D-4}$$

Equation D-3 was modified similar to 4.129 to accommodate upstream boundary conditions.

APPENDIX E

Coefficients of Bi-tridiagonal Matrix

The coefficients of the bi-tridiagonal matrix for the difference form of mass and momentum conservation evolve from Equations 4.142 to 4.155. These coefficients are presented here for Type 3 elements. Reference can be made to the computer program listing where coefficients of all other types are shown.

Conservation of Mass:

$$a_1 = \frac{1}{4} T_{i-1}^{n+1} (x_{i-1}^{n+1} - x_{i-1}^n) \quad (E-1)$$

$$a_2 = -\frac{k}{4} \quad (E-2)$$

$$b_1 = \frac{1}{2} T_i^{n+1} (x_{i+1}^{n+1} - x_{i-1}^{n+1}) \quad (E-3)$$

$$b_2 = 0.0 \quad (E-4)$$

$$c_1 = -\frac{1}{4} T_{i+1}^{n+1} (x_{i+1}^{n+1} - x_{i+1}^n) \quad (E-5)$$

$$c_2 = \frac{k}{4} \quad (E-6)$$

$$d_1 = -F \quad (E-7)$$

where F is given by Equation 4.121.

Conservation of Momentum:

$$a_3 = -\frac{kg}{4} A_{i-1}^{n+1} + \frac{k}{4} (u_{i-1}^{n+1})^2 T_{i-1}^{n+1} \quad (E-8)$$

$$a_4 = \frac{1}{4} (x_{i-1}^{n+1} - x_{i-1}^n) - \frac{k}{2} u_{i-1}^{n+1} \quad (E-9)$$

$$b_3 = \frac{kg}{4} (A_i^{n+1} \frac{\partial S_i^{n+1}}{\partial y_i^{n+1}} + T_i^{n+1} S_g^{n+1}) (x_{i+1}^{n+1} - x_{i-1}^{n+1}) \quad (E-10)$$

$$b_4 = \frac{kg}{4} A_i^{n+1} \frac{\partial S_f^{n+1}}{\partial Q_i^{n+1}} (x_{i+1}^{n+1} - x_{i-1}^{n+1}) + \frac{1}{2} (x_{i+1}^{n+1} - x_{i-1}^{n+1}) \quad (\text{E-11})$$

$$c_3 = \frac{kg}{4} A_{i+1}^{n+1} - \frac{k}{4} (u_{i+1}^{n+1})^2 T_{i+1}^{n+1} \quad (\text{E-12})$$

$$c_4 = -\frac{1}{4} (x_{i+1}^{n+1} - x_{i-1}^{n+1}) + \frac{k}{2} u_{i+1}^{n+1} \quad (\text{E-13})$$

$$d_2 = -G \quad (\text{E-14})$$

where G is given by Equation 4.122

Also,

$$S_f = \frac{Q^2 n^2}{C_c A^{4/3} R^{4/3}} \quad (\text{E-15})$$

$$\frac{\partial S_f}{\partial Q} = 2 S_f / Q \quad (\text{E-16})$$

$$\frac{\partial S_f}{\partial y} = -S_f \left(\frac{4}{3} T - \frac{10}{3} R \frac{\partial p}{\partial y} \right) / A \quad (\text{E-17})$$

APPENDIX F

More Numerical Experiment Graphical Results

In Chapter 5, a number of numerical experiments were designed and executed. Besides the experiments described in that chapter, a series of sensitivity analysis was carried out. The stage and flow hydrographs at several points and the stage and flow profiles at predetermined times were captured. These are presented without any further discussion in this appendix. Considerable amount of information, however, can be extracted even from these graphs.

The graphical presentations are further divided into the following five categories.

Series 1: In this series, Test E1, studying the passage of a surge hydrograph through the choke was undertaken. The sensitivity of further constricting the flow by pinching the size of the throat is investigated. The information is presented in Figs. F.1.1 through F.1.9.

The impact of grid sizing can be deduced from Figs. F.1.10 to F.1.15. The sensitivity of changing the temporal weighting factor and time step size is studied and depicted in Figs. F.1.16 and F.1.17.

Series 2: This series studied Test E2, namely, the passage of a surge over the Hump. Figs. F.2.1 to F.2.3 show the information not presented in Chapter 5 (eg. velocity and discharge profiles and discharge hydrographs).

A study was carried out by constricting the passage of surge both horizontally and vertically. This was achieved by combining the basic information from Tests E1 and E2. Interesting results can be deduced from Figs. F.2.4 to F.2.6.

Series 3: The impact of routing a surge through a channel expansion was studied and basic geometrical information presented in Section 5.6.4. The graphical information on this emulation of reservoir exercise is presented in Figs. F.3.1 and F.3.2. The sensitivity of changing the temporal weighting parameter is also shown on the same graphs.

Series 4: In Section 5.4, limited comparisons were shown between the moving element method and the finite element and finite difference schemes. The temporal and spatial generalization of the moving element technique, however, enabled these parameters to be varied in an orderly manner to study their impact. These are shown in Figs. F.4.1 to F.4.8. Purposely the time step in Test 'B' were selected at 5.0 seconds to introduce oscillatory behaviour at the tip the wave front. Subsequently, these oscillations were systematically removed by choosing the spatial and temporal weightings in a judicious manner.

Series 5: Information on various sensitivity analysis not reported in Chapter 5 is presented in this part to provide further insight in the mechanics of surge routing.

For the purposes of this section the following abbreviations were employed:

Moving Element Method	ME
Finite Element Method	FE
Finite Difference Method	FD

Temporal Weighting Factor	TWF
Spatial Weighting Factor	SWF
Upstream	U/S
Downstream	D/S

FLOW THRU CHOKE - PARTIAL REFLECTION

DX=20 DT=25 THETA=0.6 CHOKE 50 & 25M

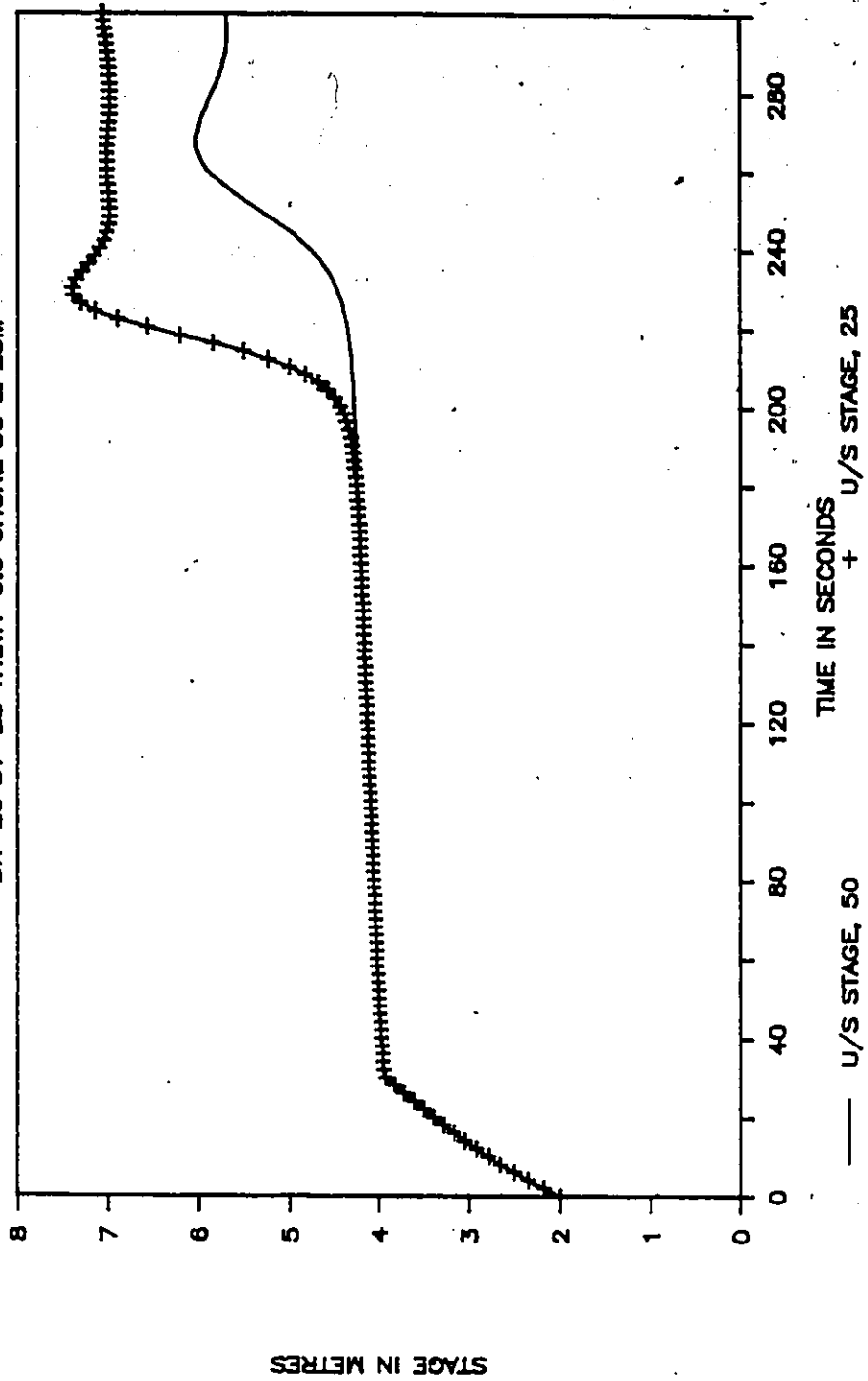


Fig. F.1.1 Impact of Choke Size Stagegraphs at U/S Boundary

FLOW THRU CHOKE - PARTIAL REFLECTION

DX=20 DT=25 THETA=0.8 CHOKE 50 & 25M

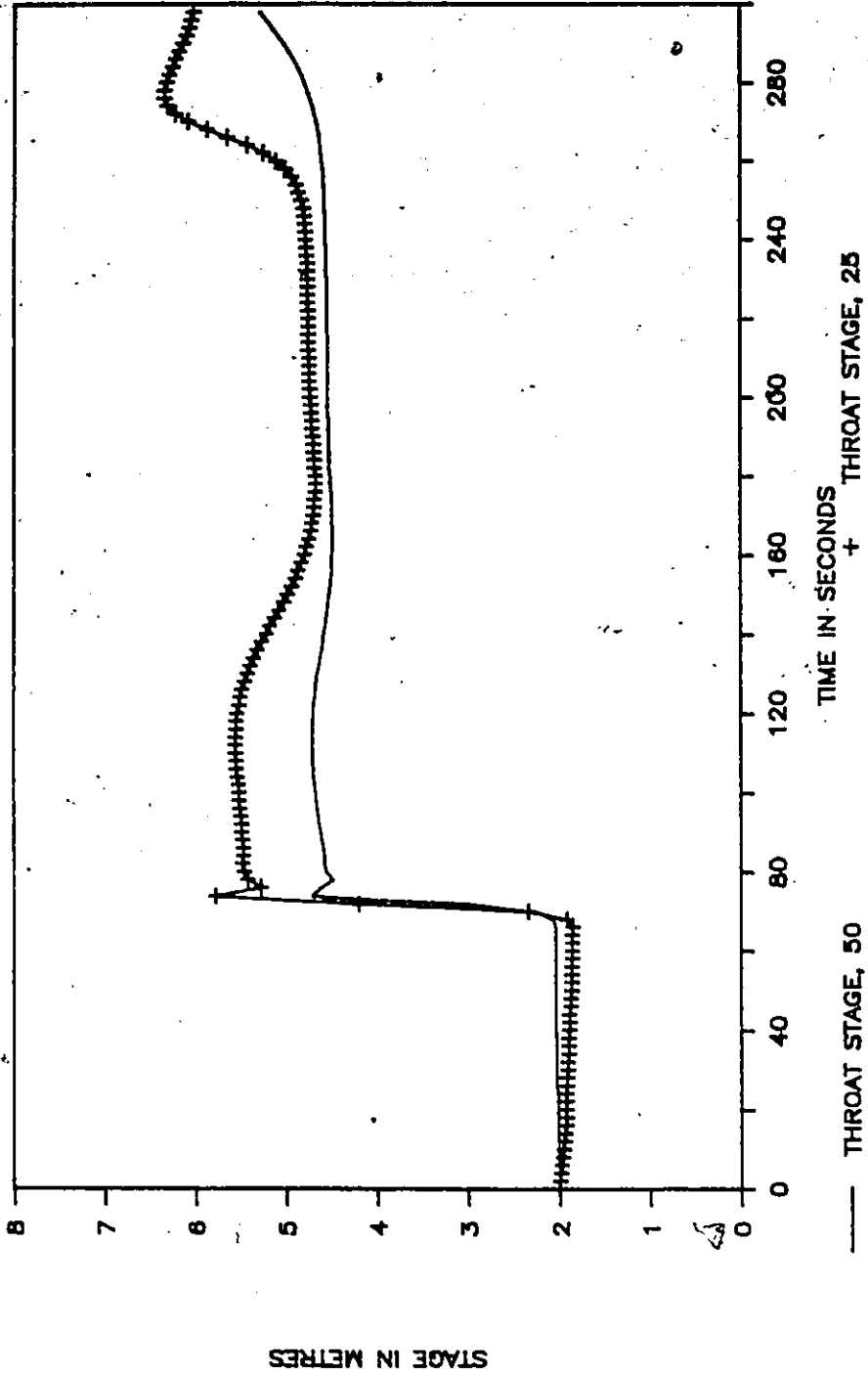


Fig. F.1.2 Impact of Choke Size Stagegraphs at Choke Section

FLOW THRU CHOKE - PARTIAL REFLECTION

DX=20 DT=2S THETA=0.6 CHOKE 50 & 25M

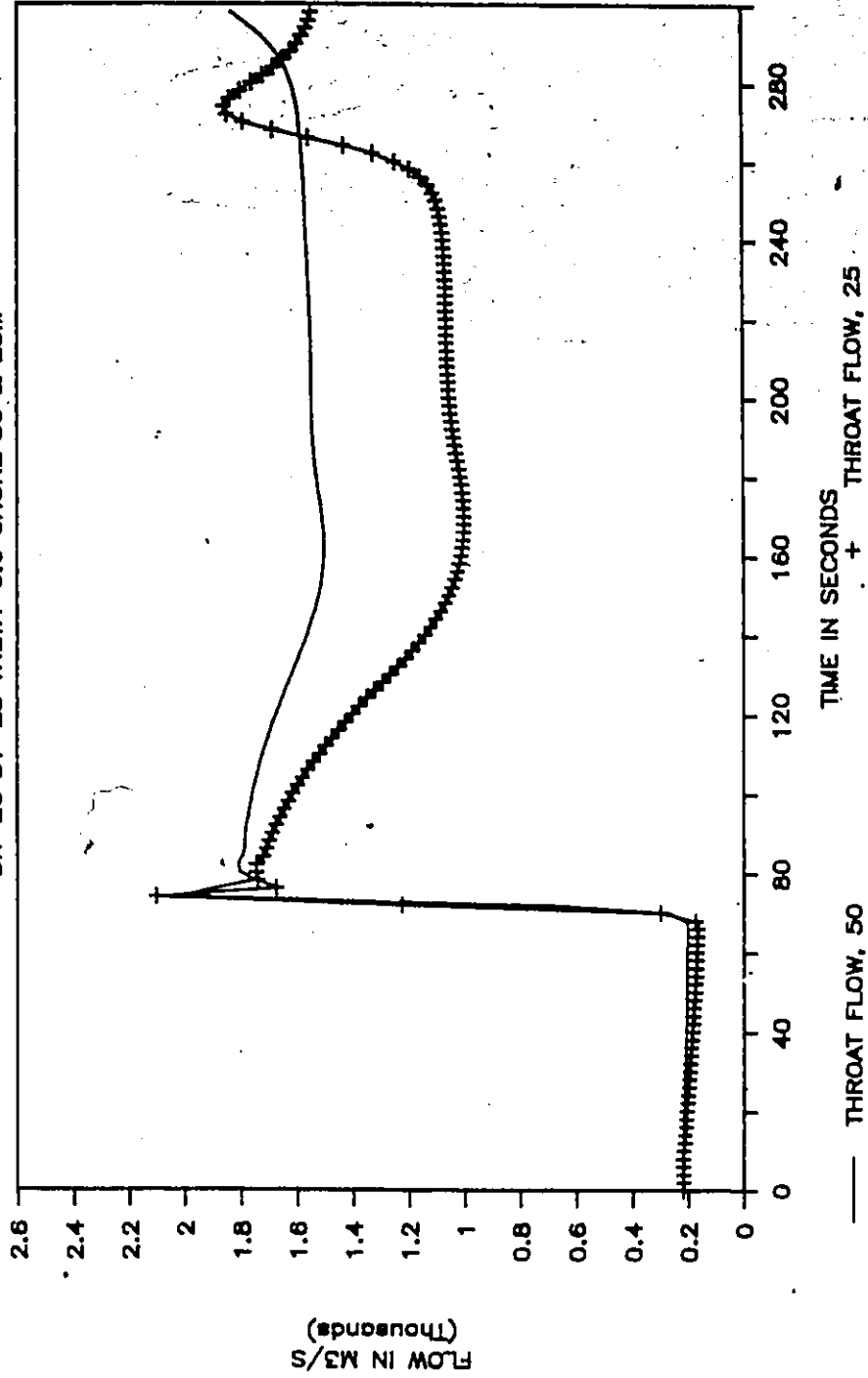


Fig. F.1.3 Impact of Choke Size - Hydrographs at Choke Section

FLOW THRU CHOKE - PARTIAL REFLECTION

DX=20 DT=2S THETA=0.6 CHOKE 50 & 25M

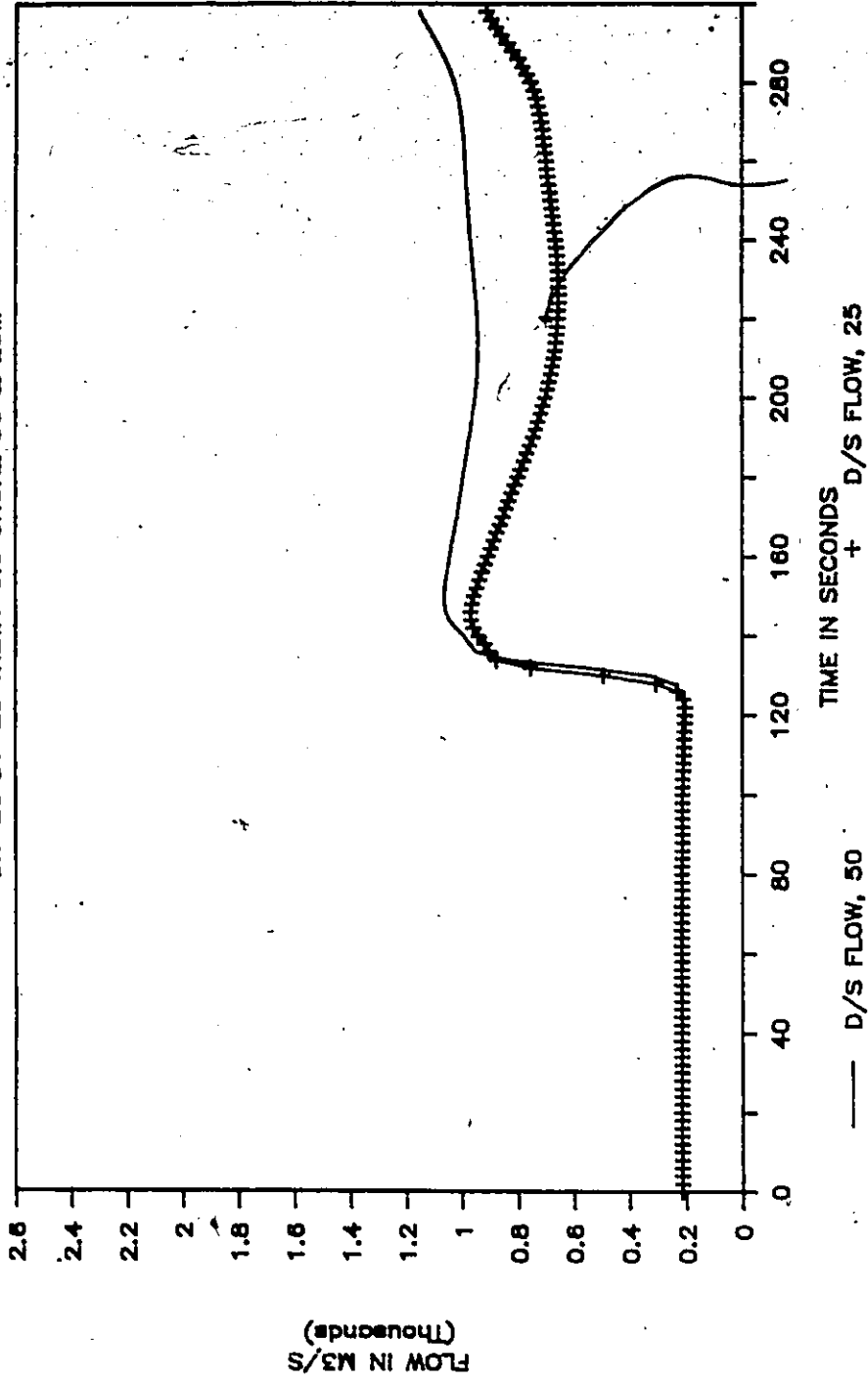


Fig. F.1.4 Impact of Choke Size - Hydrographs at D/S Boundary

FLOW THRU CHOKE - PARTIAL REFLECTION

DX=20 DT=25 THETA=0.6 CHOKES=50 & 25M

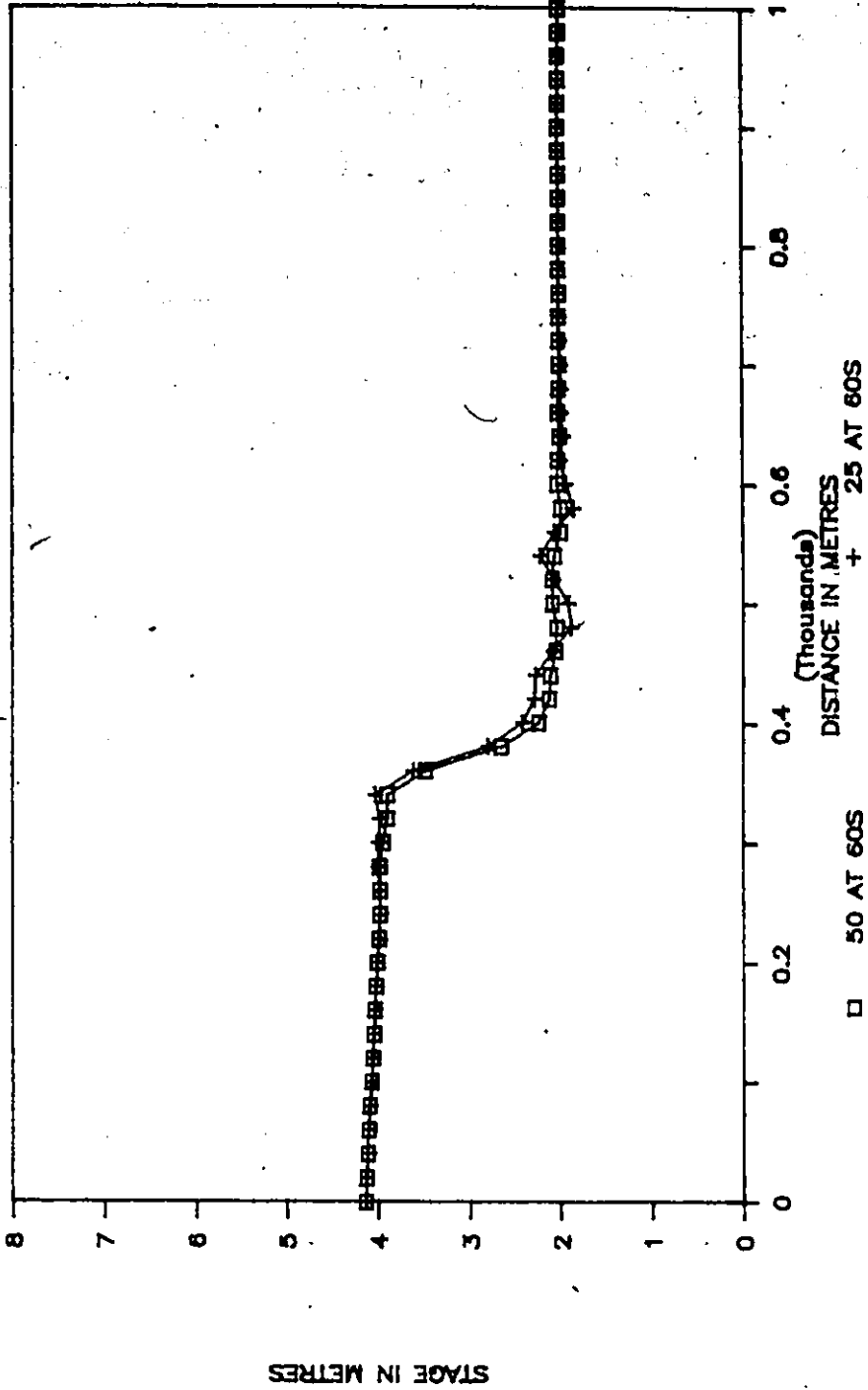


Fig. F.1.5 Surge Progress Through Choke at Time = 60.0 Seconds

FLOW THRU CHOKE -- PARTIAL REFLECTION

DX=20 DT=2S THETA=0.6 CHOKES=50 & 25M

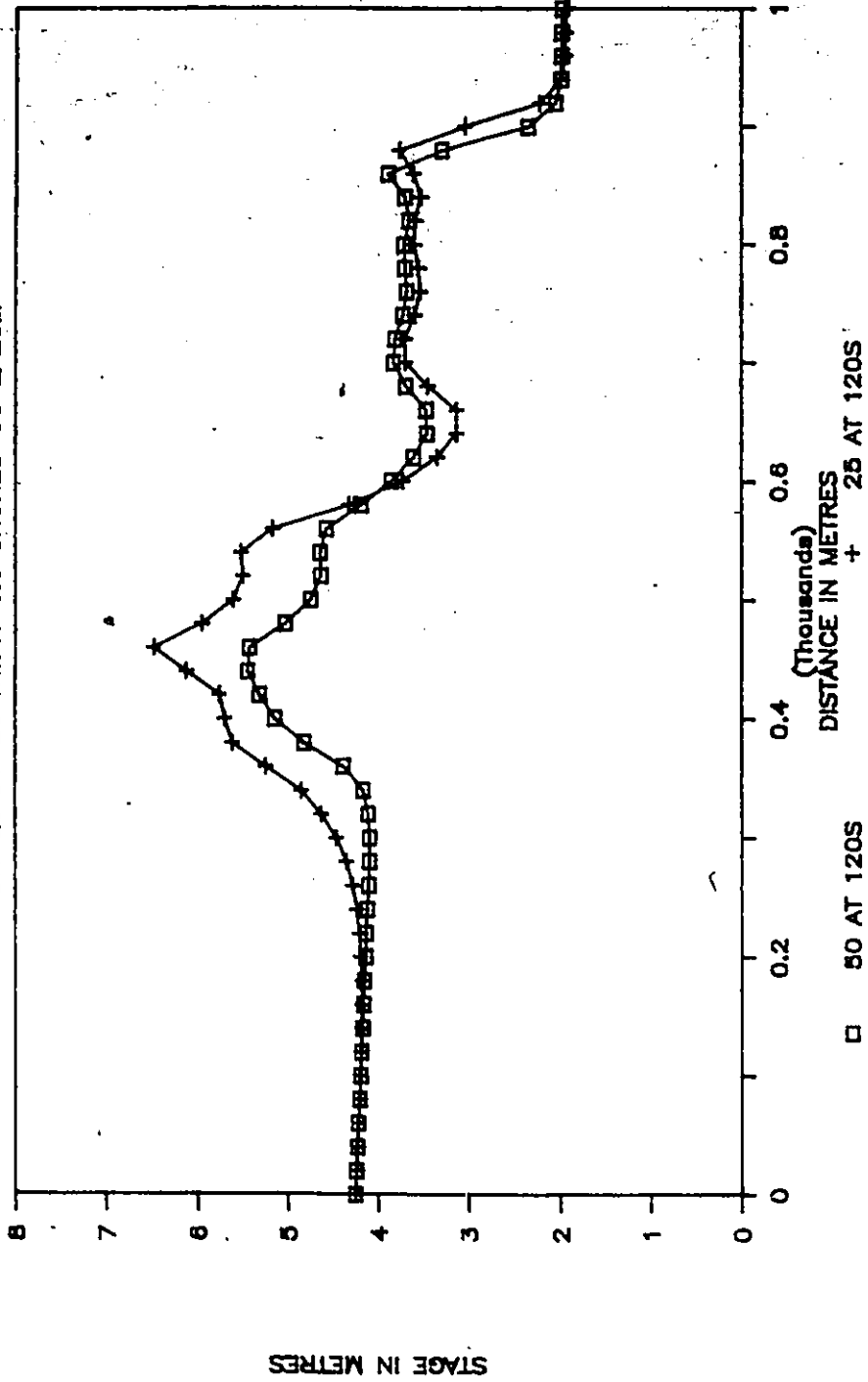


Fig. F.1.6 Surge Progress Through Choke at Time = 120.0 Seconds

FLOW THRU CHOKE - PARTIAL REFLECTION

$DX=20$ $DT=2S$ $\theta=0.6$ $CHOKES=50$ & $25M$

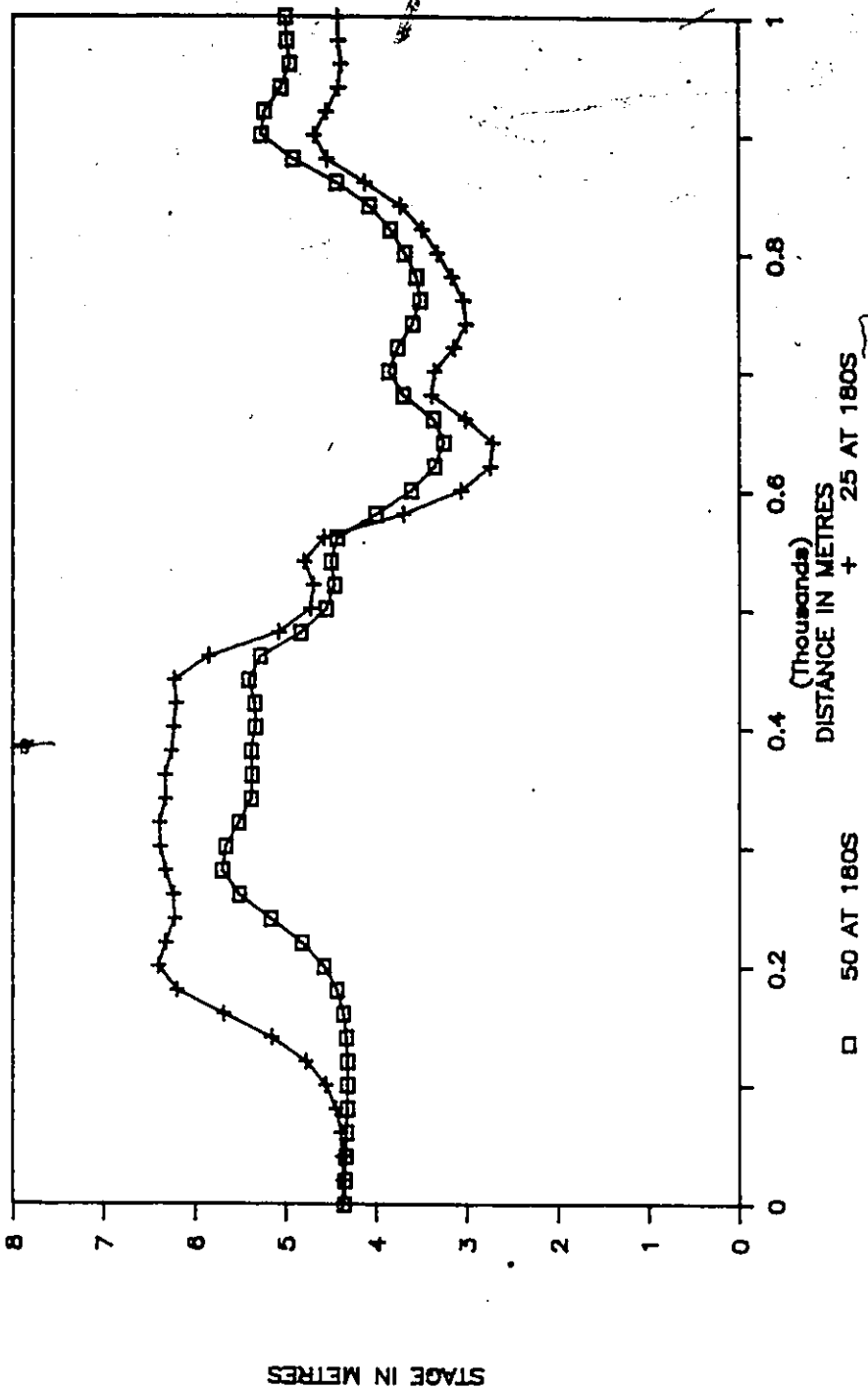


Fig. P.1.7 Surge Progress Through Choke at Time = 180.0 Seconds

FLOW THRU CHOKE -- PARTIAL REFLECTION

DX=20 DT=25 THETA=0.6 CHOKES=50 & 25M

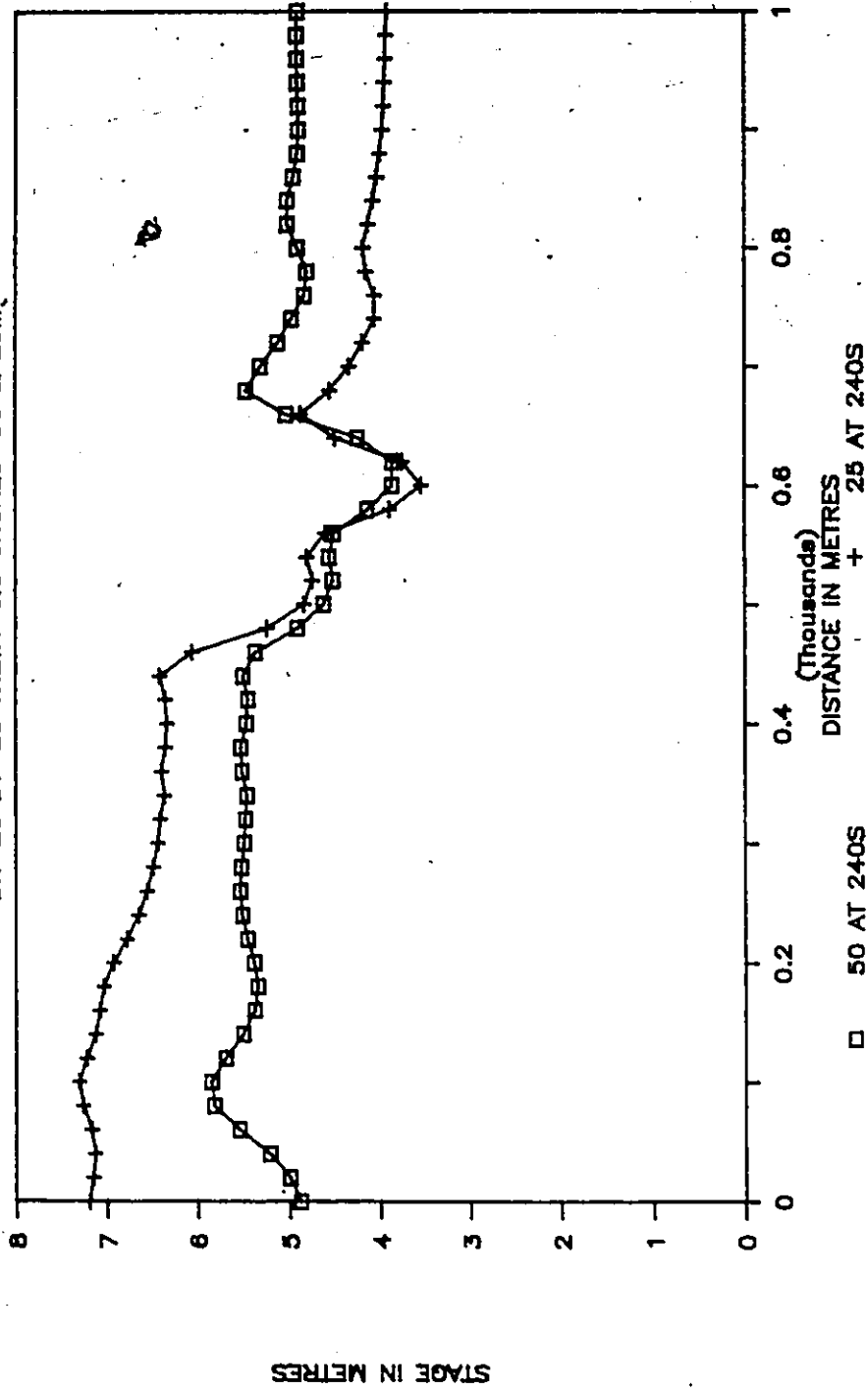


Fig. F.1.8 Surge Progress Through Choke at Time = 240.0 Seconds

FLOW THRU CHOKE - PARTIAL REFLECTION

DX=20 DT=2S THETA=0.6 CHOKES=50 & 25M

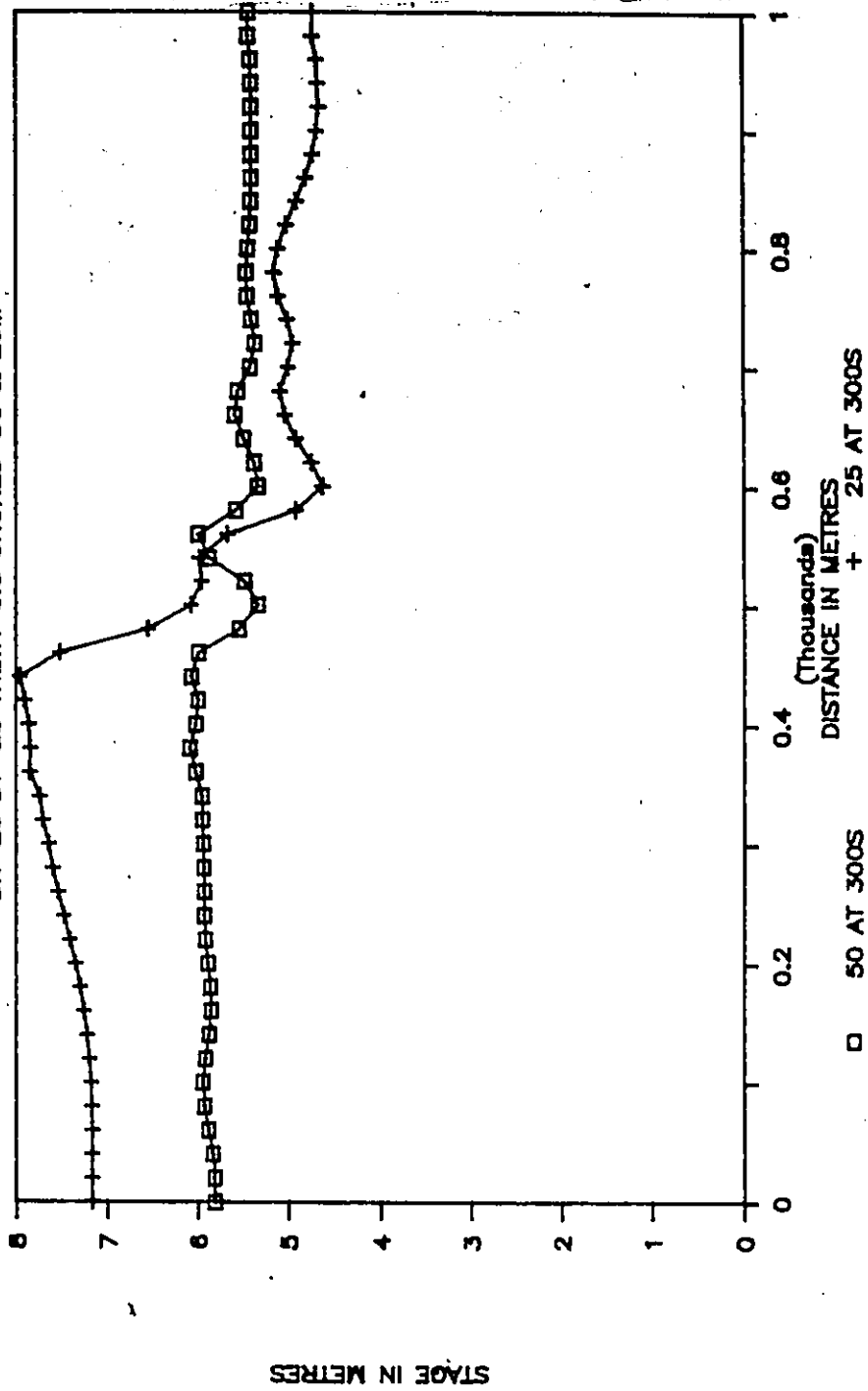


Fig. F.1.9 Surge Progress Through Choke at Time = 300.0 Seconds

FLOW-THRU CHOKE - STAGE PROFILES

$DX=25$, $DT=3$, $THETA=0.67$, $DTRISE=30$

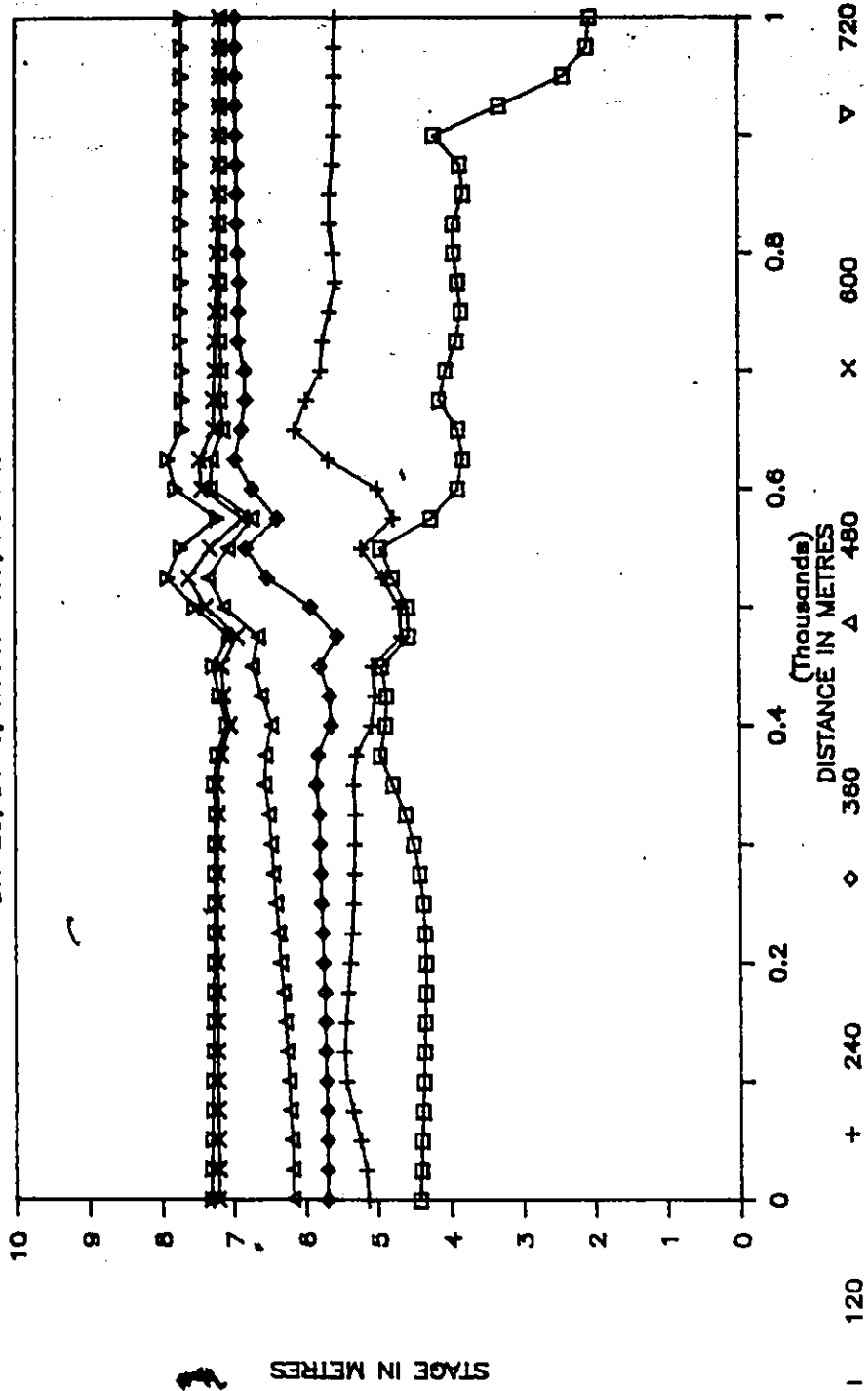


Fig. F.1.10 Surge Progress Through Choke - Grid Size Sensitivity

FLOW THRU A CHOKE -- FLOW PROFILES

$DX=10$, $DT=1$, $THETA=0.5$, $DTRISE=30$

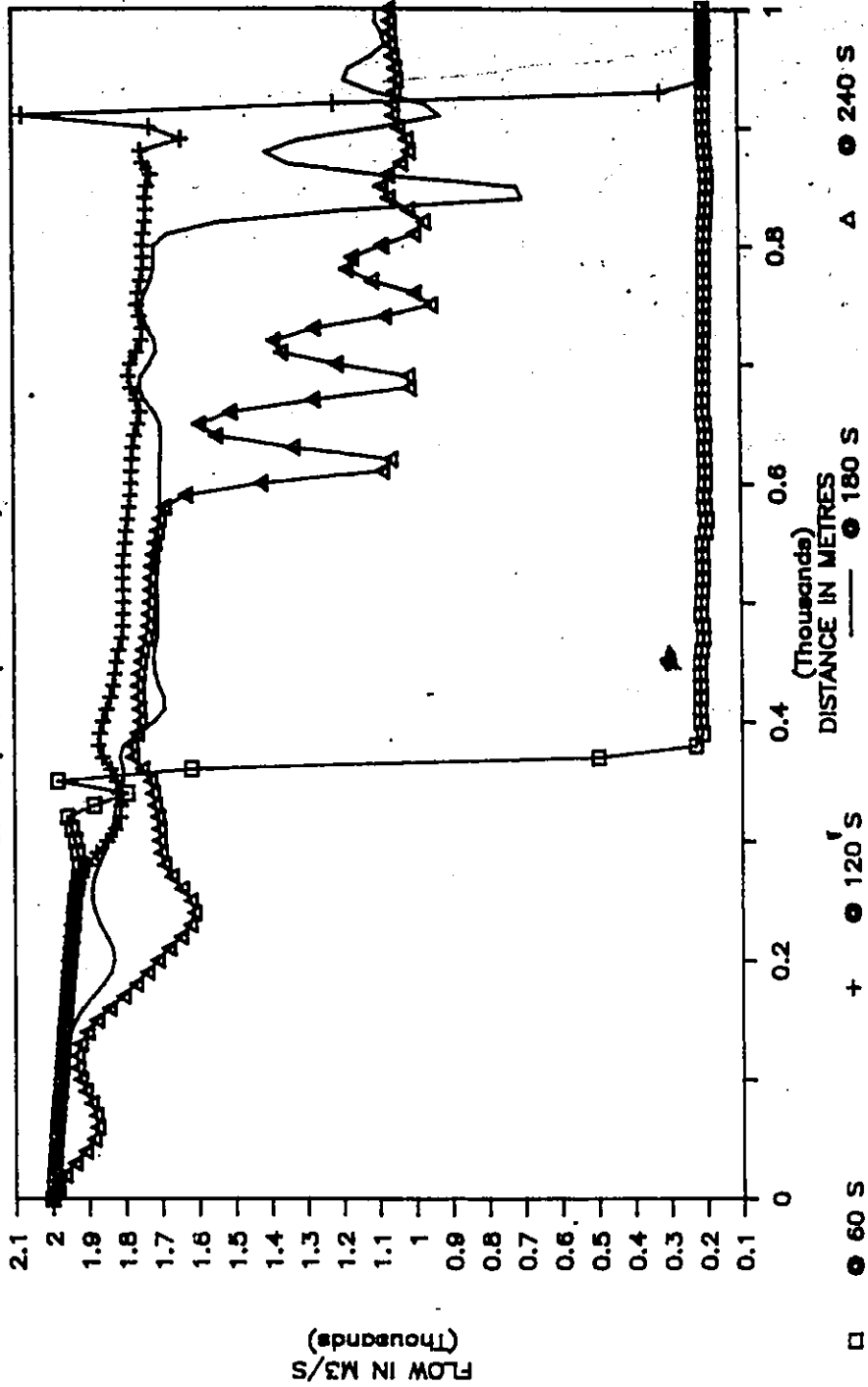


Fig. F.1.13 TWF Sensitivity on Surge Progress - Fine Grid Size

FLOW THRU A CHOKE - STAGE PROFILES

$DX=10, DT=1, THETA=0.5, DTRISE=30$

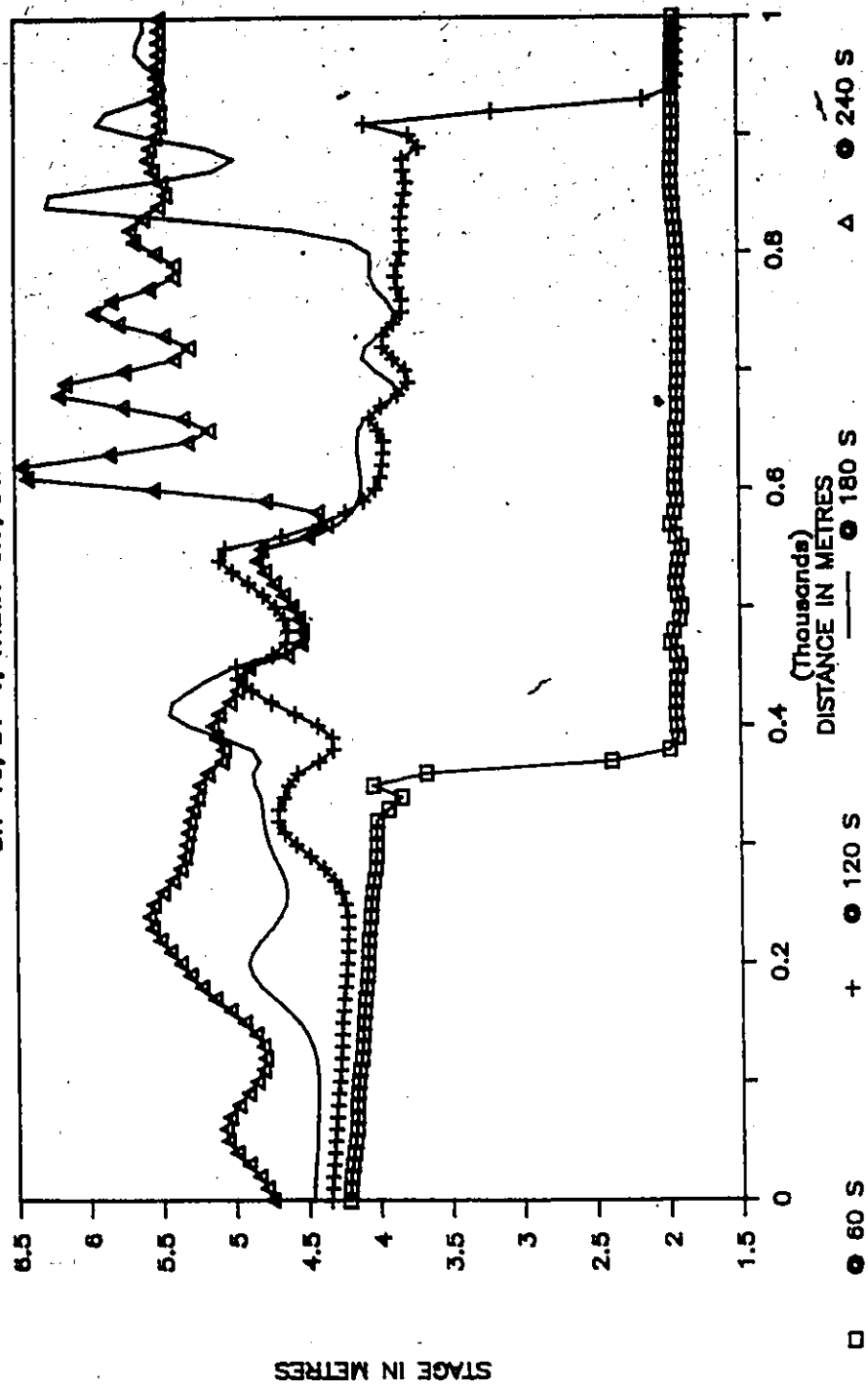


Fig. F.1.14 TWF Sensitivity on Surge Progress - Fine Grid Size

FLOW THRU A CHOKE - FLOW HYDROGRAPHS

DX=25, DT=3, THETA=0.5, DTRISE=30

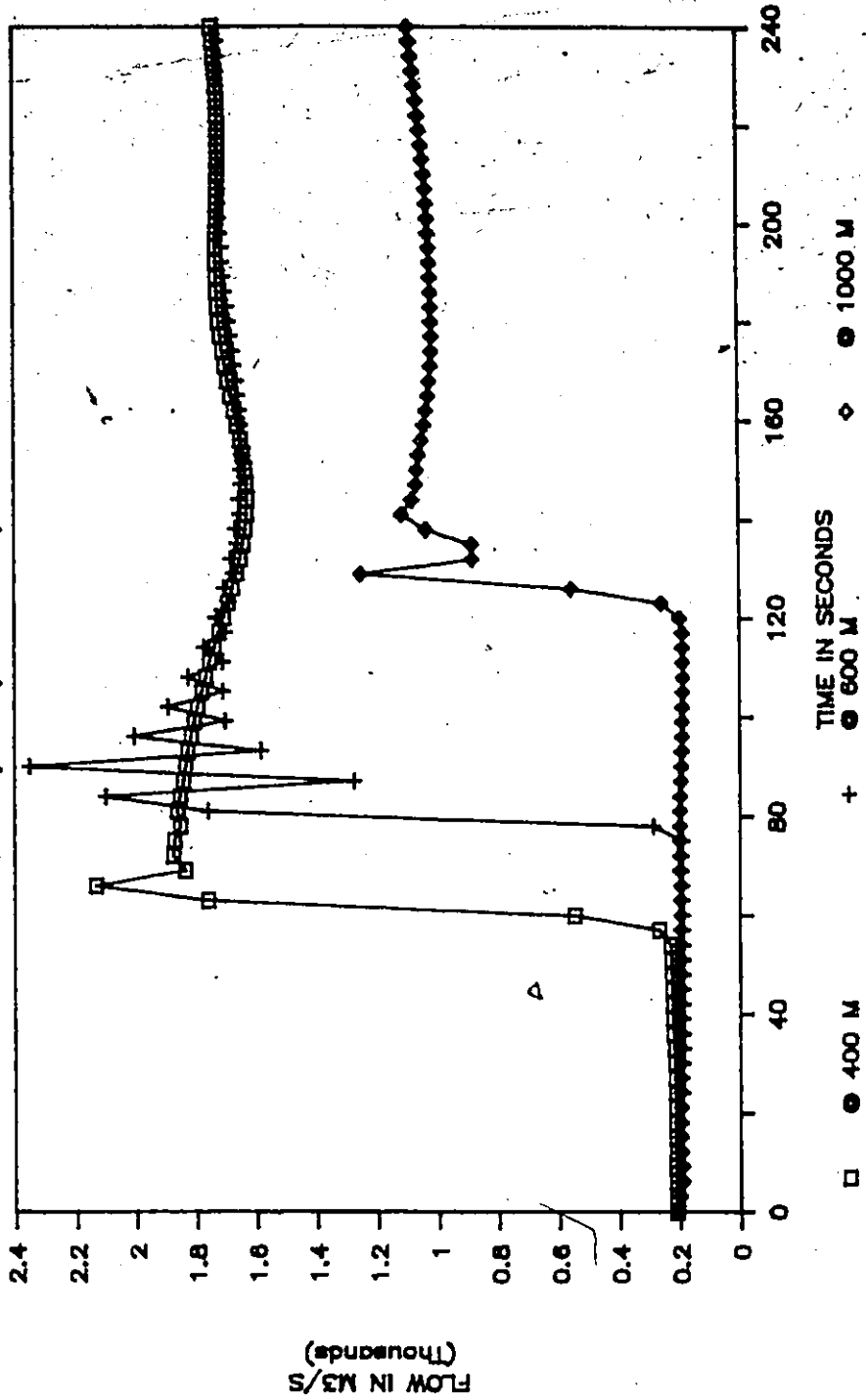


Fig. P.1.15 TWF Sensitivity on Surge Progress - Fine Grid Size

FLOW THRU A CHOKE - STAGE PROFILES

$DX=25$, $DT=3$, $THETA=0.5$, $DTR=30$ S

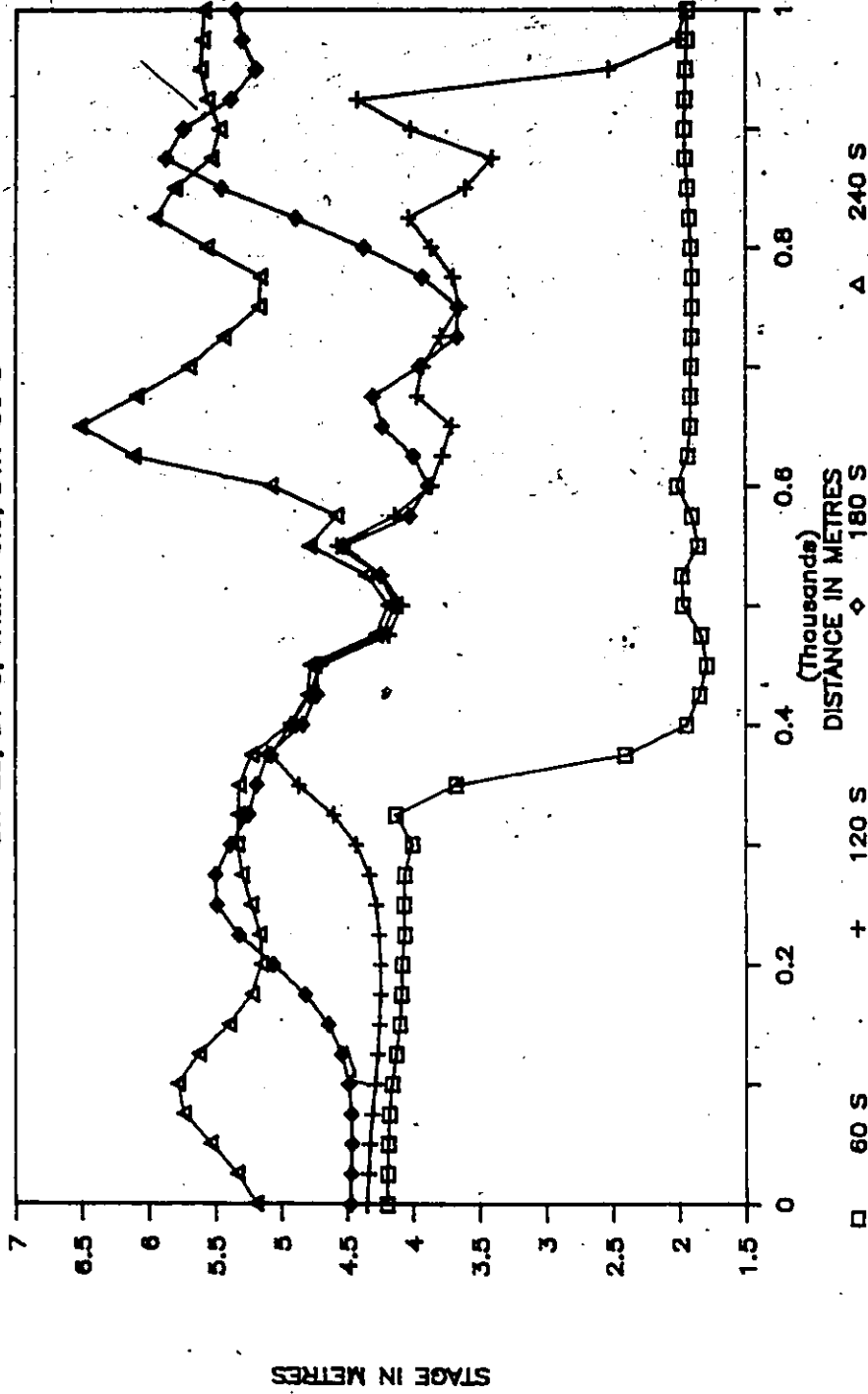


Fig. F.1.16 Time Step Sensitivity on Surge Progression

FLOW THRU A CHOKE - STAGE HYDROGRAPHS

$DX=25$, $DT=3$, $\theta=0.5$, $DRISE=30$

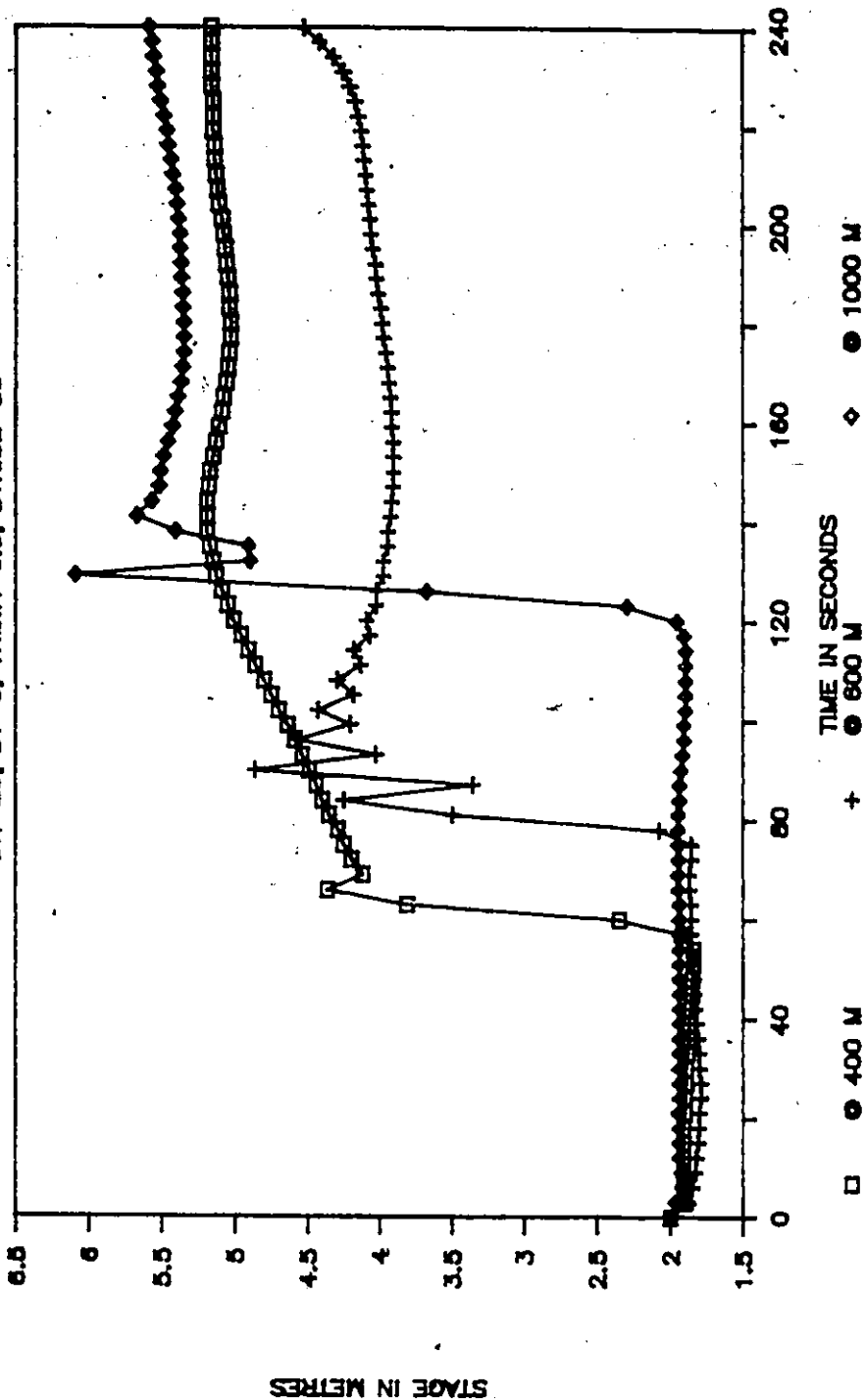


Fig. P.1.17 TWF Sensitivity on Surge Progression

EFFECT OF TIME-STEP ON FLOW THRU CHOKE

Profiles at Time = 120 Sec. TEST "E1"

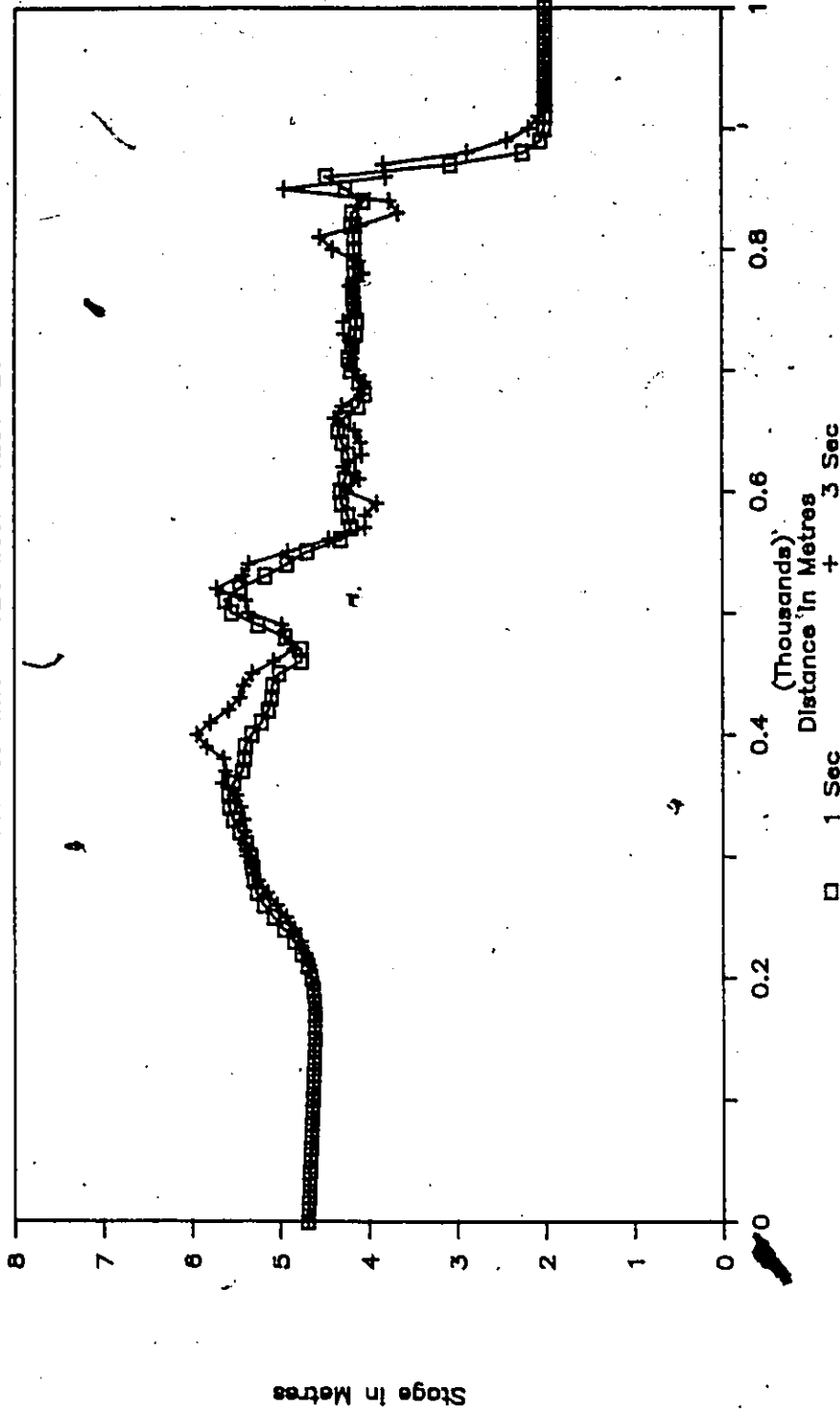


Fig. F.1.11 TWF Sensitivity on Surge Progress - Fine Grid Size

EFFECT OF THETA ON FLOW THROUGH CHOKE

Profiles at Time = 120 Sec. TEST "E1"

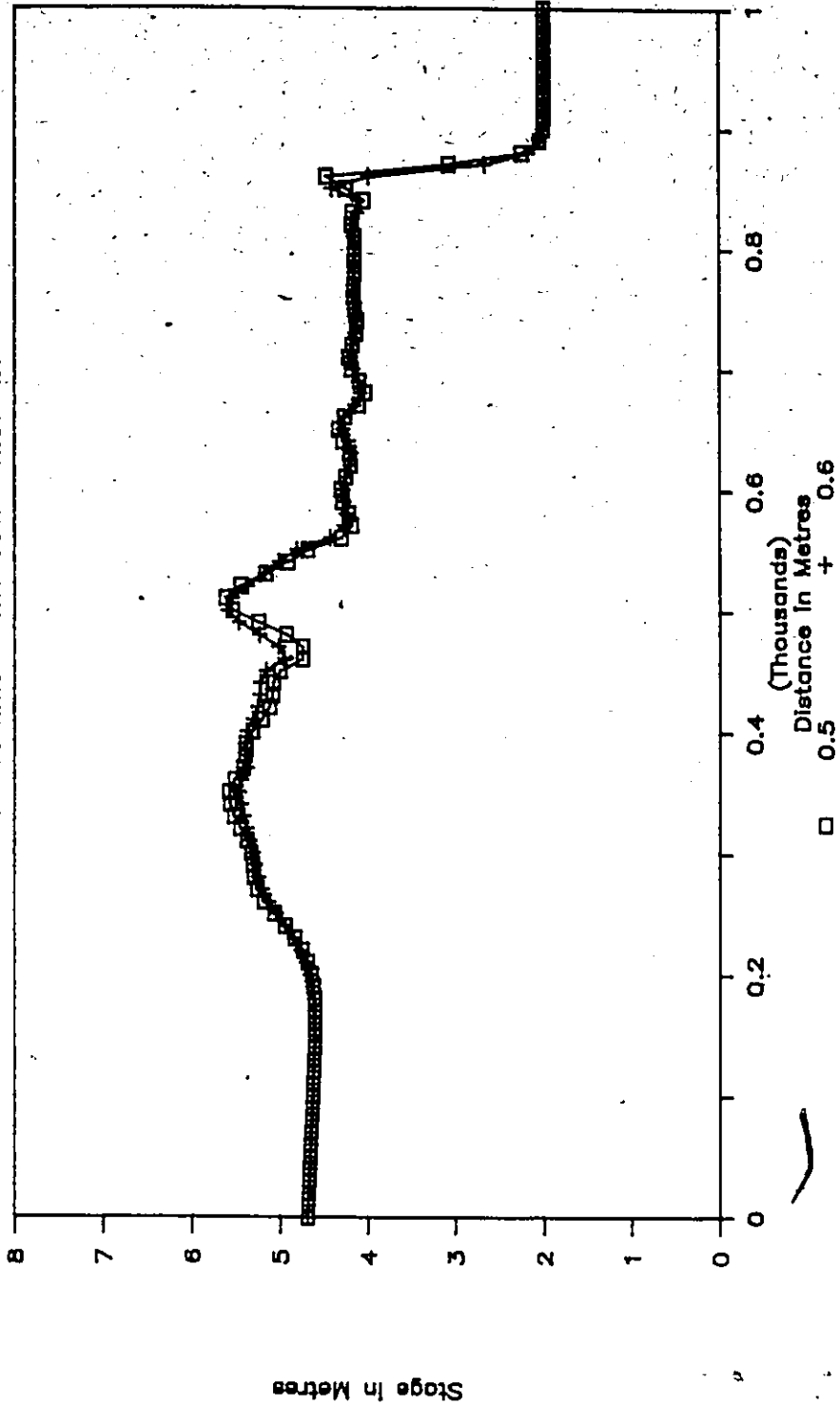


Fig. F.1.12 TWF Sensitivity on Surge Progress - Fine Grid Size

Subcritical Surge Over Hump

Discharge Profile at 120 s TEST 'E2'

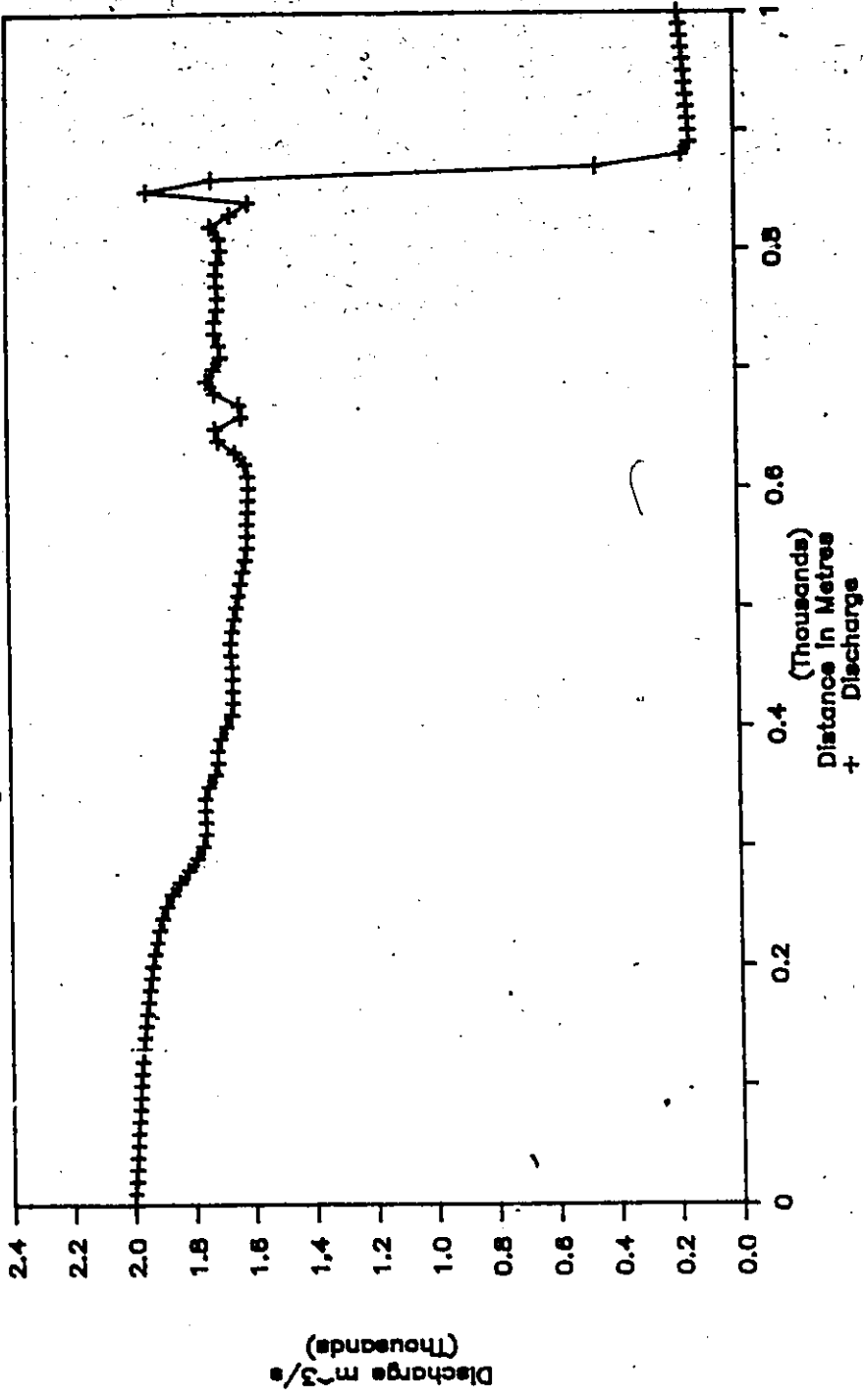


Fig. F.2.1 Test E2 - Flow Profile Over Hump

Subcritical Surge Over Hump

Velocity Profile at 120 s TEST 'E2'

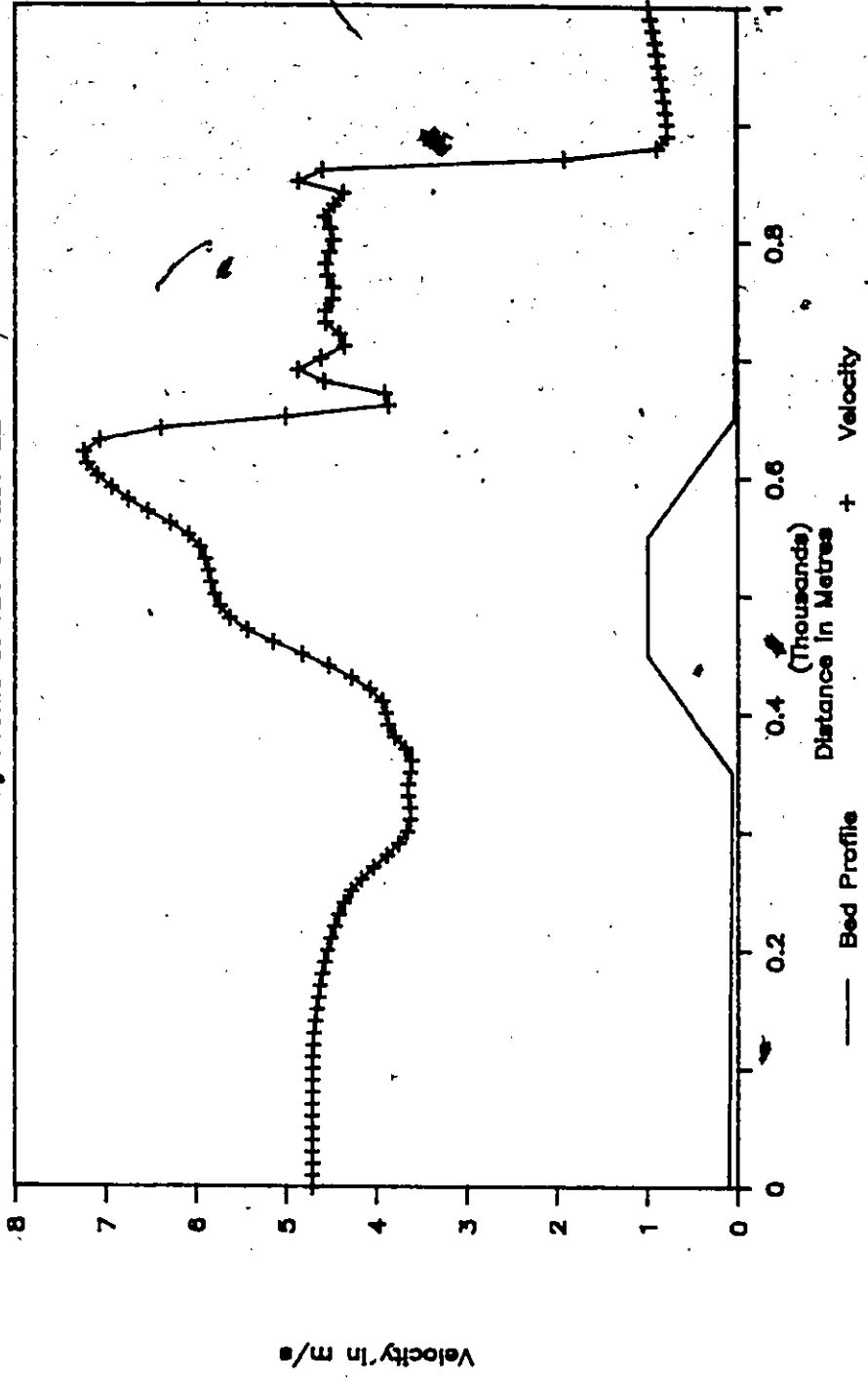


Fig. F.2.2 Test E2 - Velocity Profile Over Hump

Subcritical Surge Over Hump

Flow Hydrographs at Hump TEST 'E2'

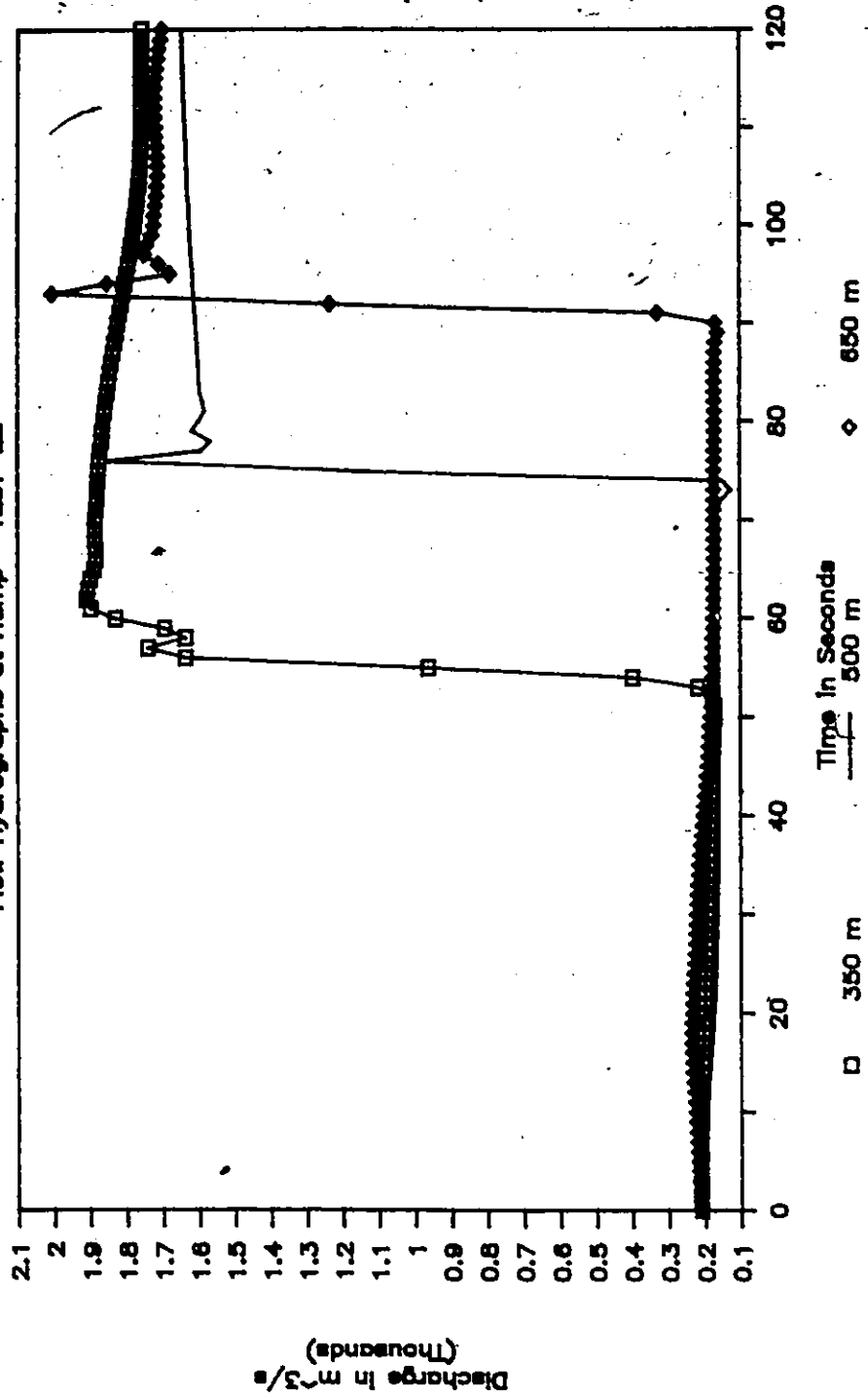


Fig. F.2.3 Test E2 - Flow Hydrographs Around Hump

Subcritical Surge Over Hump

$Dx=10m, Dt=1s, \theta=0.5$

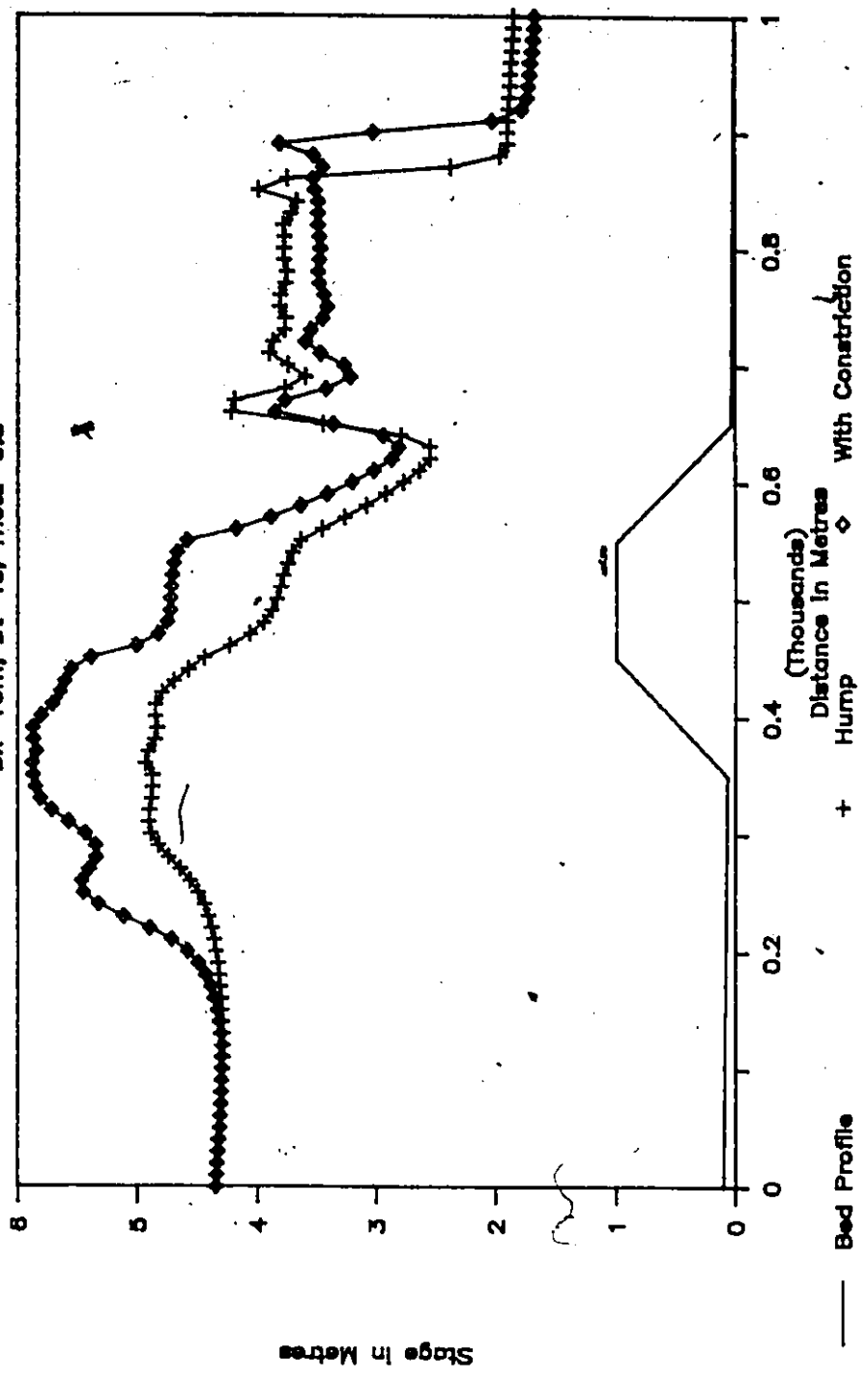


Fig. F.2.4 Constriction with Hump - Stage Profiles

Subcritical Surge Over Hump

$Dx=10m, Dt=1s, Theta=0.5$

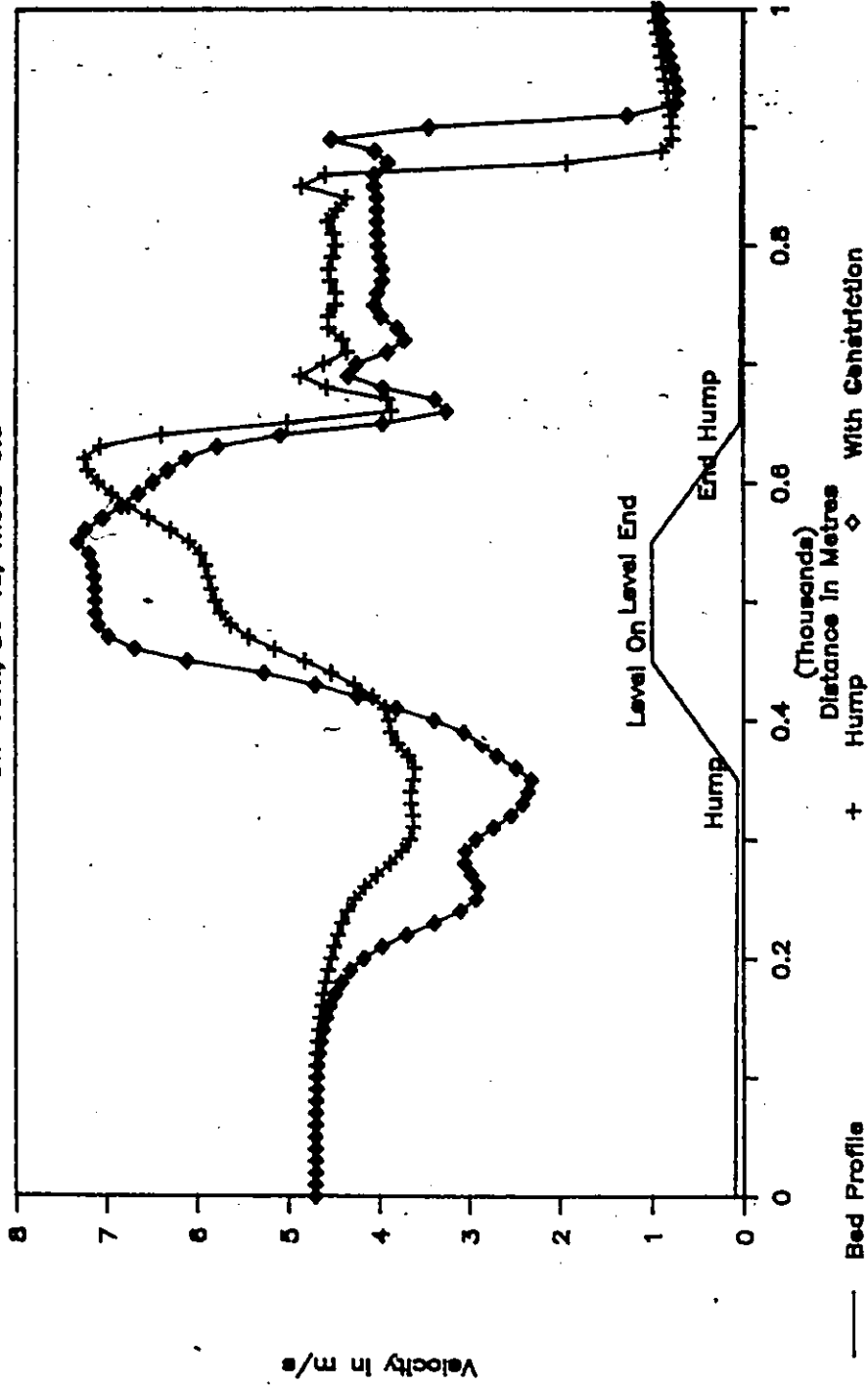


Fig. F.2.5 Constriction with Hump - Velocity Profiles

S

Subcritical Surge Over Hump

$Dx=10m, Dt=1s, Theta=0.5$

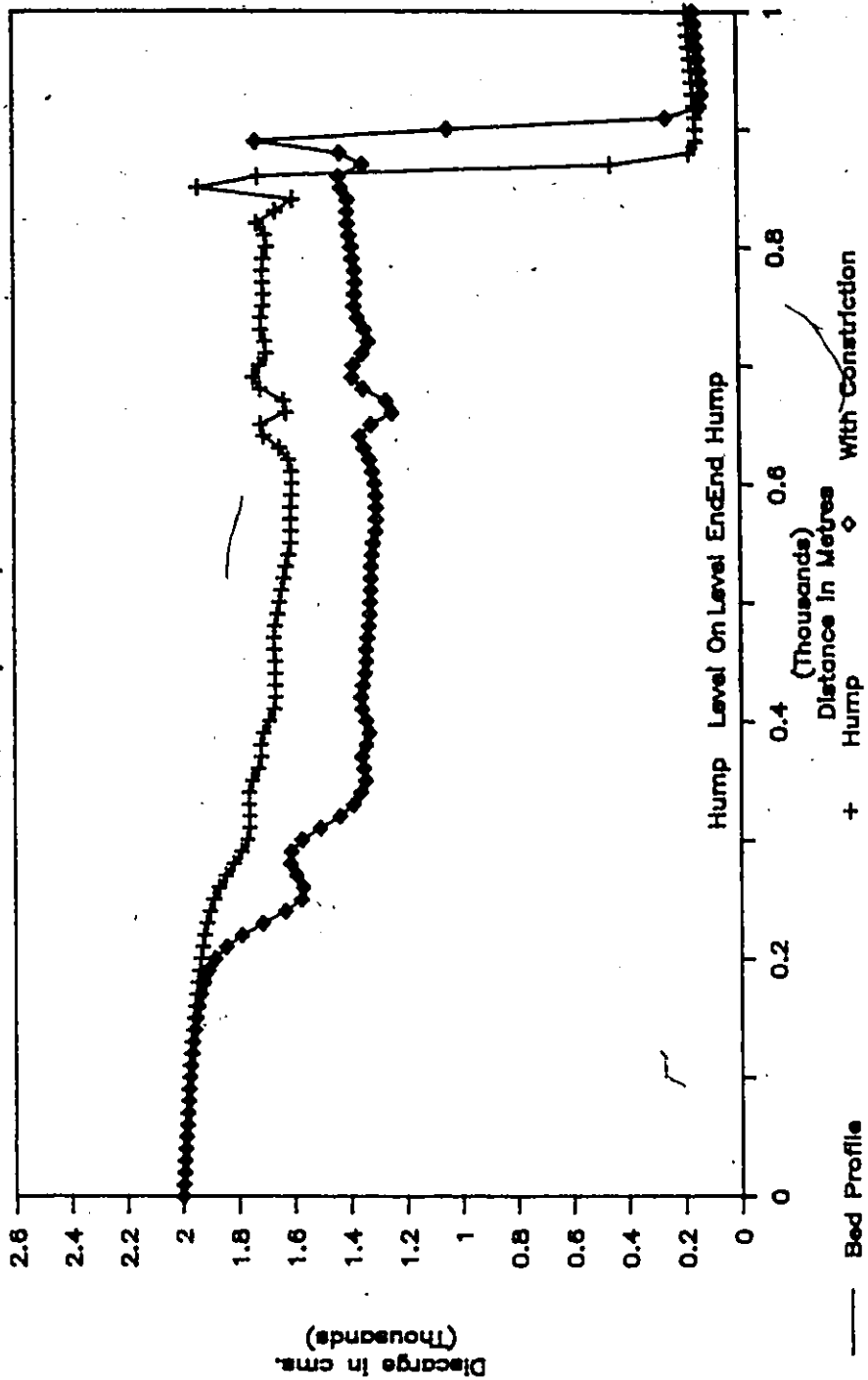


Fig. F.2.6 Constriction with Hump - Flow Profiles

FLOW THRU AN EXPANSION - PROFILES

$\Delta x = 25m, dt = 3s, \theta = 0.5 \text{ \& } 0.6$

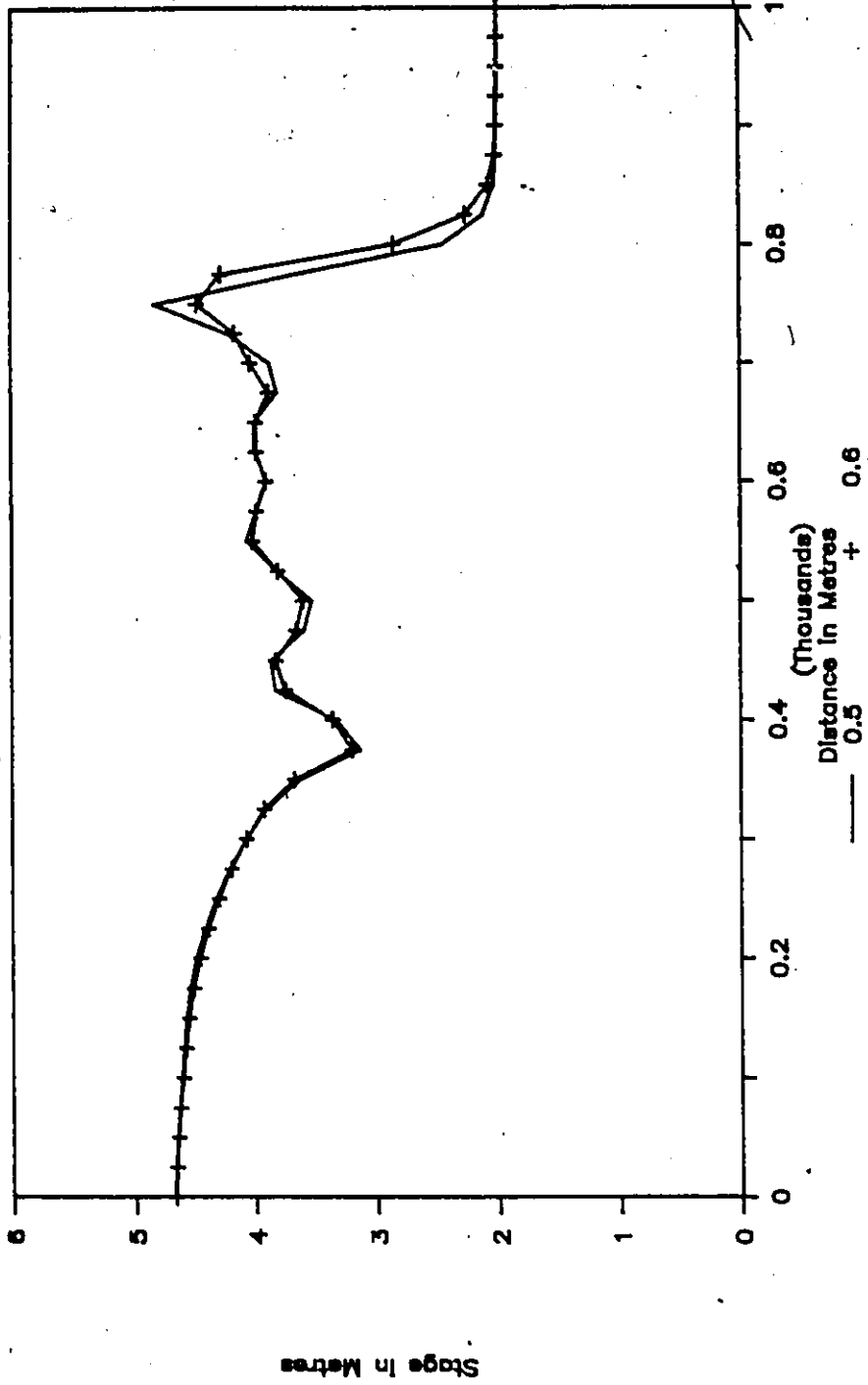


Fig. F.3.1 Surge Through an Expansion - Stage Profiles at 120 Sec

FLOW THRU AN EXPANSION -- PROFILES

$\Delta x = 25m, dt = 3s, \theta = 0.5 \text{ \& } 0.6$

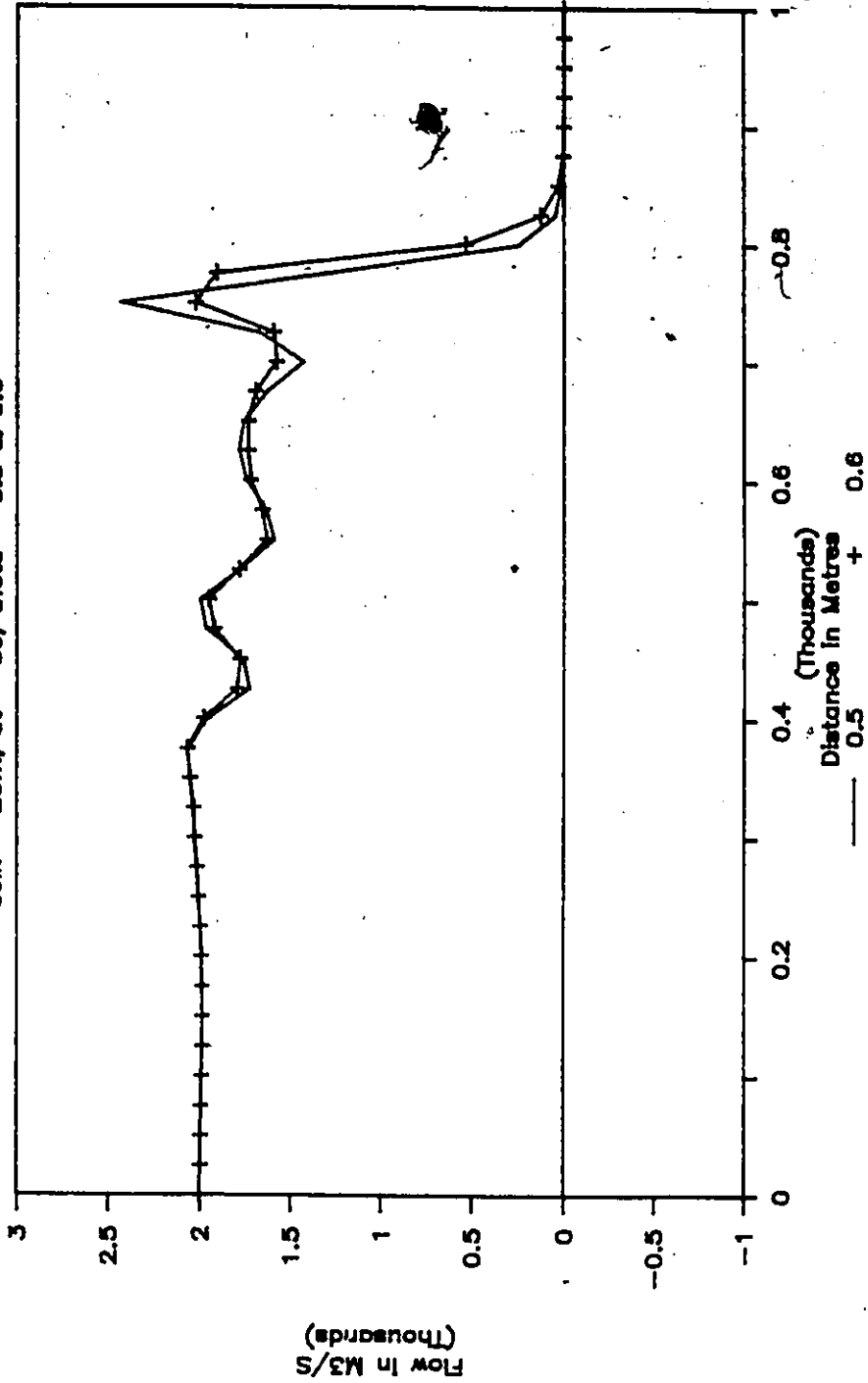


Fig. F.3.2 Surge Through an Expansion - Flow Profiles at 120 Sec

FLOW THRU AN EXPANSION - PROFILES

$De_{bx} = 10m, dt = 1s, \theta_{eta} = 0.5 \& 0.6$

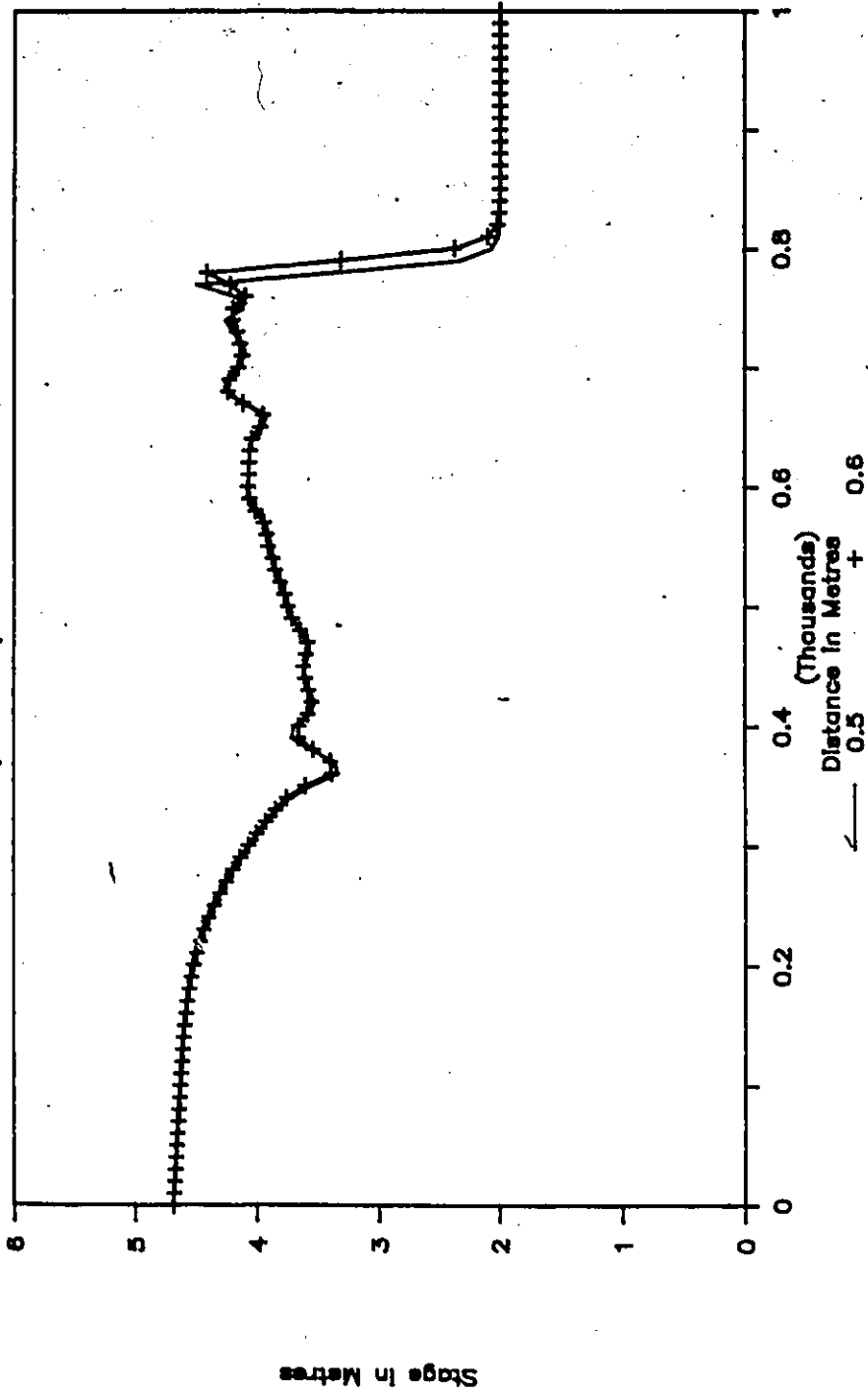


Fig. F.3.3 Surge Through an Expansion - Fine Grid Size, Stage

FLOW THRU AN EXPANSION - PROFILES

$\Delta x = 10m, dt = 1s, \theta = 0.5 \text{ \& } 0.6$

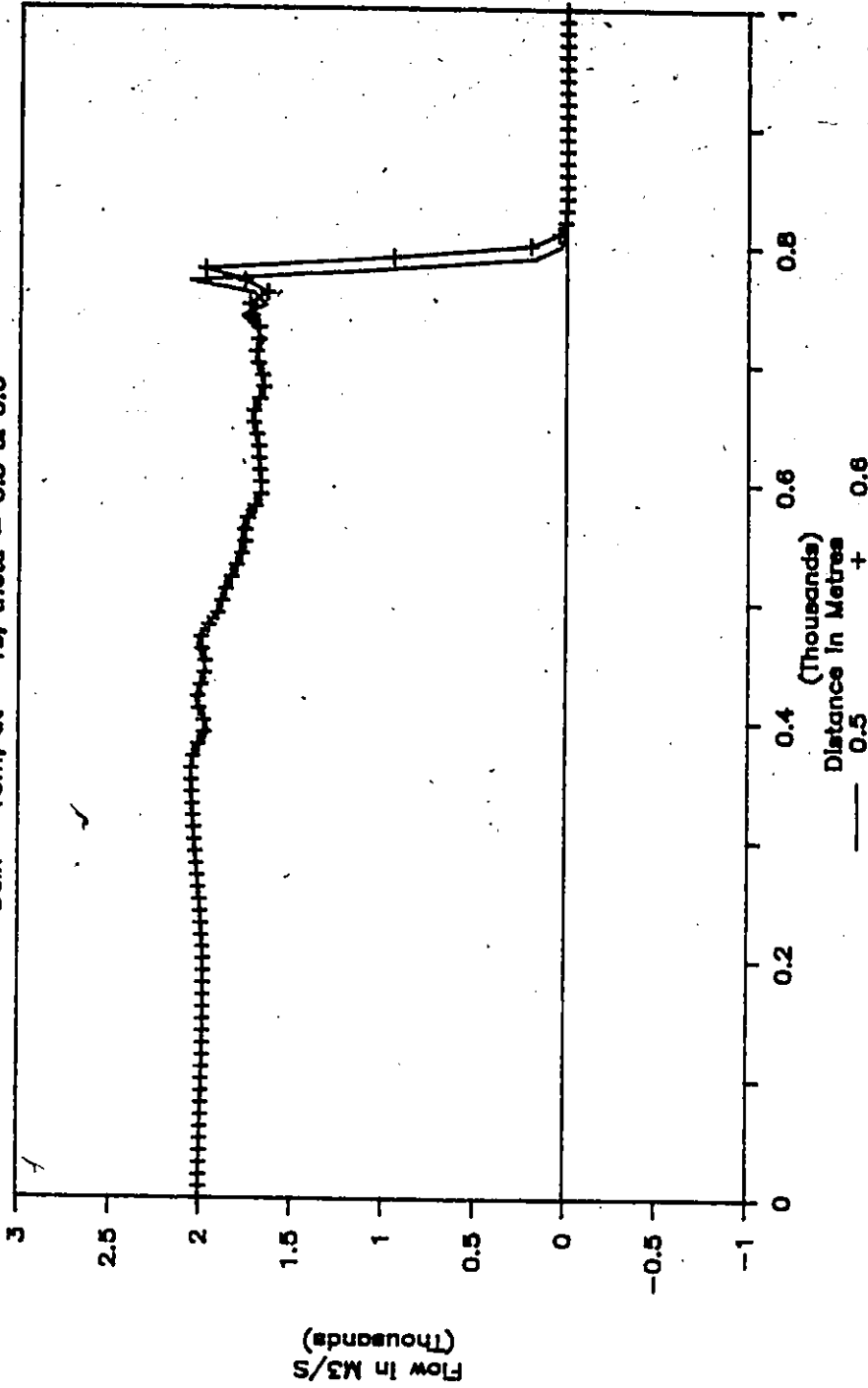


Fig. F.3.4 Surge Through an Expansion - Fine Grid Size, Flow

MOVING ELEMENT VS FINITE DIF. METHOD

Profiles at Time = 120 s TEST 'B'

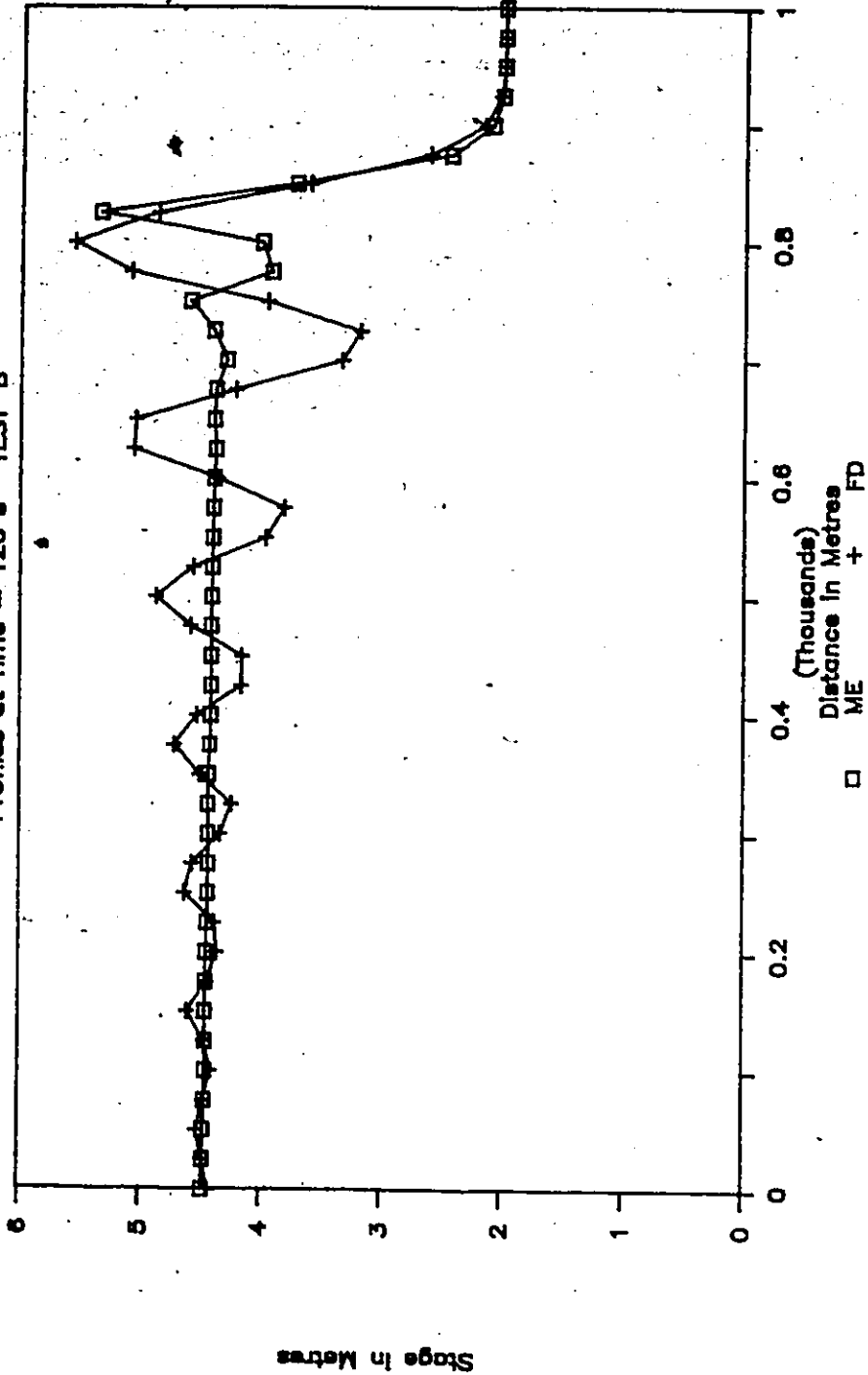


Fig. F.4.1 Stage Profiles with Time step = 5 Sec

Profile @ 120.0 Sec.

Theta=0.6, WF=0.0,0.167

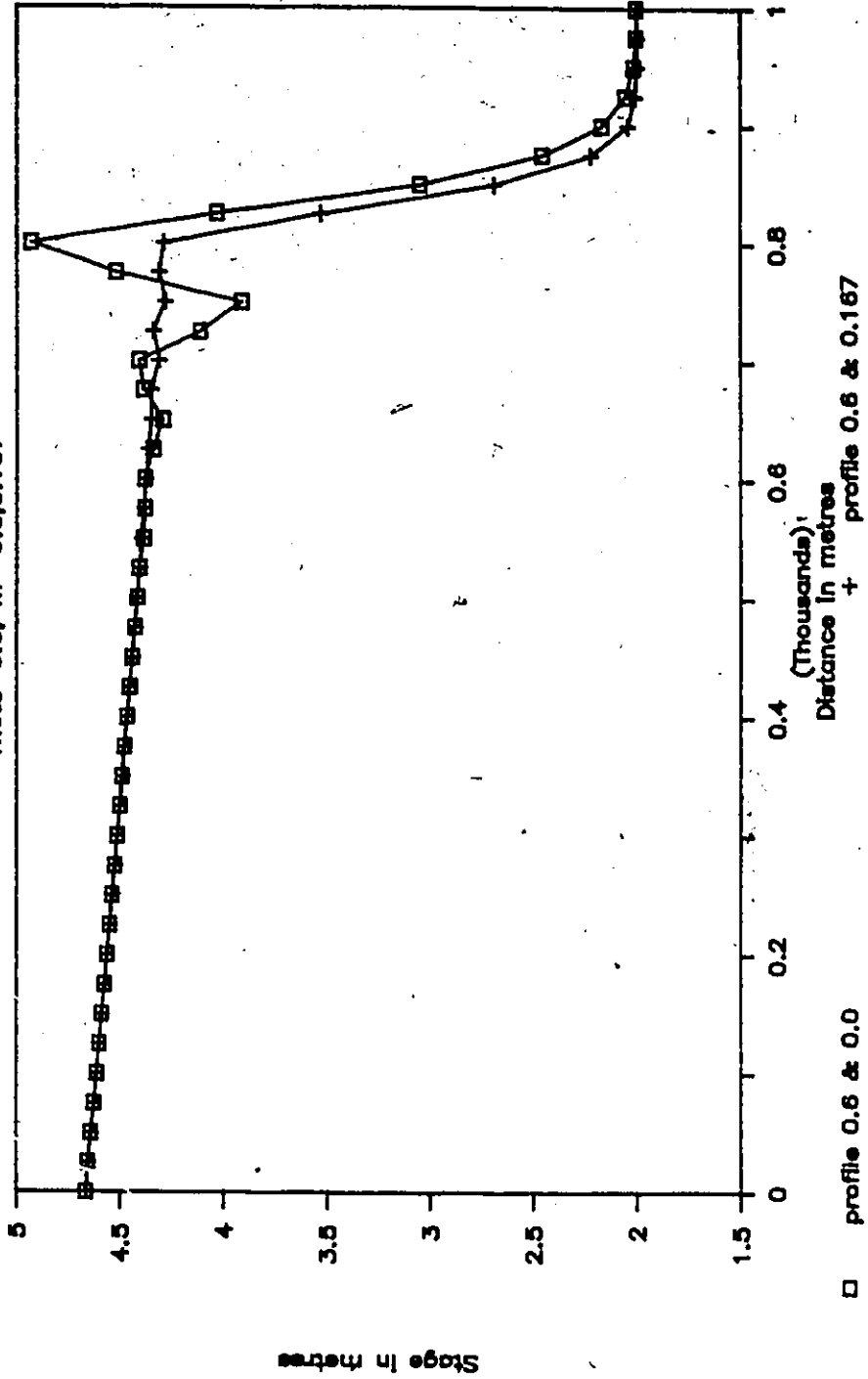


Fig. F.4.2 SWF Sensitivity for Advanced TWF

Profile @ 120.0 Sec.

Theta=0.5, WF=0.0,0.167

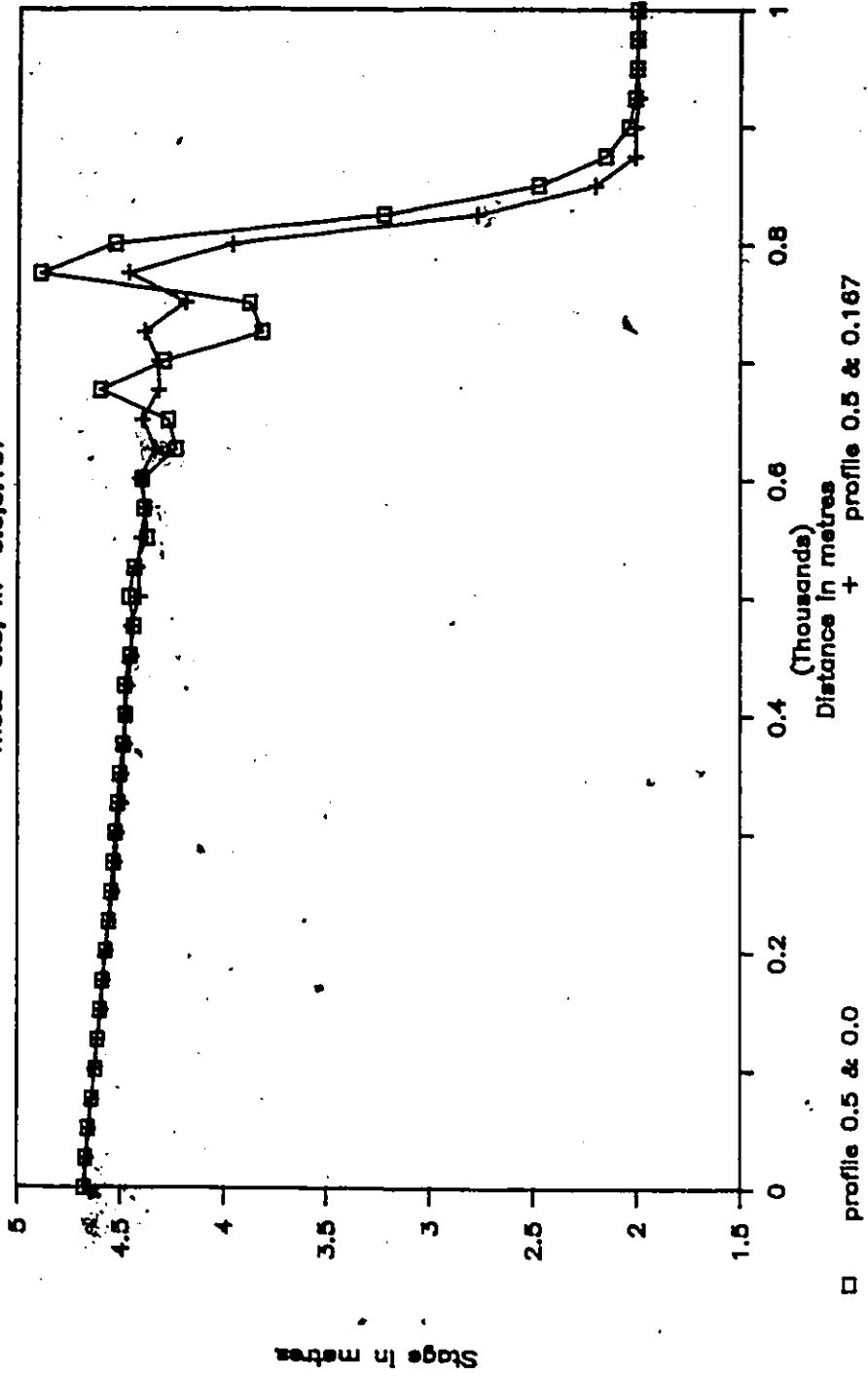


Fig. F.4.3 SWF Sensitivity for Centered TWF

Profile @ 120.0 Sec.

Theta=0.5, WF=0.0,0.25

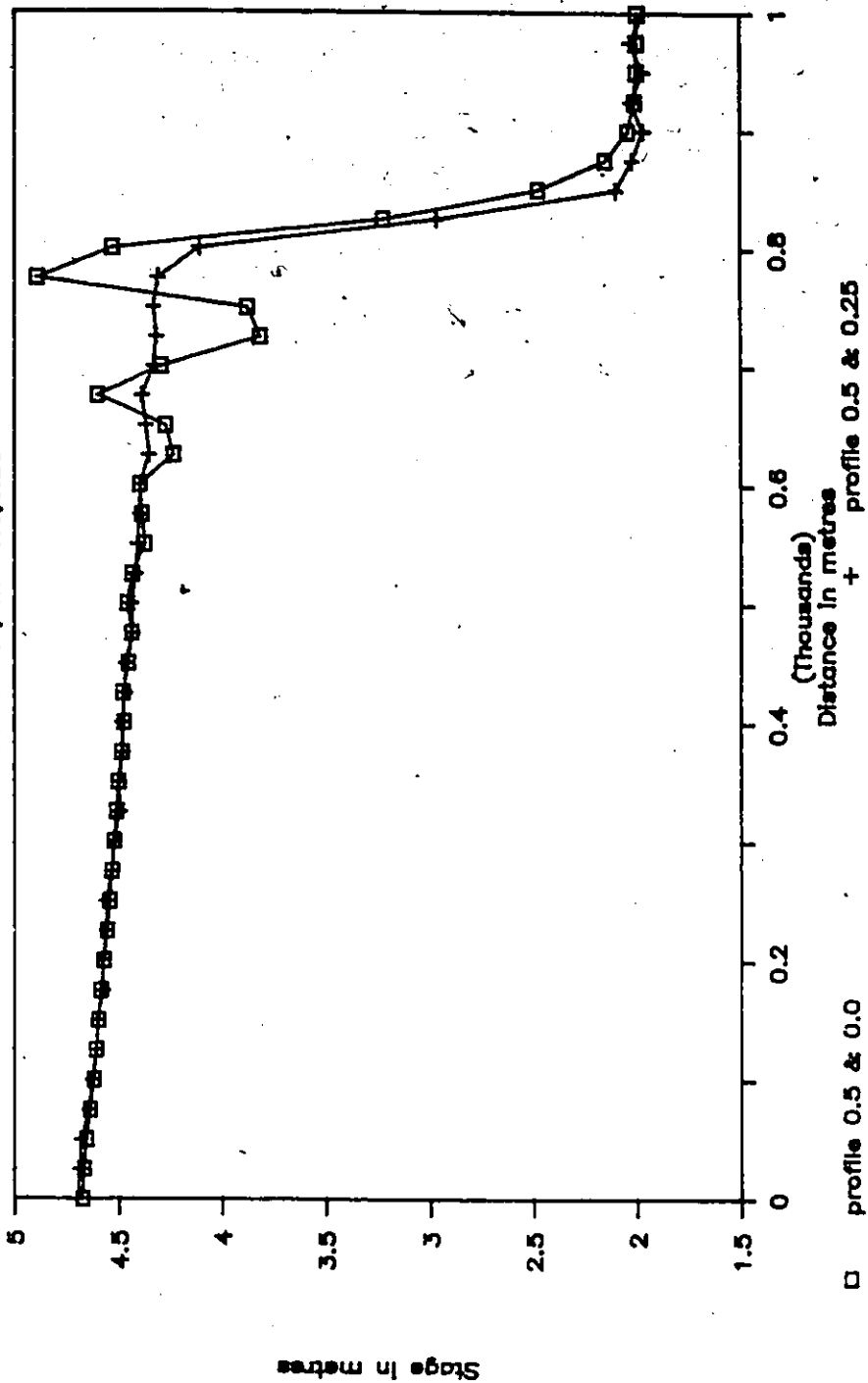


Fig. F.4.4 SWF Sensitivity for Centered TWP

Profiles @ 120.0 Sec

Comparison of ME & Vasiliev

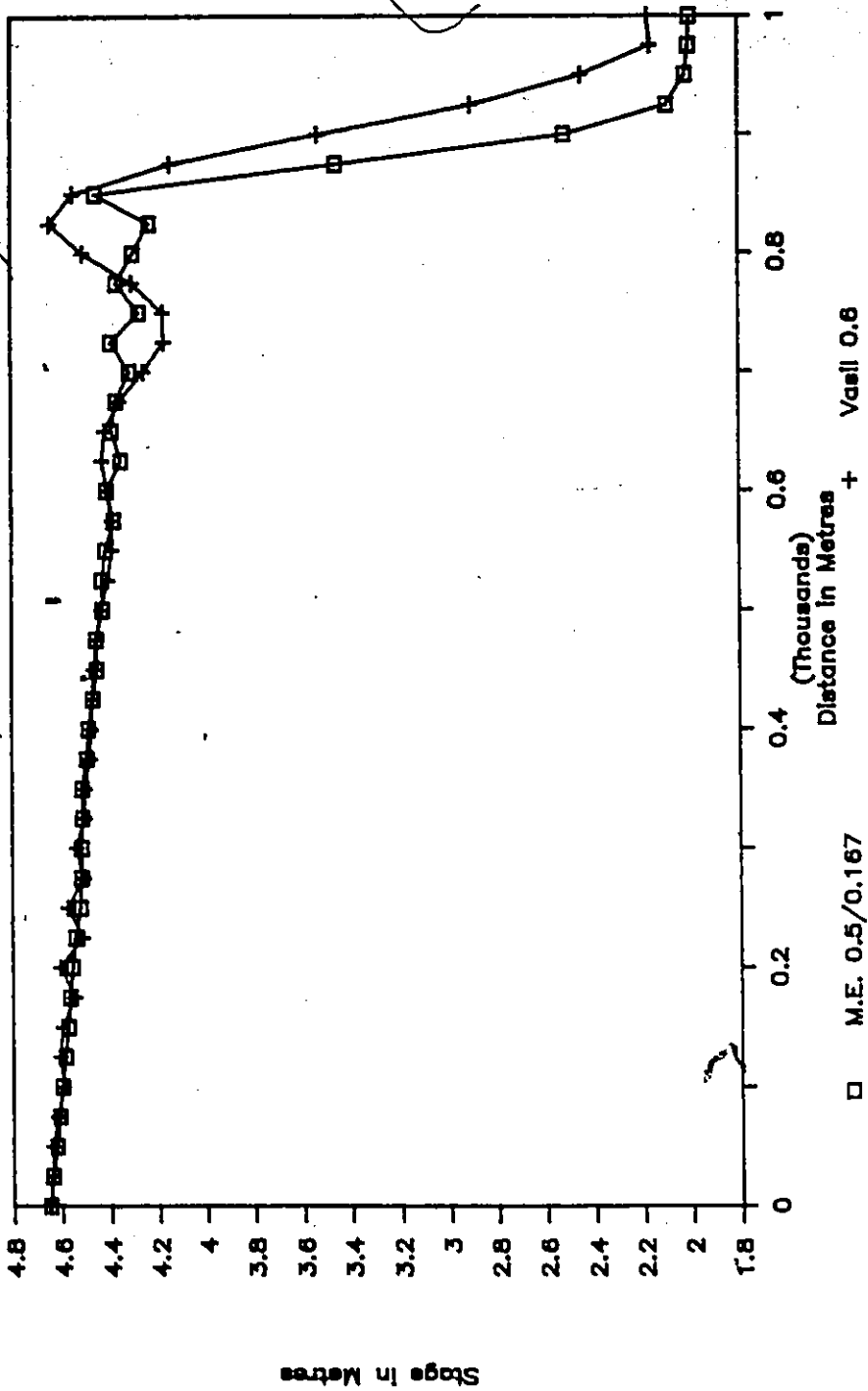


Fig. F.4.5 Comparison of ME and FD

Profiles @ 120.0 Sec

Comparison of ME & Vasiliev

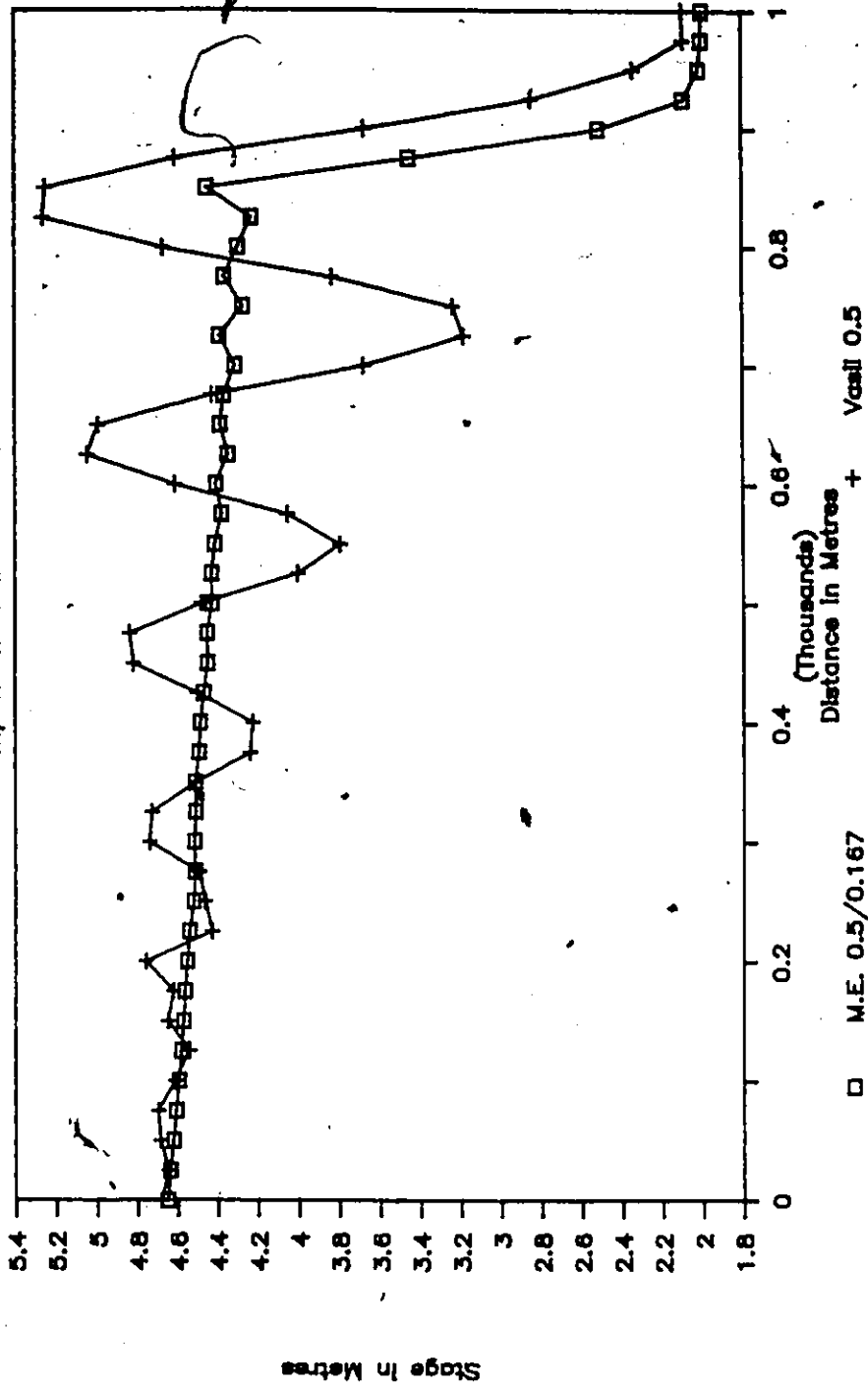


Fig. P.4.6 Comparison of ME and FD

Profiles @ 120.0 Sec

Comparison of ME & Vasiliev

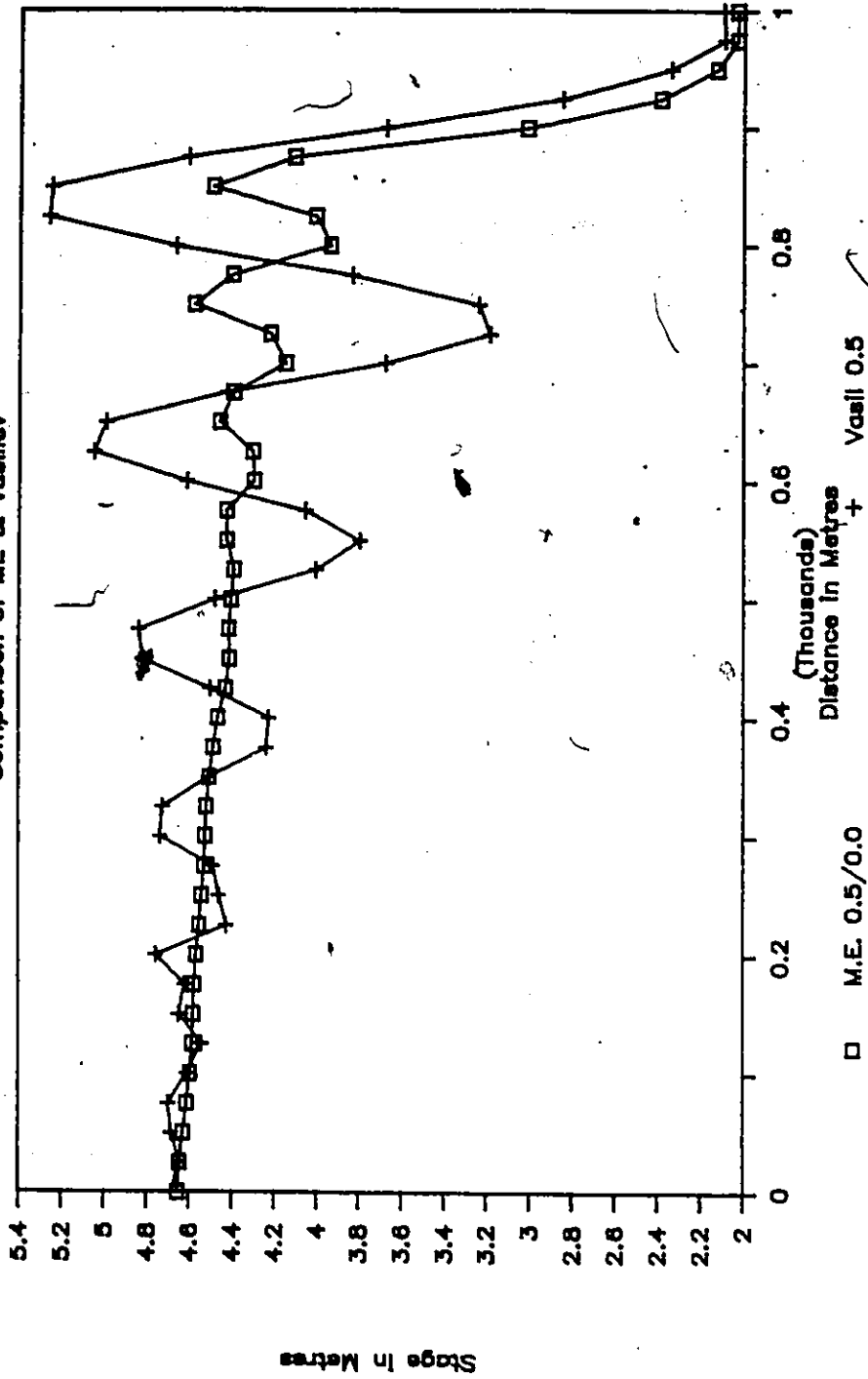


Fig. F.4.7 Comparison of ME and FD

Profiles @ 120 Sec. Comparison of FE & ME

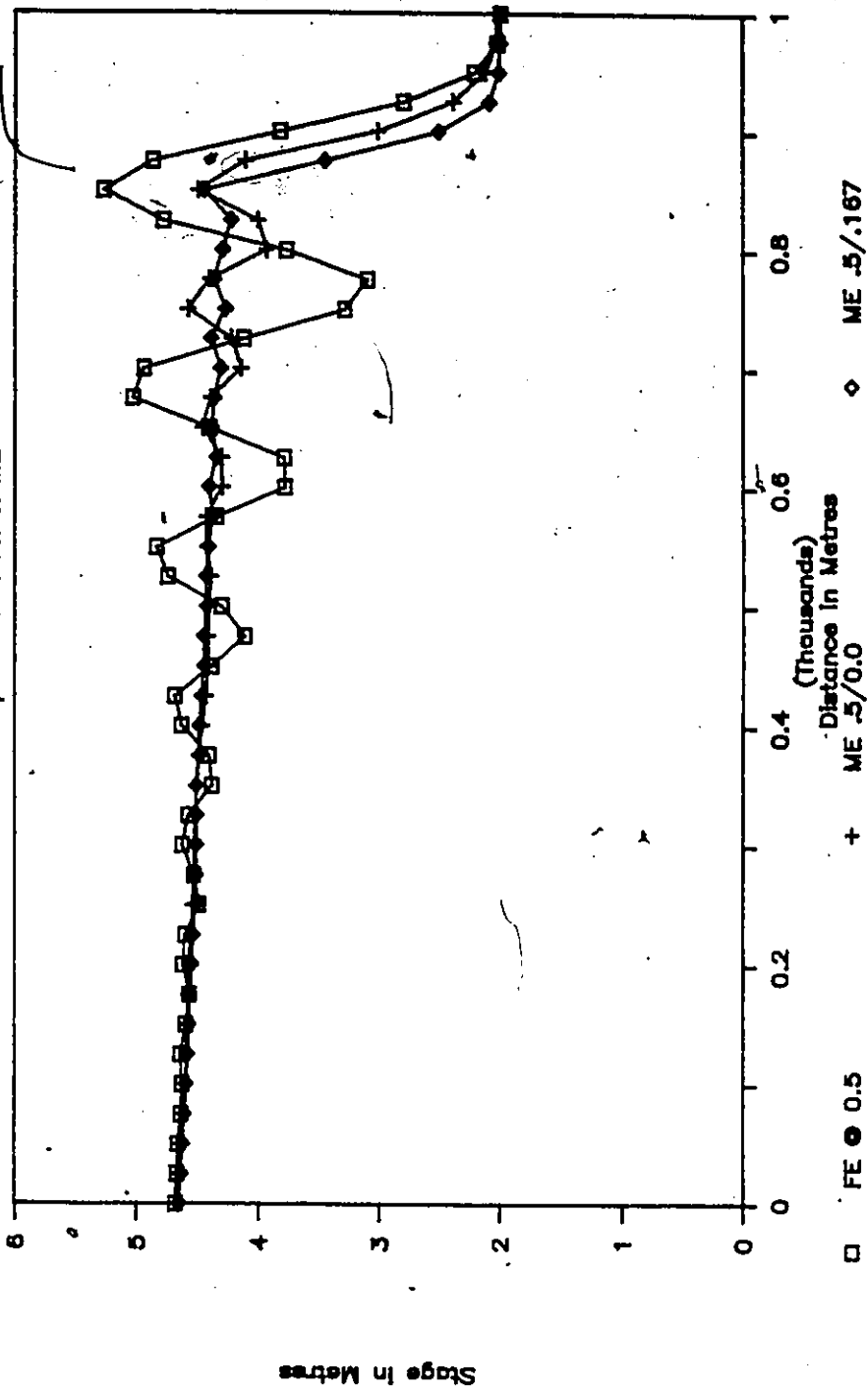


Fig. F.4.8 Comparison of ME and FE

EFFECT OF ROUGHNESS ON SURGE LOCATION

Profiles at Time = 120 Sec. TEST "B"

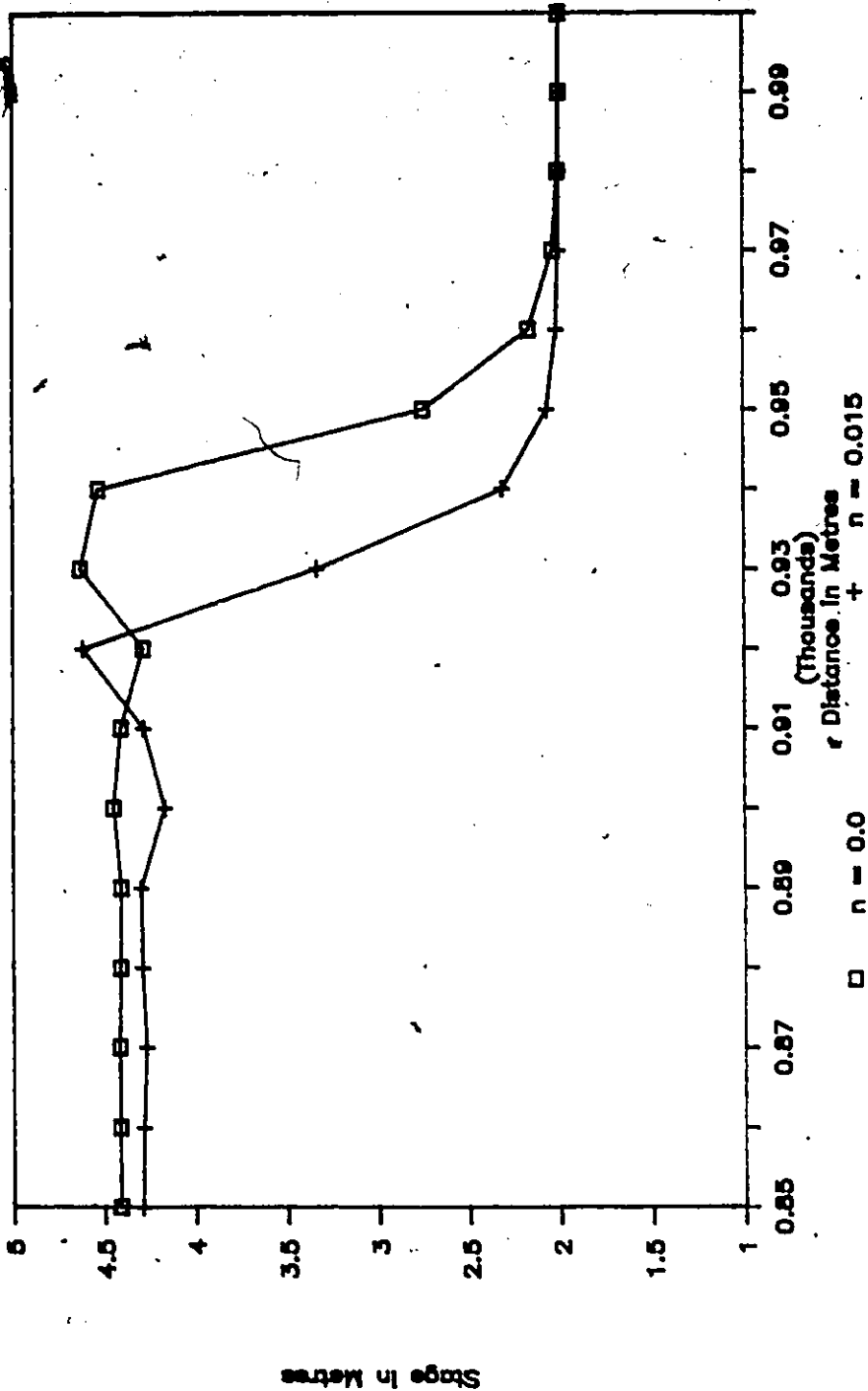


Fig. F.5.1 Channel Roughness Sensitivity on Surge Location

ELEMENT LENGTH SENSITIVITY ANALYSIS

Profiles at Time = 120 Sec. TEST "B"

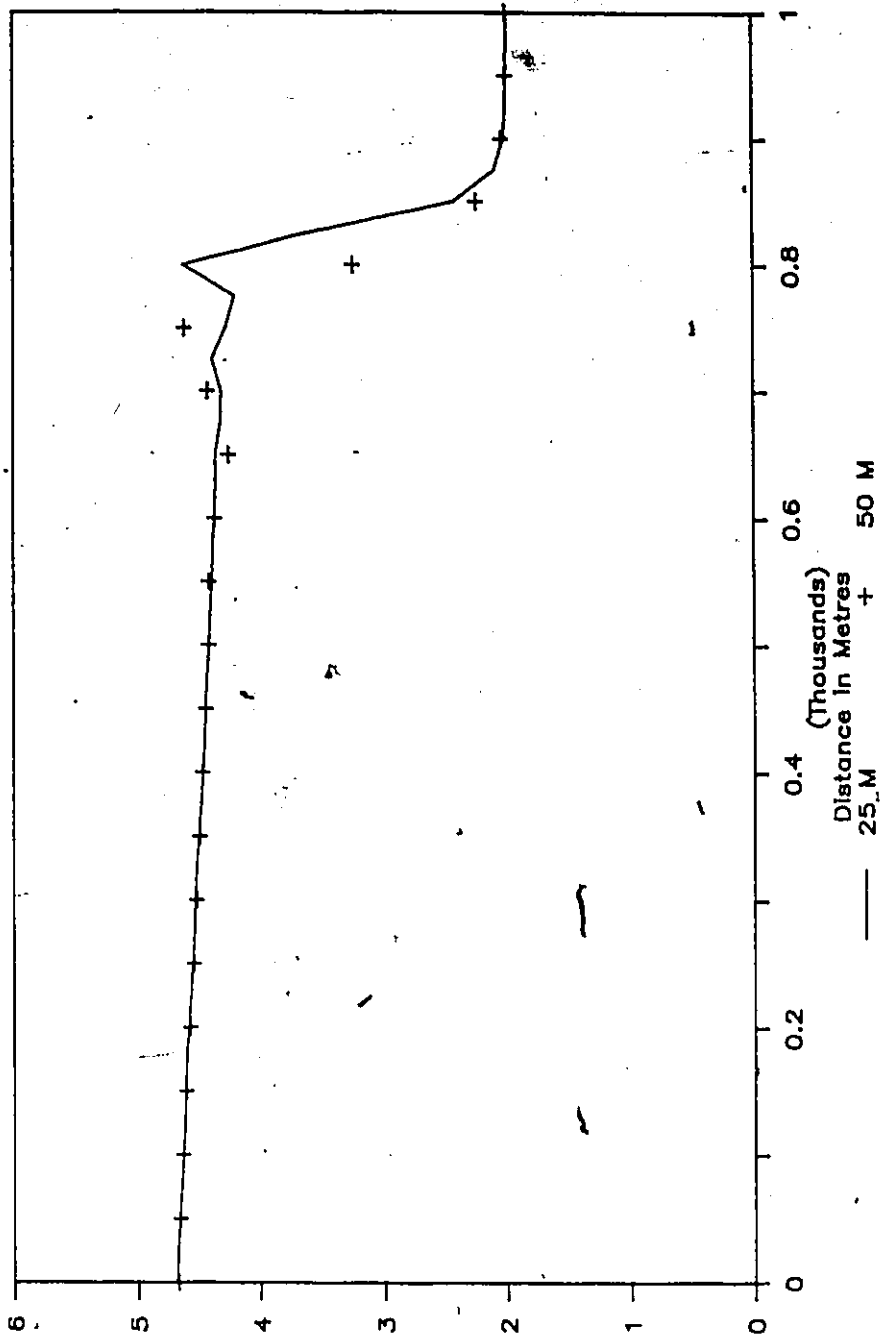


Fig. P. 5.2 Element Size Sensitivity on Front Shape

Stage in Metres

THETA VARIATION SENSITIVITY ANALYSIS

Profiles at Time = 60 sec. TEST "A"

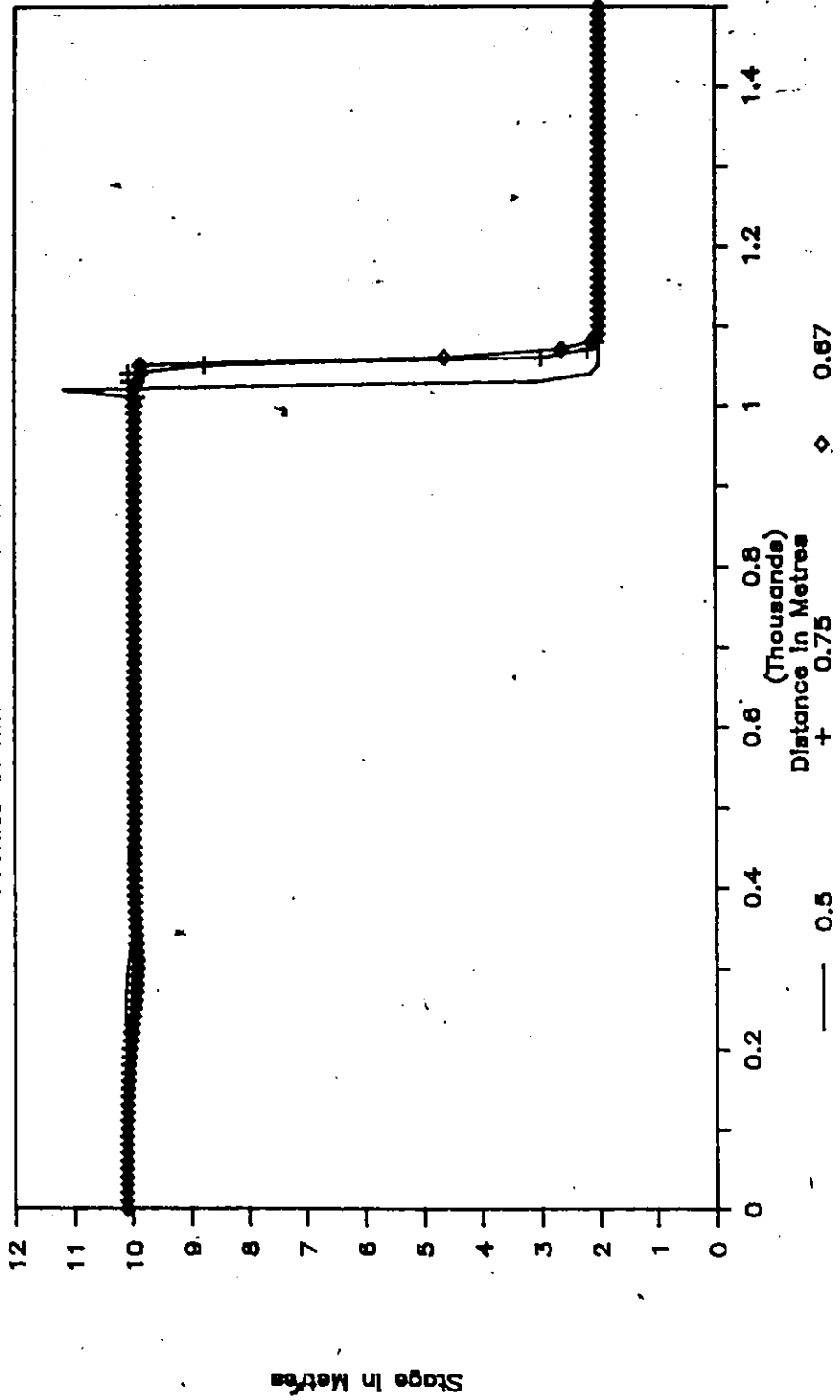


Fig. F.5.3 TWF Sensitivity on Front Shape

EULARIAN - LAGRANGIAN SOLUTION

Profiles at Time = 90 & 180 S TEST "C"

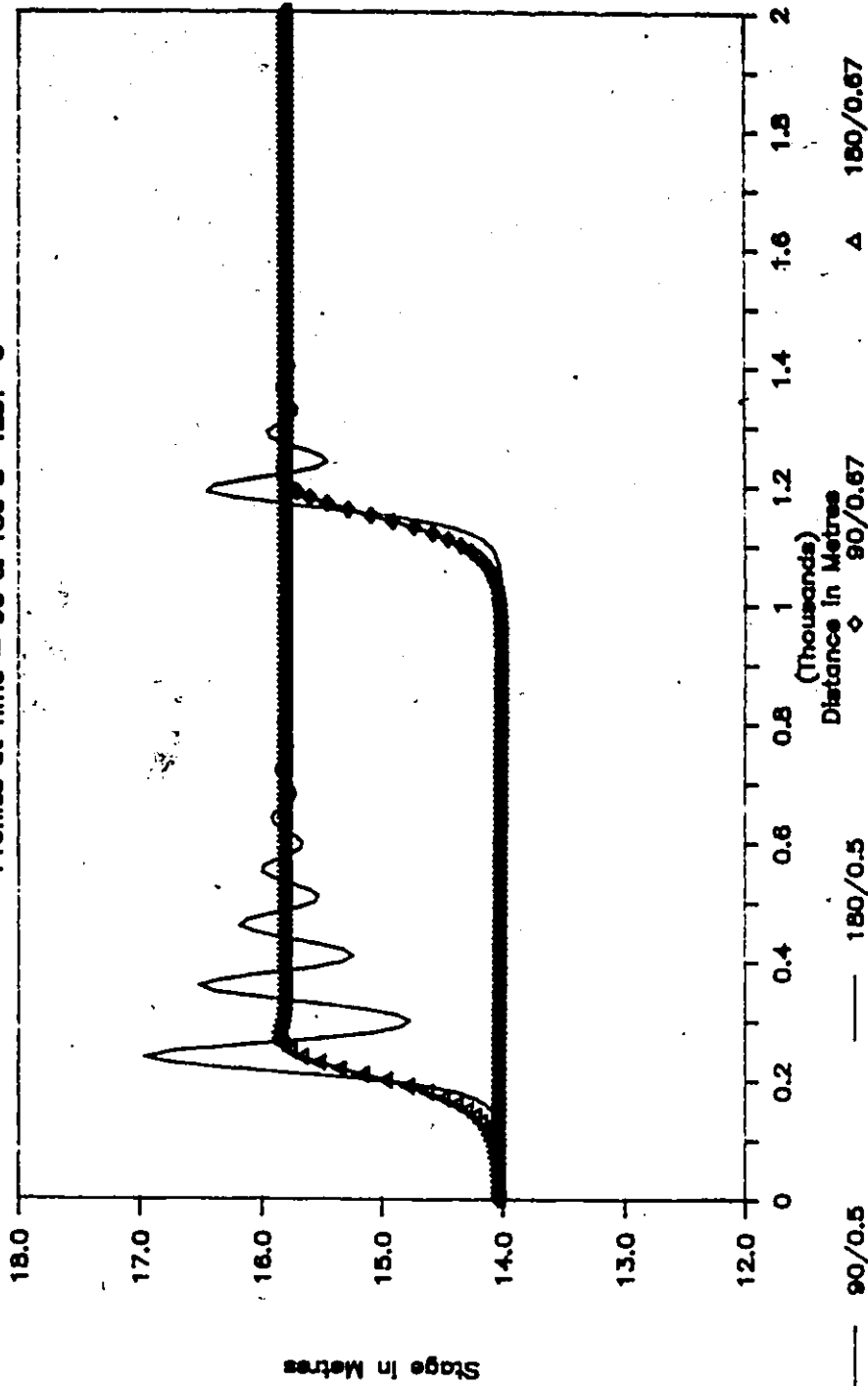


Fig. P.5.4 TWF Sensitivity on Front Shape

Linear and Nonlinear Interpolations

TimeStep=5s, Theta=0.5 @ 60s & 120s

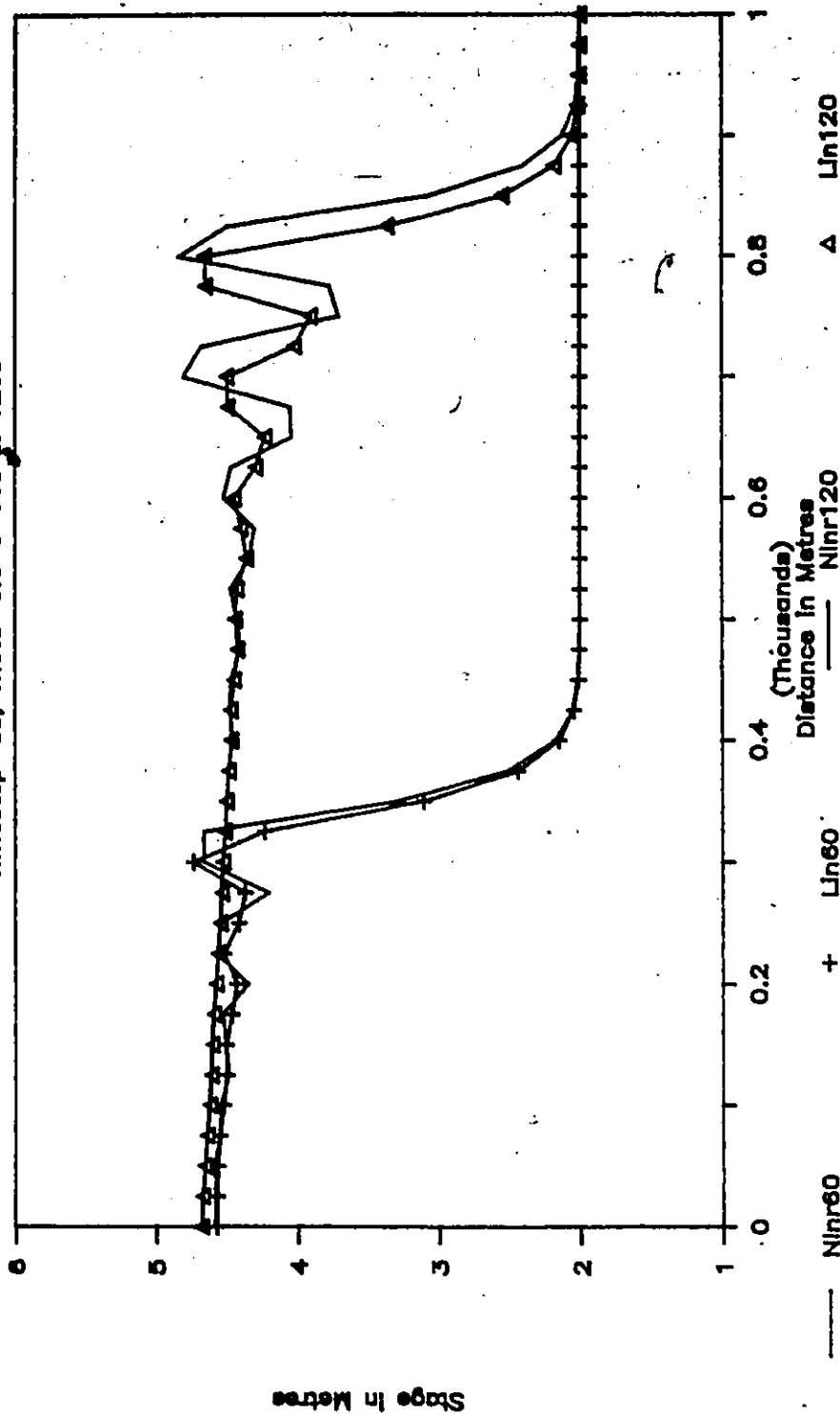


Fig. F.5.5 Interpolation Sensitivity at Eulerian Regridding Step

WAVE STEEPENING & BREAKING

$dx=10m, dt=1s, sf0=1.2\%, \theta=0.5$

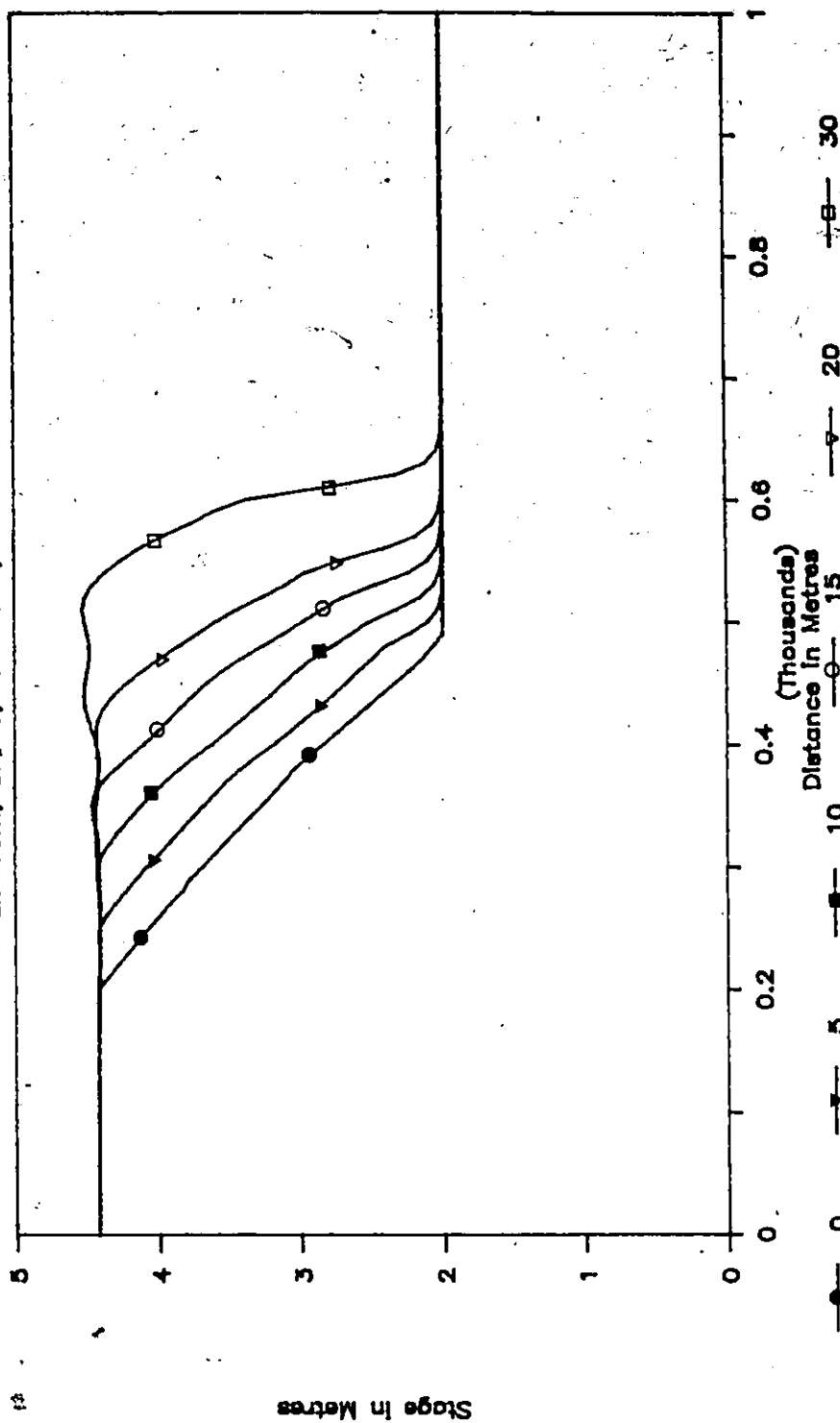


Fig. F.5.6 Wave Steepening and Breaking - Discontinuity in Domain

APPENDIX G

Input File Description

- Card A - Alphanumeric computer run identifier.
Format - A3,19A4
- Card B - Control variables
Format - I7,9I8
Field 1 - No. of Nodes
Field 2 - Eulerian-Lagrangian or Lagrangian run
Field 3 - Supercritical or subcritical run
Field 4 - No. of Hydrographs Printed
Field 5 - No. of time steps for boundary hydrographs
Field 6 - Frequency of profile capturing
Field 7 - Frequency of hydrograph ordinates capturing
Field 8 - No. of iterations in Newton-Raphson technique
Field 9 - No. of sections where channel geometry is specified
- Card C - Control variables (when Field 2 > 0)
Format - I7,I8
Field 1 - Maximum no. of nodes allowed in Lagrangian solution
Field 2 - Minimum no. of nodes allowed in Lagrangian solution
- Card D - Nodes where hydrographs are desired (when Field 4 > 0)
Format - I7,9I8
- Card E - Control variables
Format - I7,9I8
Field 1 - Type of upstream boundary
Field 2 - Type of downstream boundary
Field 3 - Type of interpolation for Eulerian regridding
Field 4 - Type of initial conditions
Field 5 - Units of simulation, Imperial or SI
- Card F - Control variables
Format - F7.0,9F8.0
Field 1 - Reach length
Field 2 - Element length
Field 3 - Temporal weighting factor
Field 4 - Spatial weighting factor
Field 5 - Tolerance for stage in Newton-Raphson iteration
Field 6 - Tolerance for flow in Newton-Raphson iteration
Field 7 - Form loss coefficient (not used in all runs)
Field 8 - Conversion factor for length scale
Field 9 - Lateral rate of inflow (negative for outflow)

Card G - Control Variables
Format - F7.0,9F8.0
Field 1 - Maximum time for simulation
Field 2 - Initial time-step
Field 3 - Final time-step
Field 4 - Conversion factor for time scale
Field 5 - Time to change time-step from initial to final
Field 6 - Time to start lateral flow rate in Field 9 of Card F

Card H - Location of channel properties
Format - F7.0,9F8.0
 Fields equal to Field 9 of Card B

Card I - Channel Geometry (equal to Field 9 of Card B)
Format - F7.0,9F8.0
Field 1 - Topwidth at bank elevation
Field 2 - Thalweg elevation
Field 3 - Bank elevation
Field 4 - Channel roughness coefficient
Field 5 - Elevation where off-channel storage begin

Card X - Channel Geometry (equal to Field 9 of Card B)
Format - F7.0,9F8.0
Field 1 - Rate of channel roughness variation above bank level
Field 2 - Side slopes below bank level (1V : ?H)
Field 3 - Side slopes of conveyance (1V : ?H)
Field 4 - Side slopes of off-channel storage (1V : ?H)

Card J - Location of initial computational nodes
Format - F7.0,9F8.0
 Fields equal to Field 1 of Card B

Card K - Initial stages at computational nodes
Format - F7.0,9F8.0
 Fields equal to Field 1 of Card B

Card L - Initial flow rate at computational nodes
Format - F7.0,9F8.0
 Fields equal to Field 1 of Card B

Card M - Starting conditions at control points
Format - F7.0,9F8.0
Field 1 - Starting water surface elevation at control point
Field 2 - Corresponding flow rate
Field 3 - Thalweg elevation (if Field 4 of Card E = 0)
Field 4 - Channel bed slope (if Field 4 of Card E = 0)

Card N - Time units for inflow stage/flow hydrographs
Format - F7.0,9F8.0
 Fields equal to Field 5 of Card B

Card O - Stage hydrograph ordinates (if Field 1 of Card E = 1)
Format - F7.0,9F8.0
 Fields equal to Field 5 of Card B

Card P - Flow hydrograph ordinates (if Field 1 of Card E = 0)
Format - F7.0,9F8.0
 Fields equal to Field 5 of Card B

Card Q - Stage hydrograph ordinates (if Field 3 of Card B = 1)
Format - F7.0,9F8.0
 Fields equal to Field 5 of Card B

Card R - Flow hydrograph ordinates (if Field 3 of Card B = 1)
Format - F7.0,9F8.0
 Fields equal to Field 5 of Card B

Card S - Stage hydrograph ordinates (if Field 2 of Card E = 1)
Format - F7.0,9F8.0
 Fields equal to Field 5 of Card B

Card T - Flow hydrograph ordinates (if Field 2 of Card E = 0)
Format - F7.0,9F8.0
 Fields equal to Field 5 of Card B

Card U - Channel bed slope at downstream boundary (if Field 2
 of Card E = 2)
Format - F7.0,9F8.0
Field 1 - Channel bed slope at D/S boundary

Table G.1

Sample Input File for Teton Dam-Break Simulation

```

A   TETON DAMFAILURE SIMULATION WITH OFF-CHANNEL STORAGE
A   3-PT LAGRANGIAN INTERPOLATION, THETA=0.5, BETA=0.0
A   TIMESTEP= 450 S, ELEMENT SIZE= 2640 FT
B   113      0      0      3      8      2      5      8
D   33      56      66
E   0      2      0      2      0
F59.5  0.5    0.50   0.0    1.5    1500.   0.0    5280.
G50.0  0.125   0.25   3600.   11.0
H0.0   8.5     16.0   27.5    32.5   41.0    51.5   59.5
I460.  5027.   5050.   0.08    5050.
I400.  4920.   4930.   0.04    4942.
I440.  4817.   4827.   0.034   4827.
I144.  4788.   4797.   0.037   4802.
I180.  4765.   4774.   0.034   4774.
I270.  4741.   4756.   0.034   4756.
I175.  4697.   4708.   0.036   4708.
I225.  4601.   4616.   0.036   4616.
X0.0   20.     2.0    0.0
X0.0   40.     250.   360.
X0.0   44.     420.   500.
X0.0   36.     300.   310.
X0.0   15.     800.   1090.
X0.0   13.5    195.   195.
X0.0   12.5    2.3    0.0
X0.0   45.     2.5    0.0
K4614.0 13000.
NO.0   0.25    1.50   2.25   3.75   8.25   10.5   50.0
P13000. 13000. 1650000.991000. 400000. 100000. 13000. 13000.
U0.00126

```


APPENDIX H

Sample of Output File Echoing Input Data

GRAND RIVER SIMULATION - BRANTFORD TO LAKE ERIE

3-PT LAGRANGIAN INTERPOLATION, THETA=0.5, BETA=0.0

TIMESTEP=450 & 900 S, ELEMENT SIZE= 2640 FT

NO. OF NODES = 122

NO. OF HYDROGRAPHS = 3

NO. OF BOUNDARY HYDROGRAPH STEPS = 153

OUTPUT PRINTED EVERY 5152 STEPS

HYDROGRAPH PRINTED EVERY 8 STEPS

NO. OF ITERATIONS = 5

X-SECTIONS DEFINED AT 10 POINTS

NLAG = 0, EULARIAN - LAGRANGIAN SOLUTION

NCRIT = 0, SUBCRITICAL FLOW SOLUTION

HYDROGRAPHS PRINTED FOR NODES 1 71 72

IF NTU= 0, FLOW HYDROGRAPH

NTU= 1, STAGE HYDROGRAPH

SPECIFIED NTU IS 0

IF NTD= 0, FLOW HYDROGRAPH

NTD= 1, STAGE HYDROGRAPH

NTD= 2, SINGLE VALUE RATING

NTD= 3, LOOPED RATING

SPECIFIED NTD IS 1

IF NINT= 0, 3-PT LAGRANGIAN INTERPOLATION

NINT= 1, MIXED LINEAR-LAGRANGIAN INTERPOLATION

NINT= 2, 2-PT LINEAR INTERPOLATION

SPECIFIED NINT IS 0

IF NINITL= 0, INITIAL CONDITIONS SPECIFIED

NINITL= 1, INITIAL CONDITIONS COMPUTED

SPECIFIED NINITL IS 2

IF METRIC= 0, IMPERIAL UNITS USED

METRIC= 1, SI UNITS USED

SPECIFIED METRIC IS 0

REACH LENGTH = 60.0000
 ELEMENT-LENGTH = 0.5000
 X UNIT CONVERSION FACTOR = 5280.0000

TEMPORAL WEIGHING PARAMETER, THETA = 0.5000
 SPATIAL WEIGHING PARAMETER, BETA = 0.0000

TOLERANCE FOR STAGE = 1.5000
 TOLERANCE FOR FLOW = 1500.0000
 EXPANSION - CONTRACTION COEF. = 0.0000
 LATERAL FLOW RATE = 0.1000

TOTAL LENGTH OF SIMULATION (TIME) = 152.0000
 INITIAL TIME STEP = 0.1250
 NORMAL TIME STEP = 0.2500
 CONVERSION FACTOR TO SEC. = 3600.0000
 TIME TO USE NORMAL TIME STEP = 100.0000
 TIME TO START LATERAL FLOW = 70.0000

END OF INITIAL INPUT DATA

SECTION PROPERTIES DEFINED AT CHAINAGES

0.000	8.000	16.000	24.000	28.000
35.000	38.500	45.000	53.000	60.000

NO.	BASE WIDTH	THALWEG EL.	BANK EL.	MANNING COEF.	OFFCHNL EL.
1	296.000	621.000	625.000	0.04500	625.000
2	538.800	610.000	633.100	0.04500	633.100
3	1178.600	610.000	640.200	0.04500	640.200
4	953.200	609.000	630.400	0.04500	630.400
5	722.500	606.000	620.600	0.03500	620.600
6	909.100	587.500	600.900	0.03200	600.900
7	820.100	573.600	584.200	0.03000	584.200
8	1166.200	561.200	588.100	0.03000	588.100
9	516.700	561.500	569.400	0.03000	569.400
10	396.400	546.400	560.400	0.03000	560.400

CONSTANTS & EXPONENTS FOR AREA RELATIONSHIPS

NO.	CONSTANT	POWER #1	POWER #2	POWER #3
1	-0.040	37.000	1.330	0.000
2	-0.040	11.700	24.000	0.000
3	-0.040	19.500	16.400	0.000
4	-0.040	22.300	29.700	0.000
5	-0.040	24.700	39.900	0.000
6	-0.040	33.800	32.100	0.000

7	-0.040	38.300	58.100	0.000
8	-0.040	21.700	5.600	0.000
9	-0.040	32.700	43.900	0.000
10	-0.040	12.800	22.100	0.000

INITIAL CONDITIONS FROM DOWNSTREAM BOUNDARY

STAGE = 570.000

FLOW = 3531.000

APPENDIX I

Envelopes of Maximum Flows and Highest Depths with Associated Times

NODE	DISTANCE	STAGE	DEPTH	TIME	DISCHARGE	TIME	TOPWIDTH
1	0.0	653.93	32.93	65.375	53318.0	64.000	372.9
2	0.5	652.88	32.57	65.750	53122.3	64.125	461.6
3	1.0	652.46	32.84	65.750	52896.9	64.125	546.6
4	1.5	651.61	32.67	66.125	52350.2	64.375	621.6
5	2.0	651.00	32.75	66.375	51712.1	64.500	692.2
6	2.5	650.51	32.95	66.500	50782.5	64.750	758.6
7	3.0	649.88	33.01	66.750	50211.2	65.000	816.6
.....							
53	26.0	629.09	21.59	74.875	36768.2	74.375	1087.9
54	26.5	628.12	21.00	75.000	36453.3	74.500	1086.5
55	27.0	627.06	20.31	75.125	36464.8	74.750	1080.0
56	27.5	625.89	19.51	75.250	36365.1	74.875	1065.0
.....							
115	57.0	574.03	21.16	85.750	34046.6	85.625	1062.6
116	57.5	573.42	21.63	85.875	34031.2	85.625	1025.7
117	58.0	572.79	22.07	85.875	34184.8	85.750	987.0
118	58.5	572.17	22.53	85.875	34040.8	85.875	949.0
119	59.0	571.53	22.97	85.875	34061.2	85.875	910.0
120	59.5	570.85	23.38	85.875	34037.9	86.000	869.2
121	60.0	570.00	23.60	86.000	33829.0	86.000	820.7

APPENDIX J

**Channel Cross-Sections for Teton Dam-Break Flood
and
Grand River Flood Simulations**

TETON DAM—BREAK FLOOD SIMULATION

Channel Cross—Section at Mile 0.0

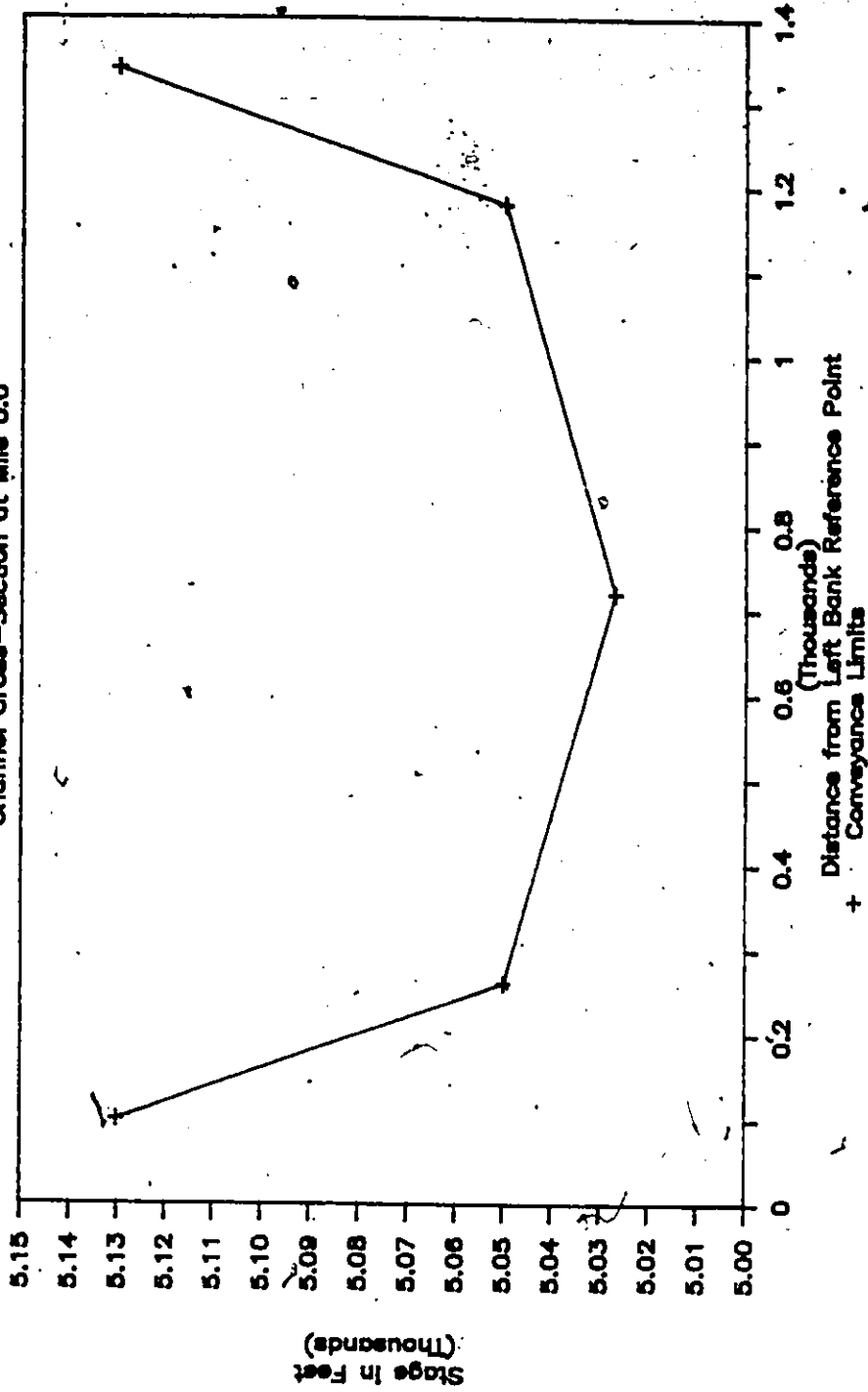


Fig. J.1.1 Section at Mile 0.0

TETON DAM—BREAK FLOOD SIMULATION

Channel Cross-Section at Mile 5.0

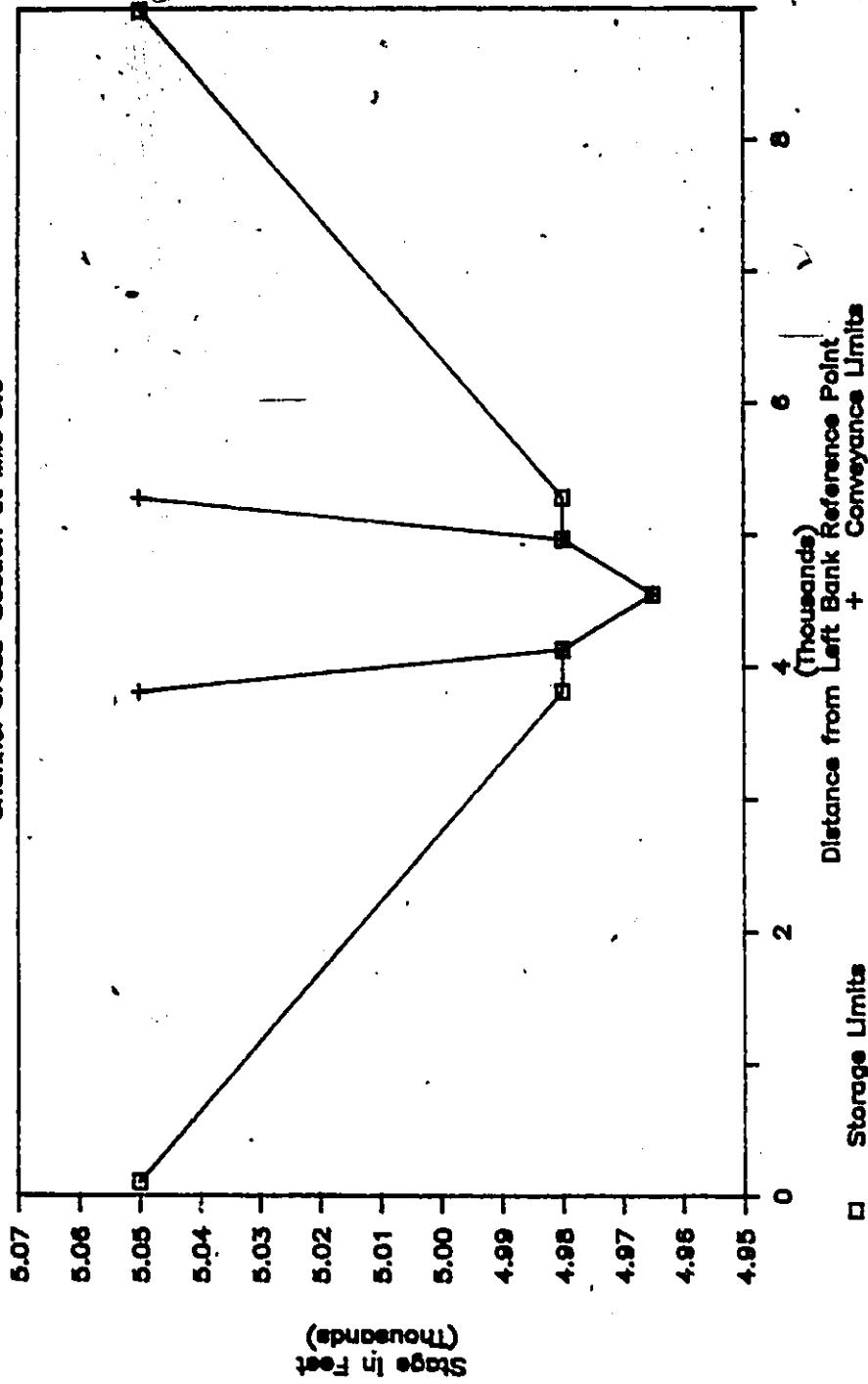


Fig. J.1.2 Section at Mile 5.0

TETON DAM—BREAK FLOOD SIMULATION

Channel Cross--Section at Mile 8.5

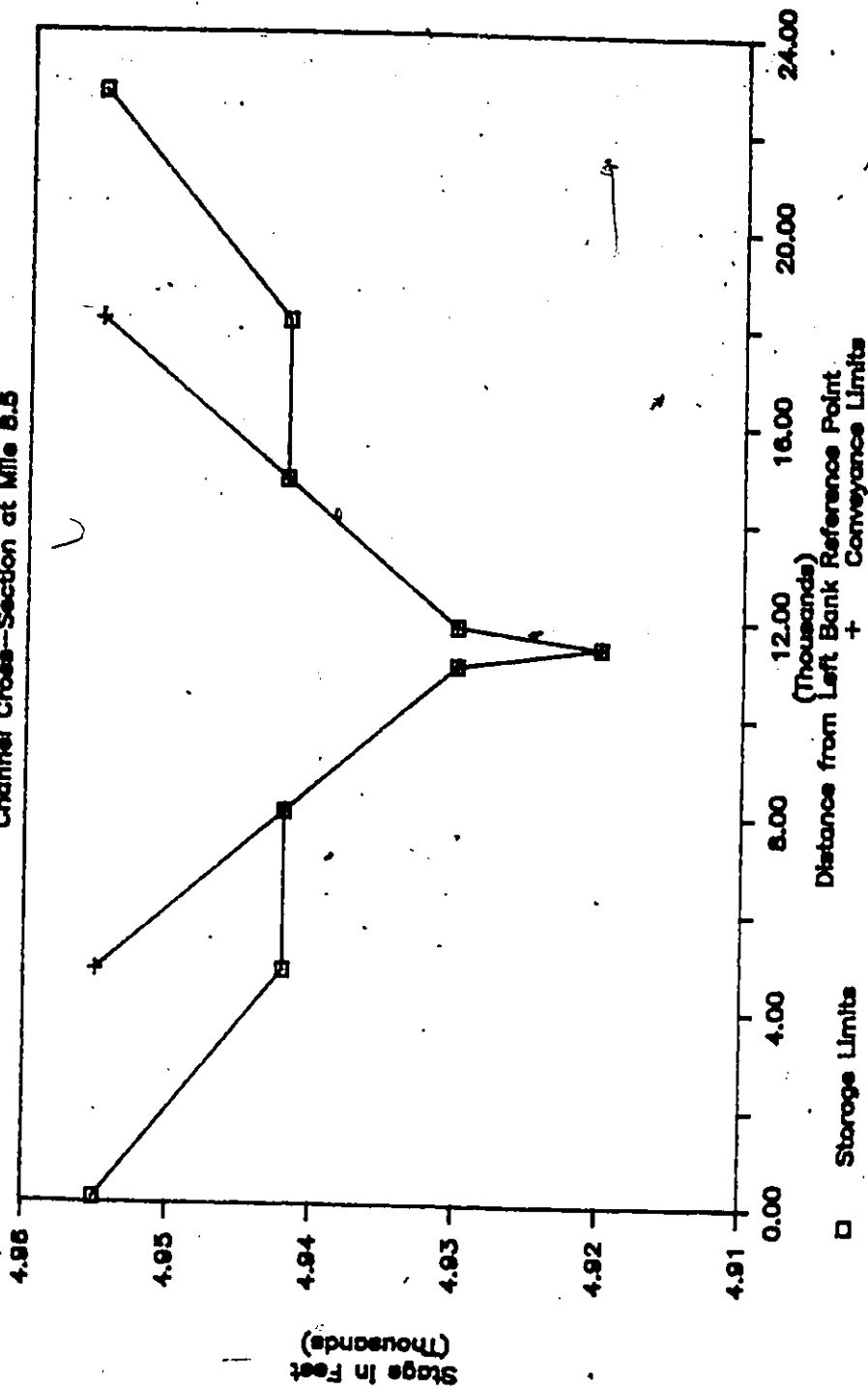


Fig. J.1.3 Section at Mile 8.5

TETON DAM—BREAK FLOOD SIMULATION

Channel Cross-Section at Mile 16.0

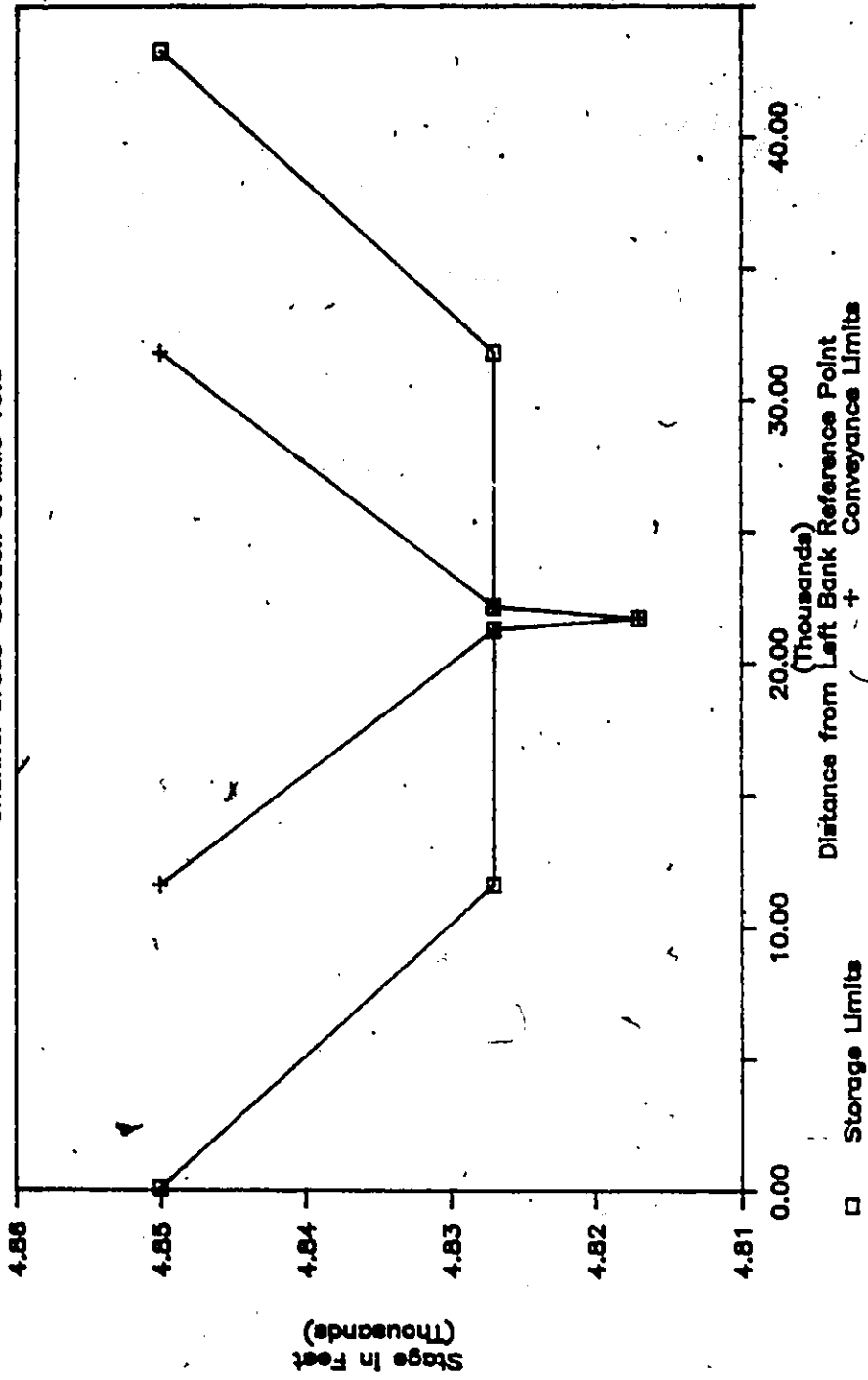


Fig. J.1.4 Section at Mile 16.0

TETON DAM--BREAK FLOOD SIMULATION

Channel Cross--Section at Mile 22.5

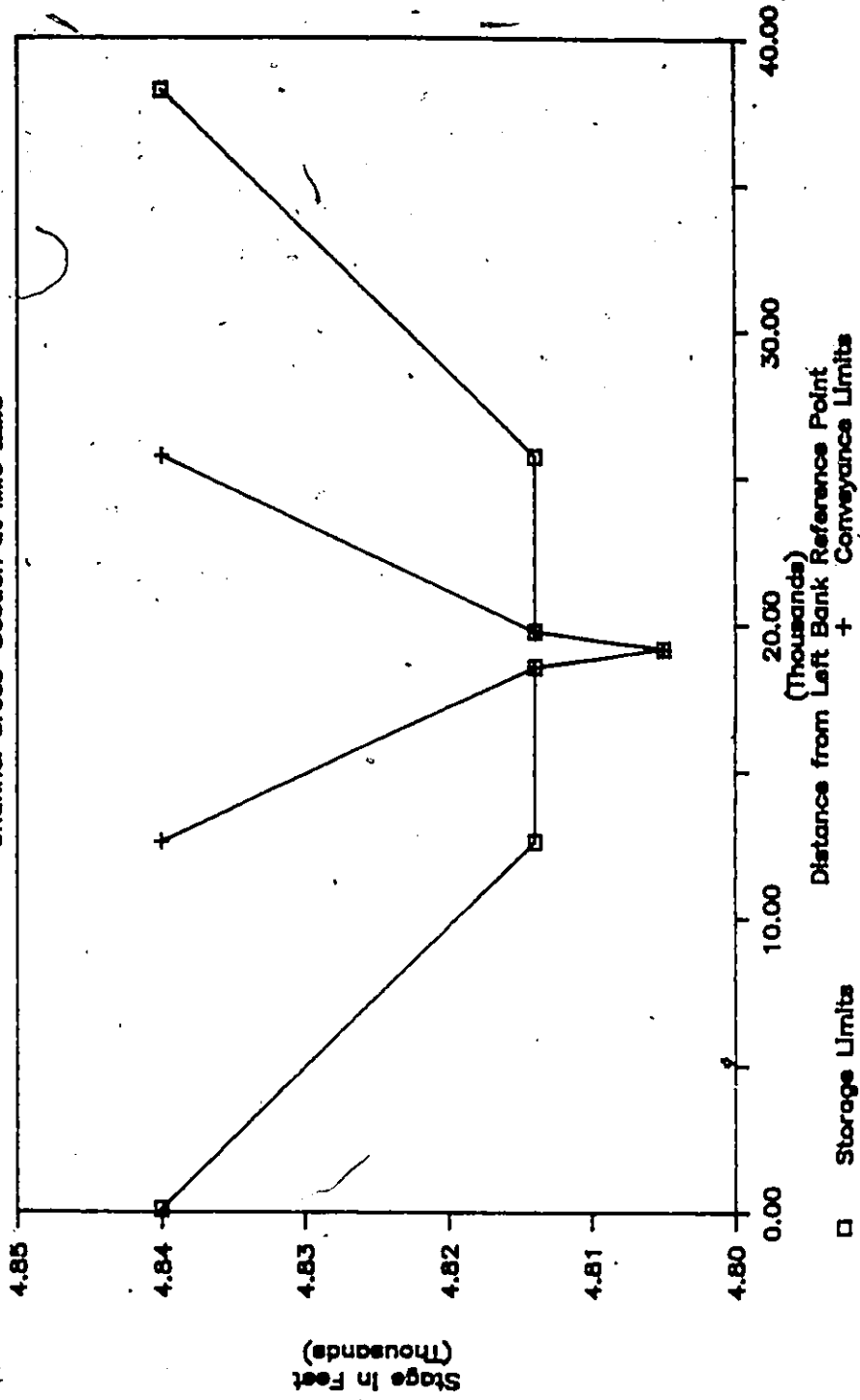


Fig. J.1.5 Section at Mile 22.5

TETON DAM—BREAK FLOOD SIMULATION

Channel Cross-Section at Mile 27.5

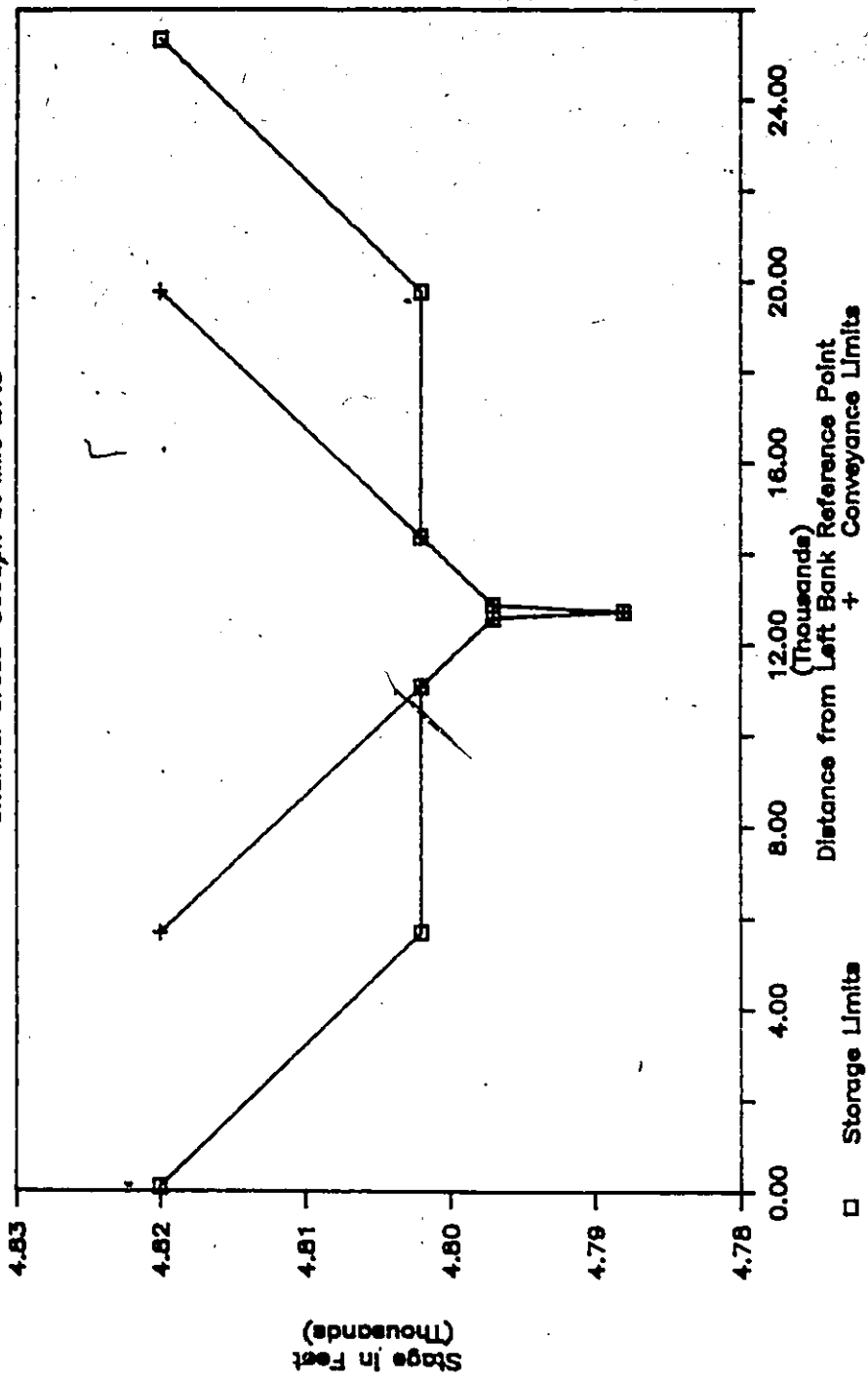


Fig. J.1.6 Section at Mile 27.5

TETON DAM—BREAK FLOOD SIMULATION

Channel Cross—Section at Mile 32.5

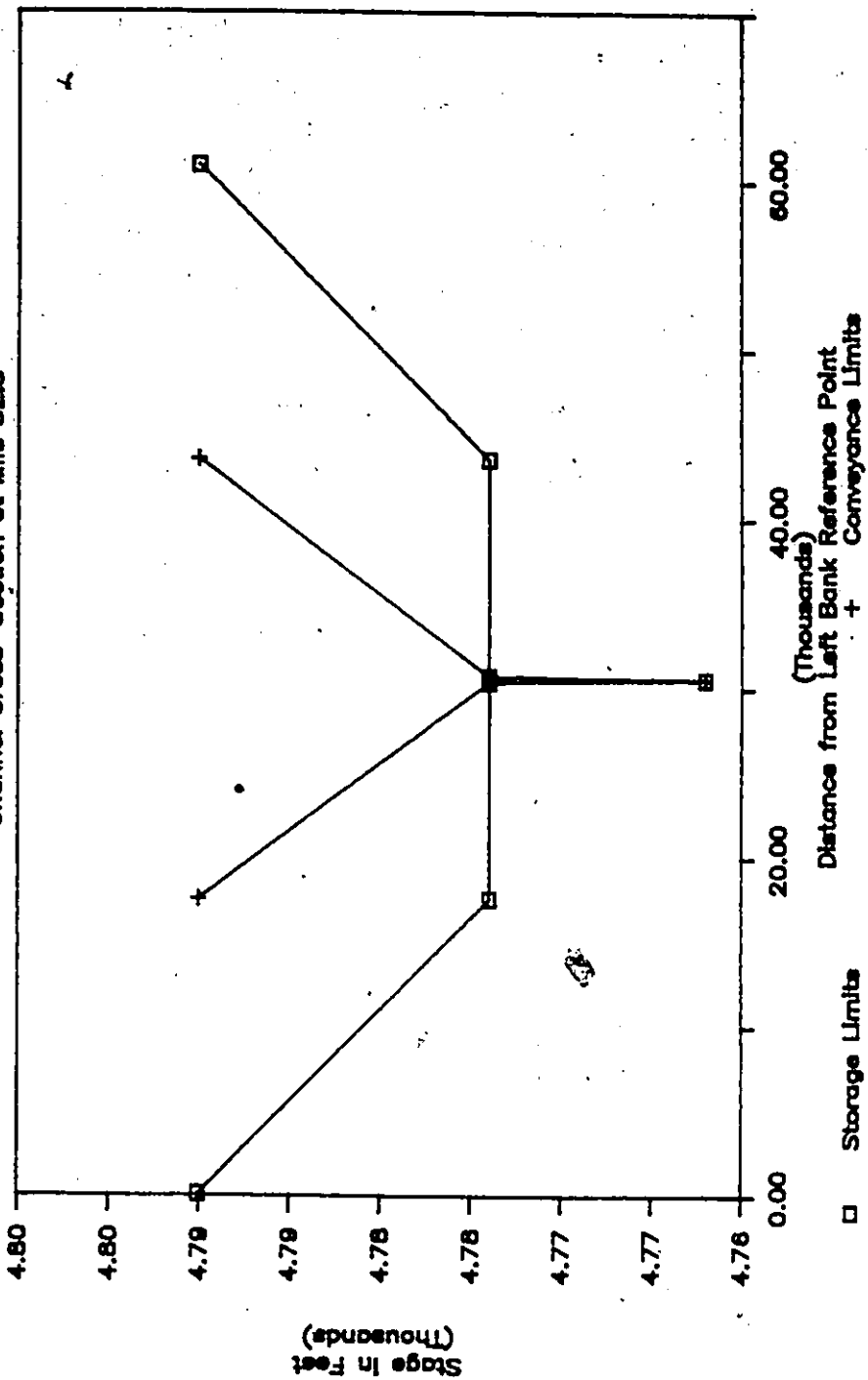


Fig. J.1.7 Section at Mile 32.5

TETON DAM—BREAK FLOOD SIMULATION

Channel Cross-Section at Mile 37.5

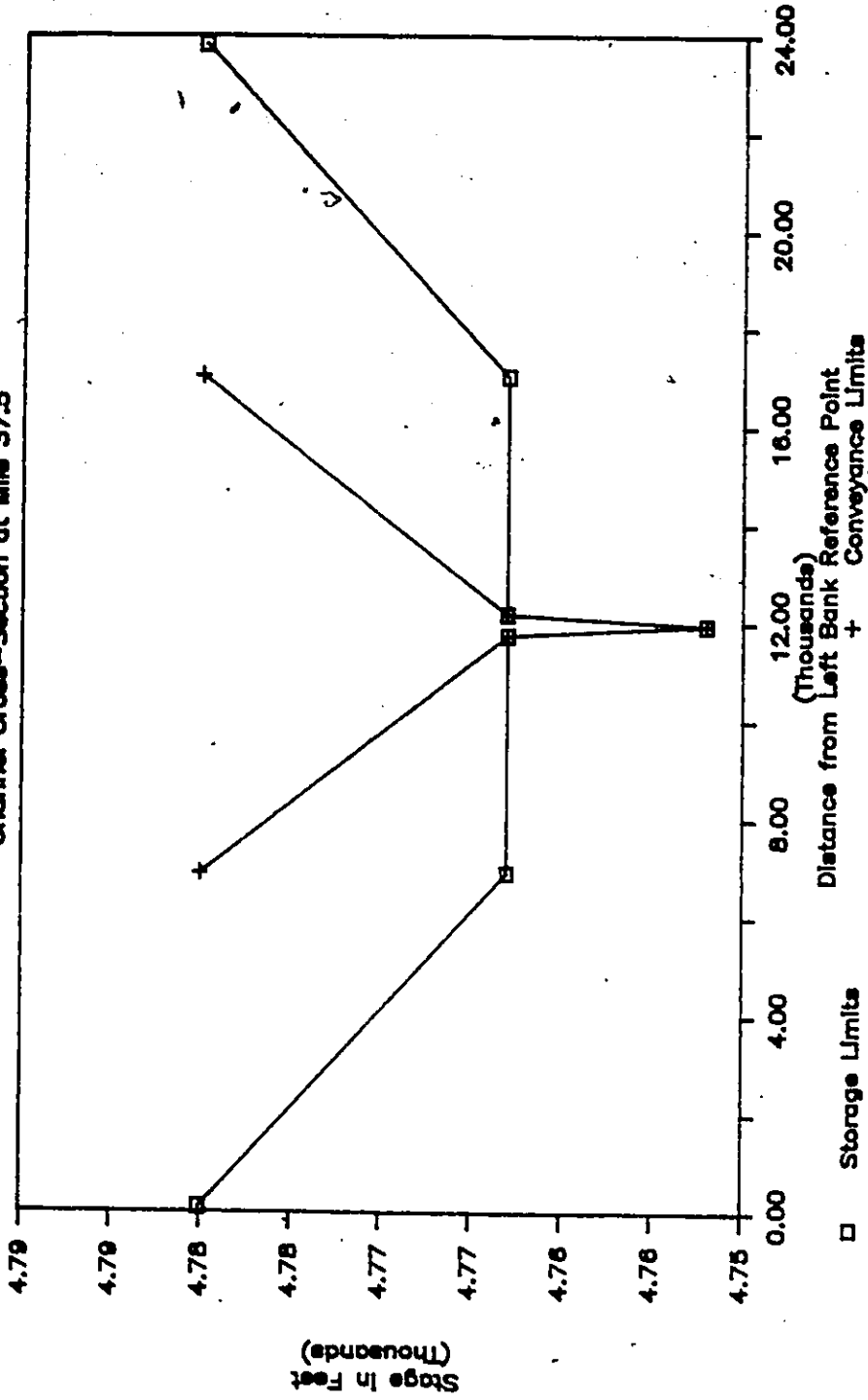


Fig. J.1.8 Section at Mile 37.5

TETON DAM—BREAK FLOOD SIMULATION

Channel Cross—Section at Mile 41.0

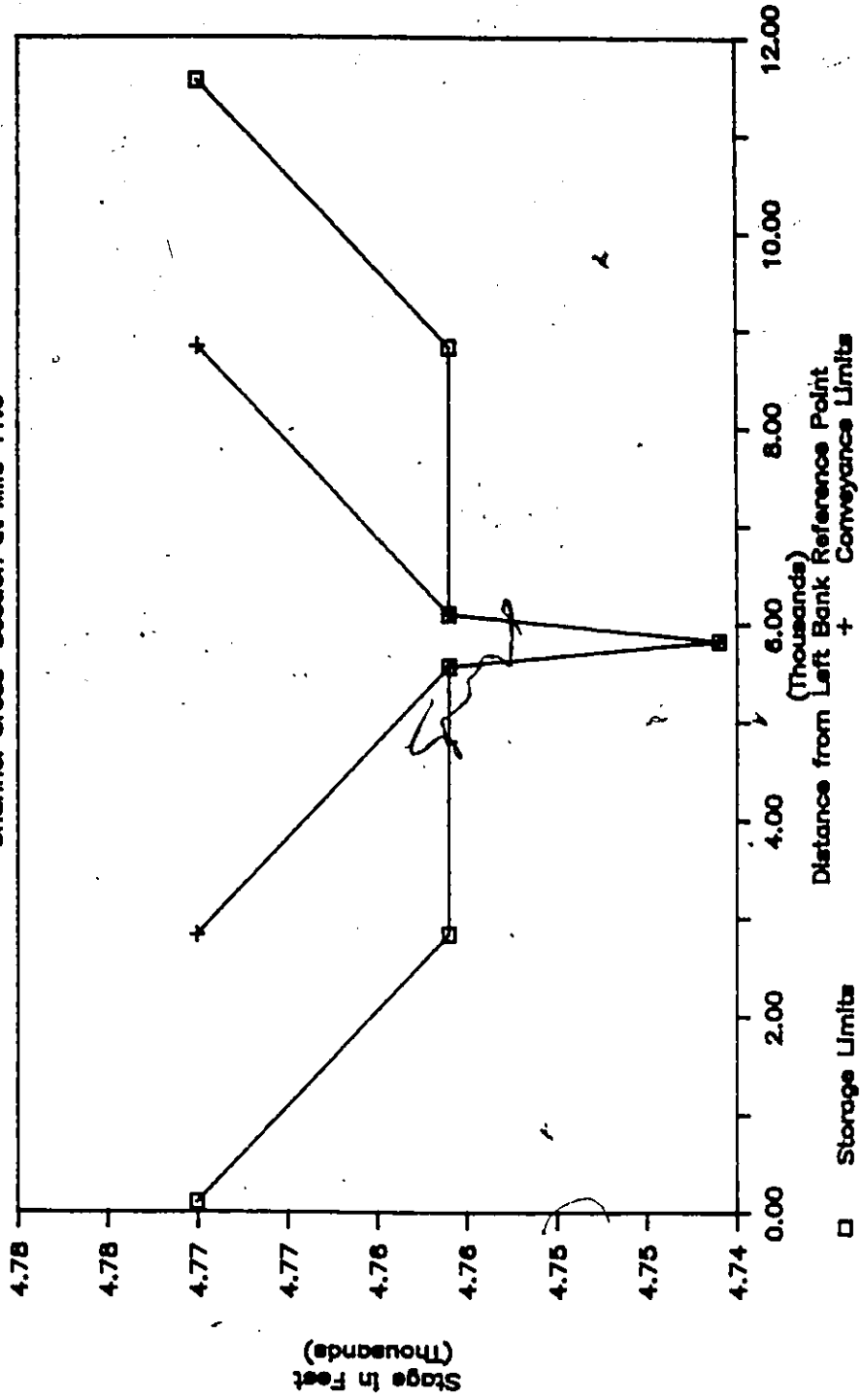


Fig. J.1.9 Section at Mile 41.0

TETON DAM—BREAK FLOOD SIMULATION

Channel Cross—Section at Mile 43.0

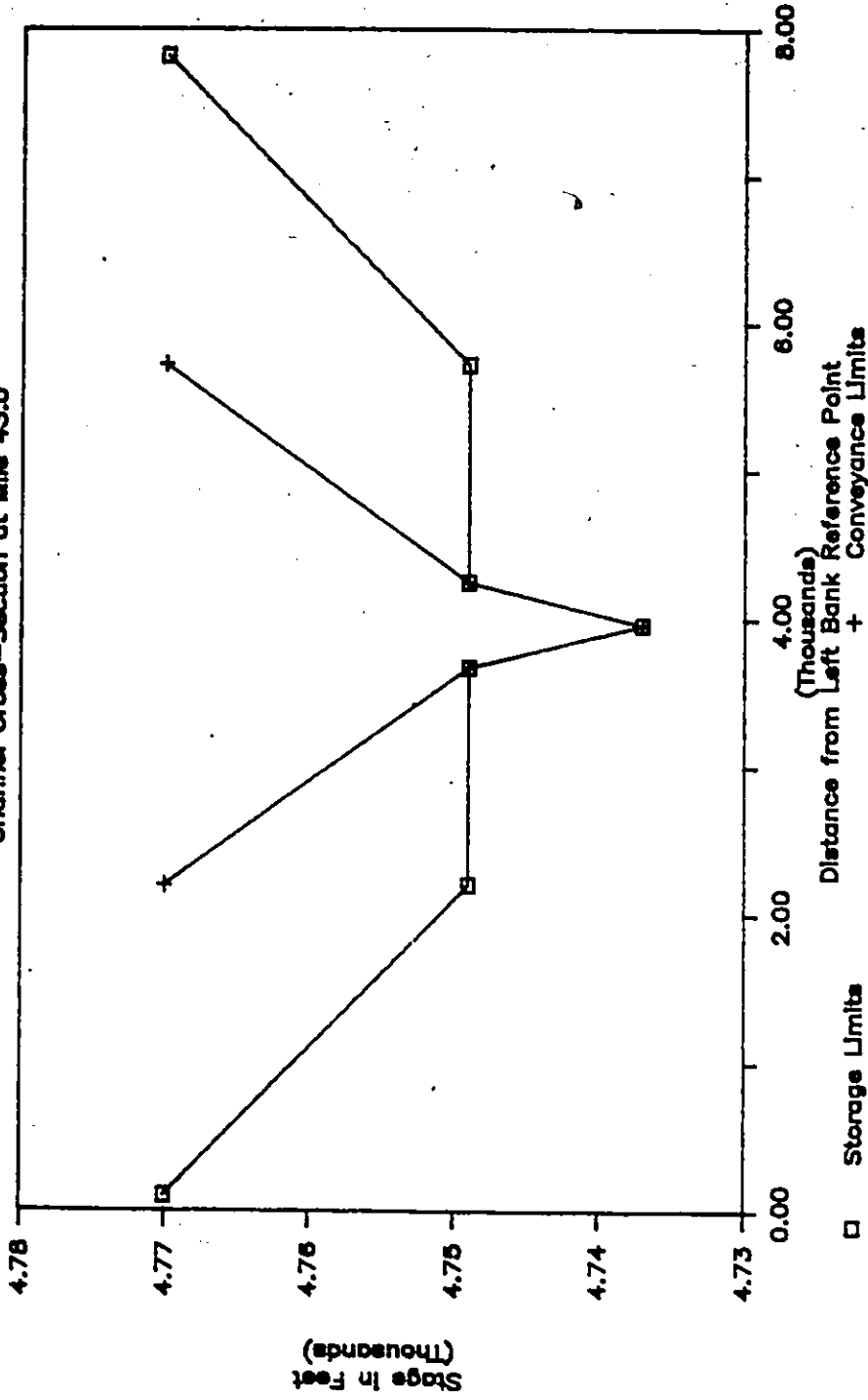
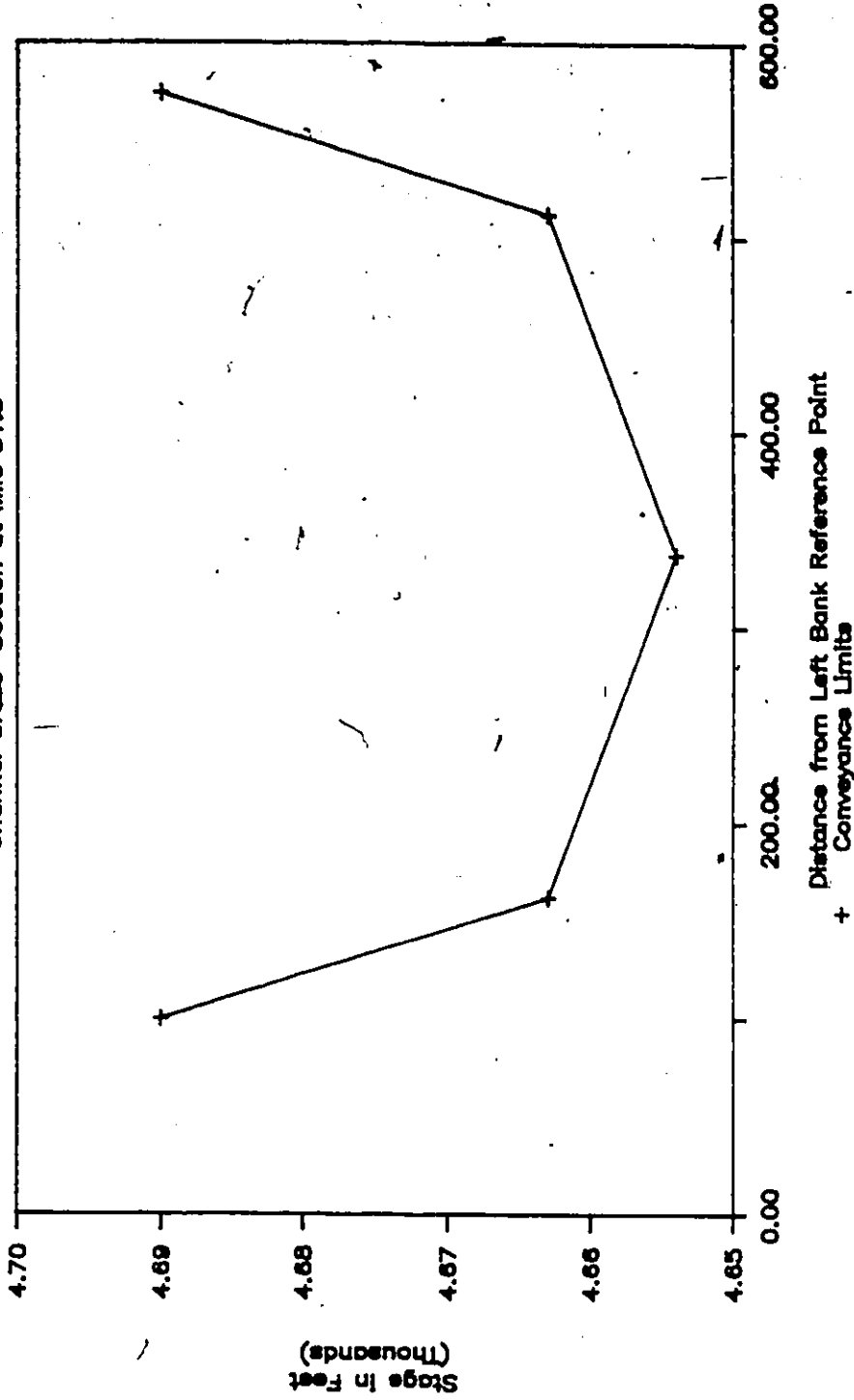


Fig. J.1.10 Section at Mile 43.0

TETON DAM—BREAK FLOOD SIMULATION

Channel Cross—Section at Mile 51.5



S

Fig. J.1.11 Section at Mile 51.5

TETON DAM-BREAK FLOOD SIMULATION

Channel Cross-Section at Mile 59.5

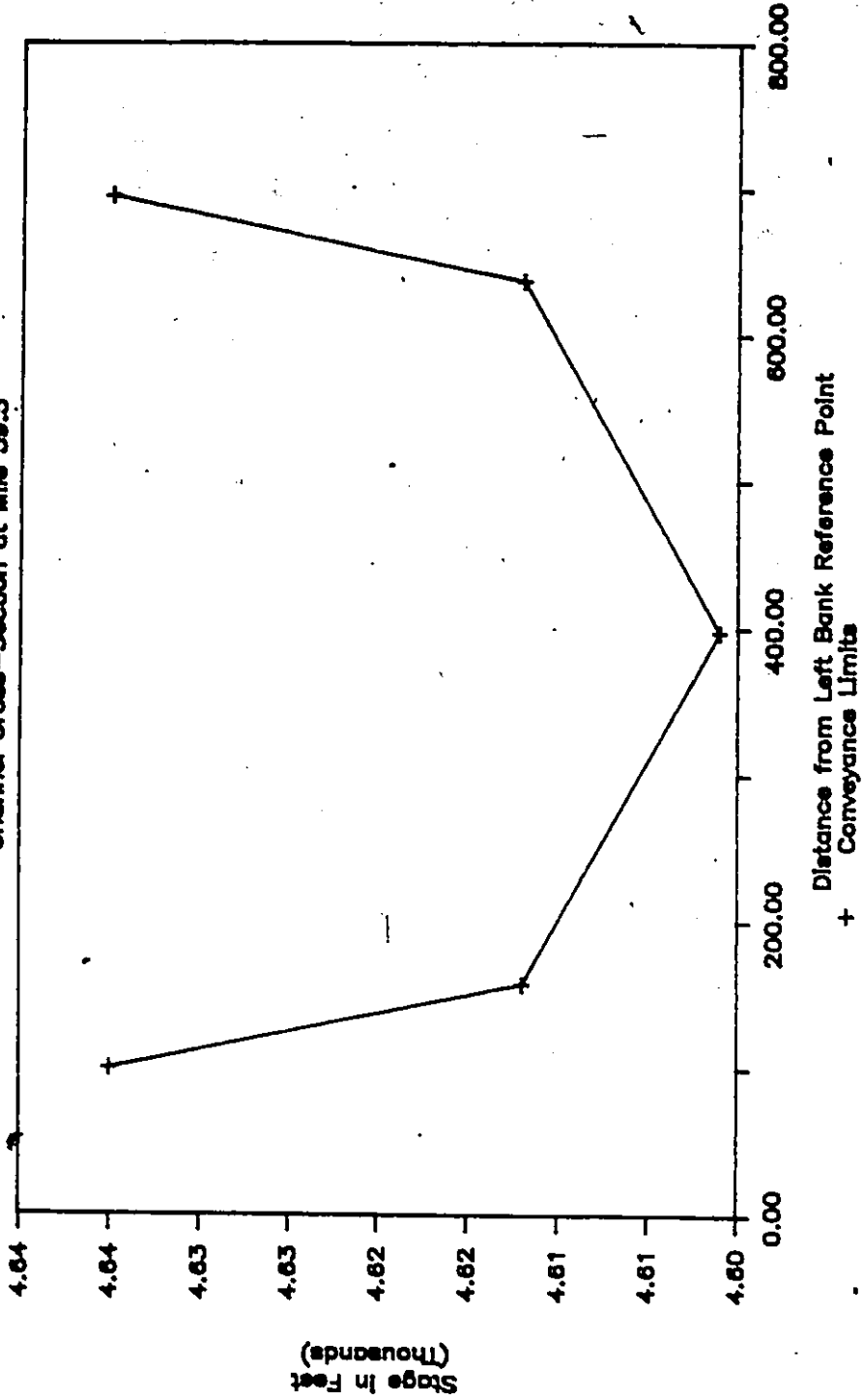


Fig. J.1.12 Section at Mile 59.5

GRAND RIVER FLOOD ROUTING

Channel Cross-Section at Mile 0.0

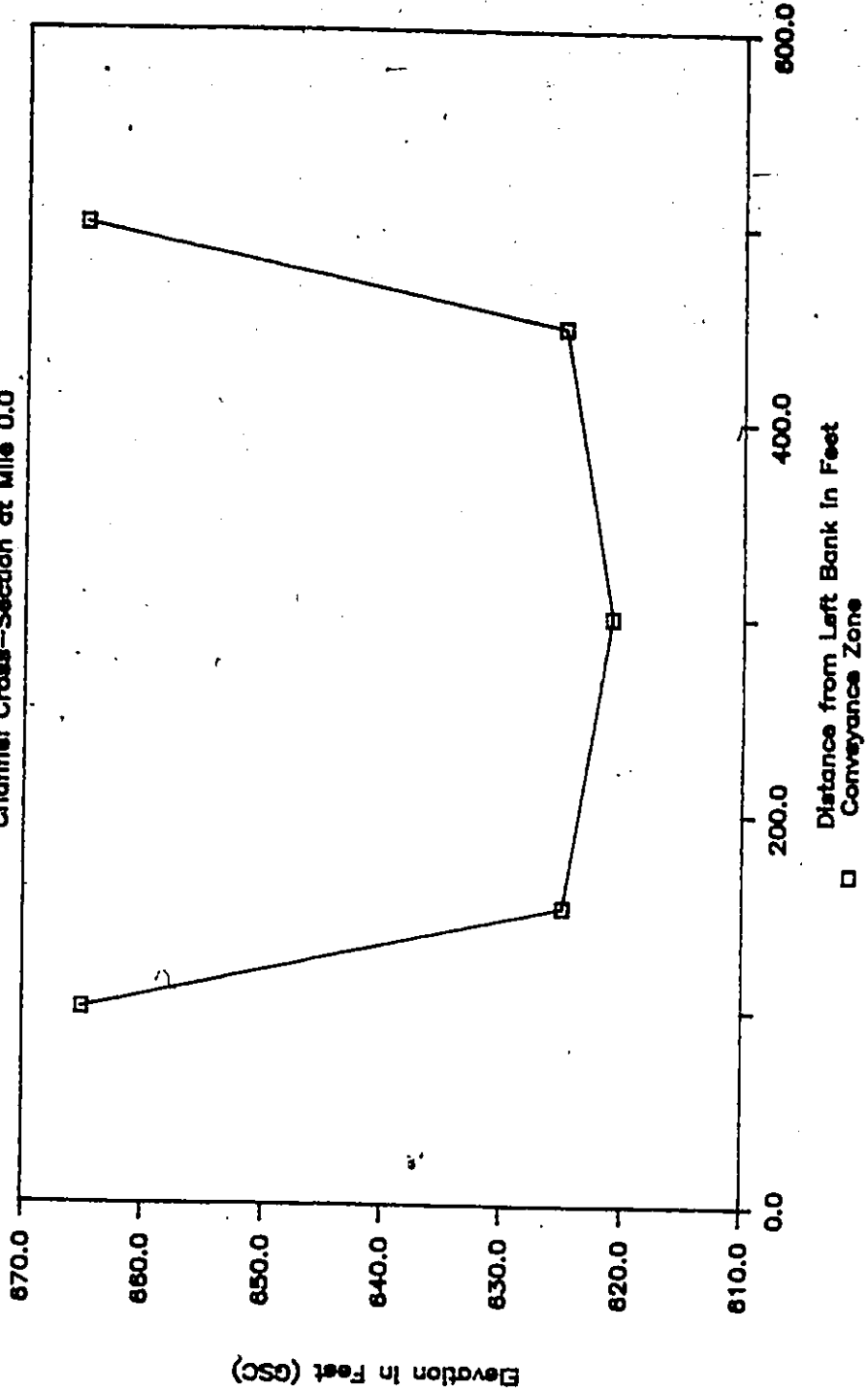


Fig. J.2.1 Section at Mile 0.0

GRAND RIVER FLOOD ROUTING

Channel Cross-Section at Mile 8.0

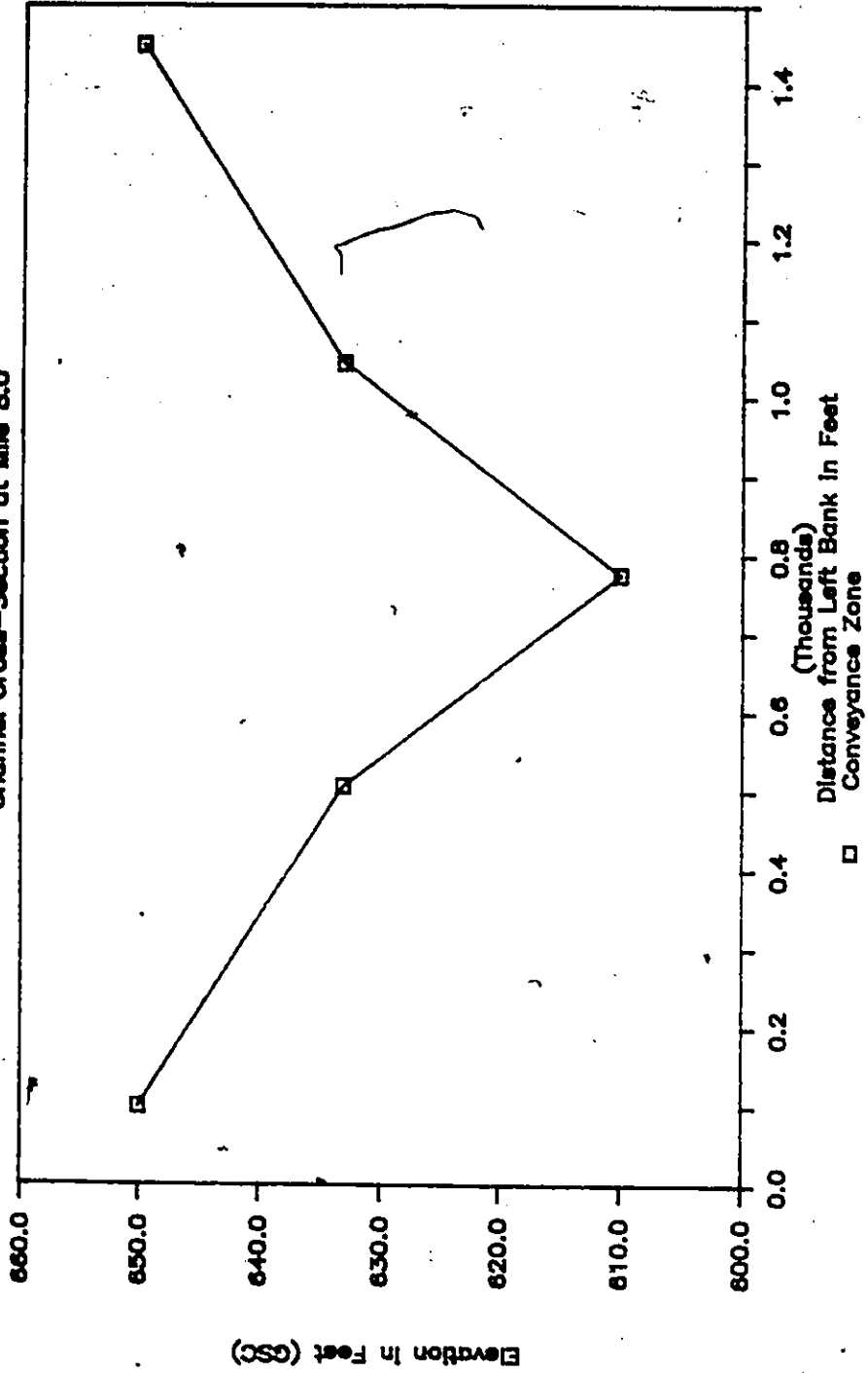


Fig. J.2.2 Section at Mile 8.0

GRAND RIVER FLOOD ROUTING

Channel Cross--Section at Mile 16.0

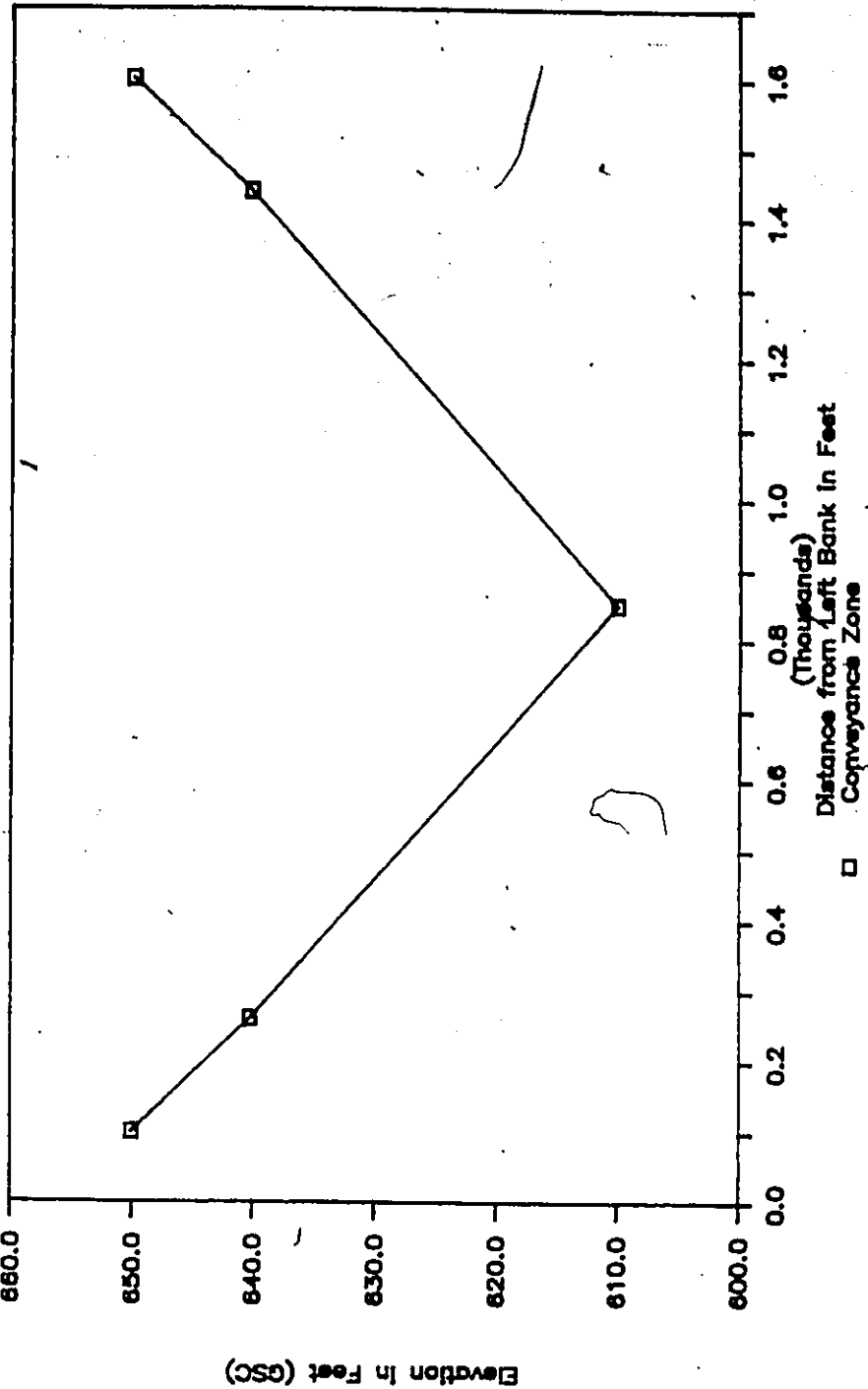


Fig. J.2.3 Section at Mile 16.0

GRAND RIVER FLOOD ROUTING

Channel Cross-Section at Mile 24.0

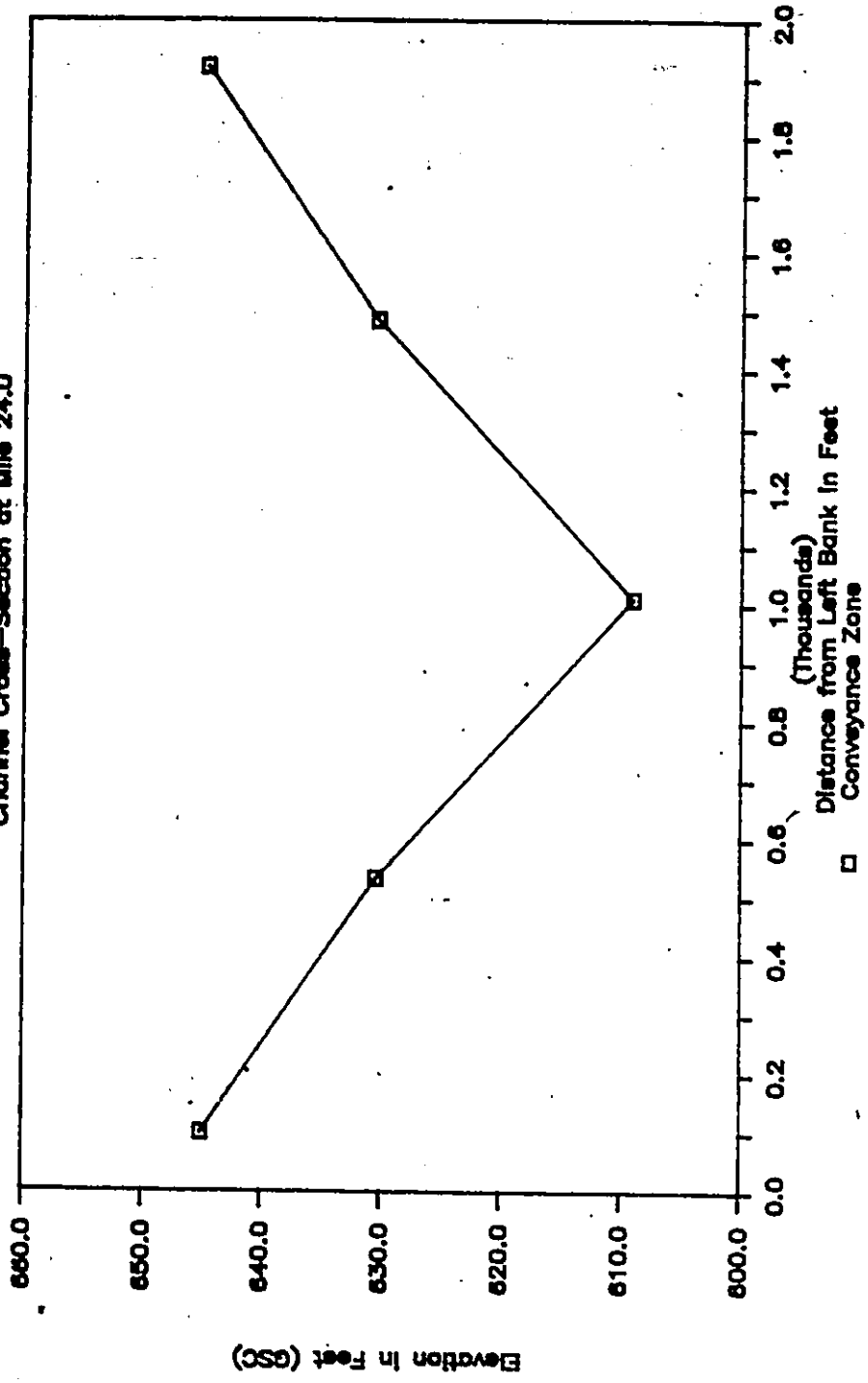


Fig. J.2.4 Section at Mile 24.0

GRAND RIVER FLOOD ROUTING

Channel Cross-Section at Mile 28.0

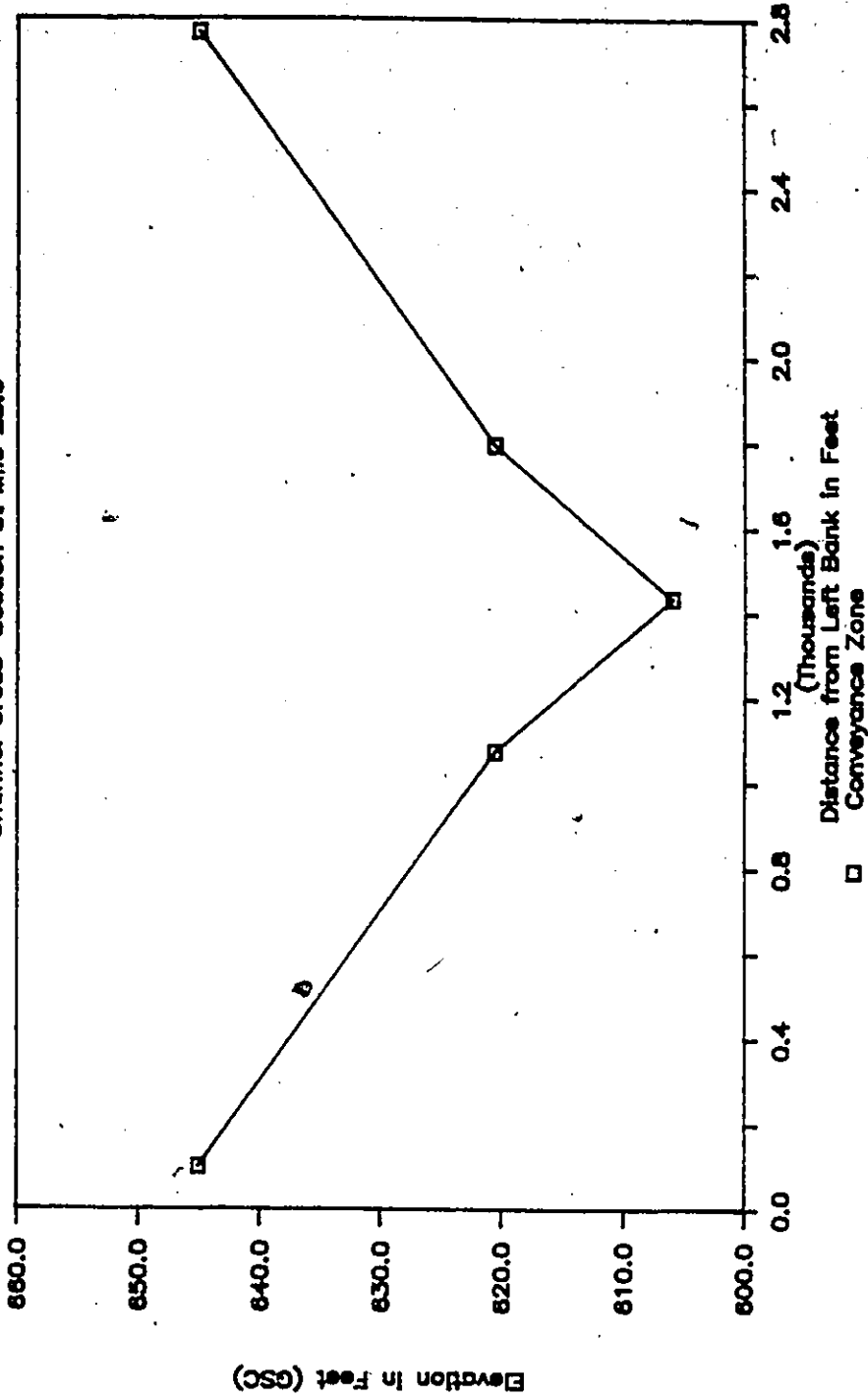


Fig. J.2.5 Section at Mile 28.0

GRAND RIVER FLOOD ROUTING

Channel Cross-Section at Mile 35.0

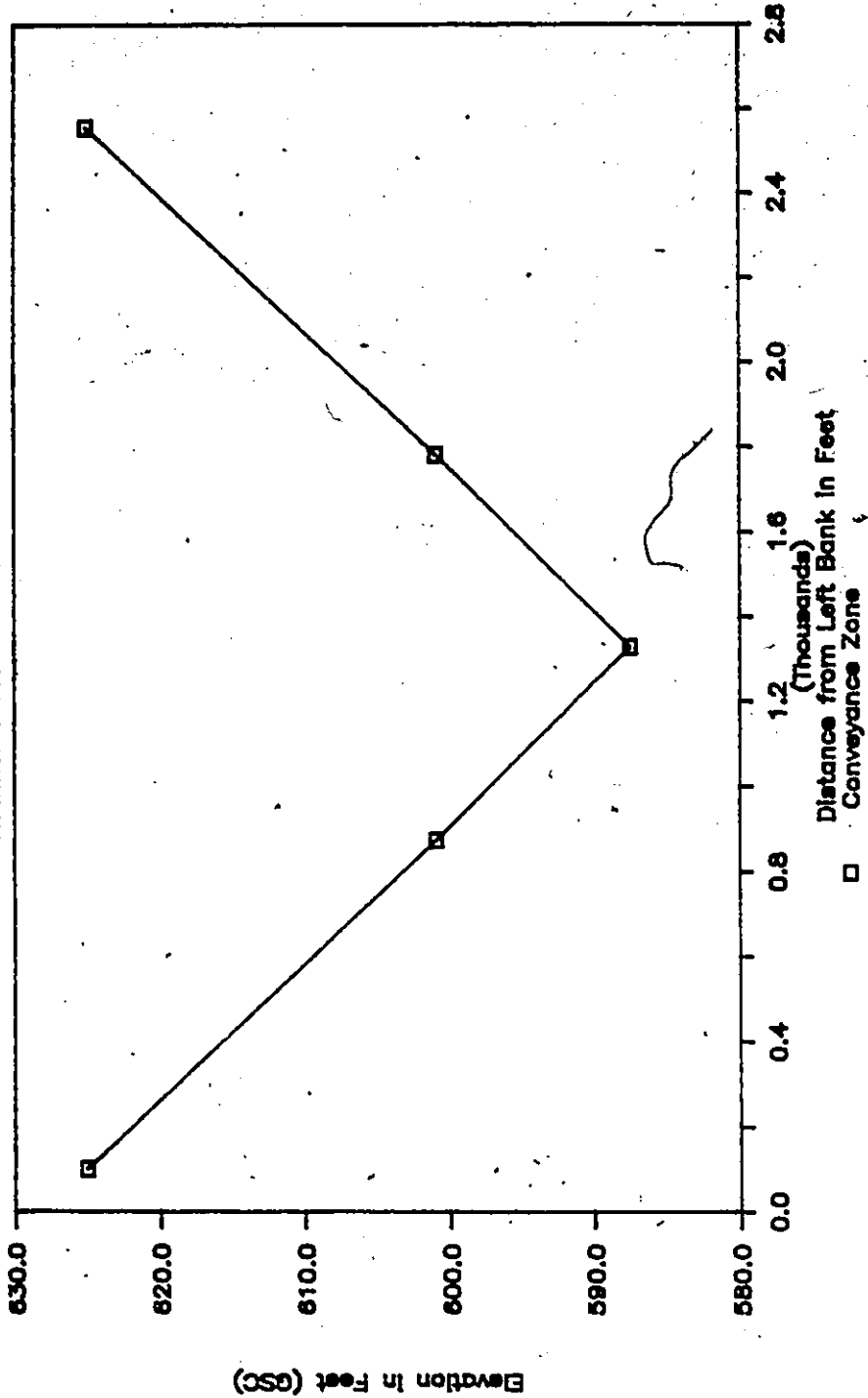


Fig. J.2.6 Section at Mile 35.0

GRAND RIVER FLOOD ROUTING (GAUGE POINT)

Channel Cross-Section at Mile 38.5

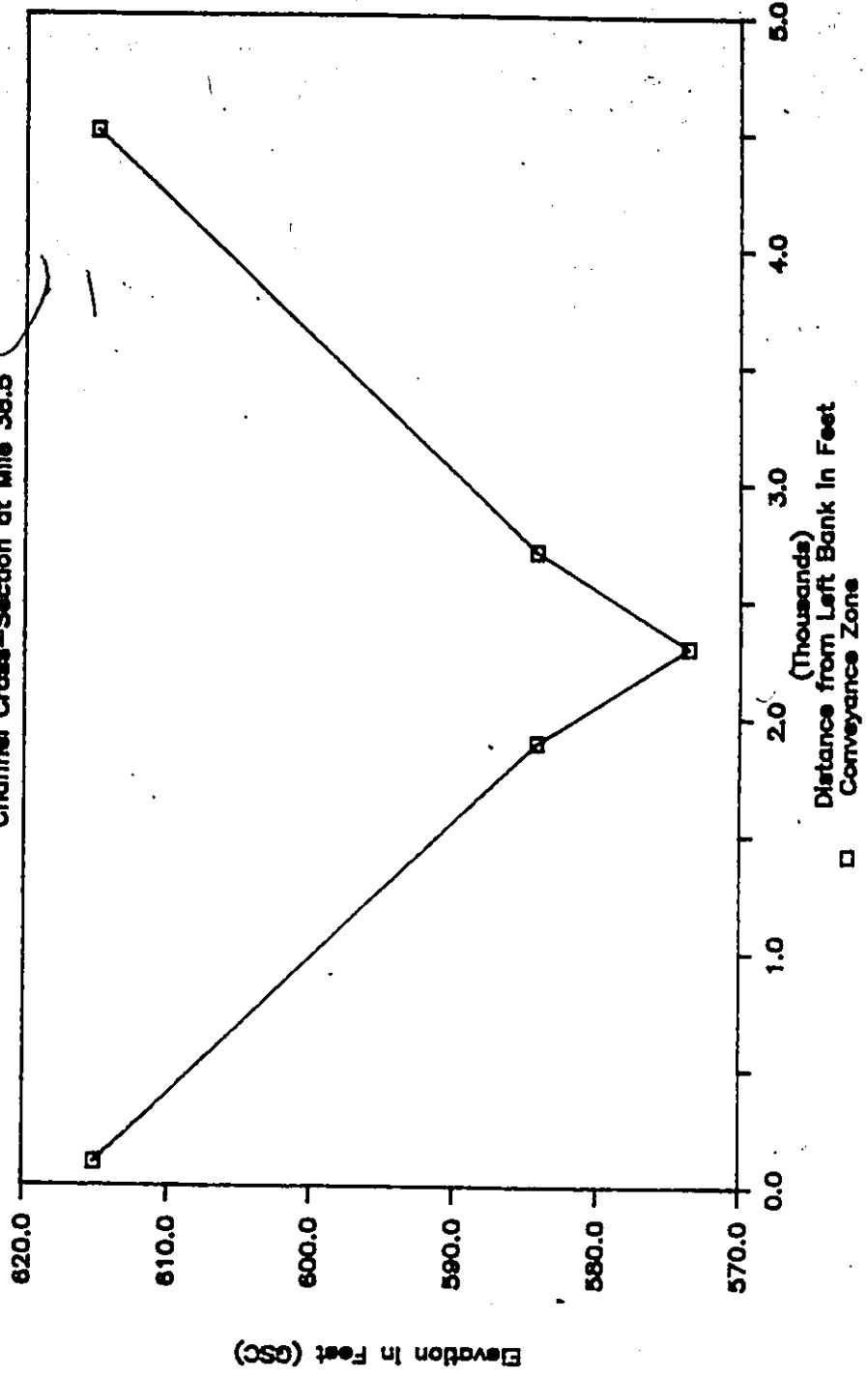
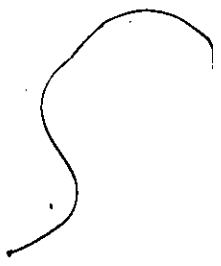


Fig. J.2.7 Section at Mile 38.5

75



GRAND RIVER FLOOD ROUTING

Channel Cross-Section at Mile 45.0

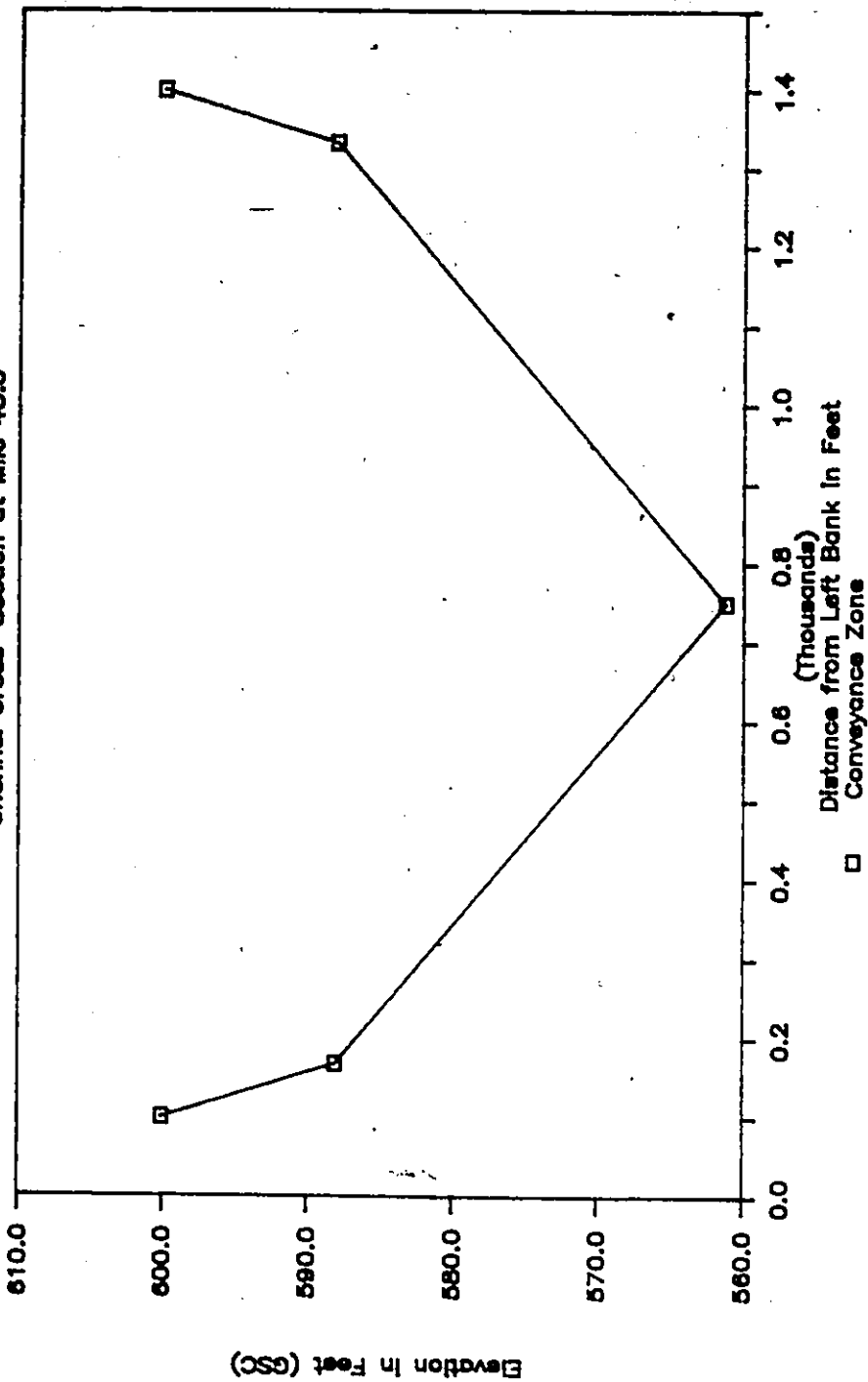


Fig. J.2.8 Section at Mile 45.0

GRAND RIVER FLOOD ROUTING

Channel Cross-Section at Mile 53.0

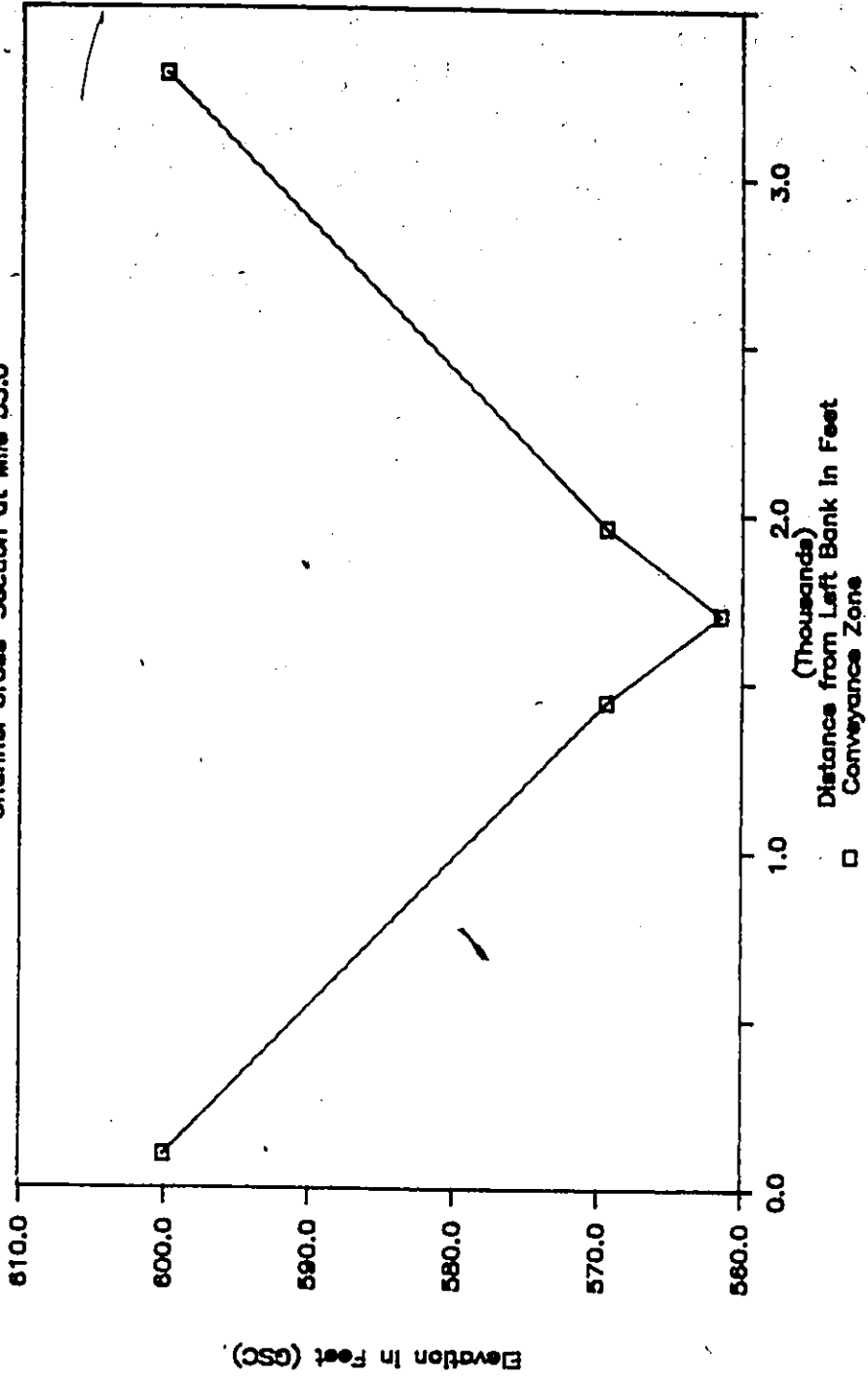


Fig. J.2.9 Section at Mile 53.0

GRAND RIVER FLOOD ROUTING

Channel Cross-Section at Mile 60.0

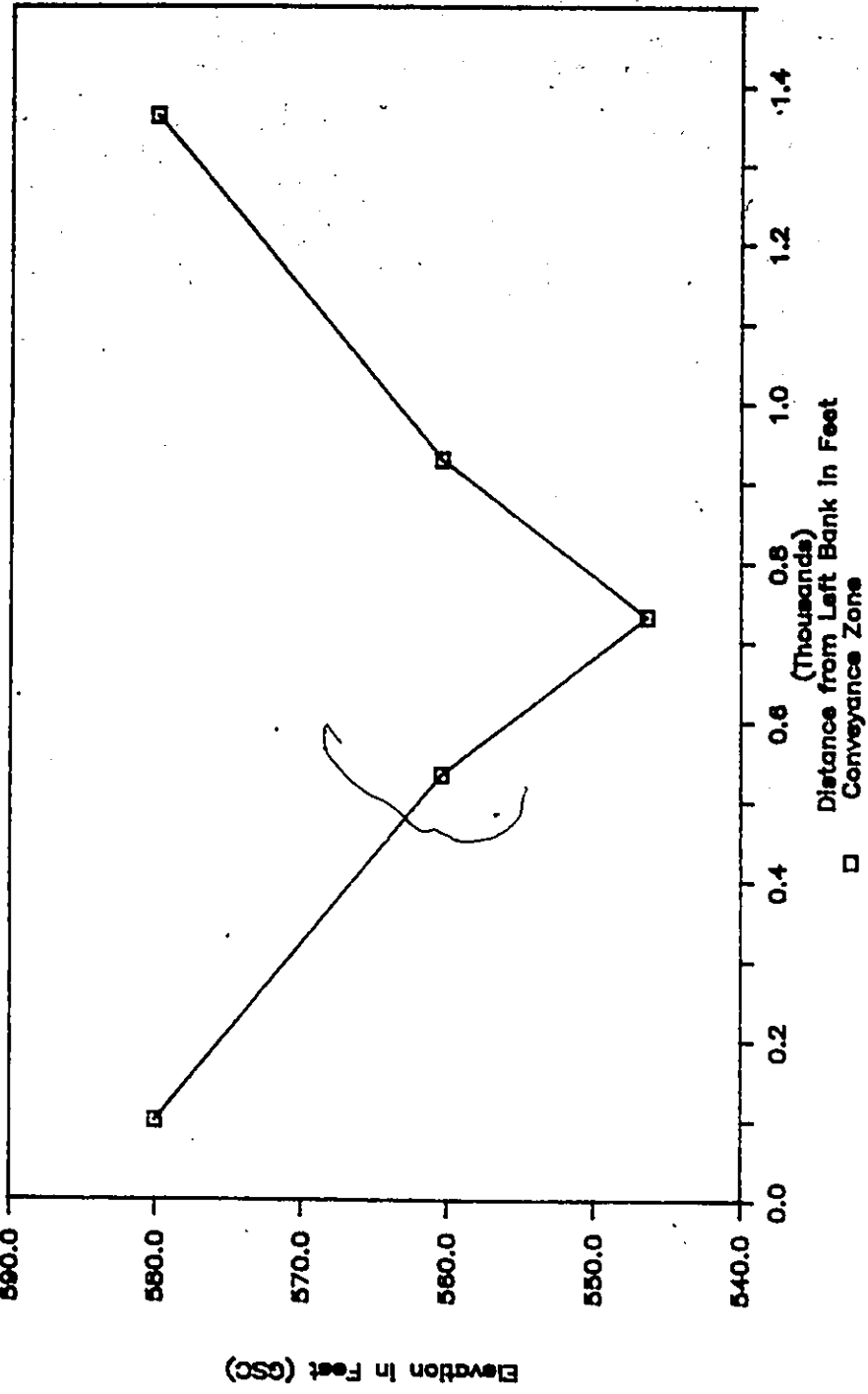


Fig. J 2.10 Section at Mile 60.0

BIBLIOGRAPHY

Abbott, M.B., "An Introduction to the Method of Characteristics", New York: American Elsevier Publishing Co., 1966, 243 p.

Abbott, M.B., "Continuous Flows, Discontinuous Flows and Numerical Analysis", *Journal of Hydraulics Research*, v. 12, no. 4, 1974, pp 417-467.

Abbott, M.B., "Computational Hydraulics", Pitman Publications, London, 1974, 374 p.

Abbott, M.B., and Ionescu, F., "On the Numerical Computation of Nearly Horizontal Flows", *Journal of Hydraulic Research*, Vol. 5, No.2, 1967, pp 97-117.

Adey, R. and Brebbia, C., "Finite Element Solution for Effluent Dispersion"; In C. Brebbia and J. Connor (Editors) *Numerical Methods in Fluid Dynamics*, Pentich Pres, London, 1973 pp 325- 354.

Amein, M., "Streamflow Routing on Computer by Characteristics", *Water Resources Research*, 1966, v. 2, no. 1, pp 123-130.

Amien, M and Fang, C.S., "Implicit Flood Routing in Natural Channels", *Journal Hydraulics Division, ASCE 96 HY12*, 1970, pp 2481-2500.

Amein, M. and Chu, Hsiao-Ling, "Implicit Numerical Modeling of Unsteady Flows", *Journal of the Hydraulics Division, ASCE, V101, HY6*, 1975, pp 717-731.

Balloffet, A., "One Dimensional Analysis of Floods and Tides in Open Channels", *Journal of the Hydraulics Division, ASCE, 95, HY4*, 1969, Vpp 1429-1451.

Baltzer, R.A., and Lai, C., "Computer Simulation of Unsteady Flows in Waterways", *Journal of the Hydraulics Division, ASCE, V94, HY4*, 1968, pp 1083-1117.

Bennett, J.P., "General Model to Simulate Flow in Branched Estuaries", in *Symposium on Modeling Techniques, Vol. I, 2nd Annual Symposium of Waterways, Harbors, and Coastal Engrg., Div. ASCE*, 1975, pp. 643-662.

Bodine, B.R., "User's Manual for FLOW SIM 1, Numerical Method for Simulating Unsteady and Spatially Varied Flow in Rivers and Dam Failures", *US Army Engineering Division, Southwestern, Dallas, TX*, Updated.

Bonnerot, R. and Jamet, P., "A Second Order Finite Element Method for the One-Dimensional Stefan Problem", *Intl. Journal of Numerical Methods in Engineering*, Vol. 8, 1974, pp 811-820.

Bonnerot, R. and Jamet, P., "Numerical Computation of the Free Boundary for the Two-Dimensional Stefan Problem by Space Time Finite Elements", *Journal of Computational Physics*, Vol. 25, 1974, pp 163-181.

Book, D., Boris, J. and Hain, K., "Flux Corrected Transport II: Generalization of the Method", *Journal of Computational Physics*, Vol 18 1975 pp 248-283.

Chaudhry, Y.M. and Contractor, D.N., 1973, "Application of the Implicit Method to Surges in Open Channels", *Water Resources Research*, v. 9, no. 6, 1973, pp 1605-1612.

Chen, Cheng-Lung, and Druffel, L.A. "Dam-Break Flood Wave Computation by Method of Characteristics and Linearized Implicit Schemes", *Proceedings of Dam-Break Flood Routing Model Workshop Held in Bethesda, Maryland, Oct. 18-20, 1977.*

Chen, Cheng-Lung, and Armbruster, J. T., "Dam-Break Wave Model: Formulation and Verification", *Journal of the Hydraulics Division, ASCE*, V106, HY5, 1980, pp 747-767.

Chen, Y.H. and Simons, D.B., "An Experimental Study on Hydraulic and Geomorphologic Changes in an Alluvial Channel Induced by Failure of a Dam", *Water Resources Research*, Vol. 15, No. 5, 1979, pp. 1183-1188.

Contractor, D.N. and Wiggert, J.M., "Numerical Studies of Unsteady Flow in the James River", *Bulletin 51, Water Resources, Research Center, Virginia Polytechnic Institute and State University, Blacksburg, Virginia, May, 1972, 50 p.*

Cooley, R.L. and Moin S.A., "Finite Element Solution of the St. Venant Equations", *Journal Hydraulics Division, ASCE 102 HY6, 1976 pp 759-775.*

Coschi, G. and Schueler, J.B., "WATFOR77 User's Guide for the IBM PC with DOS, Ver. 1.0", *WATFCOM Systems Inc., Waterloo, Ontario 1985, 137 p.*

Cunge, J.A., "Comparison of Physical and Mathematical Model Test Results on Translation Waves in the Oraison-Manosque Power Canal", *La Houille Blanche*, 1966, no.1, pp 55-70. English Translation made by the State of California Department of Water Resources.

Cunge, J.A. "Rapidly Varying Flow in Power and Pumping Canals" Chapter 14 of *Unsteady Flow in Open Channels, Vol II, K.Mahmood and V.Yevjevich Editors. Water Resources Publications, Littleton, Colorado 1975.*

Dailey, J., and Harleman, D., "A Numerical Model of Transient Water Quality in a One-Dimensional Estuary Based on the Finite Element Method", In C.Brebbia and J.Conner (Editors) *Numerical Methods in Fluid Dynamics*, Pentech Press, London 1973, pp 412-439.

De Saint-Venant, Barre, "Theory of Unsteady Flow, with Application to River Floods and to Propagation of Tides in River Channels", *Acad.Sci. (Paris) Comptis Rendus*, 73, 1871, pp 237-240.

Dronkers, J. J., "Some Practical Aspects of Tidal Computations" Proceedings, 13th Congress IAHR, Kyoto, v. 3, pp 11-20, V. 5-2, 1969, pp 260-262.

Dupont, T., "Galerkin Methods for First-Order Hyperbolics", SIAM Journal of Numerical Analysis, Vol. 10, 1973, pp 890-899.

Egiazarov, I.B., "Unsteady Wave Motion in Long Pools", Izvestija VNIIG, Leningrad VXXI, 1937.

Ehlig, C., "Comparison of Numerical Methods for Solution of the Diffusion Convection Equation in One and Two Dimensions," In W. Gray, G.Pinder and C. Brebbia (Editors) Finite Elements in Water Resources, Pentech Press, London, 1977, pp 1.91-1.102.

Ellis, J., "Unsteady Flow in Channel of Variable Cross Section", Journal of the Hydraulics Division, ASCE, V96 HY10, 1970, pp 1927-1945.

Favre, H., "The Theoretical and Experimental Study of Translation Waves in Open Channels", Paris, Dunod, 1935, pp 1-209 (in French).

Finn, W. and Varoglu, E., "An Efficient Solution of Heat Transport Problems", In R.W. Lewis and K. Morgan (Editors) Numerical Methods in Thermal Problems, Pine Ridge Press, 1979, pp 371-380.

Franz, D. D. "Dam Break Flood Wave Analysis: Problems, Pitfalls, and Partial Solutions", Proceedings of Dam-Break Flood Routing Model Workshop Held in Bethesda, Maryland, Oct. 18-20, 1977.

Fread, D. L., and Harbough, T. E., "Transient Hydraulics Simulation of Breached Earth Dams", Journal of the Hydraulics Division, ASCE, V99 HY1, 1973, pp 139-154.

Fread, D.L. "Numerical Properties of Implicit Four Point Finite Difference Equations of Unsteady Flow" NOAA Tech-Memo-NWS HYDRO-18, U.S. Dept. of Commerce, NOAA, National Weather Service, 1974, 38 pp.

Fread, D. L., "The Development and Testing of a Dam-Break Flood Forecasting Model", Proceedings of Dam-Break Flood Routing Model Workshop Held in Bethesda, Maryland, Oct. 18-20, 1977.

Fread, D. L. "NWS Operational Dynamic Wave Model", Verification of Mathematical and Physical Models, Proceedings of the 26th Annual APCE Hydraulics Division Specialty Conference, Maryland, 1978, pp 455-464.

Fread, D.L., "National Weather Service Operational Dynamic Wave Model", Hydrologic Research Laboratory, National Weather Service, Silver Spring, Md, 1978.

Fread, D.L., "Capabilities of NWS Model to Forecast Flash Floods Caused by Dam Failures", Proceedings on 2nd Conference on Flash Floods, Atlanta, GA, American Meteorological Society, 1980, pp 171-178.

Fread, D. L., "Some Limitations on Dam-Breach Flood Routing Models", Paper presented at the ASCE Fall Convention held in St. Louis, Missouri, Oct 26-30, 1981.

Fread, D.L. "DAMBRK: The NWS Dam-Break Flood Forecasting Model" Users Guide National Weather Service 1982, 56 p.

Fread, D.L., "Flood Routing: A Synopsis of Past, Present and Future Capability", in Rainfall-Runoff Relationship, V.P. Singh (Editor), Water Resources Publications, Littleton, CO, 1982.

Fread, D.L., "Channel Routing", Chapter 14 in Hydrological Forecasting, M.G. Anderson and T.P. Burt (Editors), John Wiley and Sons Ltd. 1985, pp. 437-503.

Fried, S.S., "The 8087/80287 Performance Curve", BYTE Vol 10, No 11, 1985, pp 67-88.

Garrison, Jack M., Granju, Jean-Pierre P., and Price, James T., "Unsteady Flow Simulation in Rivers and Reservoirs", Journal of the Hydraulics Division, A.S.C.E., v. 95, No. HY5, Sept., 1969, pp 1559-1576.

Gelinas, R.J., Doss, S.K. and Miller, K. "The Moving Finite Element Method: Applications to General Partial Differential Equations with Multiple Large Gradients", Journal of Computational Physics, 40, 1981, pp 202-249.

Gray, W. "An Efficient Finite Element Scheme for Two-Dimensional Surface Water Computations", Proceedings International Conference on Finite Elements in Water Resources, Water Resources Program, Princeton University, 1976.

Gray, W. and Pinder, G., "An Analysis of the Numerical Solution of the Transport Equation", Water Resources Research, Vol 12, No. 3 1976, pp 547-555.

Gray, W. and Lynch, D., "Time-Stepping Schemes for Finite Element Tidal Model Computations", Advances in Water Resources, Vol 1, No. 2, 1977, pp 83-95.

Grigo, F. and Panattoni, L., "An Implicit Method to Solve Saint Venant Equations", Journal of Hydrology, 24, 1975, pp 171- 185.

Gresho, P., and Lee, R., "Advection-Dominated Flows, with Emphasis on the Consequences of Mass-Jumping", Finite Elements in Fluids, Vol. 3, John Wiley and Sons, New York, 1978, pp 335-350.

Gresho, P.M. and Lee, R.L. "Don't Suppress the Wiggles-They're Telling You Something!" in Finite Element Methods for Convection Dominated Flows" T.R.Hughes (Editor) 1981, pp 37- 61.

Gunaratnam, D.J., and Perkins, F.E., "Numerical Solution of Unsteady Flows in Open Channels", Report No.127, Hydrodynamics Laboratory, MIT, July, 1970, 260 p.

Gundlach, D.L. and Thomas, W.A. "Guidelines for Calculating and Routing a Dam-Break Flood", Research Note No. 5 Hydrologic Engineering Center, US Army Corps of Engineers. Davis, California, 1977.

Huyakorn, P.S. and Nilkuha, K., "Solution of Transient Transport Equation Using an Upstream Finite Element Scheme", Applied Mathematical Modelling, Vol. 3, 1979, pp 7-17.

Huyakorn, P.S., "Solution of the Steady State Convective Transport Equation Using an Upwind Finite Element Scheme", Applied Mathematical Modelling, Vol. 1, 1977, p.187.

Hydrologic Engineering Center, US Army Corps of Engineers, "Gradually Varied Unsteady Flow Profiles (USTFLO)", Davis California, 1977.

Isaacson, E., Stoker, J.J., and Troesch, B.A., Numerical Solution of Flood Prediction and River Regulation Problems (Ohio- Mississippi floods), Report II, New York Univ., Inst. Sci. Rept., 1954, IMM-NYU-205, pp 1-46.

Jamet, P., and Bonnerot, R., "Numerical Solution of the Eulerian Equations of Compressible Flow by a Finite Element Method Which Follows the Free Boundary and the Interfaces", Journal of Computational Physics, Vol. 18, 1975, pp 21-45

Kamphuis, J. W., "Mathematical Tidal Study of St. Lawrence River", Journal of the Hydraulics Division, ASCE, V96, HY3, 1970, pp 643-664.

Katopodes, N.D., "A Dissipative Galerkin Scheme for Open Channel Flow", Journal of Hydraulics Division, ASCE V110, HY4, 1984, pp 450-466.

Keuning, D.H., "Application of Finite Element Method to Open Channel Flow", Journal of Hydraulics Division, ASCE, Vol 102, HY4, 1976, pp 459-468.

King, I.P., "Finite Element Models for Unsteady Flow Routing Through Irregular Channels", In Finite Elements in Water Resources, C.A. Brebbia et al. Editors, Pentech Press, London, 1976, pp 4.165-4.184.

Kowen, N., "Dynamic Wave Flood Routing Sensitivity Study with Special Emphasis on MOBED and DWOPER", Project No. 403-18, Waterloo Research Institute, University of Waterloo, Waterloo, 1986, 62 p.

Krishnappen, B.G., "Users Manual, Unsteady, Nonuniform Mobile Boundary Flow Model-MOBED", Hydraulics Division, National Water Research Institute, Burlington, Ont., 1981.

Lahey Computer Systems, "F77L Reference Manual, Version 2.22", Lahey Computer Systems Inc., Incline Village, NV, 1987.

Lai, C., "Flows of Homogeneous Density in Tidal Reaches Solution by the Method of Characteristics", Open File Report, USGS, Washington, D.C., 1965, 58 p.

Lam, D.C.L., "Comparison of Finite-Element and Finite-Difference Methods for Nearshore Advection-Diffusion Transport Models"; In W. Gray, G. Pinder and C. Brebbia (Editors) Finite Elements in Water Resources, Pentech Press, London, 1977 pp 1.115-1.129.

Lam, D.C.L. and Simpson, R.B., "Centered Differencing and the Box Scheme for Diffusion Convection Problems", *Journal of Computational Physics*, 22, 1976, pp 486-500.

Land, L. F. "Evaluation of Selected Dam-Break Flood-Wave Models by Using Field Data", US Geological Survey (National Technical Information Service PB 81-115776), Springfield, 1980.

Lapidus, L. and Pinder, G.F., "Numerical Solution of Partial Differential Equations in Science and Engineering", John Wiley and Sons, Toronto, 1980, 677 p.

Lax, P.D. and Wendroff, B., "System of Conservation Laws", *Comm. Pure and Applied Mathematics* Vol. 13, 1960, pp 217-237.

Lee, R., Gresho, P., and Sani, R., "A Comparative study of Certain Finite-Element and Finite-Difference Methods in Advection-Diffusion Simulations", 1976 Summer Computer Simulation Conference, 1976, pp 37-42.

Leonard, B.P., "A Survey of Finite Differences of Opinion on Numerical Muddling of the Incomprehensible Defective Confusion Equation", in *Finite Element Methods for Convection Dominated Flows* T.R.Hughes (Editor) 1981, pp 1-17.

Liggett, J. A., and Woolhiser, D. A., "Difference Solutions of Shallow-Water Equation", *Journal of the Engineering Mechanics Division, ASCE*, V93 EM2, 1967, pp 39-71.

Liggett, J.A., "Basic Equations of Unsteady Flow", in *Unsteady Flow in Open Channels*, Vol. II, K. Mahmood and V. Yevjevich (Editors), Water Resources Publications, Fort Collins, CO 1975, pp. 29-62.

Linsley, R.K., Kohler, M.A., and Paulhus, J.L.H. "Hydrology for Engineers 3rd Ed, McGraw-Hill, New York, 1982, 482 p.

MacLaren Atlantic Ltd., "Hydrotechnical Studies of the St. John River from McKinley to Lower Jemseg", Canada-New Brunswick Flood Damage Reduction Program, 1979.

Mahmood, K. and Yevjevich, V., (Editors), "Unsteady Flow in Open Channels", Volumes I and II, Water Resources Publications, Fort Collins, CO, 1975, 983 p.

Martin, B. "Numerical Representations Which Model Properties of the Solution to the Diffusion Equation". *J.Comp. Phys.* 17, 1975, pp 358-383.

Martin, C. S., and DeFazio, F. G., "Open-Channel Surge Simulation by Digital Computer", *Journal of the Hydraulics Division, ASCE*, V95 HY6, 1969, pp 2049-2070.

Mercer, J. and Faust, C., "The Application of Finite Element Techniques to Immiscible Flow in Porous Medium," In W. Gray, G. Pinder and C. Brebbia (Editors) *Finite Elements in Water Resources*, Pentech Press, London, 1977, pp 1.21-1.57.

Microsoft Corporation, "Microsoft FORTRAN Compiler for the MS-DOS Operating System", Microsoft Corporation, Bellevue, WA, 269 p.

Miller, K. and Miller, R.N., "Moving Finite Elements I", SIAM J. Numerical Anal. Vol. 18, No. 6, 1981, pp 1019-1032.

Miller, K., "Moving Finite Elements II", SIAM J. Numerical Anal., Vol. 18, No. 6, 1981, pp 1033-1057.

Miller, W.A., Jr. "Numerical Solution of the Equations for Steady Open-Channel Flow", Ph.D. Thesis, Georgia Institute of Technology, Atlanta, GA., 1971.

Miller, W.A., Jr., and Yevjevich, V., "Unsteady Flow in Open Channels, Vol. III, Bibliography, Water Resources Publications, Littleton, Colorado, 1975, 447 p.

Moin, S.M.A., "Finite Element River Network Simulator (FERNS)". Users Manual-Inland Waters Directorate, Burlington, Ont., 1979, 56 p.

Moin, S.M.A., "Unsteady Flow Modelling of Selected Reaches of the Truckee River" M.S. Thesis, University of Nevada, Reno, NV, 1974, 134 p.

Moin, S.M.A., "Rectangular Space-Time Finite Element Solution of Wave Equations", Unpublished Project Report for Course 754, McMaster University, 1982.

Moin, S.M.A. and Shaw, M.A., "Black and Beaver Cracks Flood Plain Mapping Study Using Dynamic Modelling Techniques, IWD Ont. Region, 1984.

Muir, L.R., "Unsteady Flow in Networks of Open Channels", Manuscript Report Series No.1. Ocean & Aquatic Sciences, Environment Canada, 1975, 115 p.

Pátry, G., "Implementation of DWOPER on Microcomputers", Personal Communications, 1987.

Perkins, F. E., "The Role of Damping in Numerical Stability", Metting Preprint 689, A.S.C.E., National Meeting on Environmental Engineering, Chattanooga, 1968, May 13-17, 12 p.

Perks, A., Moin, S. and Taylor, S., "Application of Dynamic Modelling to Flood Hazard Mapping", Proceedings of 6th Hydrotechnical Division Conference, CSCE, Ottawa, 1983.

Pinder, G.F. and Gray, W.G., "Finite Element Simulation in Surface and Subsurface Hydrology", Academic Press, New York, NY, 1972.

Preissmann, A., and Cunge, J.A., "Tidal Bore Calculation on an Electronic Computer", La Houille Blanche, no. 5, 1961, pp. 588-596.

Preissmann, A., and Cunge, J.A., "Translatory Wave Calculations by Computer", Proceedings, 9th Congress IAHR, Dubrovnik, 1961, pp. 656-664.

Preissmann, A., "Propagation of Translatory Waves in Channels and Rivers" Paper Presented at the First Congress of French. Assoc. for Computation, Grenoble, Proceedings AFCAL, 1961, pp 433-442.

Price, R. K. "Comparison of Four Numerical Methods for Flood Routing", Journal of the Hydraulics Division, ASCE, V100, HY7, 1974, pp 879-899.

Quinn, F. H., and Wylie, E. B., "Transient Analysis of the Detroit River by the Implicit Method", Water Resources Research, Dec., v.8, no. 6, 1972, pp 1461-1469.

Richtmyer, R.D., "A Survey of Difference Methods for Non-Steady Fluid Dynamics", NCAR Technical Note 63-2, National Center for Atmospheric Research, Colorado, 1962.

Ryan-McFarland Corporation, "IBM Personal Computer Professional FORTRAN, V1.0", IBM Corporation, Personal Computer, Boca Raton, FL, 1984.

Smith, D.J., "Stream Hydraulics Package, Computer Program Description (Preliminary)", Hydrologic Engineering Center, US Army Corps of Engineers, Davis, Calif., Oct., 1979.

Smith, I., "Integration in Time of Diffusion and Diffusion Convection Equations", In W. Gray, G. Pinder and C. Brebbia (Editors) Finite Elements in Water Resources, Pentech Press, London, 1977, pp 1.3-1.20.

Smith, I., Faraday, R. and O'Connor B., "Rayleigh-Ritz and Galerkin Finite elements for Diffusion-Convection Problems", Water Resources Research, Vol 9, 1973, pp 593-606.

Stoker, J.J., "Numerical Solution of Flood Prediction and River Regulation Problems", Derivation of Basic Theory and Formulation of Numerical Methods of Attack, New York Univ., 1953.

Streeter, V.L., and Wylie, E. B., "Hydraulic Transients", New York, McGraw-Hill, 1967, 321 p.

Strelkoff, T., "Numerical Solution of Sain-Venant Equations", Journal of the Hydraulics Division, ASCE, V96, HY1, 1970, pp 223-252.

Strelkoff, T., Schamber, D., and Katopodes, N., "Comparative Analysis of Routing Techniques for the Floodwave from a Ruptured Dam", Proceedings of Dam-Break Flood Routing Model Workshop Held in Bethesda, Maryland, Oct. 18-20, 1977.

Terzidis, G., and Strelkoff, T., "Computation of Open-Channel Surges and Shocks", Journal of the Hydraulics Division, A.S.C.E, v. 96, HY12, 1970, Dec. pp. 2581-2610

Thomas, W.A., "Calculating and Routing the Telton Dam-Break Flood", Proceedings of Dam-Break Flood Routing Model Workshop Held in Bethesda, Maryland, Oct. 18-20, 1977.

U.S. Army Corps of Engineers HEC, "Water Surface Profiles- HEC2", Hydrologic Engineering Center, USCOE, Davis California, 1976.

Varoglu, E. and Finn, W., "A Finite Element Method for the Diffusion-Convection Equation with constant Coefficients", *Advances in Water Resources*, Vol 1 1978 pp. 337-343.

Varoglu, E. and Finn, W., "Finite Elements Incorporating Characteristics for One-Dimensional Diffusion-Convection Equation", *Journal of Computational Physics*, Vol. 34 1980, pp 371-389.

Vasilliev, O.F., Gladyshev, M.T., Pritvits, N.A., and Sudobicher, V.G., "Methods for the Calculation of Shock Waves in Open Channels", *Proceedings, 11th Congress IAHR, Leningrad, 1965*, Paper 3.44, 14 p.

Vasilliev, O.F., "Numerical Solution of the Non-Linear Problems of Unsteady Flow in Open Channels", *Proceedings of the 2nd International Conference on Numerical Methods in Fluid Dynamics, Berkeley, sept. 1970*, pp 410-421. Published in *Lecture Notes in physics*, Vol. 8, Springer-Verlag, Bonn-New York, 1971, Edited by M. Holt.

Viesmann, W., Jr., Harbaugh, T.E. and Knapp, J.W., "Introduction to Hydrology", Intext Educational Publishers, New York, NY 1972.

Walden, R.F., "Programming the Equations of Unsteady Flow", M.Eng. Thesis, McMaster University, Hamilton, Ont., 1974.

Wetmore, J.N. and Fread, D.L., "The NWS Simplified Dam-Breach Flood Forecasting Model", *Proceedings of the 5th Canadian Hydrotechnical Conference, Fredricton, New Brunswick, 1981*.

Woolhiser, D.A., and Liggett, J.A., "Unsteady One Dimensional Flow Over a Plane--the Rising Hydrograph", *Water Resources Research*, Vol. 3, No. 3, 1967, pp 753-771.

Wurbs, R.A., "Military Hydrology; Report 13: Comparative Evaluation of Dam-Breach Flood Forecasting Methods", *Miscellaneous Paper EL-79-6, US Army Engineer Waterways Experiment Station, Vicksburg, Miss. 1986*, p 117.

Wurbs, R.A., "Military Hydrology; Report 9: State-of-the-Art Review and Annotated Bibliography of Dam-Breach Flood Forecasting", *Miscellaneous Paper EL-79-6, U.S Army Engineer Waterways Experiment Station, Vicksburg, Miss, 1985* p 157.

Wurbs, R.A., "Dam-Breach Flood Wave Models", *Journal of Hydraulic Engineering, ASCE*, Vol. 113, No. 1, 1987, pp. 29-46.

Wylie, E.B., "Unsteady Free-Surface Flow Computations", *Journal of the Hydraulics Division, ASCE*, V96, HY11, 1970, pp-2241-2251.

Zienkiwicz, O.C. "The Finite Element Method in Engineering Science", McGraw-Hill New York, 1974, 787 p.